MIXING ENHANCEMENT IN A SCRAMJET COMBUSTOR USING FUEL JET INJECTION SWIRL

BY

SONJA M. FLESBERG

Submitted to the graduate degree program in Aerospace Engineering
and the Graduate Faculty of the University of Kansas in partial fulfillment of
the requirements for the Degree of Doctor of Philosophy

Chairperson Ray Taghavi

Co-Chairperson Saeed Farokhi

Richard Hale

Ronald Barrett

Bedru Yimer

Date Defended: May 8, 2015

The Dissertation Committee for Sonja M. Flesberg
certifies that this is the approved version of the following dissertation:

MIXING ENHANCEMENT IN A SCRAMJET COMBUSTOR USING FUEL JET INJECTION SWIRL

_____
Chairperson Ray Taghavi

_____
Co-Chairperson Saeed Farokhi

Date approved: May 8, 2015

Abstract

The scramjet engine has proven to be a viable means of powering a hypersonic vehicle, especially after successful flights of the X-51 WaveRider and various Hy-SHOT test vehicles. The major challenge associated with operating a scramjet engine is the short time residence time of the fuel and oxidizer in the combustor. The fuel and oxidizer have only milliseconds to mix, ignite and combust in the combustion chamber. Combustion cannot occur until the fuel and oxidizer are mixed on a molecular level. Therefore the improvement of mixing is of utmost interest since this can increase combustion efficiency.

This study investigated mixing enhancement of fuel and oxidizer within the combustion chamber of a scramjet by introducing swirl to the fuel jet. The investigation was accomplished with numerical simulations using STAR-CCM+ computational fluid dynamic software. The geometry of the University of Virginia Supersonic Combustion Facility was used to model the isolator, combustor and nozzle of a scramjet engine for simulation purposes. Experimental data from previous research at the facility was used to verify the simulation model before investigating the effect of fuel jet swirl on mixing.

The model used coaxial fuel jet with a swirling annular jet. Single coaxial fuel jet and dual coaxial fuel jet configurations were simulated for the investigation. The coaxial fuel jets were modelled with a swirling annular jet and non-swirling core jet.

Numerical analysis showed that fuel jet swirl not only increased mixing and entrainment of the fuel with the oxidizer but the mixing occurred further upstream than without fuel jet swirl. The burning efficiency was calculated for the all the configurations. An increase in burning efficiency indicated an increase in the mixing of H_2 with O_2. In the case of the single fuel jet models, the maximum burning efficiency increase due to fuel injection jet swirl was 23.3%.

The research also investigated the possibility that interaction between two swirling jets would produce increased mixing and to study how the distance between the two fuel injector exits would affect mixing. Three swirl patterns were investigated: 1) the first swirl pattern as viewed by an observer looking downstream had the right fuel annular jet swirling counter clockwise and the left fuel annular jet swirling clockwise, 2) the second swirl pattern as viewed by an observer looking downstream had the right fuel jet swirling clockwise and the left fuel jet swirling counter clockwise, 3) the third swirl pattern as viewed by an observer looking downstream had both the right and left fuel jet swirling in the same clockwise direction.

Each one of the swirl patterns were simulated with the distances between the center points of the fuel jets modelled 3, 4, and 5 times the fuel injector radius. The swirl pattern that produced the greatest increase in burning efficiency differed according to the fuel injector spacing.

The maximum increase in burning efficiency compared to the corresponding non-swirling two jet baseline case was 24.6% and was produced by the first swirl pattern with the distance between the center points of the fuel jets being 5 times the fuel injector radius.

The burning efficiency for the single jet non-swirling baseline case and the first swirl pattern with the distance between the center points of the fuel jets being 5 times the fuel injector radius was 0.70 and 0.90 respectively indicating a 29% increase due to dual fuel injection swirl.

Acknowledgements

It is often said that the journey is more important than reaching the destination. I have found that the companions that one journeys with are as important as the journey itself.

My advisor Dr. Ray Taghavi has been there from the start. I sincerely appreciate his guidance with this research project. He has shown unlimited patience, cheerful optimism, and a sense of humor when I had little remaining.

I am honored to have Dr. Saeed Farokhi as my co-advisor. He has generously shared his expertise in the field of hypersonic aerodynamics with me and transformed what seemed to be obstacles into challenges that were to be overcome.

Thank you to my committee members, Dr. Richard Hale, Dr. Ronald Barrett and Dr. Bedru Yimer for your genuine interest in my research and for the different points of view you brought to the table that I had not considered previously.

Anna, Leslee and Amy have been indispensable for helping me with all the forms and red tape to finish my graduate work. Thank you very much.

Dr. Downing your pep talks rock! And yes, the little engine that could, did. Thank you.

I would also like to extend my thanks to Mr. N. Halliday of CD-adapco for his software support. Your advice and instructions for setting up my simulations were extremely beneficial.

Allan, my best friend and husband, there are no words. With you I soar.

I acknowledge and thank all of you for accompanying me on this memorable journey.

Table of Contents

Acronyms

AJF	Annular Jet Flow
B.L	Boundary Layer
C-D	Convergent – Divergent
CARS	Coherent Anti-Stokes Raman Spectroscopy
CFD	Computational Fluid Dynamics
CJF	Core Jet Flow
CSSI	Controlled Supersonic Swirling Injector
DARS	Digital Analysis of Reactive Systems
DCSCTF	Direct Connect Supersonic Combustion Test Facility
DLR	Deutsches Zentrum fur Luft und Raumfahrt (German Aerospace Center)
EGR	Exhaust Gas Recirculation
F.S	Free Stream
LES	Large Eddy Simulation
MF	Mole Fraction
NASA	National Aeronautics and Space Administration
PIV	Particle Image Velocimetry
PLIF	Planar Laser Induced Fluorescence
PPDF	Presumed Probability Density Function
psia	Pounds per Square Inch Atmosphere
RANS	Reynolds Averaged Navier Stokes
RMS	Root Mean Square
RST	Reynolds Stress Transport
SCFM	Standard Cubic Feet per Minute
SD	Same Direction
SST	Shear Stress Transport
TI	Top In
TKE	Turbulent Kinetic Energy
TO	Top Out
UVaSCF	University of Virginia Supersonic combustion facility
WAC	Without Any Control

Symbols

a	Area	m^2, ft^2
a	Speed of sound	m/s, ft/s
A	Constant	-
B	Constant	-
C	Constant	-
CFL	Courant-Friedrichs-Lewy number	-
D	Nozzle diameter	m, ft
d	Distance	m, ft
e	Total stored energy per unit mass	J/kg, BTU/lbm
E	Constant	-
F	Thrust	N, lbf
F	Constant	-
g	Acceleration due to gravity	m/s^2, ft/s^2
G_x	Axial flux of axial momentum	$kg \cdot m^2/s^2$
G_θ	Axial flux of swirl momentum	$kg \cdot m/s^2$
G	Constant	-
h	Specific Enthalpy	J/kg, BTU/lbm
h_t	Total Enthalpy	J/kg, BTU/lbm
H,h	Height	mm, in
I_s	Specific impulse	s
k	Turbulent kinetic energy	J/kg, m^2/s^2
L	Length	m, ft
M	Mach number	-
MW	Molecular Weight	g/mol, lbm/mol
$\dot{m}$	Mass flow	kg/s, g/s, lbm/s
P, p	Pressure	Pa, psia, bar
Pr	Prandtl Number	-
q	Dynamic pressure	Pa, psia
r	Nozzle radius	mm, in

Symbols cont…

r	Velocity ratio	-
Re	Reynolds number	-
s	Entropy	J/kg·K, BTU/lbm·°R
s	density ratio	-
S	Swirl strength	-
S	burning velocity	cm/s, in/s
S	step depth	mm
Sc	Schmidt number	-
T	Temperature	K, °C, °R, °F
t	Time	s
u, v, w	Velocity components	m/s, ft/s
V	Velocity	m/s, ft/s
x, y, z	Axis distance	m, ft
z	Distance from wall	m, ft

Greek

δ	Boundary layer thickness	mm, in
Δ	Change	-
ρ	Density	kg/m^3, lbm/ft^3
ϵ	Turbulent dissipation	J/(kg·s)
ω	Specific dissipation	s^{-1}
ϕ	Equivalence ratio	-
γ	Ratio of specific heats	-
η	Kalmogorov microscale	mm
η	Efficiency	-
ν	Kinematic viscosity	m^2/s
τ	Shear stress	Pa, lbf/ft^2
χ	Mole Fraction	-

Subscripts

atm	Atmosphere
burn	Burning
c	Convective
c	Combustion
e	Exit
f	Fuel, face
h	Hub
I	Inlet
L	Laminar
max	Maximum
mix	Mixing
o	Free stream
react	Reacting
Ref	Reference
S	Specific
T,t	Turbulent
w	Wall

Superscripts

′	Fluctuating rms value

List of Figures

List of Tables

1 Introduction

On February 24, 1949 the V-2/WAC Corporal was launched from White Sands, New Mexico and achieved hypersonic flight. The WAC Corporal was a slender needle like rocket that sat atop a V-2 rocket up to an altitude of 100 miles at which point the WAC Corporal was ignited and continued its ascent to 244 miles above the earth's surface [1]. After reaching the peak of its ascent the WAC Corporal nosed over and achieved a velocity of 5150 mph or Mach 5 [1]. Twelve years later on April 12, 1961 Flight Major Yuri Gagarin was launched into orbit aboard the Vostok I spacecraft and became the first human to travel within the hypersonic flight regime at Mach 25. In the same year Major Robert White flew the X-15 aircraft at Mach 5 on June 23, 1961. This was the beginning of realizing hypersonic flight as a viable means of travel.

By conventional rule of thumb, the hypersonic flight regime is considered flight speed equal and greater to Mach 5. Hypersonic flight is better defined as the regime where certain physical properties of the flow cannot be considered negligible. The hypersonic flight regime can start as low as Mach 3 or as high as Mach 7 [1]. Physical phenomena that help define hypersonic flow are vorticity interaction, viscous interaction, high temperature effects and low density effects [1]. Since 1961 there have been other spacecraft and aircraft travelling within the hypersonic flight regime such as the reusable space shuttle (Mach 25), SR-71 Mach (3+) and the XB-70 (Mach 3+). However the space shuttle reached hypersonic speed on re-entry in glider mode, the X-15 used a rocket engine, the SR-71 used a hybrid turbojet/ramjet engine and the XB-70 used a turbojet. For an aircraft remaining in Earth's atmosphere the SR-71 with its hybrid turbojet/ramjet engine proved to be the most viable design. The ramjet engine had the advantage over the conventional turbojet by not having any moving internal parts and the

advantage over a rocket engine by not having to carry oxidizer. One of the challenges with the ramjet was to design an inlet to slow the incoming air from supersonic to subsonic flow so that ignition of the fuel could occur. The faster the incoming air the longer the air inlet needed to be. This led to the concept of the scramjet (supersonic combustion ramjet). The air inlet needed only to reduce the incoming air to low supersonic speeds hence reducing the size of the engine.

Scramjet engines have been used in such experimental unmanned aircraft such as the X-43 as part of NASA's Hyper-X program, the X-51 as part of the Air Force Research Laboratory Hy-TECH program and HySHOT designed and launched by the University of Queensland. As the manufacturing technology improves it becomes more feasible to look towards scramjets as a means to produce hypersonic vehicles for commercial aircraft, military aircraft and military missiles.

Institutions such as NASA Langley in the USA, DLR in Germany, the University of Queensland under the Australian Hypersonic Initiative have been investigating scramjets through flight tests, experiments and numerical simulations. Flight test and experimental data is not excessive due to the expense of such projects and the difficulty of obtaining data. Flight test data is the most expensive to obtain since the flight test vehicle, such as the X-51 WaveRider, is usually destroyed after a few minutes of data collection. Experimental data obtained from hypersonic test chambers is less expensive than flight test data but is still extremely expensive with building cost in the millions of dollars and operational cost based on hourly usage. Numerical simulation has proven to be a useful tool to investigate flow characteristics of the whole or parts of hypersonic vehicles at less expense and no risk of loss of test vehicles.

Despite the scramjet engine being a viable means of powering hypersonic flight there are challenges associated with these types of engines. One of the main difficulties with the scramjet

engine is the short time that the fuel and oxidizer have to mix, ignite and combust in the combustion chamber due to the supersonic speed of both the fuel and oxidizer jets. Combustion efficiency increases with improved mixing and entrainment of the fuel flow with the oxidizer flow [2].

Another challenge with scramjet engines is related to shock waves that are produced by combustion that then travel upstream in the engine leading to the possibility of unstarting the engine. This leads to the introduction of an isolator between the inlet and combustion chamber that then increases the length and weight of the engine [2].

One more difficulty is cooling the engine especially the combustion chamber where the highest temperatures are seen. Most scramjets use active cooling which is a process that uses the fuel as the coolant for the engine [2]. The fuel is heated prior to combustion leading to greater combustion efficiency. However, this form of cooling adds weight and complexity to a scramjet engine which in turn can outweigh the combustion efficiency benefit [2].

Studies into swirling flow jets have shown that swirl enhances mixing and entrainment of two fluids [3]. Swirling flow has previously been used in fuel injectors for turbo jet engines to increase mixing by atomizing the fuel. Studies have also shown that swirling flow from an engine exhaust nozzle increases mixing and entrainment of the exhaust gases with the surrounding air [4]. However, there is usually a thrust penalty associated with this process.

The purpose of the proposed study is to investigate mixing enhancement of fuel and air within the combustion chamber of a scramjet by introducing swirl to the fuel jet. The hypothesis is that swirl added to the fuel jet will increase mixing and entrainment of the fuel with the oxidizer and increasing the combustion efficiency. Previous studies of enhanced mixing of fuel and oxidizer within the combustion chamber of a scramjet will be reviewed. Numerical

simulation will be used for the investigation due to the high cost of obtaining data through flight or experimental tests. The numerical software used for this study is STAR-CCM+ which is provided as a full package and free of cost. The simulations presented in this proposal are cases of chemical non-equilibrium reactive flow that result in combustion. The scramjet geometry used for this study is modelled after the University of Virginia's Supersonic Combustion Facility and only the isolator, combustion chamber and divergent nozzle of a scramjet engine is modelled for simulation.

2 Literature Review

Previous work and investigations that are relevant to flow field characteristics within a scramjet combustor will be presented in this chapter. The time from which air enters the engine inlet to the time it departs the engine nozzle is on the order of a millisecond. The time span for which the fuel and air have to mix and ignite is on the order of microseconds. Maximum mixing of the fuel and air is a major concern when designing a scramjet engine. Combustion occurs in the upstream portion of the combustion chamber and is kinetically controlled. Although the geometry of scramjet engines are relatively simple, the physics of the flow that occur due to fuel injection, high speed mixing and combustion is quite complex. The following review will support investigation of enhanced combustion mixing by introducing swirl to the injected fuel jet.

2.1 Physical Phenomenon of Hypersonic Flow

Once an aircraft has achieved a flight speed equal or greater than the speed of sound the aircraft is considered to be operating in the supersonic flight regime. As the aircraft flight Mach number increases so does the effect of the physical phenomenon of the flow. When the effects of certain physical properties can no longer be considered negligible the flow is considered to be hypersonic. The physical phenomenon of hypersonic flow can be significant at speeds as low as Mach 3 or can be negligible until speeds as high as Mach 7. A review of Anderson (2006) description of the physical effects associated with hypersonic flow is presented in the following four paragraphs.

One of the most noticeable physical phenomenons of hypersonic flow is a thin shock layer. Consider a 15° wedge placed in Mach 36 calorically perfect gas with a ratio of specific heat equal to 1.4 as shown in Figure 1. According to oblique shock wave theory the shock wave is only 18°. If the flow were high temperature with chemical reacting effects the shock layer would be even thinner. This can lead to the complication of the shock wave interacting with a thick viscous boundary layer.

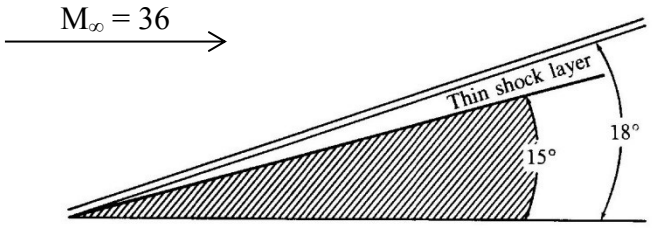

Figure 1 Thin hypersonic shock layer
[1]

Another physical phenomenon of hypersonic flow relates to the entropy layer. The effect of this can be seen in the case of a wedge similar to Figure 1 but with a blunt nose as shown in Figure 2. The bow shock is highly curved. A streamline passing through the strong normal shock at the nose experiences a larger entropy increase than the other streamlines that pass through a weaker portion of the shock wave since entropy increases with shock strength. This results in a large entropy gradient at the nose region. The entropy layer then flows downstream and essentially wets the body downstream of the nose. This affects the boundary layer that is growing on the body surface within the entropy layer. Since the entropy layer is a region of strong vorticity, the boundary layer/entropy layer interaction is called a vorticity interaction.

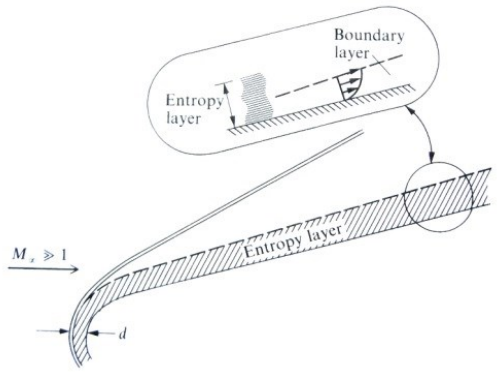

Figure 2 Entropy layer
[1]

Viscous dissipation is a phenomenon that occurs when kinetic energy from a flow is partially dissipated by friction and is transformed into internal energy within the flow. A change in internal energy causes temperature changes. Hypersonic flow is a high energy flow with large amounts of kinetic energy. Figure 3 shows the boundary layer on a flat plate in hypersonic flow. The gas flow is slowed within the boundary layer due to viscous effects and viscous dissipation occurs. The temperature increase causes the viscosity coefficient to increase which in turn thickens the boundary layer. In addition because the pressure in the normal direction of the boundary layer is constant the temperature increase results in a density decrease which results in a thicker boundary layer. The result of both of these effects causes the hypersonic boundary layer to grow more rapidly than at slower speeds. The thicker boundary layer can displace the inviscid flow outside of the boundary layer and change the outer inviscid flow which in turn feeds back to affect the boundary layer. The interaction between the boundary layer and the outer inviscid flow is called viscous interaction. The effect of viscous interaction is an increase in skin friction and heat transfer.

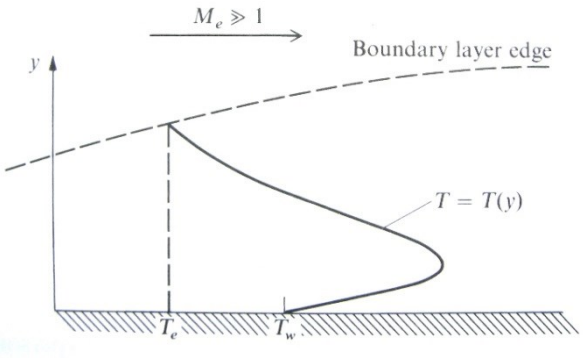

Figure 3 Temperature profile in a hypersonic boundary layer [1]

As discussed previously viscous dissipation creates high temperatures. Within a hypersonic boundary layer the temperatures can be high enough to excite vibrational energy internally in molecules and to cause dissociation and ionization within a gas. The ratio of specific heats can no longer be considered as constant. For a hypersonic flow the boundary layer and the shock layer can be dominated by chemically reacting flow. This phenomenon is a result of high temperature effects.

2.2 Scramjet Engine

As stated previously aircraft have been capable of hypersonic flight since 1949 and such vehicles initially used rocket engines. There are two major disadvantages to using rocket engines for vehicles that remain in the atmosphere; firstly, the aircraft must carry fuel and oxidizer otherwise known as the propellant and secondly, the propellant is consumed at a higher rate per unit thrust than a conventional air breathing engine.

A solution to the disadvantages of using a rocket engine for an aircraft operating within the atmosphere is to use an air breathing engine. The flight vehicle is then required to carry only

fuel, which translates into a weight reduction of the aircraft or increase in payload weight and decreases the rate of propellant burned per unit thrust. In the quest for vehicles capable of operating at higher transonic and supersonic speeds, turbojets and its variants are the preferred engines to be used for these flight regimes. Turbojets with various modifications are most commonly used in commercial airliners, business jets and military jets. A turbojet consists of an inlet to capture air and reduce its velocity, a compressor to increase the air pressure, a combustion chamber or combustor to mix the fuel with the air and to enable combustion, a turbine to extract kinetic energy to be used for mechanical work and the exhaust nozzle to increase the exhaust gas velocity. The main point at this time to note is that the air flow through the combustor is subsonic. A ramjet is a variant of the turbojet except that the internal moving turbomachinery of the engine are removed. Compression and decelerating the air flow to a subsonic speed is accomplished through shock waves and therefore the mechanical compressor is no longer required. A scramjet works with the same principle as the ramjet with the exception that the air flow is decelerated to supersonic speed in the combustion chamber. The current scramjet engines are designed to decelerate the airflow to approximately Mach 2-3 before entering the combustor. Figure 4 shows the processes that occur in the three types of engines.

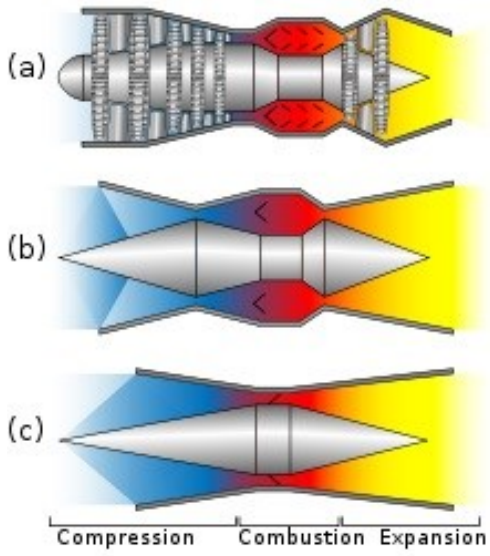

Figure 4 The compression, combustion and expansion regions of: (a) turbojet, (b) ramjet, and (c) scramjet engines.
[5]

Specific impulse, I_s, is the thrust force integrated over burn time per unit weight of propellant. Assuming a constant thrust force, F, and defining the propellant mass flow rate as $\dot{m}_p$ and g_0 as standard acceleration due to gravity on Earth, specific impulse can be shown as

$$I_S \equiv F/(\dot{m}_p g_0) \qquad \text{Equation 1}$$

The specific impulse can be used as a figure of merit and measure of propulsive efficiency of an engine. Figure 5 shows the approximate relationship between specific impulse and flight Mach number for various types of air breathing engines using hydrocarbon or hydrogen as fuel.

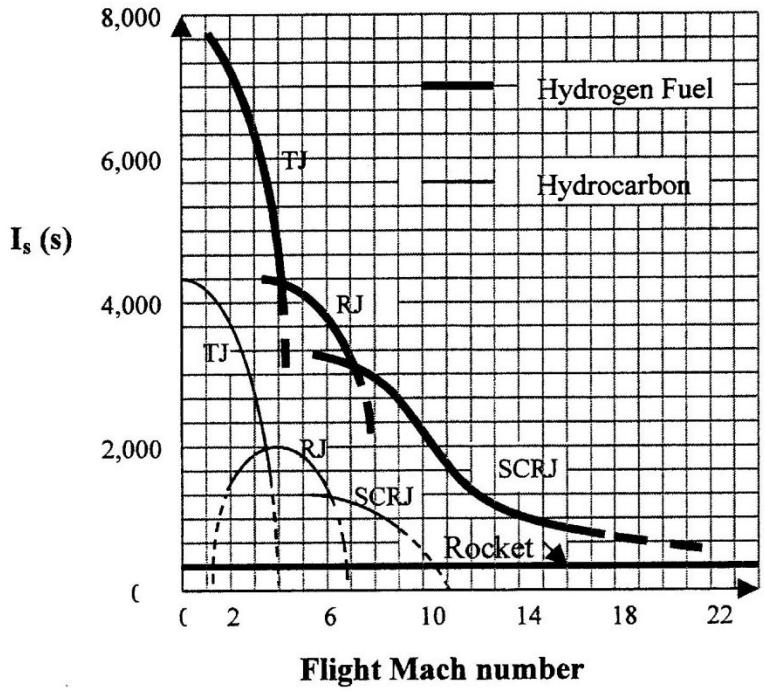

Figure 5 Approximate variation of specific impulse with flight Mach number for different air breathing engines (TJ: turbojet, RJ: ramjet and SCRJ: scramjet) and a typical chemical rocket. [6]

As aircraft are designed to travel within the hypersonic regime it can be seen that the scramjet engine is the most efficient engine for such vehicles. If a hypersonic vehicle using an air breathing engine is designed to operate through the supersonic to the hypersonic flight regime, the engine must be able to operate in multiple modes. A dual mode ramjet/scramjet allows the engine to operate as a ramjet or a scramjet [7]. As described by Curran *et al*. (1996) when the engine is operating in the ramjet mode the flow is choked downstream of the isolator resulting in a large back pressure at the combustor inlet which causes a normal shock train to form upstream of the combustor in the isolator. The shock train consists of a subsonic core. If the isolator cannot contain the shock train the engine will unstart. When operating as a scramjet the flow through the engine is supersonic. There is frequently thermal blockage, or choking, that is the result of heat addition to the flow and an adverse pressure gradient. If the pressure rises

rapidly in the combustor the wall boundary layer separates and the associated pressure disturbance propagates upstream. An oblique shock train with a supersonic core is produced in the isolator which prevents the engine unstart [8].

While the foray into the hypersonic flight regime has been slow it has been persistent. As such, it is necessary to continue researching how to make scramjets more efficient and viable for flight vehicles.

2.2.1 Scramjet Components

Although the scramjet engine has the same fundamental processes as a turbojet except the geometrical configurations of the engine components are very different. Figure 6 shows a schematic of the components and processes associated with a scramjet engine.

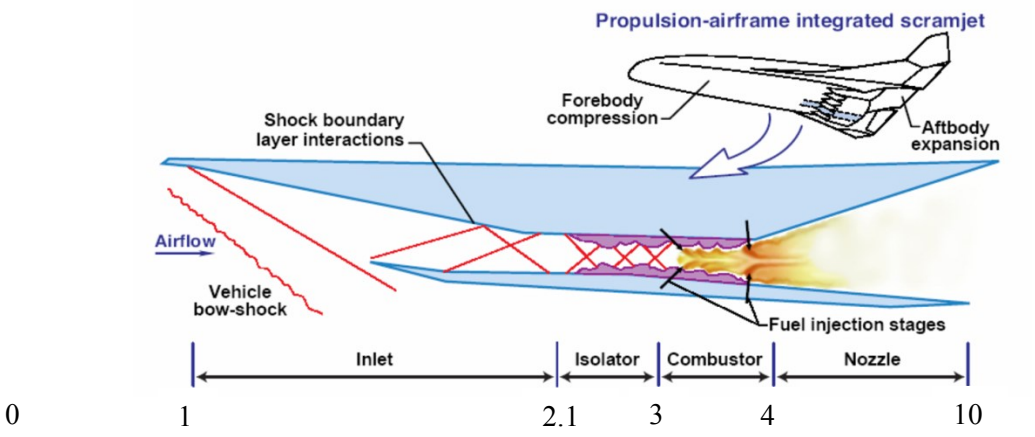

Figure 6 Schematic of a scramjet indicating engine processes, components and defining station numbers
Source: NASA Langley [2] [5]

The description of the station numbers and corresponding processes in the remainder of Section 2.2.1 are based on Segal (2006) definitions [2]:

Station 0 free stream condition.

Station 1 start of the compression process. Compression occurs through the area defined in Figure 6 as the inlet. The long compression ramp is due to the small shock wave angles that occur with hypersonic flow.

Station 2.1 entrance to the isolator. The isolator is present to protect the inlet from adverse effects occurring due to combustion in the combustion chamber. The isolator is not a desirable component because it is a source of additional pressure losses, it requires additional cooling and adds weight to the engine. For operational reasons the isolator is required to enable the presence of a shock train.

Station 3 combustion chamber entrance. The pressure at the entrance of a combustion chamber can vary over a large range depending on operational mode.

Station 4 combustion chamber exit. The air flow starts to expand at this station.

Station 10 nozzle exit. The aft section of the vehicle body may be part of the nozzle.

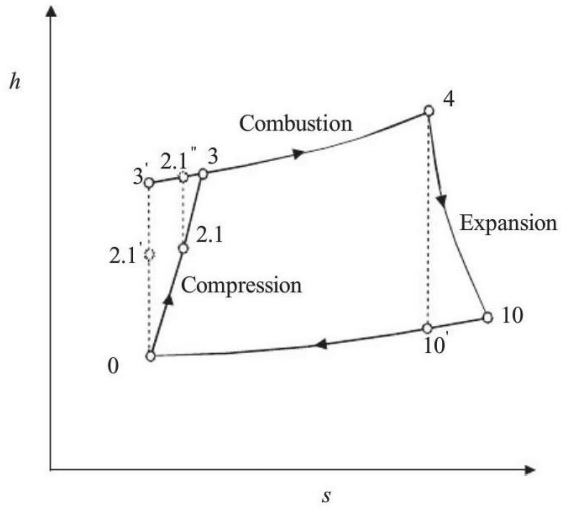

Figure 7 Scramjet cycle under real and ideal conditions [2]

Segal (2006) describes the processes of a scramjet by an *h-s* diagram of the scramjet engine cycle shown in Figure 7. The thermodynamic states are in terms of static specific enthalpy, *h,* and static specific entropy, *s,* and are indicated by engine station numbers that are shown in Figure 7.

The ideal scramjet cycle consists of an isentropic compression (stations 0 - 3'), a constant pressure heat addition, (stations 3'– 4), isentropic expansion (stations 4 - 10') and constant pressure heat rejection (stations 10'-0). Stations 0 - 2.1' represent the isentropic compression in the inlet. Stations 2.1 - 2.1' represents the isentropic compression in the isolator.

Between stations 0 and 2.1 the free stream air flow is decelerated by shock waves in the inlet. The initial compression called the external compression is created by the shock waves formed from the fore body of the vehicle. Further compression occurs within the inlet duct and is called internal compression. The departure from the isentropic compression process is due mostly to complex hypersonic flow characteristics such as multi angle shock waves, shock wave-boundary layer interaction, separation of vortices and vortex-vortex interaction.

The compression process continues between stations 2.1 and 3 in the isolator. As stated previously the isolator may have a shock train depending on the flight regime. The shock train helps to isolate the combustion process from the inlet compression process and helps to protect the engine from and unstart. It is possible for the shock train to extend into the combustion chamber allowing a combination of subsonic and supersonic flow into the combustor. Due to shock-boundary layer interactions, viscous losses and loss of heat to the walls the compression process of the isolator is not isentropic.

The combustion chamber is defined between stations 3 and 4. Inefficiencies in the combustion chamber are due mostly to friction and loss of heat to the walls. Combustion and the amount of heat released are dependent on the mixing process. Combustion chambers are generally designed to be initially of constant area for rapid heat release. The constant area is usually followed by a slowly divergent area to prevent the onset of thermally choking the flow and allow additional time/space for the flow to reach chemical equilibrium. If chemical equilibrium has not been achieved by the time the flow exits the combustion chamber, dissociated species may freeze and this will lead to a decrease in thrust.

Stations 4 – 10 define the expansion of the flow through the nozzle. The departure from the isentropic process is due to friction, heat loss to the walls or vehicle, two phase flow formation and viscous dissipation in shock waves.

2.3 Flow Physics of Mixing and Reacting Jets

> "Mixing layers are characterized by large-scale eddies that form due to the high shear that is present between the fuel and air streams. Eddies entrain the fuel and air into the mixing region. Stretching occurs in the interfacial region between the fluids leading to increased surface area and locally steep concentration gradients. Molecular diffusion then occurs across the strained interfaces."[1]

There are a variety of mixing mechanisms that exist within the flow field of a scramjet, including diffusion, mixing of parallel fluid stream of different velocities, mixing of non-parallel fluid streams, sheer layer curvature and chemical composition. Mixing of plane or curved parallel streams results in the development of shear layers at the flow boundaries. The momentum loss is relatively small but complete mixing at the molecular level requires long distances. The mixing of non-parallel fluid streams results in bulk mixing in a shorter distance but is accompanied by large momentum loss, vortical structures and sometimes strong shock waves.

2.3.1 Parallel Flow Mixing

Gupta *et al.* (1984) describes turbulence as an important and complex fluid motion that is frequently used in combustion systems to aid mixing. Turbulence is random and is produced by irregular fluctuation of small masses that is superimposed on the mean fluid flow. Turbulent motion is similar to molecular motion in that turbulent quantities corresponding to molecular

[1] Reference [27], page 121

mass and free path are not constants or properties of the medium. However, turbulence is more effective for mixing than diffusion because the turbulent mass and the mean free path are much larger than those in molecular motion.

Turbulence is a result of eddy formation in the shear flow produced by two fluid streams of different velocities. The fluid streams could be separate jets, flow around the base of a blunt body (zero velocity flow) or in boundary layers on a body. In a scramjet combustor the fluid streams velocities can be large and the densities and fluid composition are usually different. Momentum is transferred from the higher velocity flow to the slower flow and mass is exchanged at the fluid streams interface. Large eddies produced by the interaction of the two streams are initially highly anisotropic but then become nearly isotropic. The large eddies that develop transfer energy to smaller eddies that then dissipate the energy into heat that then aids mixing on a molecular level [3]. Figure 8 shows shadowgraphs of a mixing layer taken at random times.

Segal (2006) provides a clear detail of mixing due to the interaction of parallel flows that is the basis for the rest of this section [2]. A schematic of the development of the shear layer between two fluid flows with different velocities is shown in Figure 9. When the thin boundary layers of the two fluid streams coalesce, a shear layer is developed in which the two fluids can mix. When referring to the process of mixing in the context of chemical reactions and combustion, mixing has to be on the molecular level [9], which requires molecular collision. Entrainment at the interface of the two fluid flows produces large turbulent structures and rapid (macro) mixing occurs. Although molecular diffusivity is small, the diffusive flux across the interface can be large [9].

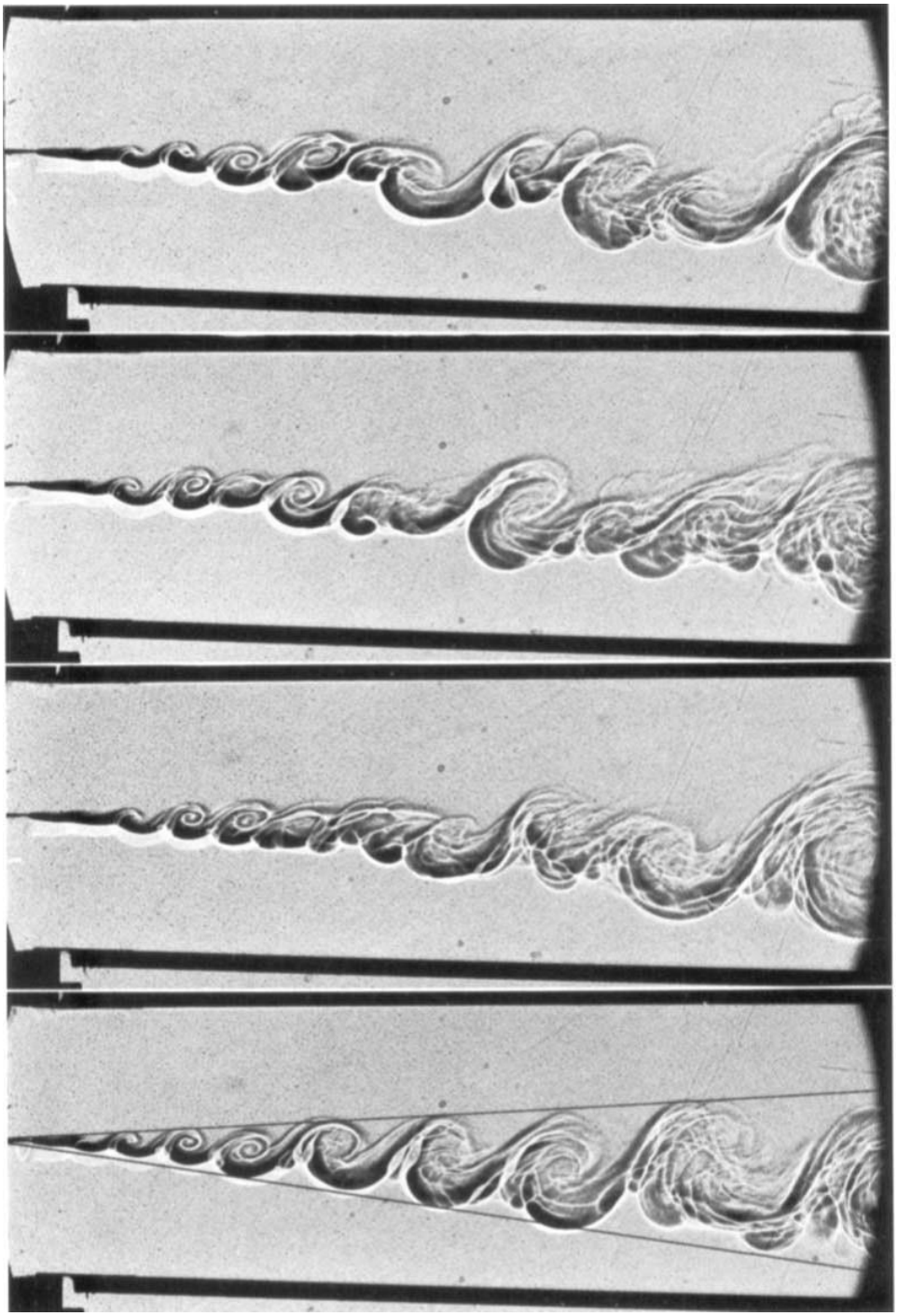

Figure 8 Shadowgraphs of helium and nitrogen mixing layer taken at different times. [10]

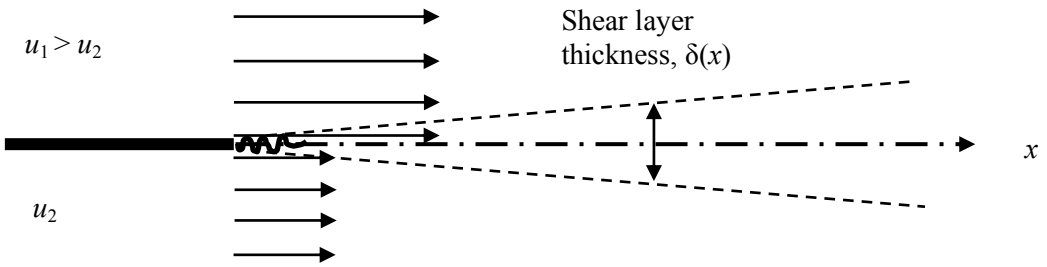

Figure 9 Schematic of shear layer thickness
[2]

Within a shear layer where combustion is present sublayers representing the mixing thickness, δ_{mix}, and chemical reaction thickness, δ_{react} can be defined. The chemical reacting layer $\delta_{react} = \delta_{react}(x)$ can then be defined as the product of the reacting layer within the mixing layer $\delta_{react}/\delta_{mix}$ and the molecularly mixed flow within the visual shear layer δ_{mix}/δ and the development of the shear layer of thickness $\delta = \delta(x)$ [10]. These representations are useful in identifying the time scales for mixing and chemical reaction.

Compressible mixing is dominated by macroscopic processes rather than microscopic diffusion. This was seen in a shear layer mixing test conducted by Wendt *et al*. (1997) when increasing the fuel stagnation temperature did not increase diffusion [11]. Increasing the stagnation temperature of one or both shear layer flows prior to mixing of the flows resulted in an increase in velocity. The increase in velocity reduced compressibility and shear forces. The reduction in shear force and macroscopic turbulence offsets any increase in diffusion. The fluids velocity, density and compressibility are the major influences on the development of a shear layer.

The development of shear layer thickness is influenced more by velocity gradient between two streams as observed by Brown and Roshko (1974) [10]. This indicates that

compressibility plays a significant role in the development of turbulent shear layers along with other factors like pressure gradient and heat released from chemical reactions. Since shear layer growth is related to large vortical structure development, compressibility effects on the shear layer growth can be analyzed within the reference frame of the motion of the vortical structures where u_c is defined as the convective velocity [12], [13]. The relative convective Mach numbers for the two streams are

$$M_{C1} = (u_1 - u_c)/a_1 \qquad M_{C2} = (u_2 - u_c)/a_2 \qquad \text{Equation 2}$$

where

M_C - convective Mach number

u - axial velocity

a - speed of sound

and subscripts *1* and *2* represent two free streams. The convective Mach numbers describe the effect of compressibility on the shear layer development. The relationship between the convective Mach number of the two free streams is

$$M_{C1} = (\gamma_1/\gamma_2)^{1/2} M_{C2} \qquad \text{Equation 3}$$

where

γ - ratio of specific heats

Two dimensional analysis indicated that the shear layer grew proportionally with free stream velocity and inversely with convective velocity as shown in Equation 4 [13].

$$\delta/x \approx \Delta u/u_C \qquad \text{Equation 4}$$

Using experimental data the relationship was further developed to include the effect of density.

$$\frac{\delta}{x} = 0.17\,\frac{(1-r)(1+\sqrt{s})}{1+r\sqrt{s}} \qquad \text{Equation 5}$$

where

δ = boundary layer thickness

x = axial distance

r $\equiv u_2/u_1$

s $\equiv \rho_2/\rho_1$

The constant 0.17 is an approximate value adjusted to the experimental results of Brown and Roshko (1974) with the observation that there is 20% or more error in determining the shear layer boundaries [13], [9]. The source of error is due to experimental inaccuracies and fundamental fluid dynamics that were not included in the analysis.

Dimotakis (1991) concluded that the cross sectional area of the shear layer would increase between consecutive flow structures due the addition of mass [9]. Equation 4 was modified to include spatial growth rate and is shown as Equation 6 [9].

$$\frac{\delta}{x}(r,s) \approx C_\delta \frac{(1-r)(1+\sqrt{s})}{2(1+r\sqrt{s})}\left\{1-\frac{(1-\sqrt{s})/(1+\sqrt{s})}{1+2.9(1+r)/(1-r)}\right\} \qquad \text{Equation 6}$$

where C_δ is a constant and is in the range 0.25 through 0.45.

Experimental data from several studies including Rossmann *et al.* (2000), Chinzei *et al.* (1985) indicate a reduction in shear layer growth as the convective Mach number increases as shown in Figure 10 [14], [15]. The shear layer growth is normalized with respect to the growth of the incompressible case, $M_{C1} = 0$. A substantial amount of data is lacking for the higher convective Mach numbers. Dimotakis (1991) suggested that the data indicated that an asymptote has been reached [9], whereas a linear stability analysis by Day *et al.* (1997) indicated the shear layer growth continued to decrease with increased convective Mach number [16]. This indicates that compressibility has a strong effect on the growth of shear layers and that growth is greatly reduced with moderate Mach numbers [17]. The use of only shear layer mixing in a scramjet engine is insufficient to fulfill the requirement of rapid mixing.

Brown and Roshko (1974) observed large scale coherent structures in the spanwise direction of free shear flows [10]. The study was conducted using helium at a velocity of 1000 cm/s and nitrogen at a velocity of 380 cm/s, both pressurized at 7 atmospheres flowing on either side of a splitter plate to produce a mixing layer for investigation. The coherent eddies viewed on a shadowgraph normal to the mixing layer that was produced was similar to two-dimensional rollers and is shown in Figure 11 [10].

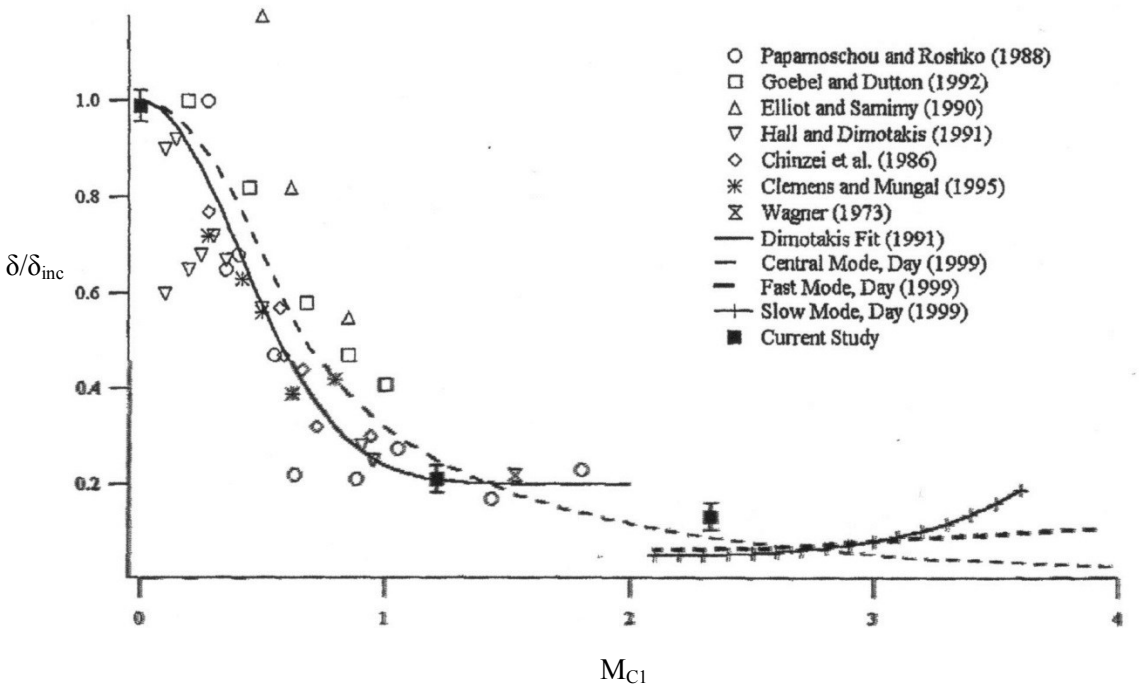

Figure 10 Experimental and computational growth rate data for compressible mixing layers vs. symmetric convective Mach number
[14]

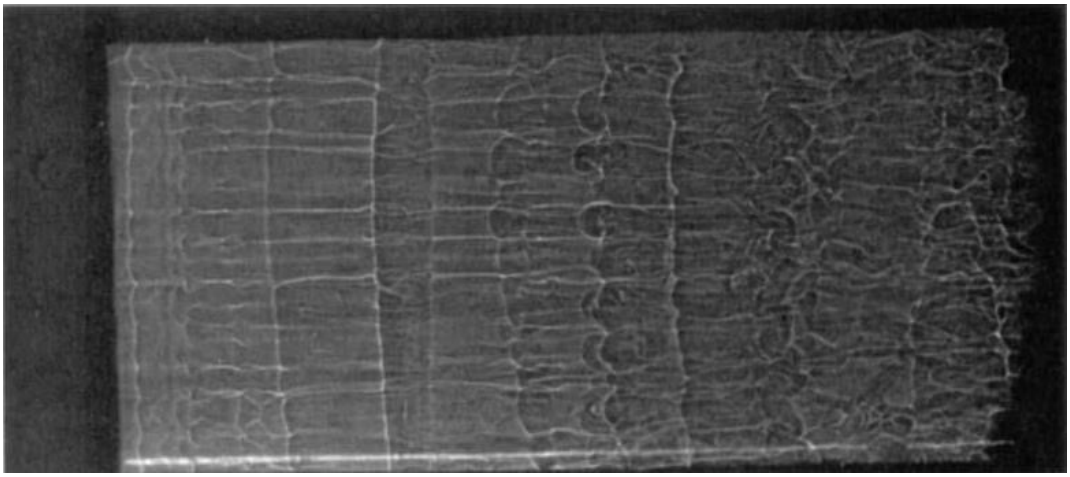

Figure 11 Shadowgraph view normal to mixing layer plane of helium and nitrogen showing spanwise eddies
[10]

These structures have been observed in other studies of mixing layer [18], [19]. At low convective Mach numbers the spanwise structures can be considered two dimensional at high convective Mach numbers the spanwsie structures are three-dimensional and oblique as observed by Samimy *et al.* (1992) [19].

2.3.2 Transverse Flow Mixing

Segal (2006) description of mixing due to the interaction of transverse flows will be the basis for this section as well [2]. As stated previously rapid mixing is accomplished with non-parallel or transverse flows. This method of mixing leads to large momentum and mass exchanges between two flows and viscous losses that cannot be considered negligible. Consider the case of an under expanded transverse jet injected into a supersonic jet. A barrel shock forms around the transverse jet. This in turn affects the supersonic flow such that a bow shock is formed upstream of the barrel shock as shown in Figure 12. The result of the formation of the bow shock is boundary layer separation and the formation of a recirculation region upstream of the transverse jet. The boundary layer separation allows the injectant to be convected upstream by spanwise voritices [18]. Axial vortices form and spill around the barrel shock with the axis of rotation eventually aligning with the supersonic stream. A second recirculation zone develops at the stagnation point of the transverse jet. The recirculation zones may have a significant effect in chemically reacting flows due to the low velocity in these regions. A flame may not be sustainable since cool air passing through the oblique shock section of the bow shock would extend the time for chemical reactions to occur beyond the residence time. The relative angle of the transverse jet with respect to the supersonic flow decreases due to the decreasing dynamic

pressure ratio of injected jet to supersonic flow. A turbulent shear layer forms as the injected jet becomes parallel with the supersonic flow. The streamwise vortices aids in mixing.

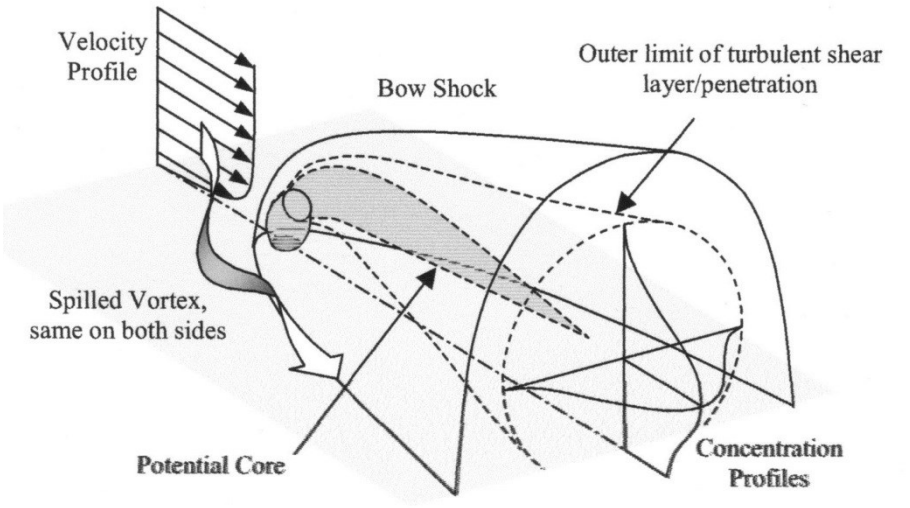

Figure 12 Model of transverse, underexpanded injection into supersonic airstream [20]

This simplified case presumes that the boundary layer thickness is less than the diameter of the injector allowing the transverse jet to penetrate the boundary layer and enabling the bow shock to form. In a scramjet the engine is integrated in the body of a hypersonic vehicle and has a long inlet ramp with a continuous, strong and adverse pressure gradient that most likely will result in a thick boundary layer at the fuel injection site. The assumption of a thin boundary layer may not occur in practice. The strength and location of the formation of the bow shock is dependent on the degree of the boundary layer separation caused by the jet, and the extent of boundary layer separation depends on a number of factors including boundary layer thickness, the jet fluid dynamic characteristics, heat released by chemical reactions interacting with the airflow and wall heat transfer [21].

Jet penetration is one of the factors that aids in the mixing process since it allows a bulk mass of injectant to penetrate the supersonic flow. It is not until the jet flow has gone through the Mach disk and starts flowing in an axial direction that mixing begins. A measure of the jet penetration is the distance from the wall to the Mach disk. A correlation that was developed for the determining the jet penetration is

$$z/D \sim (q_j/q_a)^{0.5} \qquad \text{Equation 7}$$

where

z - distance from wall

D - jet orifice diameter

q - dynamic pressure

and subscripts j and a represent the injection jet and supersonic flow respectively. This definition agrees with models that defined the jet penetration as the boundary of region that contained 99% - 99.5% molar concentration of the injectant [22], [23]. The power coefficient for the dynamic pressure ratio has varied from 0.3 to 0.56 for different studies on jet penetration. Although there were data variations with the various studies, the studies indicated rapid jet penetration within 4 – 6 jet orifice diameters from the wall. Jet penetration reduces as the jet flow turns axially and mixing due to shear layer development starts.

Equation 8 has been modified to include the effects of wall boundary layer thickness and jet/supersonic gas molecular weight ratio.

$$z/D = A(q_j/q_a)^B(x/D + C)^E(\delta/D)^F(MW_j/MW_a)^G \qquad \text{Equation 8}$$

where

z - jet penetration distance from wall

D - jet orifice diameter

q - dynamic pressure

x - axial location

δ - boundary layer thickness

MW - molecular weight

and subscripts j and a represent the transverse and supersonic flow stream, and coefficient A and exponents B, C, E, F and G are derived from studies. Portz and Segal (2004) have suggested the following to include the supersonic flow stream Mach number [20].

$A = 1.05M_{air} - 0.192$

$B = -0.0803M_{air} + 0.615$

$C = -2.34 / M_{air}$

$E = 0.406M_{air}^{(-0.823)}$

$F = -0.067M_{air} + 0.325$

$G = -0.0251$

Jet penetration increases proportionally as boundary layer thickness increases in the near field but shows no changes in the far-field [20]. The effect of molecular weight ratio on jet

penetration is an order magnitude less than that of the boundary layer thickness effect. Other factors such as jet Mach number and jet orifice shape had a negligible effect on jet penetration.

2.3.3 Effects of Turbulence on Combustion

Gupta *et al.* (1984) provides a clear explanation on the effect of turbulence on combustion and is the basis for this section [3]. Ballal and Lefebvre (1975) investigated the influence of turbulence intensity, scale and vorticity on burning velocity and flame structure [24]. A premixed propane-air mixture was supplied to a combustor with transparent side walls to enable schlieren photography. Results indicated there were three distinct models of turbulent flame structures described as a wrinkled laminar flame and combusting eddy models where the large or small eddies are dominant in the combustion process [3]. Ballal *et al.* uses the Kalmogorov microscale of turbulence, η, and laminar flame burning velocity, S_L, to describe the three regions of a turbulent flame. The Kalmogorov microscale of turbulence is given by [3]

$$\eta = (L^{0.25} \nu^{0.75}) / u'^{0.75} \qquad \text{Equation 9}$$

where

L - integral scale of turbulence in the transverse direction

ν - kinematic viscosity

u' - rms value fluctuating axial velocity

The wrinkled pulsating model as described by Ballal and Lefebvre (1975) is a region of low turbulence and low velocity where $u' < 2S_L$, $\eta > \delta_L$. The eddies wrinkle the continuous flame

sheet since the turbulence values of η are larger than laminar boundary layer thickness, δ_L. Burning velocity is increased since the wrinkling increases the surface area of the flame [24]. Figure 13 shows an illustration of the wrinkled laminar flame model [25].

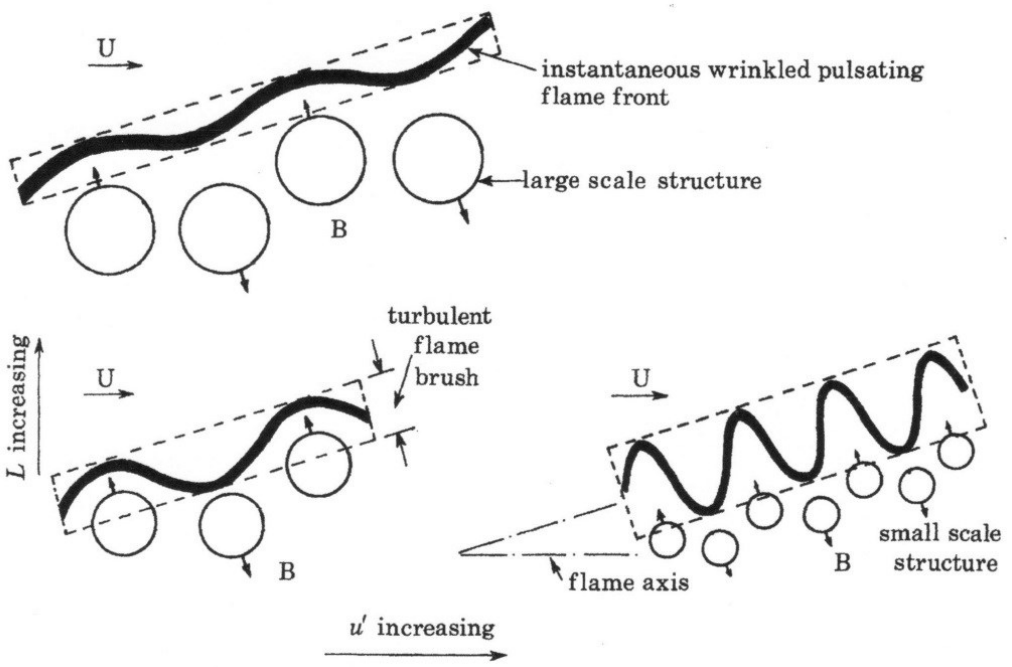

Figure 13 Illustration of the wrinkled flame model of turbulent flame structure (B, burnt: U, unburnt)
[25]

The second model is dominated by large eddies [3]. Ballal and Lefebvre (1975) describes this region as having intermediate turbulence defined as $u' \approx 2S_L$, $\eta \approx \delta_L$. The large eddies disrupt the continuous laminar flame sheet when the eddies are larger than the boundary layer thickness. Mixing is increased since the interface area between the combustion products have been extended. Turbulent diffusion is dominant. In this region combustion can be characterized as flame segments or flamelets [3]. Figure 14 illustrates this model.

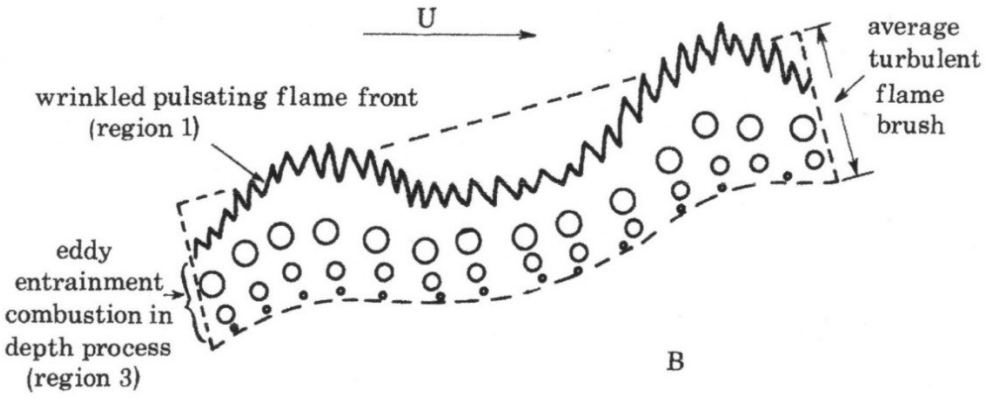

Figure 14 Combustion eddy model dominated by large eddies
(B, burnt; U, unburnt)
[25]

The third model is the combustion eddy model that is dominated by small eddies [3]. Ballal and Lefebvre (1975) describes this region as having high turbulence defined as $u' > 2S_L$, $\eta < \delta_L$. The small eddies are too small to wrinkle the flame surface however, the continuous, coherent flame is no longer realistic. Combustion occurs almost simultaneously throughout the volume of the eddy ahead of the advancing flame as shown in Figure 15. Eddy entrainment is the dominant process.

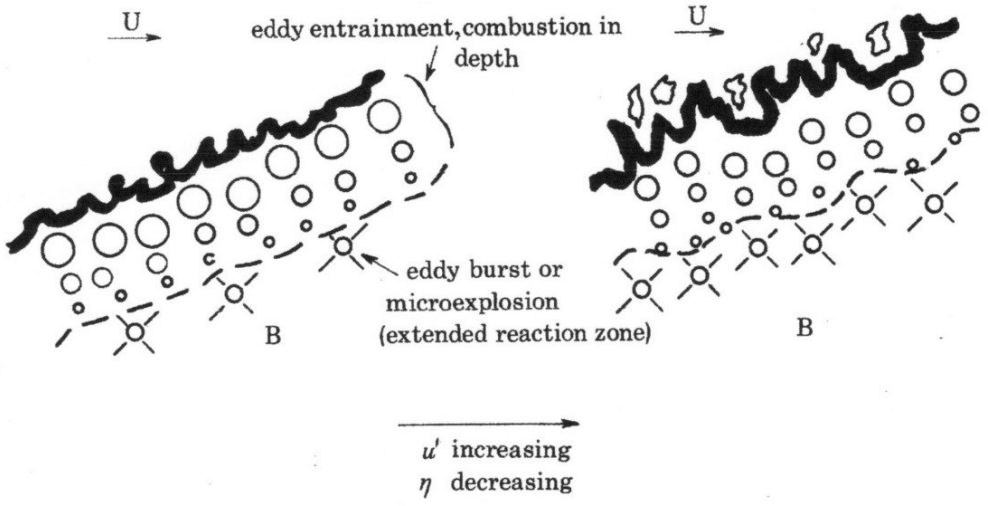

Figure 15 Combustion eddy model with high turbulence
(B, burnt; U, unburnt)
[25]

Figure 16 shows schlieren photographs of propane-air flames for low and high turbulence. It can be seen in Figure (b) that high turbulence mixing lacerates and ruptures the flame surface. This results in the noise that characterizes highly turbulent flames [24].

a)

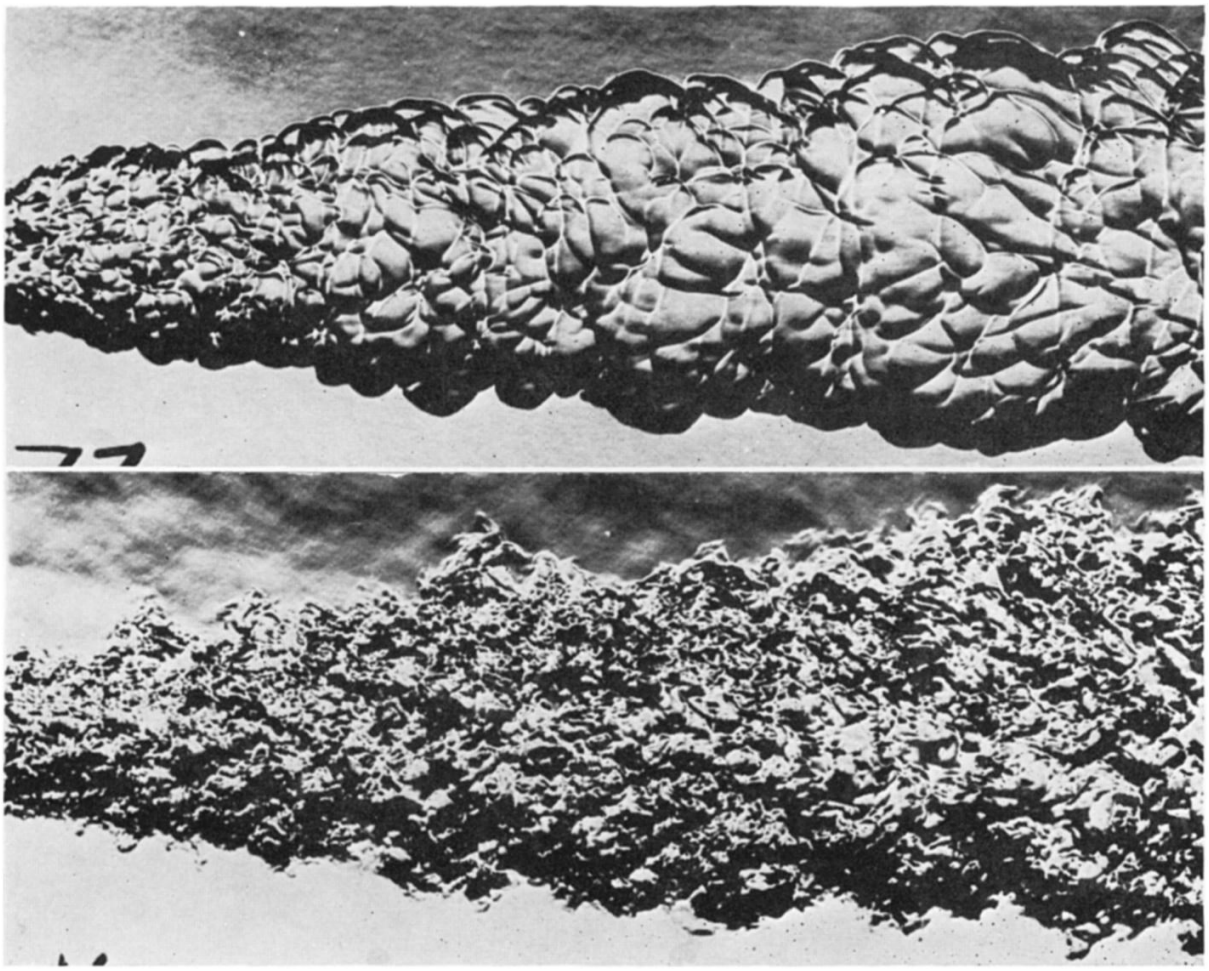

b)

Figure 16 Schlieren photograph of propane-air flames
a) low turbulence, u' = 31 cm/s b) high turbulence, u' = 305 cm/s
[24]

Ballal (1979) also proposed equations for the correlation of flame turbulence for each model [25], [26]. In the wrinkled-pulsating region ($u' < 2S_L$, $\eta > \delta_L$)

$$\frac{u'_c}{u'} = 0.62\left(\frac{S_T}{S_L}\right) / \left(\frac{u'}{S_L}\right)^{1.5} \qquad \text{Equation 10}$$

and

$$\frac{S_T}{S_L} = \left[1 + 0.03\left(\frac{u'L}{S_L\delta_L}\right)^2\right]^{1/2} \qquad \text{Equation 11}$$

where

u'_c - the total value of rms axial velocity with combustion

S_T - turbulent burning velocity

S_L - laminar burning velocity

L - integral scale of turbulence in the transverse direction

δ_L - laminar boundary layer thickness

The flame generated by intermediate turbulence levels where turbulent diffusion is dominant ($u' \approx 2S_L$, $\eta \approx \delta_L$) is given by

$$u'_c = 0.5u'^{\left(\frac{S_T}{S_L}\right)} = 2u' \qquad \text{Equation 12}$$

and

$$\frac{S_T}{S_L} = 0.5\left(\frac{u'}{S_L}\right) \qquad \text{Equation 13}$$

The high turbulence flame that is dominated by eddy entrainment ($u' > 2S_L$, $\eta < \delta_L$) is given by

$$\frac{u\prime_c}{u\prime} = 4\left(\frac{S_T}{S_L}\right) / \left(\frac{u\prime}{S_L}\right)^{1.5} \qquad \text{Equation 14}$$

and

$$\frac{S_T}{S_L} = 0.5\left(\frac{u\prime S_L}{S_L \eta}\right) \qquad \text{Equation 15}$$

Further investigation by Ballal (1979) indicated the correlations of flame turbulence equations were viable for other fuels such as acetylene and hydrogen [26].

2.4 Mixing Enhancement

The fluid residence time in a scramjet combustor is in the order of a few milliseconds in an engine that is several meters long. In that time the gaseous fuels must penetrate the airflow by injection and mix on a molecular level so that chemical reaction can occur and heat can be released. The time scale range over which a chemical reaction can occur is 10^{-8} to one second. Molecular transport processes have a smaller time scale range of 10^{-4} to 10^{-2} seconds. The exothermic process to release heat from the fuel is composed of the ignition delay time and the combustion time. Depending on pressure, temperature and concentration the combustion time can be of the same order of magnitude as the fluid residence time in the combustor. The molecular mixing process takes the longest time and is the limiting factor in the design of the combustor length [2].

There are two basic methods of fuel injection in a scramjet combustor. The first method is parallel injection such that the different velocities of the fuel flow and air flow create shear layers between the two flows where mixing can occur. This method provides good fuel-to-air ratio and there is a small degree of momentum loss. However, a long combustor length is

required to complete the mixing process. The second method is transverse injection. The interaction of non-parallel flows achieves mixing in a shorter distance but with large momentum losses and the generation of shock waves.

At the level of compressibility within a scramjet the mixing layer growth rates and mixing is decreased due to a reduced momentum transport, primary Reynolds shear stresses, size of large scale eddies and skewed, flattened turbulent eddies [27].

Other phenomena that can affect mixing within the flow field are shock and expansion waves. Under certain conditions waves can appear in the mixing layer. Local shock waves (shocklets) can occur in the mixing layer when the flow is accelerated over eddies and become supersonic. The shocklets can extend into the flow and retard eddy growth [27].

This section reviews the various methods that have been investigated to enhance mixing in scramjet combustors.

2.4.1 Ramps, Steps and Cavities

Armaly *et al.* (1983) investigated the flow characteristics of air through a rectangular channel with a backward facing step [28]. The channel was 180 mm wide and upstream of the step had a height of 5.2 mm. The step had a depth, S, of 4.9 mm increasing the channel height to 10.1 mm. The flow characteristics over a backward facing step include recirculation zones and detachment and reattachment of the flow. Figure 17 shows how the locations of flow detachment and reattachment vary with Reynolds number, Re. Laminar flow was identified as occurring when $Re < 1200$, transitional flow when $1200 < Re < 6600$, and turbulent flow when $Re > 6600$.

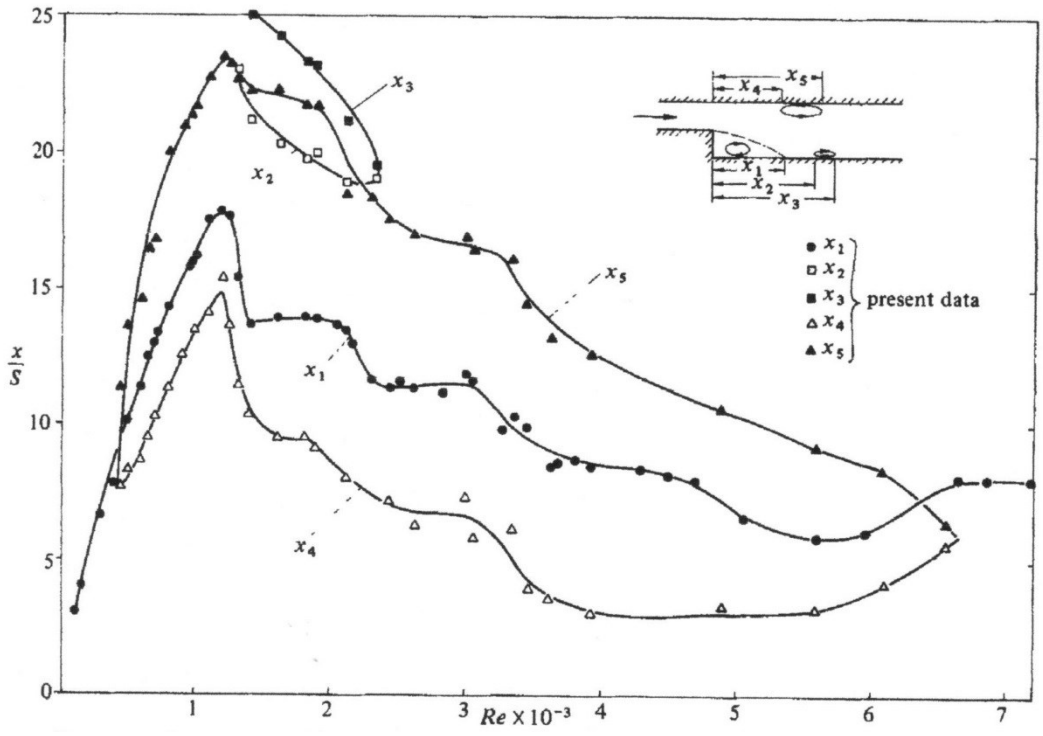

Figure 17 Variation of location of detachment and reattachment of the flow along the test section centerline with respect to Reynolds number.
[28]

The laminar regime is characterized by the reattachment length, x_1, increasing with Reynolds number. The recirculation zone on the top wall (x_4, x_5) also moves further downstream with increasing Reynolds number. In the transitional regime the reattachment length, x_1, and the recirculation zone on the top wall (x_4, x_5) start to move upstream as Reynolds number increases. A recirculation zone on the bottom wall of the channel forms in the early stages of transition between $1500 < Re < 2300$. In the turbulent regime the reattachment location remains constant and the recirculation zone on the top wall dissipates [28]. The recirculation zone at the base of the step is of particular interest since it would provide enhance mixing for two flows.

Variations of the backward facing step have been further investigated. Abdel-Salam *et al.* (2000) numerically analyzed the flow characteristics of a raised and relieved ramp with fuel

injection [29]. A raised ramp rises from the wall into the airstream producing a shock wave at the base of the ramp. A relieved ramp turns the wall away from the flow. Both ramps had a height, *H*, of 5 mm. The study by Abdel-Salam *et al.* (2000) comparing raised and relieved ramps was non-reacting. The fuel was H_2 and injected into the flow at Mach 1.7 and the air flow consisting of O_2 and N_2 was supplied at Mach 2.0. The amount of mixing produced by both configurations is shown in Figure 18 by the axial decay of the maximum amount of H_2 in the flow. The mole fraction of H_2 decreased more rapidly axially for the relieved ramp than the raised ramp. At x/h = 4.0 the mole fraction reduces to approximately 44% and 80% for the raised and relieved ramps respectively [29].

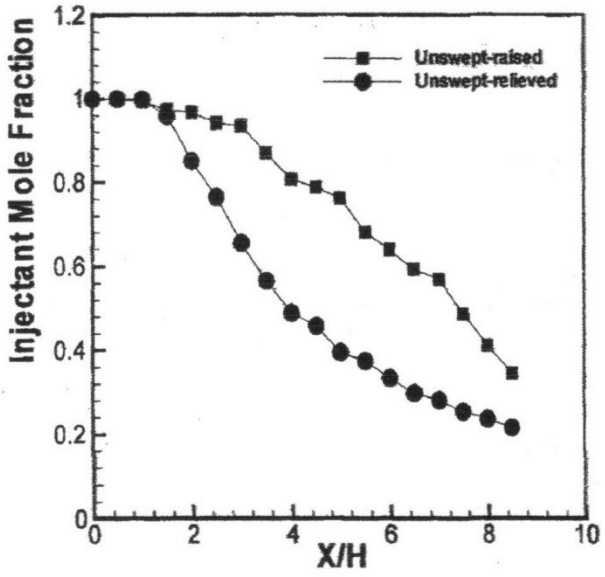

Figure 18 Decay of maximum injectant mole fraction of raised and relieved ramps [29]

A combination of ramps and steps can be used to create a cavity within a wall of the scramjet. Jeong *et al.* (2008) investigated parallel, rearward and angled fuel injection as shown

in Figure 19 [30]. Planar laser-induced fluorescence (PLIF) on the hydroxyl radical (OH) was used to visualize the flow characteristics produced with the different injection methods. In general it was found that the angled injection was the most effective for penetration and mixing and flame holding capability. The effectiveness of injection location varied with equivalence ratio. In the case of the angled injection a weak bow shock formed as the equivalence ratio increased and this aided with flame holding capability. With parallel injection at low equivalence ratios the combustion was produced along the shear layer. At higher equivalence ratios, most of the fuel moved downstream and did not mix with the air in the cavity. At low equivalence ratio the rearward injection produced similar results to the parallel injection but at higher equivalence ratios the fuel would bump the cavity leading edge and mixing was enhanced.

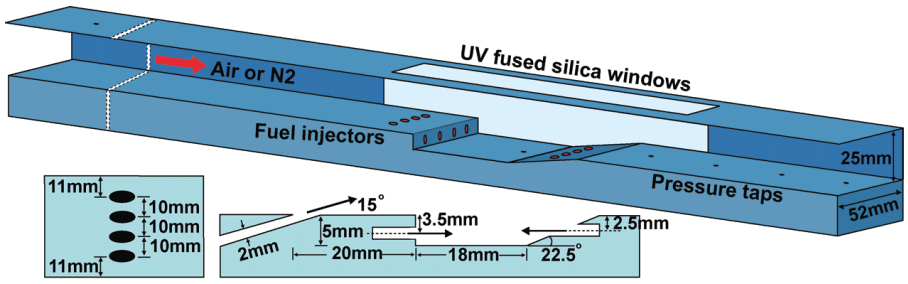

Figure 19 Schematic of Cavity Supersonic Combustor [30]

The addition of injector ramps or steps aids with mixing. The result of adding an injection ramp or a step is the presence of 2 counter rotating vortices. The vortices hold the fuel jet and aids with mixing. In fact mixing was shown to be dominated by streamwise vorticity generated by a rearward facing ramp. When the fuel injection jet interacts with vortices produced by ramps and rearward facing steps the result is improved mixing parameters such as

penetration height, vorticity and turbulent stresses [31]. Figure 20 shows a sketch of flow characteristics produced by a ramp injector [32].

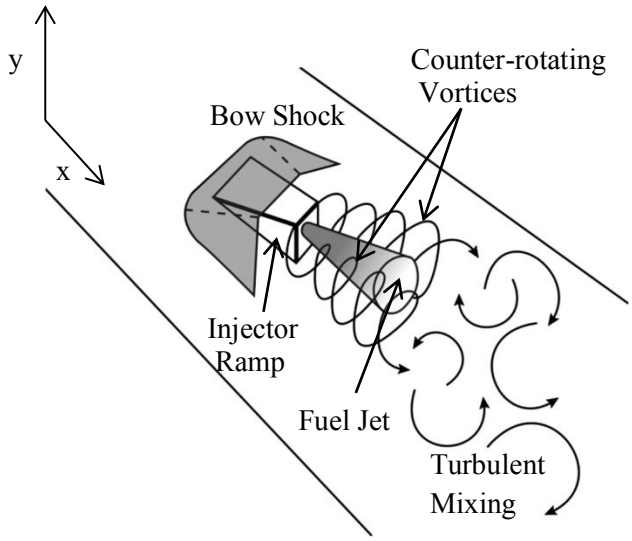

Figure 20 Sketch of ramp injector flowfield [32]

Trebs *et al.* (2014) investigated the effect of boundary layer thickness on the flow characteristics of a ramp injector and was able to show that varying the boundary layer thickness entering the test section affected flame shape, shock structure and mixing [32]. OH PLIF data showed that in the cases of thin boundary layers, flames developed away from the wall and had distinct vortex cores void of combustion. The thicker boundary layer cases showed the plume developing near the wall and the flame shape is fuller and devoid of a core. The boundary layer thickness also affected the shock structure which is coupled with mixing. As the boundary layer grew it suppressed the effectiveness of the ramp by reducing the lifting effect of the vortices. The minimum turbulent scale increased and the gas travelling in the boundary layer increased in

heat and decreased in velocity. As the boundary layer grew there was more low momentum, hot gas available near the wall for mixing.

Another variation of the backward facing step and ramp is seen in the study of a hypermixer by Kim *et al.* (2012). Kim *et al.* conducted experiments comparing a backward facing step with a transverse injector to a hypermixer which consisted of a compression wedge between two expansion ramps with a transverse injector as shown in Figure 21.

The experiment used air to flow through the test section at Mach 2.0 and air injected transversely at Mach 1.0. The main flow had a total temperature of 286 K and a total pressure of 100 kPa. The injectant had a total temperature of 286 K and total pressure of 298 kPa [33]. The constant area test section was 30 mm by 36.7 mm. The injector was located 9 mm downstream from the step or ramp.

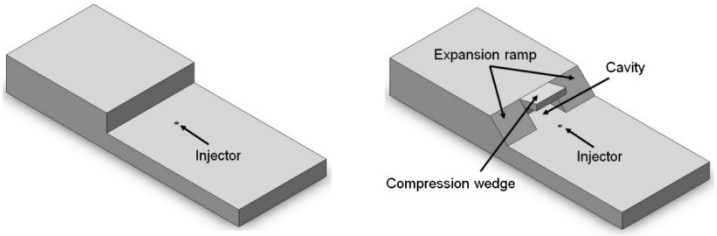

a) b)

Figure 21 Configuration of two mixer models: a) rearward facing step mixer b) hypermixer [33]

The experiment was run with and without injection. The flow field characteristics of the backward facing step without injection have already been discussed. The hypermixer configuration differed in that two counter rotating vortices were formed by the wedge and a large vortical region developed due to large pressure gradients around the wedge-ramp area. With air

injected into the system, the jet plume of the hypermixer was larger in size and had a greater penetration height than the step model. It was concluded that improved mixing was improved by the hypermixer model due to the pair of counter rotating vortices from the ramp interacting with the vortices produced from the transverse injection.

Another interesting concept for fuel injection is the aeroramp shown in Figure 22. Fuller *at al.* (1998) conducted an experiment comparing physical ramps with aerodynamic ramps [34]. The aeroramp consisted of a number of transverse fuel injectors in the combustor wall with the transverse angle increasing relative to the wall with downstream axial location. Mixing with a physical ramp was dominated by counter rotating vortices generated by the ramp. In the case of the aero ramp, mixing was produced by multiple fuel-vortex interactions in the near-field region of the injectors. The areoramp produced significantly greater mixing in the near-field region but produced poor mixing in the far-field region. This indicated that several small jets mixed fuel and air better than one single jet. Increasing the jet momentum decreased the mixing effectiveness of the physical ramp but increased mixing by the aeroramp [34].

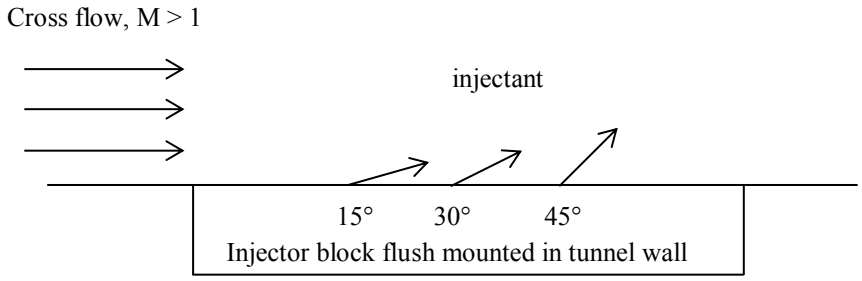

Figure 22 Schematic of an aeroramp injector [34]

2.4.2 Struts and Pylons

Another physical device that can be used for fuel injection is a strut or pylon. The strut allows fuel to be injected into the center of the flow stream and away from a wall. McClinton *et al.* (1976) investigated mixing using two swept struts in a nonreactive environment [23]. The two swept struts were located in a closed duct. Air at a stagnation pressure and temperature of 300 K and 3.896 MPa respectively flowed at Mach 4.4 through the duct. Helium at ambient temperature was injected normal to the free stream flow through injection holes on both sides of the swept struts at Mach 1.0. The experiment by McClinton *et al.* studied different injector patterns related to a range of injection hole diameters, injection hole spacing and the ratio of helium jet to free stream dynamic pressure. Results from the test showed that a fuel injector array with larger diameter injection holes and relatively small lateral injection hole spacing operating at minimum dynamic pressure ratios produced a faster mixing rate and decreased mixing length than was predicted using values based on flat plate data.

Another study using a strut with injection holes was conducted by Tomioka *et al.* (2001) in a staged supersonic combustor [35]. A schematic of the combustor is shown in Figure 23 and shows the first stage injection that is normal to the flow stream and the second stage injection consisting of three transverse injectors in the divergent section of the tunnel. The direct connect tunnel facility was supplied with Mach 2.5 airflow at a total temperature and pressure of 1500 K and 1.0 MPa respectively. It was found that the first stage strut injection by itself was limited to a maximum equivalent ratio of 0.5 and then separation of the flow penetrated the facility nozzle. When the first stage strut injector and the second stage transverse injectors were used together, the maximum equivalence ratio for the strut injection could be increased without flow separation.

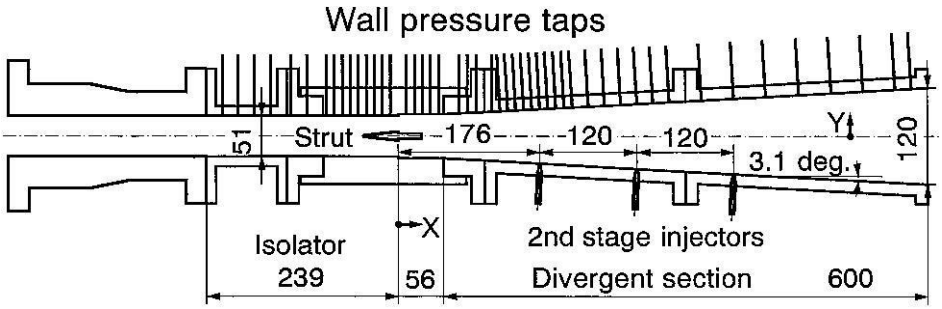

Figure 23 Schematic diagram of a staged combustor
(Dimensions in mm)
[35]

Instead of a strut Lee (2012) investigated pylon injection to increase mixing [36]. Lee (2012) was also interested in a film cooling method for the pylon. Four cases were studied numerically simulating the conditions of a Mach 8 scramjet engine. The pylon injection models are shown in Figure 24. Model A represents a transverse fuel injector such as previously discussed. Model B represents transverse fuel injection from the top of a pylon into the airstream. Models C and D include cool air jets along the surface of the pylon for cooling. The flow characteristics around the pylon are similar to that around the simple transverse injection. A bow shock is formed in front of the pylon and the fuel jet, there is boundary layer separation due to interactions with the bow shock, a barrel shock and a vortex pair are formed axially. The major differences are that the bow shock in front of the pylon is stronger and the recirculation zone in front of the pylon is larger than in the case of a simple transverse injector. The pylon injection showed an increase in fuel jet penetration and mixing. The effects from cooling models C and D were negligible when compared to Model B.

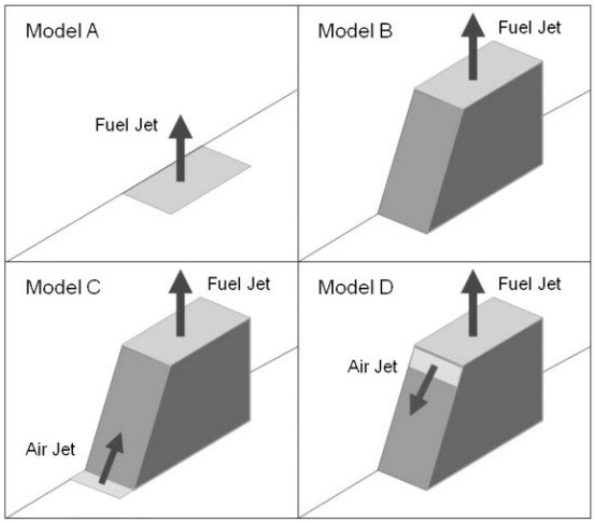

Figure 24 Four pylon injection models [36]

2.4.3 Boundary Layer Injection

The investigation by Trebs *et al.* (2014) on the effect of boundary layer thickness on the flow characteristics of a ramp injector showed that increasing the boundary layer thickness entering the test section increased mixing [32]. Kirchhartz *et al.* (2010) conducted experiments assessing combustion due to injecting fuel underneath the wall boundary layer [37]. The experiments were conducted in the T4 Stalker Tube that is a circular constant area supersonic chamber producing greater than Mach 4.0 flow to the test chamber. The H_2 fuel was injected tangentially along the combustor wall. The length of the constant area inlet upstream of the fuel injection slot was tested at two different lengths and each length was tested with sharp and blunt leading edges located upstream of the point of injection. Figure 25 shows the schematic of the inlet/combustor used for the experiments.

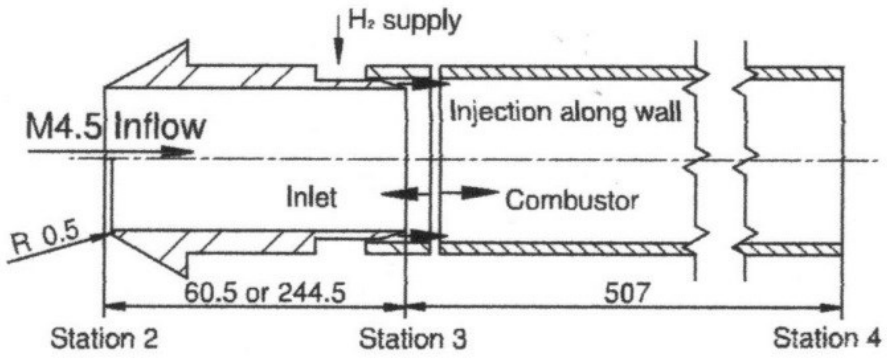

Figure 25 Schematic of inlet-combustor arrangement
(Dimensions in mm)
[37]

Data from the experiments indicated that thick, turbulent boundary layers at the entrance of the combustor could aid ignition and combustion for boundary layer fuel injection. The blunted leading edges upstream of the injection point primarily promoted ignition. In addition the shock waves generated by the blunt leading edges had a large influence on wall temperatures and the core flow in the combustor. The shock waves result in increased pressure and density in the combustor and that in turn results in a faster ignition time.

Other studies have shown that the presence of shock waves and compression fans can enhance mixing. An investigation by Mack *et al.* (2006) showed that mixing and combustion efficiency was increased when shock waves induced by transverse fuel injection and resulting reflected shock waves impinged on neighboring fuel injections [38]. Studies by Parent *et al.* (2004) showed that mixing could be increased by oblique shock waves or compression fans located in a shock induced combustion ramjet (shcramjet) [39], [40]

2.4.4 Coaxial Flow

Coaxial flow consists of a core jet surrounded by an annular jet referred to as the coflow jet. Coaxial jets are effective in producing turbulence. This is turn affects the growth rate of compressible mixing, entrainment and can also help reduce noise [41]. Cutler and White (2001) investigated the mixing within a coaxial flow [42]. The core jet was a mixture of 5% oxygen and 95% helium and the coflow jet consisted of air. The coaxial jet was discharged into stagnant air. The coaxial nozzle configuration is shown in Figure 26.

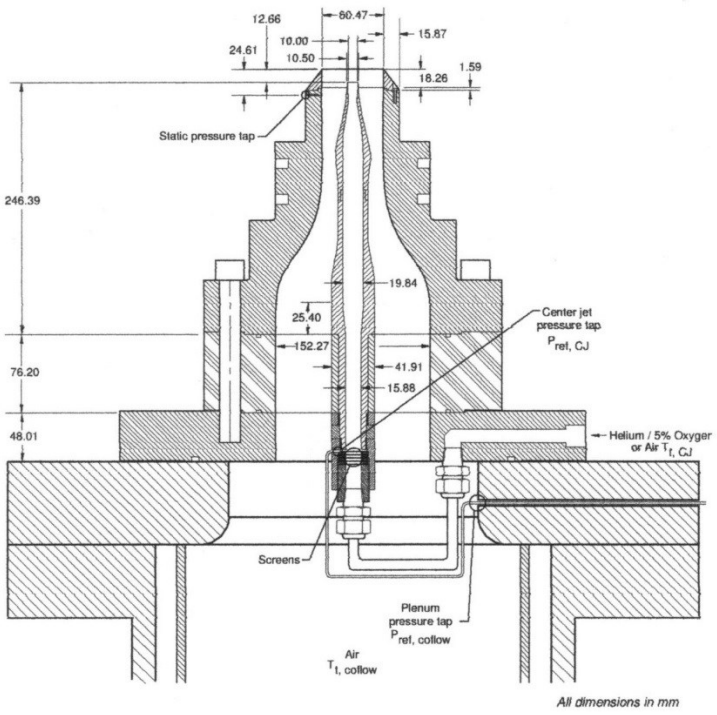

Figure 26 Coaxial jet assembly connected to Transverse Jet Facility [27]

Both jets had a nominal Mach number of 1.8 and the exit pressure for both flows at the nozzle exit was 1 atmosphere. Since the speed of sound of the core jet was greater than for the coflow jet, the two flows had different velocities. The shear layer between the two jets was

compressible and has an average convective number of 0.7. The advantage of using a free jet for experimental study is the ease of access for optical instrumentation and probes. The disadvantage is that weak shock waves that form at the nozzle exit strengthen and become normal to the axis complicating the flow. Figure 27 shows a schlieren photo of the coaxial jet flow. The development of the mixing layer between the core jet and coflow jet, as well as the development of the shear layer between the coflow jet and the stagnant laboratory air can be seen. Shock-expansion wave structures that emanate outward from the center body lip are clearly seen. Similar waves propagate inward through the helium core jet but cannot be seen in the schlieren image until the waves pass out of the core jet and into the air coflow jet.

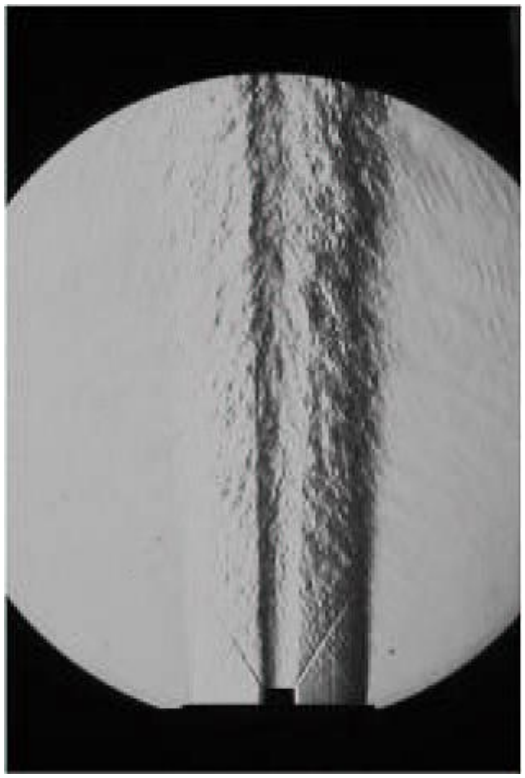

Figure 27 Schlieren image with vertical knife edge (conical extension cap removed) [27]

Abdelhafez and Gupta (2011) also investigated flow characteristics of a coaxial jet using a convergent nozzle [43]. Helium was used in the core jet and air was used in the annular jet. Figure 28 shows the nozzle assembly that is also capable of introducing swirl flow to the annular jet although only the non-swirling cases are discussed at this time. The total air temperature was 300 K with a reservoir pressure of 7.914 bar that resulted in a mass flow rate of 175 g/s, air velocity of 323 m/s and a Mach number of 1.0 at the nozzle exit. The relative Mach number between the core and annular jet was varied from -0.48 through 0.44. The shock structure for an underexpanded supersonic free jet is comprised of simple shock cell structures that repeat downstream to form a shock train. In the case of coaxial flow with no core jet the shock structure changes as shown in Figure 29. Most notable is the base separation created at the nozzle exit of the core flow. Since there is no core flow the airflow creates an inner conical boundary that completes the conical shape of the tip of the nozzle. This shock substructure interacts and changes the shock train. Adding the core jet again changes the shock structure as shown in Figure 30. The shock substructure is altered and a shear layer is formed. The airflow is gradually compressed through a compression fan which collapses into a shock wave substructure downstream.

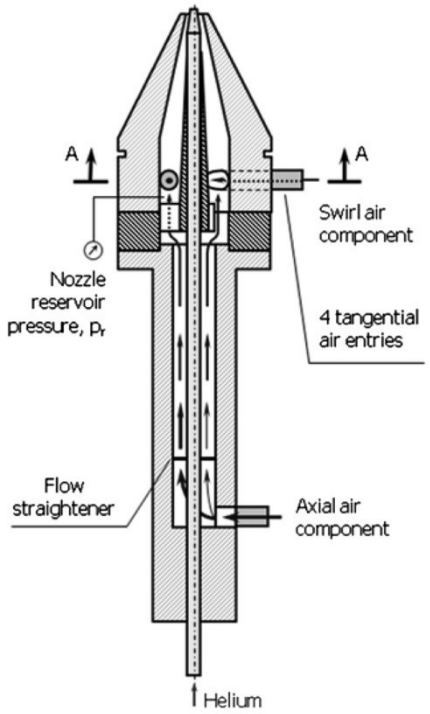

Figure 28 Schematic of the Supersonic nozzle assembly
[43]

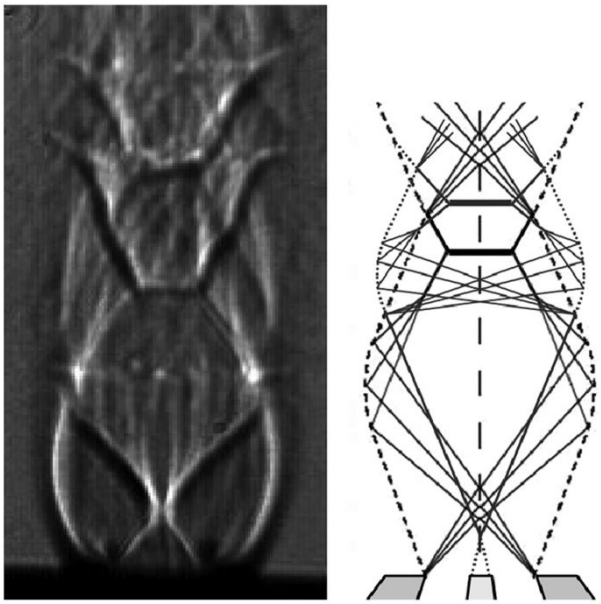

Figure 29 Shock structure of underexpanded nozzle airflow in presence of coaxial injection with no fuel injection
[43]

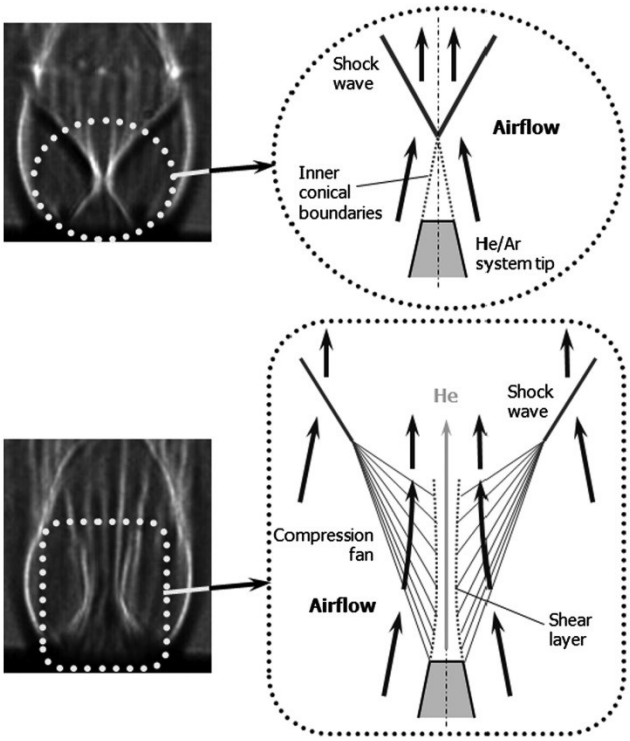

Figure 30 Effect of fuel injection on shock structure of unexpanded nozzle flow
a) no fuel injection, b) fuel injection
[43]

2.4.5 Pulsed Injection

Pulsed injection is used to enhance mixing by using fuel jet unsteadiness. A non-combustion experiment on pulsed injection by Kouchi *et al.* (2007) showed that a pulsed injection transverse jet increased mixing performance and greater jet penetration than a continuous transverse jet [44]. The experiment was conducted in a blow-down wind tunnel that provided a nominal Mach number of 2.5. The facility nozzle was capable of supplying room temperature air at a stagnation pressure 0.75 or 0.40 MPa. Helium and nitrogen gas was used for transverse injection to simulate hydrogen or a hydrocarbon fuel as needed. The facility test section width and height was 94.3 and 51 mm respectively. There were 4 jet orifice sizes

available with diameters of 2, 3, 6 and 12 millimeters and the jet was pulsed at a frequency up to 1.0 kHz. Overall results indicated that jet penetration was significantly affected by injection profile. Pulsed injection produced large eddies in the jet that was associated with bow shock fluctuations in front of the transverse jet. Jet penetration for the pulsed injection was significantly greater than for a continuous jet as seen in Figure 31 which shows Schlieren images of the freestream flow with no injection, continuous injection and pulsed injection.

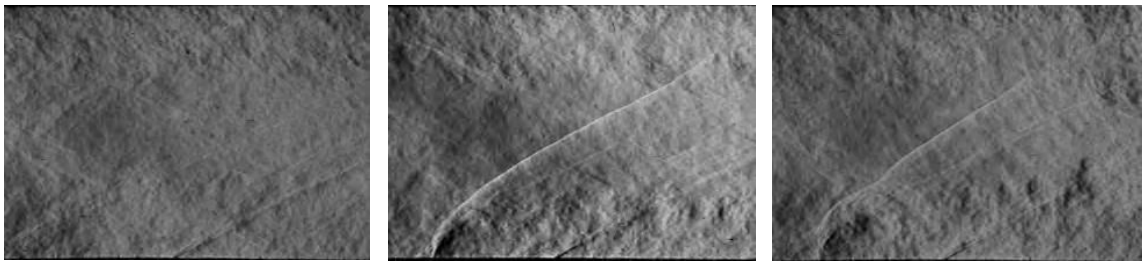

Figure 31 Schlieren images of a) freestream flow, b) continuous injection, c) pulsed injection [44]

The results of a non-combustion study on pulsed injection by Kalidas and Kurian (2007) also showed that pulsed injection provided greater mixing than continuous injection jet [45]. The blow-down tunnel provided compressed air at a stagnation pressure and temperature of 4.72 bar and 310 K respectively through a CD nozzle to obtain a nominal Mach number of 1.38. Compressed air at a stagnation pressure and temperature of 4.5 bar and 310 K was pulse injected transversely into the test section. The test section of the tunnel had a constant area of 37.5 mm x 15 mm. Configurations were run with pulse frequencies of 1 Hz and pulse widths from 160 ms up to 740 ms and at pulse frequencies at 2 Hz and the pulse widths from 160 ms to 300 ms. Results were recorded by Mie scattering images. Results indicated that pulsed injection augmented mixing and showed increased jet spread and penetration. The investigation also

indicated that the pulse width was a more significant factor for mixing enhancement than the pulse frequency. Mixing increased with decreased pulse width.

A high speed high frequency pulsed injector was studied by Cutler *et al.* (2013). In this experiment unheated air was provided at a total pressure of 793 kPa to a CD nozzle with an exit cross section of 87.88mm x 38.61 mm producing Mach 1.975 flow to a constant area duct [46]. Helium was transversely injected into the duct air flow continuously and pulsed at Mach 1.0. Various configurations were run with jet to duct pressure ratios of 16.4 and 32.7, continuously injected and pulsed injected. The pulse injected jet was investigated for various pulse frequencies up to 13 kHz. The exhaust flow ducted to the laboratory and then into an exhaust duct. Schlieren images were used to visualize the results. Results indicated that the pulsed injected jet plume was more unsteady and chaotic in shape and size than the continuous jet injection. Jet penetration for the pulsed injected jet was greater than for the continuous jet. Jet spreading and mixing for the cases of pulsed injection were less than for the continuous jet.

Smith (2014) investigated parallel pulsed injection [47]. The pulse injector was in the vertical plane of a backward step located in the test section of a wind tunnel. The throat of the wind tunnel delivered an air flow of Mach 1.8 to the test section. Carbon dioxide gas was pulse injected into the test section at a pressure of 180 psi and at frequencies between 18 kHz and 10 kHz. Results indicated that pulse injection caused the shear layer to oscillate and shed vortices downstream. Regions of turbulence formed around the regions of vorticity and could be used to enhance mixing.

An interesting modification of the pulsed injector is a pulse detonator. A pulse detonator uses a spark igniter to initiate a premixture that can lead to a flame propagation and detonation within a tube placed transversely to combustor core flow. Ombrello *et al.* experimentally

investigated the transverse injection of high pressure, high temperature exhausting flow from a pulse detonator into the supersonic flow of a combustor downstream of a transverse jet injector [48]. Using NO PLIF visualization techniques results indicated the upstream transverse injection showed enhanced mixing. There was an optimal separation distance between the upstream transverse injector and the pulsed detonator that resulted in maximum jet penetration and mixing.

2.5 Swirl Flow

A swirling flow is flow that has spiraling motion or tangential velocity. Gupta *et al.* provides an excellent description of swirl that is the basis of this section [3]. Swirl can be generated by swirl vanes (adjustable and stationary), axial flow through a rotating pipe or rotating perforated plate or by injecting air tangentially on the axial flow through a pipe. Swirl flow is anisotropic meaning the flow has unequal physical properties along different axis. Swirling flow occurs in many practical applications including cyclone separators, tornadoes, vortex shedding from aircraft wings, reduction of IR signature in stealth aircraft and aircraft combustion chamber designs resulting in higher combustion efficiencies through enhanced mixing.

Turbulent jets with an initial swirl display a different characteristic compared to turbulent flows without swirl. In the case of a subsonic jet without swirl, there is no static pressure gradient in the axial or radial direction. Spreading of the jet without initial swirl is accomplished by turbulent mixing that occurs at the interface between the jet and ambient air. In comparison, a jet with swirl shows static pressure gradients in the axial and radial direction. For weak swirl the maximum velocity occurs in the axial direction. As swirl increases the radial spread of the jet, entrainment and the rate of decay of the jet increases. Eventually a critical swirl number is

reached where the axial adverse pressure gradient exceeds the forward kinetic forces and the flow reverses direction along the centerline of the jet near the nozzle exit. The result is a central toroidal recirculation zone. In general, the length of the reverse flow region can be up to four jet diameters upon reaching the critical swirl number. The primary use of swirl is to increase the angle of spread for the jet and the rate of decay of the axial velocity and this can enhance mixing.

The degree of swirl imparted to a jet flow has a large effect on the jet growth, decay and combustion intensity. Swirl strength is defined as a non-dimensional number, *S*, which represents the axial flux of swirl momentum divided by the axial flux of axial momentum, times the equivalent nozzle radius [3].

The swirl number is defined as follows [3]:

$$S = \frac{G_\theta}{G_x (d/2)} \qquad \text{Equation 16}$$

where

the axial flux of swirl momentum, including the x-θ direction turbulent shear stress term is

$$G_\theta = \int_0^\infty \left(\rho u w + \rho \overline{u' w'}\right) r^2 dr \qquad \text{Equation 17}$$

the axial flux of axial momentum, including the x direction turbulent normal stress term and a pressure term (axial thrust) is

$$G_x = \int_0^\infty \left(\rho u^2 + \rho \overline{u'^2} + (p - p_\infty)\right) r dr \qquad \text{Equation 18}$$

d - nozzle diameter

p - pressure

r - nozzle radius

u,v,w - velocity components in (x, r, θ) cylindrical polar coordinate directions

ρ - density of medium

For a solid body plug rotation equation 2.1 can be simplified to

$$S = (G/2) / (1 - (G/2)^2) \qquad (S > 0.4) \qquad \text{Equation 19}$$

$$S = (G/2) / (1 - (G/2)) \qquad (S < 0.4) \qquad \text{Equation 20}$$

where

$G = w_{mo}/u_{mo}$

w_{mo} - tangential velocity at outer wall of nozzle

u_{mo} - axial velocity

and for a nozzle with a vane pack and hub

$$S = \frac{2}{3}\left[\frac{1-(d_h/d)^3}{1-(d_h/d)^2}\right] tan\phi \qquad \text{Equation 21}$$

where

d_h - diameter of central jet

For a hubless swirler Equation 2.8 reduces to

$$S = 2/3 \tan \phi \qquad \text{Equation 22}$$

Figure 32 illustrates the flow characteristics of weak and strong swirl. For a very low swirl number, ($S < 0.2$) the pressure gradient in the lateral axis is insignificant. Although a weak swirl will increase the width of the jet the swirl velocity does not drastically change the jet flow. Since there is no recirculation in the flow downstream events do not affect upstream flow.

a) 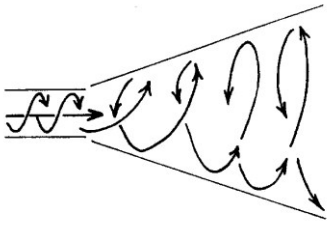 b) 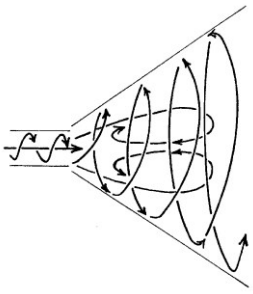

Figure 32 Swirl Strength
a) Weak Swirl Strength Jet Flow ($S < 0.4$) b) Strong Swirl Strength Jet Flow ($S > 0.6$)
[3]

Jet growth, mixing and decay are enhanced as the strength of swirl increases. This level of swirl produces significant pressure gradients in the lateral (radial) axis, and insignificant pressure gradients in the longitudinal (axial) axis. At higher degrees of swirl, ($S > 0.6$), strong radial and axial pressure gradients are produced at the nozzle exit. The point at which the flow will break down is considered the critical swirl number and has a value of approximately $S = 0.6$. The result of strong swirl results in a recirculation zone located on the longitudinal axis and is shown in Figure 32b. The axial recirculation is affected by the swirl number, nozzle geometry and the particular nozzle exit velocity profiles.

Swirling flow through a pipe consists of three regions based on tangential velocity; the wall, the annular region and the core. The flow in the annular region is skewed and has high anisotropic turbulence. Flows in stirred vessels, such as a cyclone separator, are highly anisotropic also.

2.5.1 Mixing Enhancement with Swirl

An experimental study by Flesberg (2000) on the effect of imparting swirl to supersonic rectangular jets showed enhanced mixing of the jet exhaust with ambient air [4]. Three nozzle exit shapes were examined with and without swirl vanes as shown in Figure 33. Each nozzle had an aspect ratio of 6.0 and the vane angles were at 30 degrees and placed on the large dimension of the nozzle only. The swirl vanes protruded 0.04" into the boundary layer. The mean Mach number of air flow was 1.2

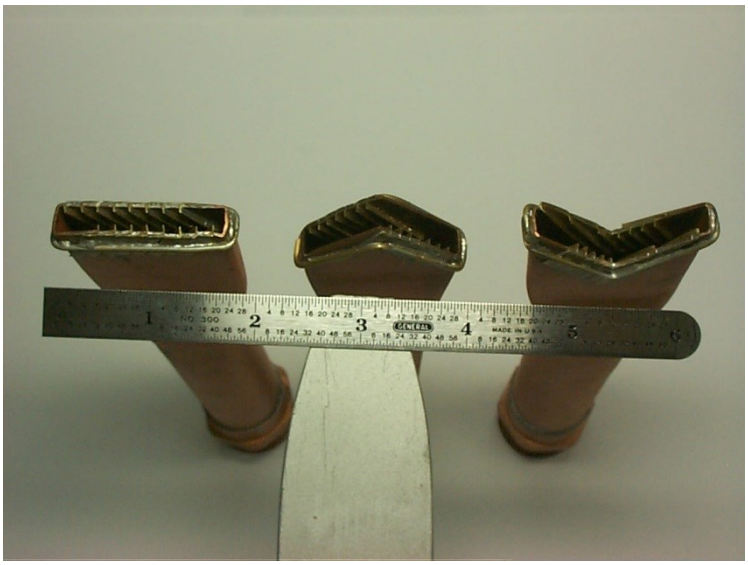

Figure 33 Rectangular Nozzles with Swirl Vanes
a) Straight, b) notched, c) double-beveled
[4]

Regardless of nozzle exit shape, it was observed that the centerline pressure distribution for nozzles with swirl vanes began decreasing closer to the nozzle exit and at a more rapid rate than their non-swirling counterparts. The nozzles with boundary layer swirl vanes eliminated or decreased the number and strength of shock waves independent of nozzle geometry. Results from the experiment also indicated that swirl promoted a faster rate of decay for the centerline pressure distribution or velocity which is an indication of enhanced mixing. Regardless of nozzle exit geometry, the pressure contour plots for non-swirling jets had more uniform and tightly packed contours than with swirl as seen in Figure 34. This is another indication that the addition of boundary layer swirl vanes enhanced mixing and agreed with previous results by Frank (1994) [49].

Other indications of enhanced mixing included a decrease of maximum pressure ratios when swirl was added to the jet, the swirling jets had no potential core unlike the non-swirling counterparts and the maximum velocity downstream of the nozzle exit became subsonic in less distance for swirling jets than for the non-swirling counterparts.

The results of a numerical investigation by Han and Taghavi (2001) [50] reiterate the previously discussed results. Han and Taghavi (2001) investigated the effects of boundary layer swirl on a straight rectangular nozzle with vane angles of 0, 10, 25, 30 and 45 degrees. The aspect ratio of the nozzles was 5.0 and the fully expanded jet Mach number was 1.526. The results showed that shock strength decreased with increasing boundary layer swirl angle. Increasing the boundary swirl angle of the jet resulted in an earlier start and a faster rate of jet velocity decay and increased the jet spreading rate. The numerical results showed that boundary layer swirl enhanced mixing but imposed a thrust penalty that increased with increasing swirl angle.

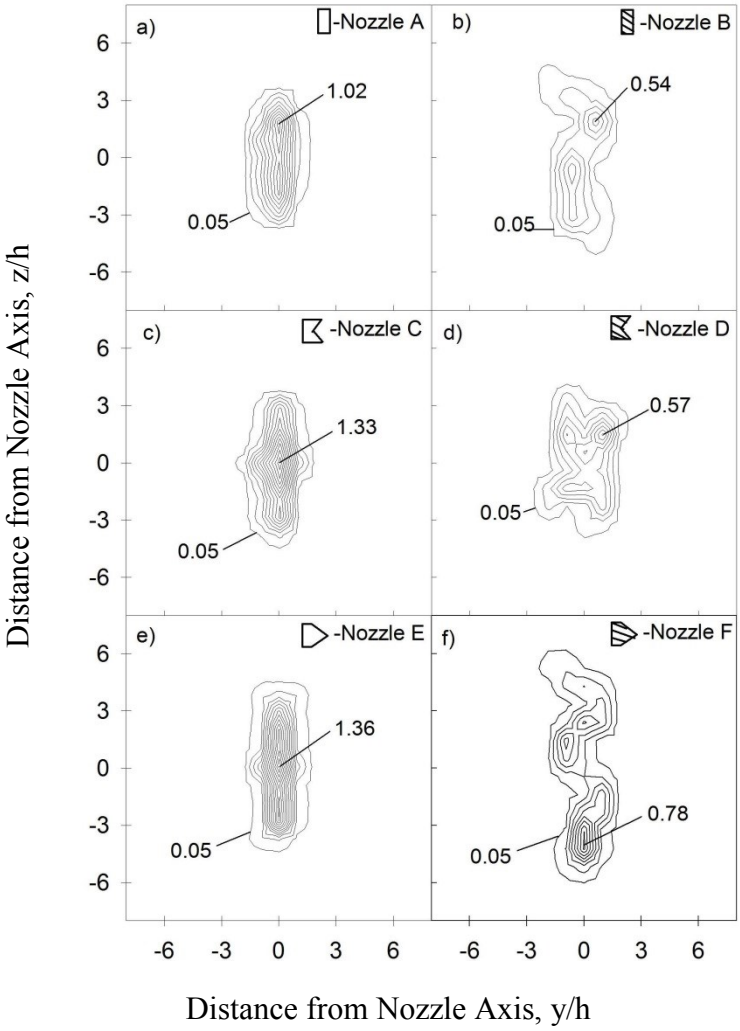

Figure 34 Comparison of Cross Sectional Pressure Ratio Contours for Rectangular Nozzles at x = 6h (h = 0.25"; contour interval = 0.1): a) straight, b) straight with swirl, c) notched, d) notched with swirl, e) double-beveled, f) double-beveled with swirl [4]

One investigation by Farokhi and Taghavi (1992) of a subsonic, circular jet with swirl found that the characteristics of the near field jet were found to be significantly affected by the initial swirl tangential velocity distribution [51]. The swirl number alone was shown to be insufficient for predicting the swirl characteristics of the jet and it was concluded that other parameters needed to be developed in order to better describe this behavior. It was also seen that that vortex breakdown was observed at a lower swirl number than the critical value. The

research indicated that the diameter of the vortex core and the tangential velocity influence the evolution of swirling turbulent jet flow.

Another experiment investigating the effects of swirl on mixing was conducted by Gilchrist and Naughton (2003). Gilchrist and Naughton (2003) compared a non-swirling circular jet with swirling jets that had tangential velocity profiles describing solid body rotation and q-vortex, each at swirl strengths of 0.10 and 0.25 [52]. The incompressible swirling jets had a Reynolds number of 1×10^6 and exhausted into laboratory. It was found that the swirling jets had spreading rates up to 45% greater than the non-swirling case. Regardless of swirl strength jets with a solid body velocity profile grew faster than jets with q-vortex velocity profiles. This indicates swirl strength alone does not predict mixing enhancement. Measurements of the fluctuating velocity at the jet nozzle exit showed high levels of turbulence several magnitudes higher than for the non-swirling jet.

Benim *et al.* (2007) numerically investigated the effect of velocity profile on the decay of swirl [53]. The study showed that inlet swirl profile had an effect on swirl decay in steady-state, incompressible, laminar pipe flows. The investigation was simulated for a Reynolds number of 2000 and for swirl numbers of 0.2 and 0.5. Results indicated that swirl decay was influenced by velocity profile regardless of swirl number.

Murugappan and Gutmark (2003) suggested the use of a controlled supersonic swirling injector (CSSI) to control jet spreading and improve mixing in high speed flows [54]. Murugappan *et al.* (2006) conducted an experiment with the CSSI to modify the spreading rate and mixing of a transverse jet in a high speed crossflow [55]. A swirling jet has a vortex core and while the vortex core remains intact, the flow will have high penetration rate. However, the vortex core becomes unstable when the swirl number is too high. The CSSI has swirl vanes in

the fuel nozzle as shown in Figure 35 thus providing a swirling injector with a central jet. In this manner the CSSI produces a high swirl with active control to manipulate growth rate and spreading characteristic. Large scale mixing and entrainment was shown in a study using visualization with ice crystals and planar laser induced fluorescence (PLIF) of NO molecules. It was seen that the central jet encouraged penetration while the swirl wanes induced swirl resulting in increased mixing area.

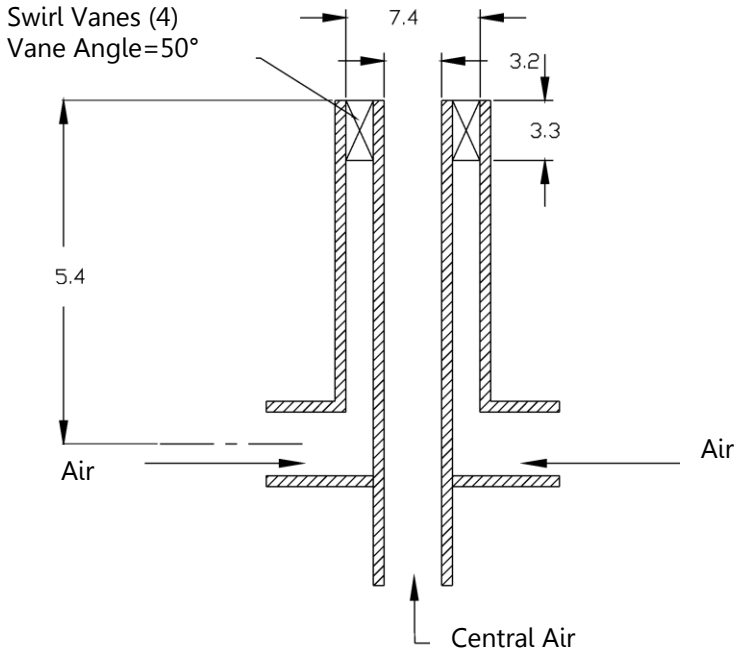

Figure 35 Schematic of the CSSI (dimensions in mm) [55]

Air was used for the core flow and the coflow. The guide vanes were set at an angle of 50° producing a swirl strength of approximately 0.89. The pressure ratio and flow rates ranged from 7.11 to 10.45 and 6.1 g/s to 9.0 g/s respectively for the swirling jet and 10.78 to 19.11 and 0 g/s to 10.2 g/s respectively for the core jet. The CSSI injected the swirling coflow jet transversely into air flow at a nominal Mach number of 2.0. A circular jet with no swirl with a flow rate of 10.2 g/s and pressure ratio of 19.11 was also studied for comparison.

Results indicated that the CSSI arrangement provided a higher penetration rate than a non-swirling or full swirling injector. The optimal case resulted in a 78% increase in total jet area when compared to the non-swirling jet case. The study showed that the CSSI was capable of controlling jet penetration and jet growth independently.

Linck and Gupta (2003) used particle image velocimetry, PIV, to characterize the effect of radial distribution of swirl on spray flames [56]. The nozzle used to produce the flame is shown in Figure 36 and was designed to resemble a gas turbine injector. The inner and outer annuli jets used air with a flow rate of 14.3 standard cubic feet per minute, SCFM, and had swirl guide vane angles of 30° or 45° for the inner annulus and 50° for the outer annulus. Kerosene was used to fuel the flame at a flow rate of 0.5 gallons/hour. Non-combusting and combusting cases were run and results indicated that the effect of the fuel mass flow dominated the flow field when the fuel spray was introduced to the flow. Additional results showed that strong swirl produced wider and more distributed combustion regions.

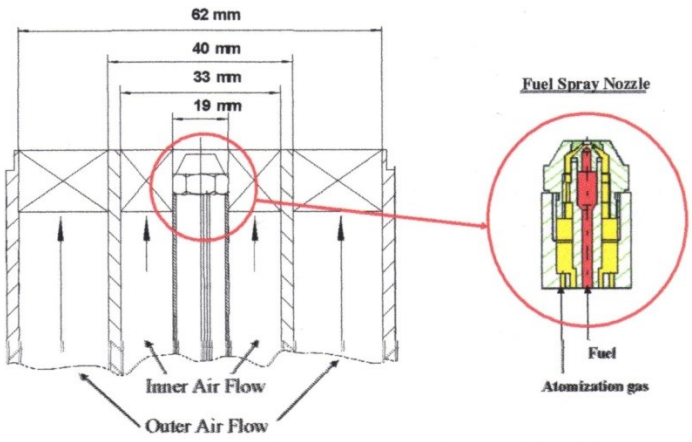

Figure 36 Schematic of injector of swirl stabilized burner [57]

In a later study Linck and Gupta (2005) studied the effect of pressure on the characteristics of a swirling jet [57]. The experiment was setup to produce a flame in a pressurized container in order to simulate a combustor. The nozzle used to produce the flame is shown in Figure 36. The inner and outer annuli jets used air and had swirl numbers of 0.385 and 0.795 respectively. The total mass airflow was 15 g/s. Methanol was used to fuel the flame and had a mass flow rate of 0.82 g/s. The exhaust nozzle for the pressurized container was designed to produce a Mach 1 exhaust jet. Figures 38(a) and (b) show the methanol flame in the pressurized container at 1 bar and 2.19 bar respectively with the same swirl configuration, air flow rates and fuel rates. It can be seen that the higher container pressure resulted in a longer, more elongated flame with less jet spreading than at the lower container pressure.

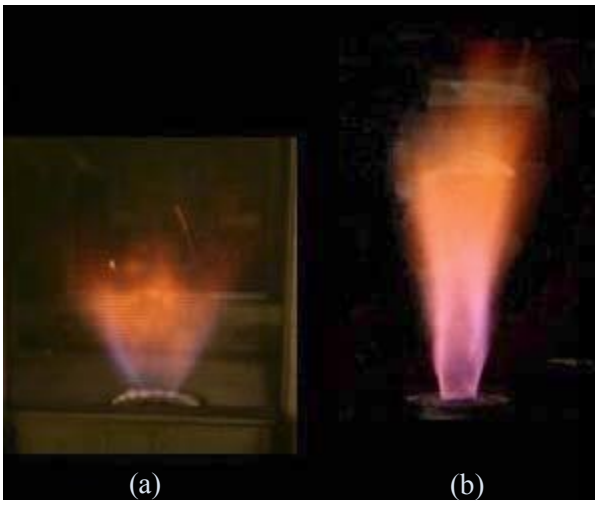

Figure 37 Methanol spray flames under different container pressures
a) 1 bar, b) 2.19 bar
[57]

Abdelhafez and Gupta (2011) also investigated flow characteristics of a swirling jet [43]. Mie scattering was used to analyze mixing in a nonintrusive manner. Cases simulated an annular swirling jet with swirl strength of 0.68 and coaxial jets with swirl strength of 0.36. Inert

mixtures containing a combination of helium, argon and krypton were used in the core jet and air was used in the swirling annular jet. Figure 39 shows a cutaway of the nozzle and the axial plus tangential system used to produce swirling coaxial flow. The total air temperature was 300 K with a reservoir pressure of 8.82 bar resulting in an air flow rate of 175 g/s. The study also investigated the effect of fuel-to-air density ratio on mixing. The air-to-fuel density ratio at the injection plane varied from 35.5 for 100% helium to 2.29 with a 50/50 ratio of argon and krypton.

a) 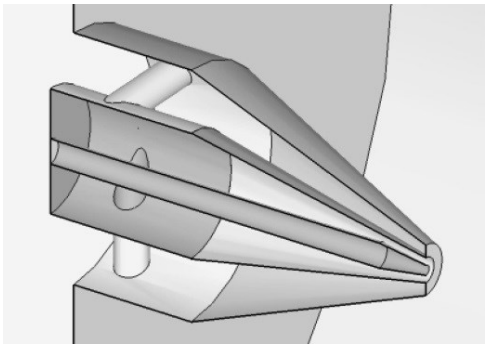 b) 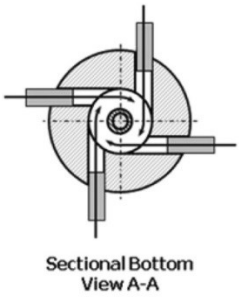

Figure 38 Schematic of axial plus tangential system for a supersonic nozzle
a) cutaway of nozzle, b) cross section al view of nozzle (See Figure 28)
[43]

The Mie scattering images of the non-swirling case and the swirling case are shown in Figure 40. Figure 40(a) compares well with the Schlieren image from Figure 30(a). The white horizontal lines in Figure 40 indicate the location of the first Mach discs in the jet flow. The Mie scattering images have a dark core area at the nozzle exit where there are few seeding particle. This area is believed to be composed of toroidal vortices of subsonic flow where the kinetic energy dissipates into viscous heating. It can be seen that swirl greatly influenced this area. Results indicated that even a small amount of swirl enhanced mixing in the jet. This can be seen

in the narrower subsonic core of the jet after the first Mach disc and in the smeared slip lines that separate the subsonic core from the supersonic outer jet. The slip lines can be considered to be shear layers. The compressible mixing layer thickness was found to increase with swirl. In addition a decrease in the air-to-fuel density ratio at the nozzle exit resulted in decreased mixing while a decrease in the core jet Mach number, or decreasing the compressibility of the core jet, resulted in increased mixing.

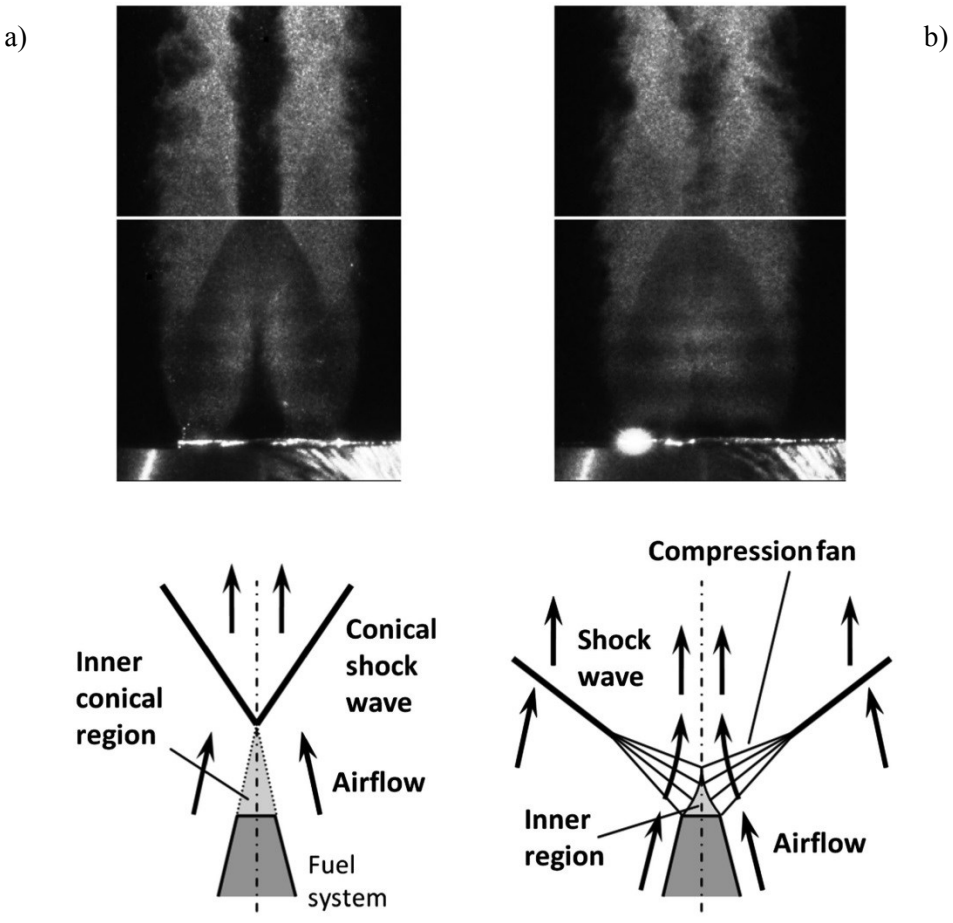

Figure 39 Mie scattering images of underexpanded airflow (no flow injection)
a) non-swirling, reservoir pressure = 7.91 bar, b) swirling, reservoir pressure = 8.82 bar
[43]

An experimental non-combustion investigation into fuel penetration using a pair of swirling jets was performed by Cutler and Johnson (1995). The study used injection at low angles with respect to the airflow of the tunnel [58]. The wind tunnel used convergent-divergent nozzle that provided Mach 2.0 air to the test section which was a 1.52 inches by 3.46 inches constant area duct. The airflow then exhausted into the laboratory for a short distance before being expelled from the building via a catch cone and muffler. The flow pressure in the duct was nominally atmospheric. Helium or air at ambient conditions was used to simulate fuel. Injection was accomplished by ramp injection or flush wall injection. Ramp injection angles were 10 degrees and 20 degrees with respect to the tunnel airflow and had swirl flow and was compared with flushed wall injection provided a single injected jet at 30 degrees with respect to the tunnel airflow. Effective penetration can be provided when a trailing vortex pair is created in the fuel-air plume. The vortex pair affects each other by moving the other vortex in a normal direction away from a line connecting the vortices centers. This allows the fuel to be moved away from the wall and into the airflow. Both the 10 degrees and 20 degrees twin swirl jets from the ramp produced greater jet penetration than for the 30 degree wall flushed non-swirling single jet. The 20 degrees twin swirl jets from the ramp produced greater jet penetration than the 10 degree twin swirl jet although it was not doubled.

Koike *et al*. (2005) investigated the flow field developed by ramp vortices interacting with two swirling jets without combustion [59]. Three configurations were tested; no jet swirl, jet swirl in same direction as the ramp vortices and jet swirl in opposite direction to the ramp vortices. A suction type wind tunnel was used for the test. Unheated atmospheric air was pulled through a two dimensional contoured nozzle resulting in a Mach number of 2.35 flowing through the test section before exhausting into a vacuum tank with 5 kPa of pressure. The constant area

test section was 30 mm by 30 mm and 330 mm in length. Air was injected into the flow from a 30 degree unswept ramp through two converging-diverging nozzles with throat and exit diameters of 2.7 mm and 3.5 mm respectively. The swirl number of the injectant was 0.22. Results were obtained from particle image velocimetry, PIV, and Mie scattering images. Results indicated that the case of jet swirl opposite in direction to the ramp vortices had greater jet spreading than the case of no swirl or jet swirl in the same direction as the ramp vortices.

3 Numerical Analysis

A variety of numerical simulation software is available with fluid dynamic capability. However, not all codes are capable of solving for supersonic/hypersonic flows. Some of the codes that have been used for numerical simulation of scramjets are NASA Langley's VULCAN, CRAFT CFD®, FLUENT and Wind-US. There are a number of experiments that can be used for validation of numerical simulations [60]. Some of the experiment data requirements that are to be used for validation of numerical simulations are that the flow field be relatively simple but has features relevant to high speed engine flow and have regions of subsonic flow and recirculation. The geometry model and boundary conditions should be well controlled and described and experimental uncertainties should be qualified. One such experiment (SCHOLAR) for a supersonic combustor was conducted in NASA Langley's Direct-Connect Supersonic Combustion Facility (DCSCTF) and the numerical analysis used VULCAN [61].

3.1 Computational Turbulence Models

The governing equations for unsteady, compressible, viscous, three dimensional flow are the Navier-Stokes equations described by equations 23 through 27. The have a mathematically elliptic behavior that allows flow field information and flow disturbances to travel downstream and upstream. The equations are in a form suitable for a time dependent solution.

Continuity: Equation 23

$$\frac{\partial \rho}{\partial t} = -\left[\frac{\partial(\rho u)}{\partial x} + \frac{\partial(\rho v)}{\partial y} + \frac{\partial(\rho w)}{\partial z}\right]$$

x momentum: Equation 24

$$\frac{\partial u}{\partial t} = -u\frac{\partial u}{\partial x} - v\frac{\partial u}{\partial y} - w\frac{\partial u}{\partial z} + \frac{1}{\rho}\left[-\frac{\partial p}{\partial x} + \frac{\partial \tau_{xx}}{\partial x} + \frac{\partial \tau_{yx}}{\partial y} + \frac{\partial \tau_{zx}}{\partial z}\right]$$

y momentum: Equation 25

$$\frac{\partial v}{\partial t} = -u\frac{\partial v}{\partial x} - v\frac{\partial v}{\partial y} - w\frac{\partial v}{\partial z} + \frac{1}{\rho}\left[-\frac{\partial p}{\partial y} + \frac{\partial \tau_{xy}}{\partial x} + \frac{\partial \tau_{yy}}{\partial y} + \frac{\partial \tau_{zy}}{\partial z}\right]$$

z momentum: Equation 26

$$\frac{\partial w}{\partial t} = -u\frac{\partial w}{\partial x} - v\frac{\partial w}{\partial y} - w\frac{\partial w}{\partial z} + \frac{1}{\rho}\left[-\frac{\partial p}{\partial z} + \frac{\partial \tau_{xz}}{\partial x} + \frac{\partial \tau_{yz}}{\partial y} + \frac{\partial \tau_{zz}}{\partial z}\right]$$

Energy: Equation 27

$$\begin{aligned}\frac{\partial (e + V^2/2)}{\partial t} = {} & -u\frac{\partial (e + V^2/2)}{\partial x} - v\frac{\partial (e + V^2/2)}{\partial y} - w\frac{\partial (e + V^2/2)}{\partial z} + \dot{q} \\ & + \frac{1}{\rho}\left[\frac{\partial}{\partial x}\left(k\frac{\partial T}{\partial x}\right) + \frac{\partial}{\partial y}\left(k\frac{\partial T}{\partial y}\right) + \frac{\partial}{\partial z}\left(k\frac{\partial T}{\partial z}\right) - \frac{\partial (pu)}{\partial x} - \frac{\partial (pv)}{\partial y} - \frac{\partial (pw)}{\partial z} + \frac{\partial (u\tau_{xx})}{\partial x}\right. \\ & + \frac{\partial (u\tau_{yx})}{\partial y} + \frac{\partial (u\tau_{zx})}{\partial z} + \frac{\partial (v\tau_{xy})}{\partial x} + \frac{\partial (v\tau_{yy})}{\partial y} + \frac{\partial (v\tau_{zy})}{\partial z} + \frac{\partial (w\tau_{xz})}{\partial x} + \frac{\partial (w\tau_{yz})}{\partial y} \\ & \left. + \frac{\partial (w\tau_{zz})}{\partial z}\right]\end{aligned}$$

There is no direct analytical solution for the above set of equations. However with the use of computers a numerical solution of the discretized equations can be attained. An important factor in simulating the flow accurately is the choice of turbulence model. Turbulent flow is dominated by continual fluctuating velocities and are inherently time dependent. Since there is no pure theory on turbulence any analysis of turbulent flow or turbulent boundary layers is based on empirical data [62].

The most common models are Reynolds-Averaged Navier-Stokes equation, RANS, based turbulence models. These models use the mean velocity instead of the time dependent fluctuation velocities and the Reynolds stresses [63]. CFD-Wiki is the basis for the following descriptions of RANS based turbulence models [64]. There are three categories of RANS based models: linear eddy viscosity models, nonlinear eddy viscosity models and Reynolds stress models.

Within the category of linear eddy models are a variety of models based on algebraic models, one equation models and two equation models. Of the one equation models (Prandtl's one-equation, Baldwin-Barth, Spalart-Allmaras) the Spalart-Allmaras model is more commonly used these days. This turbulence model solves a transport equation for a viscosity like variable. It is not recommended for flows where complex recirculation occurs. Of the two equation models the most widely used are the k-ε turbulence models and k-ω turbulence models. The k-ε turbulence models (standard k-ε, Realisable k-ε and RNG k-ε) are the most common models and describe turbulence by using two transport equations. The transport variables are turbulent kinetic energy, k and turbulent dissipation, ϵ. This model is a good compromise between robustness, computational cost and accuracy. These models are useful for flows with free-shear layer and small pressure gradients. The model is based on the assumption that the ratio of

turbulent stresses to rates of deformation are in one direction or isotropic. Another popular turbulence model is the k-ω turbulence models (Wilcox's k-ω, Wilcox's modified k-ω, SST k-ω). They are similar to k-ε turbulence models in that turbulence is described by using two transport equations. The transport variables are turbulent kinetic energy, k and specific dissipation, ω. The SST k-ω models are capable of integrating the transport variables through the viscous sublayer.

Nonlinear eddy viscosity models use an eddy viscosity coefficient to relate the turbulence field to the velocity field in a nonlinear relationship.

Reynolds stress transport (RST) models are higher level, complex turbulence models. This model has a higher computational cost than the linear eddy viscosity models. With this model the Reynolds stresses are directly computed.

Bui (2008) compared the modeling capabilities of a k-ε turbulence model versus a RST turbulence model in finding a solution involving turbulent flow in a stirred vessel that was highly anisotropic. Results showed that the k-ε turbulence model that is based on isotropic eddy viscosity assumptions was not able to provide reasonable solutions. The RST model performed much better but was computational expensive [65].

A RANS/LES model (combination of a RANS model and Large Eddy Simulation (LES) model) was used to simulate flow with a small swirl number. Results indicated that the length scales governing the swirl and axial velocity were different and simulations would be more accurate if they could cover a large range of mixing length scales [66].

Recent numerical studies of supersonic flow or interior scramjet flow field simulations have used k-ε, k-ω turbulence models or combinations of both. Numerical investigation of scramjet combustors with combustion conducted by Vyas (2010) [7] and Tourani (2011) [67]

used a k-ε turbulence, Mack (2006) [38] and Jianwen (2008) [68] used a k-ω turbulence model while Rodriguez (2005) [61] and Bhagwandin (2009) [69] used Mentor's SST k-ω turbulence model. However numerical studies using 2 equation k-ε turbulence models have been shown to under predict mixing rates for swirl flows.

3.2 Modeling Combustion for Computational Simulations

In most investigations of generic scramjet engines the fuel is usually a gas such as H_2 although other gases have been used to simulate fuel in the study of flow field characteristics. In situations where vitiation effects are studied, H_2O is added to the air flow. The X-43 used H_2 as fuel and the X-51 used ethylene to start the engine and then burned JP-7.

Chemical processes occur due to molecular collisions and/or radiative interactions. As the temperature of a gas increases the molecules will begin to dissociate. For instance oxygen gas, O_2, and nitrogen gas, N_2, start to dissociate at 2500K and 4000K respectively at 1 atm pressure [1]. Oxygen and hydrogen gases are inert but once dissociated oxygen and hydrogen atoms react energetically with each other and the main result of the reaction is water, H_2O.

For studies using H_2 as fuel the species group used has been as small as 4 species (H_2, O_2, N_2, H_2O) [29] and as large as 9 species (N_2, O_2, H_2O, H_2, OH, O, H, HO_2, H_2O_2) [61] [7] . The effects of NOx are not usually modelled in most studies. Kindler *et al.* (2011) [70] investigated NOx formations in scramjet combustors. The study showed that NOx emissions were dependent on the type of fuel injection method, the flight Mach number and the boundary layer thickness in the combustor.

Two parameters that have a substantial effect on combustion modelling and the subsequent numerical simulation are the turbulent Schmidt number and the turbulent Prandtl

number. The turbulent Schmidt Number, Sc_t, affects the mixing behavior of the various species. It is defined as follows:

$$Sc_t = \frac{momentum\ diffusivity}{mass\ diffusivity} \qquad \text{Equation 28}$$

Increasing the value of Sc_t reduces the mixing capability and increases the possibility of a flameout. Decreasing the value of Sc_t increases mixing, decreases ignition delay and causes higher pressure rise in the combustor that can lead to shock waves travelling upstream and unstarting the engine [69], [7]. Typical values of Sc_t are 0.7 – 0.9.

Another turbulent flow property is the turbulent Prandtl Number, Pr_t, which is defined in equation 29.

$$Pr_t = \frac{momentum\ diffusivity}{thermal\ diffusivity} \qquad \text{Equation 29}$$

Pr_t affects reaction rates. Decreasing the value of Pr_t reduces the rate of reaction and delays ignition. The typical value for Pr_t is 0.9. However, Sc_t has a greater effect on ignition and combustion behavior since Sc_t affects the concentration of species and therefore chemical reaction.

If the chemical reaction is considered to be in a chemical equilibrium state then statistical thermodynamics can be used for simulating the combustion. STAR-CCM+ uses a Chemkin database [71] for statistical thermodynamics to create a table to model chemical equilibrium.

For a chemical non-equilibrium state the reactions of the species can be modeled using kinematic mechanism tables. STAR-CCM+ uses a flamelet model to simulate chemical non-equilibrium combustion. The flamelet model is used when the chemical time scale is short compared to the convection and diffusion times as is the case with combustion in a scramjet. The advantage of using a flamelet model is the ability to account for ignition and extinction [72] [68]. In addition a numerical study by Jianwen (2008) indicated that the turbulence/combustion interaction at the flame ignition vicinity was not negligible and that a flamelet model simulated the turbulence/combustion interaction well when compared to experimental results [68]. In a flamelet model combustion is modelled in asymptotically thin layers that are embedded in turbulent flow as shown in Figure 40. CD-adapco uses Veynante and Vervisch (2002) turbulent combustion modelling techniques [73] to create a flamelet library with another CD-adapco software called DARS. DARS directly solves the flamelet equations and constructs library tables over a range of EGRs, oxidizer pressures and temperatures for a specified fuel temperature and pressure [71]. The table is then exported to STAR-CCM+ to simulate combustion.

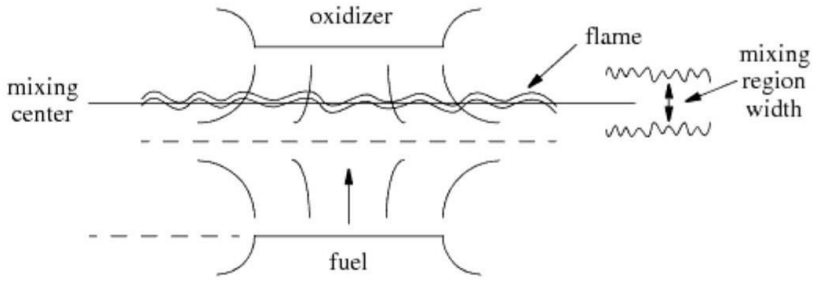

Figure 40 Schematic of a flamelet model [71]

4 Supersonic Combustion Chambers

Institutions such as NASA Langley in the USA, DLR in Germany, the University of Queensland under the Australian Hypersonic Initiative have been investigating hypersonic vehicles through flight tests, experiments and numerical simulations. In recent years there have been successful flights of hypersonic vehicles such as the X-51 WaveRider and the HyShot research vehicles. Flight test data is not excessive due to the expense of such projects and the difficulty of obtaining data. Experimental data can be obtained using supersonic wind tunnels and shock tunnels to simulate flow in supersonic combustion chambers. However, not all facilities are capable of combustion and these facilities are costly to build and operate. The supersonic wind tunnel is usually built to represent the isolator, combustion chamber and nozzle of a scramjet engine. In this section two such supersonic combustion chambers and consequent experimental and numerical data from previous investigations will be reviewed.

4.1 NASA Langley Direct-Connect Supersonic Combustion Test Facility

4.1.1 Test Facility

The Langley DCSCTF is used to test ramjet and scramjet combustor models. Information from a NASA brochure [74] provided details on the facility for this section. The facility is capable of duplicating stagnation enthalpies that correspond to flight between Mach 4 and Mach 7.5 [74]. The facility is directly connected to the combustor model so that the entire test gas mass flow will flow through the model. The flow from the facility nozzle exit simulates the flow entering the combustor of a ramjet or scramjet. The combustor model can exhaust freely, or directly to an air ejector or to a vacuum sphere.

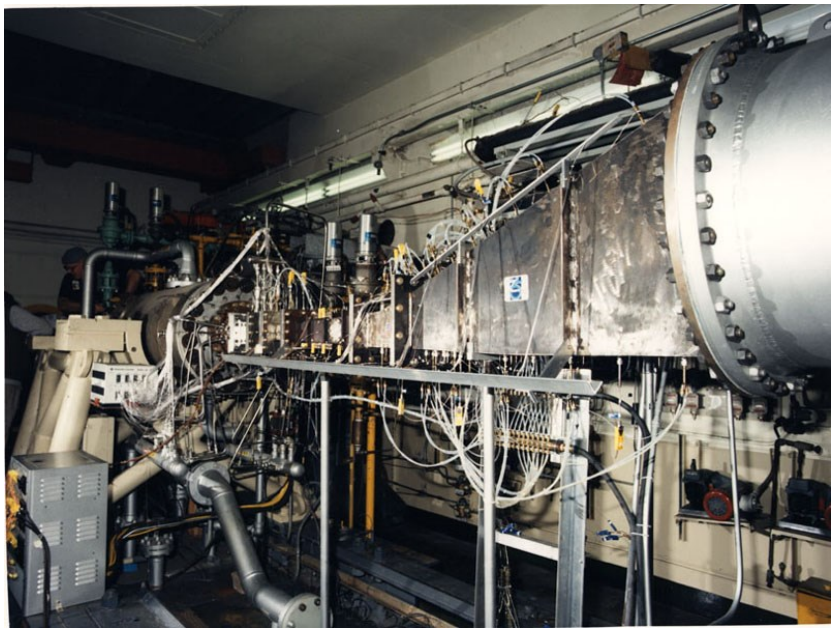

Figure 41 The Direct-Connect Supersonic Combustion Test Facility (DCSCTF) Combustor Test Section
[74]

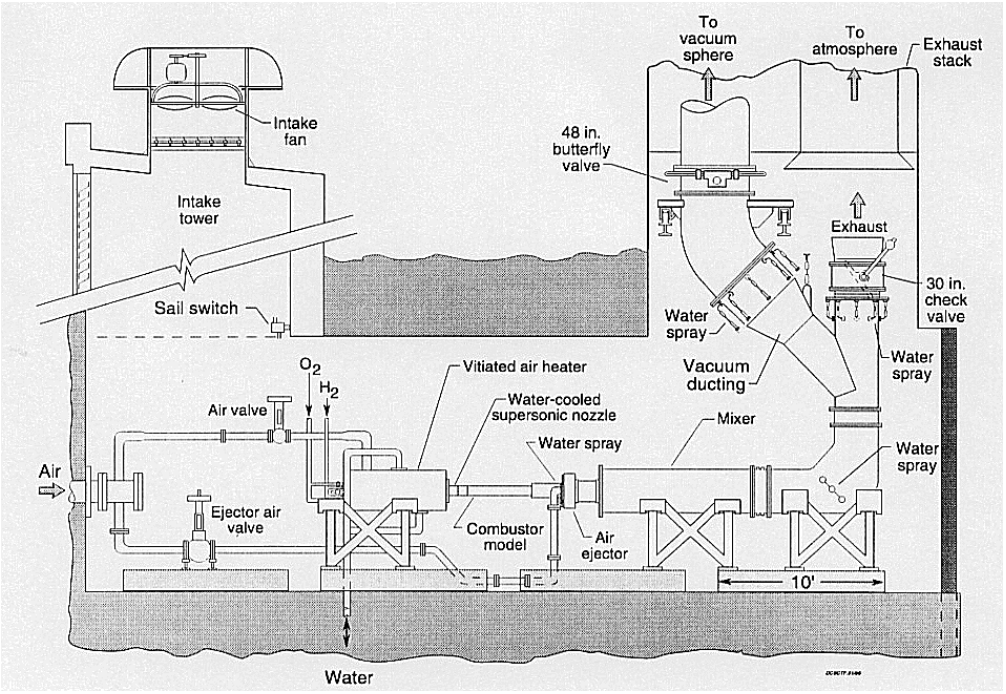

Figure 42 Schematic of DCSCTF
[74]

The DCSTF shown in Figure 42 is located in a 16' x 16' x 52' test cell with forced air ventilation [74]. Test air is regulated at 550 psia prior to entering the test cell. Hydrogen gas, oxygen and nitrogen gas are supplied separately through tube trailers and are regulated to 720 psia, 720 psia and 230 psia respectively. The DCSTF uses a hydrogen and air combustion heater. Oxygen is added to the airstream and premixed and then hydrogen is added to the air/oxygen mixture. Ignition is achieved with an electric spark activated hydrogen and oxygen torch igniter. The heated test gas then flows through the facility nozzle into the combustor model. There are currently two facility nozzles available. Both are rectangular contoured nozzles. The first is a Mach 2 nozzle with throat dimensions of 0.846" x 3.46" and exit dimensions of 1.52" x 3.46". The second facility nozzle is a Mach 2.7 nozzle with throat dimensions of 0.356" x 6.69" and exit dimensions of 1.5" x 6.69". The primary fuel used in the DCSCTF is gaseous hydrogen. The hydrogen supplied to the fuel injector comes from the same tube trailers as the hydrogen gas for the facility heaters but may be used at the maximum pressure of 2400 psia. Oxygen can also be supplied to the combustor models at 2400 psia. The pilot and igniter for the combustor model is a 20% silane and 80% hydrogen mixture (by volume). The DCSCTF can operate between heater stagnation pressures of 115 to 500 psia and temperatures between 1600°R and 3800°R. The test gas mass flow rates are between 1 to 7 pounds mass per second. The average run for a test lasts 20 to 30 seconds.

4.1.2 SCHOLAR

SCHOLAR is a benchmark case of supersonic combustion that was conducted at NASA Langley DCSCTF for the purpose of providing data for CFD validation. The test case was designed to be simple by avoiding subsonic/recirculating flow. However, it was discovered that

the chemical reactions lagged mixing so that most of the combustion occurred well downstream of fuel injection. This resulted in a more challenging test case to model for CFD simulation than was originally intended [61].

The work of Rodriguez *et al.* (2003) is the basis for the description of the experiment in this section [75]. The combustor model used for the SCHOLAR experiment is shown in Figure 43(a). The combustor model consisted of a constant area isolator that ended with a step on the top wall. This was followed by another constant area section and then the top wall diverged at a 3° angle until the model nozzle exit. The section containing the isolator, injector and a portion of the divergent nozzle was constructed of copper while the rest of the model was made of carbon steel. The combustor model required no cooling due to the thermal conductivity and thickness of the fabrication materials. The fuel injector was located on the top wall at the location where the top wall started to diverge.

Hydrogen gas was used as the fuel and it was injected at an angle of 30° from the horizontal into the vitiated air flow. The fuel injection nozzle was designed to produce Mach 2.5 flow at its exit with a stagnation pressure of 3.44 ± 0.07 MPa and a stagnation temperature of 302 ± 4 K. The five pilot injectors shown in Figure 43(b) were not used for this experiment.

For this experiment vitiated air was used as the test gas. The vitiated air was heated in the combustion heater to a stagnation enthalpy corresponding to Mach 7 flight. The vitiated mass flow rate was 1.24 kg/s. The heater stagnation pressure was 0.765 ± 0.008 MPa. The nominal heater stagnation temperature was found to be 1827 ± 75 K. The vitiated air was then accelerated through the Mach 2 facility nozzle to produce facility nozzle outlet conditions of Mach 1.989 ± 0.005, static temperature of 1187 ± 60 K and a static pressure of 100 ± 1.5 kPa. The facility nozzle exit condition was the combustor model inlet condition.

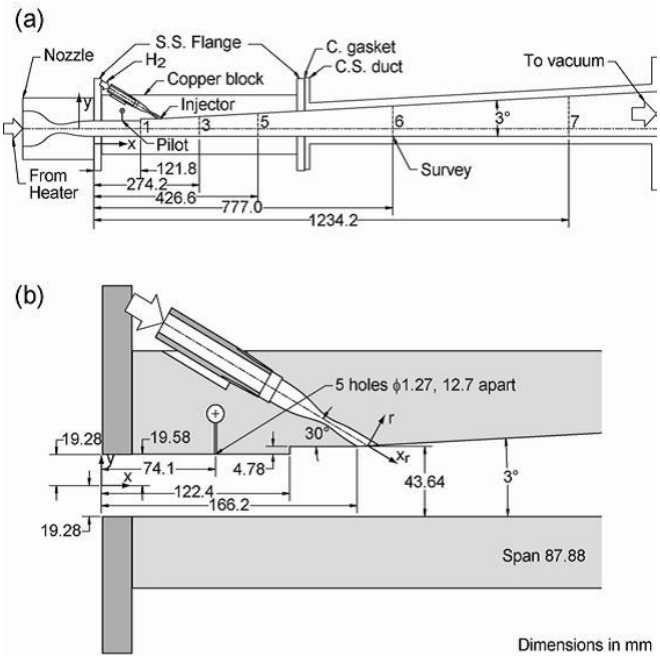

Figure 43 Schematic of SCHOLAR Combustor model: (a) details of combustor model (b) details of fuel injection section [61]

The combustor model was instrumented with static pressure taps located on the centerline of the bottom wall. Static pressure taps were also located on the top wall near to the sidewall in the copper section and centerline for the carbon steel section of the model. There were additional static pressure taps on the side wall of the carbon steel section. Data from the static pressure taps are shown in Figure 44 [61]. Temperature was measure with thermocouples located on the top wall of the model. There are 7 transverse slots in the combustor model located at the locations numbered 1, 3, 5, 6 and 7 shown in Figure 43(a). The slots are used to measure static temperature fields by Coherent Anti-Stokes Raman Spectroscopy, CARS, beams. The results are shown in Figure 45 [75].

(a)

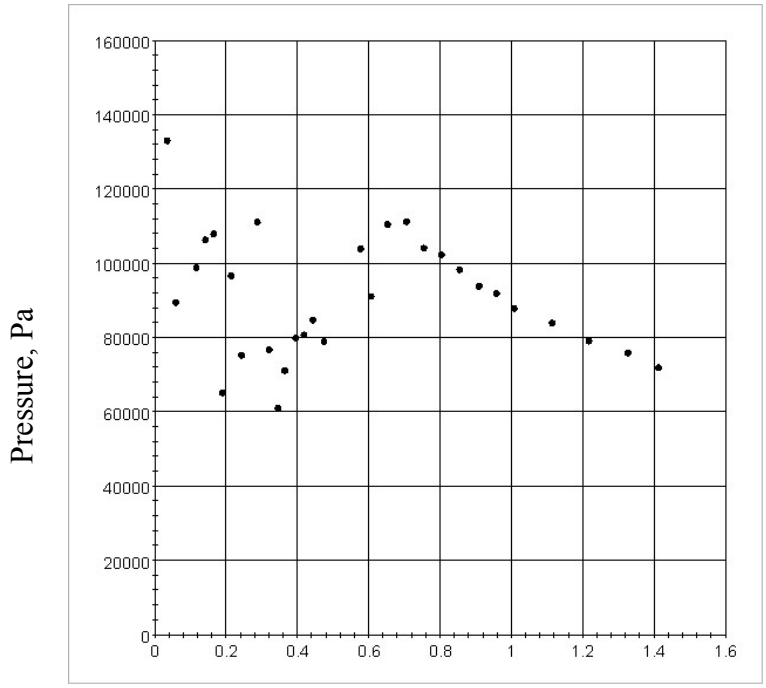

(b)

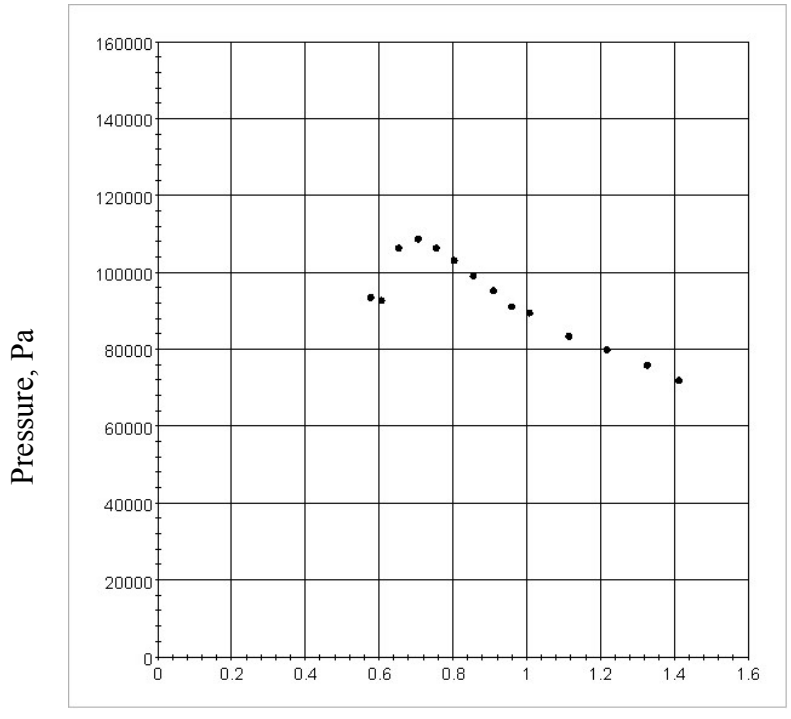

Figure 44 Centerline wall pressures: (a) bottom wall, (b) top wall [61]

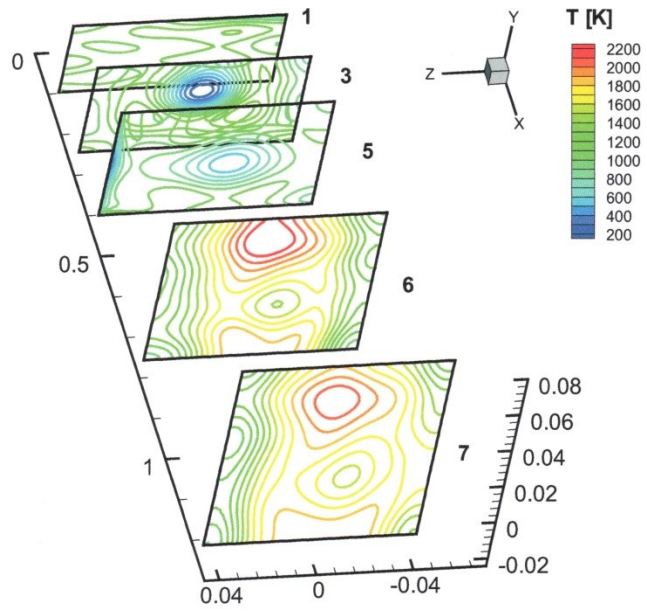

Figure 45 Cutaway planes with contours of mean temperature (dimensions in meters)
[75]

4.2 University of Virginia Supersonic Combustion Facility

4.2.1 Test Facility

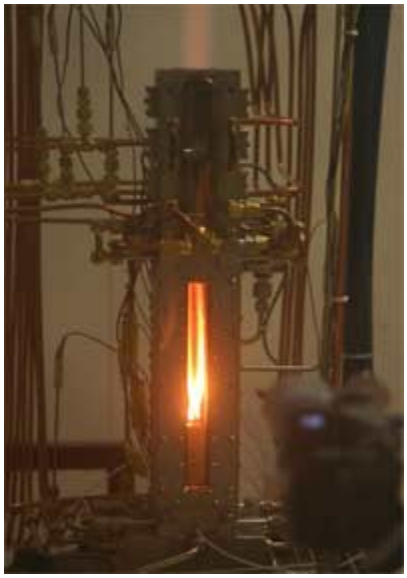

Figure 46 University of Virginia Supersonic Combustion Facility (UVaSCF)
[76]

The University of Virginia Supersonic Combustion Facility has the capability to obtain experimental data representative of a scramjet engine corresponding to flight at Mach 5. The works of Bhagwandin *et al.* (2009) and Vyas *et al.* (2010) are the basis for the description of the experiments and facility in this section. Air flow from the facility convergent divergent nozzle exit simulates flow entering the isolator of the scramjet engine which then passes through the combustor and finally exhaust to ambient air. A schematic of the facility is shown in Figure 47.

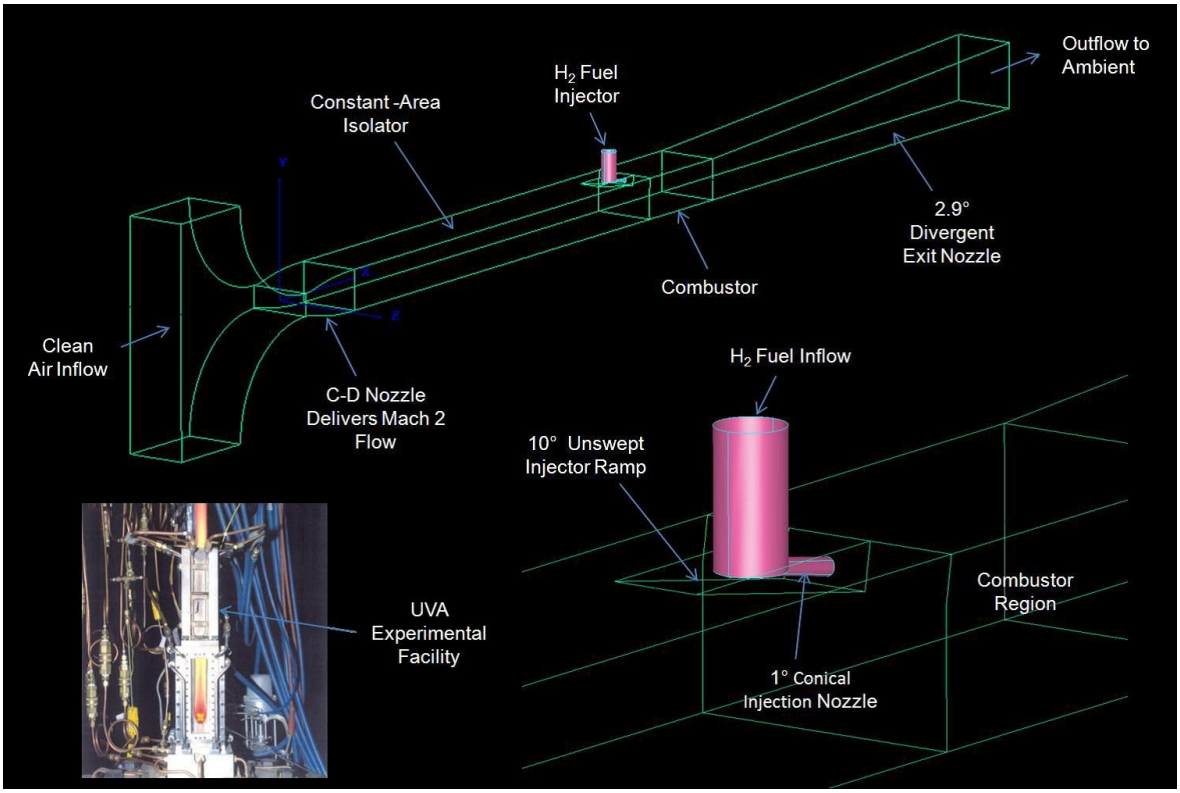

Figure 47 Experimental Configuration of the University of Virginia Supersonic Combustion Facility
[69]

The facility supply nozzle is connected to a 300 kW electrical resistance heater which accomplishes air heating to approximately 1200 K for clean air experiments. The facility is also capable of providing vitiated air by adding steam to the airflow from an external source upstream

of the heater. Oxygen gas is also added to the airflow to obtain 21% mass fraction to the airflow. The facility nozzle is a rectangular contoured nozzle that delivers Mach 2 air flow to the inlet of the isolator. The facility's convergent divergent nozzle has a throat dimension of 0.395" x 1.5" and exit dimension of 1.0" x 1.5" [7]. Hydrogen is used to fuel the combustor.

The airflow from the facility nozzle exits into a constant area isolator and then continues to the fuel ramp region. The compression ramp in the fuel ramp region has a width of 0.5" and a normal height of 0.25". The compression ramp has an angle of 10° into the airflow. The test gas flows into a constant area combustor. At the exit of the combustor the top wall diverges at a 2.9° angle to the nozzle exit. Exhaust gases are captured by a catch-cone and directed vertically out of the building. The fuel injector is located within the fuel ramp region as shown in Figure 47 and designed to deliver Mach 1.7 fuel flow at the injector exit. Combustion ignition is achieved with an oxygen-hydrogen wave igniter. With the exception of the fuel injector and 3 optical windows, the components of the facility were cooled with water [69] [7].

Additional dimensions for the UVaSCF are provided in Figure 48.

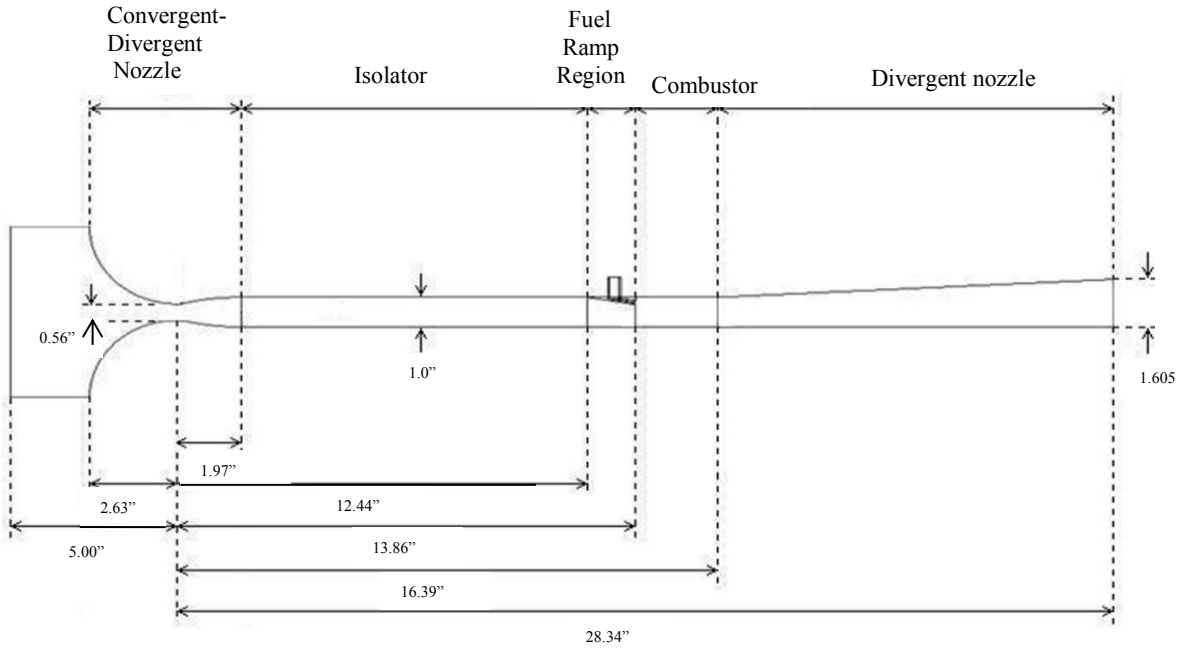

Figure 48 Dimensions of the University of Virginia Supersonic Combustion Facility [69]

4.2.2 Experimental Data

The experimental data collected from test runs using the UVaSCF are in the form of temperature and pressure measurements that are taken along the centerline of the top wall. Data from test runs are presented in this section. Table 1 provides the operating conditions of the UVaSCF for the various runs. The naming convention for each experimental test is the same as used in the reference for each test. Scan4 Case1 was run as a no combustion case with no fuel injected into the airflow. Test cases Scan 14 tand Scan 18 were run with fuel added and combustion. Data of static pressure measured along the centerline of the top wall is shown in Figure 49.

Table 1 Conditions for Three Experimental Cases

	Experimental Cases		
Research Paper	[69]	[69]	[7]
Experimental Case	Scan4 Case1	Scan 14	Scan 18
Clean Air Inlet Total Conditions	P_0 = 331 kPa T_0 = 1033 K $\dot{m}$ = 0.220 kg/s	P_0 = 330 kPa T_0 = 1203 K $\dot{m}$ = 0.203 kg/s	P_0 = 326.87 kPa T_0 = 1203 K $\dot{m}$ = 0.196 kg/s
Clean Air Species	Air	21% O_2 79% N_2	21% O_2 12% H_2O 79% N_2
CD Nozzle Exit Mach Number	M = 2	M = 2	M = 2
H_2 Fuel Inlet Total Conditions	No Fuel Injection $\dot{m}$ = 0 kg/s	P_0 = 829 kPa T_0 = 297 K $\dot{m}$ = 1.54E-3 kg/s	P_0 = 829.67 kPa T_0 = 298.64 K $\dot{m}$ = 1.59E-3 kg/s
Fuel Injector Exit Mach Number	N/A	M = 1.7	M = 1.7
Ambient Exit Pressure	101.3 kPa	102.7 kPa	99.1 kPa
Wall Temperatures			
Inflow & C-D Nozzle	375 K	410 K	N/A
Isolator	375 K	428 K	N/A
Fuel Ramp Region & Combustor	Adiabatic	Adiabatic	1000 K
Divergent Nozzle	400 K	500 K	N/A
Fuel Injector	Adiabatic	Adiabatic	N/A

(a)

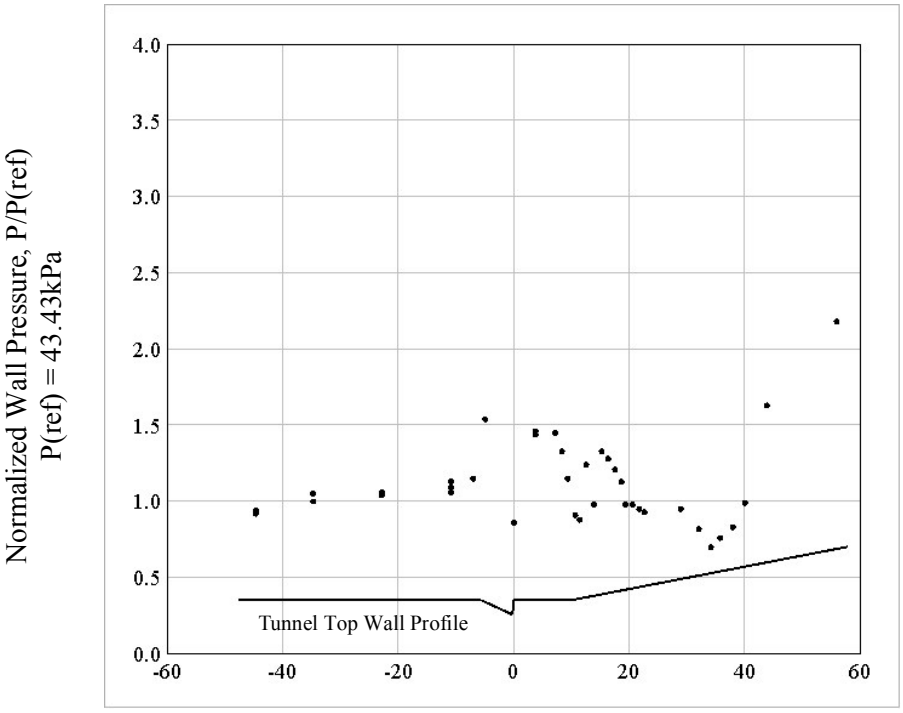

(b)

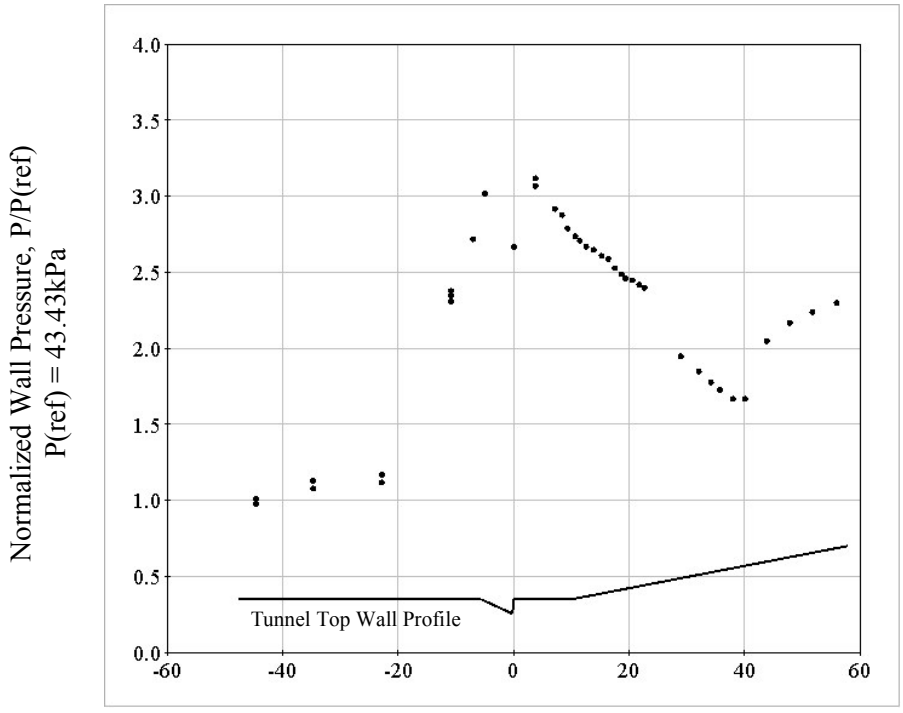

Figure 49 Wall static pressure along axial centerline:
(a) Scan4 Case1, (b) Scan 14

(c)

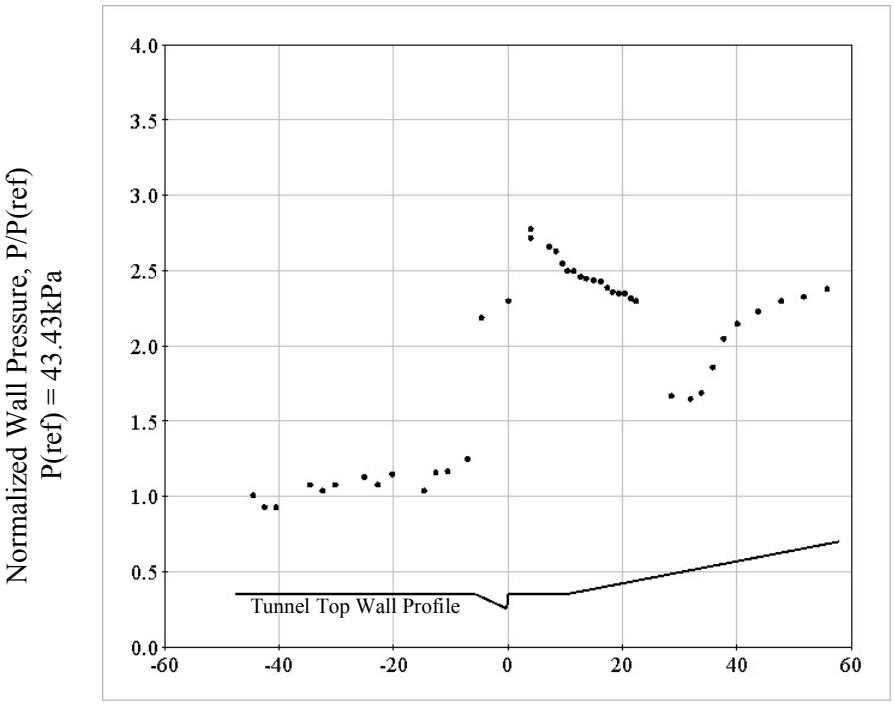

Figure 49 Wall static pressure along axial centerline:
(c) Scan 18

P(ref) is the absolute static pressure at the inlet of the isolator. The zero axial point is located at the start of the combustor so that the isolator and fuel ramp region is shown in negative axial distance. The axial distance, x, is normalized by the vertical height of the fuel injector ramp, $H = 0.25$”.

5 Computational Fluid Dynamic Simulation Validation

This chapter presents the evaluation of the computational fluid dynamic (CFD) simulation that will be used to study mixing enhancement within the combustor of a scramjet. The simulation software used is STAR-CCM+ and the combustor used for the study of fuel nozzle swirl is based on the geometry of the University of Virginia's Supersonic Combustion Facility (UVaSCF).

STAR-CCM+ is a single integrated simulation package that provides numerical solutions involving flow, heat transfer and stress [70]. The software package includes pre-processing, solving and post-processing capabilities.

The capabilities and a description of the UVaSCF were discussed in Section 4.2. The three test runs shown in Table 1 will be simulated with STAR-CCM+. The simulations will be compared and evaluated with the experimental data and Wind-US CFD numerical solutions. The Wind-US CFD parameters used for the numerical solution will be used as closely as possible for the STAR-CCM+ simulations for comparison purposes.

5.1 Simulation Cases

Since the tunnel is symmetrical and symmetrical flow is expected half the tunnel width was used for the simulation. The simulations used a medium grid size of approximately 300 K cells that was chosen after a grid sensitivity study. The no combustion case referred to as Scan4 Case1 ran for 1300 iterations to obtain a converged solution. The simulations for the chemically reacting combustion cases Scan14 and Scan18 were run for a total of approximately 8000 and

2400 iterations respectively to obtain a converged solution. Convergence of the numerical solution for chemically reacting combustion cases was determined by the following:

- residuals of Navier-Stokes equations
- mass flow balance sum of zero
- successive profile of absolute static pressure along top wall centerline of engine
- constant mass fraction of water at nozzle exit

Cases simulating chemically reacting combustion used a multi gas component model based on 9 species; O, O_2, H, H_2, OH, H_2O, HO_2, H_2O_2 and N_2. The chemical reactions for a non-equilibrium state for O_2 and H_2 are shown in Table 3. There are 19 reversible reactions with one third body species, or catalysts, represented by *M*. Kinematic mechanism tables for H_2 and O_2 are calculated using Arrhenius coefficients and NASA polynomials for a range of gas pressures and temperatures.

Table 2 Chemical reactions for H_2 and O_2

$O_2 + H \Leftrightarrow OH + O$	$2HO_2 \Leftrightarrow H_2O_2 + O_2$
$H_2 + O \Leftrightarrow OH + H$	$2OH + M1 \Leftrightarrow H_2O_2 + M1$
$H_2 + OH \Leftrightarrow H_2O + H$	$H_2O_2 + H \Leftrightarrow H_2 + HO_2$
$2OH \Leftrightarrow H_2O + O$	$H_2O_2 + H \Leftrightarrow H_2O + OH$
$H + O_2 + M1 \Leftrightarrow HO_2 + M1$	$H_2O_2 + O \Leftrightarrow OH + HO_2$
$HO_2 + H \Leftrightarrow 2OH$	$H_2O_2 + OH \Leftrightarrow OH + HO_2$
$HO_2 + H \Leftrightarrow H_2 + O_2$	$2H + M1 \Leftrightarrow H2 + M1$
$HO_2 + OH \Leftrightarrow H_2O + O_2$	$H + OH + M1 \Leftrightarrow H_2O + M1$
$HO_2 + H \Leftrightarrow H_2O + O$	$2O + M1 \Leftrightarrow O_2 + M1$
$HO_2 + O \Leftrightarrow OH + O_2$	

The turbulence model chosen for these simulations was a SST k-ω turbulence model. This model has the advantage of using the k-ω formulation in the boundary layer so that the model is usable through the viscous sub layer and to the wall and acts like a k-ε model in free stream where the k-ω model can be too sensitive [64].

A Courant-Friedrichs-Lewy number, *CFL*, of 5 was used for the simulations. This allowed the simulations to run faster but not cause the solution to be unstable.

Table 2 shows the similarity and differences between the numerical parameters for the two software solutions.

Table 3 CFD Numerical Parameters for Three Simulation Cases

Research Paper	**[69]**		**[69]**		**[7]**	
Experimental Case	Scan4 Case1		Scan 14		Scan 18	
CFD Software	Wind-US	STAR-CCM+	Wind-US	STAR-CCM+	Wind-US	STAR-CCM+
Grid Size	≈ 435 K	≈ 310 K	≈ 435 K	≈ 310 K	≈ 435 K	≈ 310 K
Number of Iterations	≈ 5 K	≈ 1.3 K	≈ 5 K	≈ 8 K	N/A	≈ 2.5 K
Turbulent Model	B.L. - k-ω F.S. - k-ε	k-ω	B.L. - k-ω F.S. - k-ε	k-ω	k-ε	k-ω
Turbulent Schmidt Number, Sc_t	0.9	0.9	1.1	1.1	0.6	0.6
Turbulent Prandtl Number, Pr_t	0.9	0.9	0.9	0.9	0.9	0.9
Courant-Friedrichs-Lewy Number, CFL	0.5 – 1.0	5	0.5 – 1.0	5	0.5 – 1.0	5

Note: B.L – boundary layer, F.S – free stream

5.1.1 Grid Sensitivity Study

In order to assess the accuracy of the numerical solution a grid sensitivity study was performed. The variation of solutions from grids of different refinement is one indication as to the accuracy of the solution. For this study three different grid sizes were used to simulate a solution using test conditions and CFD parameters for Scan4 Case1. The coarse, medium and fine grids consisted of 73K, 305K and 1108K cells respectively. Figure 50 shows the normalized absolute static pressure, *P/P(ref),* measured on the top wall along the axial distance of the UVaSCF tunnel. The results from Figure 50 show the majority of inaccuracy will occur in the divergent nozzle when the axial position $x/H > 32$. It can also be seen that the grid size had little effect on the results of the normalized wall pressure in the isolator. The accuracy in the combustor at axial locations $x/H \approx 0.9$, 4.5 and 11.0 for the coarse grid with respect to the fine grid was 12.6%, -2.7% and 16.5% respectively. The accuracy of the medium grid with respect to the fine grid results in the combustor at axial locations $x/h \approx 0.9$, 4.5 and 11.0 was 6.3%, -0.2% and 8.1% respectively. The iteration solver time for the coarse, medium and fine grids were 28.4 minutes, 2.25 hours, and 10.48 hours per 1000 iterations respectively. Since this study is primarily interested in investigating flow characteristics within the combustor and due to the higher time costs of the fine grid, simulations were run with the medium grid. The medium grid used in this research for the UVaSCF is shown in Figure 51.

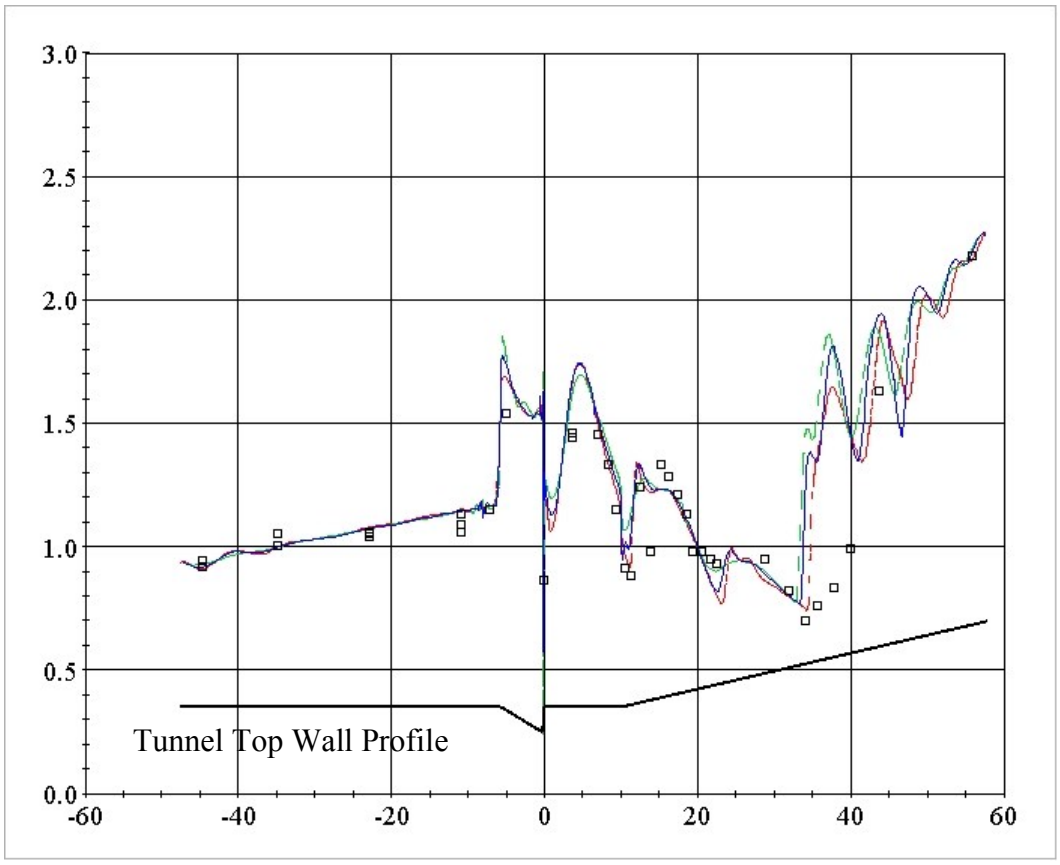

Figure 50 STAR CCM+ Grid Sensitivity Study Scan 4 Case 1; Coarse, Medium and Fine Grid

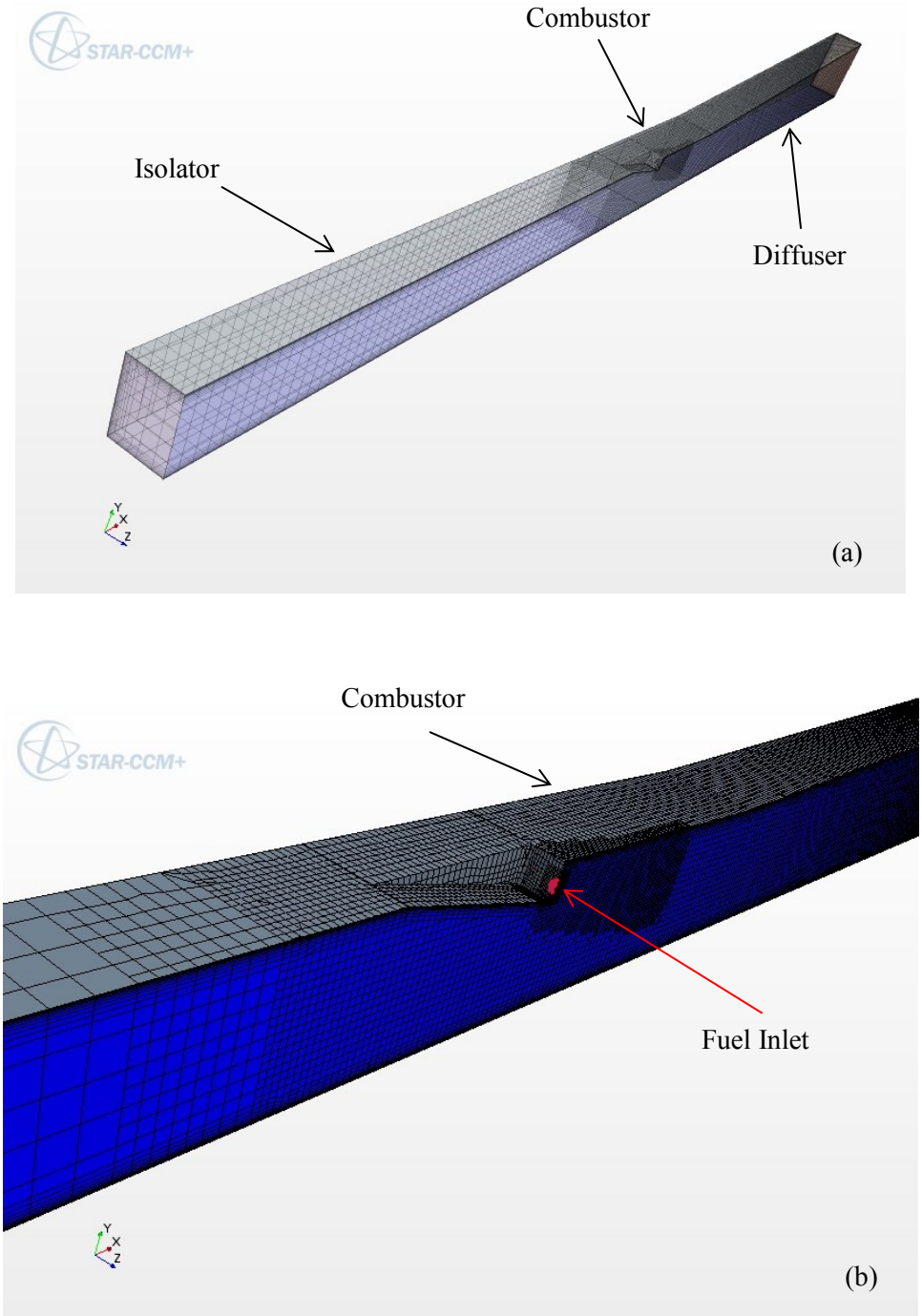

Figure 51 STAR-CCM+ 3-D Medium Grid of Isolator, Combustor and Nozzle Half Sections
a) full tunnel, b) detail showing fuel inlet in magenta

5.1.2 Scan4 Case1

The result for the no fuel run of the UVaSCF is shown in Figure 52. The test conditions are in Table 1 and experimental data of the static pressure on the centerline of the top wall is from Figure 49(a). STAR-CCM+ was capable of simulating the conditions of the isolator and fuel ramp region very well. The simulation results agree with the experimental data for the combustor also. Discrepancies between the simulation result and the experimental data start to have greater variance in the diverging the nozzle. The section where the simulation results do not agree with experimental data is approximately at x/H= 32 through x/H = 45. This is probably due to incorrect predication of the separated air flow on the top wall of the divergent nozzle.

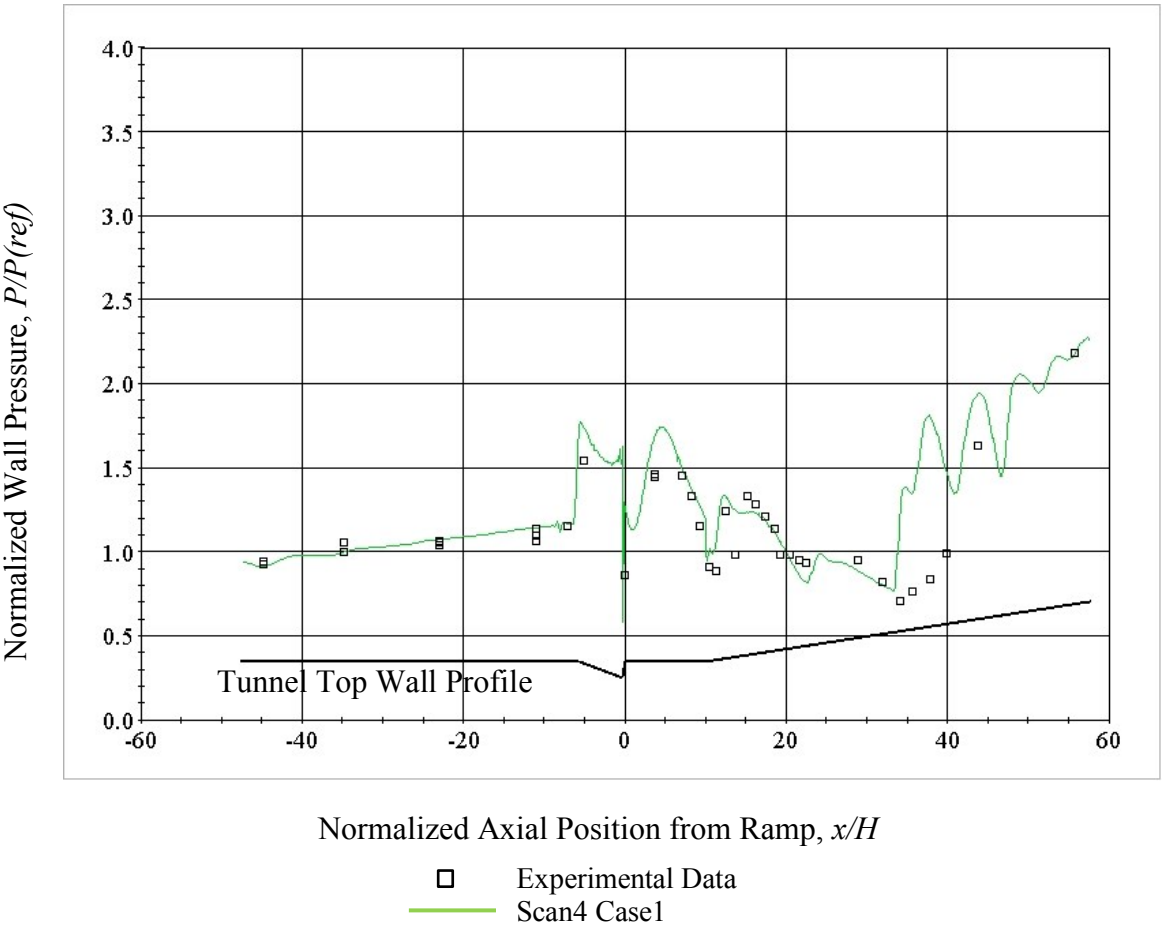

Figure 52 STAR-CCM+ Results: Top wall static pressure along the axial centerline for Scan4 Case1

Figure 53 shows numerical results with Wind-US [69]. Test case Scan4 Case1 is listed as Φ=0 WIND-US Case 1 and the numerical result is represented by the green line. The simulation results from STAR-CCM+ shown in Figure 52 compare well with the Wind-US simulation results. The STAR-CCM+ simulation agreed with experimental data for a longer axial distance downstream of the combustor exit.

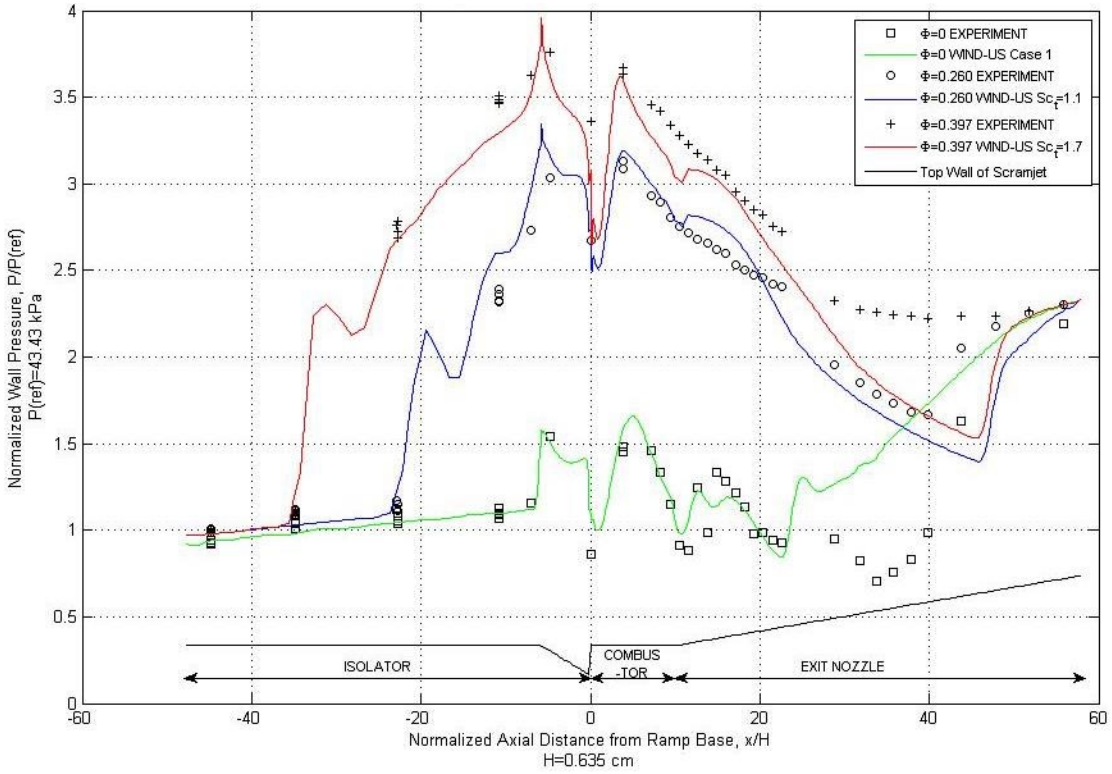

Figure 53 Wind-US Results: Top wall static pressure along the axial centerline [69]

In Scan4 Case1 there is no fuel injection and no combustion. Although the STAR-CCM+ simulation does not account for the inflow and convergent-divergent nozzle that is connected to the inlet of the isolator, the static pressure contours located on the symmetry plane shown in Figures 54 compare very well with the results from Wind-US shown in Figure 55. Both results

show the initial oblique shock wave due to the ramp, the reflected shock waves and expansion waves clearly. Both simulation results also show the increase in static pressure to indicate the location of a shock wave in the divergent nozzle.

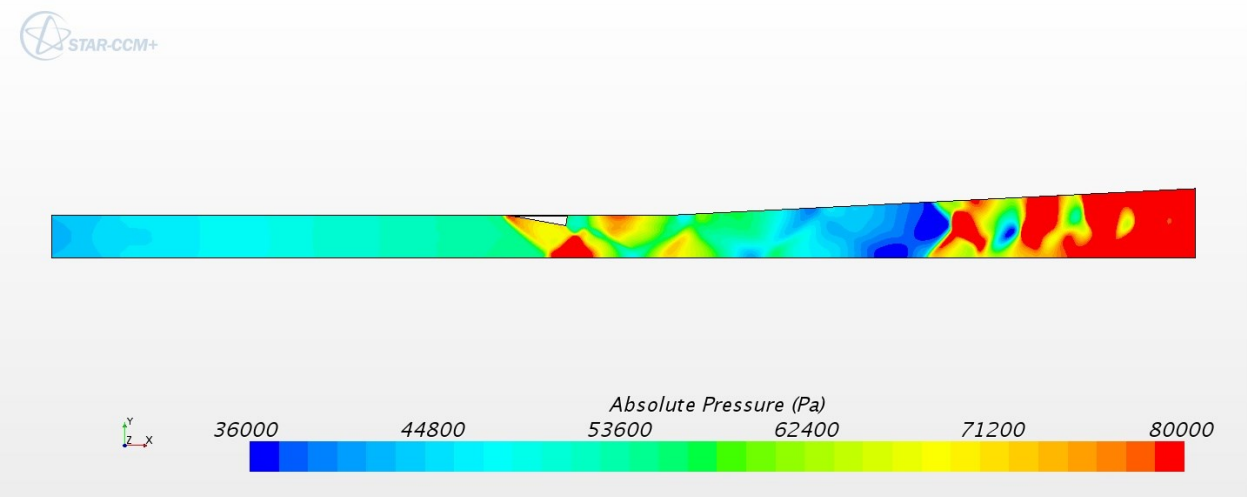

Figure 54 STAR-CCM+ Results: Static pressure contours (Pa) on the symmetry plane (z=0) for Scan4 Case1

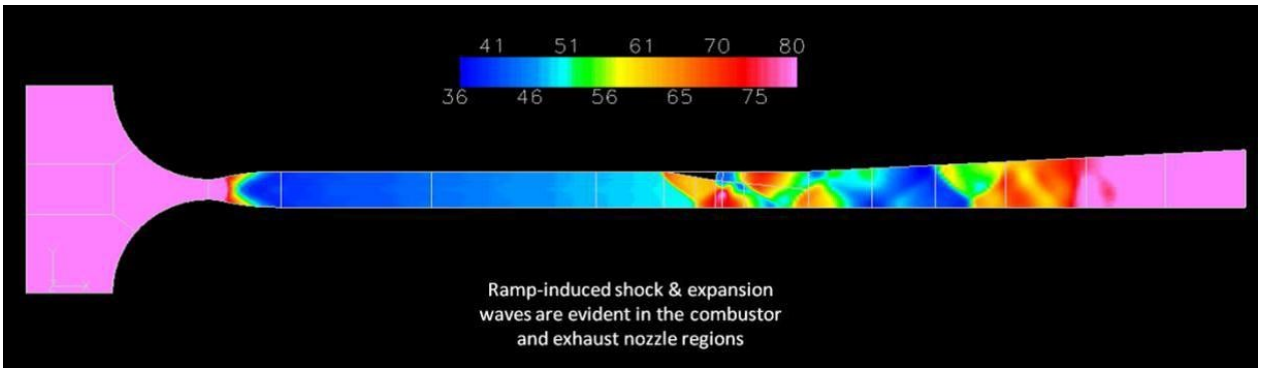

Figure 55 Wind-US Results: Static pressure contours (kPa) on the symmetry plane (z=0) for $\Phi = 0$; clean air
[69]

5.1.3 Scan14

The STAR-CCM+ simulation result for Scan 14 is shown in Figure 56. For this simulation chemical combustion was modeled. The simulation used a multi-gas component model based on 9 species; O, O_2, H, H_2, OH, H_2O, HO_2, H_2O_2 and N_2. The simulation was run twice. The first simulation used a combustion model that assumed local instantaneous chemical equilibrium called a presumed probability density function, PPDF, model and the second used a non-equilibrium model in the form of a flamelet.

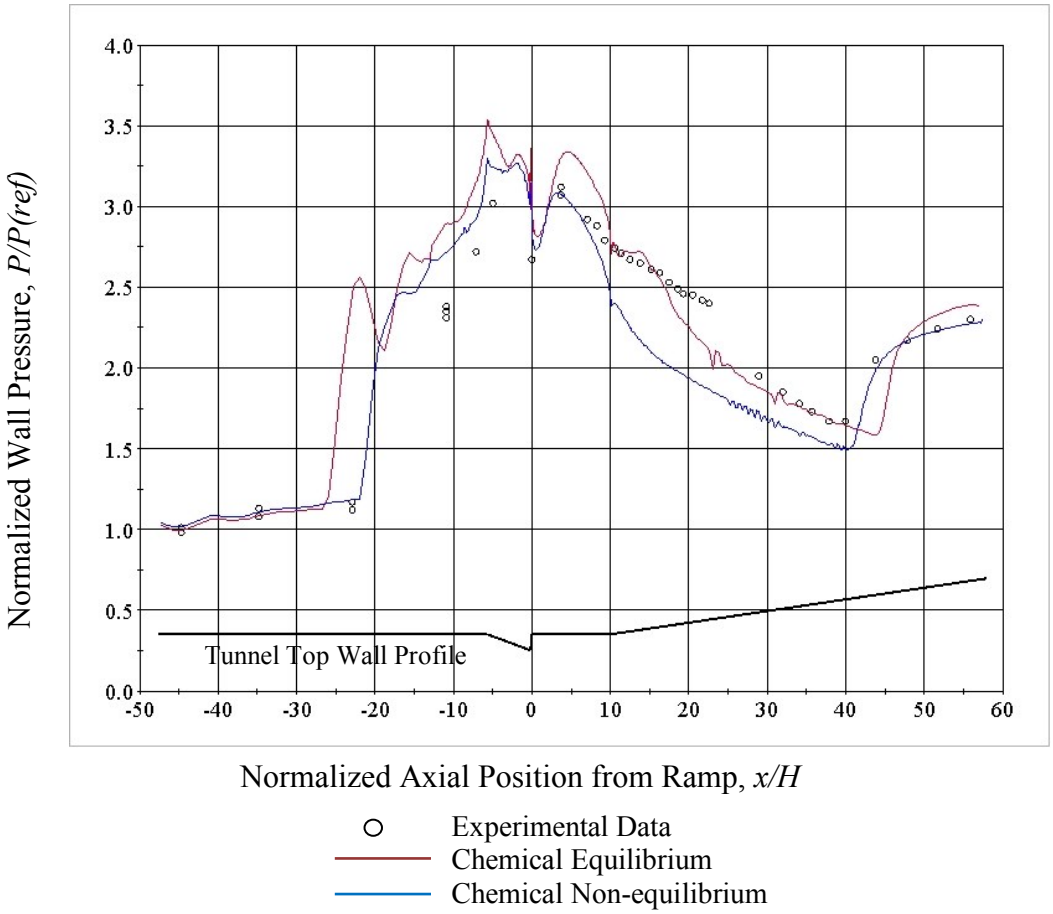

Figure 56 STAR-CCM+ Results: Top wall static pressure along the axial centerline for Scan14

As previously stated in Chapter 2.2.1 the gases in the combustor are expected to experience chemical non-equilibrium combustion but then reach chemical equilibrium by the combustor exit.

The results from the chemical non-equilibrium simulation were closer to the pressure ratio experimental data than the chemical equilibrium simulations at axial locations $x/H \approx -47$ through 7 and then from $x/H \approx 42$ through 58. The chemical equilibrium simulation provided more accurate results than the non-equilibrium simulation from $x/H \approx 7$ through 42. This would indicate that the exhaust gas reached chemical equilibrium near to the combustor exit at $x/H \approx 10$ but reverted back to chemical non-equilibrium after the shock wave at $x/H \approx 40$. The greatest inaccuracy for the chemical non-equilibrium simulation results occurred at $x/H \approx 20$ with an error of 21% compared with the experimental data.

The Wind-US simulation used a chemical non-equilibrium combustion model. The Wind-US pressure ratio along the top wall results are shown in Figure 53 and Scan 14 is labelled as Φ=0.260 WIND-US Sc_t=1.1 and represented by the blue line in the figure. Plots of static pressures and Mach numbers along the symmetry plane are shown in Figures 57 through 60 for comparison.

It can be seen that the Wind-US software simulates the centerline top wall pressure of the isolator more accurately than either STAR-CCM+ simulations although the STAR-CCM+ chemical non-equilibrium model correctly captures the start of the shock train in the isolator at $x/H = -22$. The STAR-CCM+ chemical non-equilibrium model predicts the centerline top wall pressure in the divergent nozzle after the shock wave and to the nozzle exit more accurately than the Wind-US model. Both STAR-CCM+ and Wind-US simulated the shock train in the isolator

as can be seen in Figures 57 through 60. Figures 59 and 60 show that the airflow entering the combustor has a supersonic core surrounded by subsonic flow.

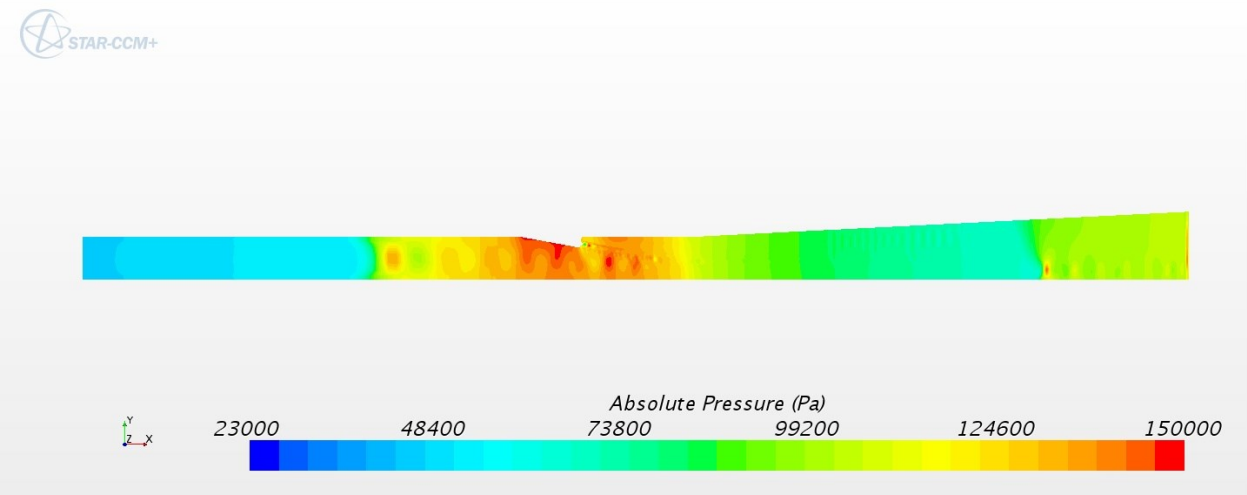

Figure 57 STAR-CCM+ Results: Static pressure contours (Pa) on the symmetry plane (z=0) for Scan14

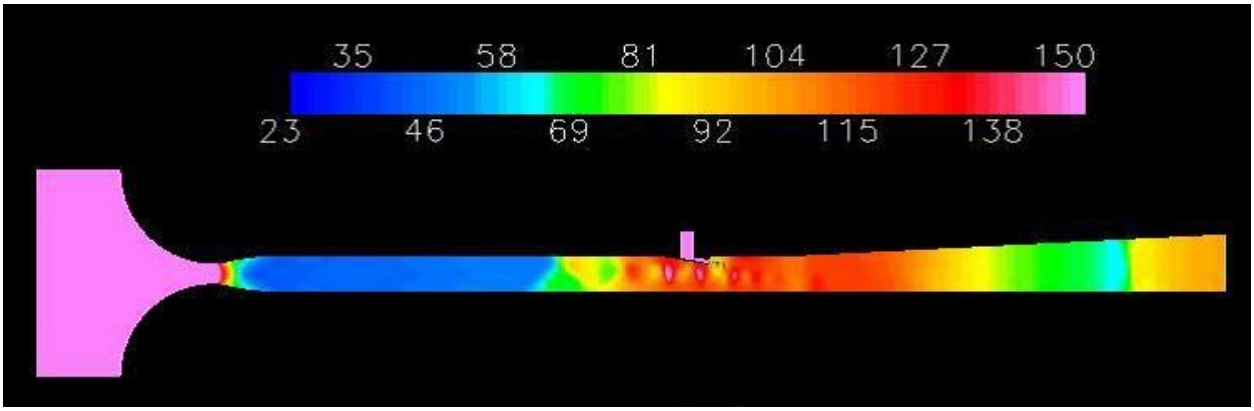

Figure 58 Wind-US Results: Static pressure contours (kPa) on the symmetry plane (z=0) for $\Phi = 0.260$; clean air
[69]

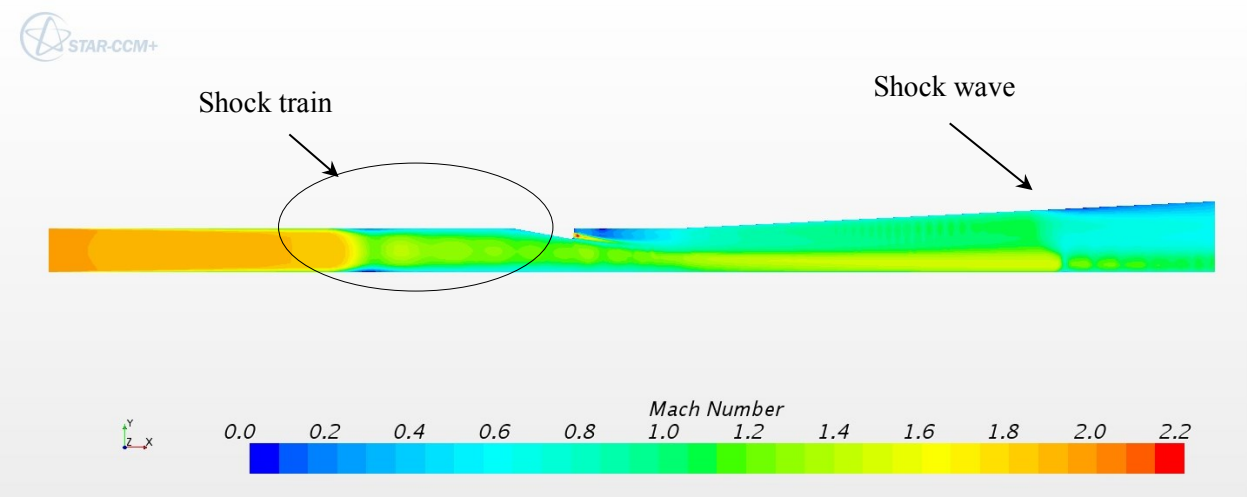

Figure 59 STAR-CCM+ Results: Mach number contours on the symmetry plane (z=0) for Scan14

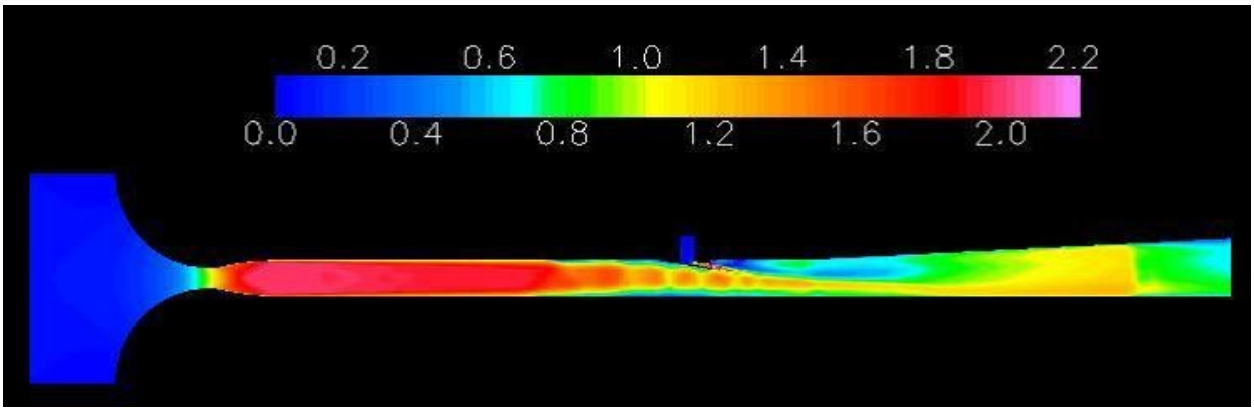

Figure 60 Wind-US Results: Mach number contours on the symmetry plane (z=0) for Φ=0.260; clean air
[69]

5.1.4 Scan18

Scan 18 is a repeat of Scan 14 but with vitiated air instead of clean air with the addition of 12% H_2O. Once again the simulation is run first with a chemical equilibrium combustion model and then with a chemical non-equilibrium model. The comparison of the pressure ratio along the centerline of the top wall results from the two combustion models is shown in Figure 61. Overall the result from the chemical non-equilibrium model is more accurate to the experimental data. This is particularly noticeable from $x/H \approx 0$ through $x/H \approx 37$. The largest inaccuracy to the experimental data for the chemical equilibrium and chemical non-equilibrium models occurred at $x/H \approx 5$ and was 12% and 8% respectively.

The WIND-US simulation result is shown in Figure 62. Scan 18 is labelled as WIND-US, 12% H_2O, Φ_{exp} =0.267 and is represented by a blue line with the experimental results shown as blue circles. The STAR-CCM+ simulation results compared to the experimental data more closely than the WIND-US simulation result particularly from approximately x/H = -6 through x/H = 47.

Both Figures 61 and 62 shows that the vitiated air case reduces the static pressure sufficiently to prevent a shock train from developing and travelling upstream into the isolator. This is confirmed by the Mach contours of Figures 63 and 64. The addition of vitiated air to this scramjet model results in a fully developed scramjet rather than a dual-mode scramjet [7].

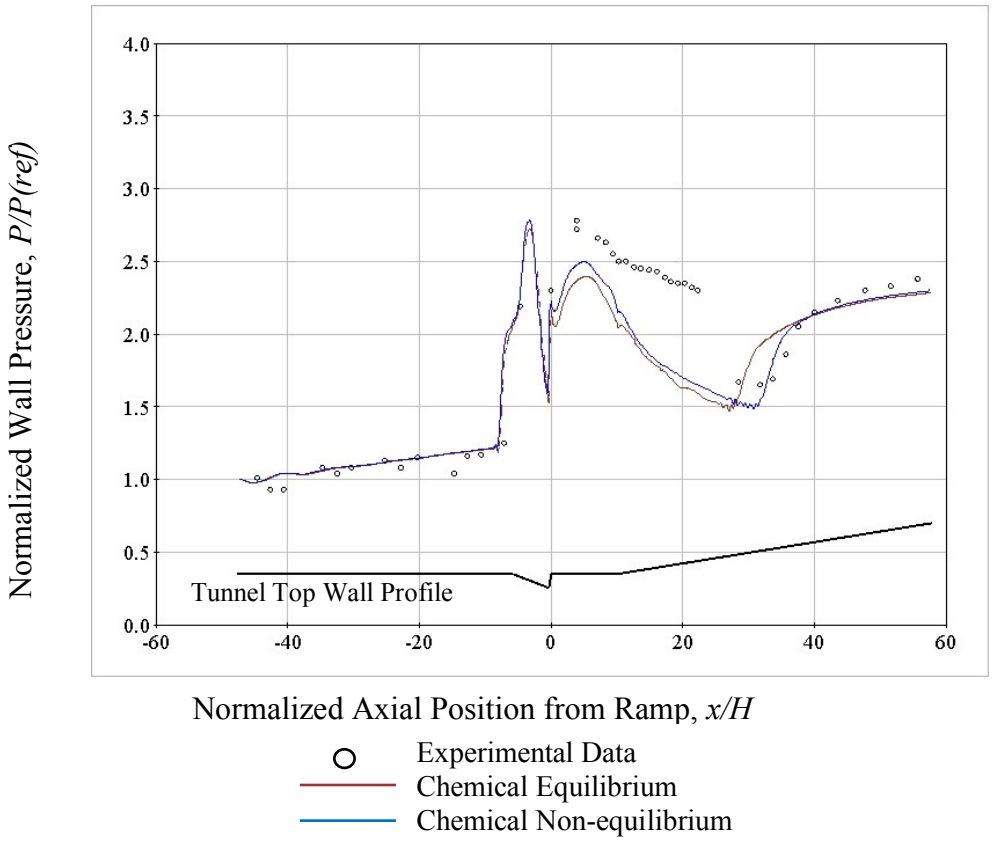

Figure 61 STAR-CCM+ Results: Top wall static pressure along the axial centerline for Scan18

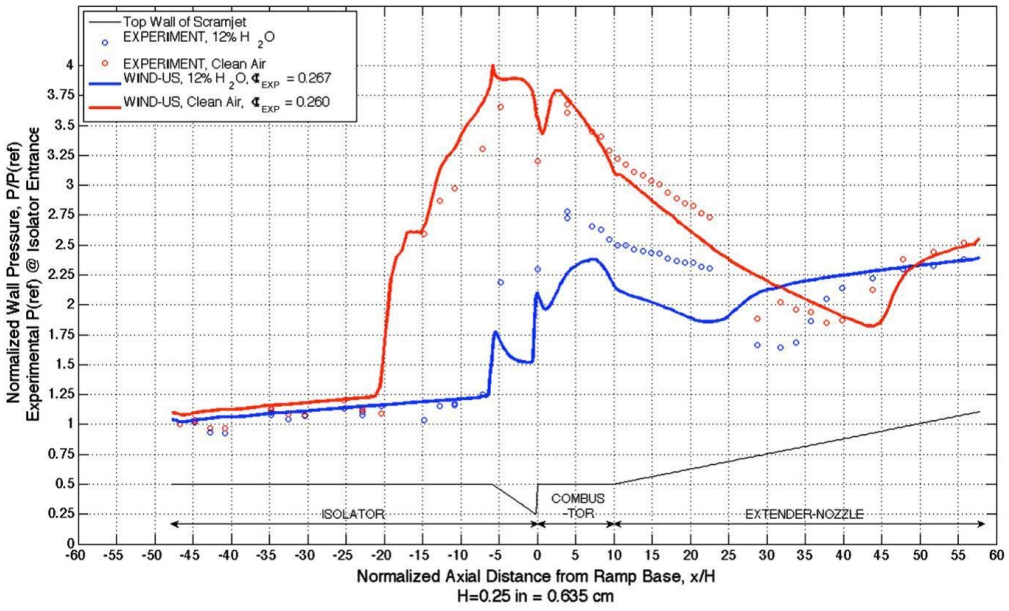

Figure 62 WIND-US Results: Top wall static pressure along the axial centerline for Φ = 0.260, 0.267; clean and vitiated air
[7]

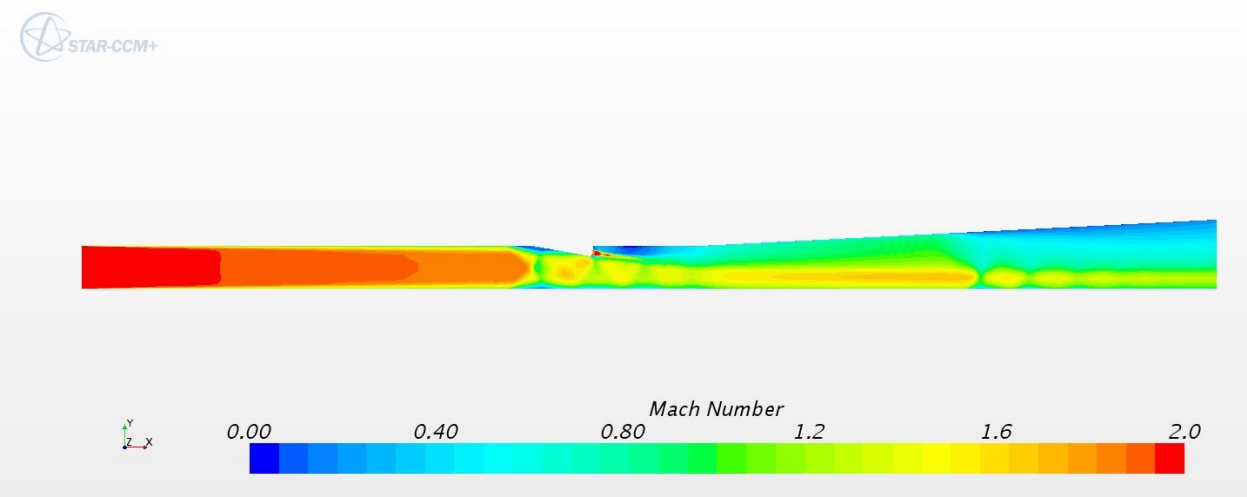

Figure 63 STAR-CCM+ Results: Mach number contours on the symmetry plane (z=0) for Scan18

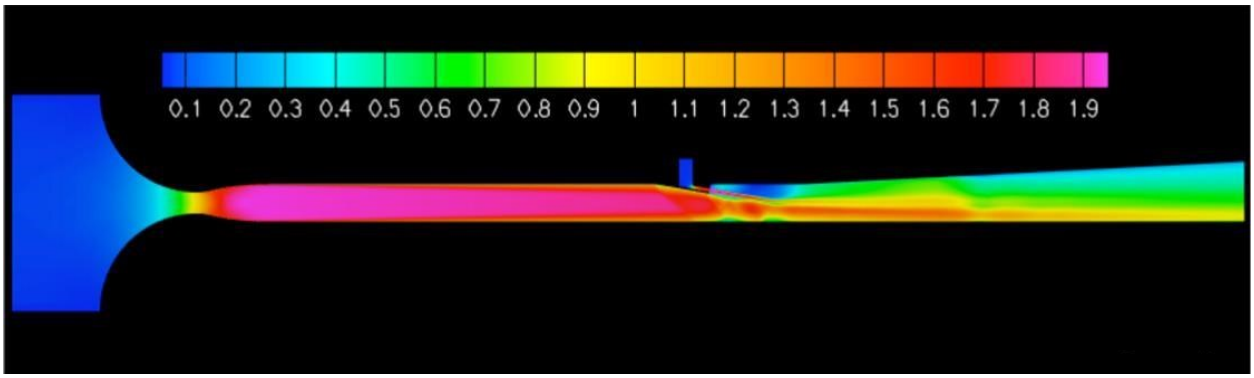

Figure 64 WIND-US Results: Mach number contours on the symmetry plane (z=0) for Φ = 0.267; vitiated air
[7]

5.1.5 Modeling NO_X Formation

This study on the effect of fuel jet swirl on mixing enhancement in the combustor of a scramjet does not include the formation of nitride oxides. Nitrogen, N_2 has a high activation energy and low reaction rate [70]. Nitrogen oxide, NO and nitrogen dioxide, NO_2 contribute to NO_X emissions. Nitrogen oxide, NO, contributes 90 – 95% of NO_X. There are three NO_X emission models: thermal NO_X, prompt NO_X and fuel NO_X.

The thermal NO_X model is important when temperatures reach within the 1600 – 1800 K range. The prompt NO_X model is used when hydrocarbon radicals react with N_2. The fuel NO_X model is used when the combusting fuel consists of nitrogen.

Since the combustor model simulated for this study uses hydrogen fuel the thermal NO_X model is applicable for simulation purposes. The thermal NO_X model uses the Zeldovich reaction mechanism shown below to compute NO_X [71].

$$O + N_2 \rightarrow NO + N$$

$$N + O_2 \rightarrow NO + O$$

$$N + OH \rightarrow NO + H$$

The case Scan 14 from the verification process was simulated again with Zeldovich reaction mechanism included. The STAR-CCM+ simulation used a chemical non-equilibrium NO_X flamelet library. Results of case Scan 14 with and without the thermal NO_X model are shown in Figures 65 – 68 for comparison.

The iteration solver time for chemical non-equilibrium with thermal NOX model was 3.63 hours per 1000 iterations. The results of the top wall static pressure ratio along the axial centerline shown in Figure 65 indicated that the shock train in the isolator starts further upstream when the Zeldovich reaction mechanism is included for the simulation. The greatest difference

in the top wall static pressure ratio between the two simulation models occurs at $x/H \approx -21$ where the Zeldovich reaction mechanism result is greater by 30%. Within the combustor region the simulation model with the Zeldovich thermal NO_X model resulted in a maximum increase of top wall static pressure ratio of 1.7% at $x/H \approx 3.2$.

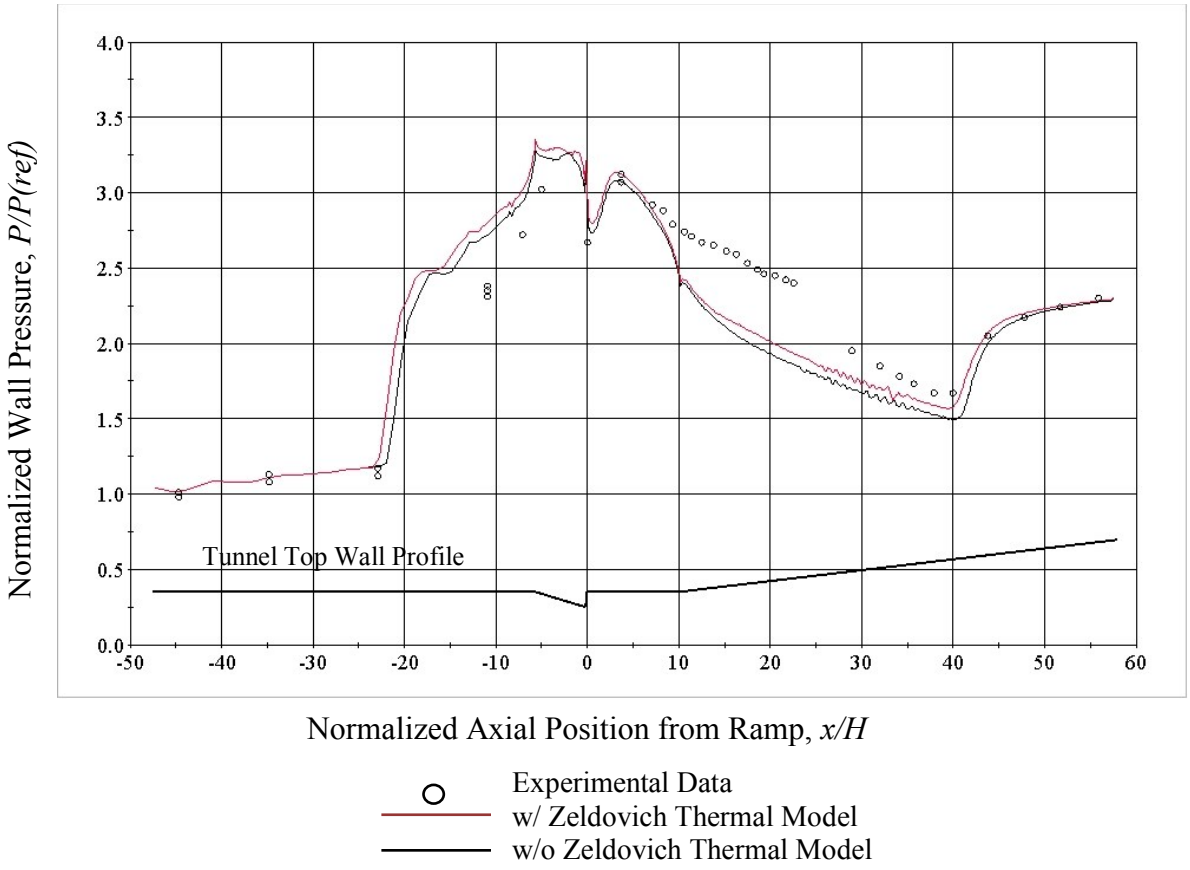

Figure 65 Top wall static pressure along the axial centerline for Scan 14 with and without Zeldovich Thermal NO_X model

Figure 66 (a) and (b) show the temperature contours on the symmetry plane z = 0 and cross planes at $x/H \approx 0.01$, 2.26, 4.24, 6.62, 9.79, 19.68, 31.56, 43.44 and 57.92. The maximum temperature for the simulation without the thermal NO_X model is 2568 K. The maximum temperature for the simulation with the thermal NO_X model is higher by 1.8% at 2613 K.

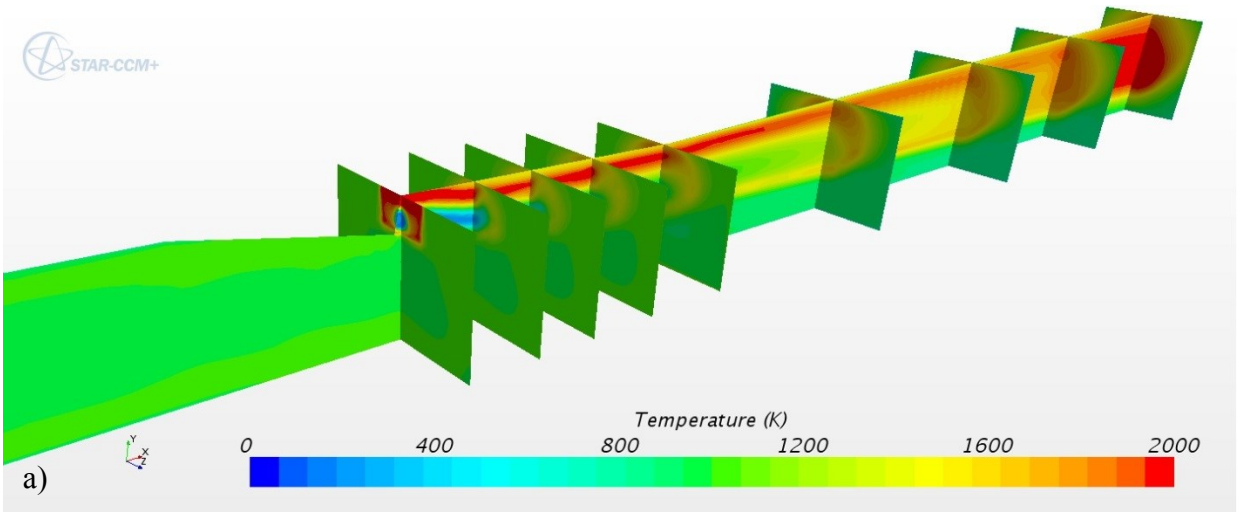

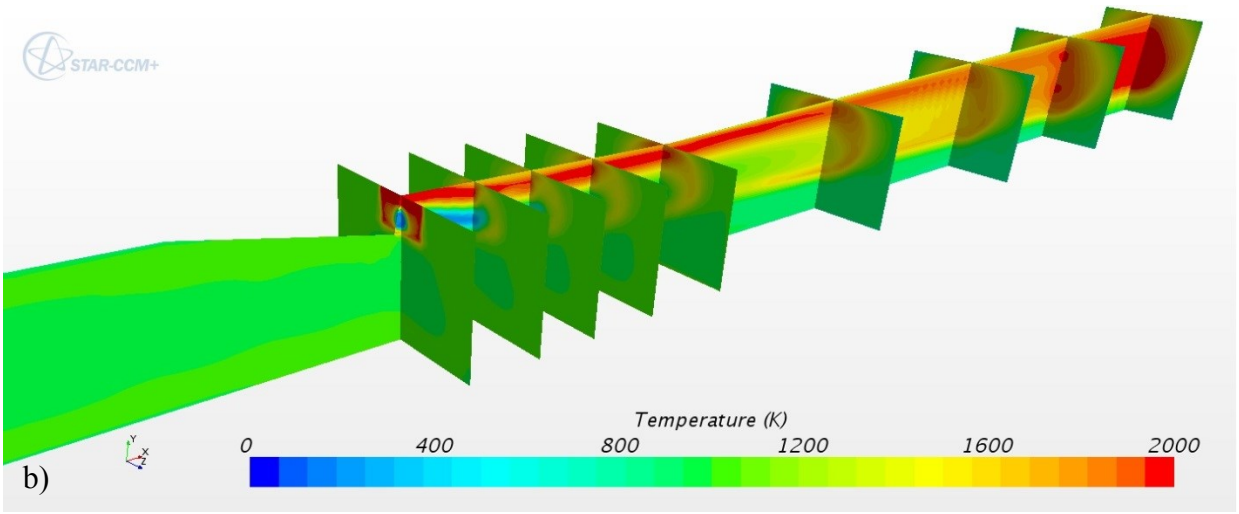

Figure 66 Temperature contours on the symmetry plane (z=0) and y-z cross planes a) without Zeldovich thermal NO_X model b) with Zeldovich thermal NO_X model

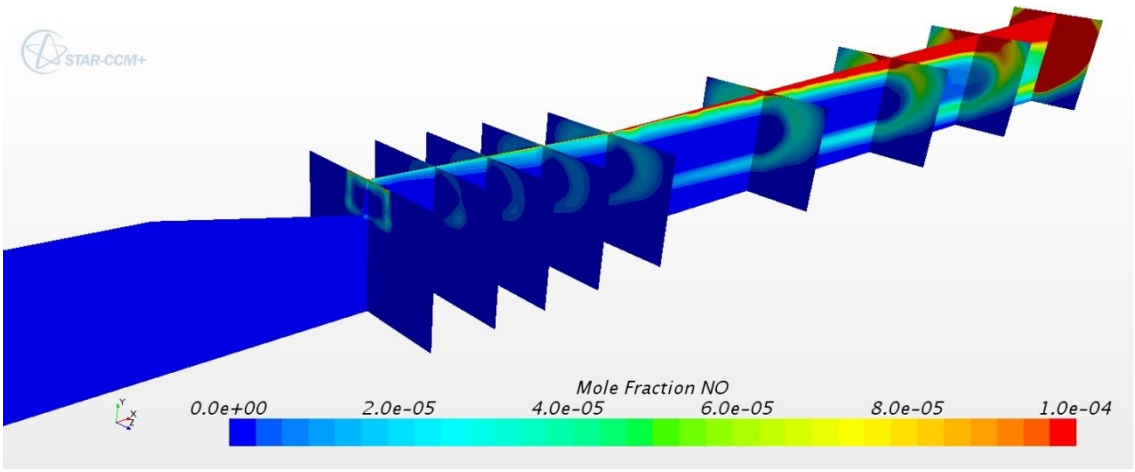

Figure 67 Mole fraction contours of nitrogen oxide, NO, on the symmetry plane (z = 0) and y-z cross planes with Zeldovich thermal NO_X model

Contours showing the mole fraction of NO on the axial symmetry plane and on cross planes $x/H \approx 0.01$, 2.26, 4.24, 6.62, 9.79, 19.68, 31.56, 43.44 and 57.92 are shown in Figure 67. It indicates that the majority of NO formation occurs in the divergent nozzle towards the tunnel exit. The maximum mole fraction of NO formed was 0.0012.

Figure 68 (a) and (b) show the mole fraction of H_2O contours on the symmetry plane z = 0 and cross planes $x/H \approx 0.01$, 2.26, 4.24, 6.62, 9.79, 19.68, 31.56, 43.44 and 57.92. The maximum mole fraction of H_2O for the simulations without and with the thermal NO_X model is 0.286 and 0.285 respectively. The maximum mole fraction of NO is 0.4% of the maximum mole fraction of H_2O.

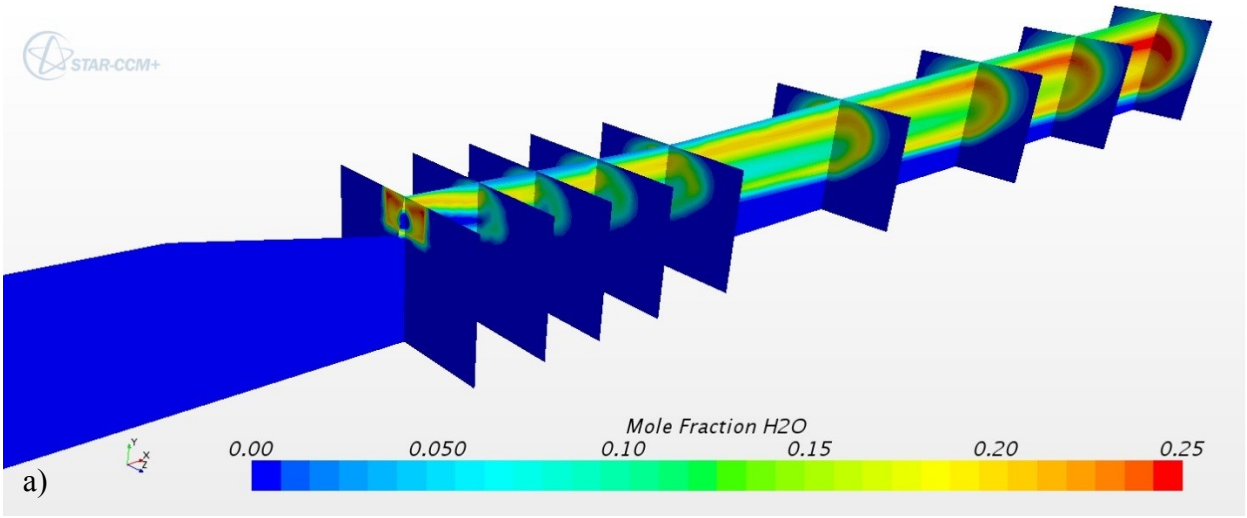

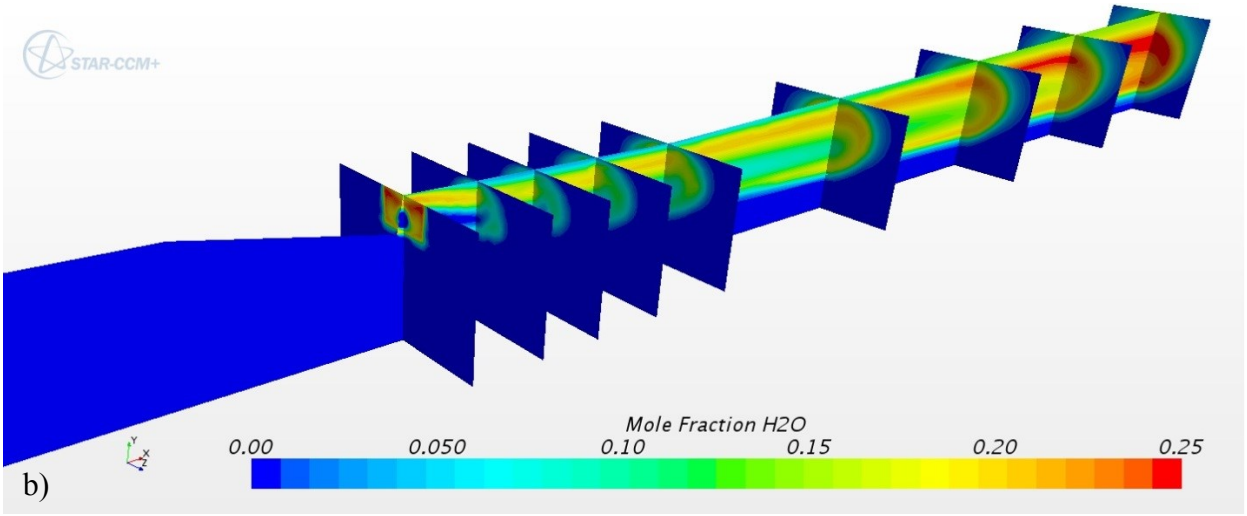

Figure 68 Mole fraction contours of water, H_2O on the symmetry plane (z = 0) and y-z cross planes a) without Zeldovich thermal NO_X model b) with Zeldovich thermal NO_X model

5.2 Results of Simulation Validation

The STAR-CCM+ software was used to simulate three different cases of a scramjet engine. The results of the simulations were compared to experimental data of pressure ratios along the axial centerline of the top wall of the tunnel and numerical results from Wind-US.

Overall, the results from STAR-CCM+ compared well to the experimental data. The largest inaccuracies occurred within the divergent nozzle, more specifically from the nozzle entrance to the point of flow separation or a shock. The results from STAR-CCM+ were more accurate than Wind-US in locating point of separation or shock in the isolator and divergent nozzle.

The primary objective of this research was to investigate the near-field flow characteristics and the effect of fuel jet swirl on mixing within the combustor. The conditions used to simulate case Scan14 was used in this research since the production of H_2O is a sign of combustion which can only occur upon molecular mixing. The chemical non-equilibrium combustion model was used since the numerical solution of the static pressure ratio along the top wall centerline more accurately simulated the experimental results. The Zeldovich thermal NO_X model was not used since there was a 61% increase in iteration solver time when compared to the 2.25 hours per 1000 iteration for the model without thermal NO_X included.

6 Results of the Effect of Fuel Injection with Swirl on Mixing

As previously discussed in section 2.5.1 the effect of adding swirl to flow is an increase in jet spreading and mixing. Most of the experimental results were obtained from non-combusting cases. Experiments with combustion concentrated on coaxial nozzles. Experiments that simulated fuel jet swirl injected into Mach 2 or greater air flow were non-combustion cases [58], [59]. The primary purpose of this investigation is to determine the effect of fuel jet swirl on mixing within a scramjet combustor with non-equilibrium chemically reacting combustion. This study is a numerical investigation due to the expense and complexity of data acquisition for an experimental study.

6.1 Methodology

Since swirl flow is being investigated the flow from the fuel nozzle is not symmetrical. Therefore the full tunnel width was used for the simulations. Due to the simple geometry and previously validated simulation results the investigation uses the geometry of the UVaSCF and the CFD software STAR-CCM+. The baseline case will be based on Scan 14 that was discussed previously.

The full tunnel model is shown in Figure 69. Figure 70 shows that there is negligible error in the comparison of simulation results from the half tunnel and full tunnel with regards to the pressure on the centerline top wall.

The boundary conditions and numerical parameters that were used for the validation of Scan 14 were used for the study of the effects of a swirling fuel jet. Due to the interest of mixing in the combustor, the chemical non-equilibrium combustion model was used for the study.

Although the flow from the nozzle is anisotropic [65] and a RST model is available in STAR-CCM+ the SST k-ω turbulence model was chosen for the simulations for the following reasons:

- The flow through the fuel nozzle which is highly anisotropic is not modeled in the simulation. Velocity profiles are used to input the swirl at the fuel nozzle exit.
- The majority of flow in the simulation is isotropic and the RST turbulence model would have high computational costs.

User defined functions were created for computing the fuel inlet velocity profiles and are shown in Appendix A.

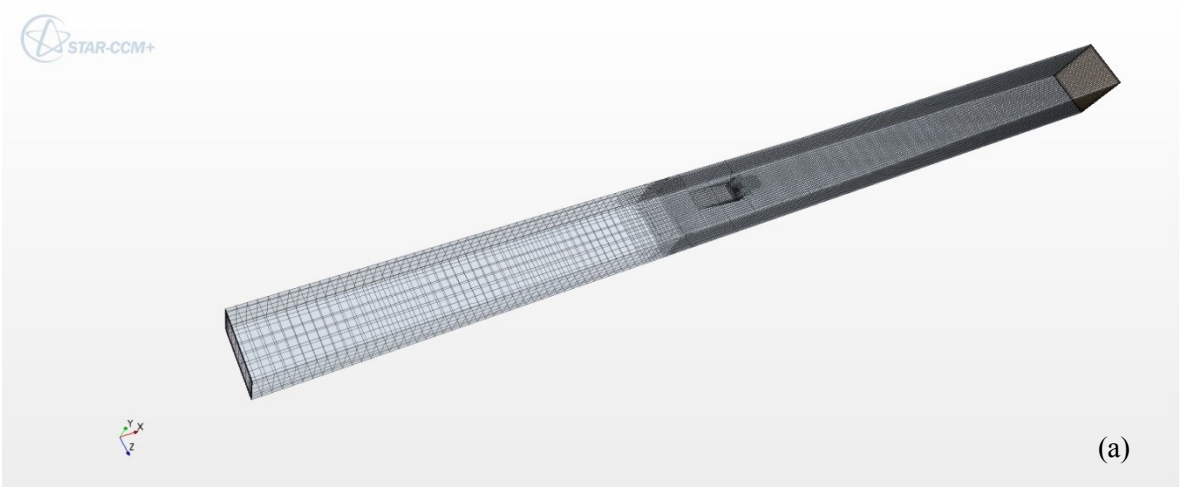

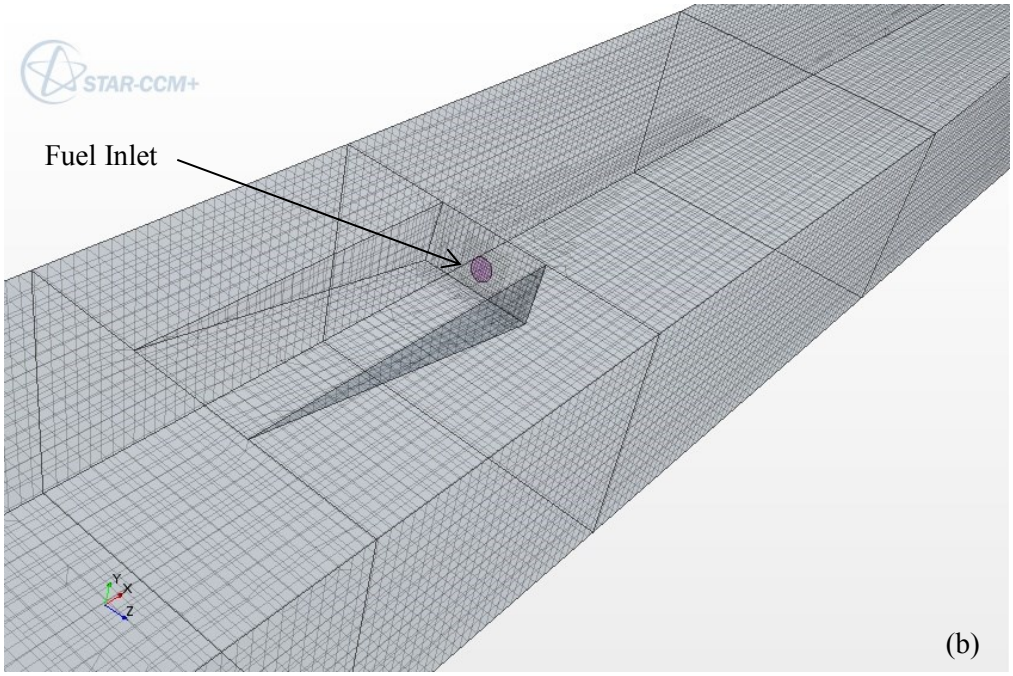

Figure 69 STAR-CCM+ 3-D Mesh of Isolator, Combustor and Nozzle Sections
a) Full tunnel grid b) detail of full tunnel grid in fuel ramp region

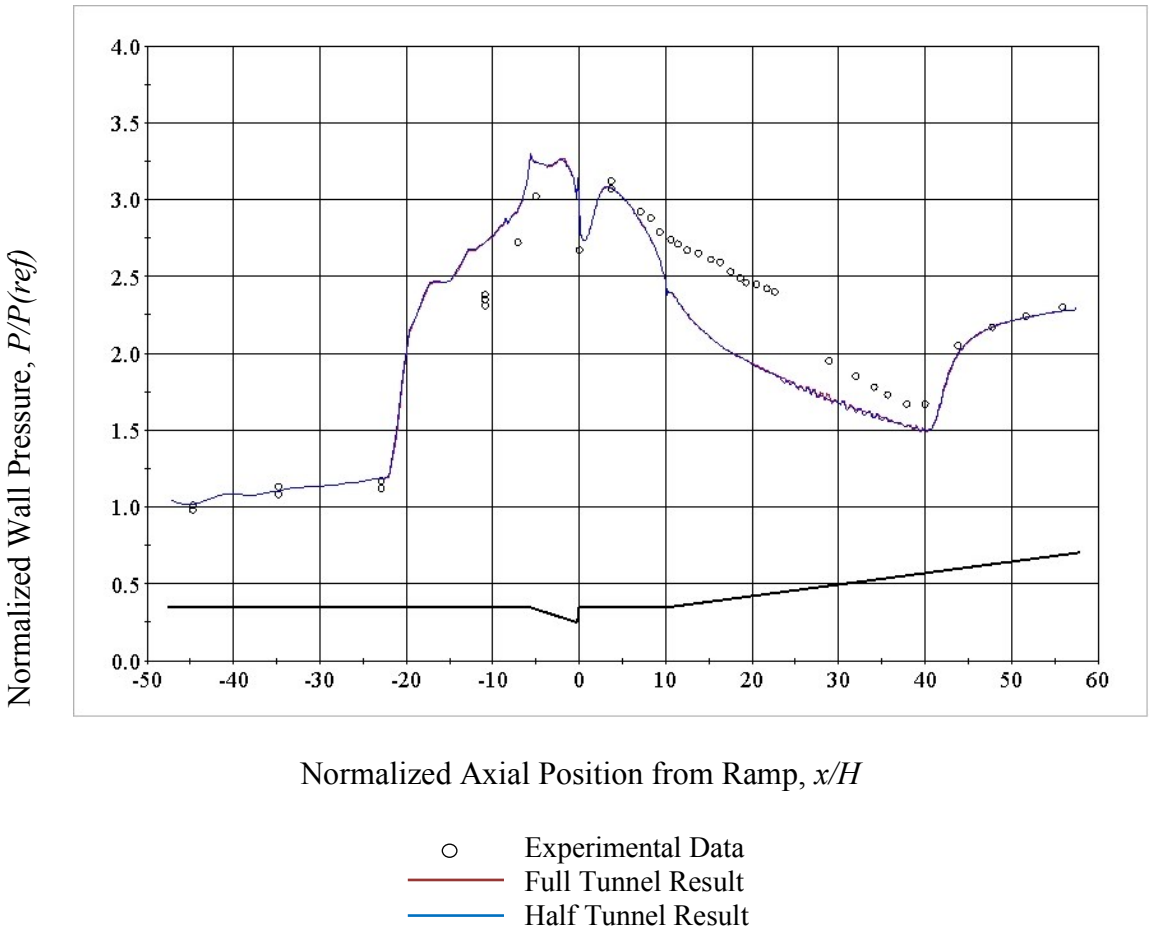

Figure 70 STAR-CCM+ Results: Comparison of half tunnel and full tunnel results of top wall static pressure along the axial centerline for Scan14 (chemical non-equilibrium combustion model)

6.1.1 Near-field Normalized Axial Locations

Previously the axial location of x was normalized by H the normal height of the ramp. This study is interested in the near-field effects of chemical combustion and mixing in the combustor. For this reason the axial distance x will be normalized by d, the diameter of the fuel inlet which is 2.514 mm or 0.099" and the reference or $x/d = 0$ location is the center of the fuel inlet. Figure 71 shows the reference or $x = 0$ location defined for both scales.

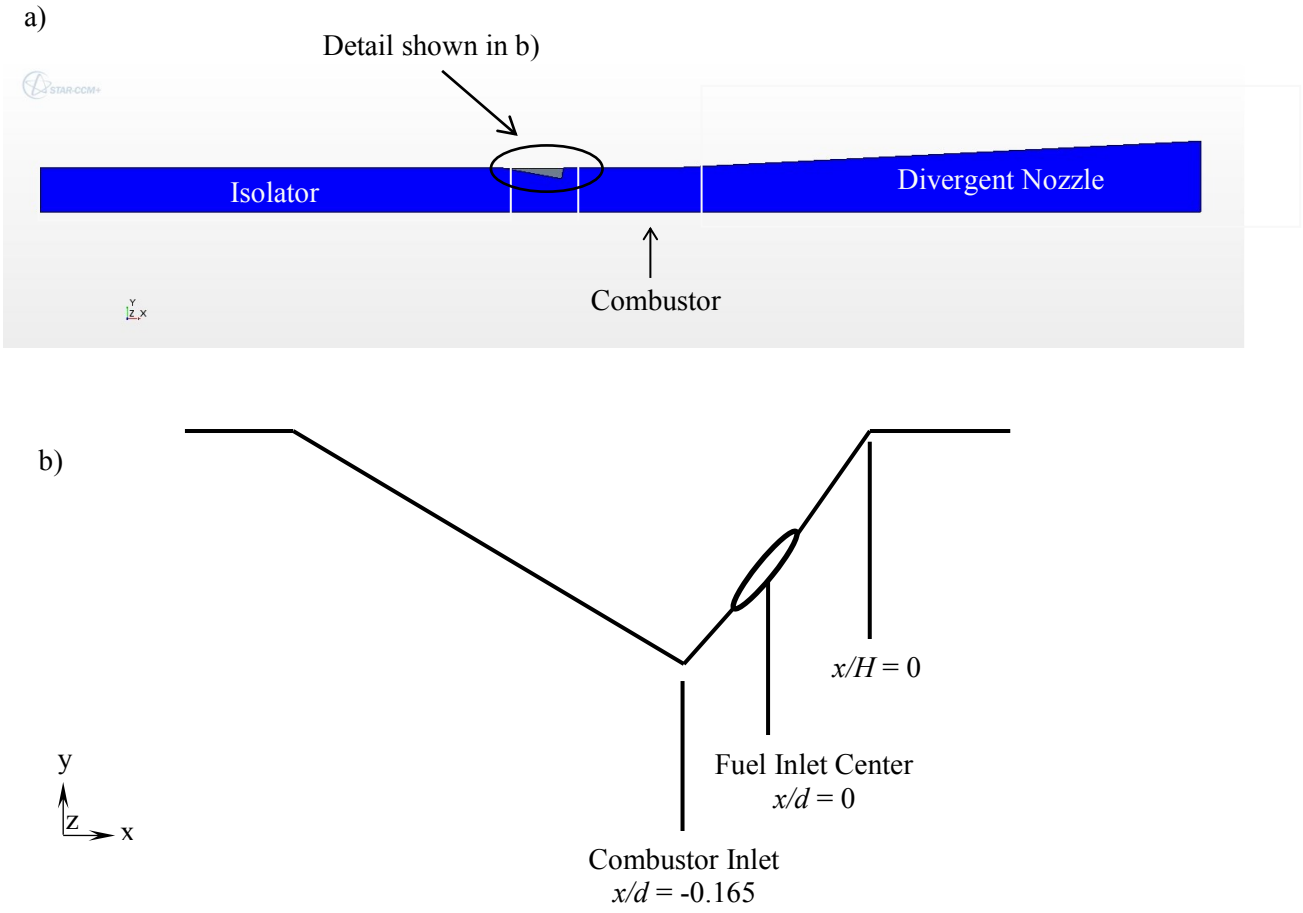

Figure 71 Normalized reference axial locations
a) full tunnel geometry, b) detail of combustor inlet and fuel inlet area (not to scale)

6.1.2 Numerical Simulation of Swirl

The introduction of swirl to the fuel jet is accomplished at the fuel inlet to the scramjet since the fuel nozzle is not simulated. Swirl is simulated by defining the tangential vector of the fuel jet velocity. The non-swirling fuel jet has a velocity, *V*, of 1771.5 m/s The fuel jet comprises of two separate regions; the core jet flow (CJF) and the annular jet flow (AJF). The core flow is non-swirling while the annular jet flow is swirling flow that represents the swirl produced with guide vanes. Three configurations with different core jet flow radius were investigated. Configuration R2, R4 and R6 were defined as having a core jet flow radius (R_{CJF}) / fuel inlet radius (R_I) of 20%, 40% and 60% respectively as shown in Figure 72. The fuel inlet radius, R_I, is 0.0494" or 1.255mm. The swirl flow is clockwise as viewed by an observer looking downstream from the fuel inlet into the scramjet.

The swirl flow was defined to represent swirl guide vane angles of 10, 20, 30, 40 or 50 degrees. The naming convention for each case involves the radius configuration and the vane angle represented. As an example a case labelled R4 V30 represents the case where the core flow is non-swirling with a radius that is 40% of the fuel inlet radius and the swirl in the annular region represents the flow produced by 30° swirl guide vanes.

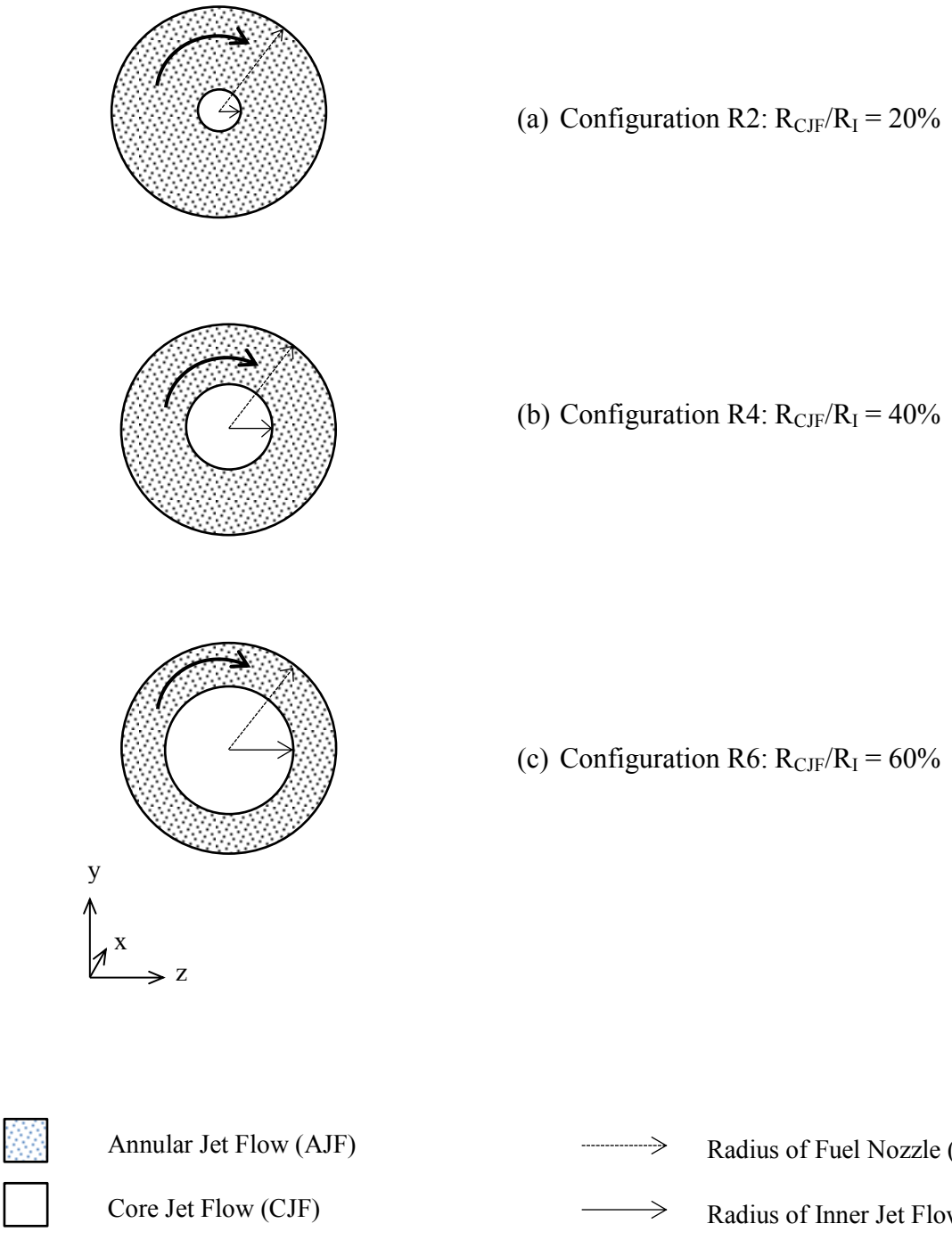

Figure 72 Radius configuration of fuel jet

6.2 Results: Fuel Jet Swirl

The swirl flow was defined to represent swirl guide vane angles of 10, 20, 30, 40 or 50 degrees. The swirl number, *S* is calculated using Equation 16 [3] and shown in Table 4. Swirl is simulated by defining the tangential vector of the fuel jet velocity. The axial and tangential velocity profiles for configuration R2, R4 and R6 are shown in Appendix B. The baseline configuration had no fuel jet swirl and is referred to as V00. The critical swirl number was found to be 0.735 as shown in Appendix C.

Table 4 Nozzle Vane Angle and Swirl Number

	R2	*R4*	*R6*
Vane Angle (Deg)	*Swirl Number, S*		
10	0.12	0.11	0.09
20	0.24	0.22	0.18
30	0.38	0.34	0.27
40	0.54	0.47	0.35
50	0.75	0.61	0.41

The reference values used to normalize data in this section are listed below:

Pabs(ref) = 176.7 kPa - absolute pressure at the fuel inlet of the baseline case V00

d = 2.514 mm or 0.099" - fuel inlet diameter

H = 6.35 mm or 0.25" - normal height of fuel ramp

P(ref) = 42.18kPa - static pressure (gauge) at isolator inlet

Since this study investigated the effect of swirl on mixing the burning efficiency was examined. The burning efficiency measures how much injected fuel was consumed prior to reaching the nozzle exit. An increase in burning efficiency would indicate an increase in the mixing of H_2 with O_2. The burning efficiency as defined by Kindler *et al*. (2011) [70] and Pandey *et al*. (2011) [77] is given in equation 6.1

$$\eta_{burn} = 1 - (\dot{m}_{H2}|_x / \dot{m}_{H2,inj}) \qquad \text{Equation 30}$$

where

η_{burn} - burning efficiency

$\dot{m}_{H2}|_x$ - mass flow at and normal to the divergent nozzle exit

$\dot{m}_{H2,inj}$ - mass flow at the fuel injector exit

6.2.1 The Effect of Swirl on Mixing

The primary visual indication of jet swirl is increasing jet diameter with increasing swirl strength. This characteristic is not as discernable for the fuel jet in this research due to the high fuel jet pressure which produces an elongated jet although swirl is present [57]. However, increasing swirl strength results in decreasing length of the potential core of a jet. Figure 73 shows the velocity contours along the centerline plane for the baseline case V00.

Figure 74 shows the centerline absolute pressure distribution of the fuel jet from the fuel inlet face to $x/d \approx 6$. This plot shows the locations of shock cells in the fuel jet flow. The centerline absolute pressure is normalized with respect to the absolute pressure at the center of the fuel inlet for the baseline no swirling case. Figure 74 shows the results for configuration R2 where the radius of the inner non swirling jet is 20% of the fuel inlet radius.

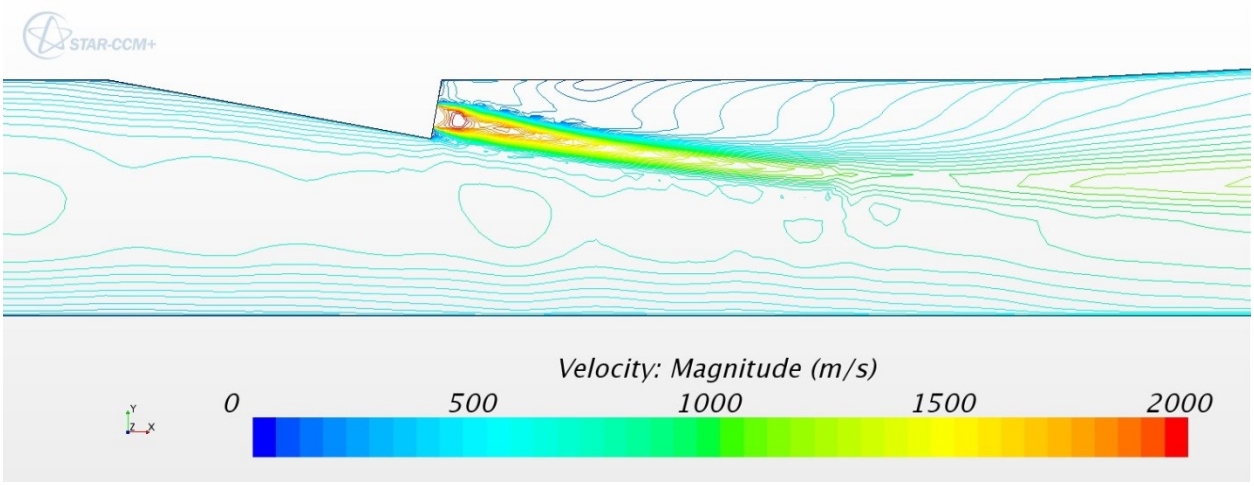

Figure 73 Velocity contours on the centerline plane for the baseline case V00

The baseline case V00 is represented by the black line. The first shock cell starts to develop at an axial location of $x/d \approx 0.25$. The centers of the shock cells occur at $x/d \approx 1.1$, 3.125 and 4.75 with each shock cell becoming progressively weaker. The shock cells also become

more elongated as distance increases from the fuel inlet. The fuel jet potential core can be seen in Figure 73 and has a length approximately equal to 4.25*d*.

Case R2 V10 has a weak swirl of 0.12 and is represented by the red line in Figure 74. Similar to the baseline case the first shock cell starts to develop at an axial location of $x/d \approx 0.25$. The centers of the shock cells occur at $x/d \approx 1.1$, 3.2 and 5.0. Once again each shock cell is weaker than the previous one. The third shock cell barely exists. The fuel jet potential core is shown in Figure 75(a) and has a length approximately equal to 5.75*d*.

Case R2 V20 has a weak swirl of 0.24 and is represented by the gold line in Figure 74. Unlike the previous two cases the first shock cell starts to develop almost at the start of the fuel inlet. The centers of the shock cells occur at $x/d \approx 1.1$ and 3.0 and 4.75. Once again each shock cell is weaker than the previous one and the third shock cell barely exists. The fuel jet potential core is shown in Figure 75(b) and has a length approximately equal to 3.55*d*.

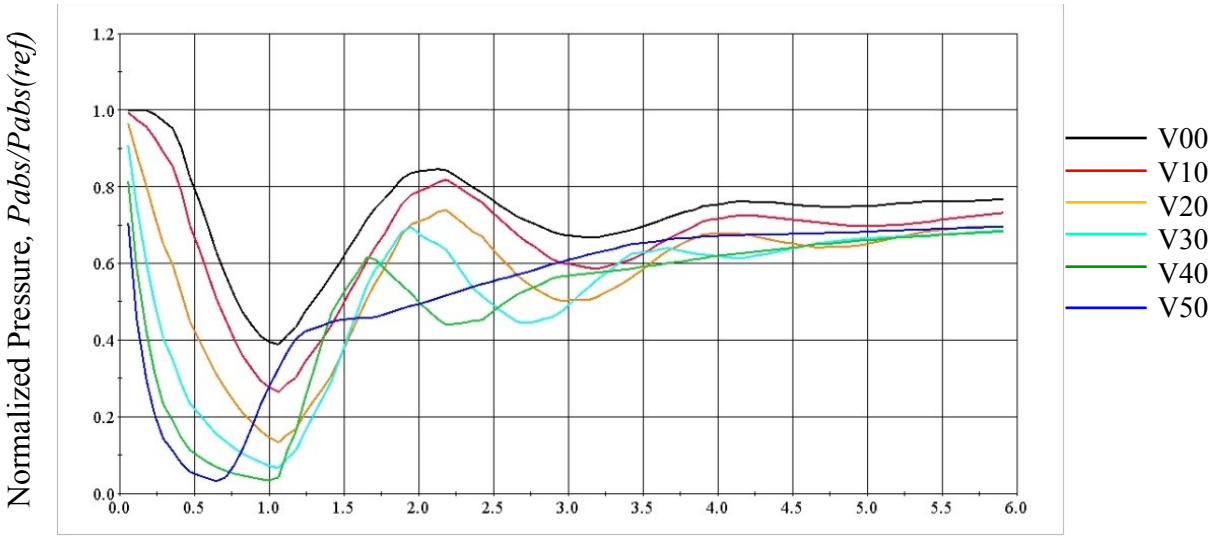

Figure 74 Normalized absolute pressure along the fuel jet potential core for configuration R2

Case R2 V30 has a weak swirl of 0.38 and is represented by the cyan line in Figure 74. The first shock cell starts to develop almost at the start of the fuel inlet. The centers of the shock cells occur at $x/d \approx 1.1$, 2.75 and 4.2. Once again each shock cell is weaker than the previous one and the third shock cell barely exists. The fuel jet potential core is shown in Figure 75(c) and has a length approximately equal to 1.5*d*. It can be seen that the potential core becomes shorter with the addition of swirl and the fuel jet flow has become weaker.

Case R2 V40 has a strong swirl of 0.54 and is represented by the dark green line in Figure 74. The first shock cell develops at the start of the fuel inlet. The centers of the shock cells occur at $x/d \approx 1.1$ and 2.25. The velocity contours shown in Figure 75(d) show the final stages of the breakdown of the fuel jet. The fuel jet potential core is $x/d \approx 1.3$d in length.

Case R2 V50 has a strong swirl of 0.75 and is represented by the dark blue line in Figure 74. Not only is the first shock cell starting to develop at the start of the fuel inlet but it is now being pushed upstream into the fuel inlet. There is one strong shock cell with a center at $x/d \approx 0.65$ and as seen in Figure 75(e). The length of the fuel jet potential core is approximately 0.75*d* and a strong recirculation zone can be seen.

Increasing the swirl number of the fuel jet flow causes a decrease in the length of the fuel jet potential core. However, since there is no swirl in the inner core of the fuel jet the swirl does not eliminate it. The number of shock cells in the potential core decrease as the swirl number of the fuel jet increases. Figure 75(e) shows the recirculation zone that is produced by the strong swirl as previously described in section 2.5.1 [3]. This is due to strong radial and axial pressure gradients at the fuel inlet. Figure 75 also indicates that increasing the swirl number increases jet spreading.

(a)

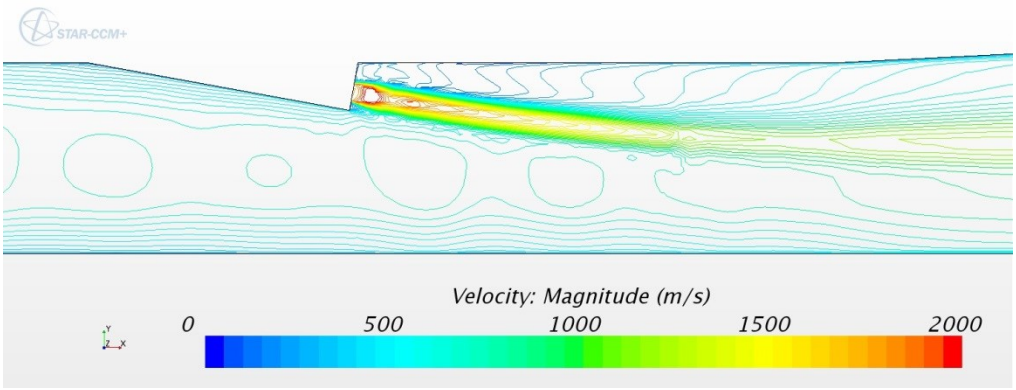

(b)

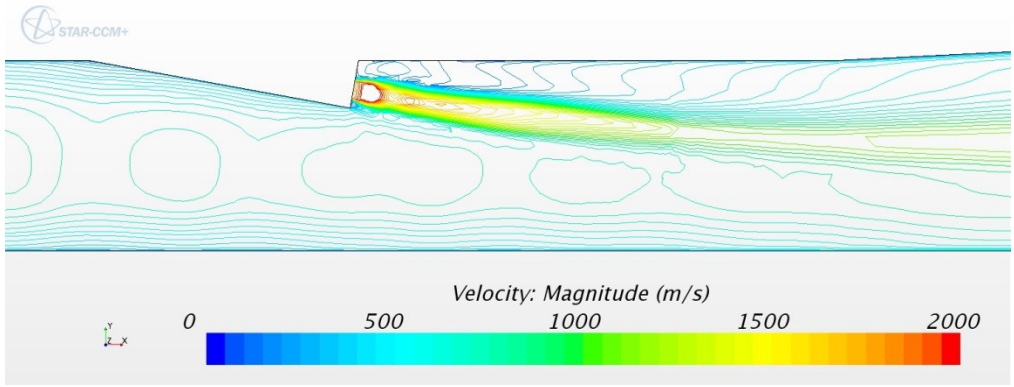

(c)

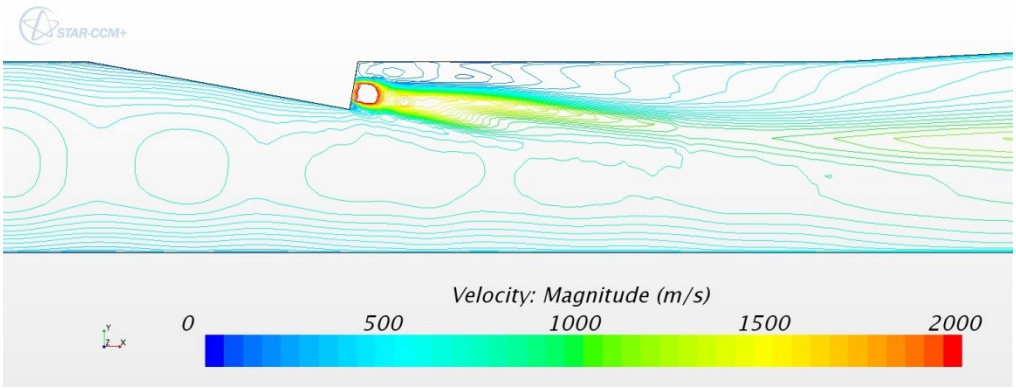

Figure 75 Velocity contours on the centerline plane (z = 0) showing potential core of fuel jet for Configuration R2
a) R2 V10, b) R2 V20 c) R2 V30

(d)

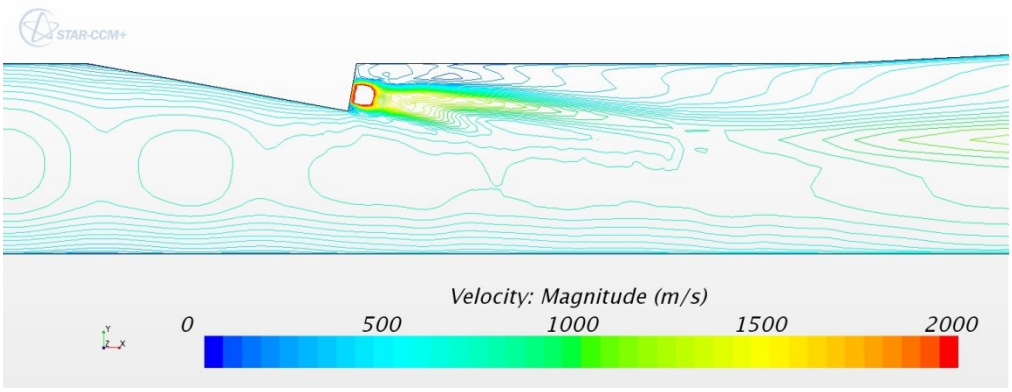

(e)

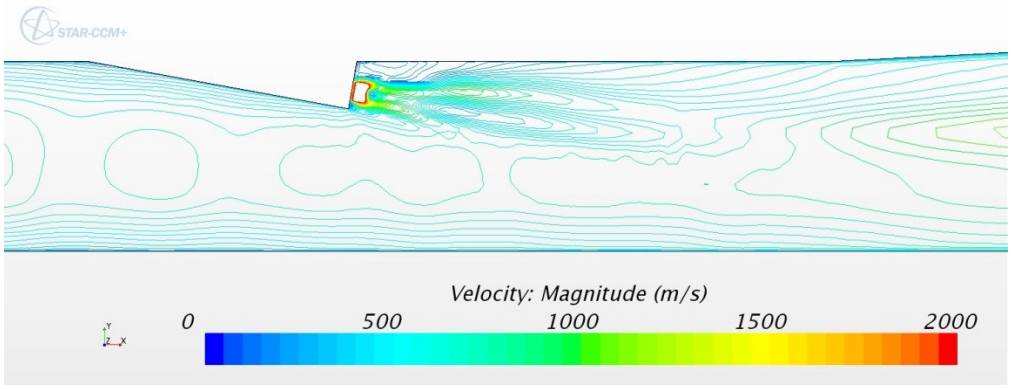

Figure 75 Velocity contours on the centerline plane (z = 0) showing potential core of fuel jet for Configuration R2
d) R2 V40, e) R2 V50

One primary indication of combustion of hydrogen fuel and oxygen is the production of H_2O. Figure 76 shows plots of the mole fraction of H_2O on the fuel inlet wall and the upper combustor wall.

The red areas on the contour plots represent H_2O mole fractions equal to or greater than 0.25. The maximum value of H_2O mole fraction in this research was approximately 0.29. The red areas on the H_2O mole fraction plots are referred to as high H_2O mole fraction zones in this research.

Figure 76(a) shows the plot of H_2O mole fraction for the baseline case V00. In this case there are four distinct areas of high H_2O mole fraction zones; two zones located on either side of the fuel inlet and two more zones on the combustor upper wall approximately 1.5*d* downstream of the fuel inlet center point. Once swirl is introduced one of the high H_2O mole fraction zones is eliminated and the areas on either side of the nozzle become asymmetric. As swirl strength increases the two zones on the fuel inlet wall seem to rotate clockwise as viewed looking upstream. Finally for the case of R2 V40 a large area of the fuel inlet wall is covered by a high H_2O mole fraction zone and starts to spill over to the upper combustor wall. In the final case R2 V50 the high H_2O mole fraction zone on the fuel inlet wall reduces and the high H_2O mole fraction zone is seen trailing downstream on the combustor upper wall. This is likely due to the fuel jet break down due to strong swirl. Figure 76 shows that increasing swirl results in an earlier combustion especially in the case of R2 V40. Swirl aids in ensuring combustion within the short resident time of the fuel and air in the combustor.

Figure 77 shows a progression of H_2O mole fraction contour plots at axial distances $x/d \approx$ 0.3, 3.0, 6.0, 11.0, 17.0 and 25 within the combustor. It can be seen that the addition of swirl has more of an effect on near-field flow characteristics ($x/d \leq 10$) than for far field characteristics ($x/d > 10$). This can be seen in the more pronounced differences of the H_2O mole fraction contours at $x/d = 0.3$, 3.0 and 6.0.

A progression of temperature contour plots at axial distances $x/d \approx$ 0.3, 3.0, 6.0, 11.0, 17.0 and 25 within the combustor is shown in Figure 78. The effect of swirl on temperature is seen throughout the combustor length. Temperature within the combustor flow decreases with an increase in swirl except for case R2 V50. Once again the recirculation zone that was created by strong swirl causes the temperature to increase downstream of axial position x/d ≈ 6.

(a)

(b)

(c)

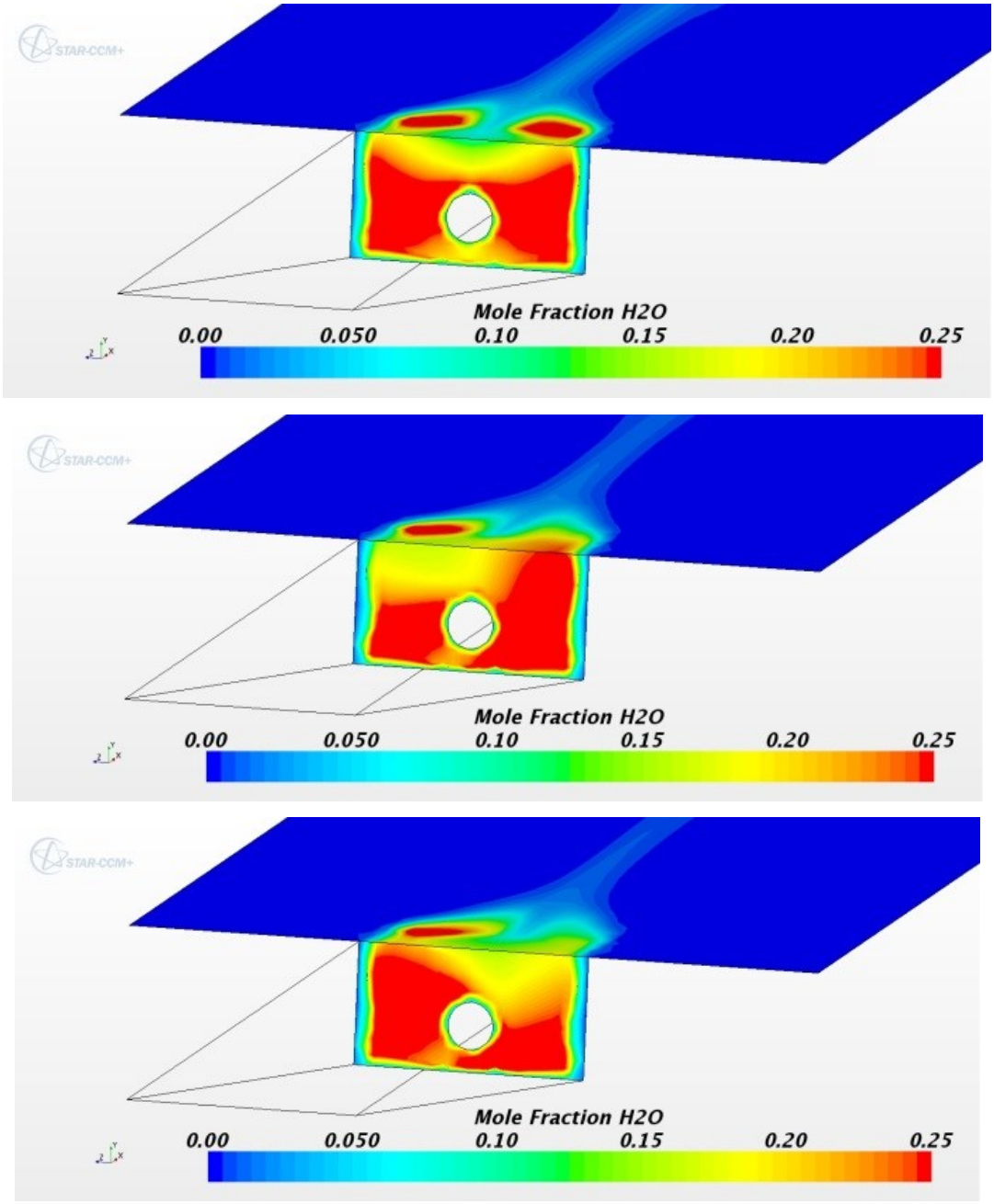

Figure 76 Mole fraction of H_2O on the fuel inlet wall and the upper combustor wall for Configuration R2
a) V00, b) R2 V10, c) R2 V20

(d)

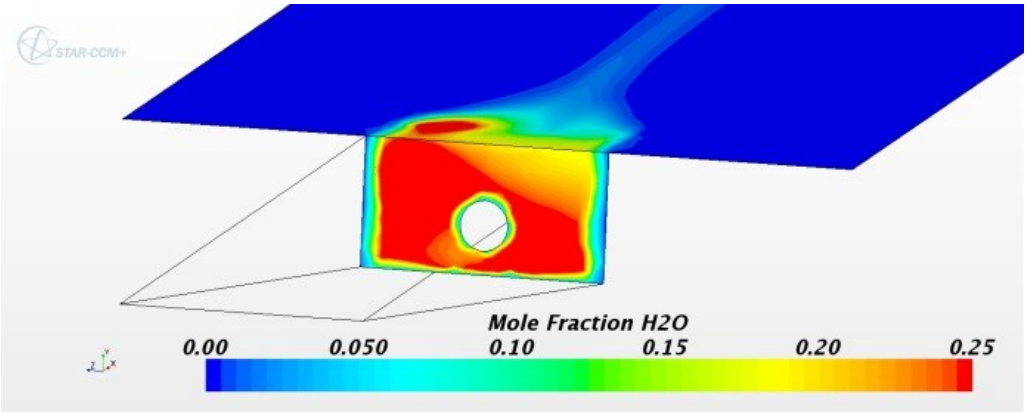

(e)

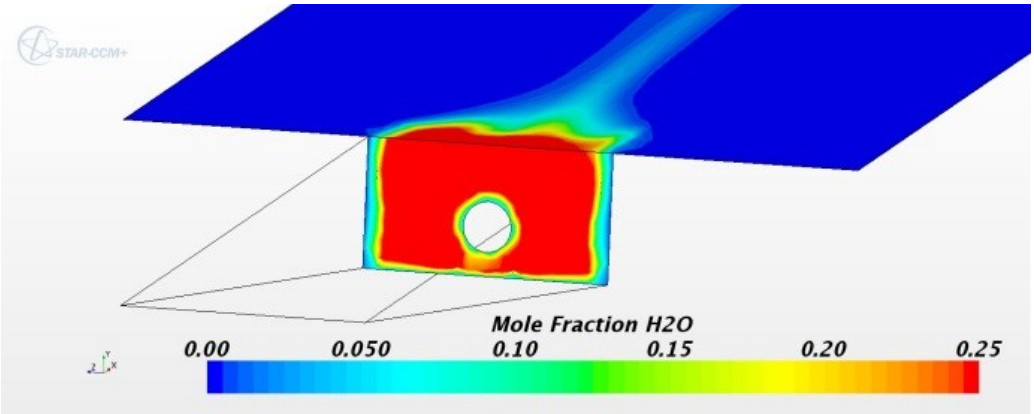

(f)

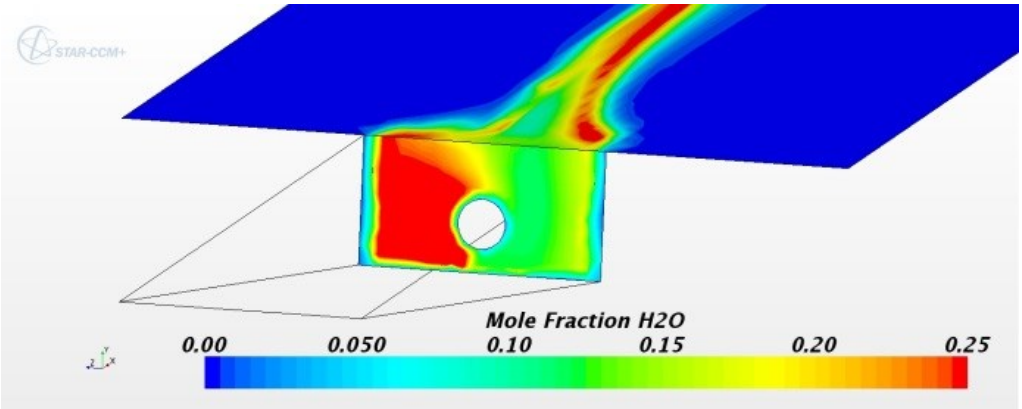

Figure 76 Mole fraction of H_2O on the fuel inlet wall and the upper combustor wall for Configuration R2
d) R2 V30, e) R2 V40, f) R2 V50

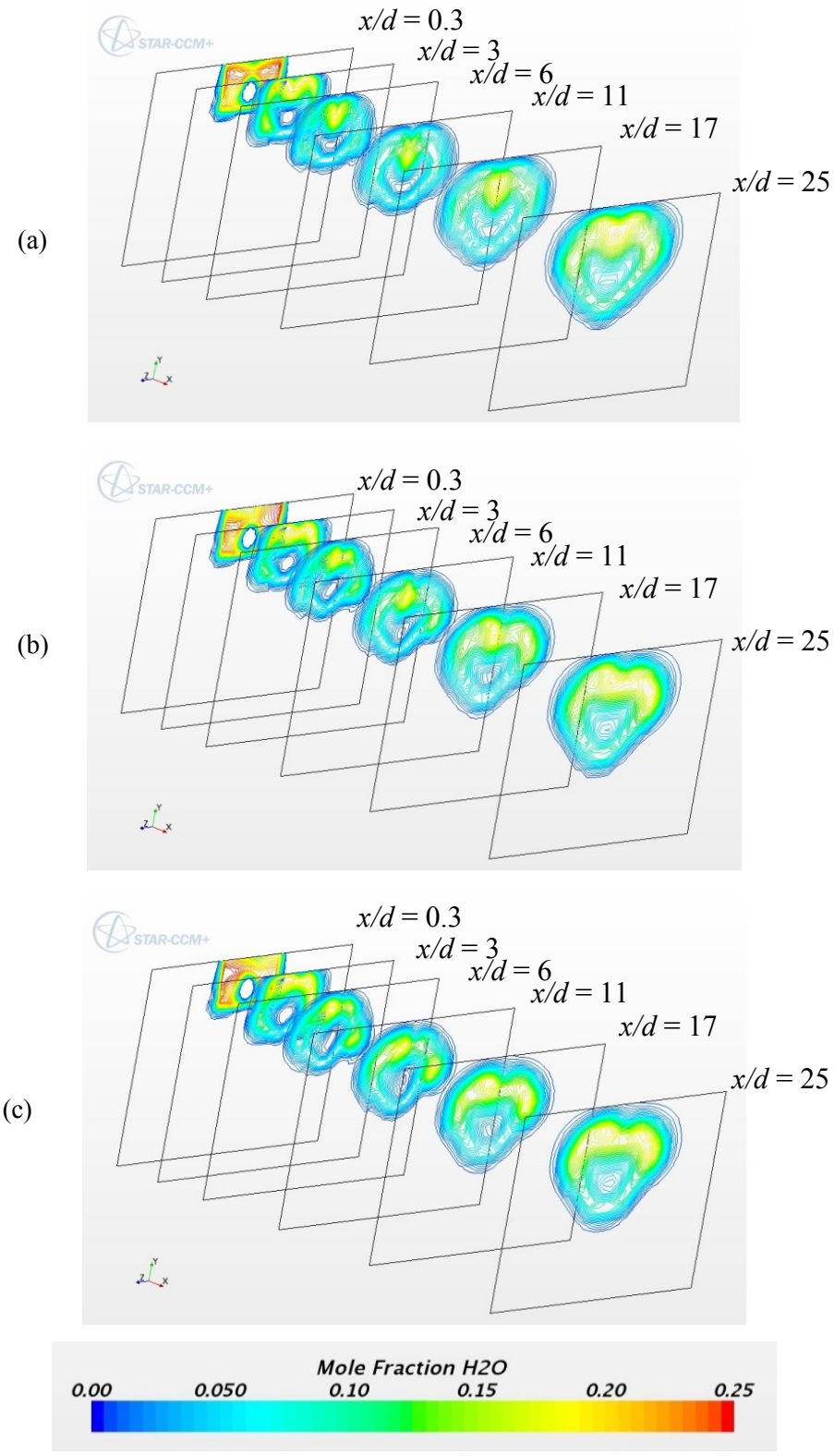

Figure 77 Mole fraction contours of H_2O in the combustor for Configuration R2
a) V00, b) R2 V10, c) R2 V20

(d)

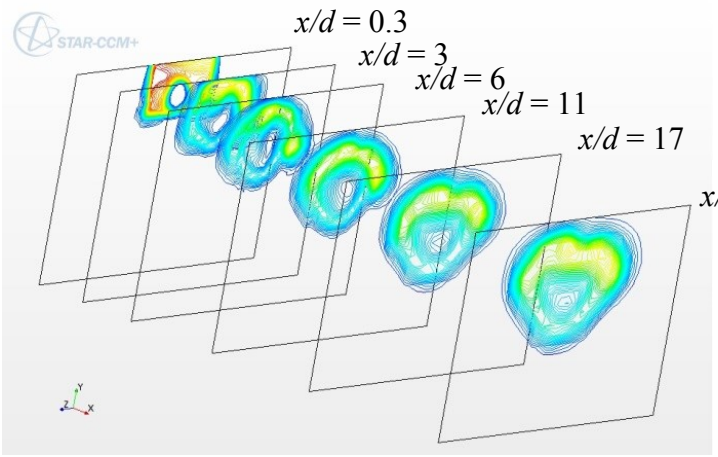

(e)

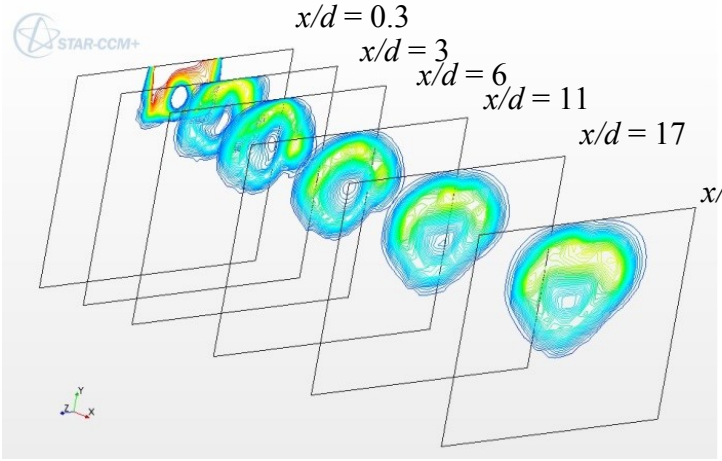

(f)

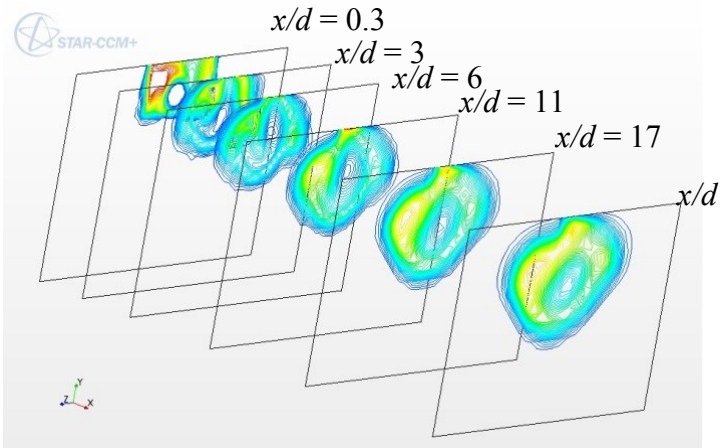

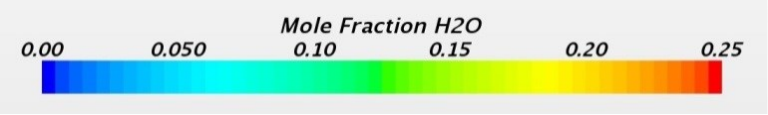

Figure 77 Mole fraction contours of H_2O in the combustor for Configuration R2
d) R2 V30, e) R2 V40, f) R2 V50

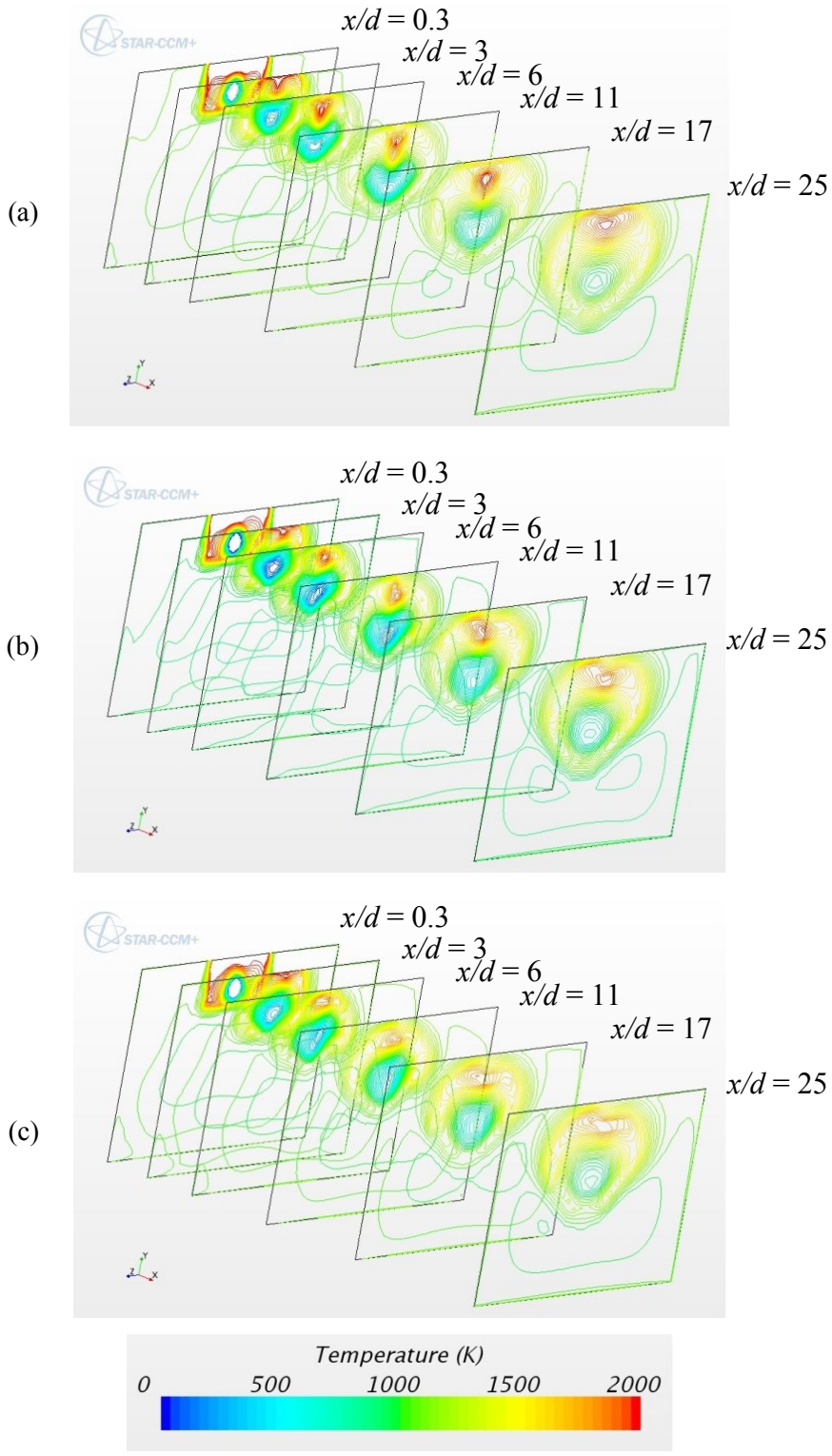

Figure 78 Temperature contours in the combustor for Configuration R2
a) V00, b) R2 V10, c) R2 V20

(d)

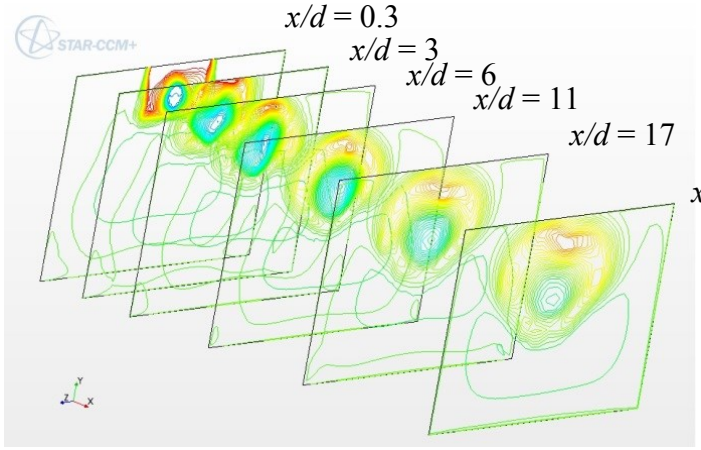

(e)

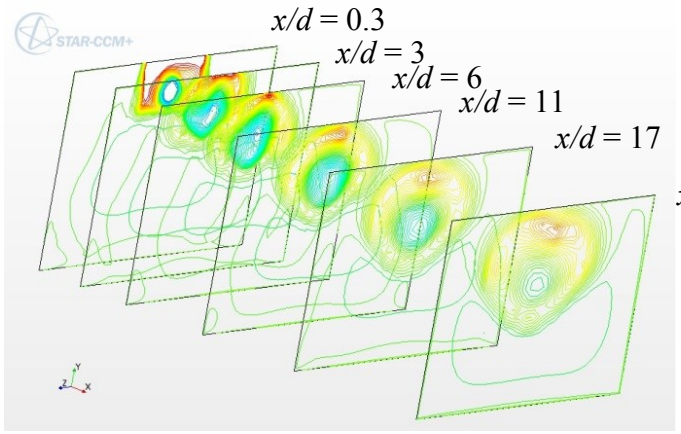

(f)

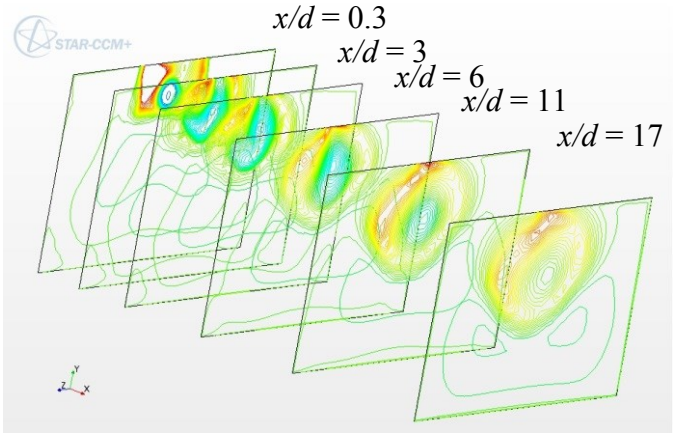

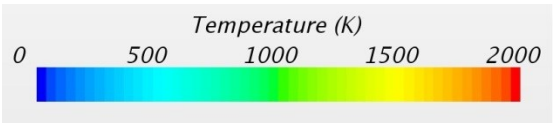

Figure 78 Temperature contours in the combustor for Configuration R2
d) R2 V30, e) R2 V40, f) R2 V50

One indication of possible mixing is turbulent kinetic energy. Turbulent kinetic energy is associated with eddies in turbulent flow that then promotes mixing. The red areas on the contour plots represent areas of turbulent kinetic energy that equal to or greater than 50,000 J/kg. The maximum value of turbulent kinetic energy for a single nozzle configuration was 115,763 J/kg. The red areas on the turbulent kinetic energy contour plots are referred to as high TKE zones in this research paper.

Figure 79 shows that introducing and increasing swirl to the fuel jet increases the turbulent kinetic energy in the flow. In addition the high TKE zone occurs earlier and lasts over a longer distance on the tunnel centerline plane ($z = 0$). Figure 79(d) indicates the axial length that mixing can occur starts to decrease and relates to the start of a recirculation zone. Figure 79(f) shows that the high turbulent kinetic energy zone starts to occur further downstream of the fuel inlet as the fuel jet breaks down.

(a)

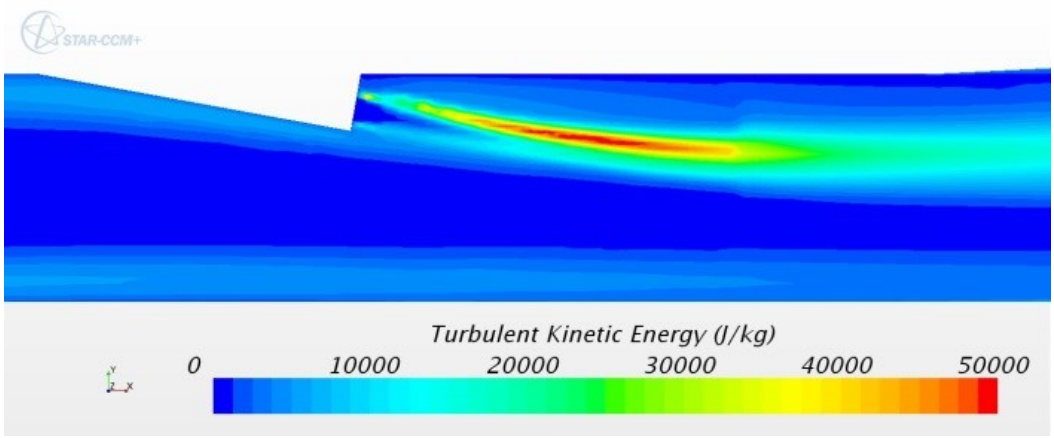

(b)

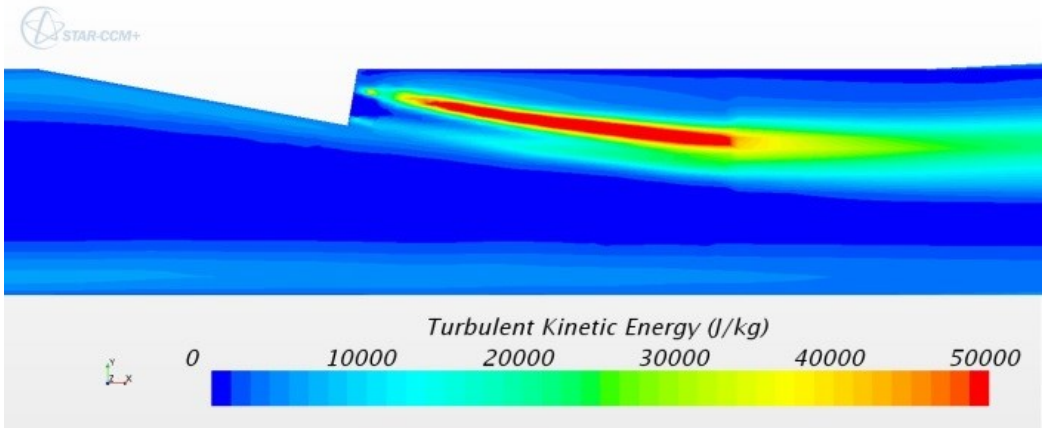

(c)

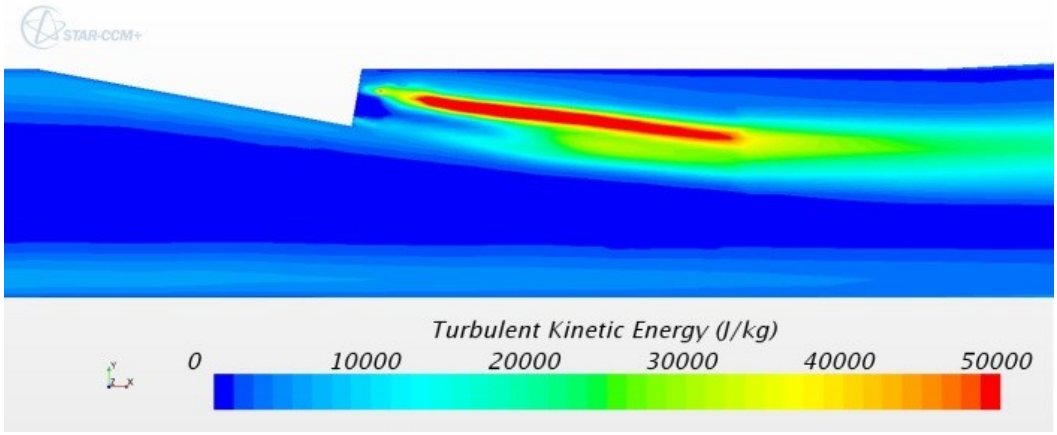

Figure 79 Turbulent kinetic energy plots on the centerline plane (z = 0) in the combustor for Configuration R2
a) V00, b) R2 V10, c) R2 V20

(d)

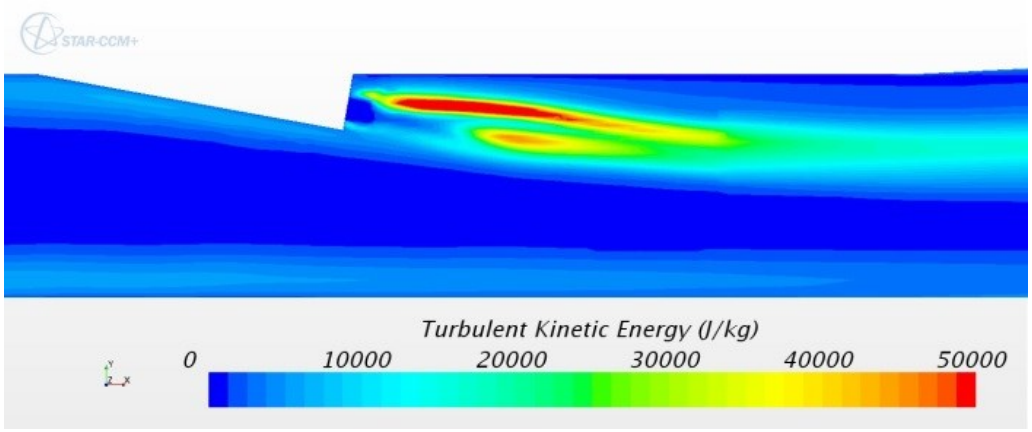

(e)

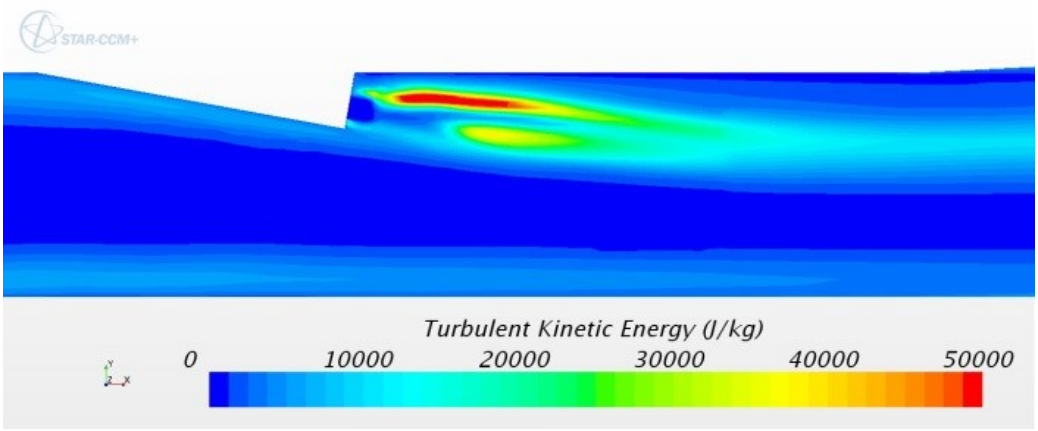

(f)

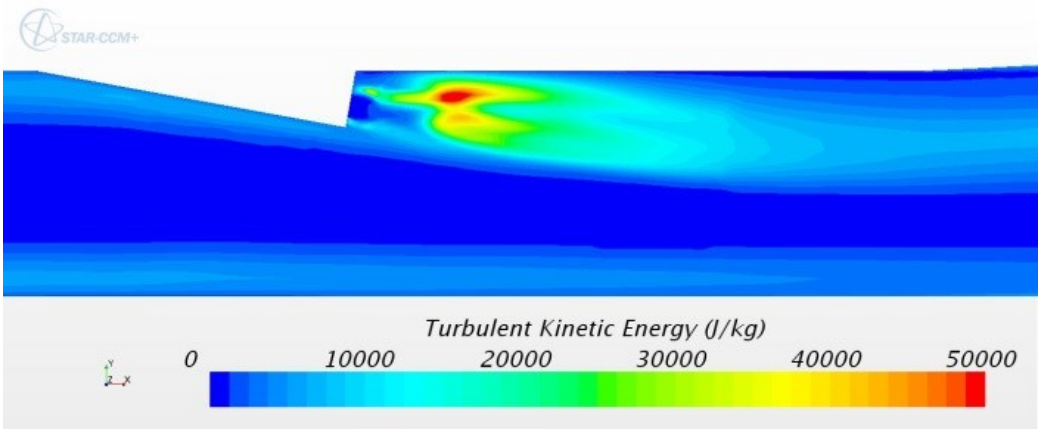

Figure 79 Turbulent kinetic energy plots on the centerline plane (z = 0) in the combustor for Configuration R2
d) R2 V30, e) R2 V40, f) R2 V50

The data shown in Table 5 shows the start location and length of the high TKE zone, the burning efficiency and the increase in burning efficiency due to swirl. As swirl is introduced to the fuel jet and increased the location that the high TKE zone moves closer to the fuel injector exit. This would allow the fuel and oxidizer to mix earlier than the case with no swirl. The high TKE zone start location reaches a minimum with the R2 V30 configuration at only 0.88*d* from the fuel injector exit but then the zone start location moves downstream as more swirl is added. The length of the high TKE zone increases with swirl until a maximum length is achieved 15.67*d* for configuration R2 V20. An increase in the high TKE zone length provides a greater opportunity for the fuel and oxidizer to continue mixing. The zone length then decreases with increasing swirl. Finally, burning efficiency increases with increasing swirl and the configuration R2 V50 provides a 23.3% increase in burning efficiency compared to the case with no swirl.

Table 5 Mixing Data for Configuration R2

	High Turbulent Kinetic Energy Zone			
Configuration	*Zone start location (x/d)*	*Zone Length (d)*	*Burning Efficiency, η_{burn}*	*$\Delta\ \eta_{burn}$ (%)*
Baseline V00	4.57	8.39	0.70	n/a
R2 V10	2.67	14.20	0.70	0.6
R2 V20	0.99	15.67	0.72	3.1
R2 V30	0.88	10.26	0.75	7.6
R2 V40	2.23	5.41	0.81	15.3
R2 V50	3.10	2.31	0.86	23.3

The centerline normalized absolute pressure distribution of the fuel jet for configuration R4 is shown in Figure 80. Configuration R4 has an inner non swirling jet that is 40% of the fuel inlet radius.

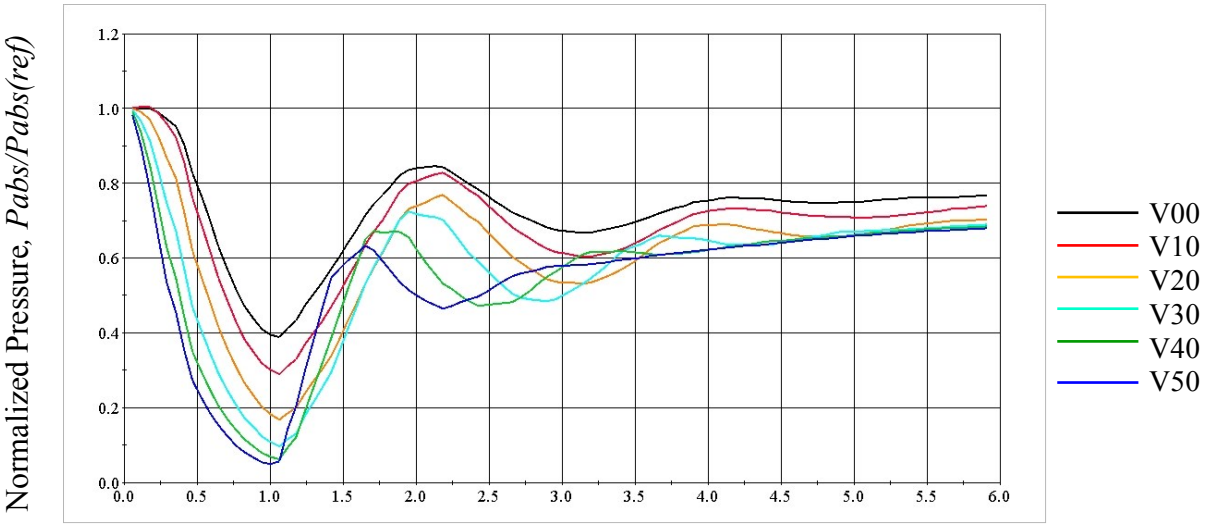

Figure 80 Normalized absolute pressure along the fuel jet potential core for configuration R4

Case R4 V10 has a weak swirl of 0.11 and is represented by the red line in Figure 80. Similar to the baseline case the first shock cell starts to develop at an axial location of $x/d \approx 0.25$. However, the introduction of swirl has decreased the strength of the bow shock from the fuel inlet. The centers of the shock cells occur at $x/d \approx 1.1$, 3.2 and 5.0. Once again each shock cell is weaker than the previous one. The third shock cell barely exists. The fuel jet potential core is shown in Figure 81(a) and has a length approximately equal to 5.5*d*.

Case R4 V20 has a weak swirl of 0.22 and is represented by the gold line in Figure 80. Similar to the baseline case the first shock cell starts to develop at an axial location of $x/d \approx 0.25$.

The centers of the shock cells occur at $x/d \approx 1.1$, 3.15 and 4.75. Once again each shock cell is weaker than the previous one and the third shock cell barely exists. The fuel jet potential core is shown in Figure 81(b) and has a length approximately equal to 3.7*d*.

Case R4 V30 has a weak swirl of 0.34 and is represented by the cyan line in Figure 80. The first shock cell starts to develop almost at the start of the fuel inlet. The centers of the shock cells occur at $x/d \approx 1.1$, 2.75 and 4.2. Once again each shock cell is weaker than the previous one and the third shock cell barely exists. The fuel jet potential core is shown in Figure 81(c) and has a length approximately equal to 2.9*d*.

Case R4 V40 has a swirl strength of 0.47 and is represented by the dark green line in Figure 80. The first shock cell develops at the start of the fuel inlet. The centers of the shock cells occur at $x/d \approx 1.1$ and 2.5. In Figure 81(d) the fuel jet potential core has a length of approximately 1.45*d*.

Case R4 V50 has a strong swirl of 0.61 and is represented by the dark blue line in Figure 80. The first shock cell develops at the start of the fuel inlet. The centers of the shock cells occur at $x/d \approx 1.1$ and 2.2. The fuel jet potential core as shown in Figure 81(d) shows the initial stages of the breakdown of the fuel jet. The fuel jet potential core is approximately 1.2*d* in length.

(a)

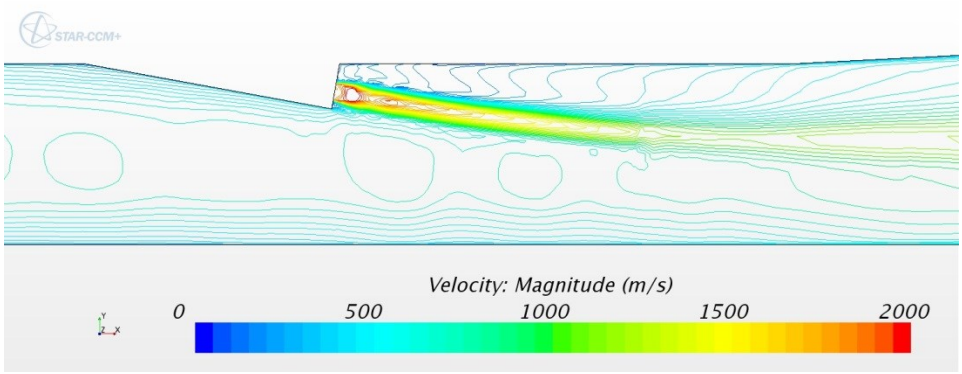

(b)

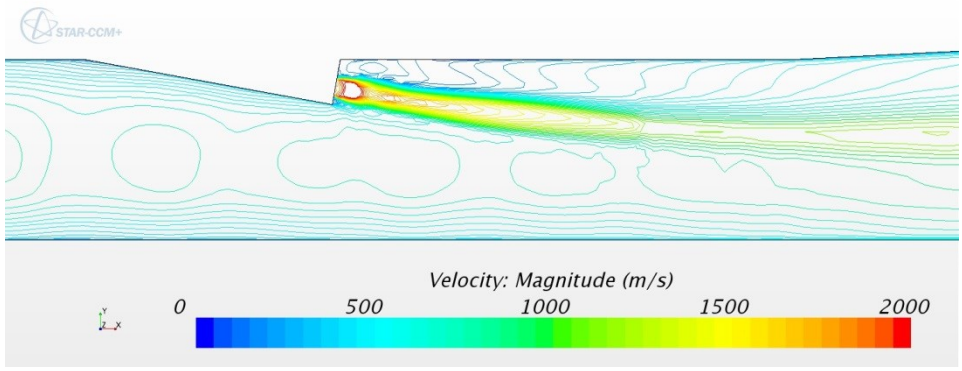

(c)

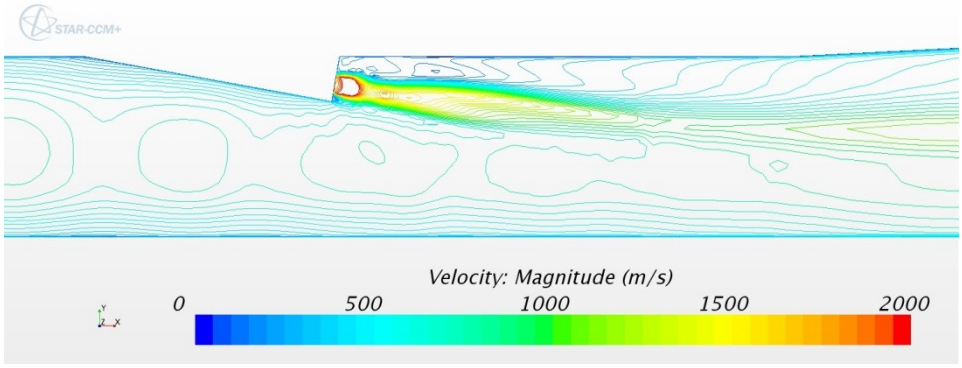

Figure 81 Velocity contours on the centerline plane (z = 0) showing potential core of fuel jet for Configuration R4
a) R4 V10, b) R4 V20, c) R4 V30

(d)

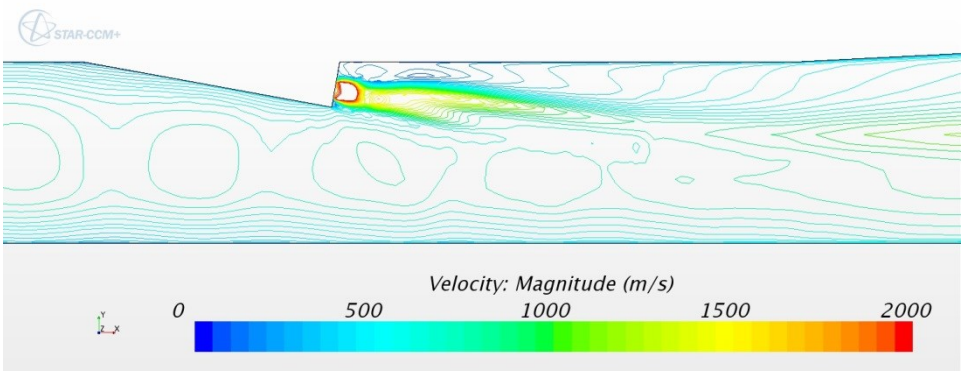

(e)

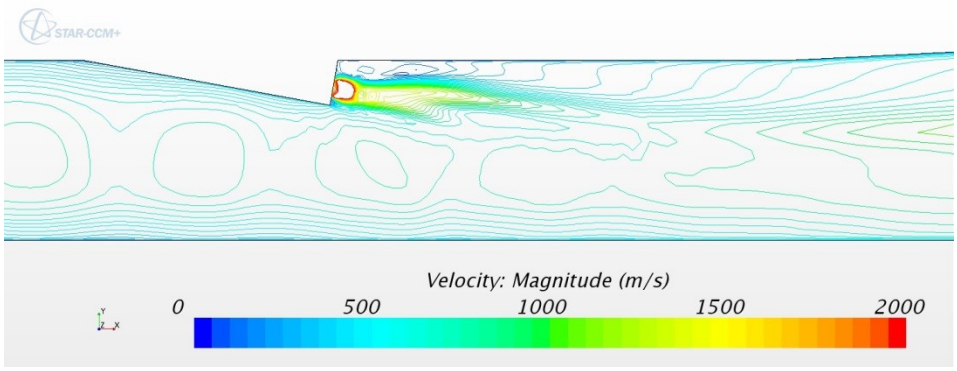

Figure 81 Velocity contours on the centerline plane (z = 0) showing potential core of fuel jet for Configuration R4
d) R4 V40, e) R4 V50

Figure 82(a) shows the contour plot of H_2O mole fraction for the baseline case V00. The contour plots are similar to those for Configuration R2. Once swirl is introduced one of the high H_2O mole fraction zones on the combustor upper wall is eliminated and the areas on either side of the nozzle become asymmetric. As swirl strength increases the two areas on the fuel inlet wall seem to rotate clockwise as viewed looking upstream. The most noticeable difference is in Figure 82(f) case R4 V50. Although the high H_2O mole fraction zone is reduced on the nozzle wall the high H_2O mole fraction zone has only just started trailing downstream on the combustor upper wall. This is likely due to the onset of the fuel jet break down.

Again the introduction of swirl indicates a tendency to assist combustion to occur further upstream than for a non-swirling fuel jet.

(a)

(b)

(c)

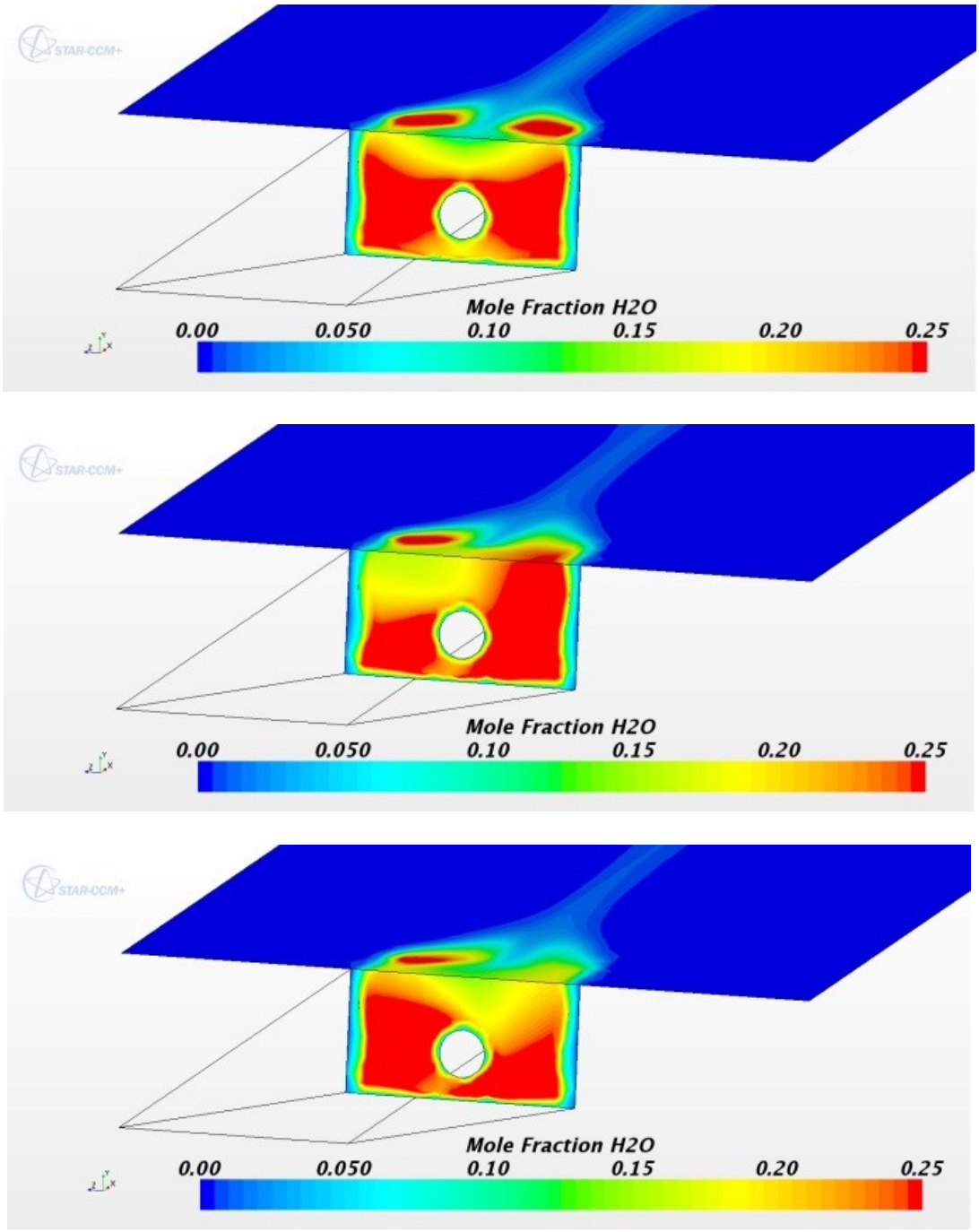

Figure 82 Mole fraction contours of H_2O on the fuel inlet wall and combustor upper wall for Configuration R4
a) V00, b) R4 V10, c) R4 V20

(d)

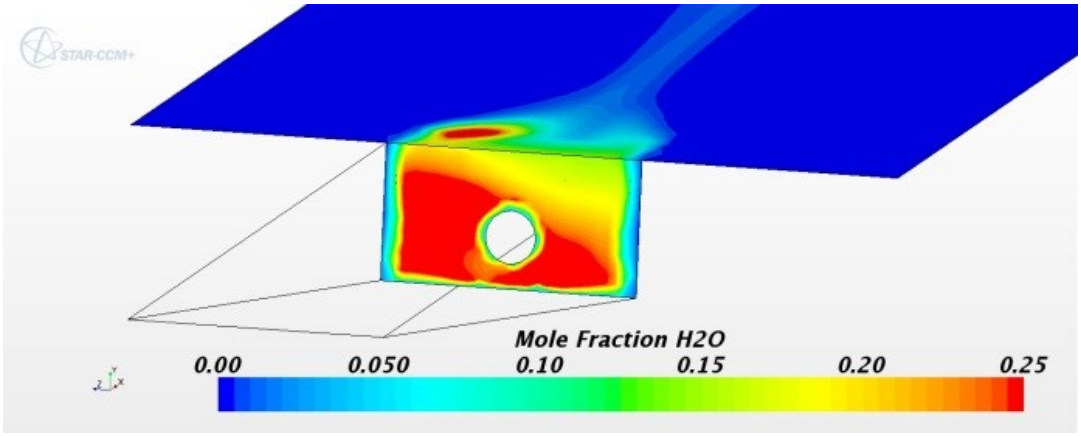

(e)

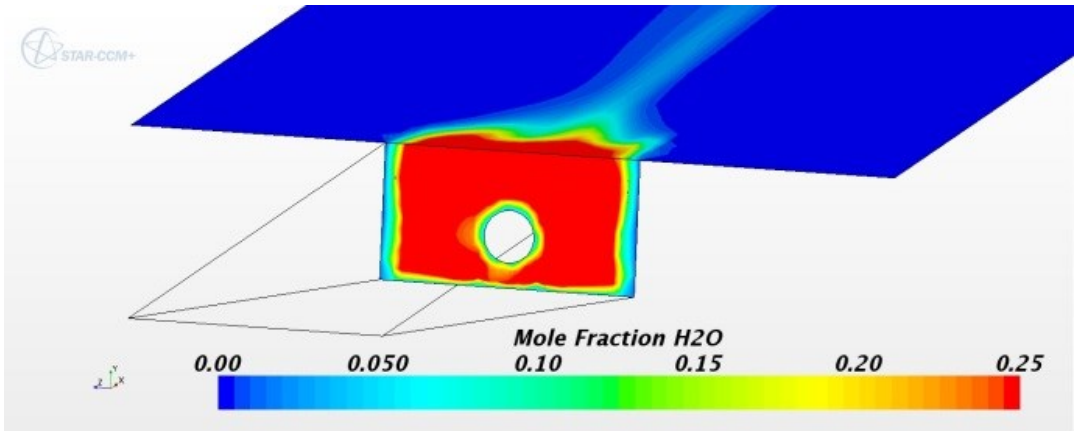

(f)

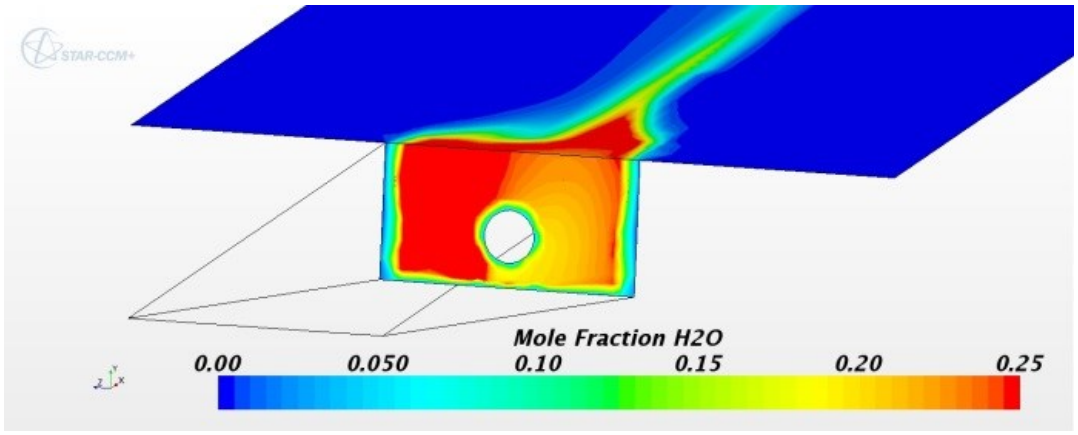

Figure 82 Mole fraction of H2O on the fuel inlet wall and combustor upper wall for Configuration R4
d) R4 V30, e) R4 V40, f) R4 V50

Figure 83 shows a progression of H_2O mole fraction contour plots at axial distances $x/d \approx$ 0.3, 3.0, 6.0, 11.0, 17.0 and 25 within the combustor. As with Configuration R2 swirl has more of an effect on near-field flow characteristics than far field characteristics. The more pronounced differences of the H_2O mole fraction contours can still be seen between $x/d = 0.3$ and 6.0.

The temperature contour plots at axial distances $x/d \approx$ 0.3, 3.0, 6.0, 11.0, 17.0 and 25 within the combustor are shown in Figure 84. Again the effect of swirl on temperature is seen throughout the combustor length with the temperature decreasing as swirl increases.

The turbulent kinetic energy on the tunnel centerline plane (z = 0) is shown in Figure 85. Results from Configuration R4 show similar trends when compared with the results from Configuration R2. Increasing swirl to the fuel jet increases the high turbulent kinetic energy zone in the flow, encourages the zone to occur closer to the fuel inlet and extends over a longer distance. Again Figure 85(f) indicates the axial distance over which the promotion of mixing occurs starts to decrease as a recirculation zone starts.

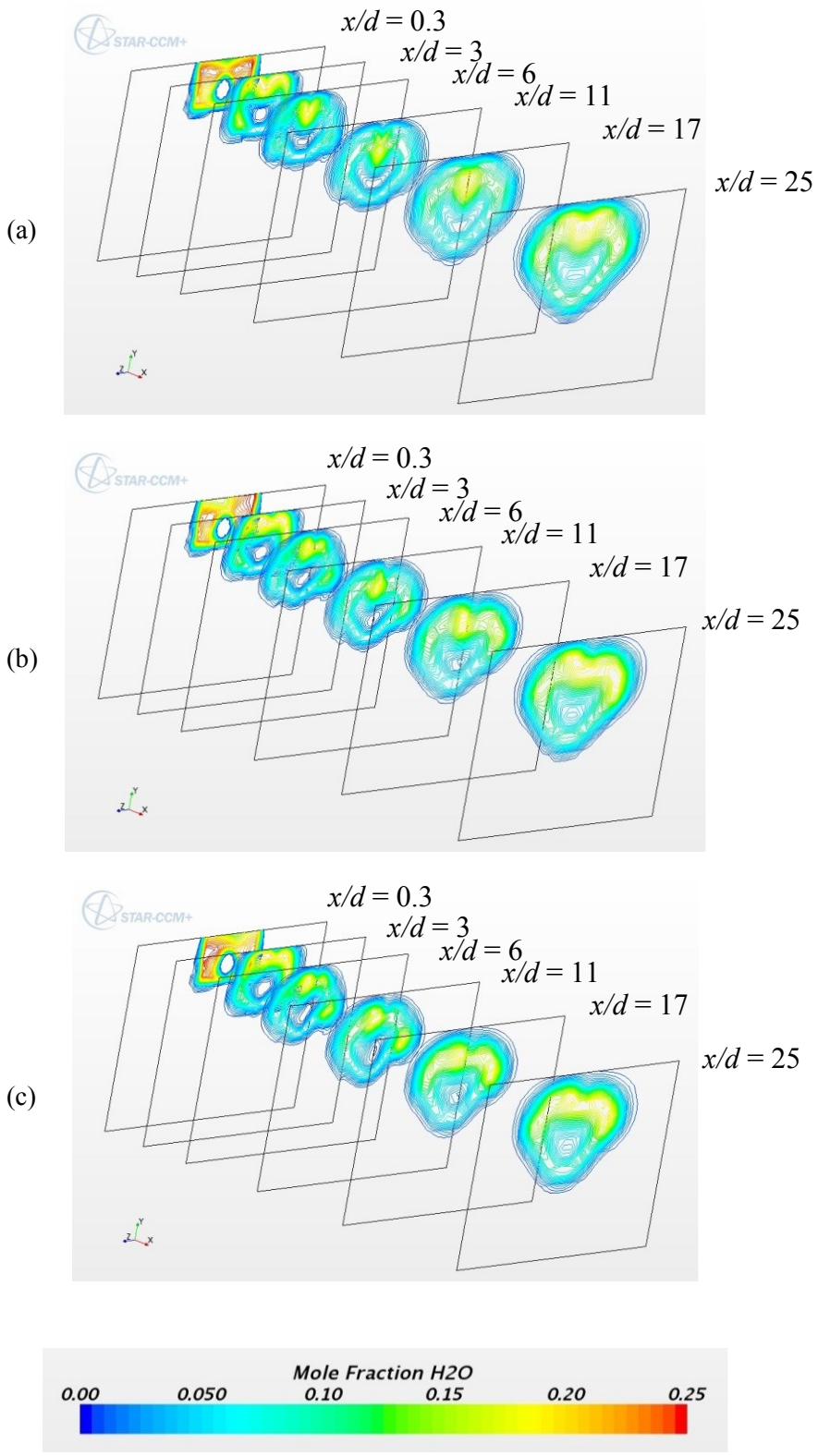

Figure 83 Mole fraction contours of H_2O in the combustor for Configuration R4
a) V00, b) R4 V10, c) R4 V20

(d)

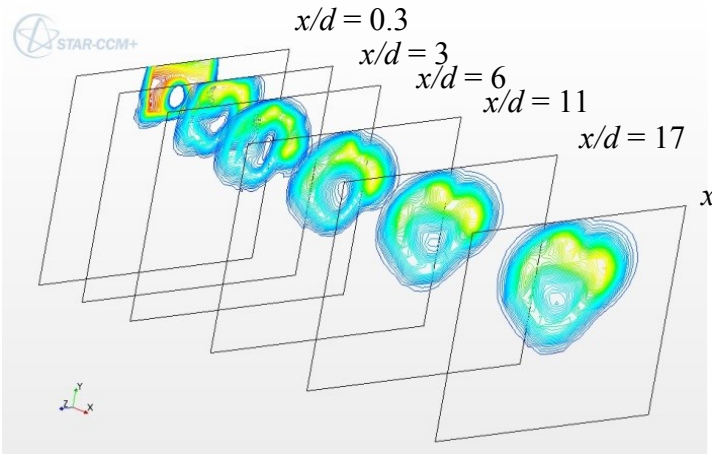

(e)

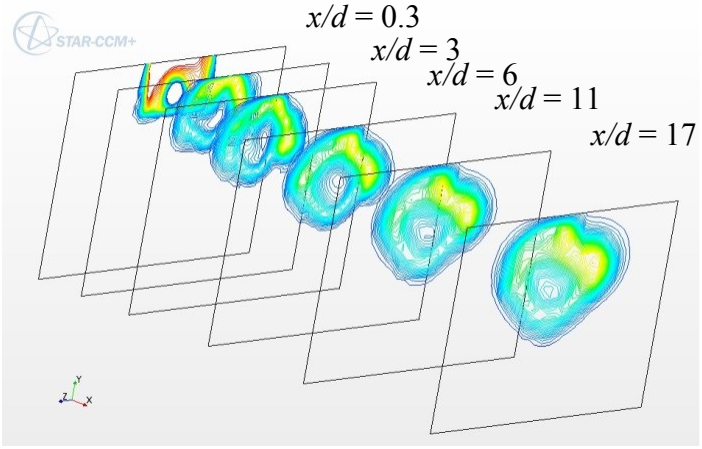

(f)

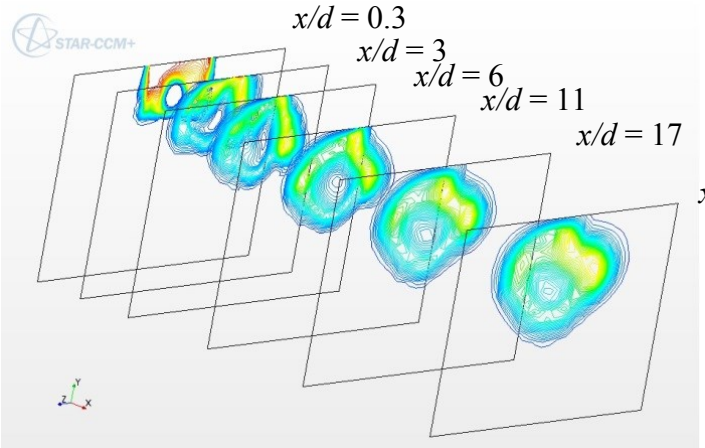

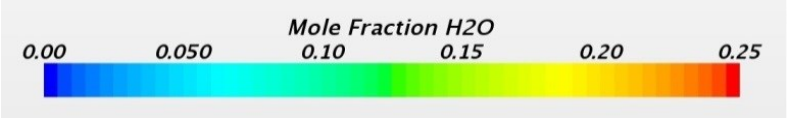

Figure 83 Mole fraction contours of H_2O in the combustor for Configuration R4
c) R4 V20, d) R4 V30, e) R4 V40, f) R4 V50

(a)

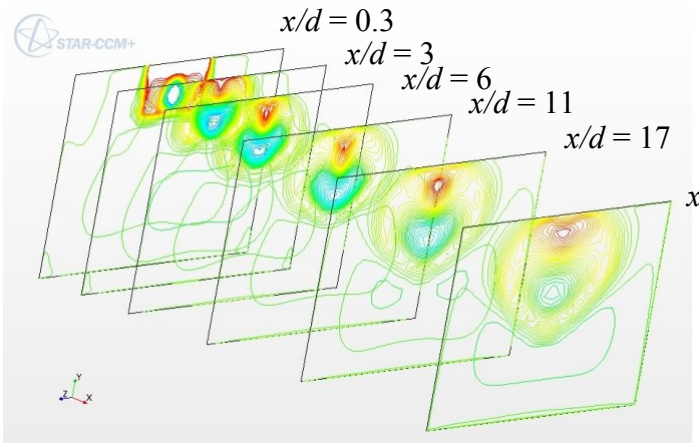

(b)

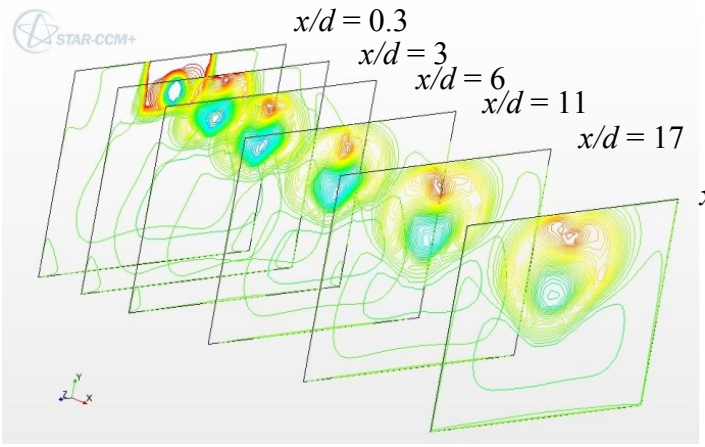

(c)

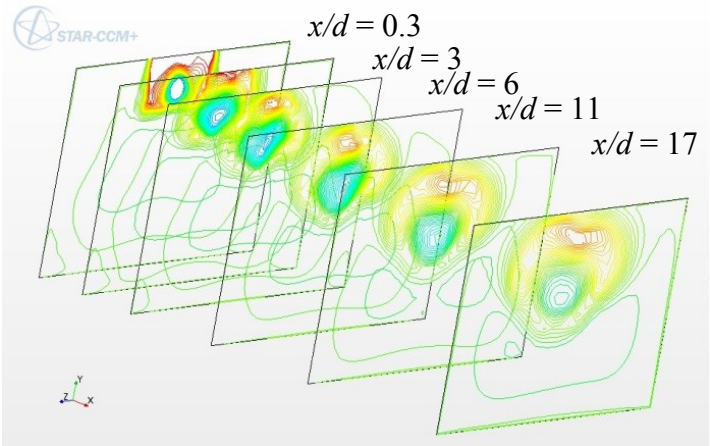

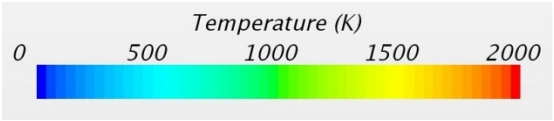

Figure 84 Temperature contours in the combustor for Configuration R4
a) V00, b) R4 V10, c) R4 V20

(d)

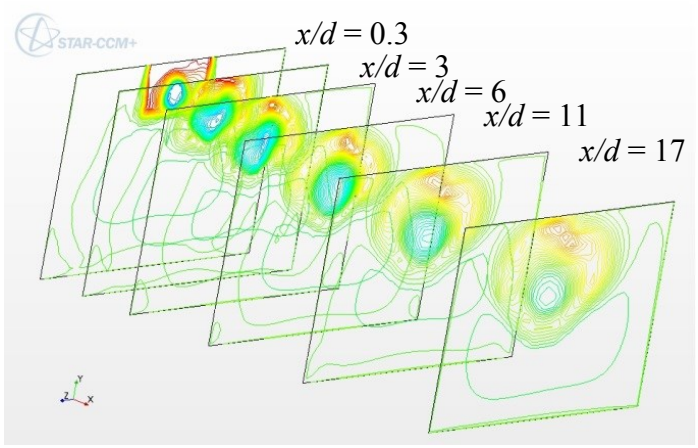

(e)

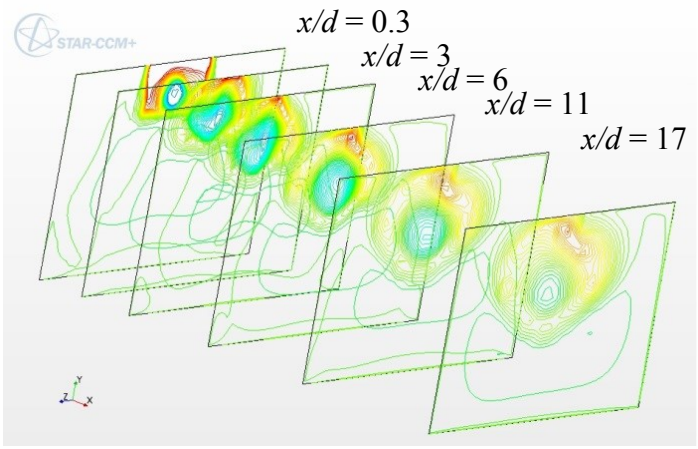

(f)

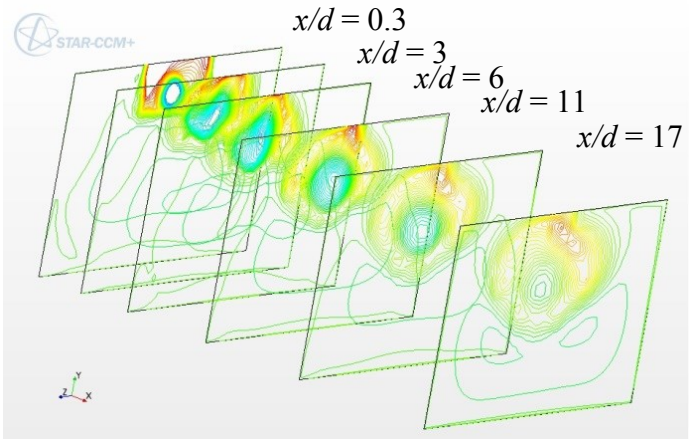

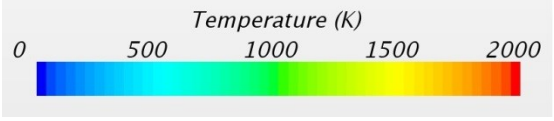

Figure 84 Temperature contours in the combustor for Configuration R4
d) R4 V30, e) R4 V40, f) R4 V50

(a)

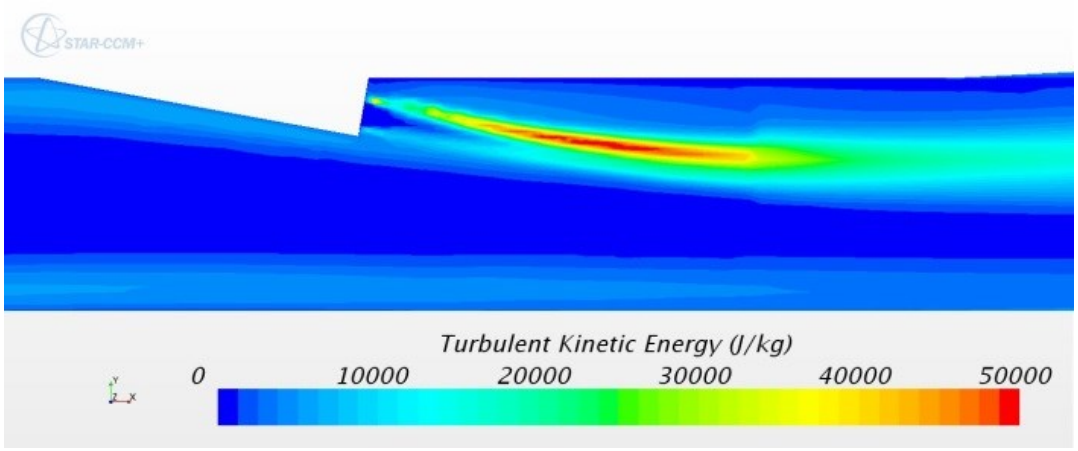

(b)

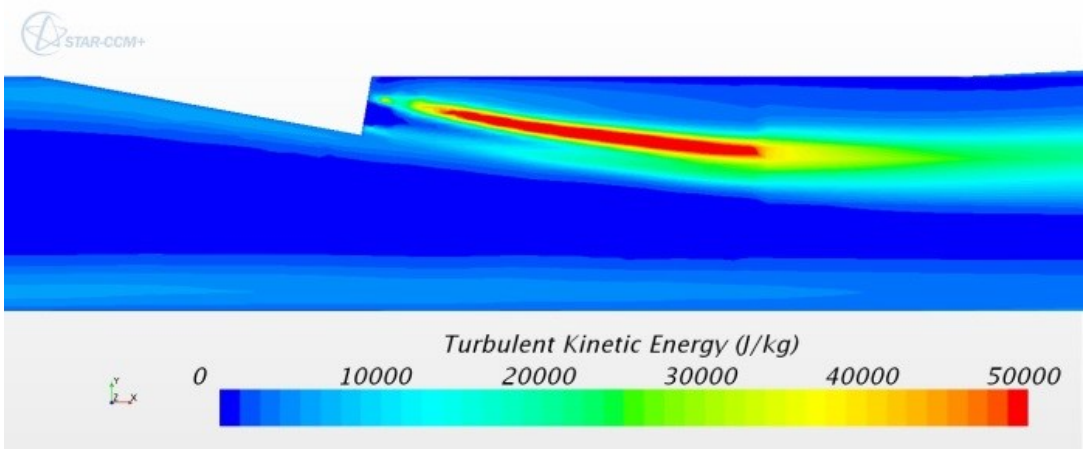

(c)

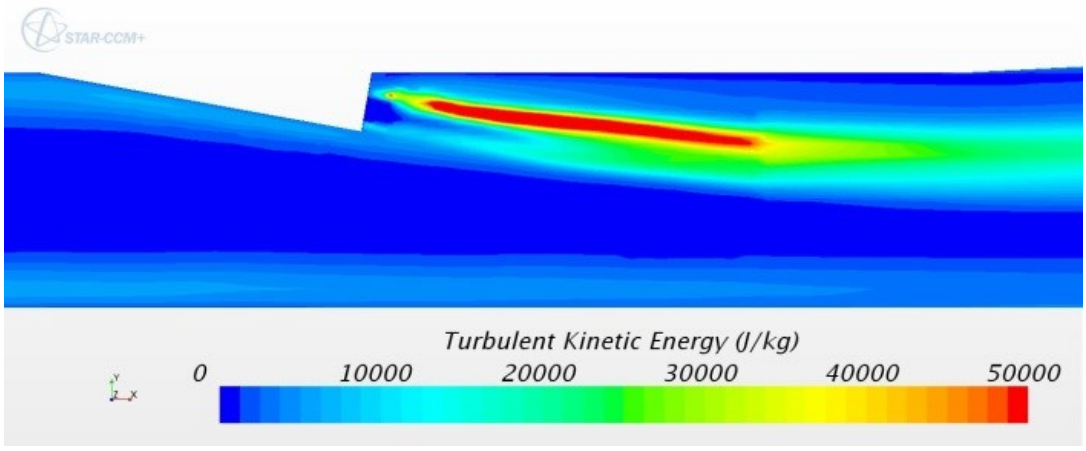

Figure 85 Turbulent kinetic energy plots on the centerline plane (z = 0) in the combustor for Configuration R4
a) V00, b) R4 V10, c) R4 V20

(d)

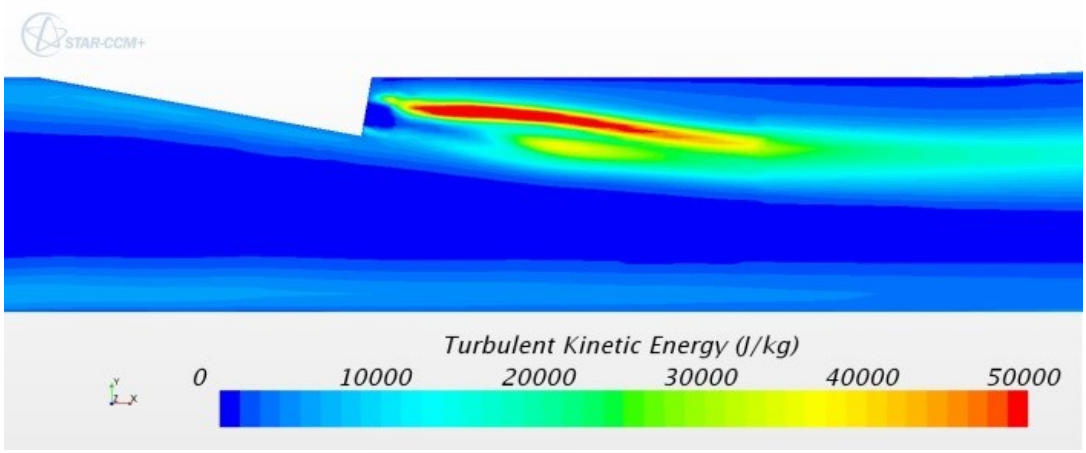

(e)

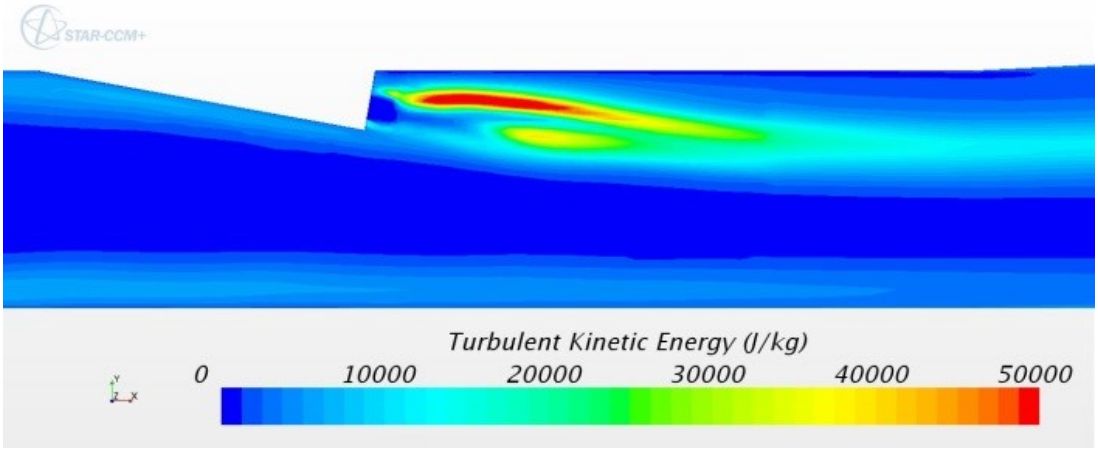

(f)

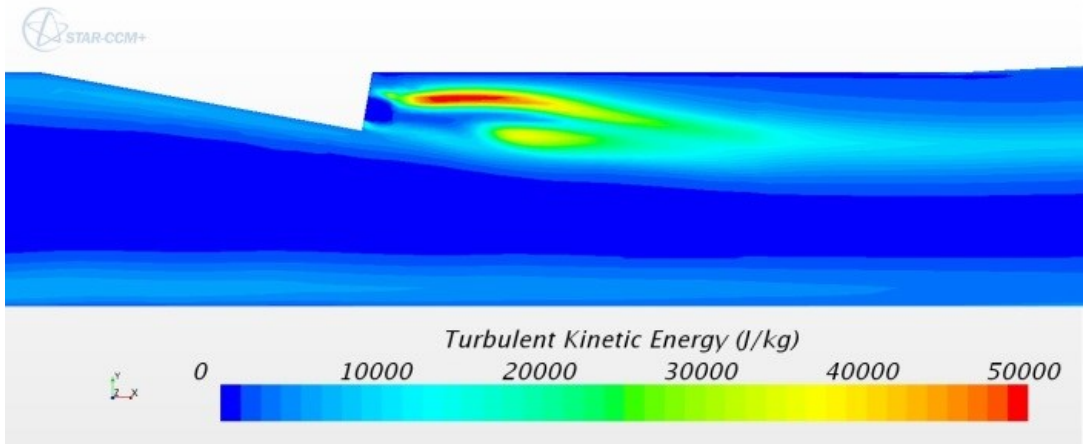

Figure 85 Turbulent kinetic energy plots on the centerline plane (z = 0) in the combustor for Configuration R4
d) R4 V30, e) R4 V40, f) R4 V50

The results shown in Table 6 indicate the same trend as shown in Table 5 for configuration R2. The start location of the high turbulent kinetic energy zone moves closer to the fuel injector exit with increasing swirl until a minimum distance of 1.19*d* is reached for configuration R4 V20. The high TKE zone start location then moves downstream with higher swirl intensity. Configuration R2 results in a closer start location of the high TKE zone to the fuel injector exit than configuration R4. A maximum zone length of 15.47*d* is achieved with configuration R2 V20 and then the length decreases with increasing swirl. The burning efficiency increases with increasing swirl and configuration R4 V50 results in a 20.2% increase in burning efficiency compared to the case with no swirl.

Table 6 Mixing Data for Configuration R4

	High Turbulent Kinetic Energy Zone			
Configuration	*Zone start location (x/d)*	*Length of zone (d)*	*Burning Efficiency,* η_{burn}	$\Delta\ \eta_{burn}$ *(%)*
Baseline V00	4.57	8.39	0.70	-
R4 V10	2.70	14.24	0.70	0.7
R4 V20	1.19	15.47	0.72	2.5
R4 V30	2.11	10.58	0.74	6.2
R4 V40	2.39	7.08	0.78	12.5
R4 V50	2.47	4.42	0.84	20.2

The centerline normalized absolute pressure distribution of the fuel jet for configuration R6 is shown in Figure 86. Configuration R4 has an inner non swirling jet that is 60% of the fuel inlet radius.

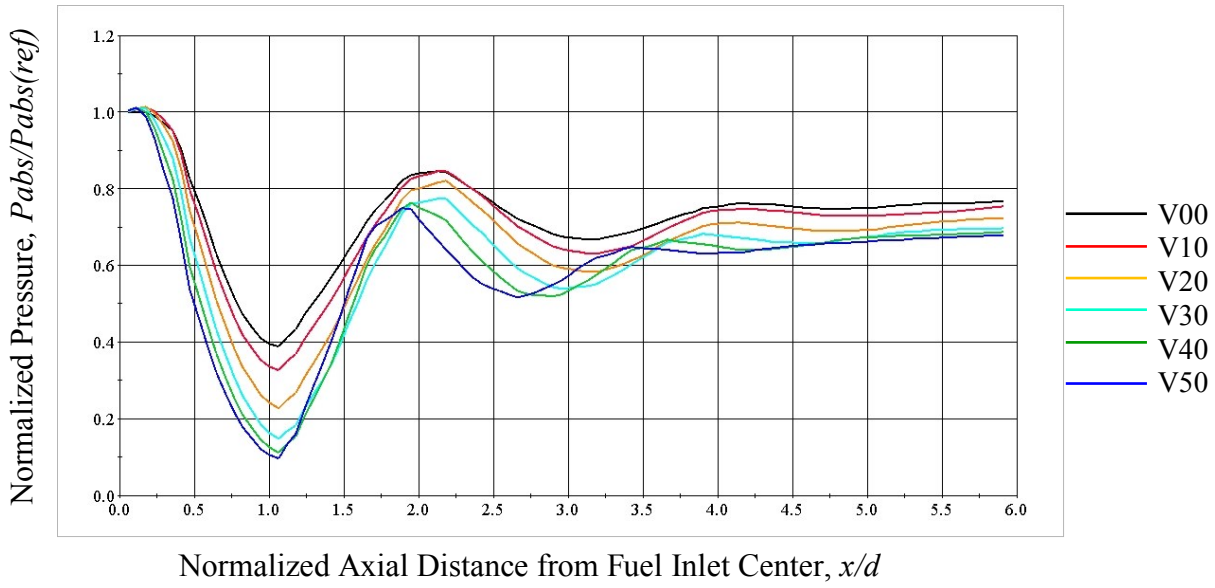

Figure 86 Normalized absolute pressure along the fuel jet potential core for configuration R6

Case R6 V10 has a weak swirl of 0.09 and is represented by the red line in Figure 86. The first shock cell starts to develop at an axial location of $x/d \approx 0.25$. The centers of the shock cells occur at $x/d \approx 1.1$, 3.2 and 5.0. The third shock cell barely exists. The fuel jet potential core has a length approximately equal to $4.75d$ and is shown in Figure 87(a).

Case R6 V20 has a weak swirl of 0.18 and is represented by the gold line in Figure 86. Again the first shock cell starts to develop at an axial location of $x/d \approx 0.25$. The centers of the shock cells occur at $x/d \approx 1.1$, 3.15 and 4.75. The fuel jet potential core is shown in Figure 87(b) and has a length approximately equal to $3.7d$.

Case R6 V30 has a weak swirl of 0.27 and is represented by the cyan line in Figure 86. The first shock cell starts to develop at an axial location of $x/d \approx 0.25$. The centers of the shock

cells occur at $x/d \approx 1.1$, 3.0 and 4.6. The fuel jet potential core is shown in Figure 87(c). The fuel jet potential core has a length approximately equal to 3.25*d*.

Case R6 V40 has a weak swirl of 0.35 and is represented by the dark green line in Figure 86. The first shock cell develops at an axial location of $x/d \approx 0.2$. The centers of the shock cells occur at $x/d \approx 1.1$, 2.8 and 4.2. In Figure 87(d) the fuel jet potential core has a length of approximately 2.9*d*.

Case R6 V50 has a swirl strength of 0.41 and is represented by the dark blue line in Figure 86. The first shock cell develops at the start of the fuel inlet. The centers of the shock cells occur at $x/d \approx 1.1$, 2.7 and 3.9. The fuel jet potential core shown in Figure 87(d) is approximately 1.5*d* in length.

Figure 88(a) shows the plot of H_2O mole fraction for the baseline case V00. The contour plots are similar to those used for Configurations R2 and R4 and the same trend of the high H_2O mole fraction zones on the combustor upper wall and fuel inlet wall moving in a clock wise direction can be seen.

Figure 89 shows a progression of H_2O mole fraction contour plots at axial distances $x/d \approx$ 0.3, 3.0, 6.0, 11.0, 17.0 and 25 within the combustor. As with Configurations R2 and R4 swirl has more of an effect on near-field flow characteristics than far field characteristics. The more pronounced differences of the H_2O mole fraction contours can still be seen between $x/d = 0.3$ and 6.0.

The temperature contour plots at axial distances $x/d \approx 0.3$, 3.0, 6.0, 11.0, 17.0 and 25 within the combustor are shown in Figure 90. Again the effect of swirl on temperature is seen throughout the combustor length with the temperature decreasing as swirl increases.

(a)

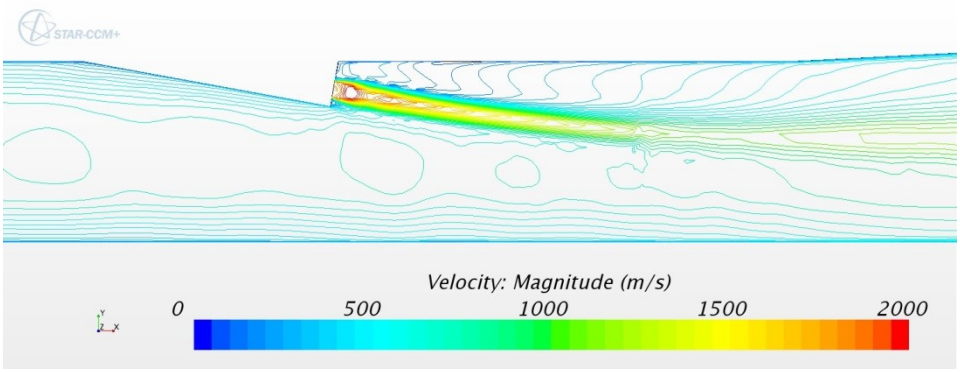

(b)

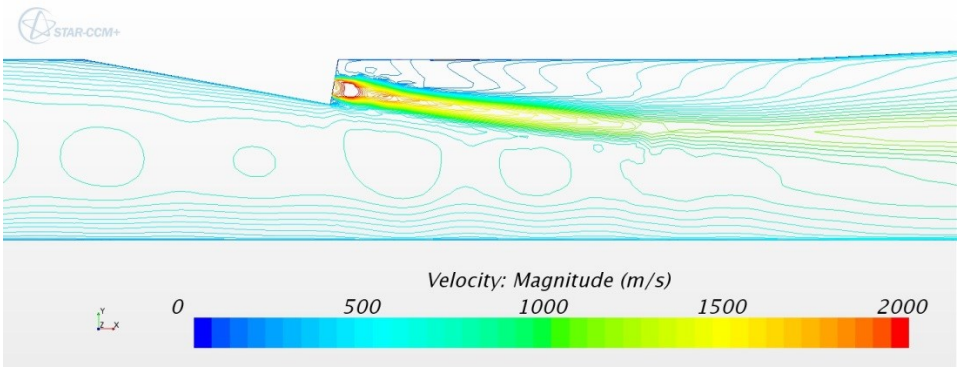

(c)

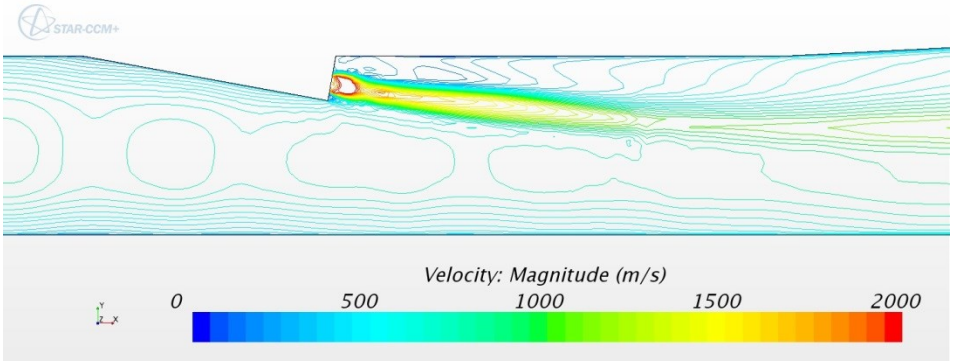

Figure 87 Velocity contours on the centerline plane (z = 0) showing potential core of fuel jet for Configuration R6
a) R6 V10, b) R6 V20, c) R6 V30

(d)

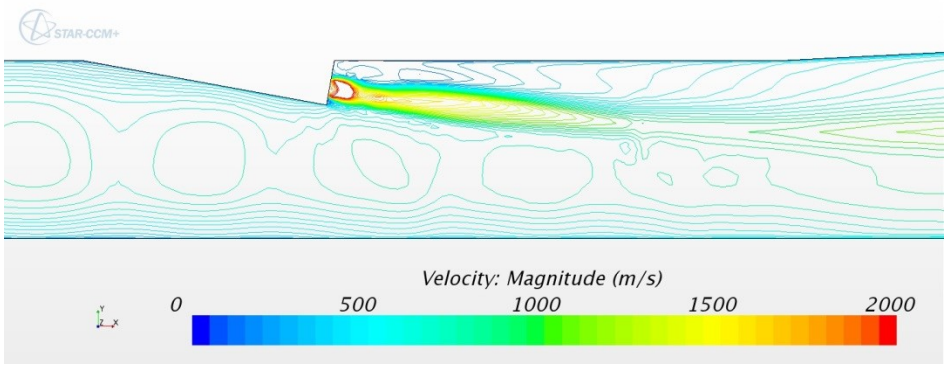

(e)

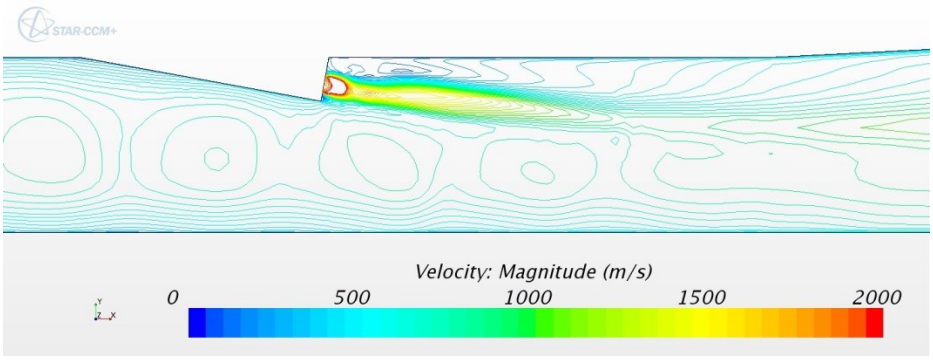

Figure 87 Velocity contours on the centerline plane (z = 0) showing potential core of fuel jet for Configuration R6
d) R6 V40, e) R6 V50

The turbulent kinetic energy on the centerline plane (z = 0) is shown in Figure 91. Results from Configuration R6 show the same trends as the results from Configurations R2 and R4. Increasing swirl to the fuel jet increases the turbulent kinetic energy in the flow, the promotion of mixing occurs earlier and lasts over a longer distance.

(a)

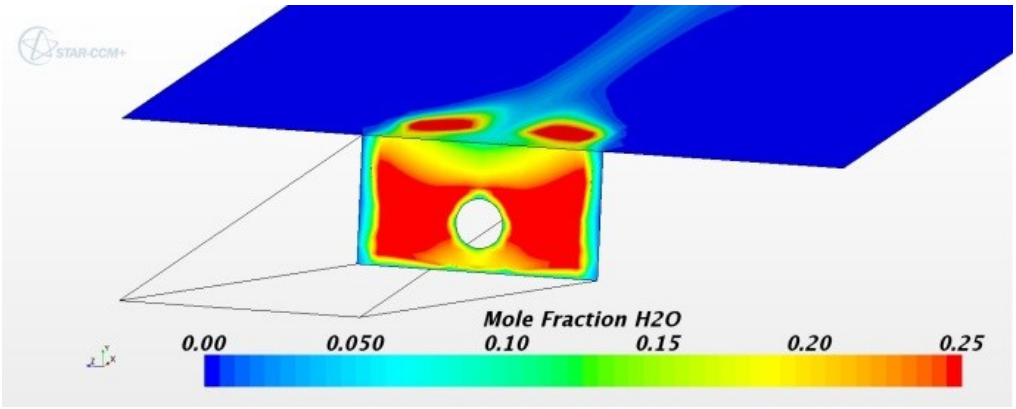

(b)

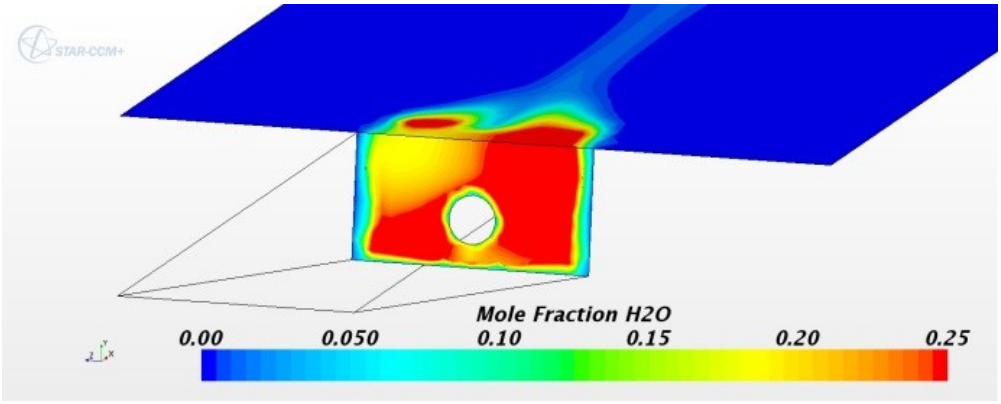

(c)

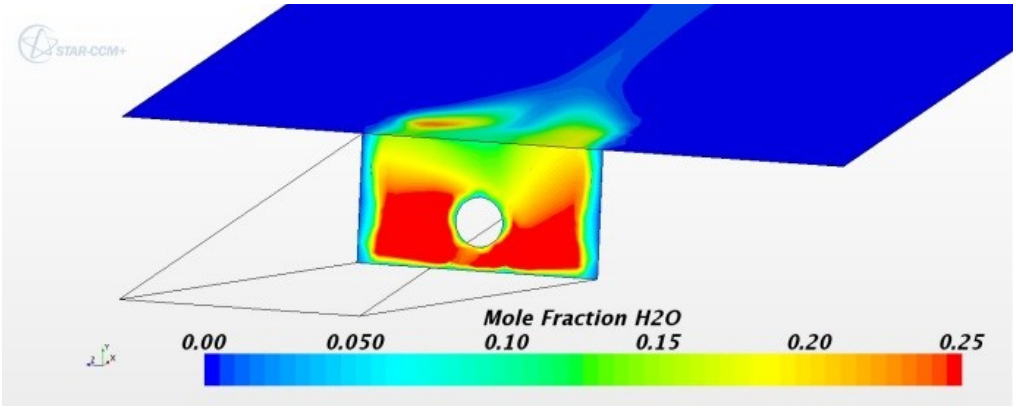

Figure 88 Mole fraction contours of H_2O on the fuel inlet wall and combustor upper wall for Configuration R6
a) V00, b) R6 V10, c) R6 V20

(d)

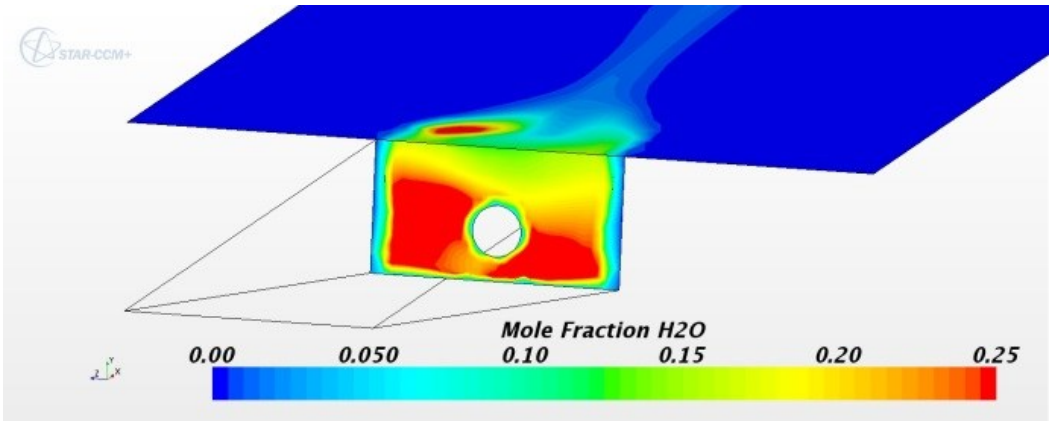

(e)

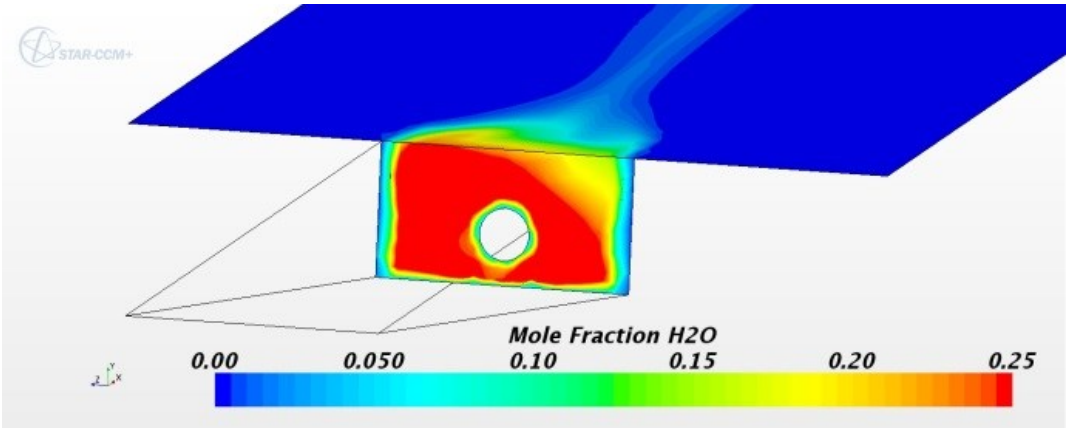

(f)

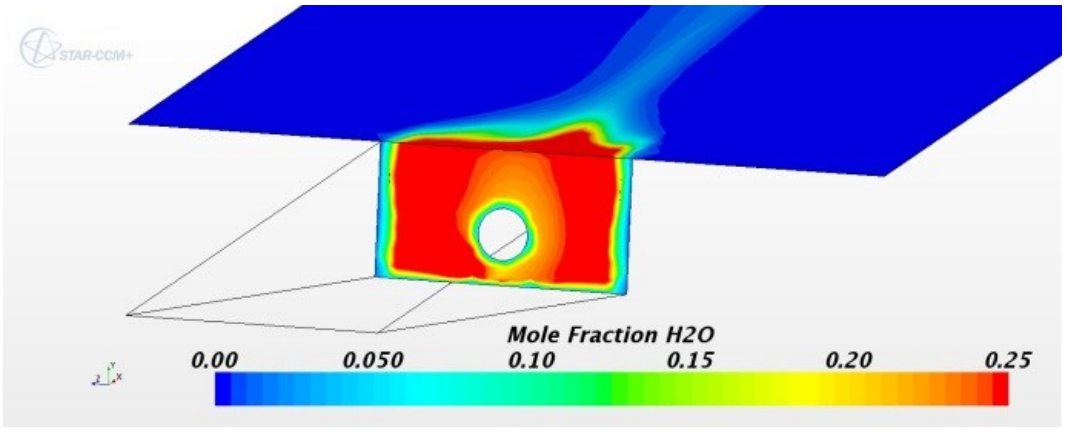

Figure 88 Mole fraction contours of H2O on the fuel inlet wall and combustor upper wall for Configuration R6
d) R6 V30, e) R6 V40, f) R6 V50

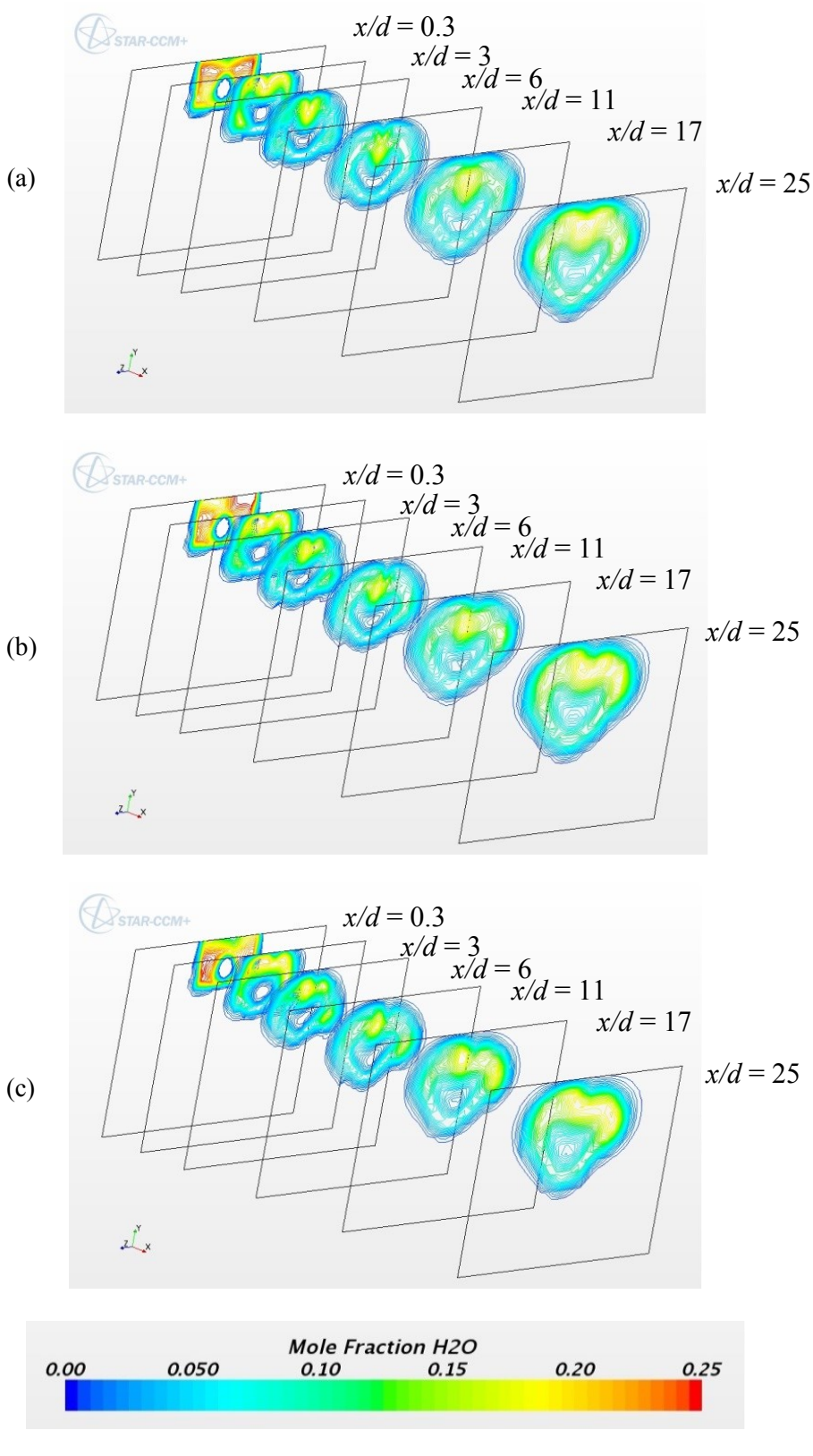

Figure 89 Mole fraction contours of H_2O in the combustor for Configuration R6
a) V00, b) R6 V10, c) R6 V20

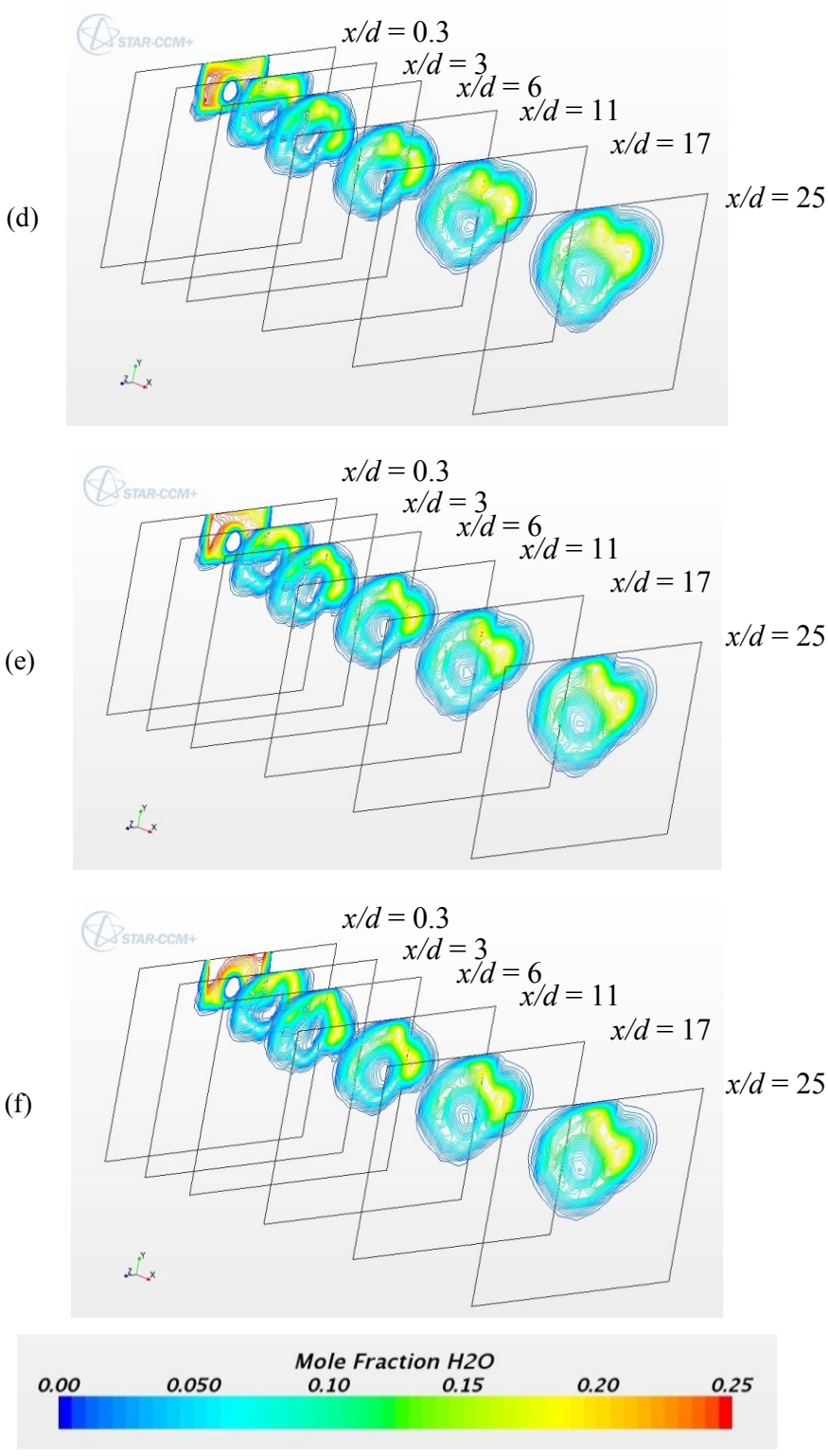

Figure 89 Mole fraction contours of H_2O in the combustor for Configuration R6
d) R6 V30, e) R6 V40, f) R6 V50

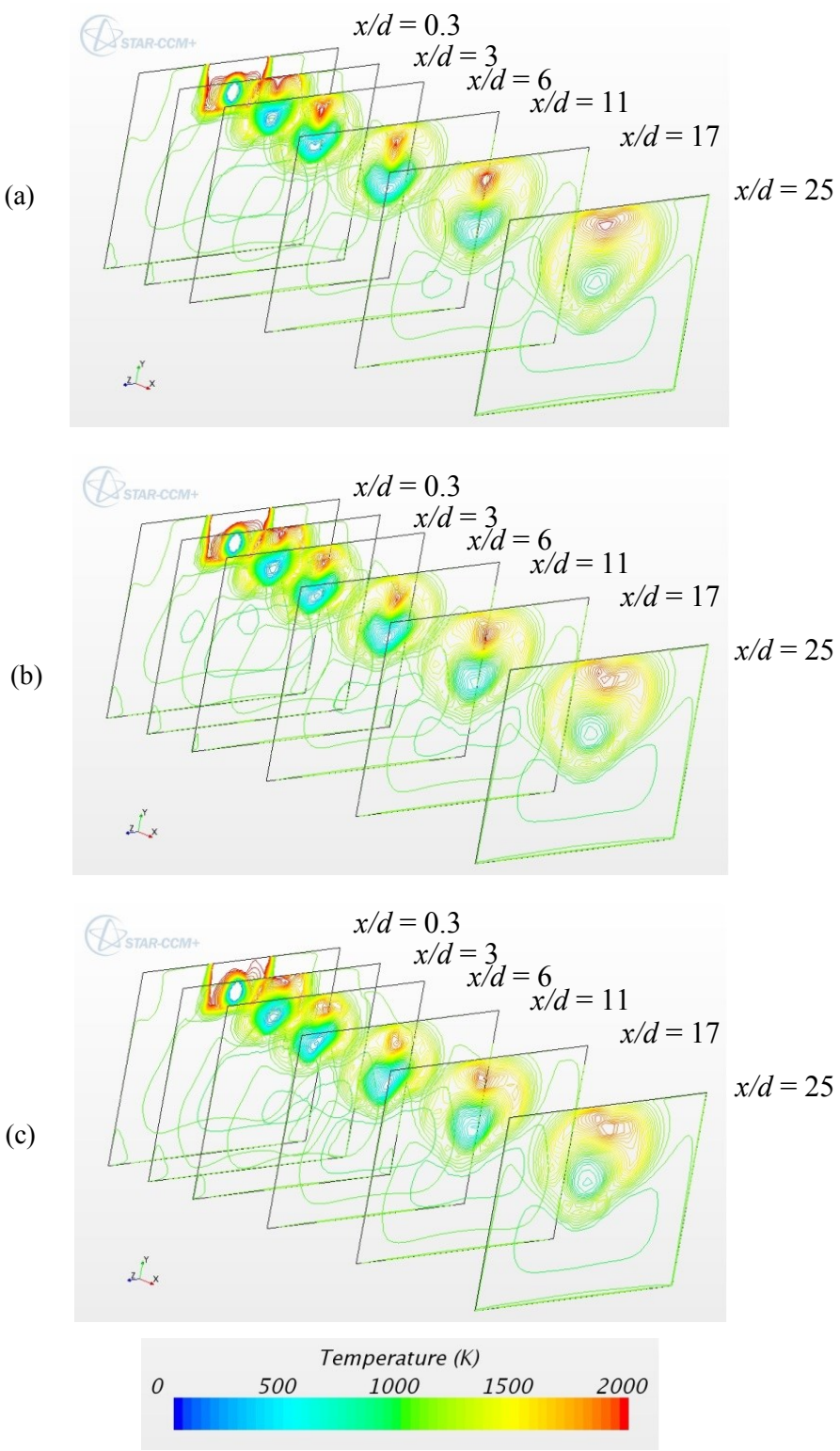

Figure 90 Temperature contours in the combustor for Configuration R6
a) V00, b) R6 V10, c) R6 V20

(d)

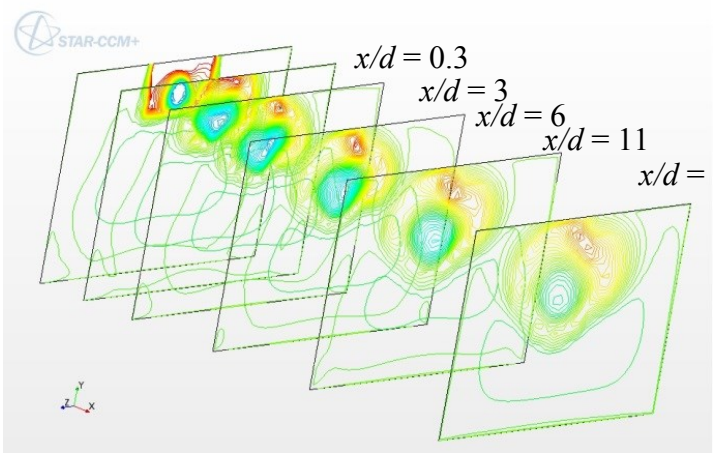

(e)

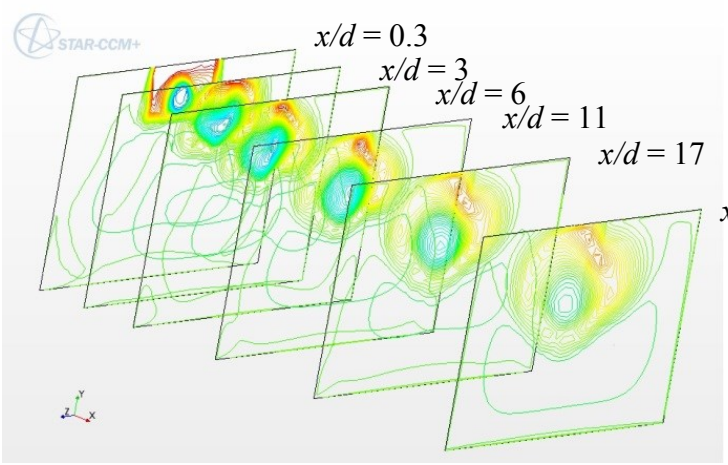

(f)

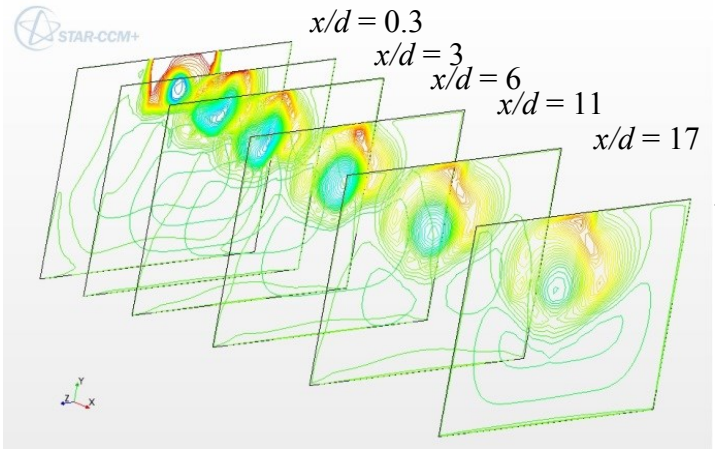

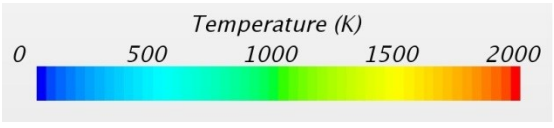

Figure 90 Temperature contours in the combustor for Configuration R6
d) R6 V30, e) R6 V40, f) R6 V50

(a)

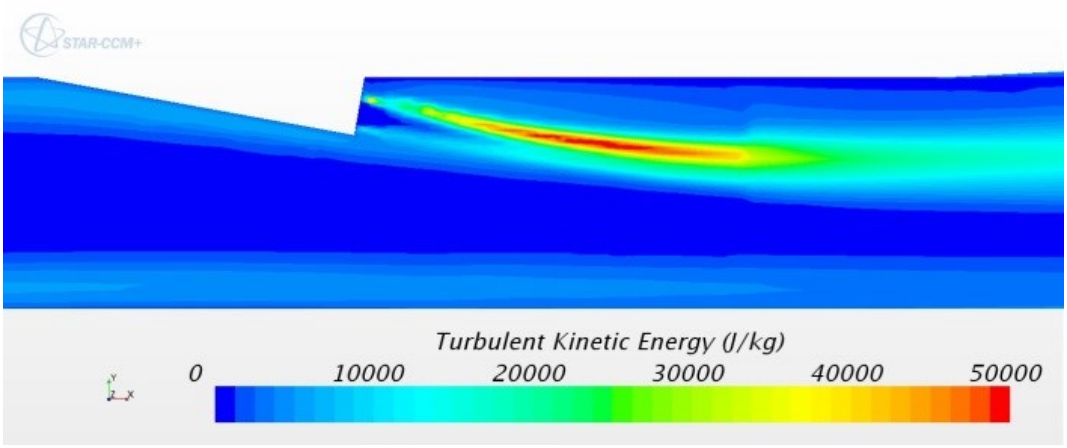

(b)

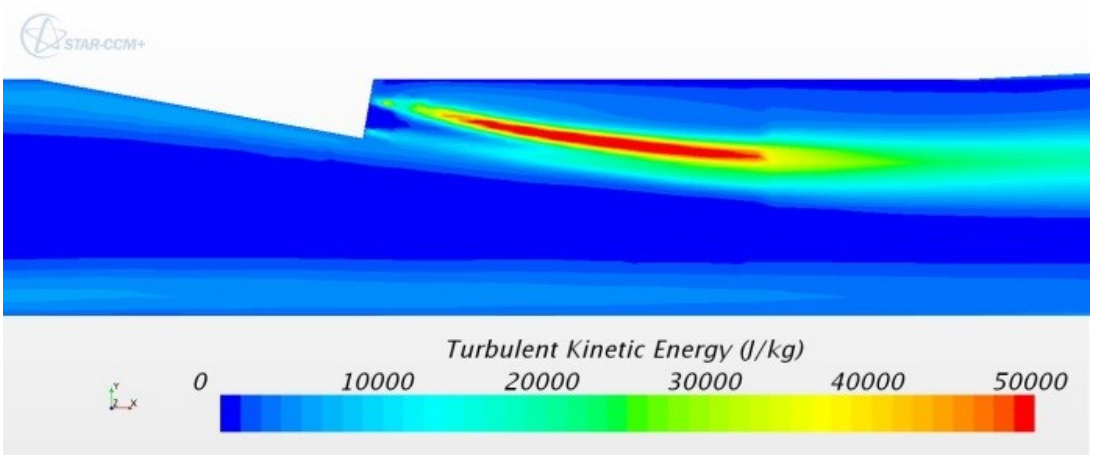

(c)

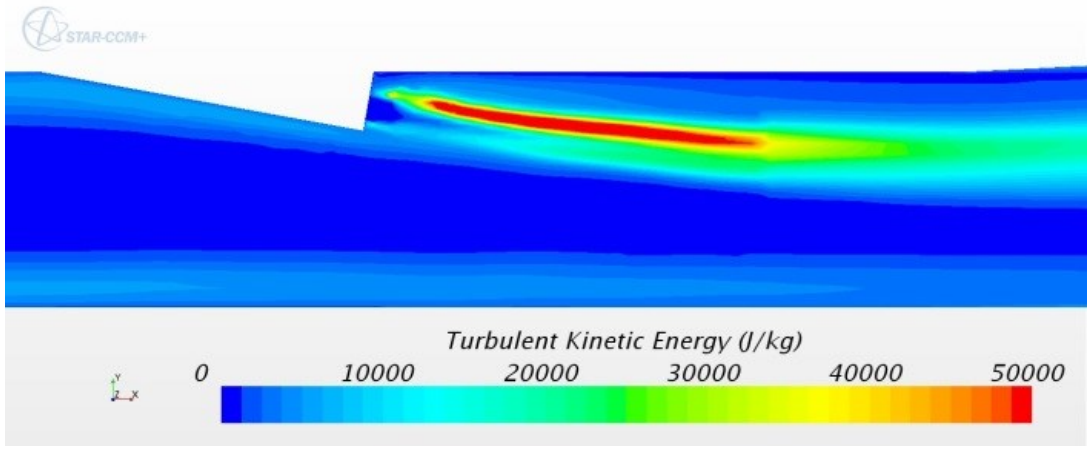

Figure 91 Turbulent kinetic energy plots on the centerline plane (z = 0) in the combustor for Configuration R6
a) V00, b) R6 V10, c) R6 V20

(d)

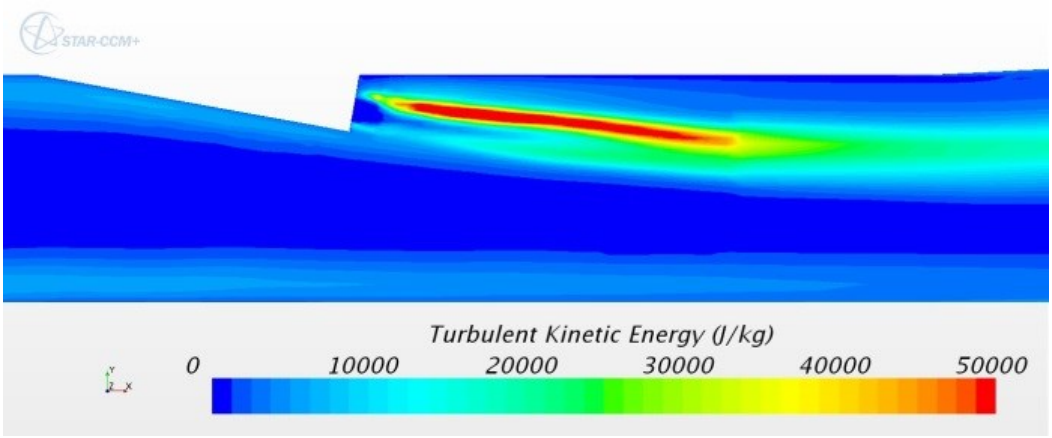

(e)

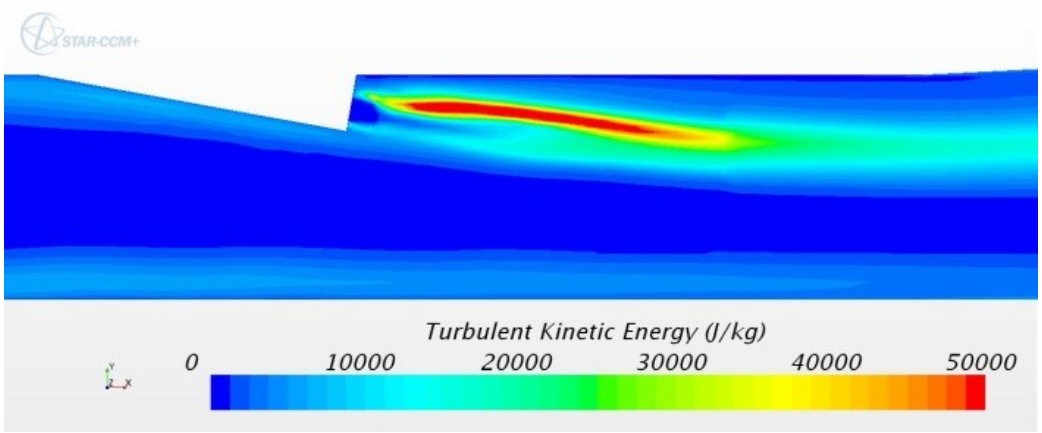

(f)

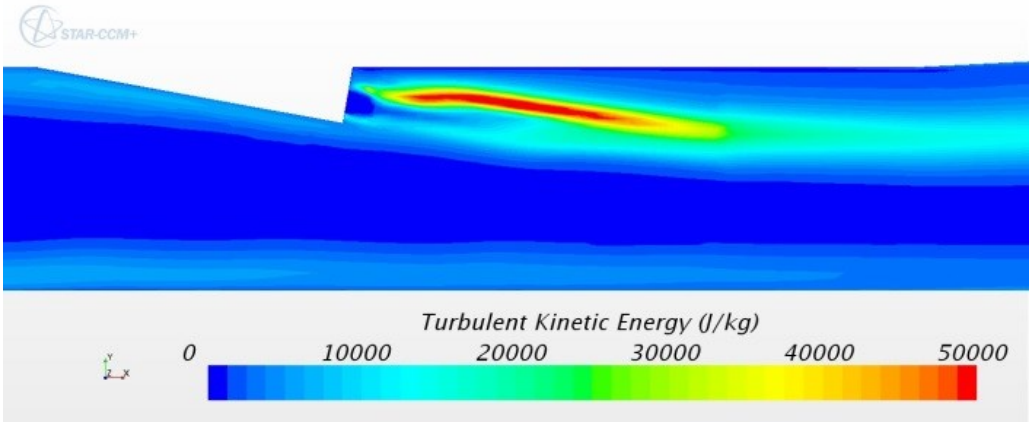

Figure 91 Turbulent Kinetic energy plots on the centerline plane (z = 0) in the combustor for Configuration R6
d) R6 V30, e) R6 V40, f) R6 V50

Once again the results for configuration R6 follows the same trend as for configurations R2 and R4. The minimum start location of the high turbulent kinetic energy zone is 0.60*d* for configuration R6 V10. Configuration R6 V10 also resulted in the maximum high turbulent kinetic energy zone length of 15.91*d*. The maximum burning efficiency increase is 13.8% for configuration R6 V50.

Table 7 Mixing Data for Configuration R6

	High Turbulent Kinetic Energy Zone			
Configuration	*Zone start location (x/d)*	*Length of zone (d)*	*Burning Efficiency,* η_{burn}	$\Delta\ \eta_{burn}$ *(%)*
Baseline V00	4.57	8.39	0.70	-
R6 V10	0.60	15.91	0.71	0.9
R6 V20	2.39	14.24	0.71	1.9
R6 V30	2.43	13.29	0.73	4.3
R6 V40	2.63	10.82	0.76	8.5
R6 V50	3.22	8.71	0.80	13.8

6.2.2 The Effect of Swirl on the Isolator Shock Train

One of the interesting characteristics of this scramjet model is the presence of a shock train that is produced by combustion and travels upstream into the isolator. The isolator then has to be long enough to prevent the shock train from traveling upstream to the inlet and causing the engine to unstart.

Figure 92 shows the normalized static pressure along the axial centerline of the top wall of the UVaSCF tunnel for the simulation cases of configurations R2, R4 and R6. The baseline case that has no fuel jet swirl is labelled as V00 and is represented by a solid black line. The shock train for the baseline case V00 starts at $x/H \approx -22.05$ and the maximum normalized static pressure on the axial centerline of the upper wall of the combustor is 3.08. As the swirl strength of the fuel jet is increased the pressure along the centerline of the combustor upper wall decreases. As the pressure in the combustor decreases, the strength and the length of the shock train decreases as well [7]. Figure 93 shows the approximate decrease in shock train length for each configuration.

Figure 93 indicates that for each configuration there is a minimum shock train length. However, in case R2 V50 the decrease in shock train length due to increasing swirl starts to reverse due to strong swirl.

(a)

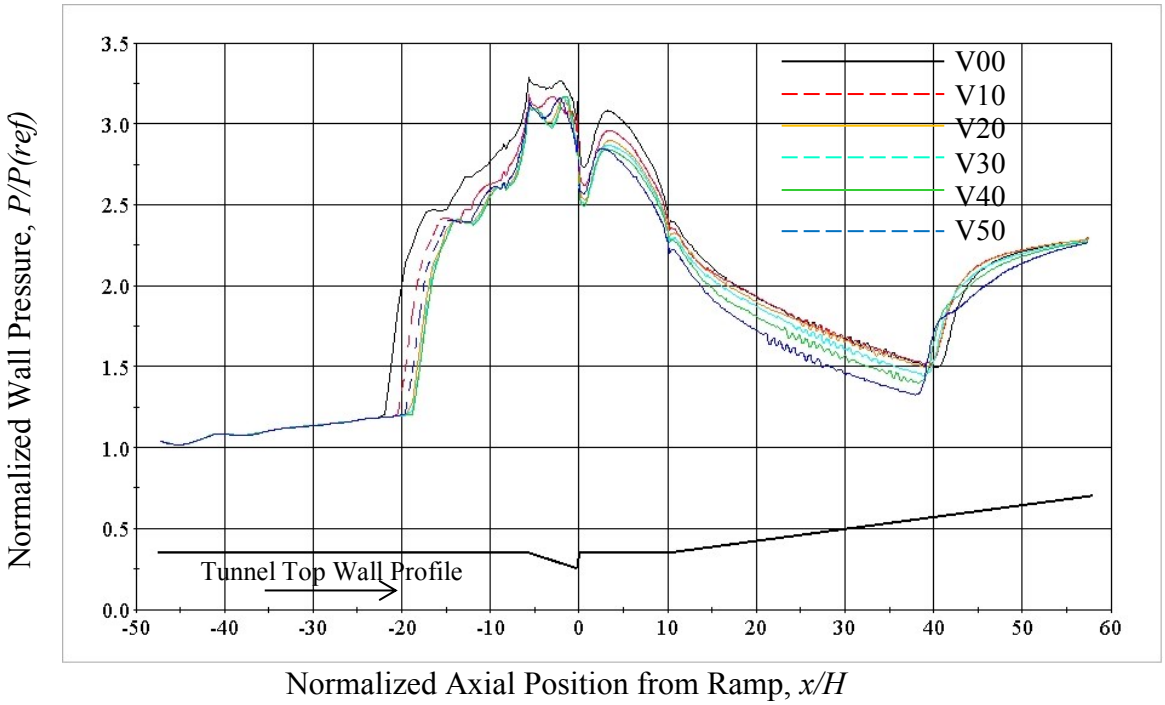

(b)

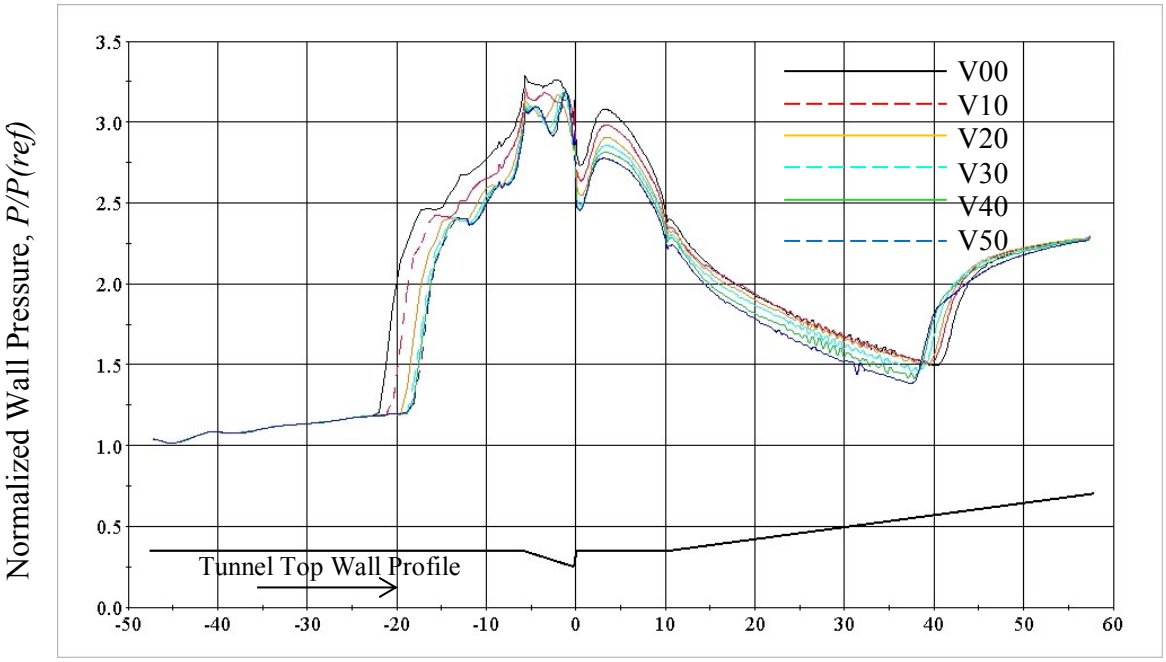

Figure 92 Normalized static pressure along the axial centerline of the top wall for Configurations R2, R4 and R6
(a) R2 (b) R4

(c)

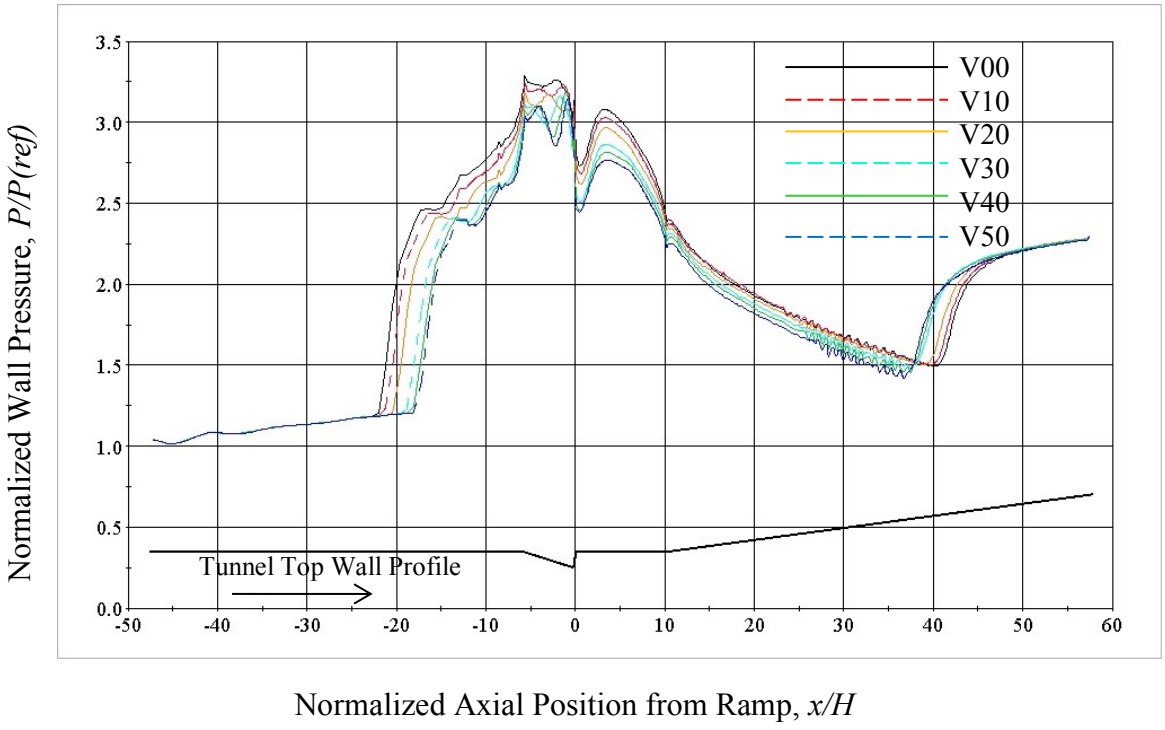

Figure 92 Normalized static pressure along the axial centerline of the top wall for Configurations R2, R4 and R6
(c) R6

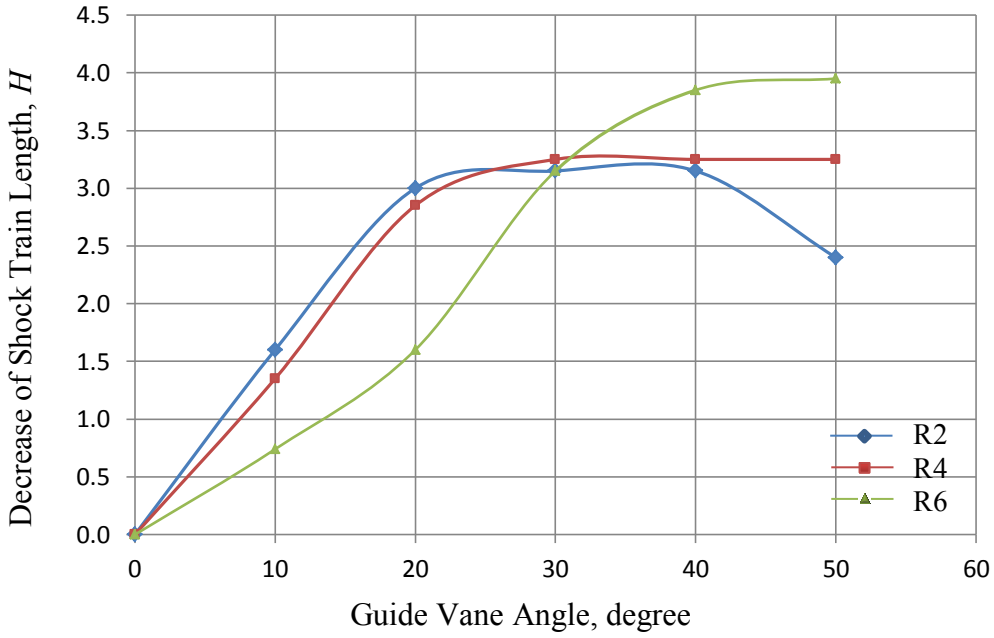

Figure 93 Effect of Swirl on Isolator Shock Train Length for Configurations R2, R4 and R6

6.2.3 Summary of Single Nozzle Fuel Jet Injection Swirl

Simulation results show that as the swirl strength of the fuel jet flow is increased the length of fuel jet potential core will decrease and if the swirl is strong enough the fuel jet will break down. This is seen in all three configuration cases. Comparing configuration R2, R4 and R6 it can be seen that swirl affects the jet flow more as the radius of the non-swirling core of the jet decreases. This can be seen when comparing R2 V50, R4 V50 and R6 V50. In the case of R2 V50 where the radius of the non-swirling core is only 20% of the fuel inlet, swirl will break down the fuel jet creating two recirculation zones. R4 V50 with a non-swirling core radius that is 40% of the fuel inlet radius indicates the start of jet flow break down. R6 V50 with a non-swirling core radius that is 60% of the fuel inlet radius shows no sign of jet break down.

One primary indication of the hydrogen fuel and oxygen combustion is the production of H_2O. Contour plots of H_2O mole fraction indicate an increase in swirl assists H_2O to form further upstream than a non-swirling fuel jet until the start of fuel jet breakdown. This is particularly seen in R2 V50 and R4 V50. There are four distinct areas of high H_2O mole fraction zones on the fuel nozzle wall and upper combustor wall for the non-swirling fuel jet flow case; two zones located on either side of the fuel inlet and two more zones on the combustor upper wall approximately 1.5d downstream of the fuel inlet center point. As fuel jet swirl is introduced one of the high H_2O mole fraction zones is eliminated and the areas on either side of the nozzle become asymmetric. As swirl strength increases the two zones on the fuel inlet wall seem to rotate clockwise as viewed by an observer looking upstream. A large area of the fuel inlet wall is covered by a high H_2O mole fraction zone and starts to spill over to the upper combustor wall. Finally due to the fuel jet break down due to strong swirl the high H_2O mole fraction zone reduces on the fuel inlet wall reduces and increases on the combustor upper wall.

Swirl aids in ensuring combustion within the short resident time of the fuel and air in the combustor.

The temperature within the non-swirling fuel jet case decreases when swirl is introduced to the fuel jet. The temperature decrease is seen throughout the combustor length especially on the upper combustor wall.

Turbulent kinetic energy is associated with eddies in turbulent flow that then promotes mixing. Introducing and then increasing swirl to the fuel jet increases the turbulent kinetic energy in the flow. The high turbulent kinetic energy zone for the baseline non-swirling case started at $x/d \approx 4.57$ and had a length of approximately $8.4d$. As swirl is introduced to the fuel jet and increased the start location of the high turbulent kinetic energy zone moves closer to the fuel injector exit and the zone length increases providing a greater opportunity for the fuel and oxidizer to continue mixing. The fuel jet swirl of case R2 V30 resulted in the high turbulent kinetic energy zone starting at $x/d \approx 1.0$ had a length $\approx 10.3d$. The length and start location of the turbulent kinetic energy zone starts to decrease and increase respectively as the swirl continues to increase.

The burning efficiency measures how much injected fuel was consumed prior to reaching the nozzle exit. An increase in burning efficiency would indicate an increase in the mixing of H_2 with O_2. In all cases the burning efficiency increased with increasing swirl. The maximum increase in burning efficiency compared to the non-swirling baseline case reached an impressive level of 23.3% for case R2 V50.

6.3 The Effect of Swirl on the Interaction between Two Nozzles

The simulation results for single fuel jet swirl injection indicated that increasing swirl increased the burning efficiency. The introduction of swirl to the fuel jet also resulted in an increase of high H_2O mole fraction zone to be formed on the fuel nozzle wall indicating that combustion was occurring earlier. In addition swirl could help lengthen the high turbulent kinetic energy zone and enable the zone to start closer to the fuel injector exit. These factors indicate that mixing increased with fuel jet injection swirl. The research continued with two fuel jet injectors with swirl in order to investigate the possibility that interaction, or coupling, between two swirling jets will produce increased mixing. Nine configurations were examined for a range of swirl numbers described by vane angles 10° - 50° in ten degree intervals. There were three swirl patterns as viewed by an observer looking downstream as shown in Figure 94. Swirl pattern TI (top in) has the right fuel jet swirling counter clockwise and the left fuel jet swirling clockwise. Swirl pattern TO (top out) has the right fuel jet swirling clockwise and the left fuel jet swirling counter clockwise. Swirl pattern SD (same direction) has both the right and left fuel jet swirling clockwise. For each swirl pattern the distance between the center point of the fuel jets were distanced at three times the fuel injector radius (3xr), four times the radius (4xr) and five timed the radius (5xr) as shown in Figure 95. Therefore configuration 3xr-V20-TO describes the distance between the center point of the fuel jets as three times the fuel injector radius, swirl produced by a 20° vane guide and with the right fuel jet swirling clockwise and the left fuel jet swirling counter clockwise. All the simulations investigating two nozzle fuel jet swirl injection has a core flow that is non-swirling with a radius that is 40% of the fuel injector radius and swirl in the annular region as shown in Figure 72(b). The combined area of the two fuel jet injectors is equal to the area of the single fuel inlet previously investigated in Section 6.2.

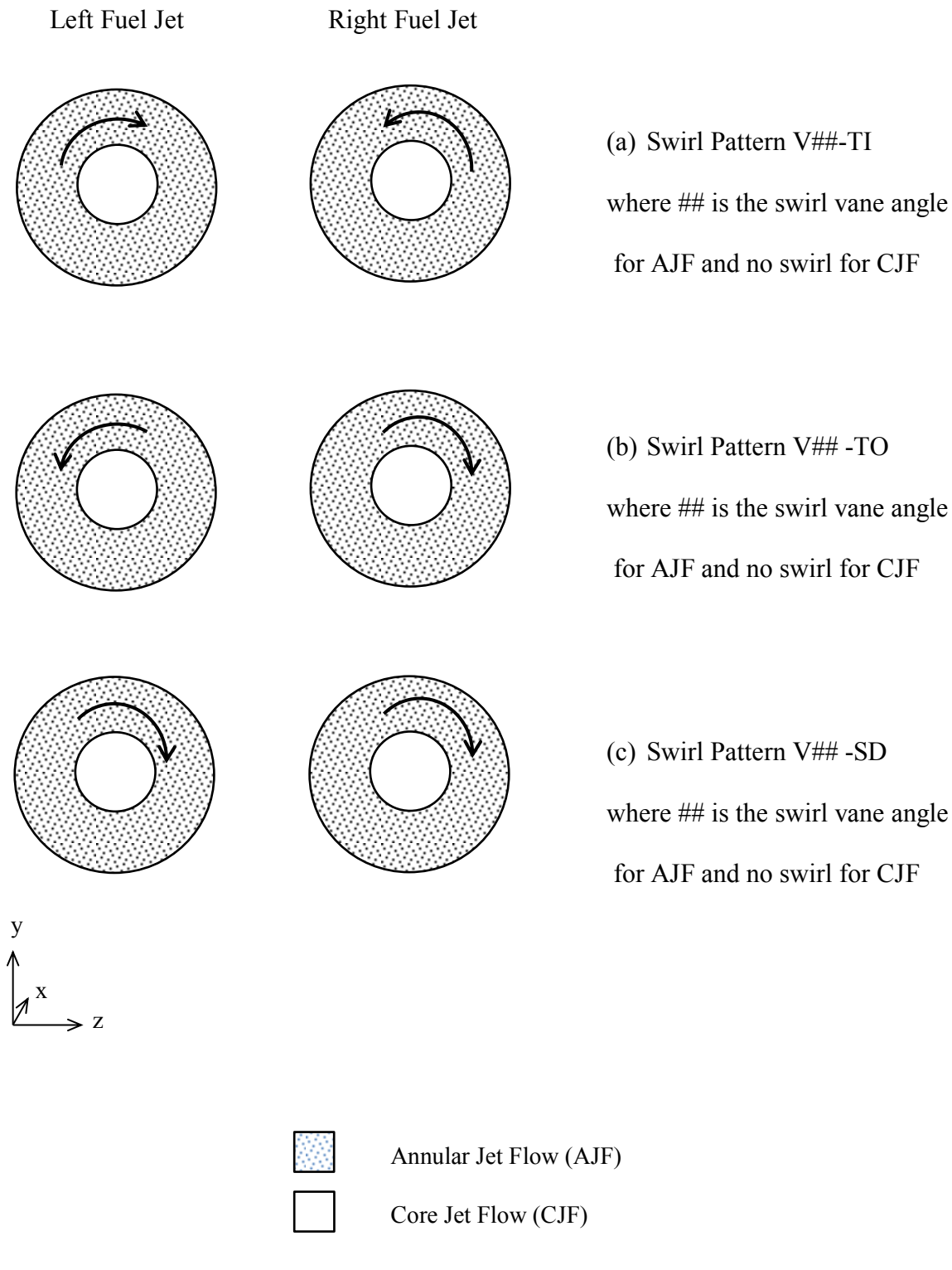

Figure 94 Swirl pattern for two nozzle cases

Left Fuel Jet Right Fuel Jet

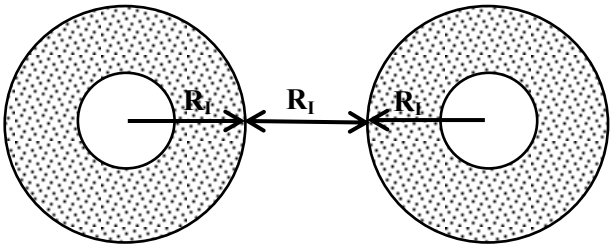

a) Distance configuration 3xr

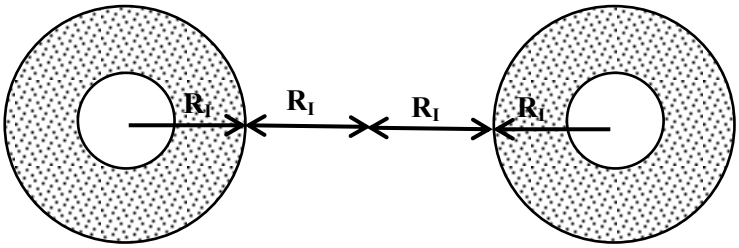

b) Distance configuration 4xr

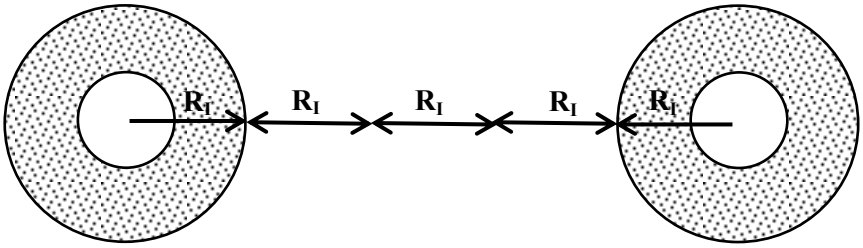

c) Distance configuration 5xr

Figure 95 Distance configuration for two nozzle cases

6.3.1 Distance Configuration 3xr, Swirl Pattern TI

Figure 96(a) shows the H_2O mole fraction contours on the fuel inlet and upper combustor walls for the non-swirling baseline case for the distance configuration 3xr. The H_2O mole fraction contours shown in Figure 96(a) are similar to those shown for the single nozzle non-swirling baseline case shown in Figure 76(a). There are two distinct areas of high H_2O mole fraction zones on the upper combustor wall but the two zones that are located on side of the fuel inlets have merged into one large zone. Unlike the single nozzle case, the high H_2O mole fraction zones on the upper combustor wall are not eliminated and the zones on the fuel nozzle wall do not rotate as swirl increases. The high H_2O mole fraction zones on the fuel nozzle wall increase in area moving towards the upper combustor wall and eventually combining with the zones on the upper combustor wall. Finally the high H_2O mole fraction zone starts to transfer to the upper combustor wall completely. The interaction of this swirl pattern produces similar results to high swirl in single fuel jet.

Figure 97 shows that the two fuel jets merge together faster with increasing swirl. In addition, the areas of higher H_2O mole fraction spread out from the upper wall and further into the flow as swirl increases.

The temperature contours shown in Figure 98 indicate that decreases with increasing fuel jet swirl. This is similar to the results from the single nozzle cases.

Turbulent kinetic energy is shown on the tunnel centerline ($z = 0$) in Figure 99 and on the right fuel injector centerline plane ($z = 1.5r$) in Figure 100. The flow through the tunnel is symmetrical for this swirl pattern. Therefore Figure 100 is the same for the right and left fuel jets. The high TKE zones on the tunnel centerline indicate cells of high TKE unlike the high TKE zones on the fuel jet centerline. The high TKE zones on the fuel jet centerline are similar

to those shown in Figure 79 for the single fuel jet configuration R2. Figure 101 shows a progression of contour plots of TKE.

Table 8 shows the start location and length of the high TKE zone, the burning efficiency and the increase in burning efficiency due to swirl. The results show a similar trend as the single fuel jet configurations. The start location of the high TKE zone for the fuel jet swirl cases is upstream of the start location of the high TKE zone for the non-swirling baseline case. The earliest start location is 1.03*d* from the fuel injector exit for configuration 3xr-V20-TI. The high TKE zone length increases with swirl, reaches a maximum of 9.15*d* and then decreases as more swirl is added to the fuel jet.

The burning efficiency increases with increasing swirl as shown in Table 8. Configuration 3xr-V50-TI resulted in an impressive 16.1% increase in burning efficiency compared to the case with no swirl.

Table 8 Mixing Data for Configuration 3xr-TI

	High Turbulent Kinetic Energy Zone			
Configuration	*Zone start location (x/d)*	*Zone Length (d)*	*Burning Efficiency, η_{burn}*	*$\Delta\ \eta_{burn}$ (%)*
3xr-V00	2.11	8.23	0.72	n/a
3xr-V10-TI	1.19	8.99	0.72	0.0
3xr-V20-TI	1.03	9.15	0.74	2.3
3xr-V30-TI	1.11	7.80	0.76	5.5
3xr-V40-TI	1.07	5.21	0.79	9.4
3xr-V50-TI	1.03	3.54	0.84	16.1

a)

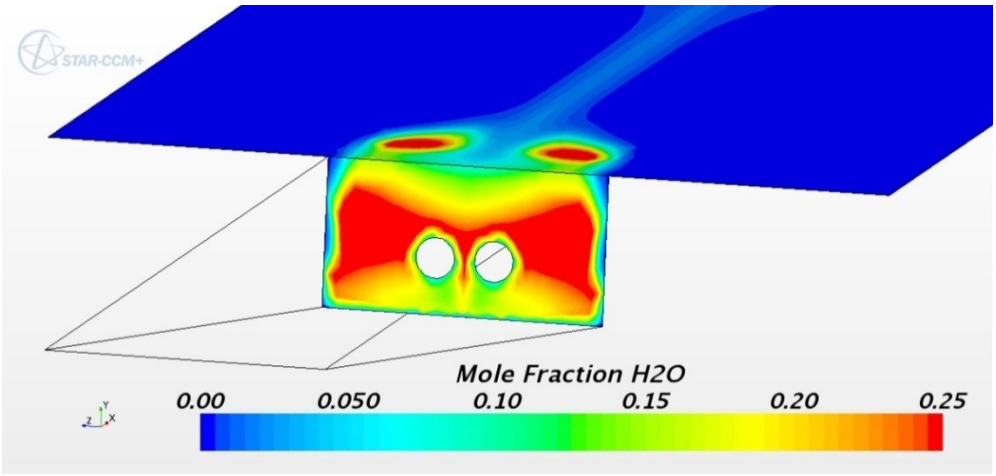

b)

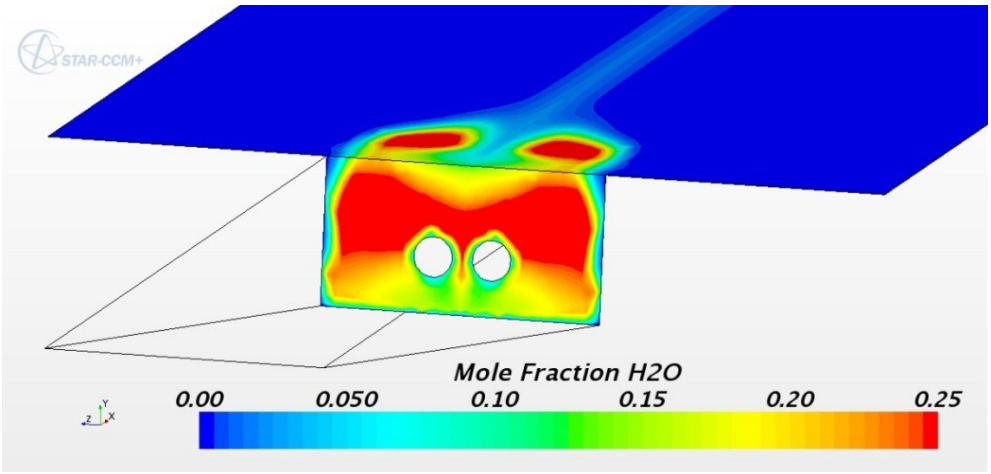

c)

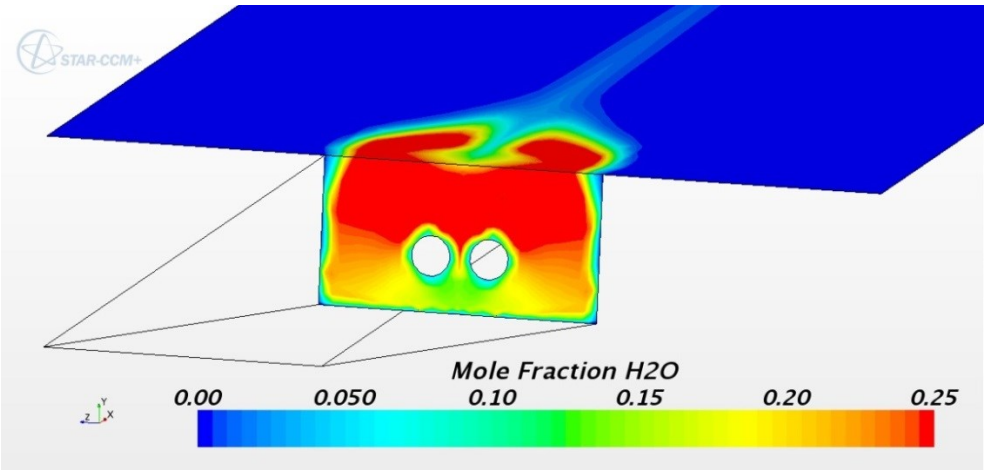

Figure 96 Mole fraction contours of H_2O on the fuel inlet wall and combustor upper wall for Configuration 3xr-TI
a) 3xr-V00, b) 3xr-V10-TI, c) 3xr-V20-TI

d)

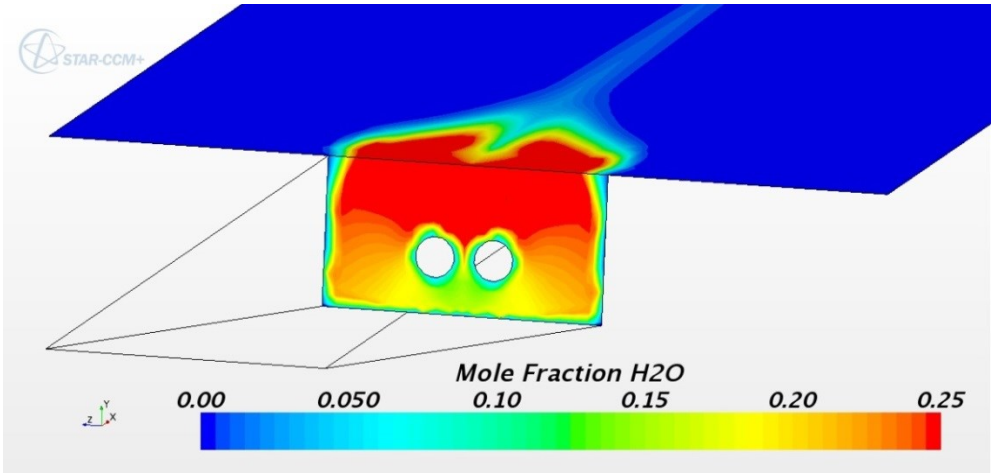

e)

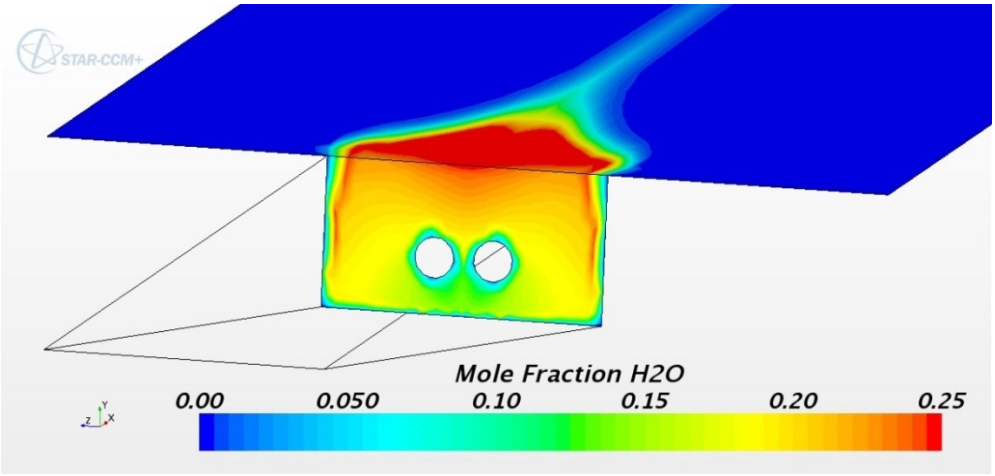

f)

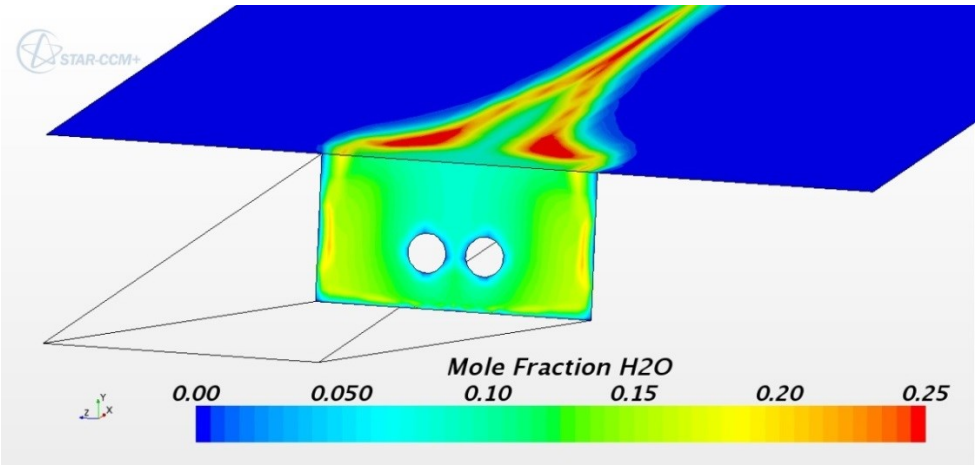

Figure 96 Mole fraction contours of H_2O on the fuel inlet wall and the combustor upper wall for Configuration 3xr-TI
d) 3xr-V30-TI, e) 3xr-V40-TI, f) 3xr-V50-TI

a)

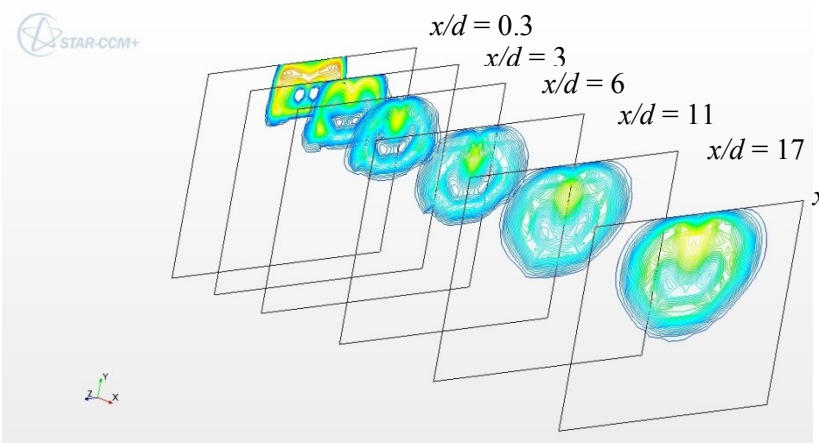

b)

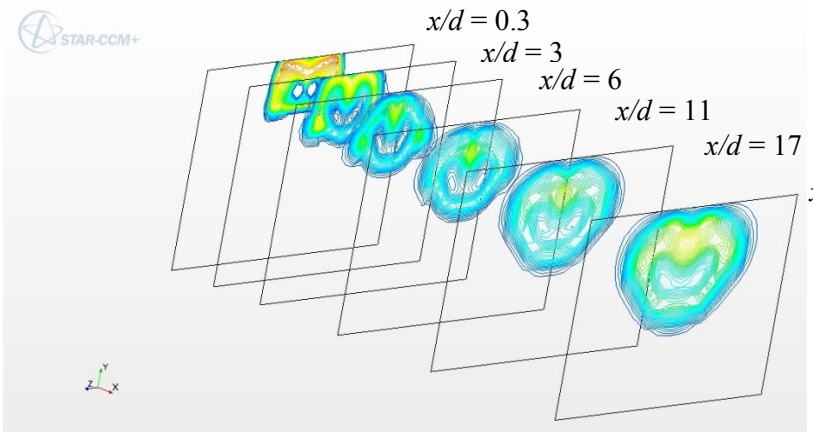

c)

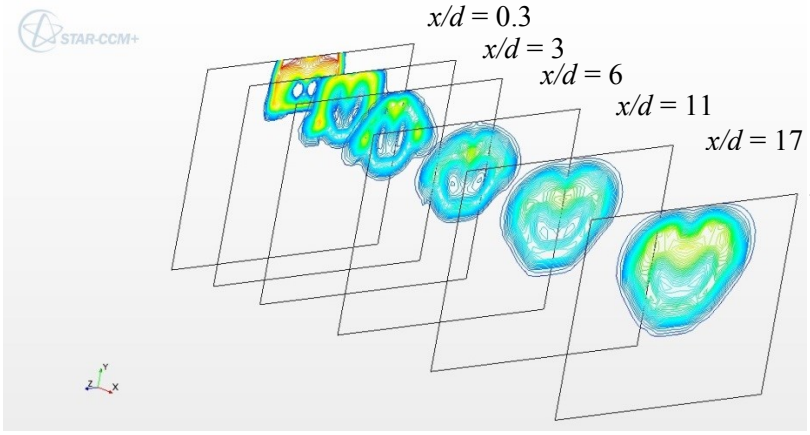

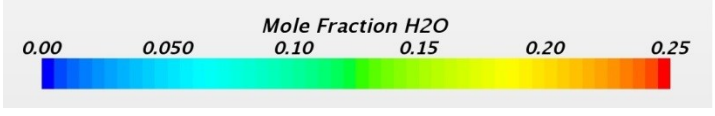

Figure 97 Mole fraction contours of H_2O in the combustor for Configuration 3xr-TI
a) 3xr-V00, b) 3xr-V10-TI, c) 3xr-V20-TI

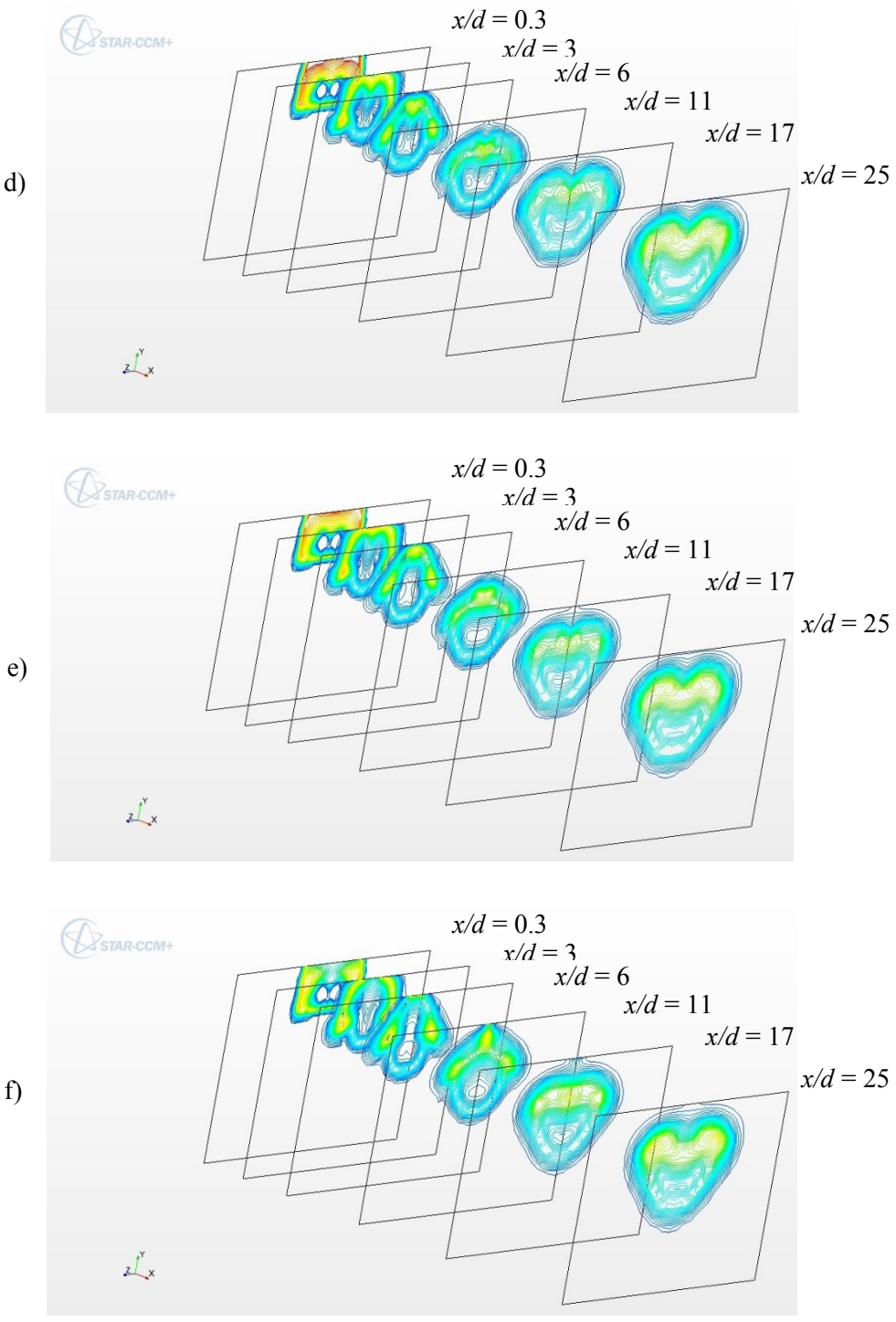

Figure 97 Mole fraction contours of H_2O in the combustor for Configuration 3xr-TI
d) 3xr-V30-TI, e) 3xr-V40-TI, f) 3xr-V50-TI

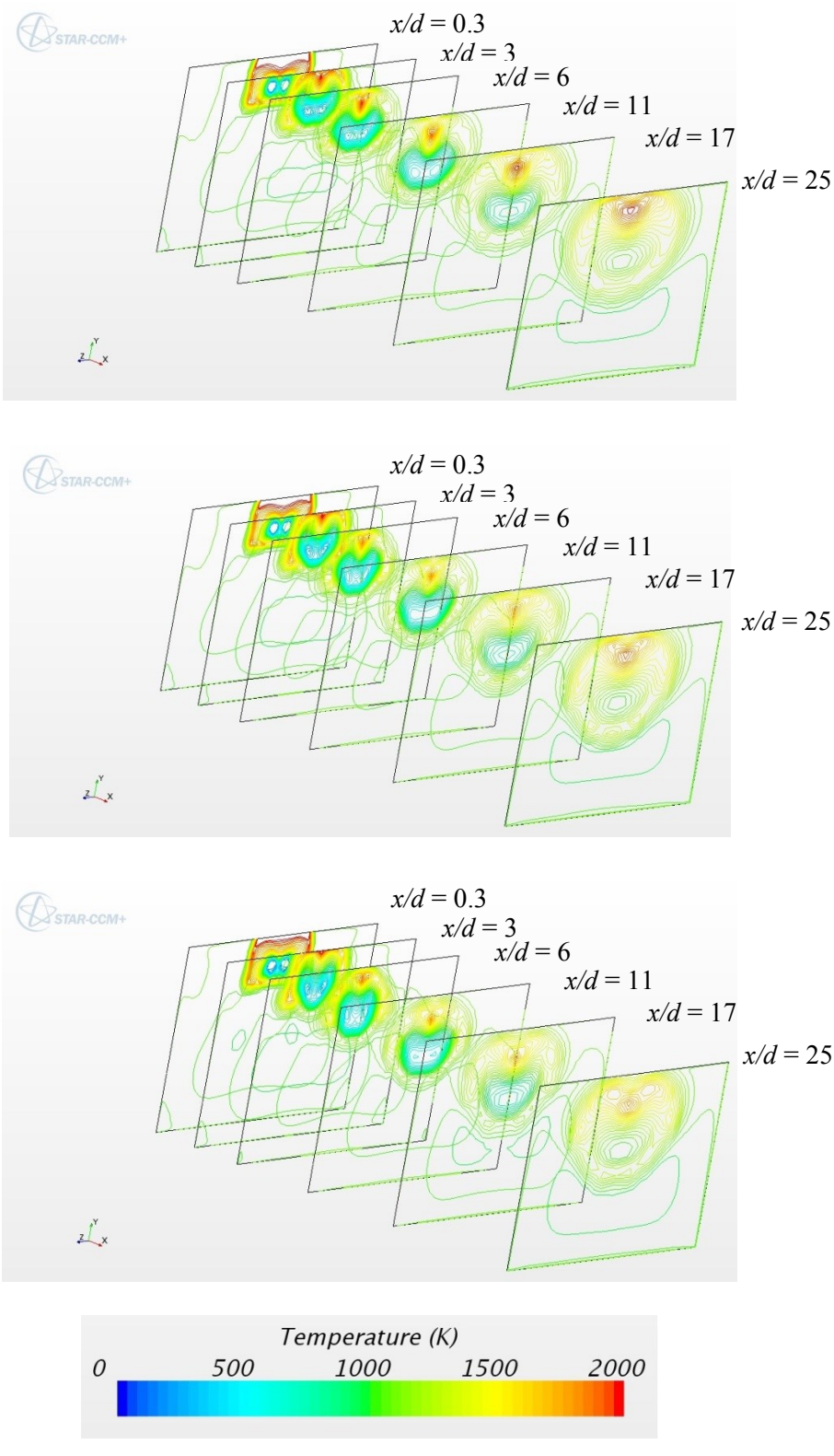

Figure 98 Temperature contours in the combustor for Configuration 3xr-TI
a) 3xr-V00, b) 3xr-V10-TI, c) 3xr-V20-TI

d)

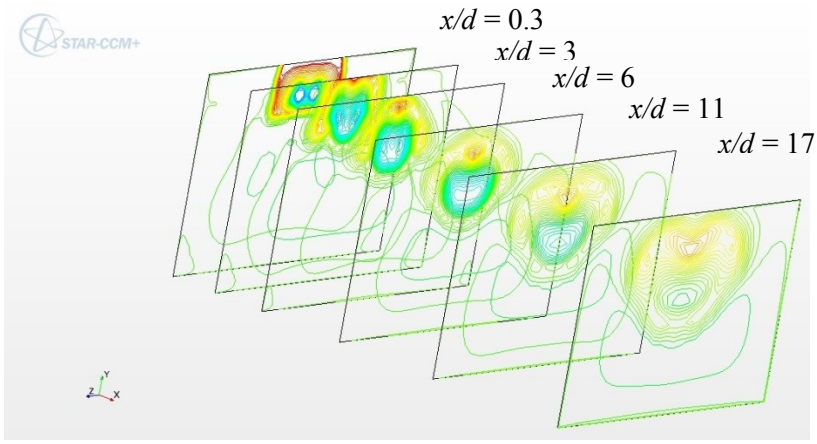

e)

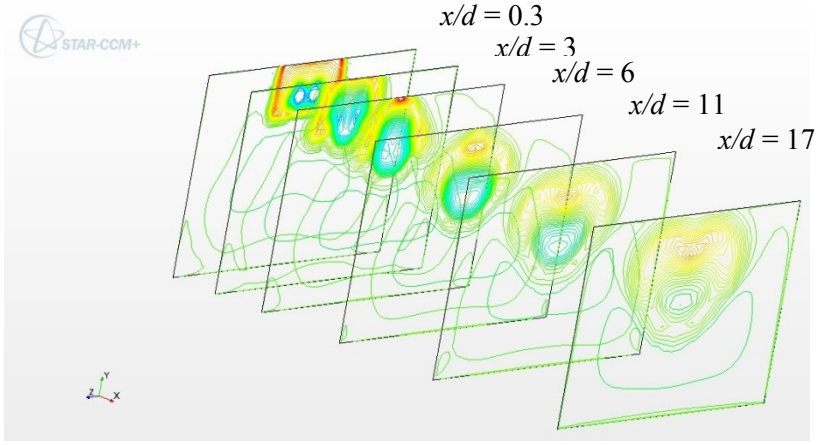

f)

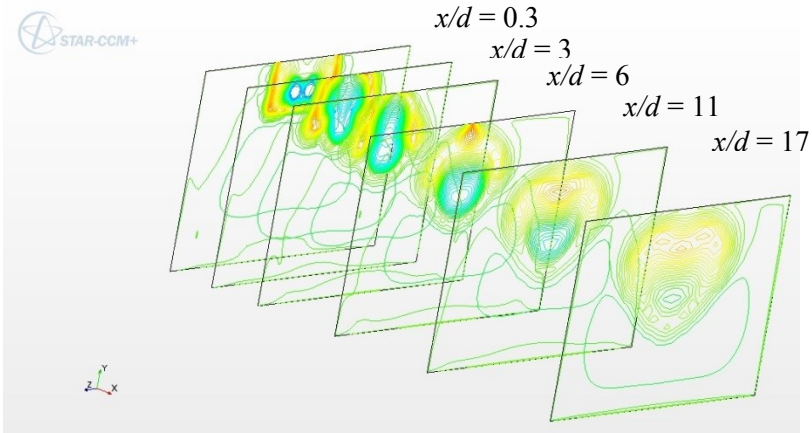

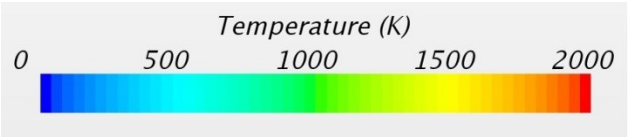

Figure 98 Temperature contours in the combustor for Configuration 3xr-TI
d) 3xr-V30-TI, e) 3xr-V40-TI, f) 3xr-V50-TI

(a)

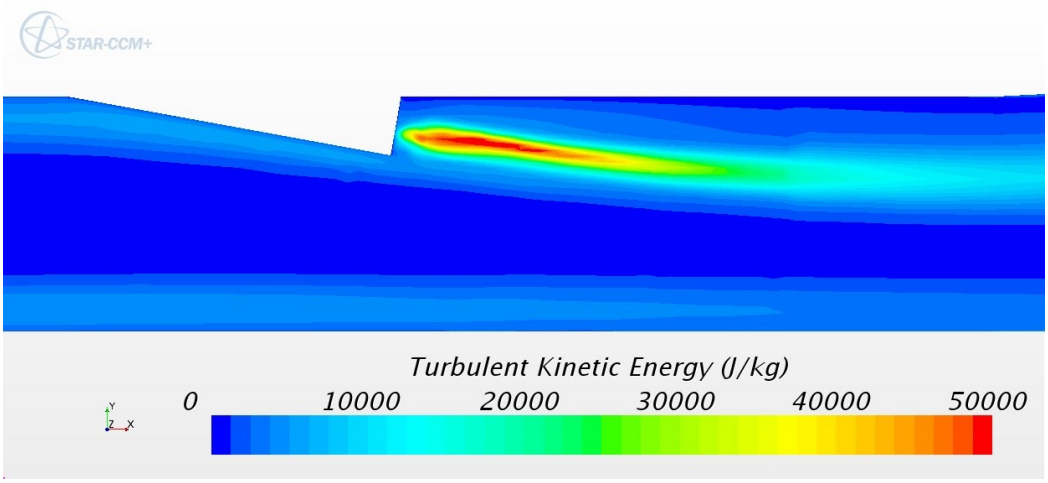

(b)

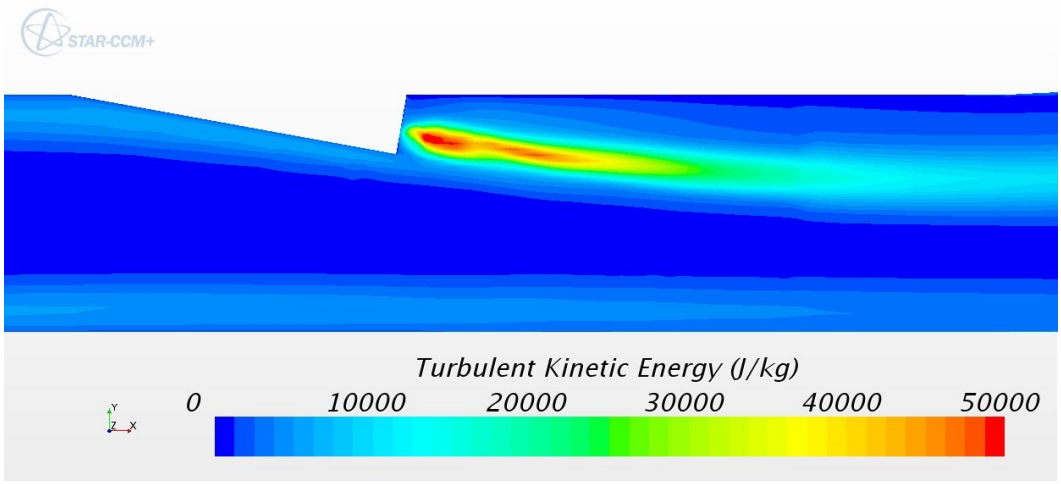

(c)

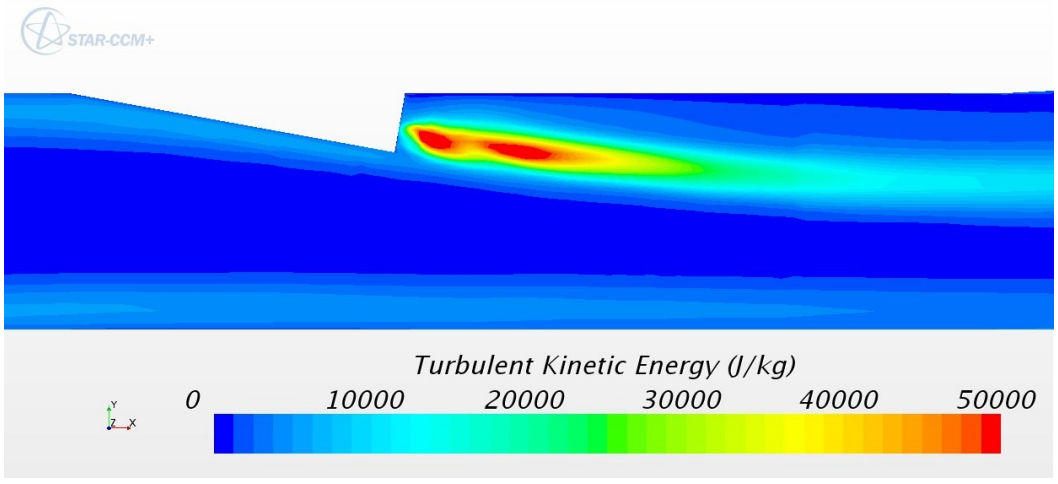

Figure 99 Turbulent kinetic energy plots on the centerline plane (z = 0) in the combustor for Configuration 3xr-TI
a) 3xr-V00, b) 3xr-V10-TI, c) 3xr-V20-TI

(d)

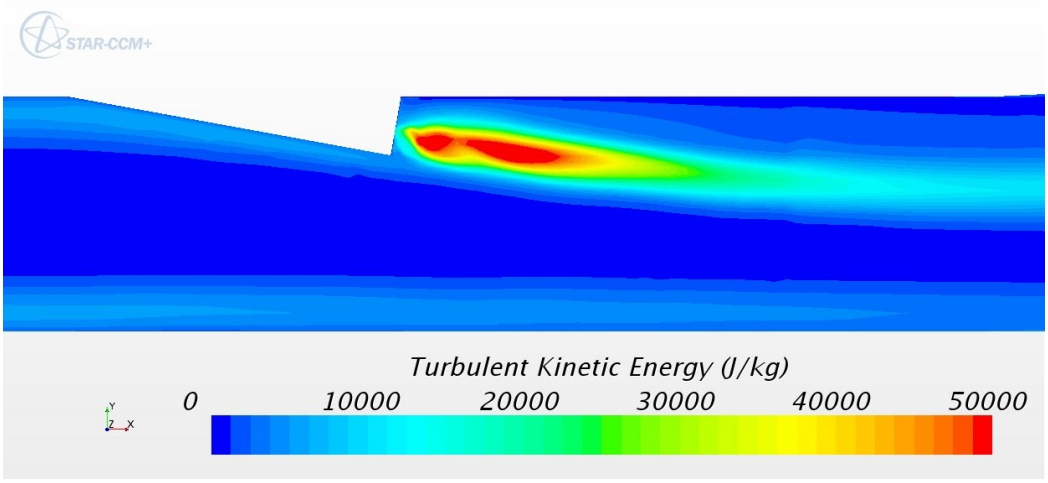

(e)

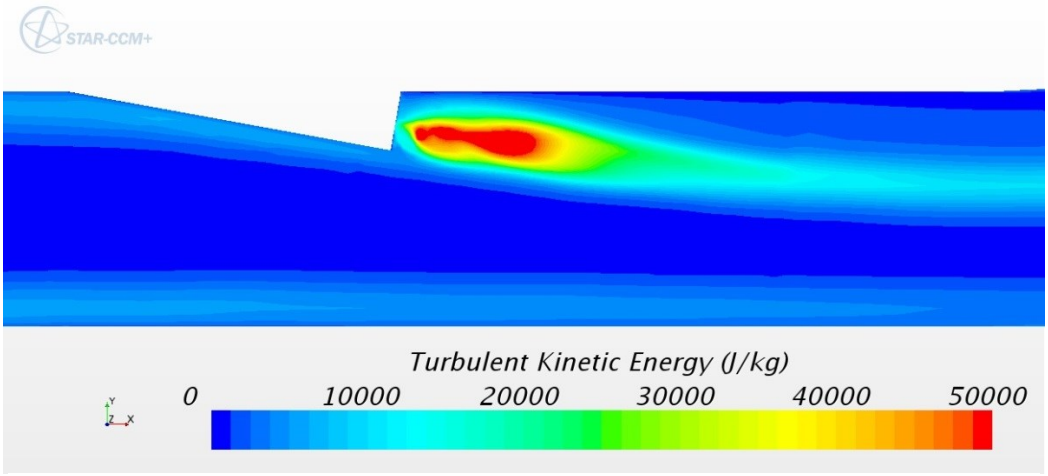

(f)

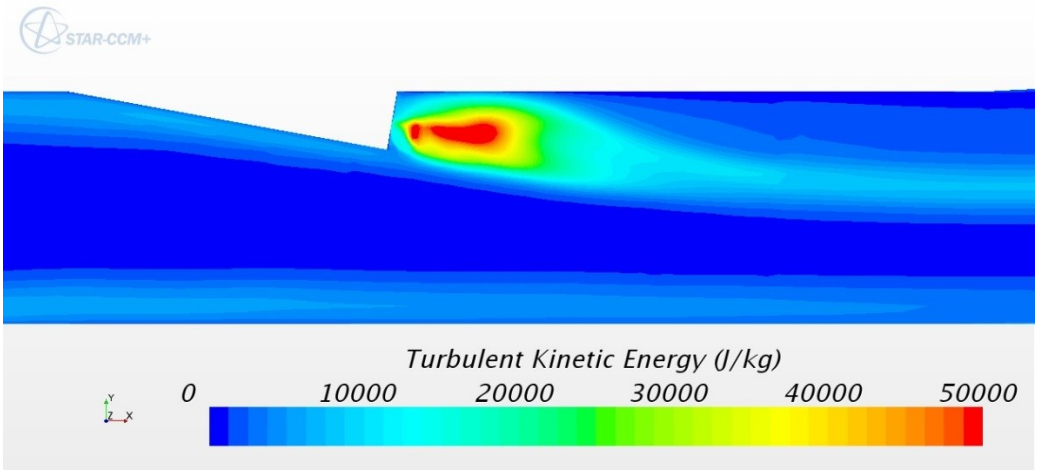

Figure 99 Turbulent kinetic energy plots on the centerline plane (z = 0) in the combustor for Configuration 3xr-TI
d) 3xr-V30-TI, e) 3xr-V40-TI, f) 3xr-V50-TI

(a)

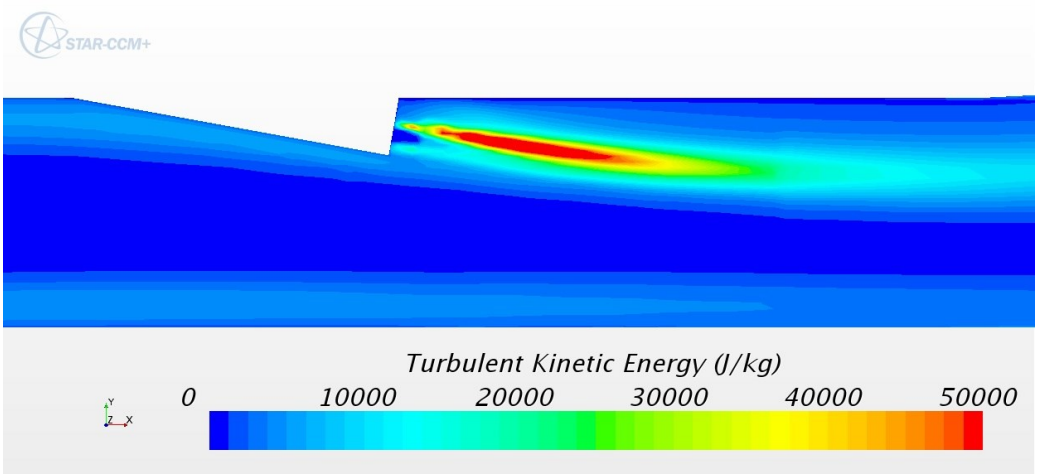

(b)

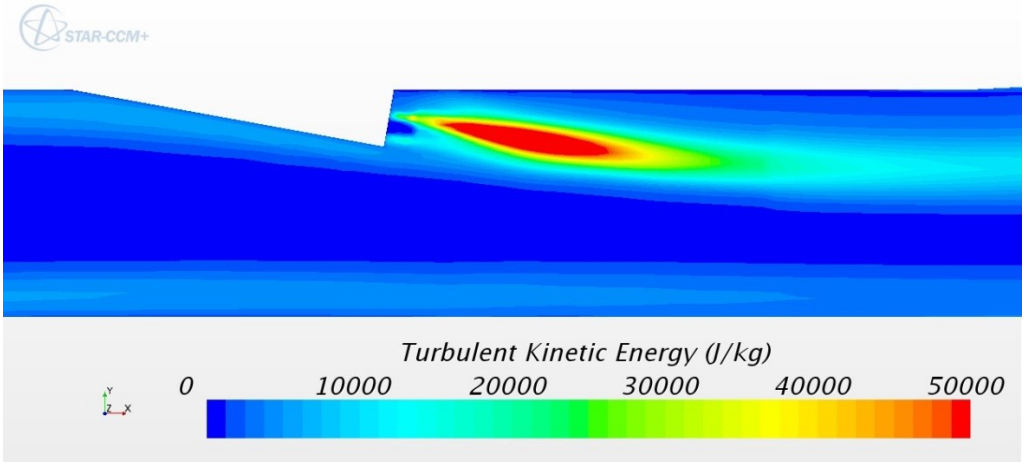

(c)

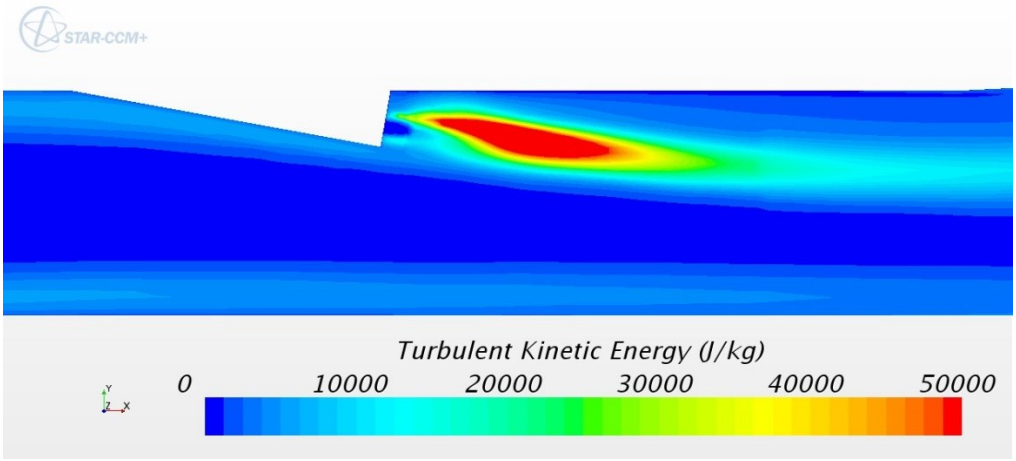

Figure 100 Turbulent kinetic energy plots on the fuel nozzle centerline plane (z = 1.5r) in the combustor for Configuration 3xr-TI
a) 3xr-V00, b) 3xr-V10-TI, c) 3xr-V20-TI

(d)

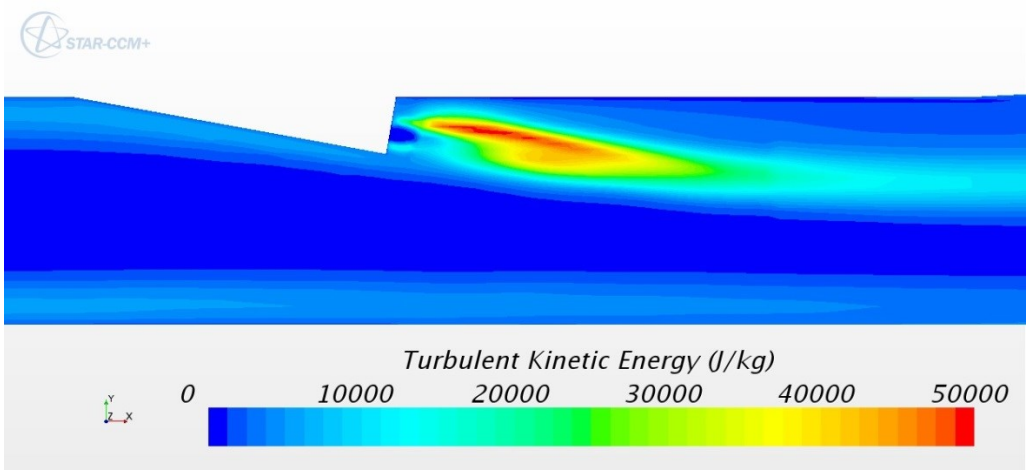

(e)

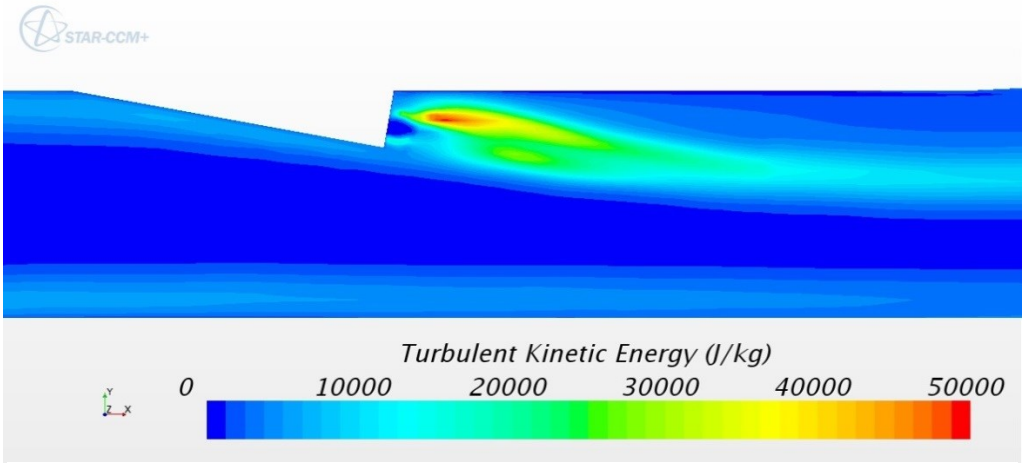

(f)

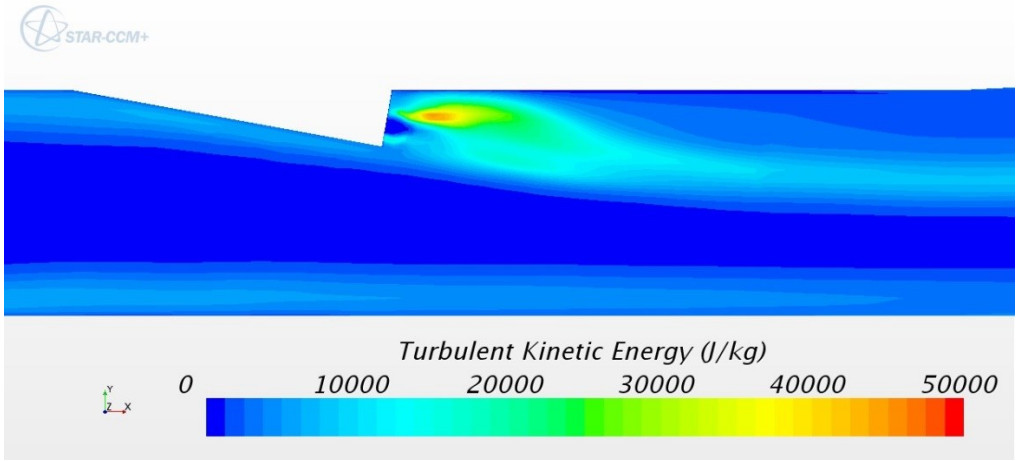

Figure 100 Turbulent kinetic energy plots on the fuel nozzle centerline plane (z = 1.5r) in the combustor for Configuration 3xr-TI
d) 3xr-V30-TI, e) 3xr-V40-TI, f) 3xr-V50-TI

a)

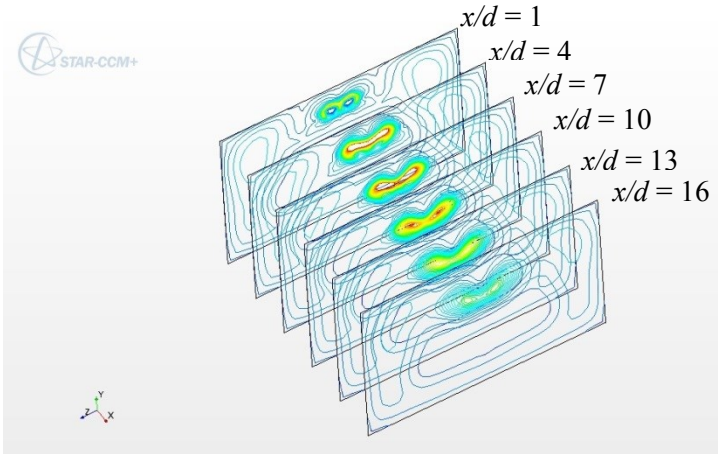

b)

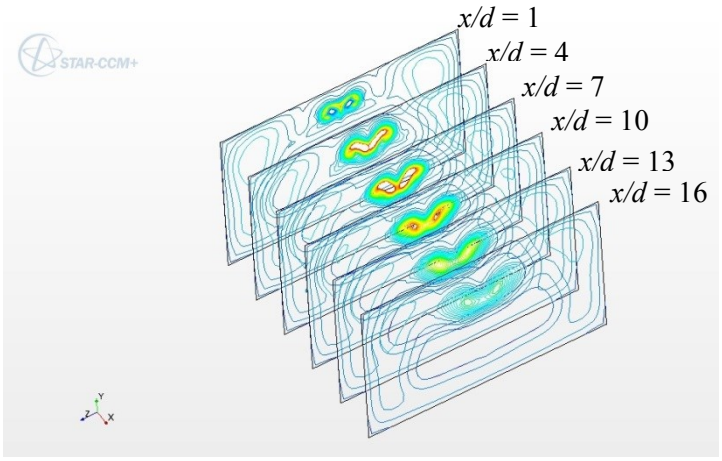

c)

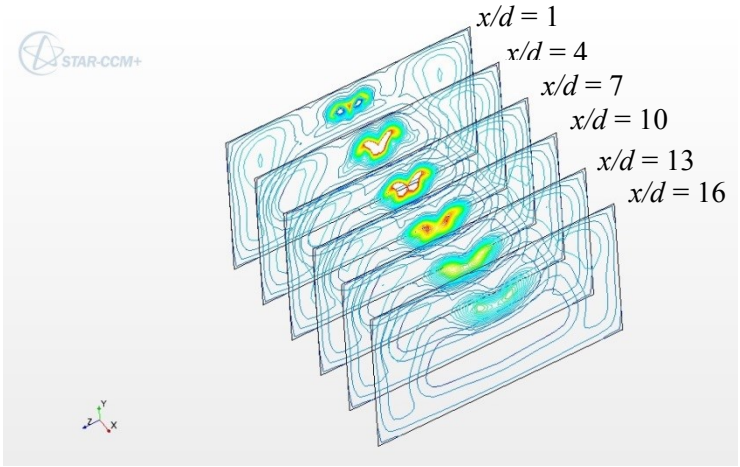

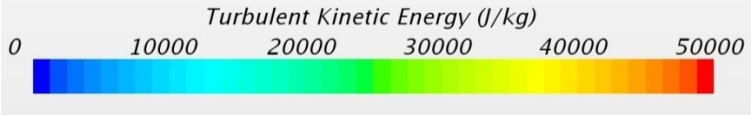

Figure 101 Turbulent kinetic energy contours in the combustor for Configuration 3xr-TI
a) 3xr-V00, b) 3xr-V10-TI, c) 3xr-V20-TI

d)

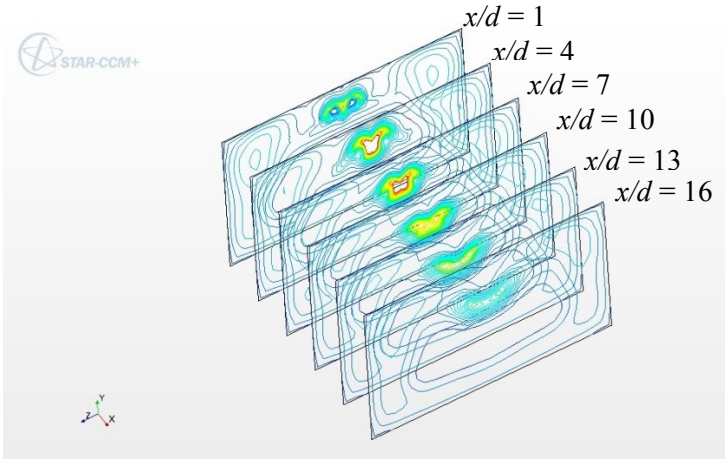

e)

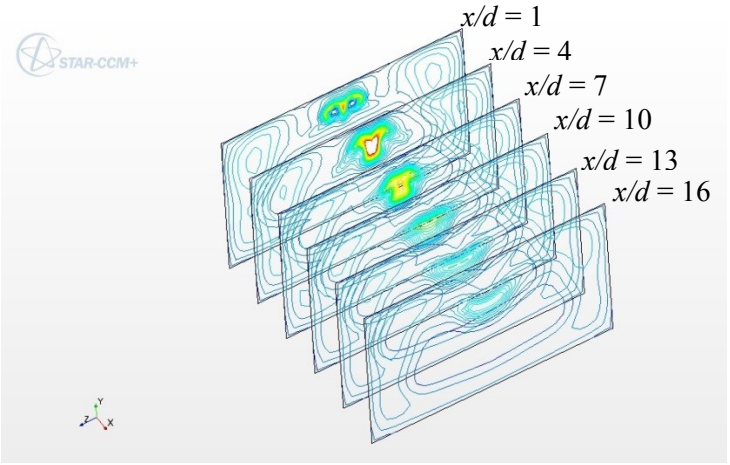

f)

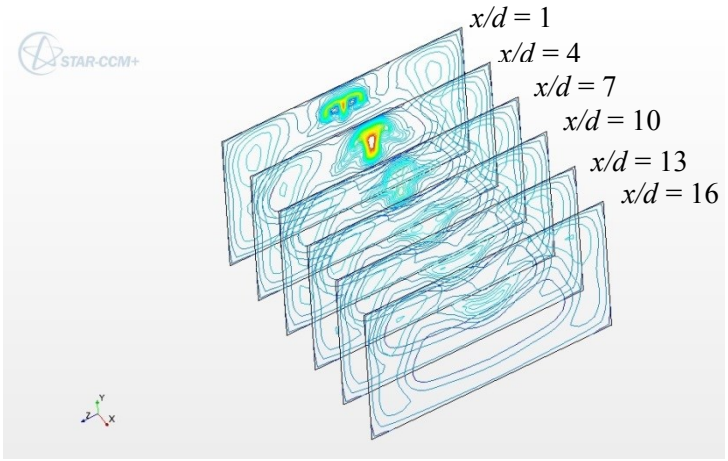

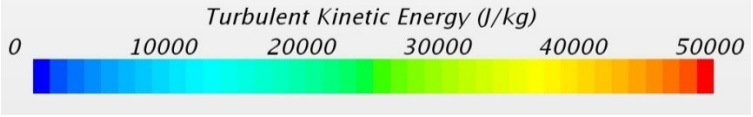

Figure 101 Turbulent kinetic energy contours in the combustor for Configuration 3xr-TI
d) 3xr-V30-TI, e) 3xr-V40-TI, f) 3xr-V50-TI

6.3.2 Distance Configuration 3xr, Swirl Pattern TO

Figure 102(a) shows the H_2O mole fraction contours on the fuel inlet and upper combustor walls for the non-swirling baseline case for the distance configuration 3xr. Configuration 3xr-TO is similar to the single fuel jet cases in that the high H_2O mole fraction zones on the upper combustor wall are eliminated with increasing swirl and then the high H_2O mole fraction zones on the fuel nozzle wall transfer to the combustor wall and move downstream. Configuration 3xr-TO is similar to 3xr-TI in that the high H_2O mole fraction zones on the fuel nozzle wall do not rotate as swirl increases. As swirl increases the high H_2O mole fraction zones on the fuel nozzle wall increase in area moving away from the upper combustor wall and then move away from the fuel injector exits prior to moving unto the upper combustor wall. The interaction of this swirl pattern produces similar results as with the single fuel jet except with less fuel jet swirl.

Contour plots showing the progression of the H_2O mole fraction in the combustor are shown in Figure 103. The previous TI swirl pattern produced a heart shaped fuel jet. The TO swirl pattern turns the heart shaped fuel jet flow upside down. This is also seen in the temperature contours shown in Figure 104.

Turbulent kinetic energy is shown on the tunnel centerline (z = 0) in Figure 105 and on the right fuel injector centerline plane (z = 1.5r) in Figure 100. The flow through the tunnel is symmetrical for this swirl pattern. Therefore Figure 106 is the same for the right and left fuel jets. The high TKE zones on the tunnel centerline and the fuel jet centerline decrease with increasing fuel jet swirl but decreases faster on the tunnel centerline. Figure 101 shows a progression of contour plots of TKE. The high TKE zones are upside down in comparison to the previous TI configuration.

Table 9 shows the start location and length of the high TKE zone, the burning efficiency and the increase in burning efficiency due to swirl. Unlike the previous simulation cases, the start location of the high TKE zone for the fuel jet swirl cases is not always upstream of the start location of the high TKE zone for the non-swirling baseline case. The earliest start location is 1.07*d* from the fuel injector exit for configuration 3xr-V10-TO. The high TKE zone length increased with the 3xr-V10-TO swirl to 8.95*d* and then decreased as more swirl was added to the fuel jet.

The burning efficiency increases as the swirl increases. Configuration 3xr-V50-TO resulted in a 18.4% increase in burning efficiency compared to the case with no swirl.

Table 9 Mixing Data for Configuration 3xr-TO

	High Turbulent Kinetic Energy Zone			
Configuration	*Zone start location (x/d)*	*Zone Length (d)*	*Burning Efficiency, η_{burn}*	*$\Delta\ \eta_{burn}$ (%)*
3xr-V00	2.11	8.23	0.72	n/a
3xr-V10-TO	1.07	8.95	0.74	3.2
3xr-V20-TO	2.19	6.60	0.76	5.8
3xr-V30-TO	1.87	4.97	0.77	7.5
3xr-V40-TO	2.63	3.86	0.79	10.3
3xr-V50-TO	2.47	2.31	0.85	18.4

a)

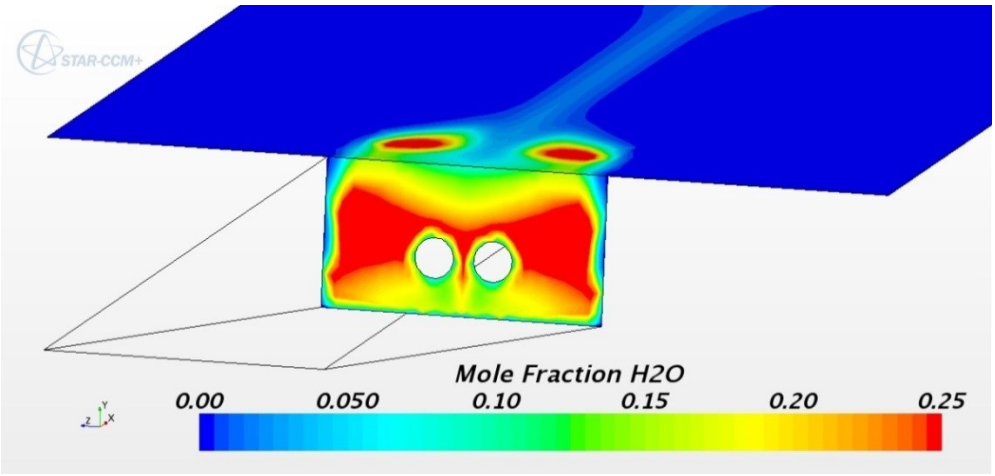

b)

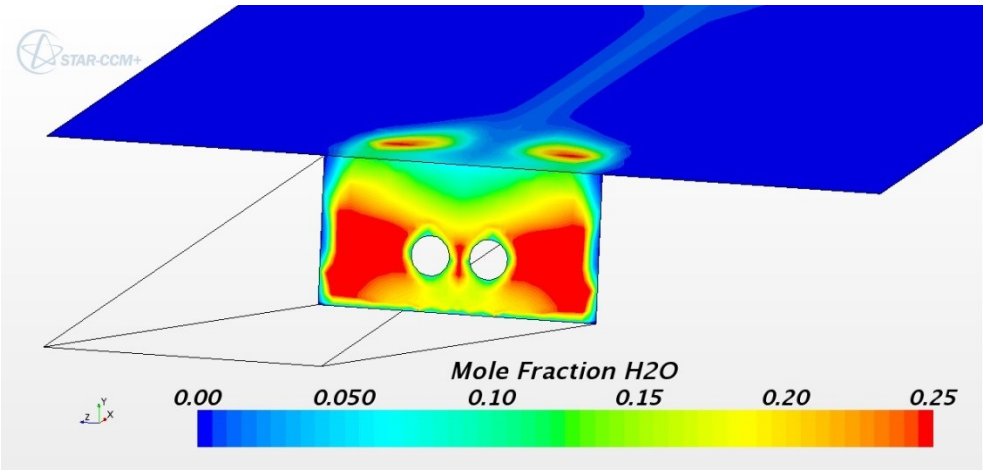

c)

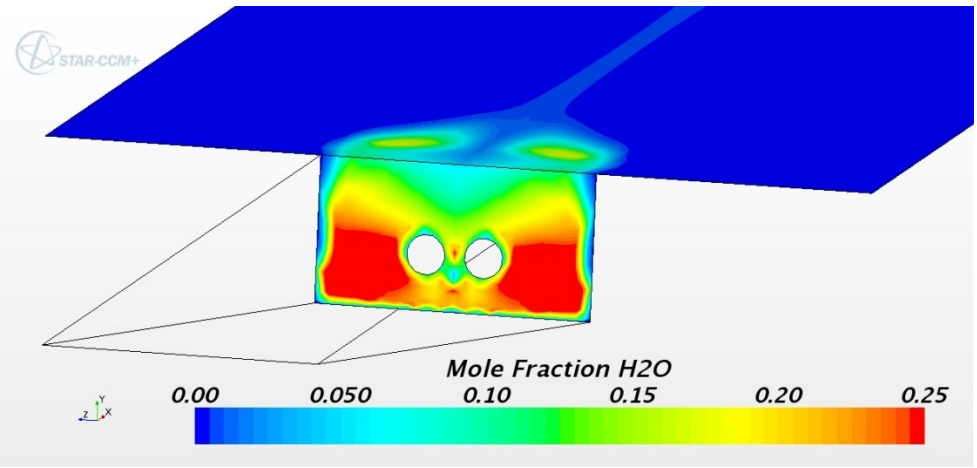

Figure 102 Mole fraction contours of H_2O on the fuel inlet wall and combustor upper wall for Configuration 3xr-TO
a) 3xr-V00, b) 3xr-V10-TO, c) 3xr-V20-TO

d)

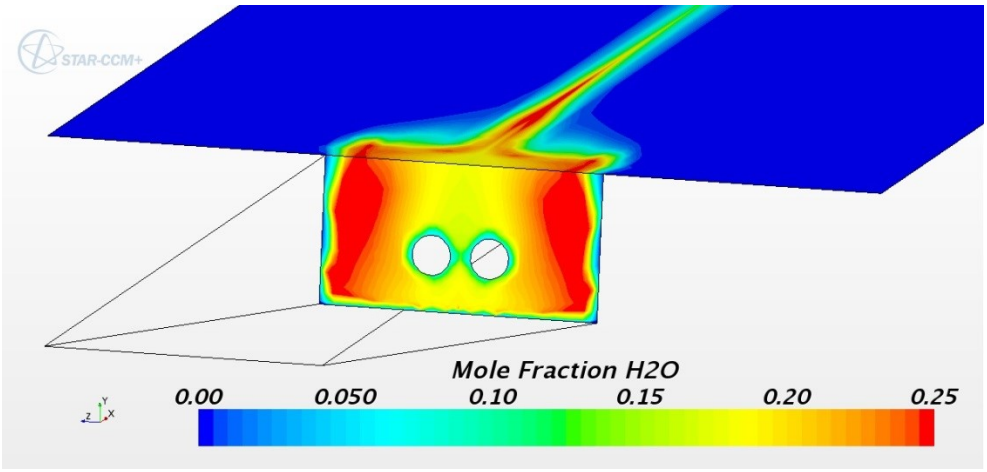

e)

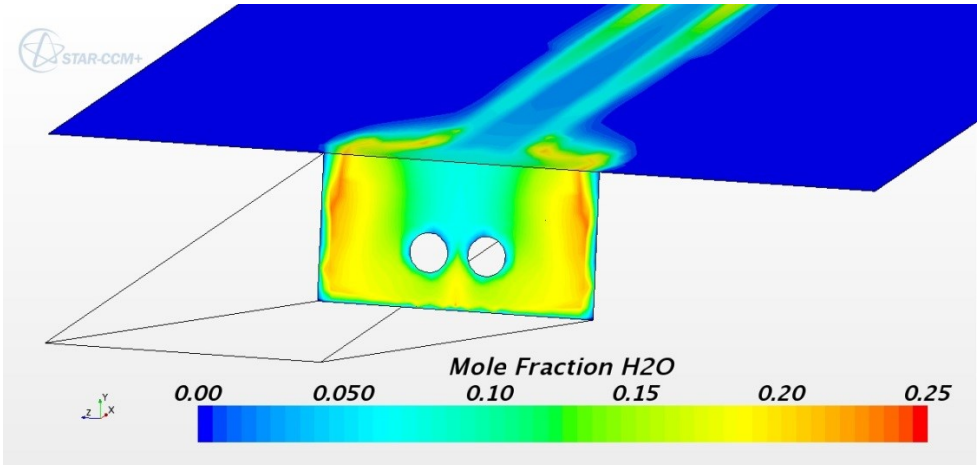

f)

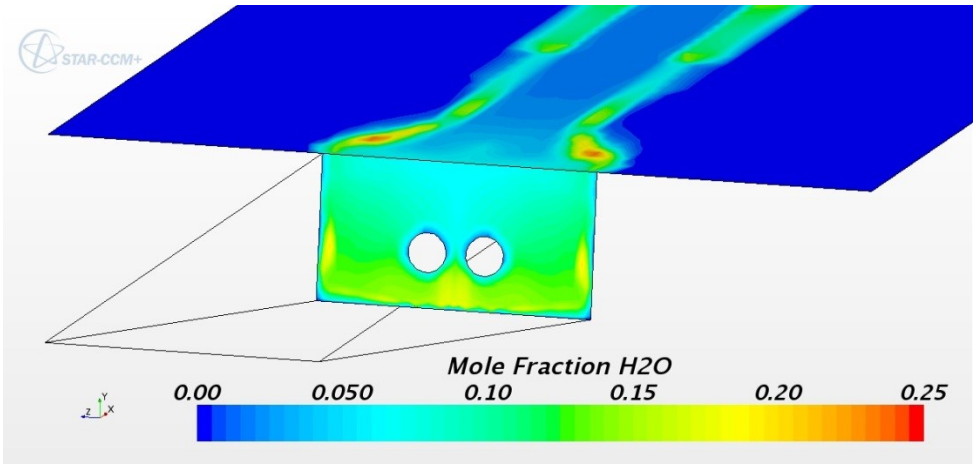

Figure 102 Mole fraction contours of H_2O on the fuel inlet wall and the combustor upper wall for Configuration 3xr-TO
d) 3xr-V30-TO, e) 3xr-V40-TO, f) 3xr-V50-TO

a)

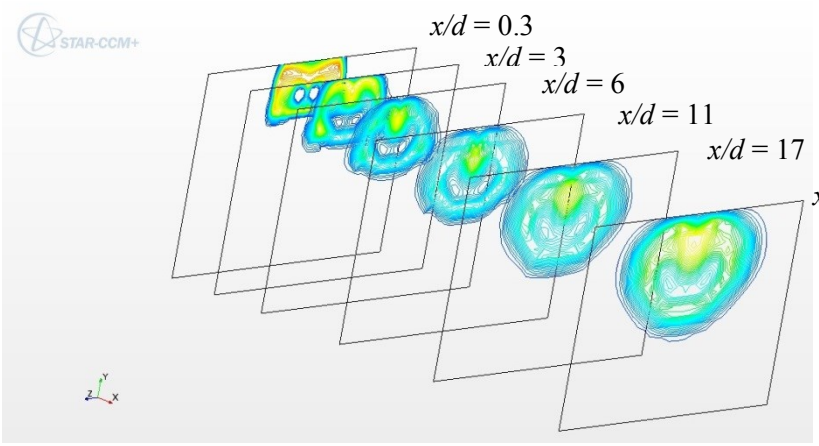

b)

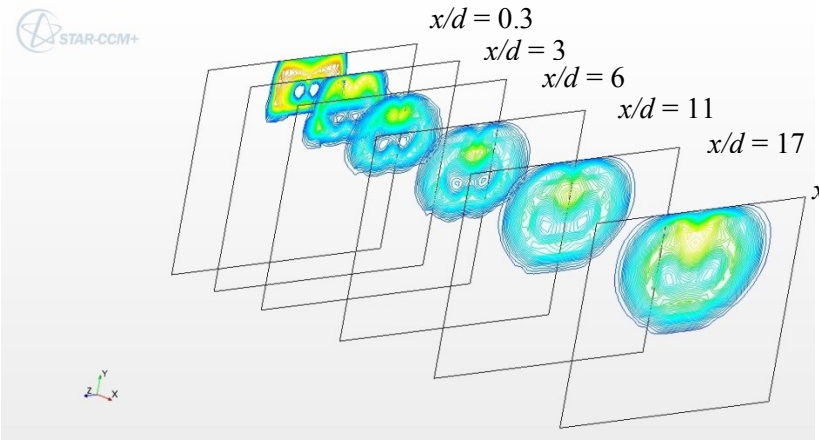

c)

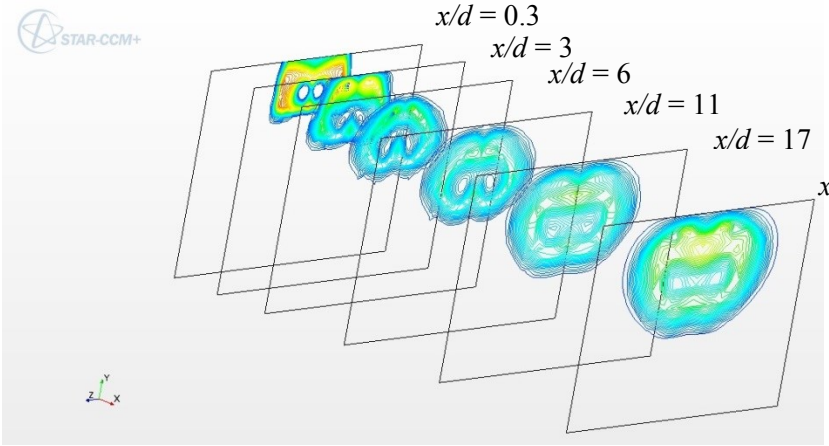

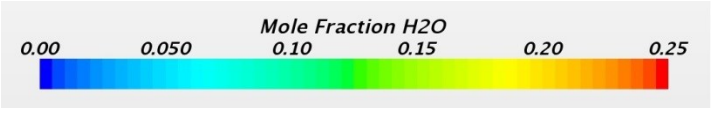

Figure 103 Mole fraction contours of H_2O in the combustor for Configuration 3xr-TO
a) 3xr-V00, b) 3xr-V10-TO, c) 3xr-V20-TO

d)

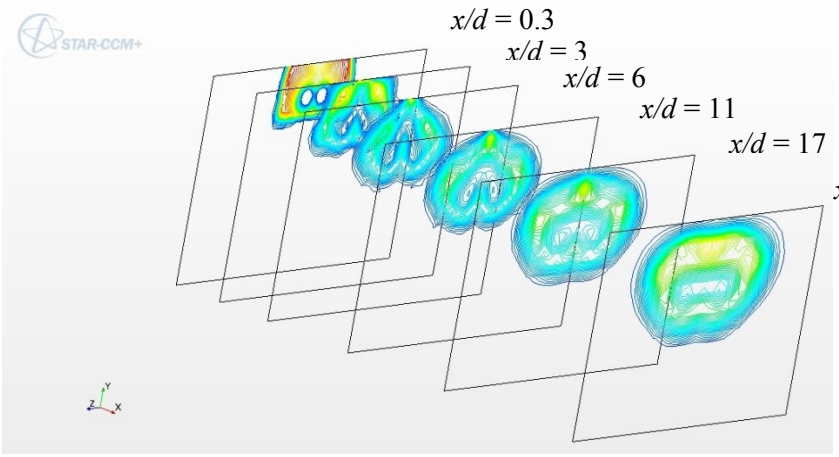

e)

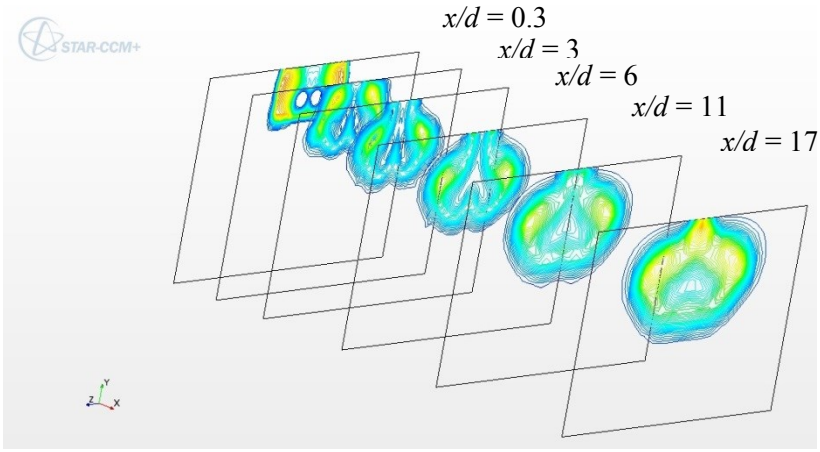

f)

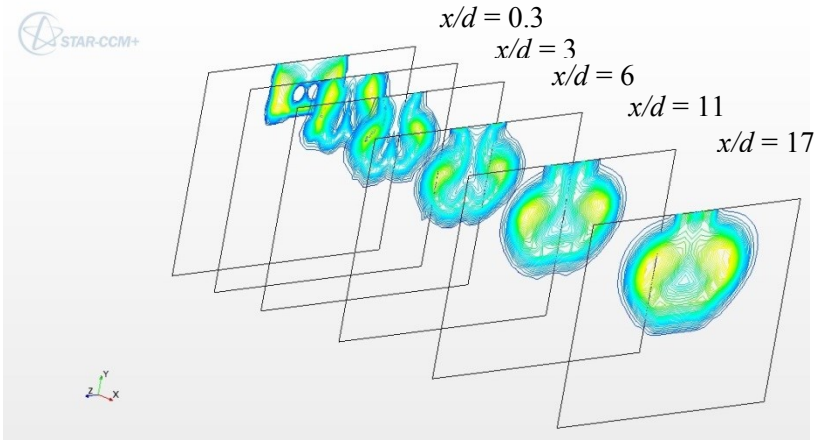

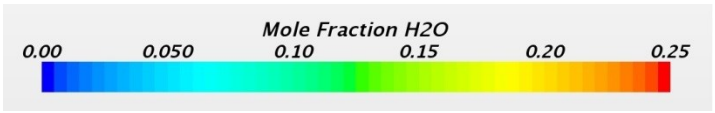

Figure 103 Mole fraction contours of H_2O in the combustor for Configuration 3xr-TO
d) 3xr-V30-TO, e) 3xr-V40-TO, f) 3xr-V50-TO

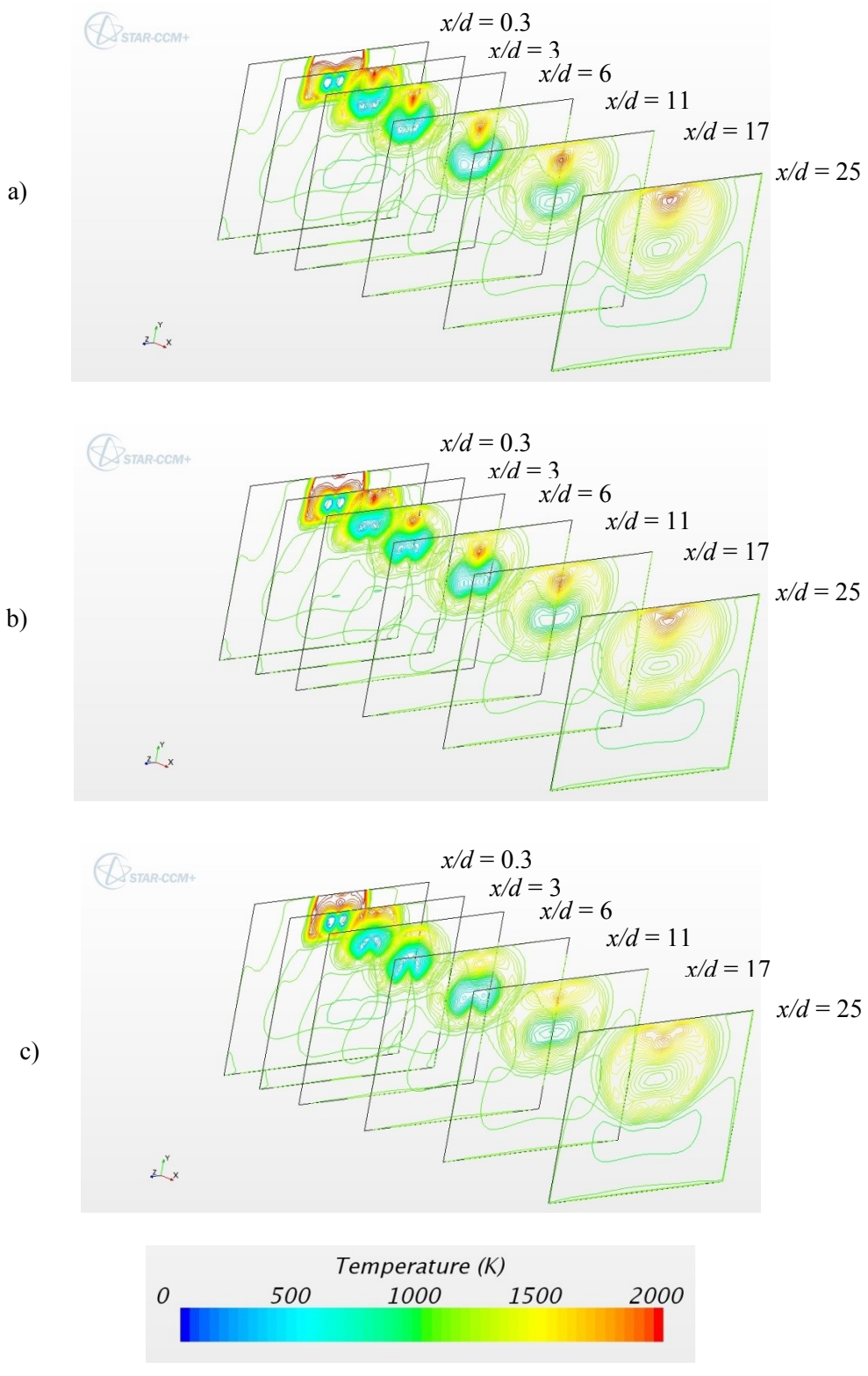

Figure 104 Temperature contours in the combustor for Configuration 3xr-TO
a) 3xr-V00, b) 3xr-V10-TO, c) 3xr-V20-TO

d)

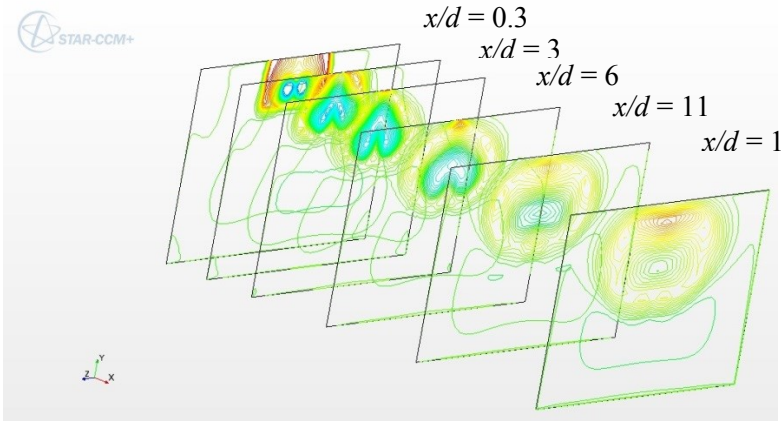

e)

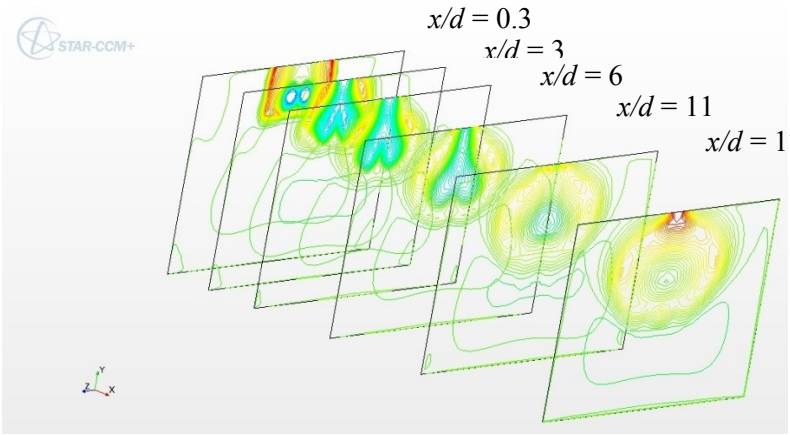

f)

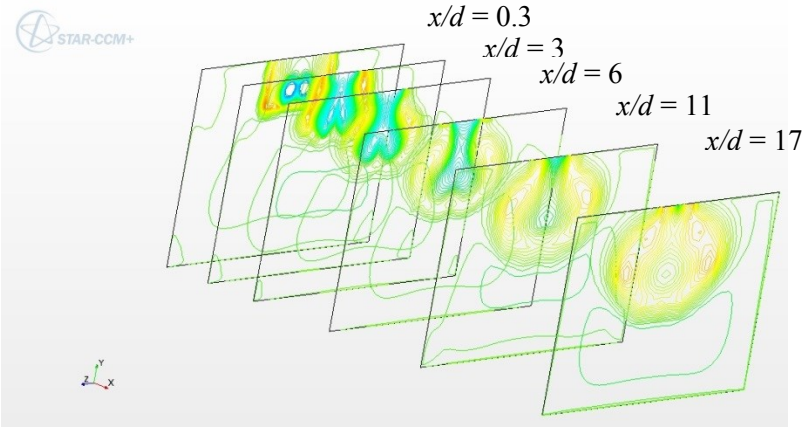

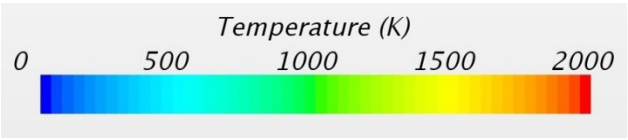

Figure 104 Temperature contours in the combustor for Configuration 3xr-TO
d) 3xr-V30-TO, e) 3xr-V40-TO, f) 3xr-V50-TO

(a)

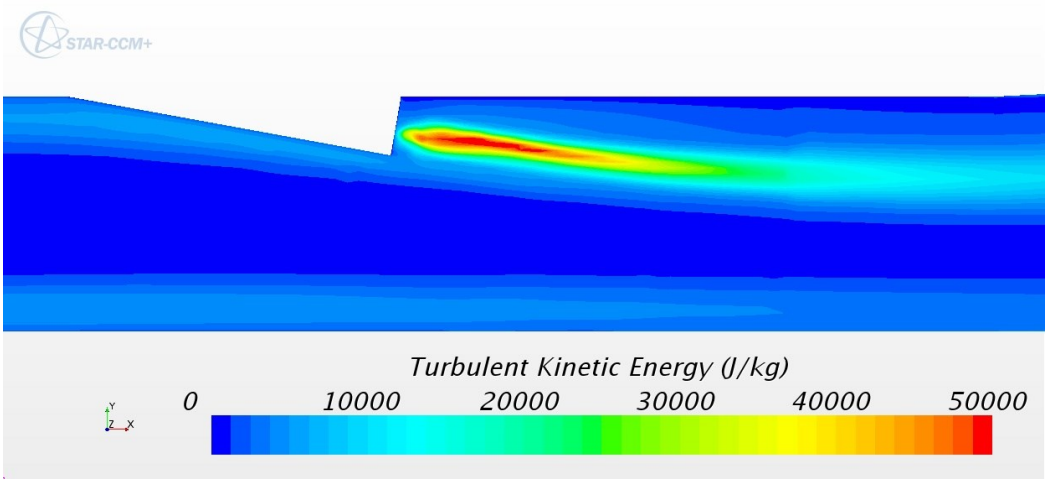

(b)

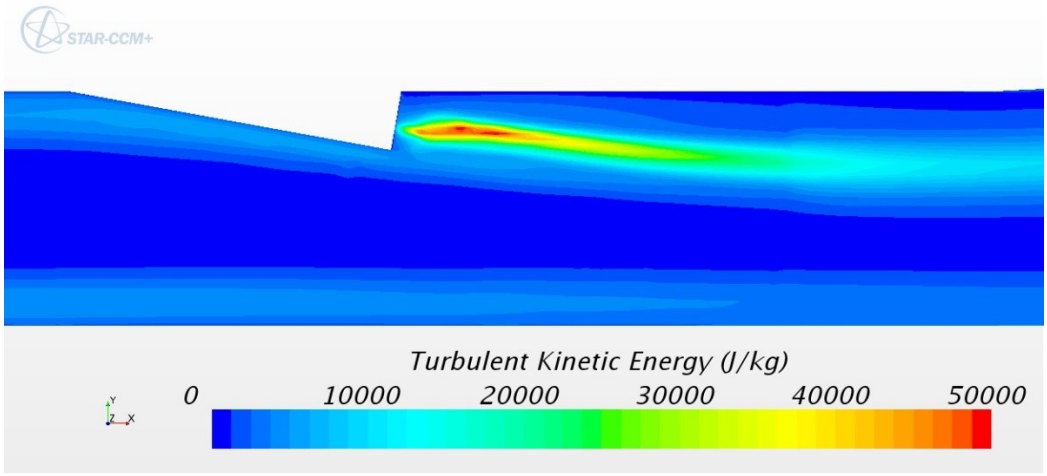

(c)

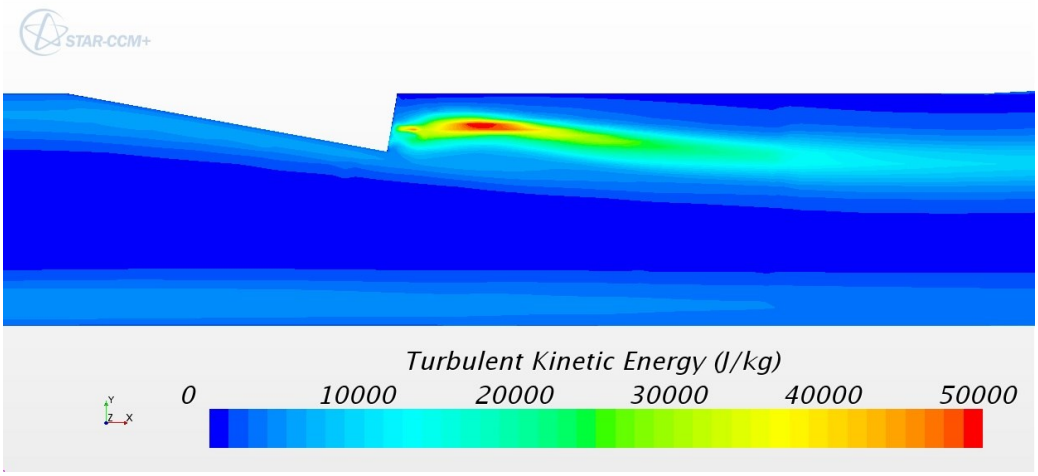

Figure 105 Turbulent kinetic energy plots on the centerline plane (z = 0) in the combustor for Configuration 3xr-TO
a) 3xr-V00, b) 3xr-V10-TO, c) 3xr-V20-TO

(d)

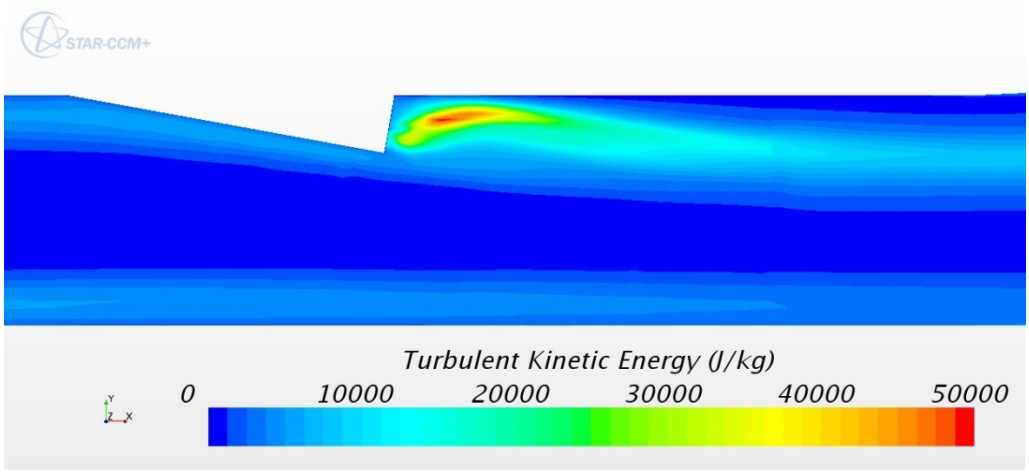

(e)

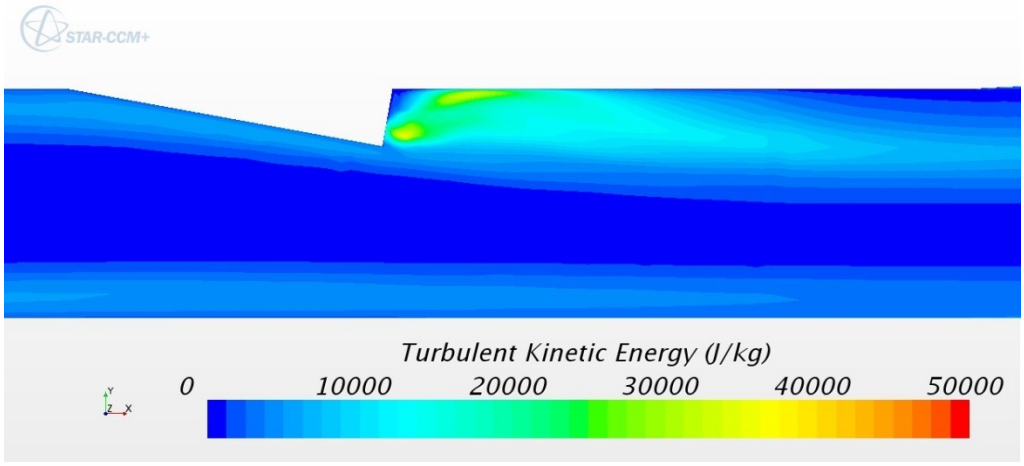

(f)

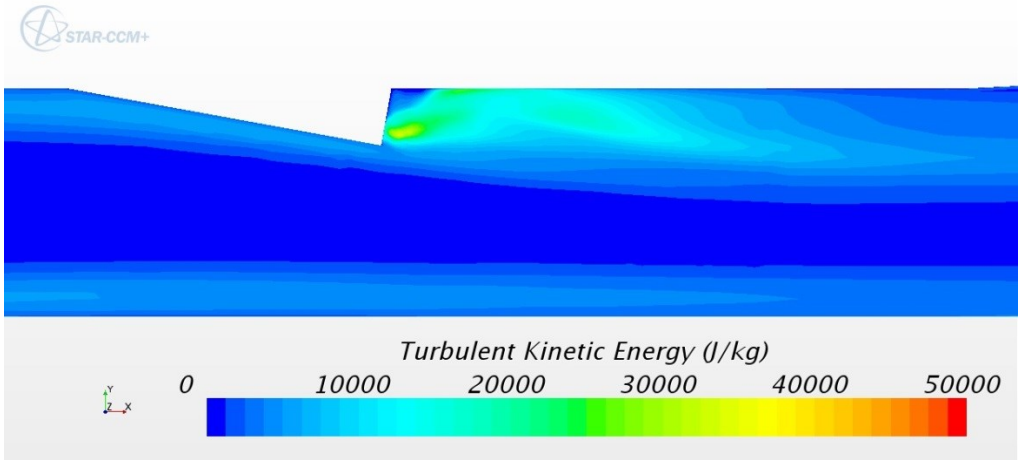

Figure 105 Turbulent kinetic energy plots on the centerline plane (z = 0) in the combustor for Configuration 3xr-TO
d) 3xr-V30-TO, e) 3xr-V40-TO, f) 3xr-V50-TO

(a)

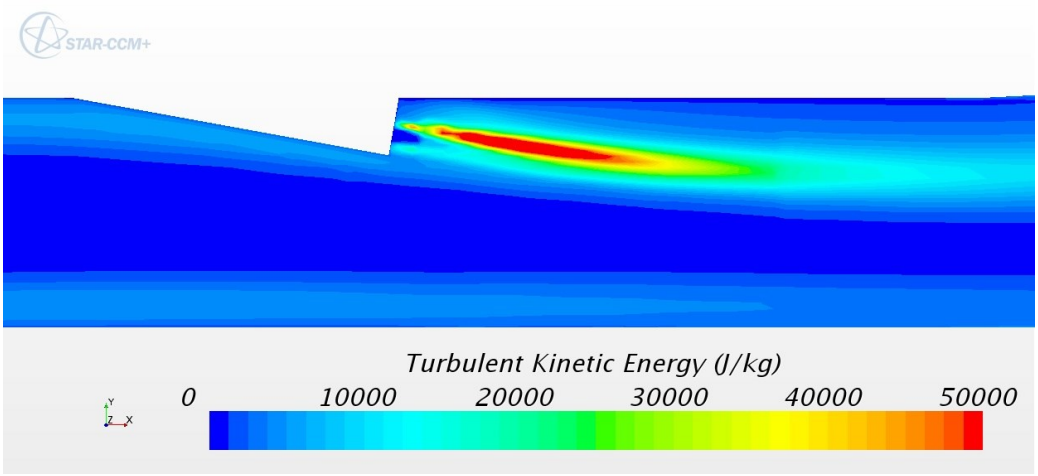

(b)

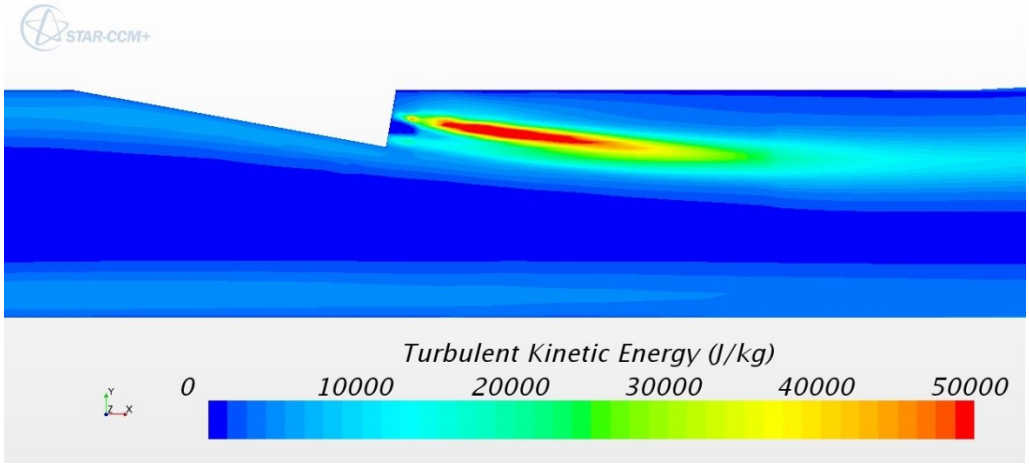

(c)

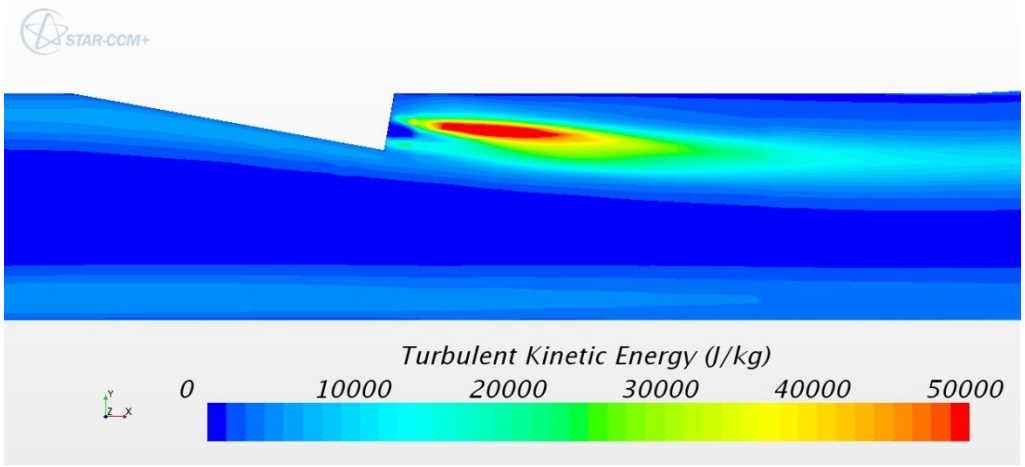

Figure 106 Turbulent kinetic energy plots on the fuel nozzle centerline plane (z = 1.5r) in the combustor for Configuration 3xr-TO
a) 3xr-V00, b) 3xr-V10-TO c) 3xr-V20-TO

(d)

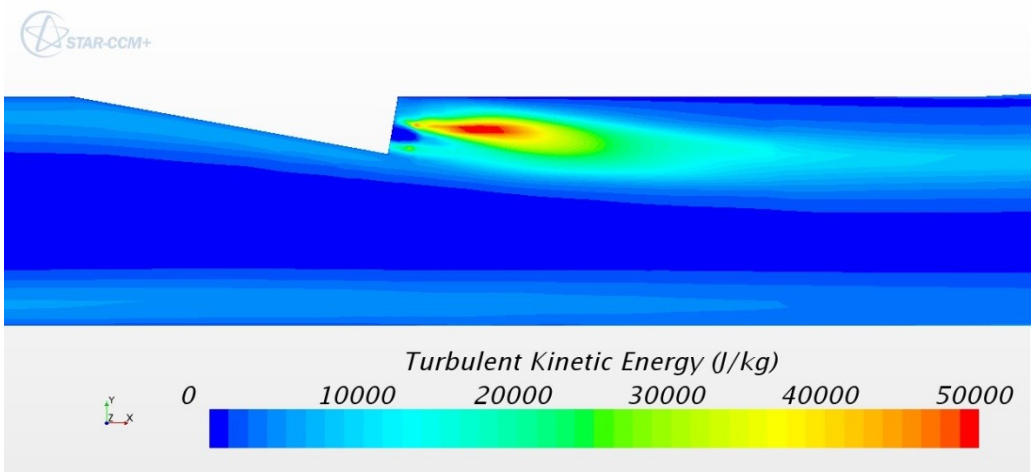

(e)

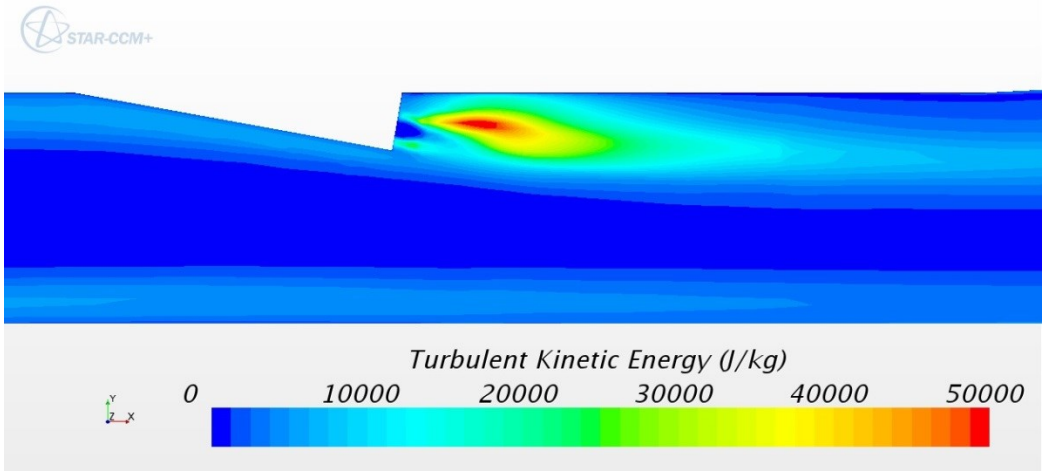

(f)

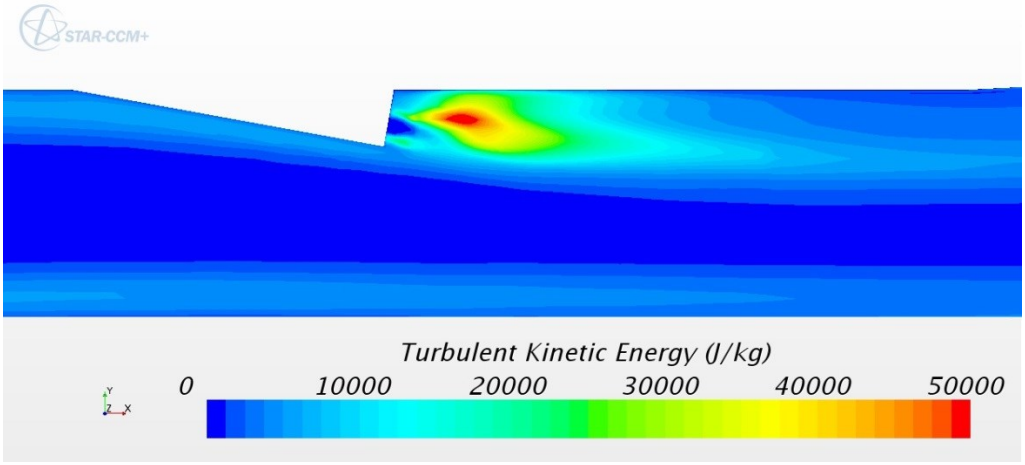

Figure 106 Turbulent kinetic energy plots on the fuel nozzle centerline plane (z = 1.5r) in the combustor for Configuration 3xr-TO
d) 3xr-V30-TO, e) 3xr-V40-TO, f) 3xr-V50-TO

a)

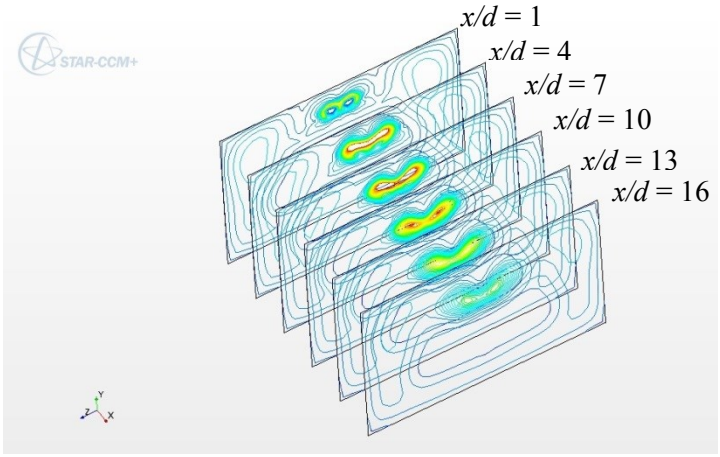

b)

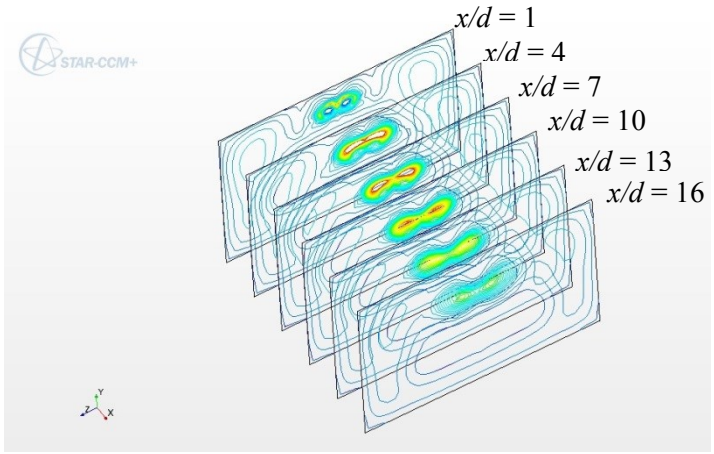

c)

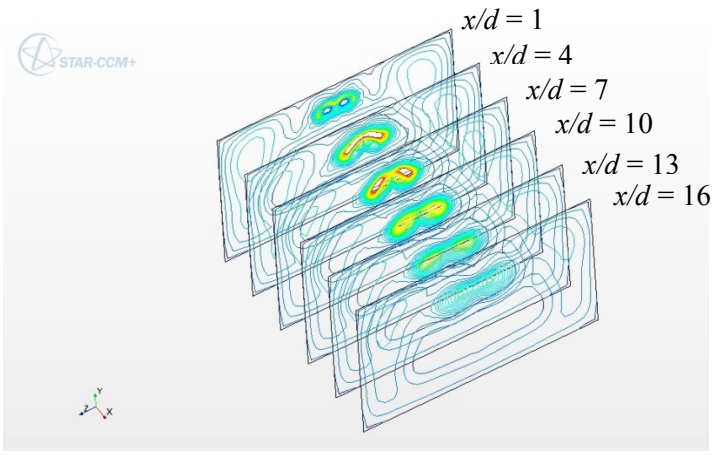

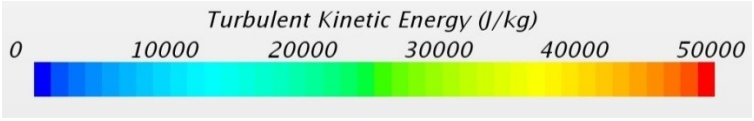

Figure 107 Turbulent kinetic energy contours in the combustor for Configuration 3xr-TO
a) 3xr-V00, b) 3xr-V10-TO, c) 3xr-V20-TO

d)

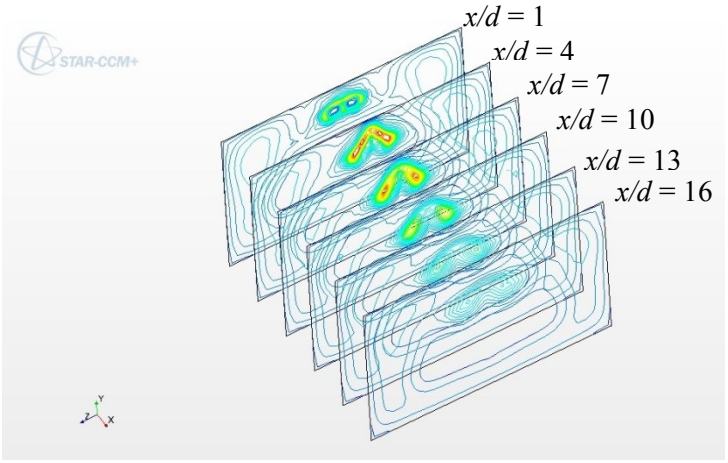

e)

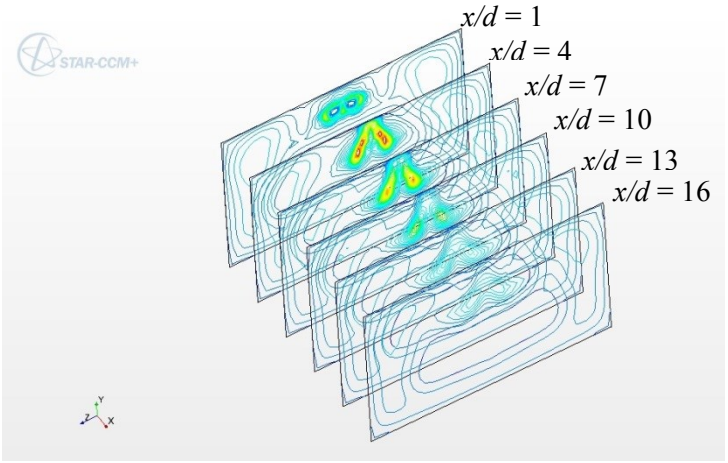

f)

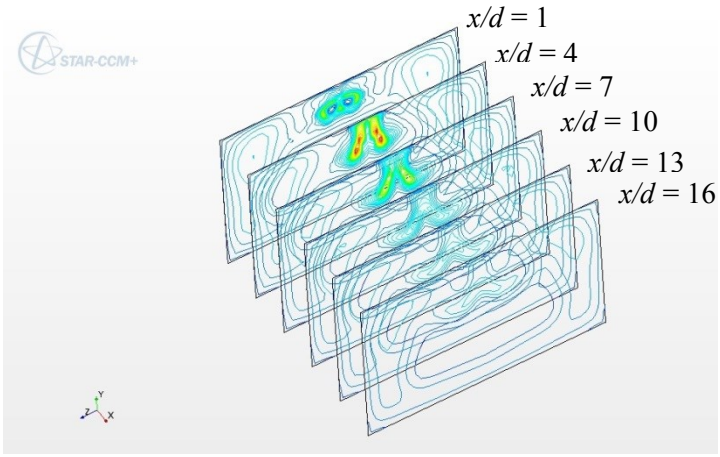

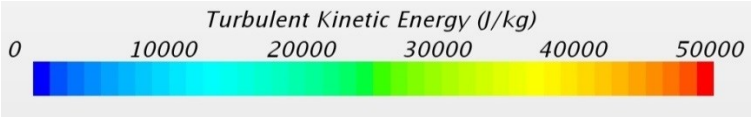

Figure 107 Turbulent kinetic energy contours in the combustor for Configuration 3xr-TO
d) 3xr-V30-TO, e) 3xr-V40-TO, f) 3xr-V50-TO

6.3.3 Distance Configuration 3xr, Swirl Pattern SD

Figure 108(a) shows the H_2O mole fraction contours on the fuel inlet and upper combustor walls for the non-swirling baseline case for the distance configuration 3xr. Configuration 3xr-SD is similar to the single fuel jet cases in that the high H_2O mole fraction zones on the upper combustor wall are eliminated with increasing swirl and then the high H_2O mole fraction zones on the fuel nozzle wall transfer to the combustor wall. Configuration 3xr-SD is similar to the single fuel jet cases in that the high H_2O mole fraction zones on the fuel nozzle wall rotate as swirl increases. The interaction of this swirl pattern also produces similar trends as with the single fuel jet.

Contour plots showing the progression of the H_2O mole fraction in the combustor are shown in Figure 109. Unlike the previous TI and TO swirl pattern, the fuel jets remain distinctly separate. This new trend is not as obviously seen in the temperature contours shown in Figure 110.

Turbulent kinetic energy is shown on the left fuel injector centerline plane (z = -1.5r) in Figure 111, on the tunnel centerline (z = 0) in Figure 112 and on the right fuel injector centerline plane (z = 1.5r) in Figure 113. The high TKE zones decrease as the swirl increases. However, The high TKE zone decreases on the left fuel injector centerline plane faster than on the tunnel centerline plane which in turn decreases faster than on the right fuel injector centerline plane. Figure 114 shows a progression of contour plots of TKE. At first there are two high TKE zones. The high TKE zone on the left side decreases as the swirl increases. Figure 114(f) shows only one high TKE zone at $x/d = 4$.

Table 10 shows the start location and length of the high TKE zone, the burning efficiency and the increase in burning efficiency due to swirl. Unlike the previous simulation cases, the start location of the high TKE zone for the fuel jet swirl cases is not always upstream of the start location of the high TKE zone for the non-swirling baseline case. The earliest start location is 2.31*d* from the fuel injector exit for configuration 3xr-V10-SD. The high TKE zone length increased with the 3xr-V10-SD swirl to 7.96*d* and then decreased as more swirl was added to the fuel jet.

The burning efficiency increases as the swirl increases. Configuration 3xr-V50-SD resulted in an 20.9% increase in burning efficiency compared to the case with no swirl.

Table 10 Mixing Data for Configuration 3xr-SD

	High Turbulent Kinetic Energy Zone			
Configuration	*Zone start location (x/d)*	*Zone Length (d)*	*Burning Efficiency,* η_{burn}	$\Delta\ \eta_{burn}$ *(%)*
3xr-V00	2.11	8.23	0.72	n/a
3xr-V10-SD	2.31	7.96	0.74	2.8
3xr-V20-SD	2.55	6.88	0.77	6.7
3xr-V30-SD	2.82	5.05	0.80	10.6
3xr-V40-SD	2.94	2.63	0.83	15.2
3xr-V50-SD	n/a	0.00	0.87	20.9

a)

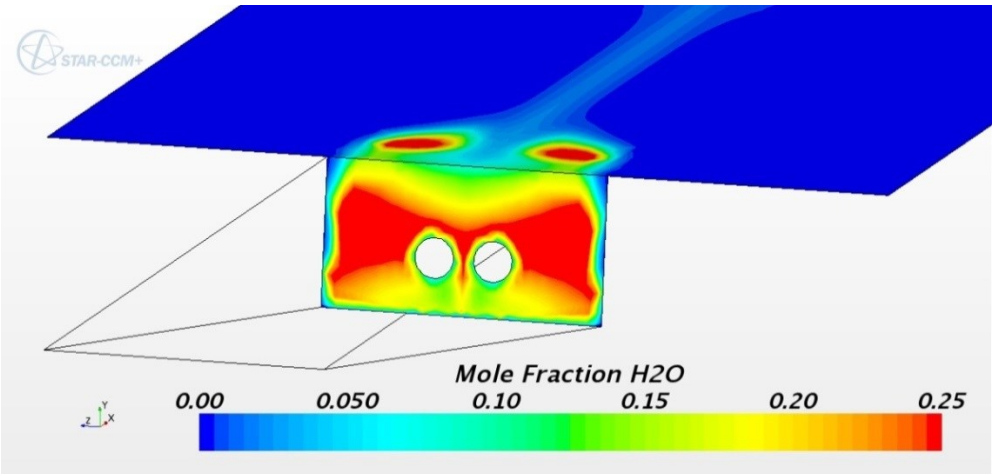

b)

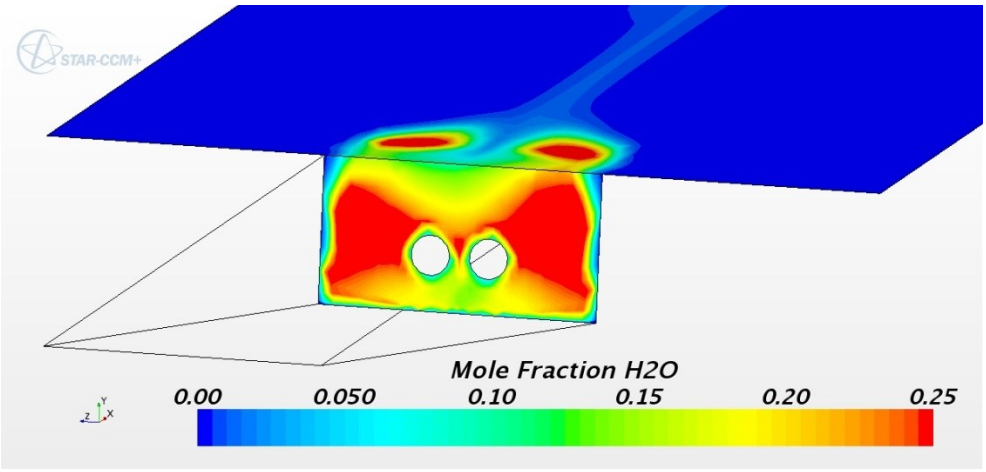

c)

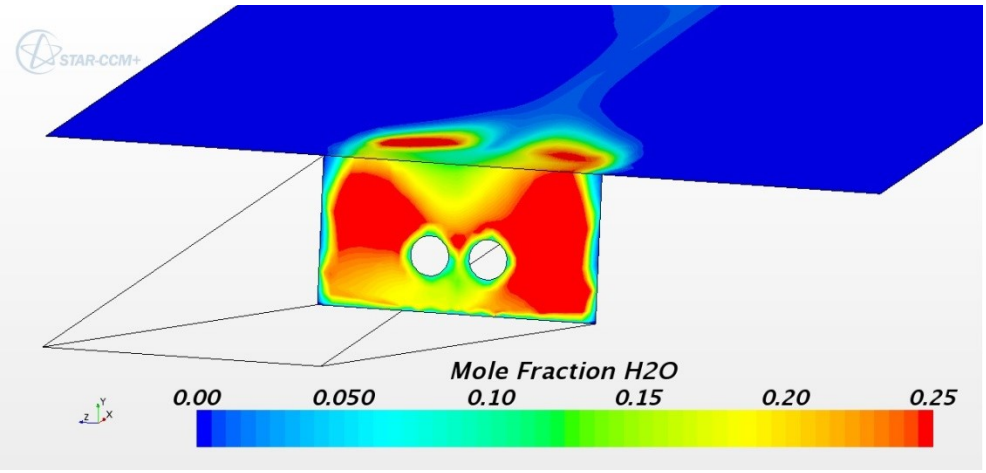

Figure 108 Mole fraction contours of H_2O on the fuel inlet wall and combustor upper wall for Configuration 3xr-SD
a) 3xr-V00, b) 3xr-V10-SD, c) 3xr-V20-SD

d)

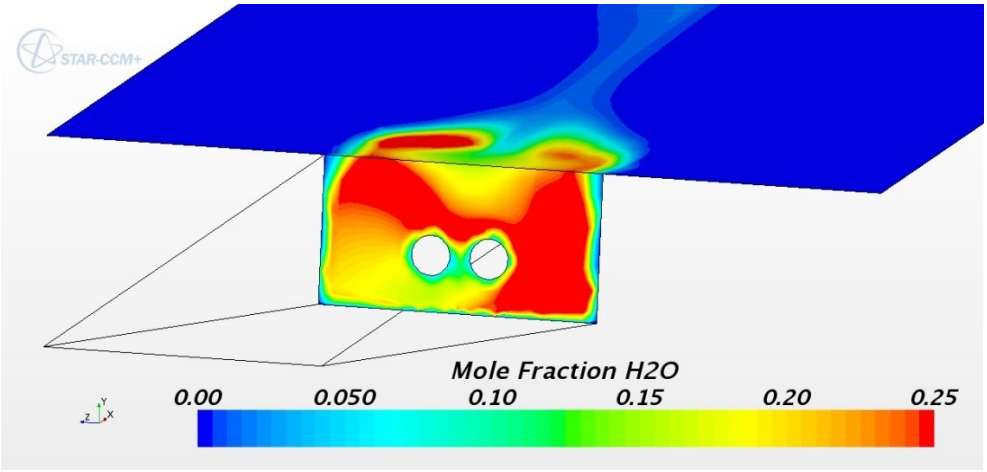

e)

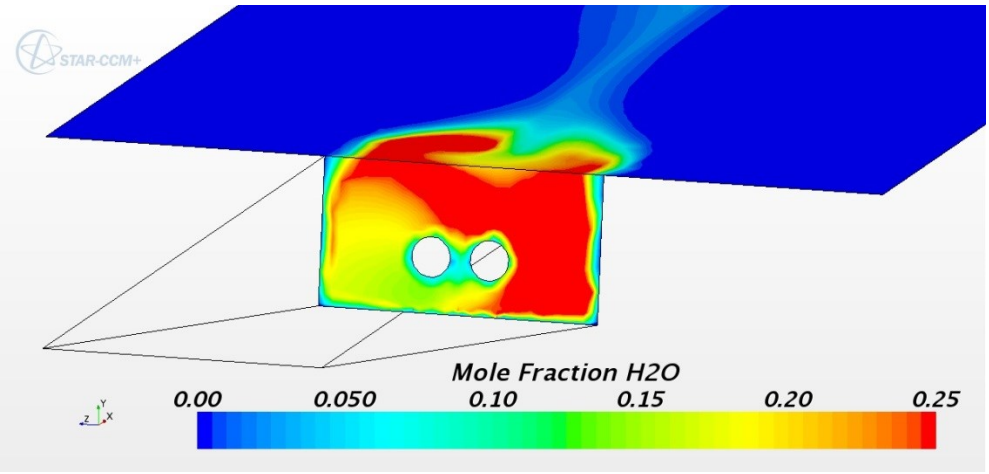

f)

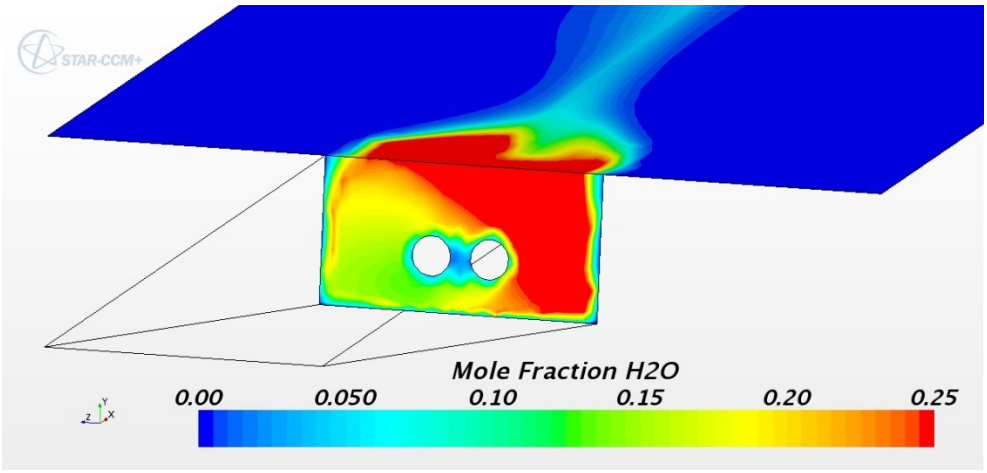

Figure 108 Mole fraction contours of H_2O on the fuel inlet wall and the combustor upper wall for Configuration 3xr-SD
d) 3xr-V30-SD, e) 3xr-V40-SD, f) 3xr-V50-SD

a)

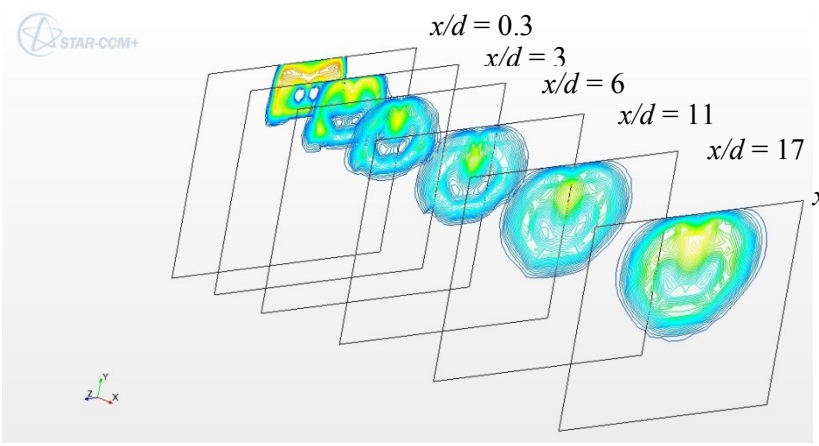

b)

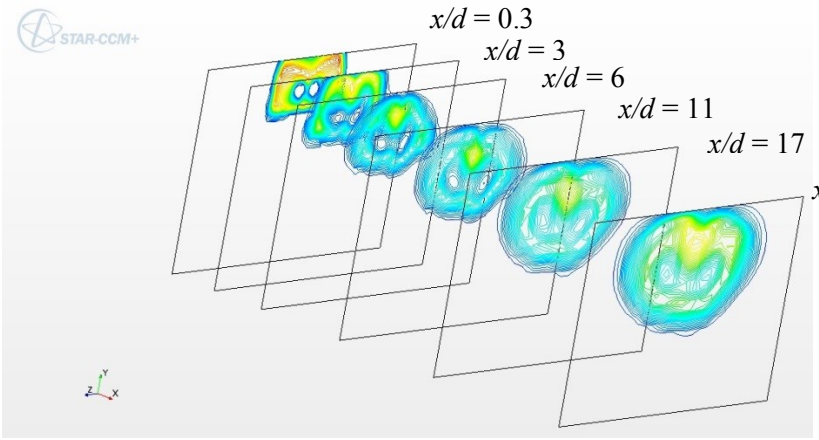

c)

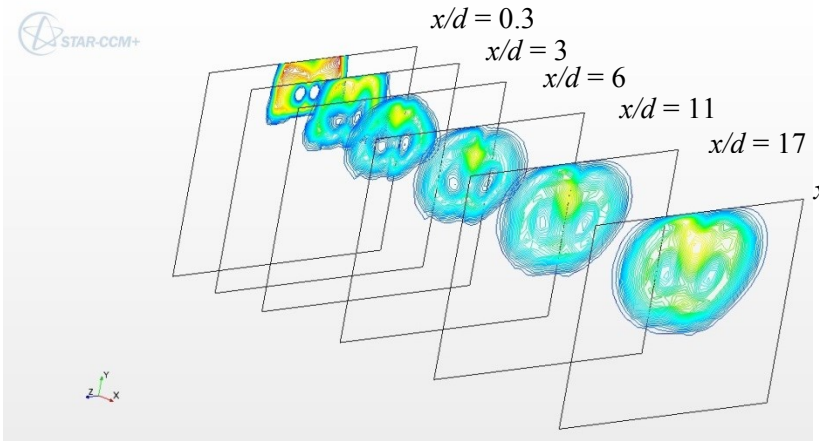

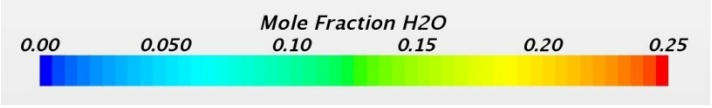

Figure 109 Mole fraction contours of H_2O in the combustor for Configuration 3xr-SD
a) 3xr-V00, b) 3xr-V10-SD, c) 3xr-V20-SD

d)

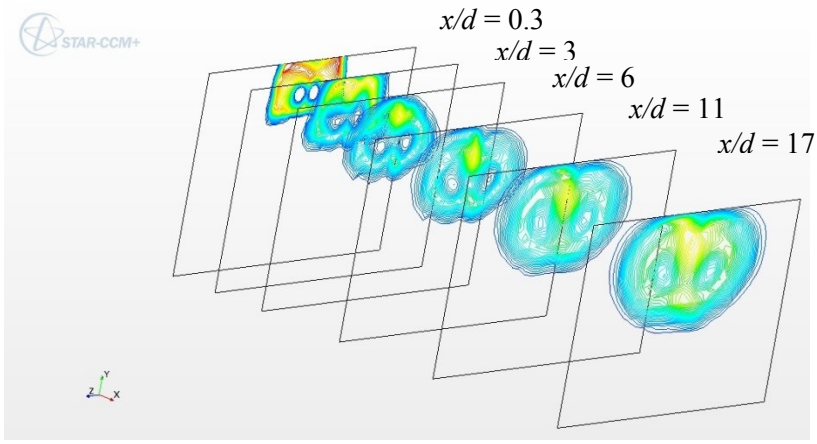

e)

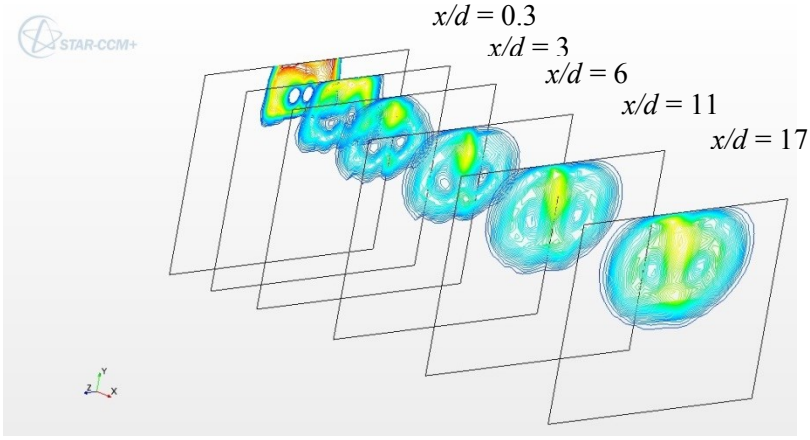

f)

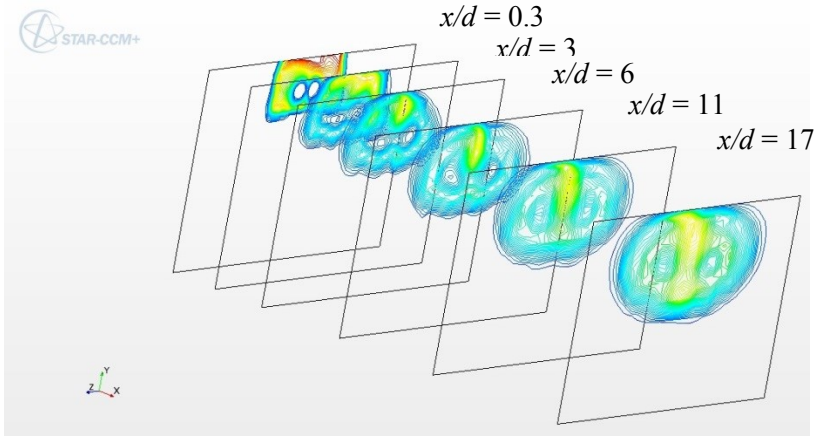

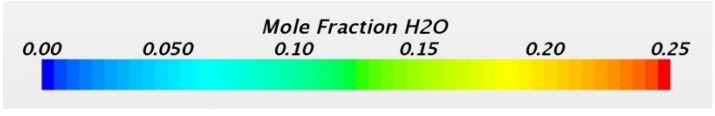

Figure 109 Mole fraction contours of H_2O in the combustor for Configuration 3xr-SD
d) 3xr-V30-SD, e) 3xr-V40-SD, f) 3xr-V50-SD

a)

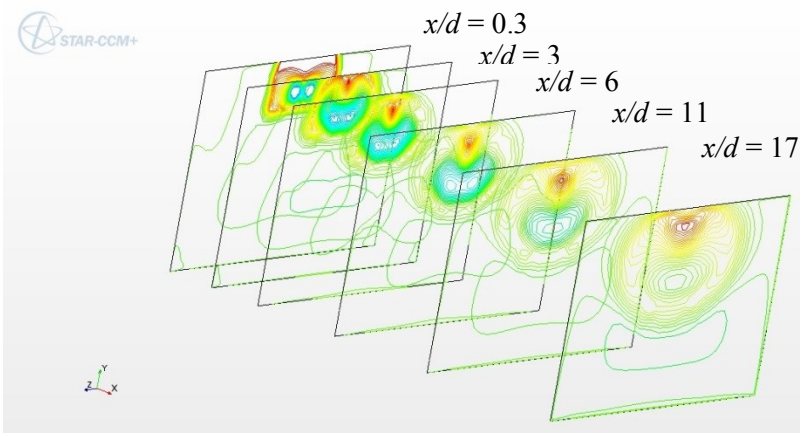

b)

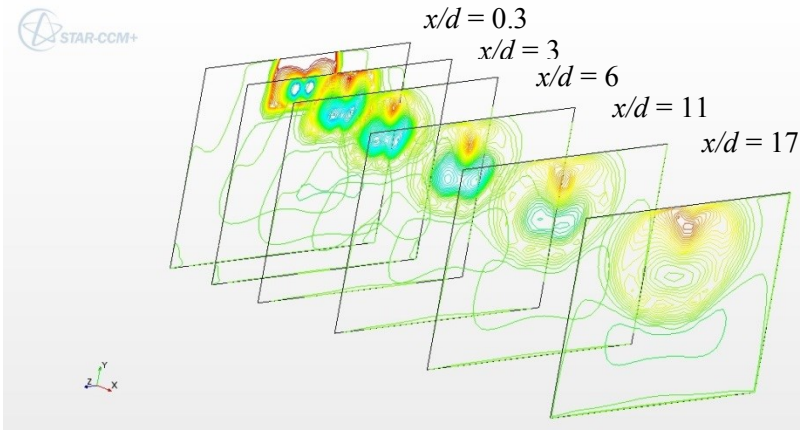

c)

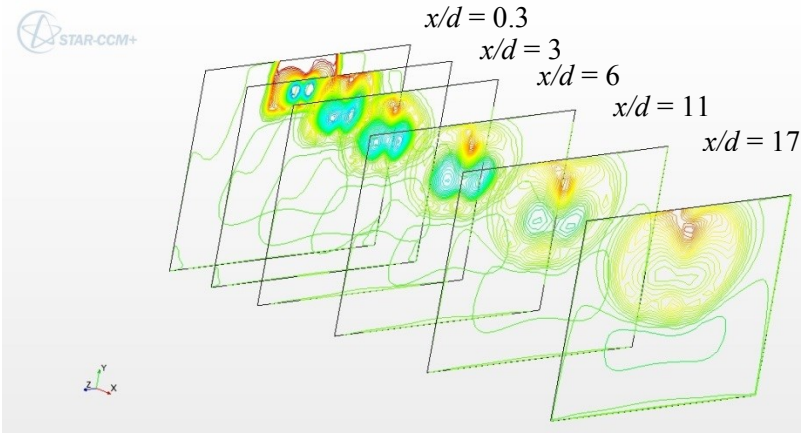

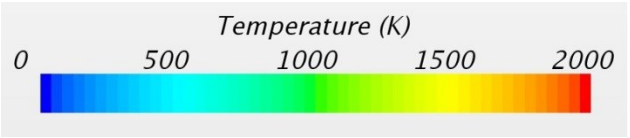

Figure 110 Temperature contours in the combustor for Configuration 3xr-SD
a) 3xr-V00, b) 3xr-V10-SD, c) 3xr-V20-SD

d)

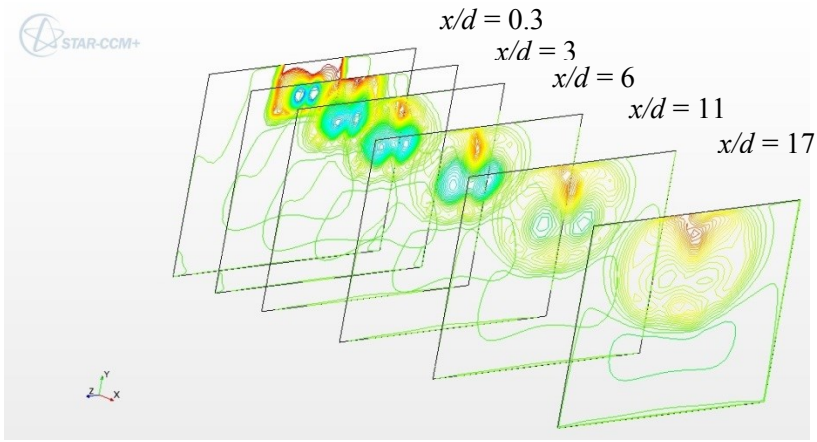

e)

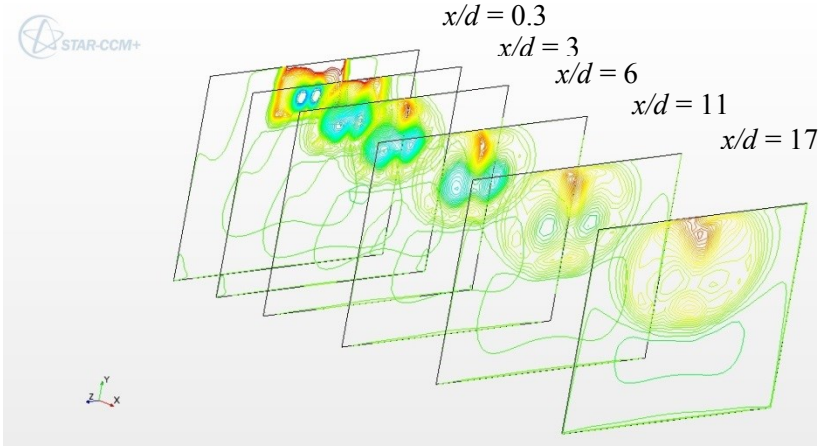

f)

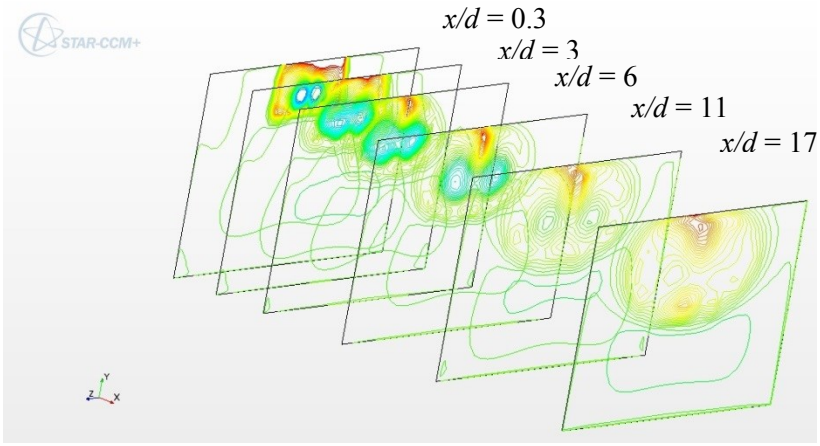

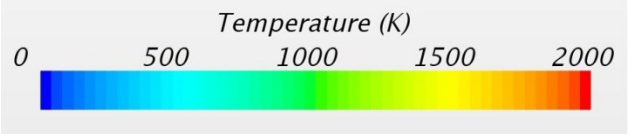

Figure 110 Temperature contours in the combustor for Configuration 3xr-SD
d) 3xr-V30-SD, e) 3xr-V40-SD, f) 3xr-V50-SD

(a)

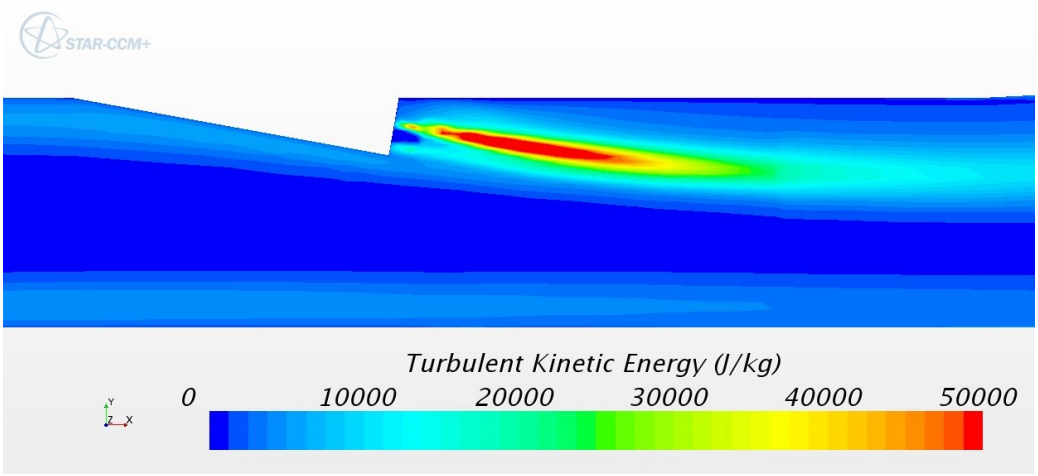

(b)

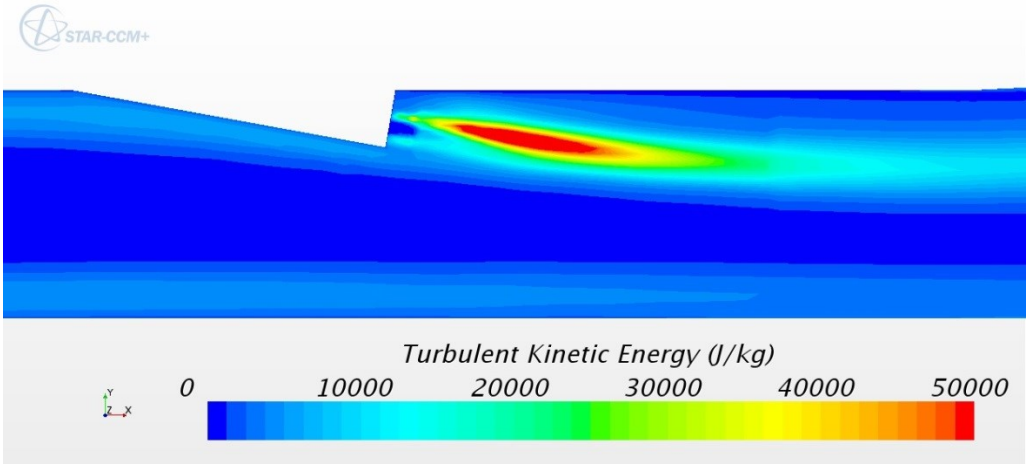

(c)

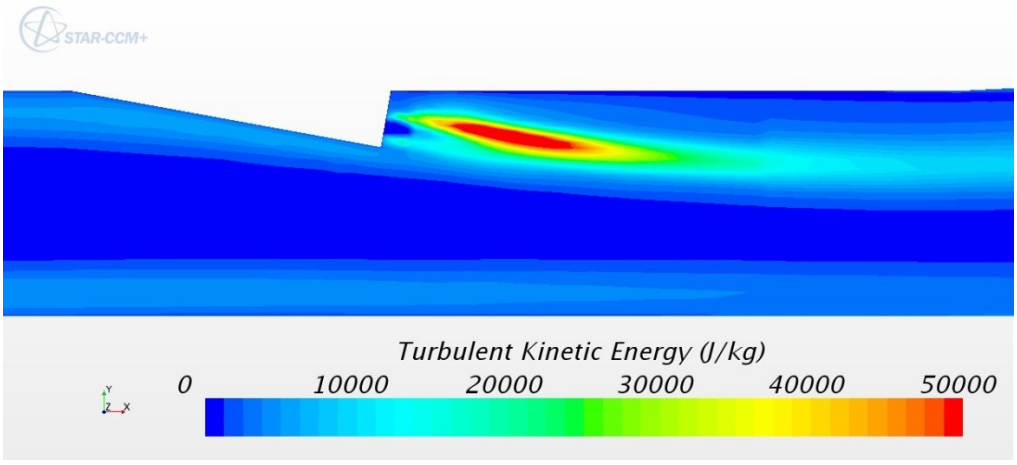

Figure 111 Turbulent kinetic energy plots on the left fuel nozzle centerline plane (z = -1.5r) in the combustor for Configuration 3xr-SD
a) 3xr-V00, b) 3xr-V10-SD, c) 3xr-V20-SD

(d)

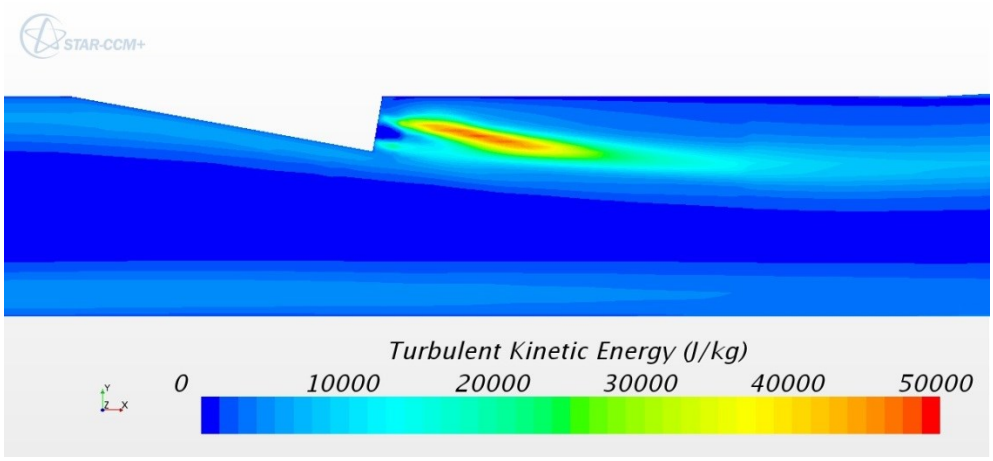

(e)

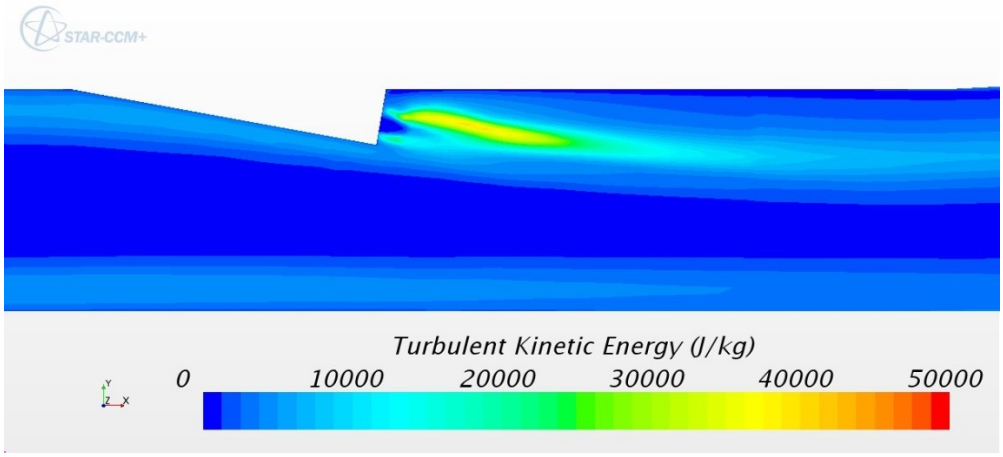

(f)

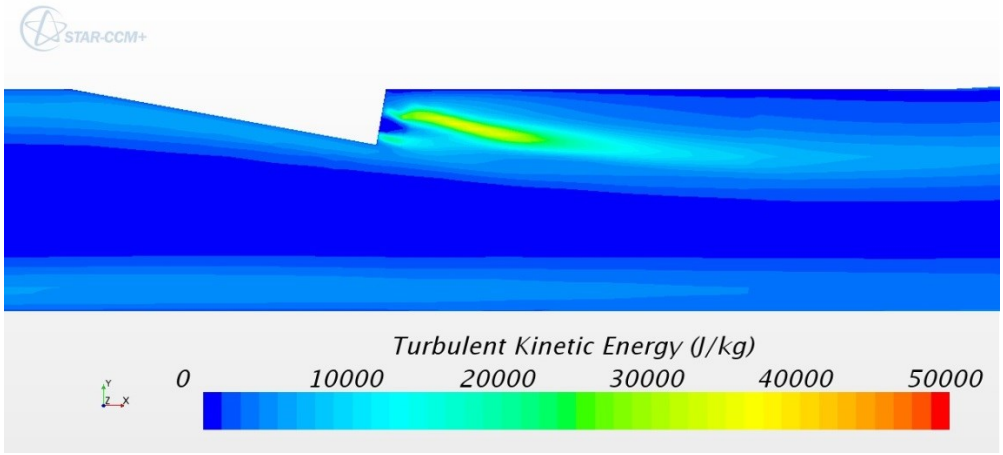

Figure 111 Turbulent kinetic energy plots on the left fuel nozzle centerline plane (z = -1.5r) in the combustor for Configuration 3xr-SD
d) 3xr-V30-SD, e) 3xr-V40-SD, f) 3xr-V50-SD

(a)

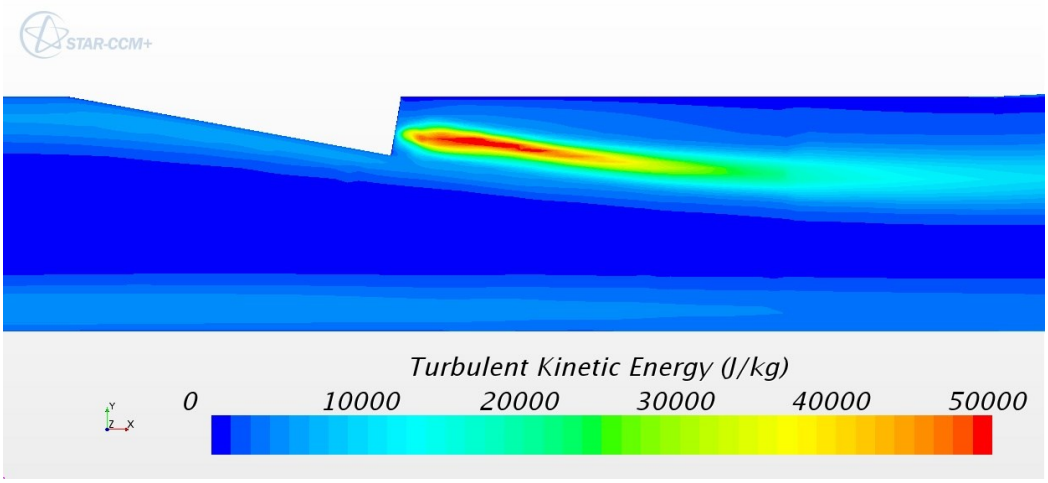

(b)

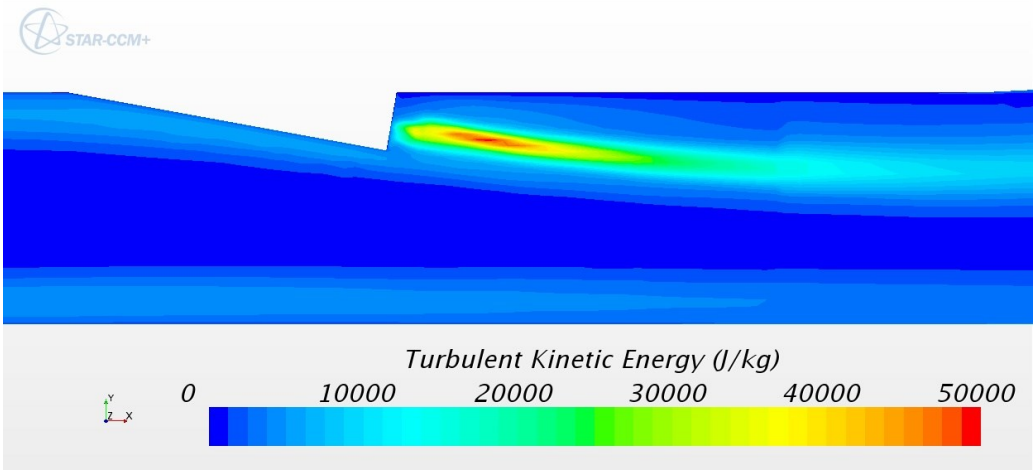

(c)

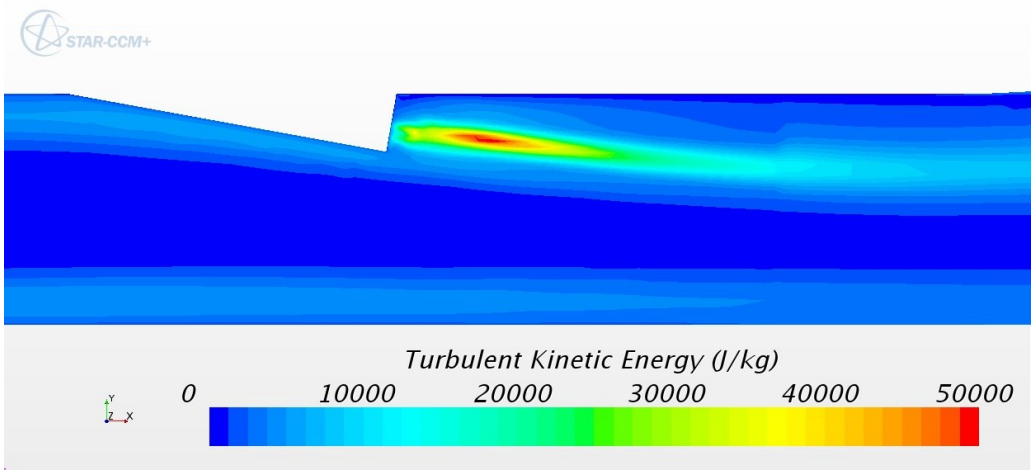

Figure 112 Turbulent kinetic energy plots on the centerline plane (z = 0) in the combustor for Configuration 3xr-SD
a) 3xr-V00, b) 3xr-V10-SD, c) 3xr-V20-SD

(d)

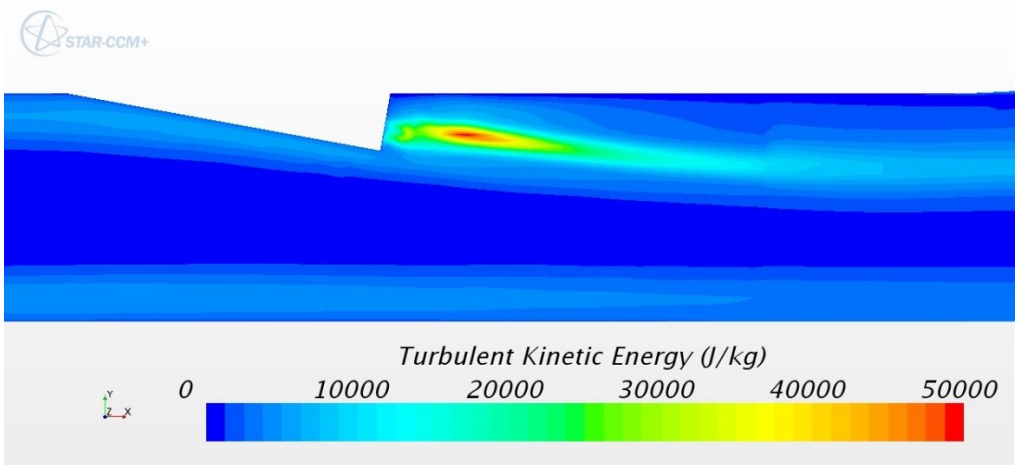

(e)

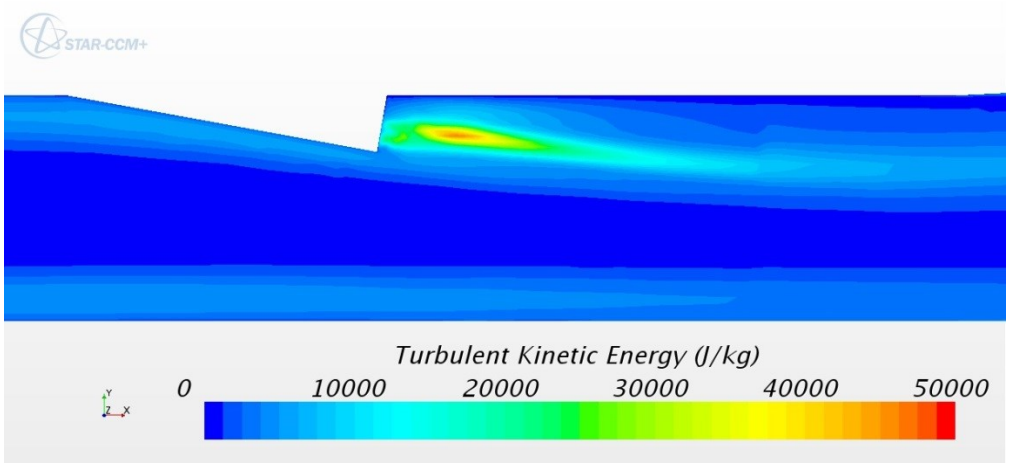

(f)

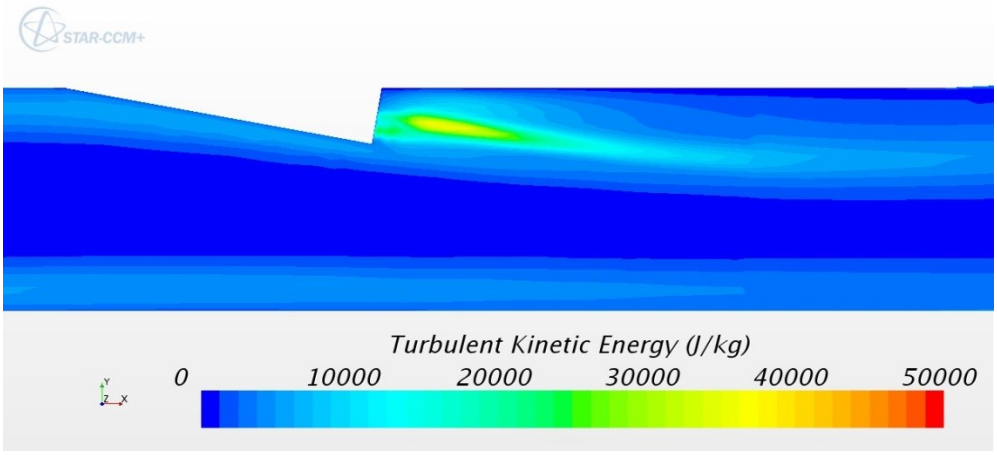

Figure 112 Turbulent kinetic energy plots on the centerline plane (z = 0) in the combustor for Configuration 3xr-SD
d) 3xr-V30-SD, e) 3xr-V40-SD, f) 3xr-V50-SD

(a)

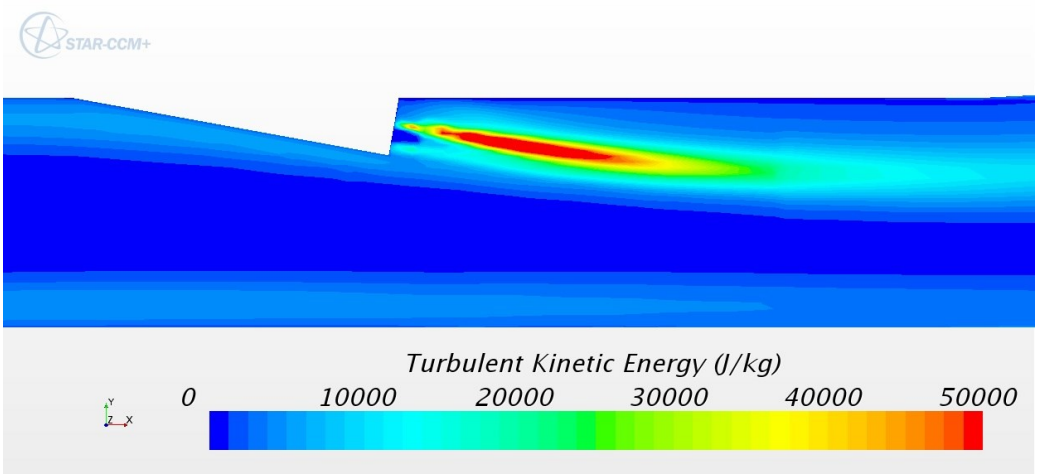

(b)

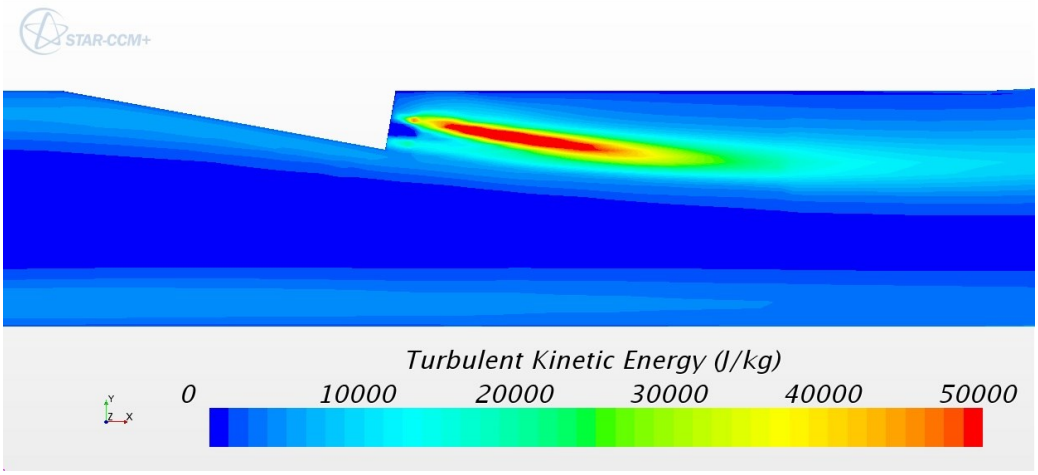

(c)

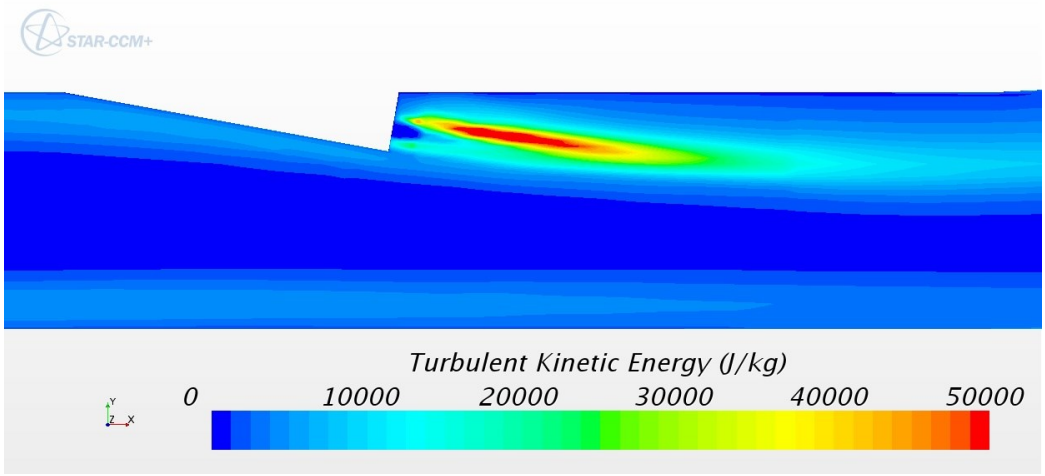

Figure 113 Turbulent kinetic energy plots on the right fuel nozzle centerline plane (z = 1.5r) in the combustor for Configuration 3xr-SD
a) 3xr-V00, b) 3xr-V10-SD, c) 3xr-V20-SD

(d)

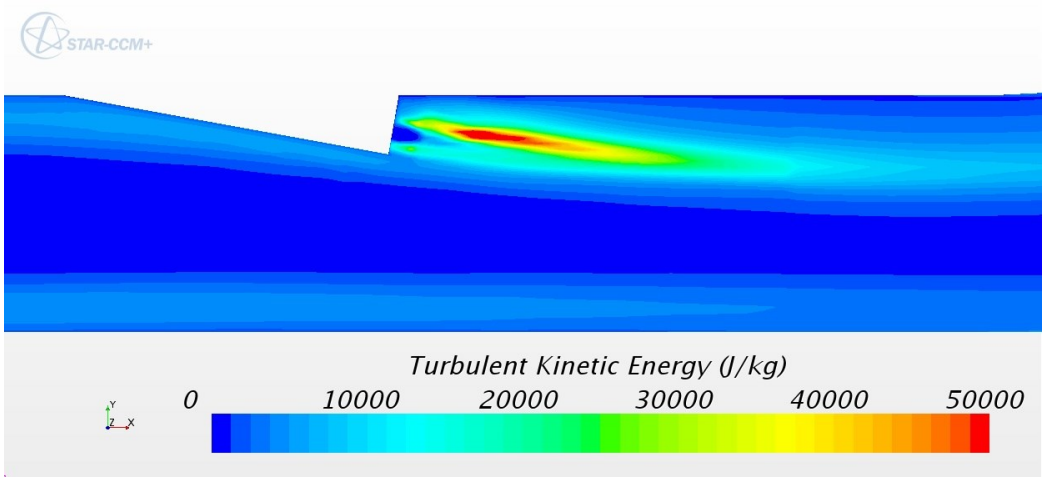

(e)

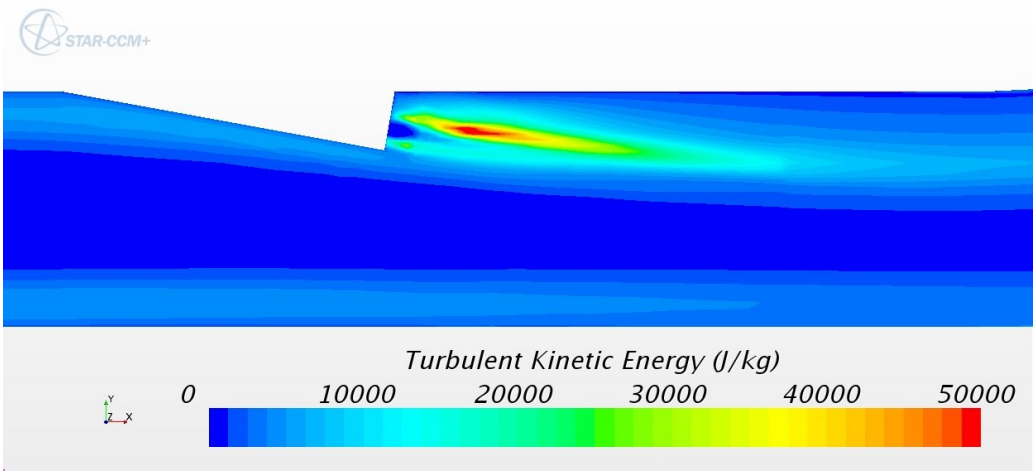

(f)

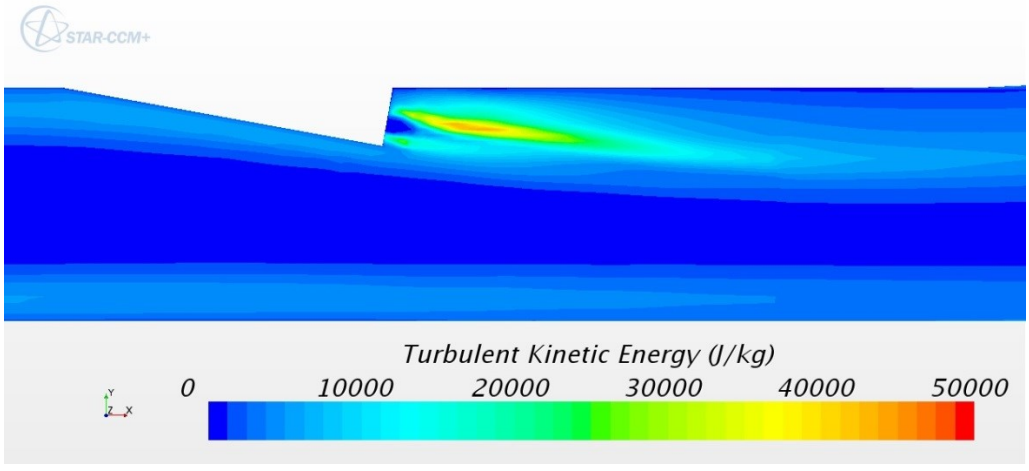

Figure 113 Turbulent kinetic energy plots on the right fuel nozzle centerline plane (z = 1.5r) in the combustor for Configuration 3xr-SD
d) 3xr-V30-SD, e) 3xr-V40-SD, f) 3xr-V50-SD

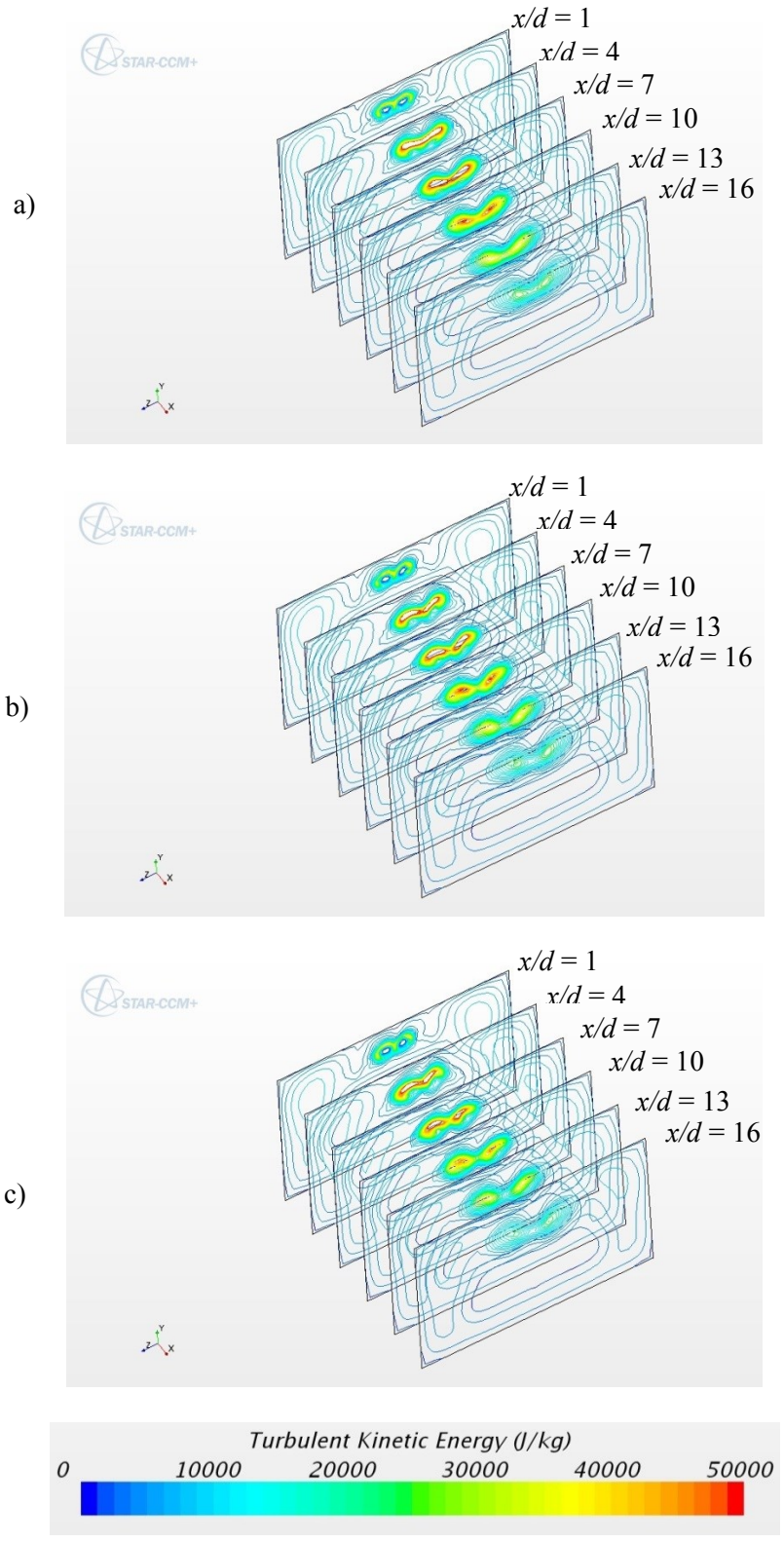

Figure 114 Turbulent kinetic energy contours in the combustor for Configuration 3xr-SD
a) 3xr-V00, b) 3xr-V10-SD, c) 3xr-V20-SD

d)

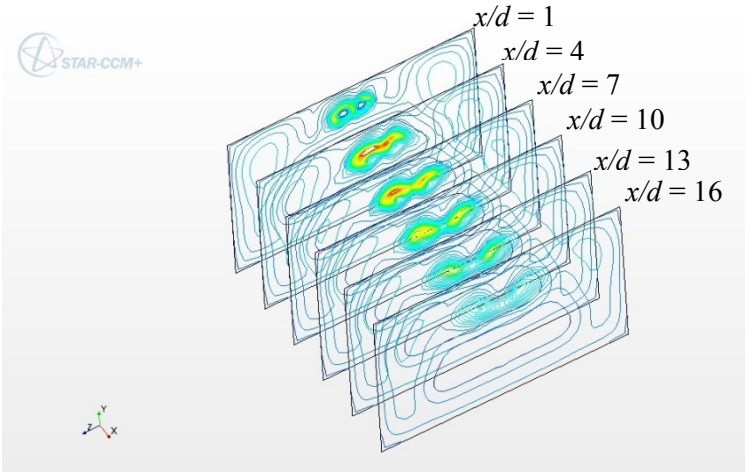

e)

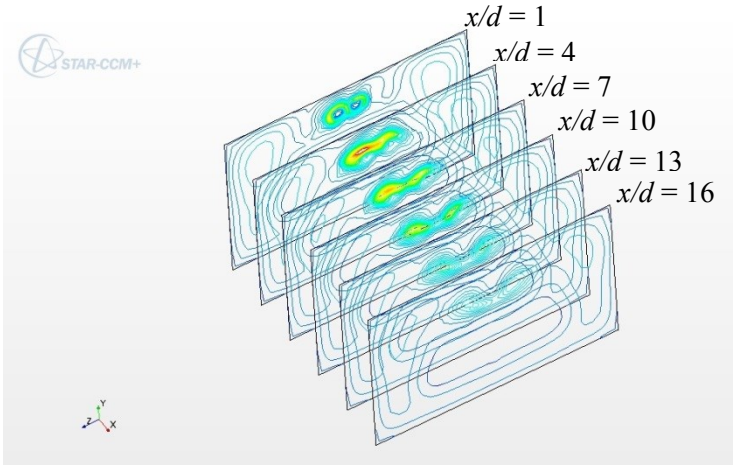

f)

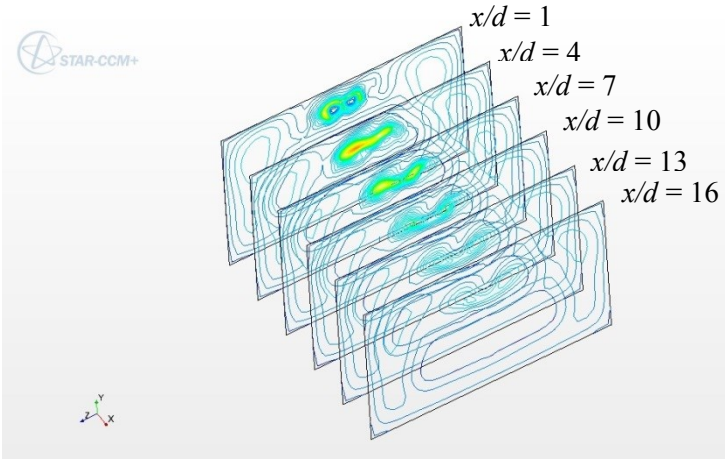

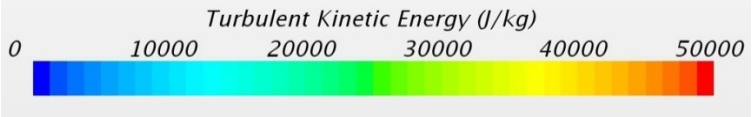

Figure 114 Turbulent kinetic energy contours in the combustor for Configuration 3xr-SD
d) 3xr-V30-SD, e) 3xr-V40-SD, f) 3xr-V50-SD

6.3.4 Distance Configuration 4xr, Swirl Pattern TI

Figure 115(a) shows the H_2O mole fraction contours on the fuel inlet and upper combustor walls for the non-swirling baseline case for the distance configuration 4xr. The H_2O mole fraction contours shown in Figure 115(a) are similar to those shown for the single nozzle non-swirling baseline case shown in Figure 76(a). There are two distinct areas of high H_2O mole fraction zones on the upper combustor wall but there are three zones that are located on the fuel nozzle wall. The high H_2O mole fraction zone on the upper combustor wall increases prior to decreasing as swirl increases as seen in Figure 115(b). Unlike the single nozzle case the zones on the fuel nozzle wall do not rotate as swirl increases. The high H_2O mole fraction zones on the fuel nozzle wall increase in area and then transfer to the upper combustor wall prior to decreasing. The interaction of this swirl pattern indicates the production of H_2O on the fuel nozzle wall and combustor wall is greater than the single nozzle as swirl increases.

Figure 116 shows that the two fuel jets merge together by $x/d = 3$ regardless of swirl.

Temperature contours are shown in Figure 117 and indicate that the temperature decreases with increasing fuel jet swirl until the last case shown in Figure 117(f).

Turbulent kinetic energy is shown on the tunnel centerline (z = 0) in Figure 118 and on the right fuel injector centerline plane (z = 2r) in Figure 119. The flow through the tunnel is symmetrical for this swirl pattern. Therefore Figure 119 is the same for the right and left fuel jets. The high TKE zones on the tunnel centerline last longer as swirl increases than the high TKE zones on the fuel jet centerline. Figure 120 shows a progression of contour plots of TKE.

Table 11 shows the start location and length of the high TKE zone, the burning efficiency and the increase in burning efficiency due to swirl. The results show a similar trend as the 3xr-TI configuration. The only major difference is that the start location of the High TKE zone

plateaus at 0.60*d* downstream of the fuel injector exit despite increasing the swirl. The high TKE zone length increases with swirl, reaches a maximum of 8.59*d* and then decreases as more swirl is added to the fuel jet.

As with the other simulation cases increasing swirl increase the burning efficiency. Configuration 4xr-V50-TI resulted in an impressive 15.31% increase in burning efficiency compared to the case with no swirl.

Table 11 Mixing Data for Configuration 4xr-TI

	High Turbulent Kinetic Energy Zone			
Configuration	*Zone start location (x/d)*	*Zone Length (d)*	*Burning Efficiency, η_{burn}*	*$\Delta\ \eta_{burn}$ (%)*
4xr-V00	2.07	8.19	0.73	n/a
4xr-V10-TI	1.75	8.59	0.73	0.8
4xr-V20-TI	0.84	7.24	0.75	2.7
4xr-V30-TI	0.60	4.73	0.77	5.5
4xr-V40-TI	0.60	2.98	0.80	10.0
4xr-V50-TI	0.60	0.76	0.84	15.3

a)

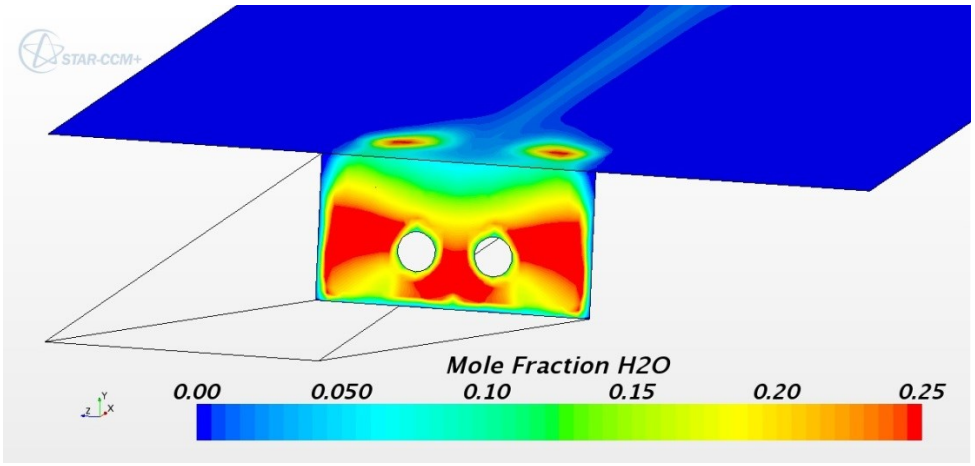

b)

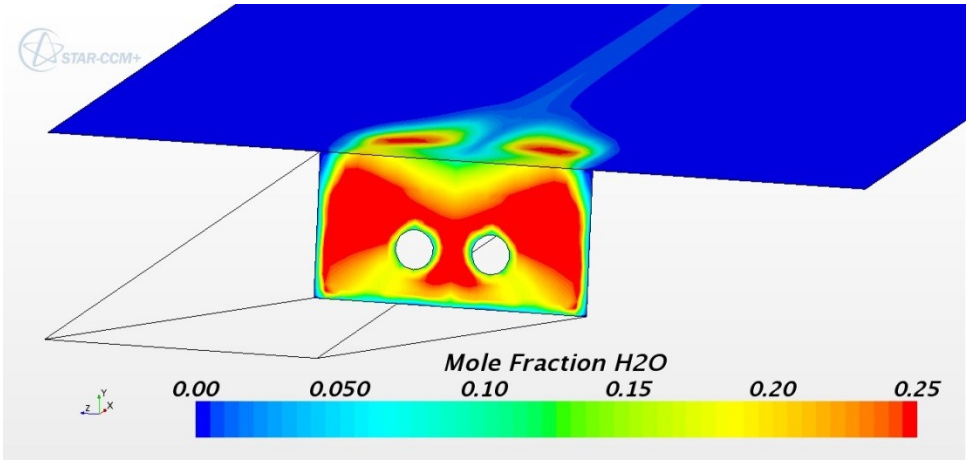

c)

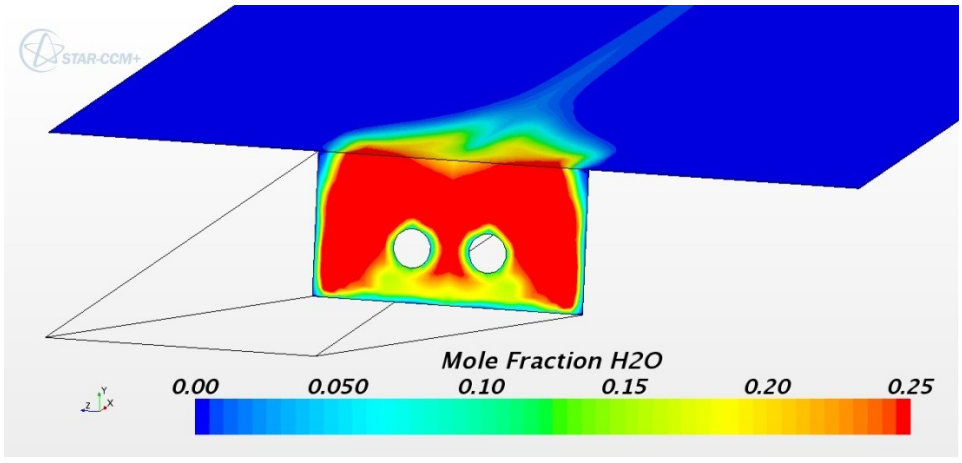

Figure 115 Mole fraction contours of H_2O on the fuel inlet wall and combustor upper wall for Configuration 4xr-TI
a) 4xr-V00, b) 4xr-V10-TI, c) 4xr-V20-TI

d)

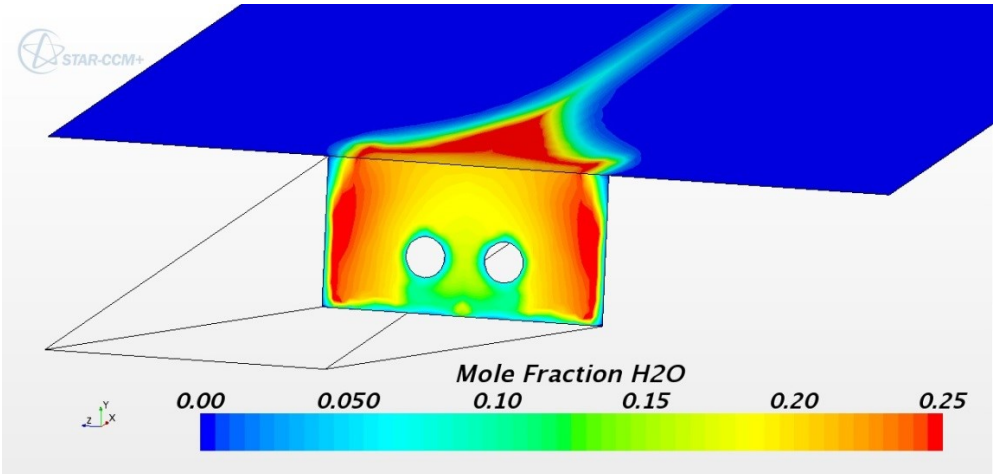

e)

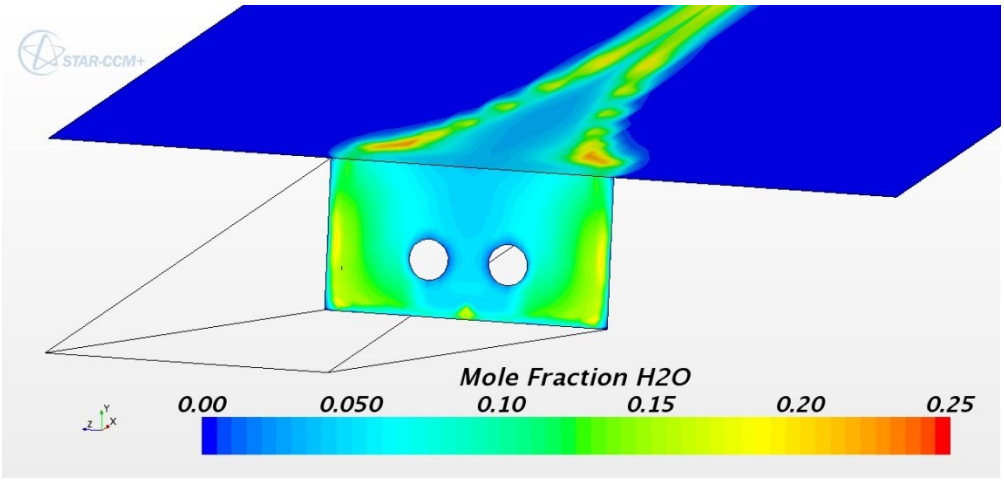

f)

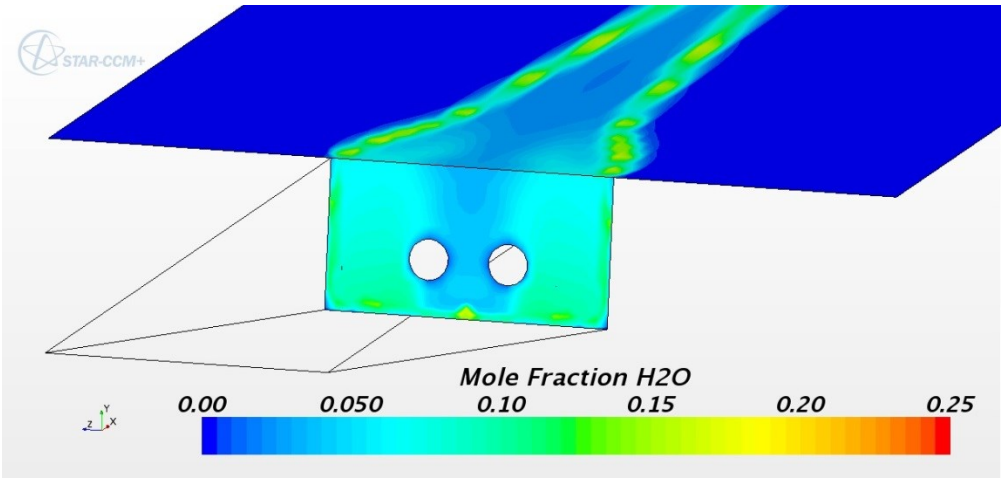

Figure 115 Mole fraction contours of H_2O on the fuel inlet wall and the combustor upper wall for Configuration 4xr-TI
d) 4xr-V30-TI, e) 4xr-V40-TI, f) 4xr-V50-TI

a)

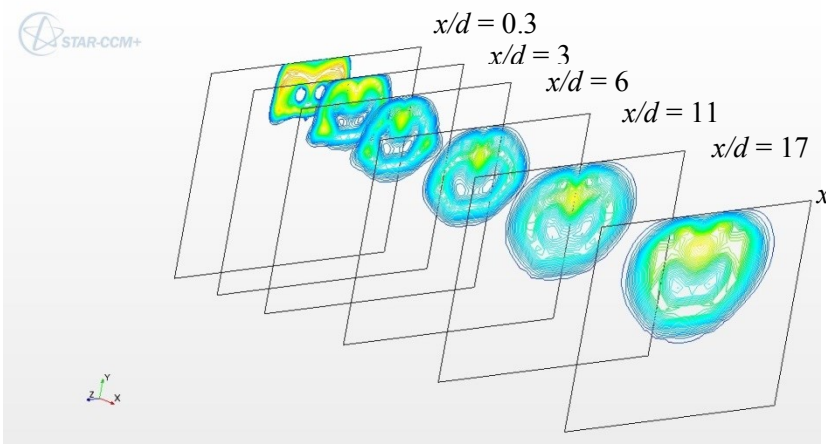

b)

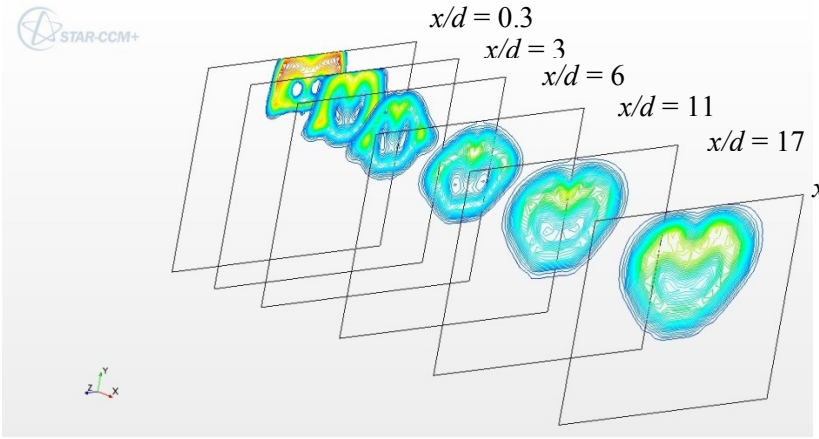

c)

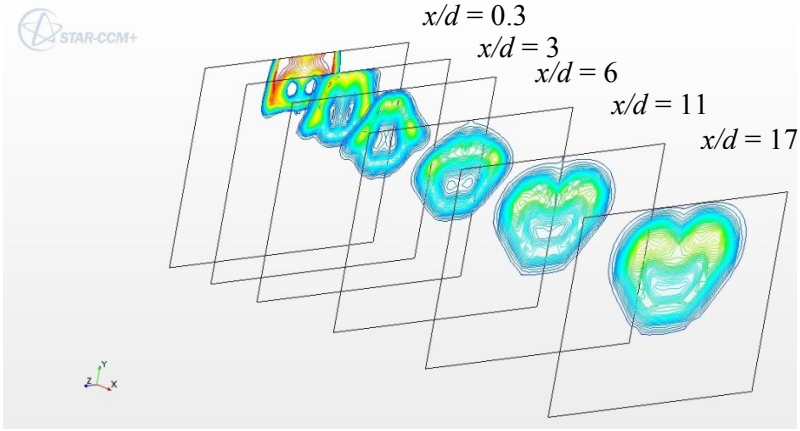

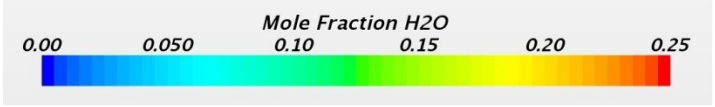

Figure 116 Mole fraction contours of H_2O in the combustor for Configuration 4xr-TI
a) 4xr-V00, b) 4xr-V10-TI, c) 4xr-V20-TI

d)

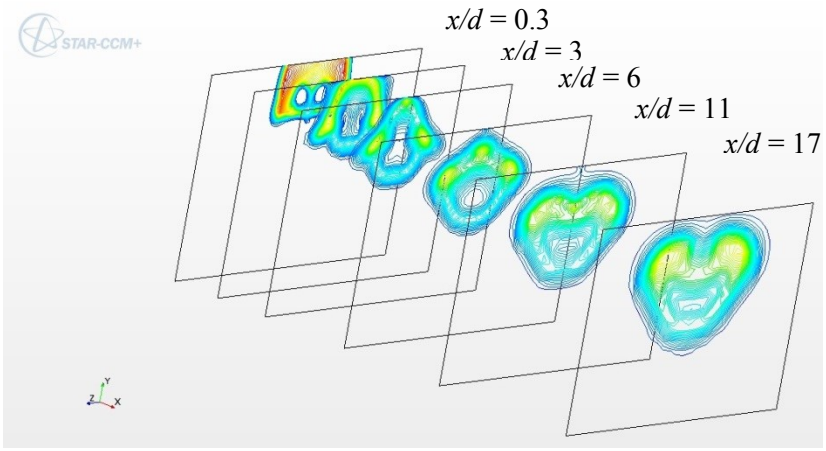

e)

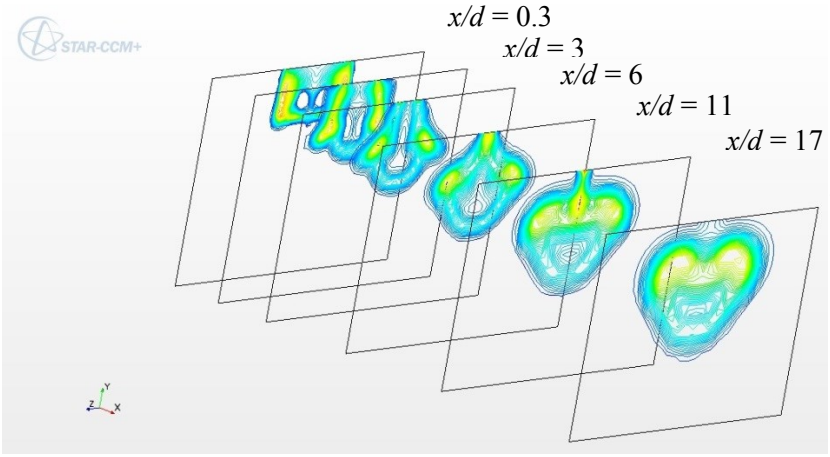

f)

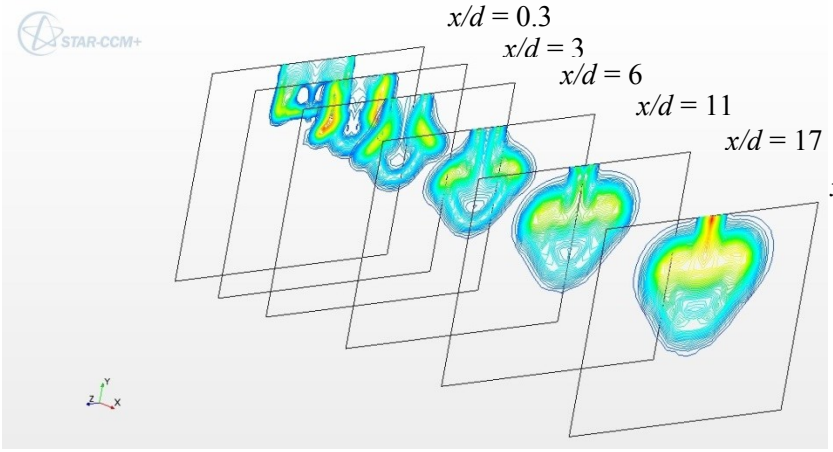

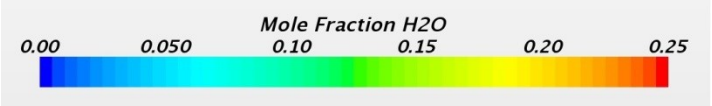

Figure 116 Mole fraction contours of H_2O in the combustor for Configuration 4xr-TI
d) 4xr-V30-TI, e) 4xr-V40-TI, f) 4xr-V50-TI

a)

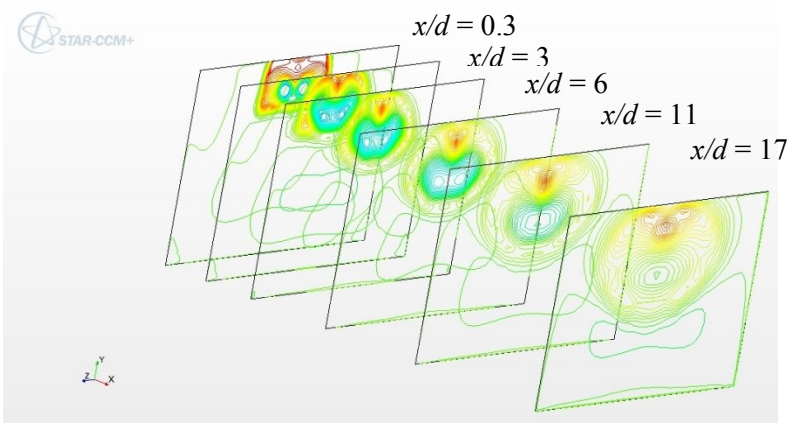

b)

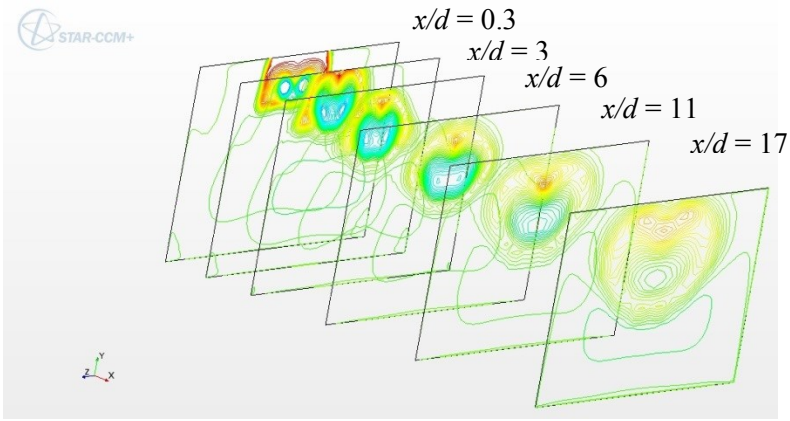

c)

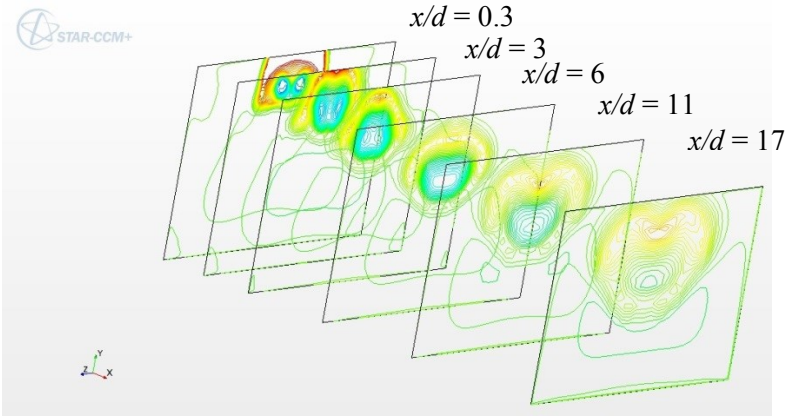

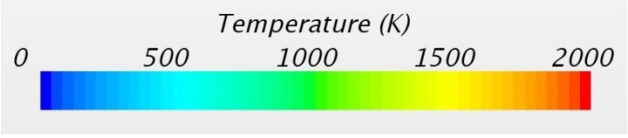

Figure 117 Temperature contours in the combustor for Configuration 4xr-TI
a) 4xr-V00, b) 4xr-V10-TI, c) 4xr-V20-TI

d)

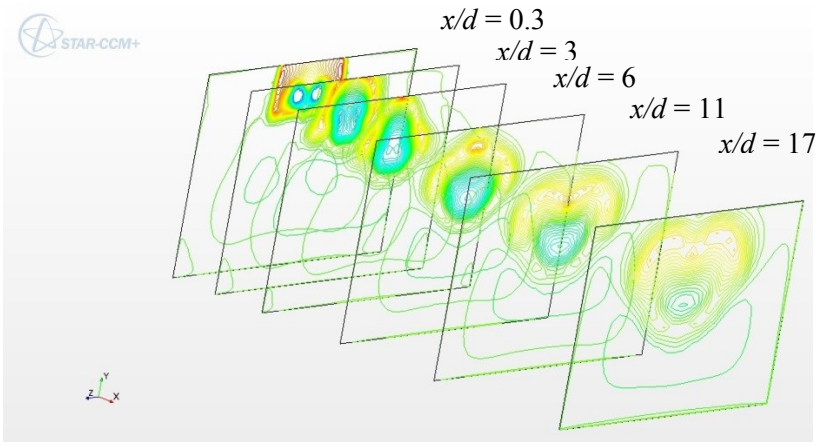

e)

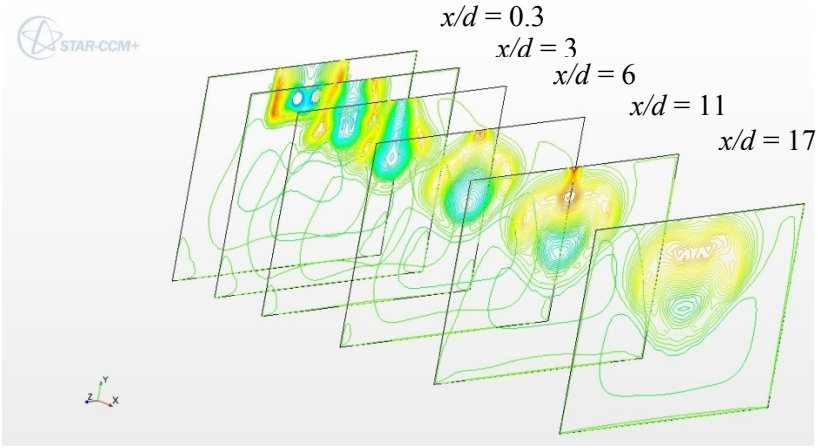

f)

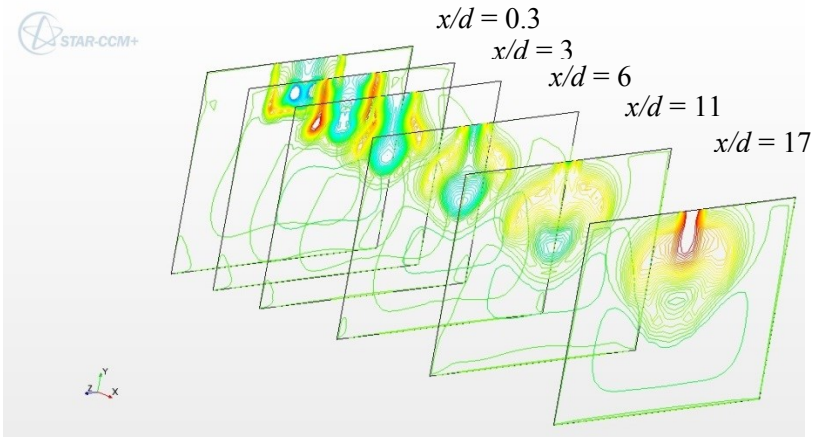

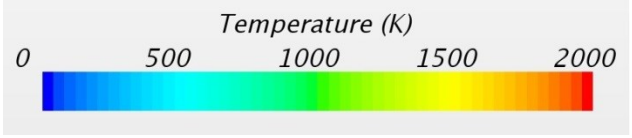

Figure 117 Temperature contours in the combustor for Configuration 4xr-TI
d) 4xr-V30-TI, e) 4xr-V40-TI, f) 4xr-V50-TI

(a)

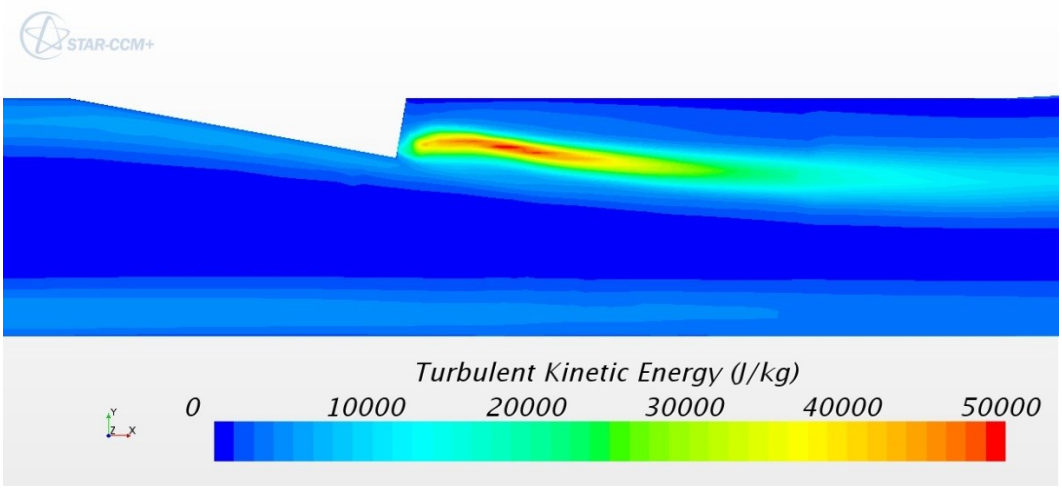

(b)

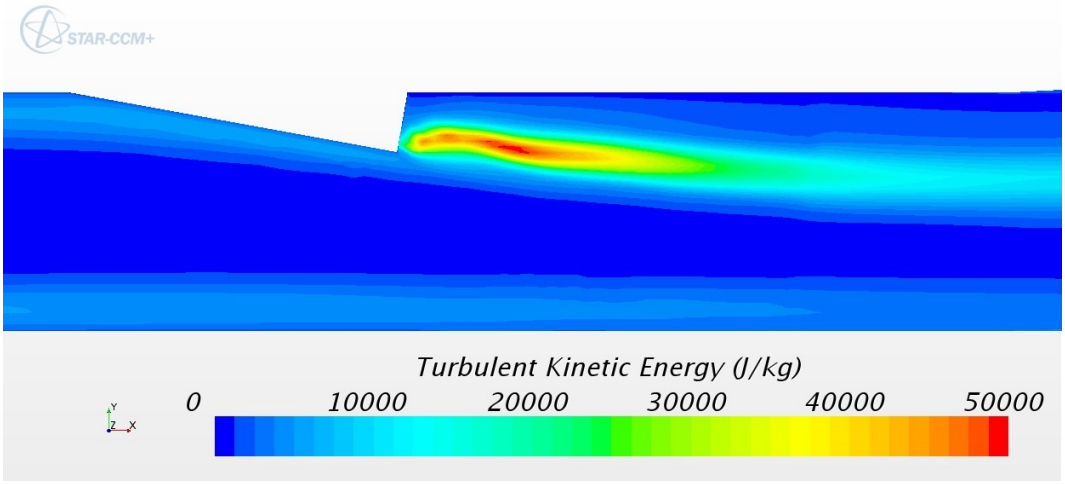

(c)

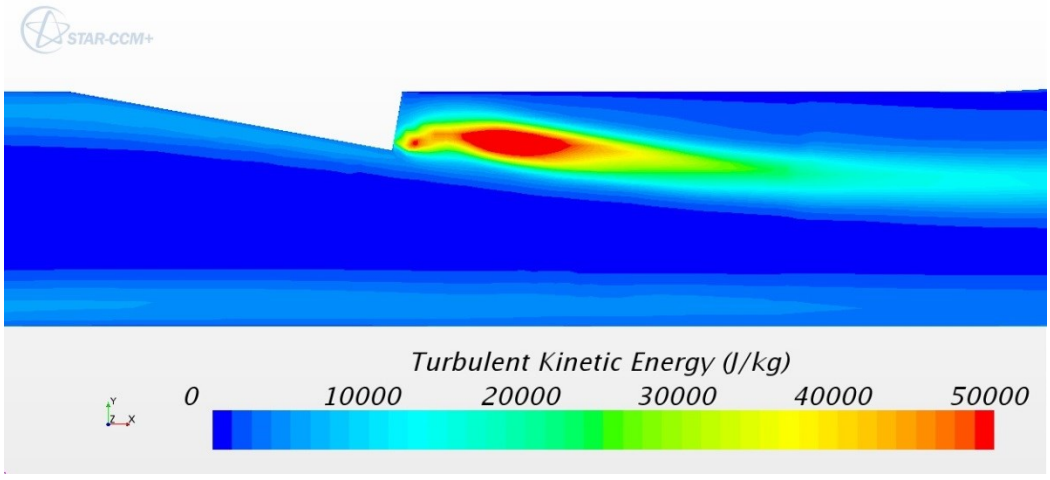

Figure 118 Turbulent kinetic energy plots on the centerline plane (z = 0) in the combustor for Configuration 4xr-TI
a) 4xr-V00, b) 4xr-V10-TI, c) 4xr-V20-TI

(d)

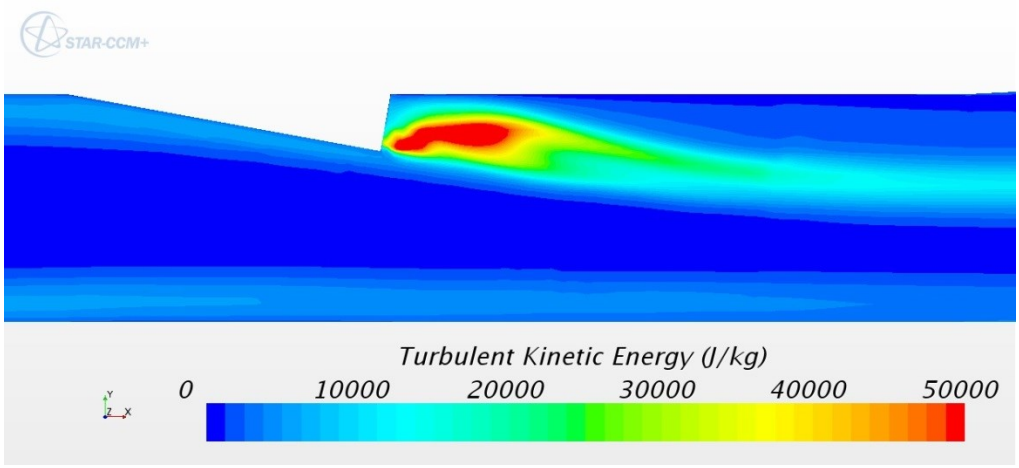

(e)

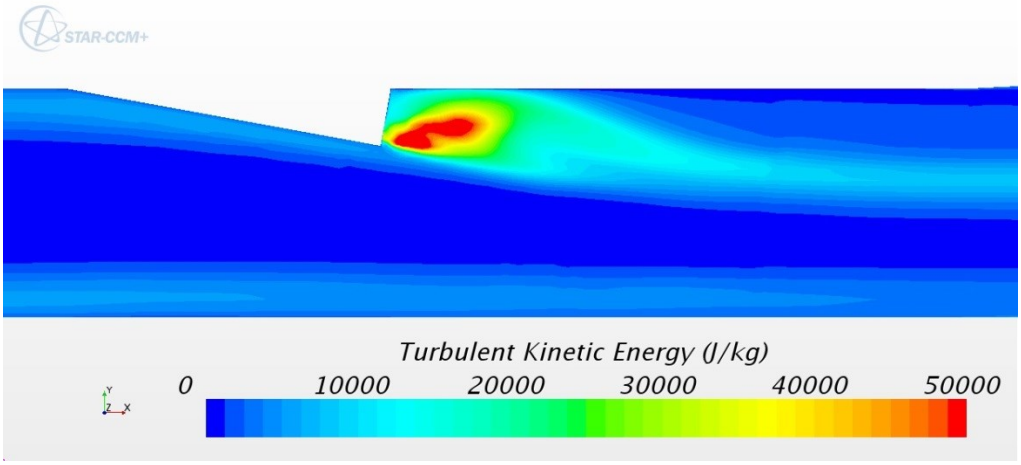

(f)

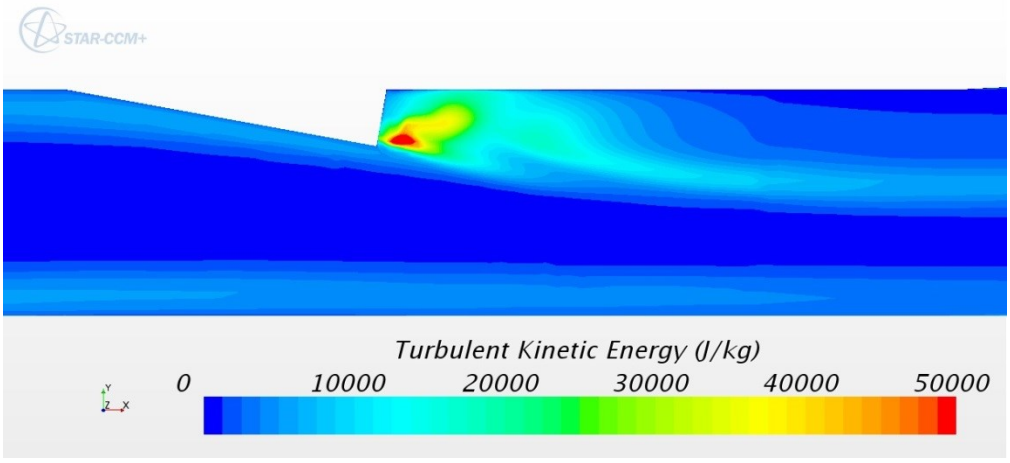

Figure 118 Turbulent kinetic energy plots on the centerline plane (z = 0) in the combustor for Configuration 4xr-TI
d) 4xr-V30-TI, e) 4xr-V40-TI, f) 4xr-V50-TI

(a)

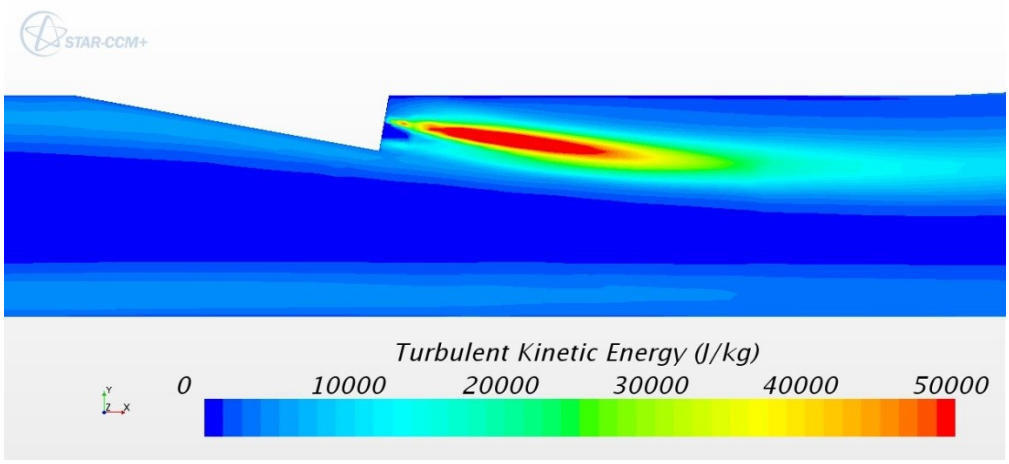

(b)

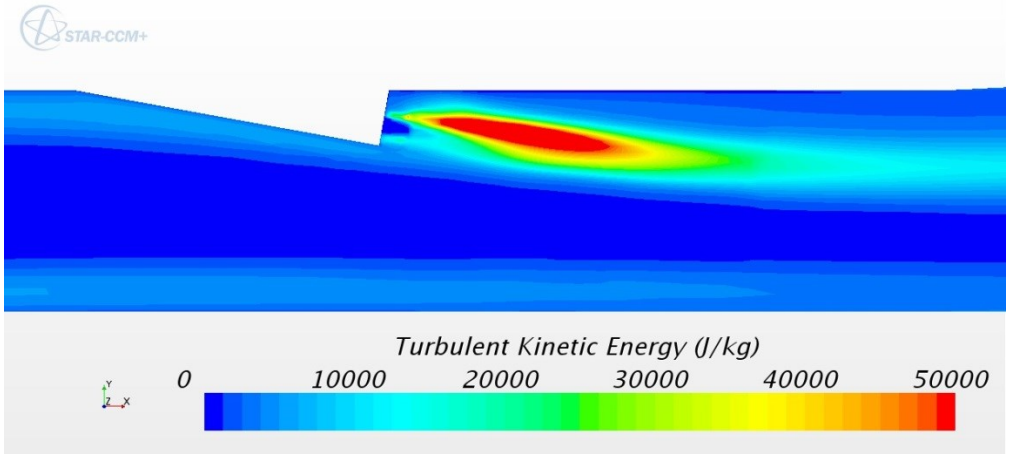

(c)

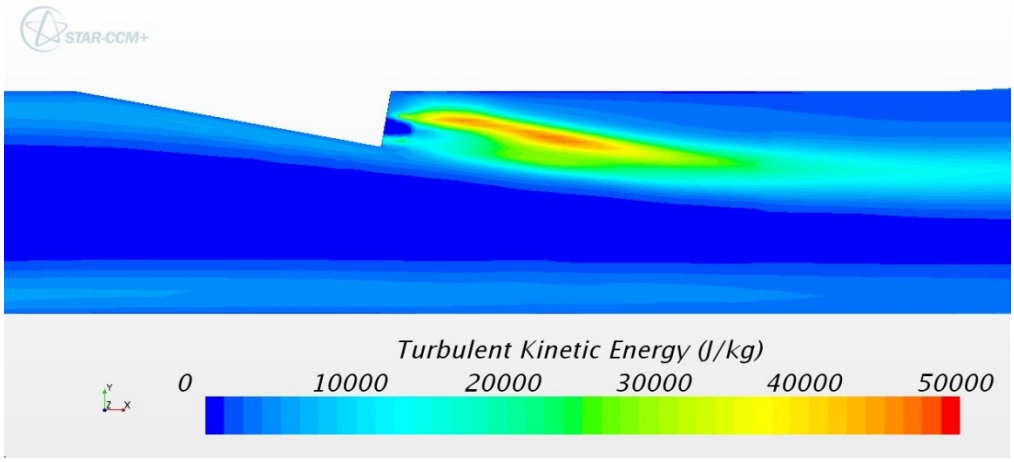

Figure 119 Turbulent kinetic energy plots on the fuel nozzle centerline plane (z = 2r) in the combustor for Configuration 4xr-TI
a) 4xr-V00, b) 4xr-V10-TI, c) 4xr-V20-TI

(d)

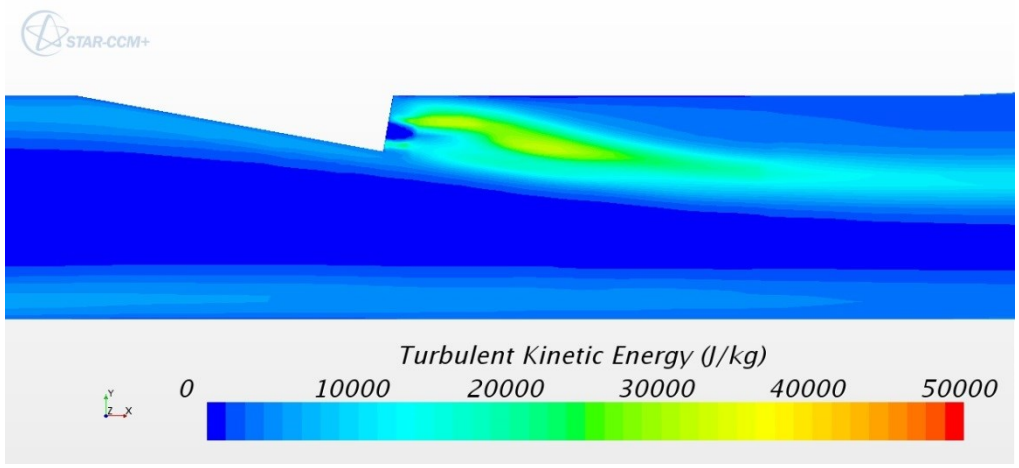

(e)

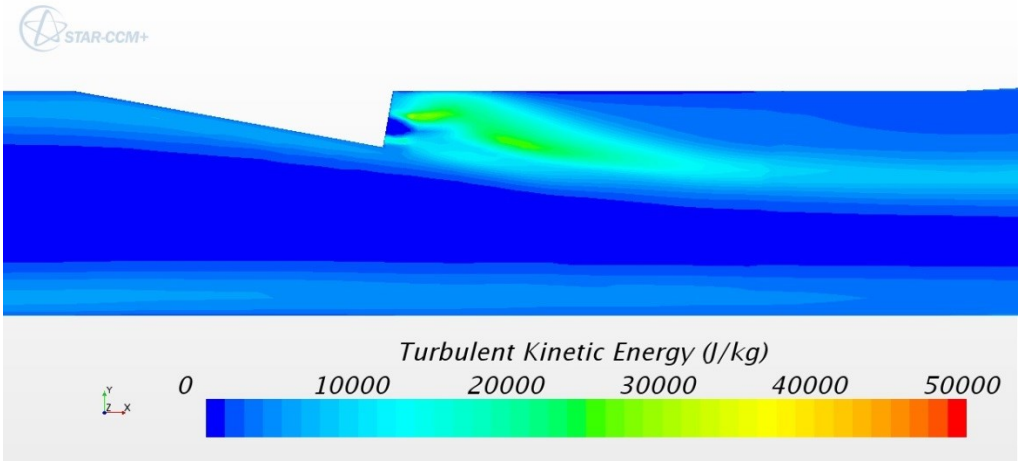

(f)

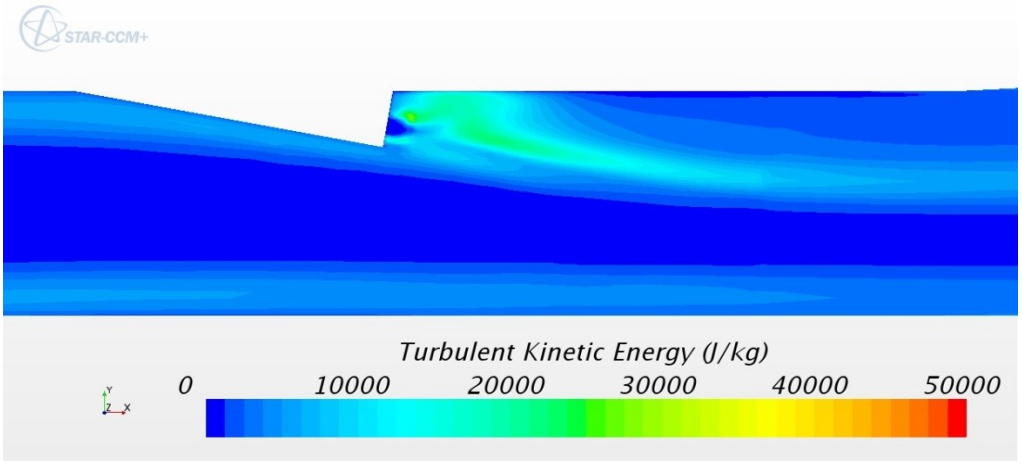

Figure 119 Turbulent kinetic energy plots on the fuel nozzle centerline plane (z = 2r) in the combustor for Configuration 4xr-TI
d) 4xr-V30-TI, e) 4xr-V40-TI, f) 4xr-V50-TI

a)

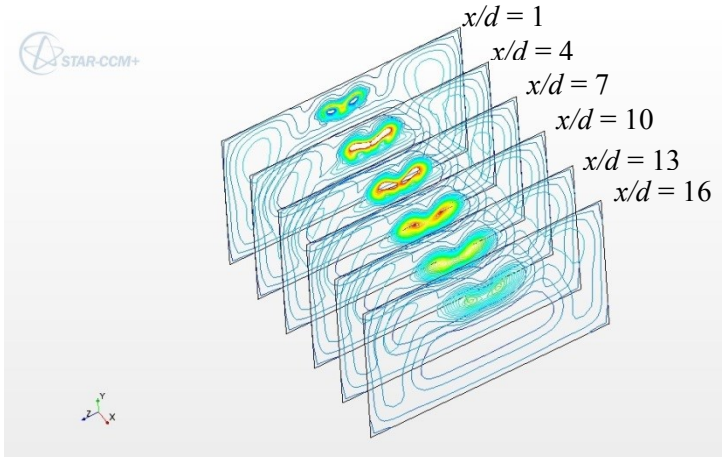

b)

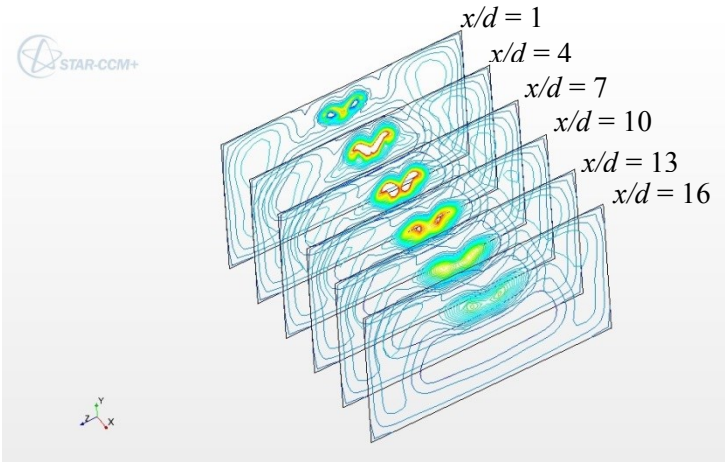

c)

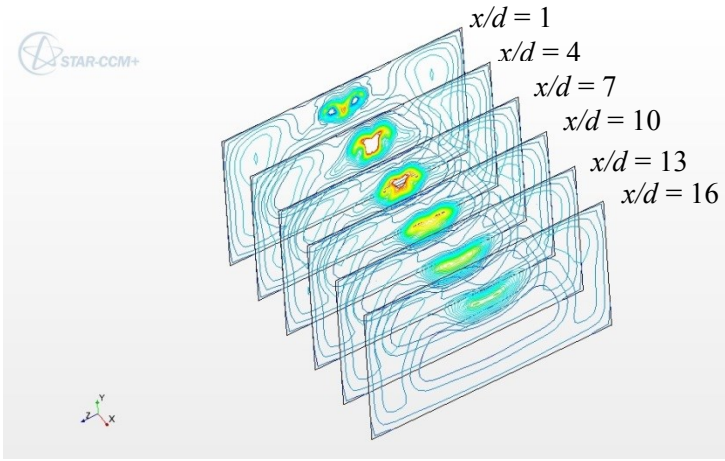

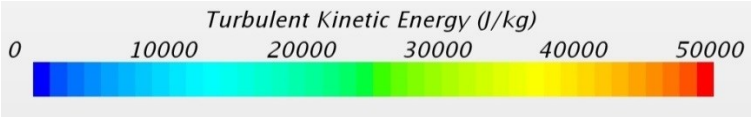

Figure 120 Turbulent kinetic energy contours in the combustor for Configuration 4xr-TI
a) 4xr-V00, b) 4xr-V10-TI, c) 4xr-V20-TI

d)

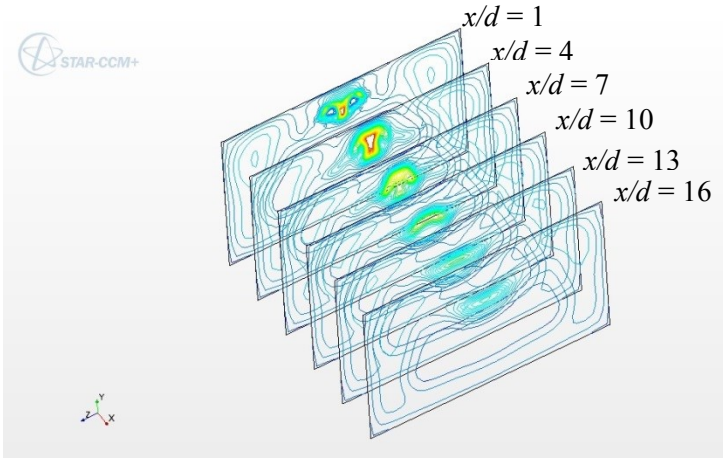

e)

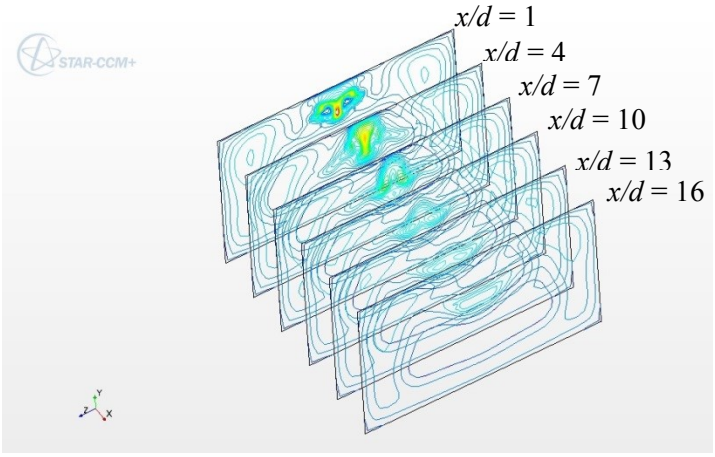

f)

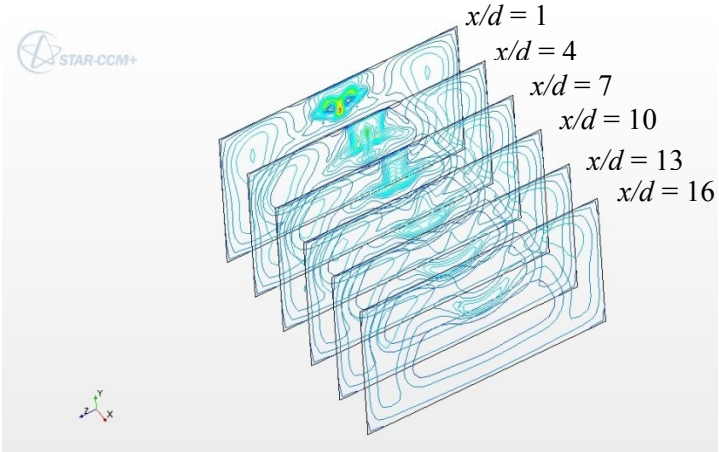

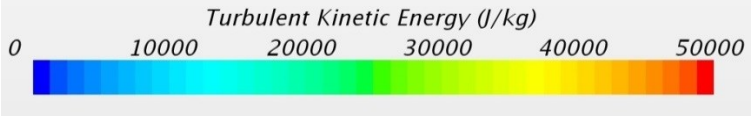

Figure 120 Turbulent kinetic energy contours in the combustor for Configuration 4xr-TI
d) 4xr-V30-TI, e) 4xr-V40-TI, f) 4xr-V50-TI

6.3.5 Distance Configuration 4xr, Swirl Pattern TO

Figure 121(a) shows the H_2O mole fraction contours on the fuel inlet and upper combustor walls for the non-swirling baseline case for the distance configuration 4xr. The high H_2O mole fraction zones on the upper combustor wall are eliminated and the H_2O mole fraction zones on the fuel nozzle wall increase in area but do not rotate as swirl increases. The interaction of this swirl pattern produces similar results as the single fuel jet R6 Configuration.

Contour plots showing the progression of the H_2O mole fraction in the combustor are shown in Figure 122. The H_2 jets combine in shorter distance with lower swirl intensity. This is also seen in the temperature contours shown in Figure 123 where the H_2 jets have a lower temperature than the surrounding flow.

Turbulent kinetic energy is shown on the tunnel centerline (z = 0) in Figure 124 and on the right fuel injector centerline plane (z = 1.5r) in Figure 125. The flow through the tunnel is symmetrical for this swirl pattern. Therefore Figure 125 is the same for the right and left fuel jets. The high TKE zones on the tunnel centerline and the fuel jet centerline decrease with increasing fuel jet swirl. Two high TKE zones can be seen in Figure 125(a), (b) and (c). Figure 126 shows a progression of contour plots of TKE.

Table 12 shows the start location and length of the high TKE zone, the burning efficiency and the increase in burning efficiency due to swirl. The results show a similar trend as the 3xr-TO configuration. One major difference is that the start location of the high TKE zone plateaus at 0.32*d* downstream of the fuel injector exit then the high TKE zone is eliminated. The high TKE zone length increases with swirl, reaches a maximum of 8.83*d* and then decreases as more swirl is added to the fuel jet.

As with the other simulation cases increasing swirl increase the burning efficiency. Configuration 4xr-V50-TO resulted in an impressive 22.5% increase in burning efficiency compared to the case with no swirl.

Table 12 Mixing Data for Configuration 4xr-TO

	High Turbulent Kinetic Energy Zone			
Configuration	*Zone start location (x/d)*	*Zone Length (d)*	*Burning Efficiency,* η_{burn}	$\Delta\ \eta_{burn}$ *(%)*
4xr-V00	2.07	8.19	0.73	n/a
4xr-V10-TO	1.03	8.83	0.75	3.3
4xr-V20-TO	0.48	8.00	0.78	7.3
4xr-V30-TO	0.32	5.61	0.82	127
4xr-V40-TO	0.32	3.82	0.85	17.2
4xr-V50-TO	n/a	0.00	0.89	22.5

a)

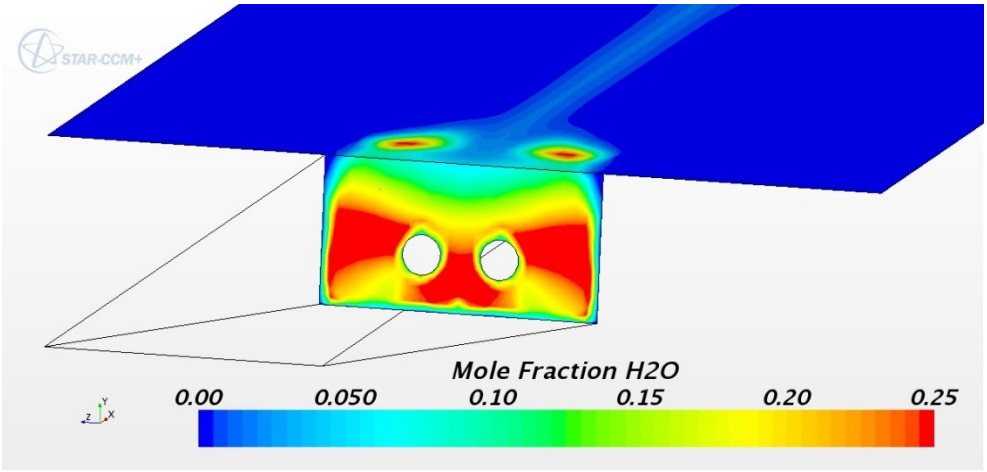

b)

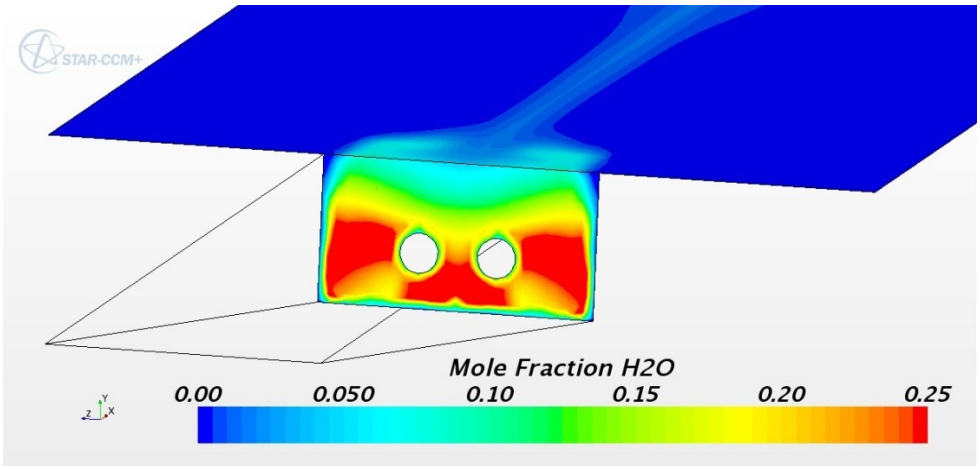

c)

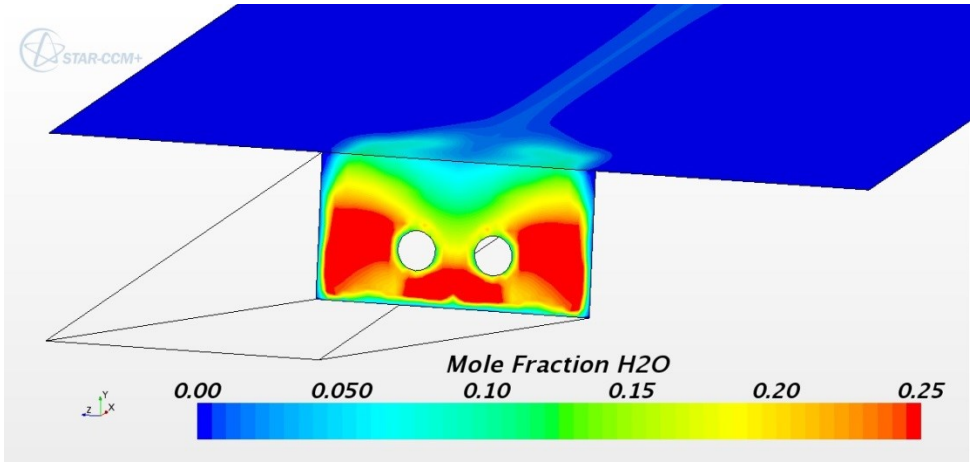

Figure 121 Mole fraction contours of H_2O on the fuel inlet wall and combustor upper wall for Configuration 4xr-TO
a) 4xr-V00, b) 4xr-V10-TO, c) 4xr-V20-TO

d)

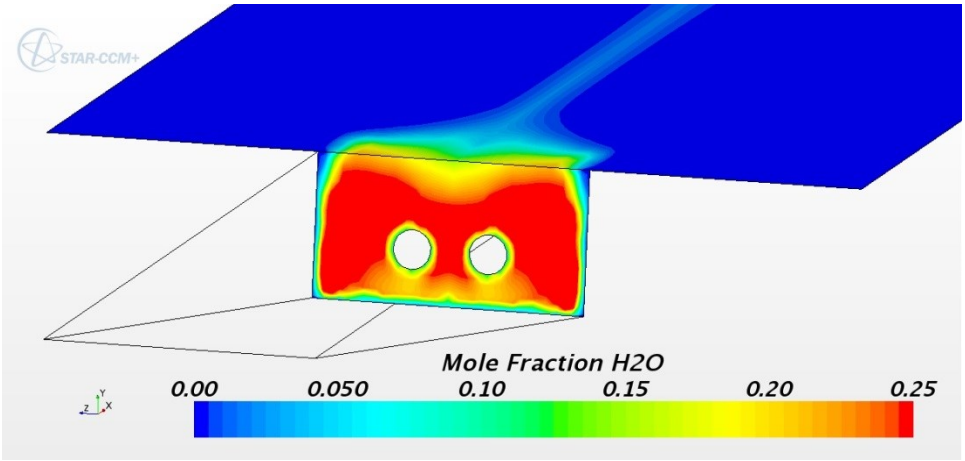

e)

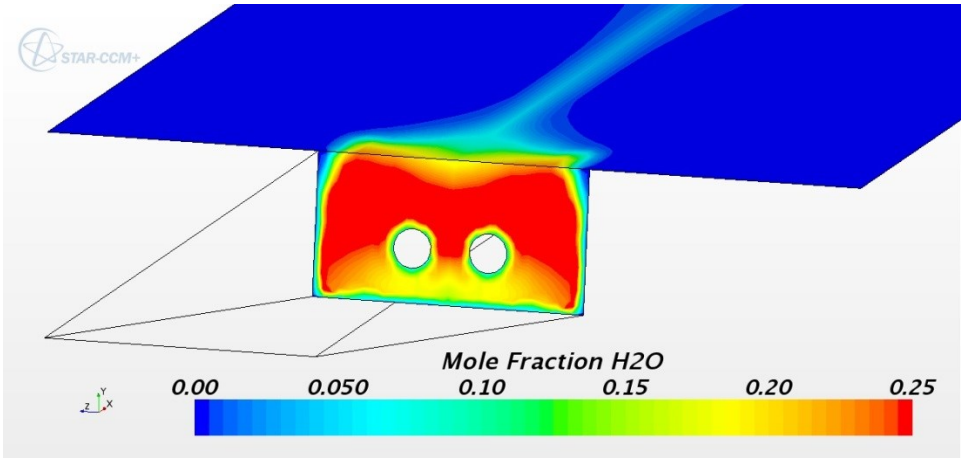

f)

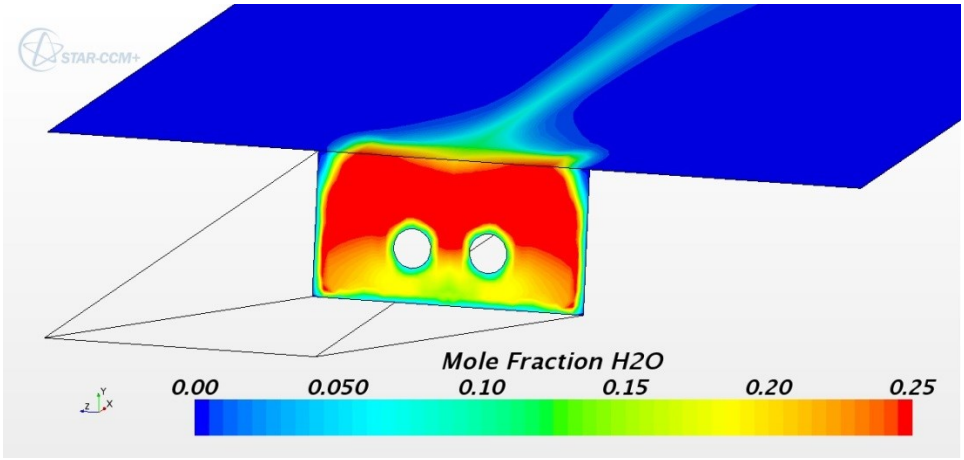

Figure 121 Mole fraction contours of H_2O on the fuel inlet wall and the combustor upper wall for Configuration 4xr-TO
d) 4xr-V30-TO, e) 4xr-V40-TO, f) 4xr-V50-TO

a)

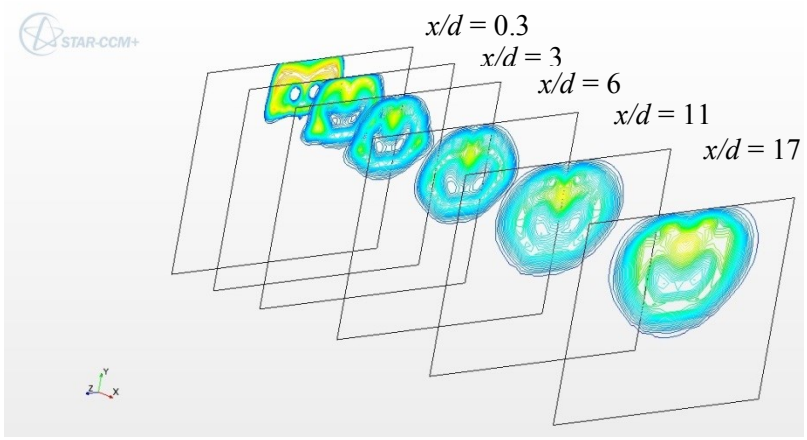

b)

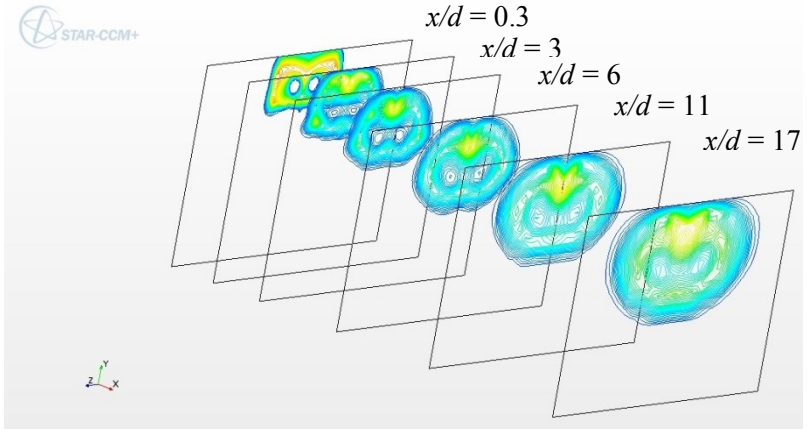

c)

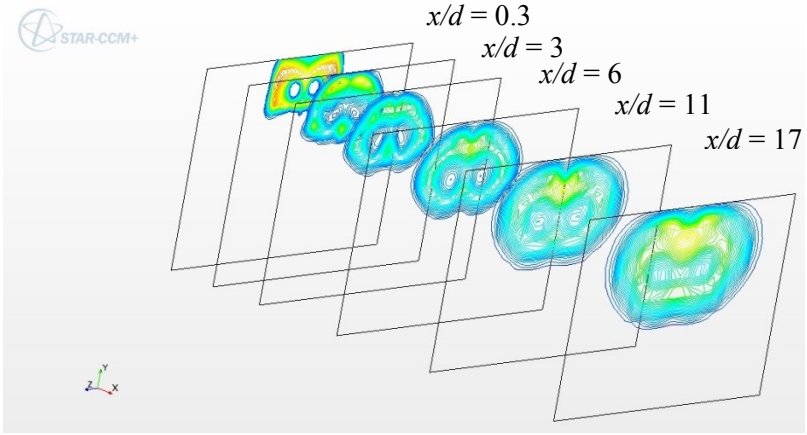

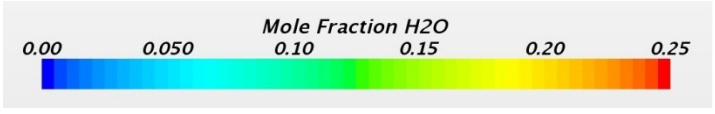

Figure 122 Mole fraction contours of H_2O in the combustor for Configuration 4xr-TO
a) 4xr-V00, b) 4xr-V10-TO, c) 4xr-V20-TO

d)

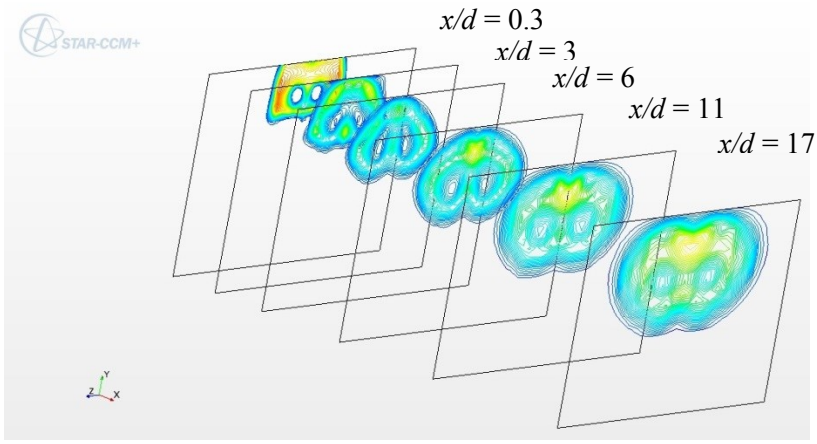

e)

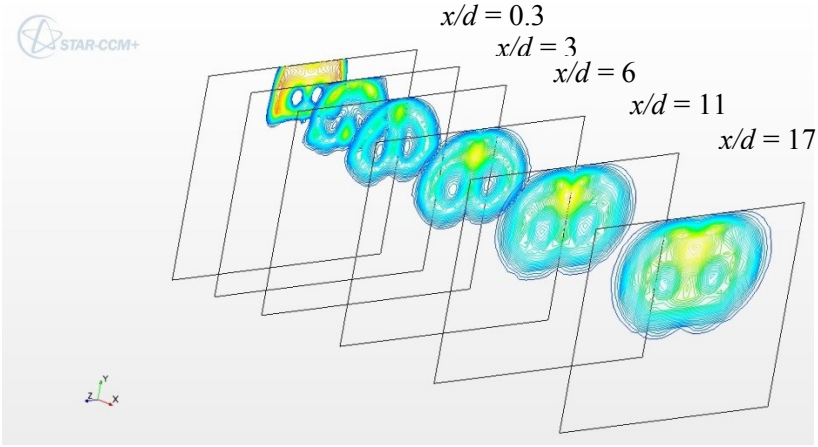

f)

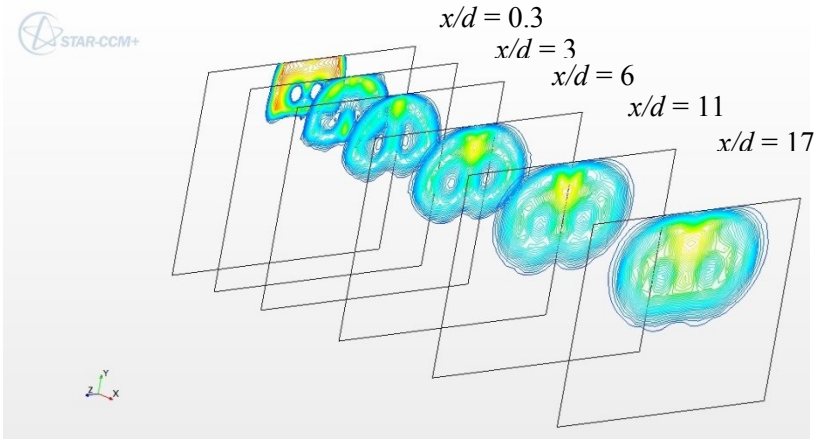

Figure 122 Mole fraction contours of H_2O in the combustor for Configuration 4xr-TO
d) 4xr-V30-TO, e) 4xr-V40-TO, f) 4xr-V50-TO

a)

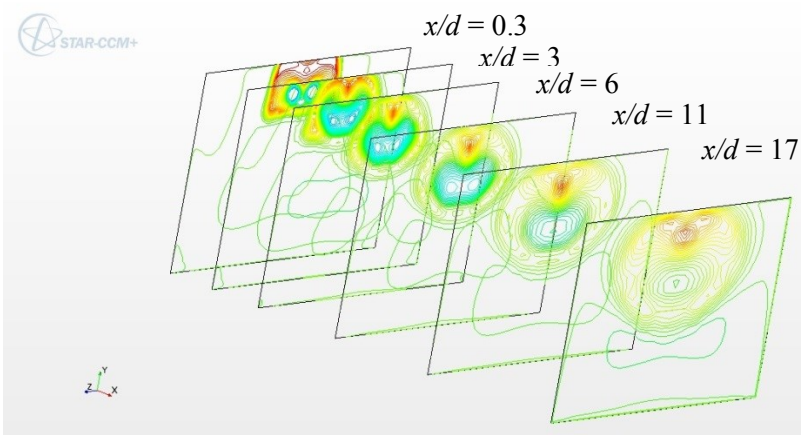

b)

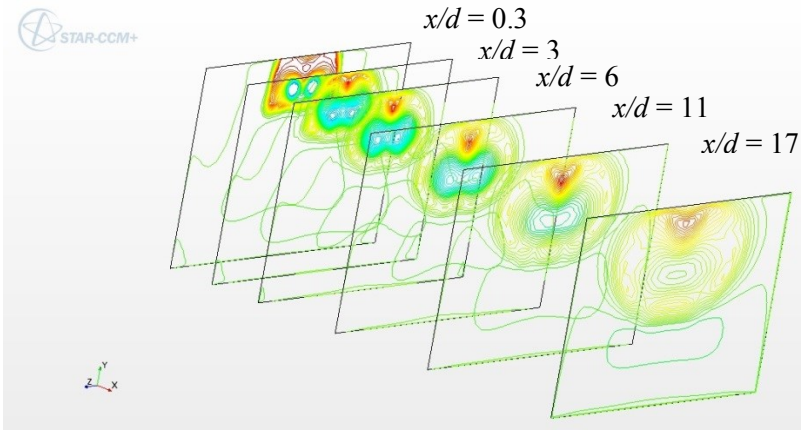

c)

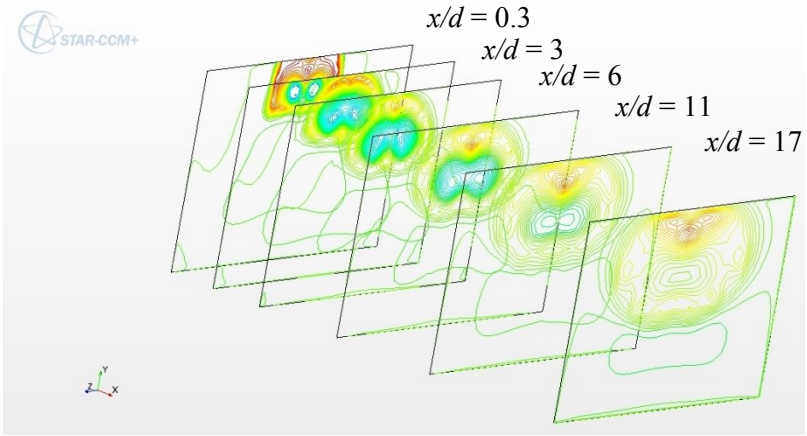

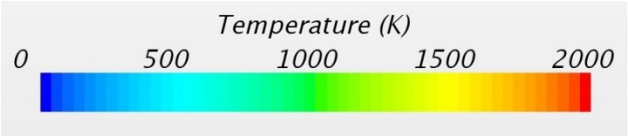

Figure 123 Temperature contours in the combustor for Configuration 4xr-TO
a) 4xr-V00, b) 4xr-V10-TO, c) 4xr-V20-TO

d)

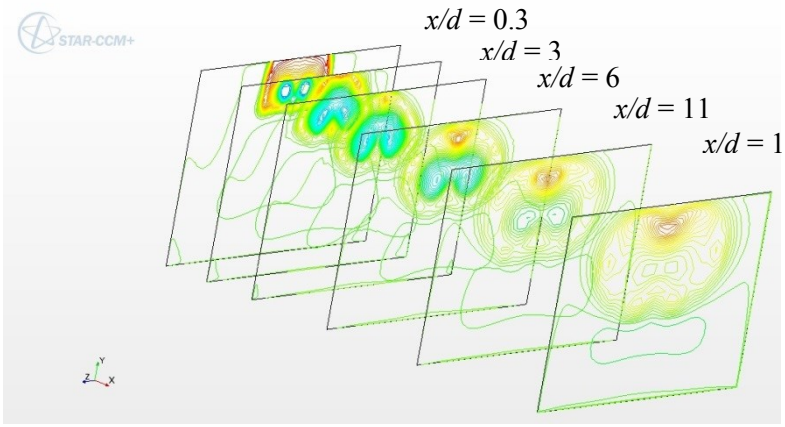

e)

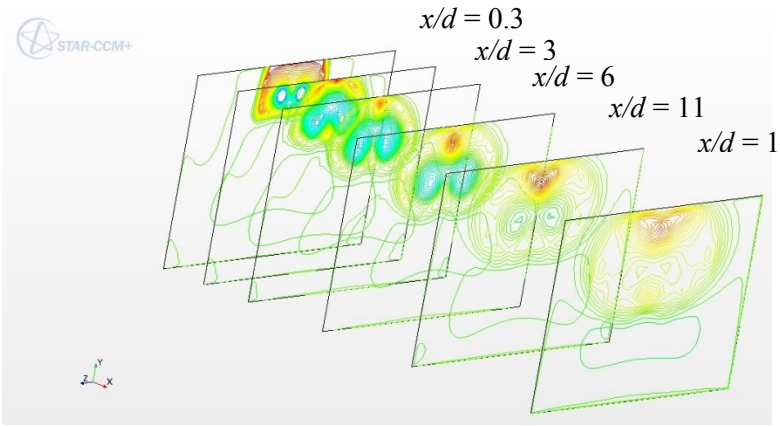

f)

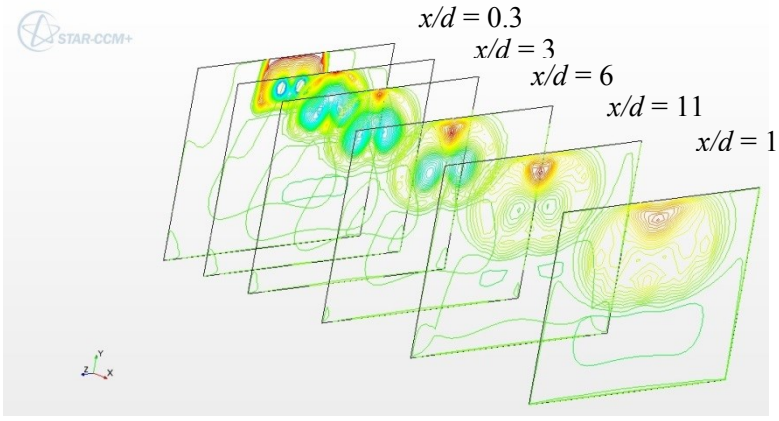

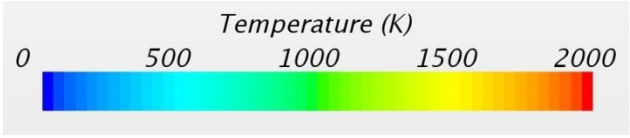

Figure 123 Temperature contours in the combustor for Configuration 4xr-TO
d) 4xr-V30-TO, e) 4xr-V40-TO, f) 4xr-V50-TO

(a)

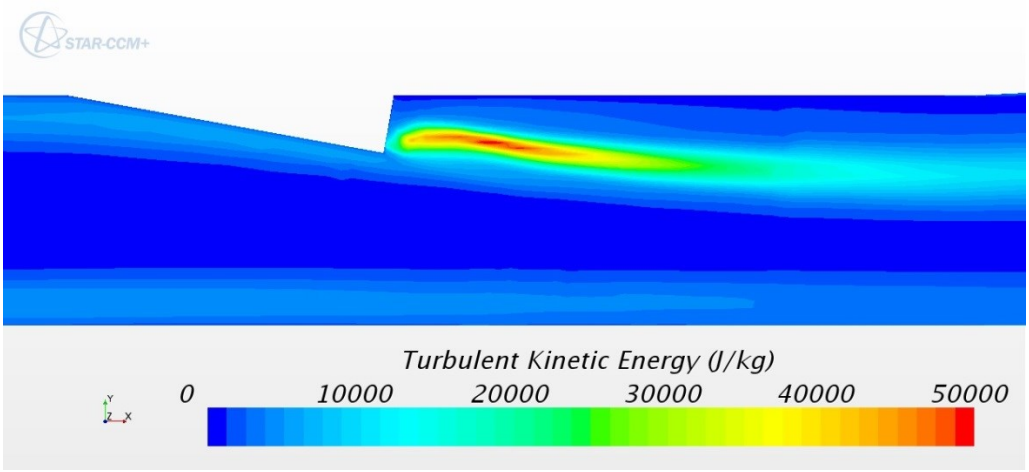

(b)

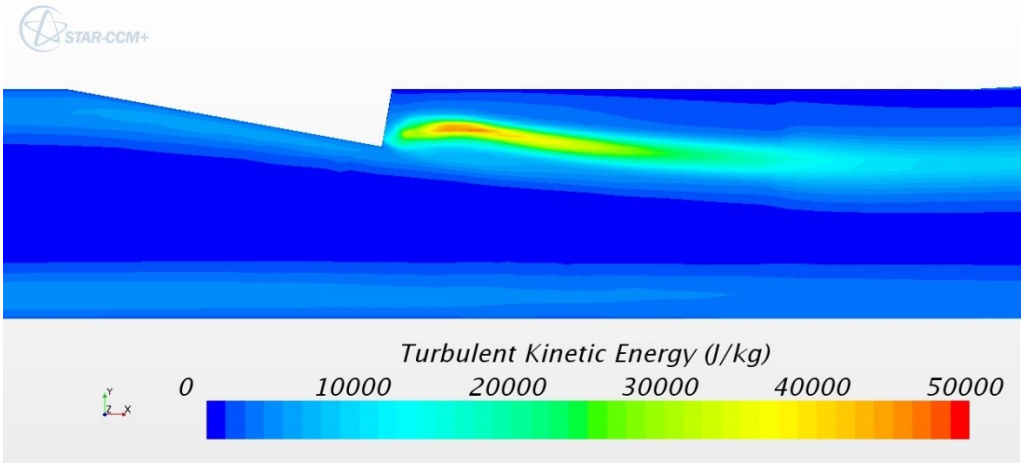

(c)

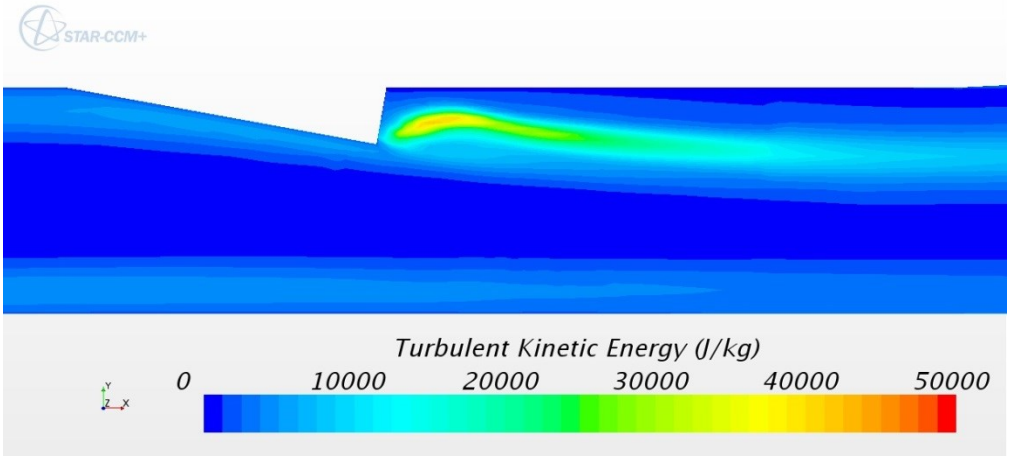

Figure 124 Turbulent kinetic energy plots on the centerline plane (z = 0) in the combustor for Configuration 4xr-TO
a) 4xr-V00, b) 4xr-V10-TO, c) 4xr-V20-TO

(d)

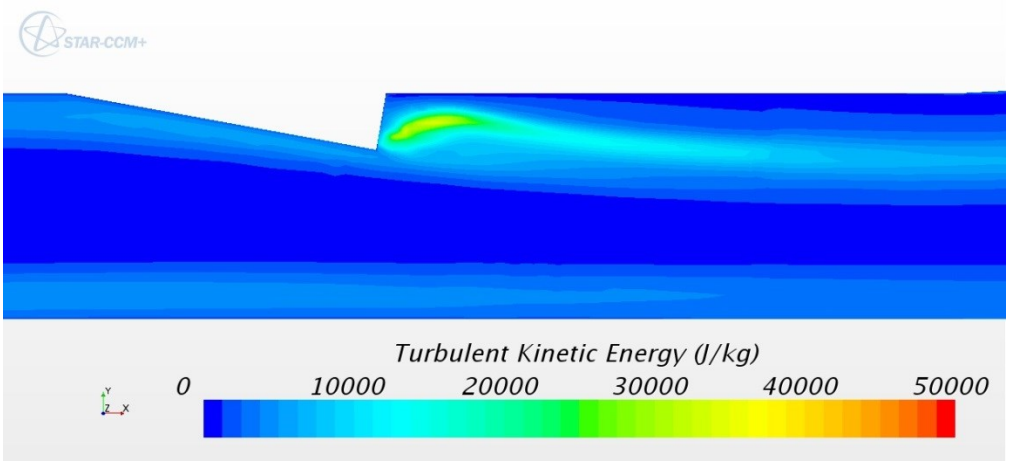

(e)

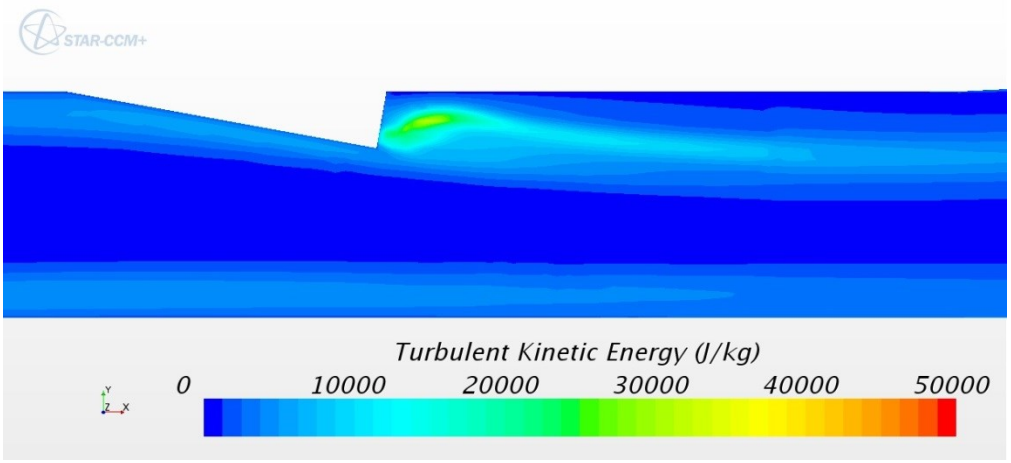

(f)

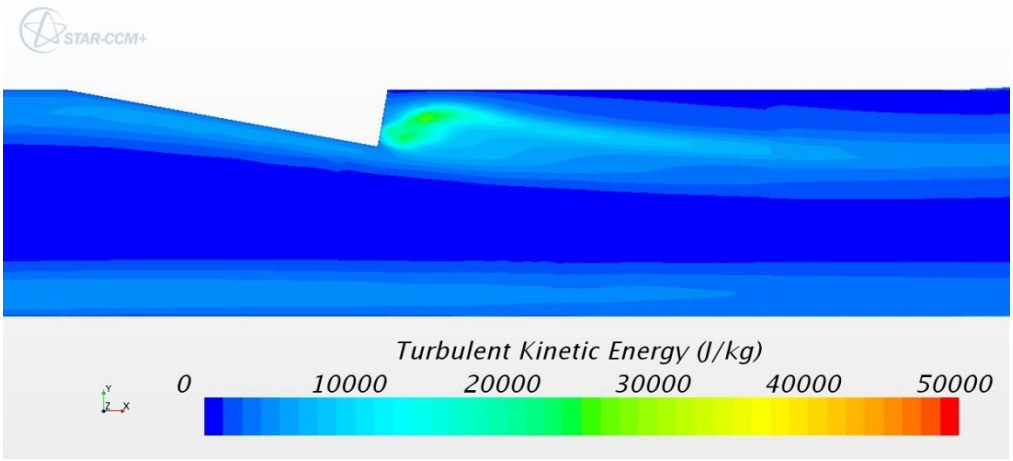

Figure 124 Turbulent kinetic energy plots on the centerline plane (z = 0) in the combustor for Configuration 4xr-TO
d) 4xr-V30-TO, e) 4xr-V40-TO, f) 4xr-V50-TO

(a)

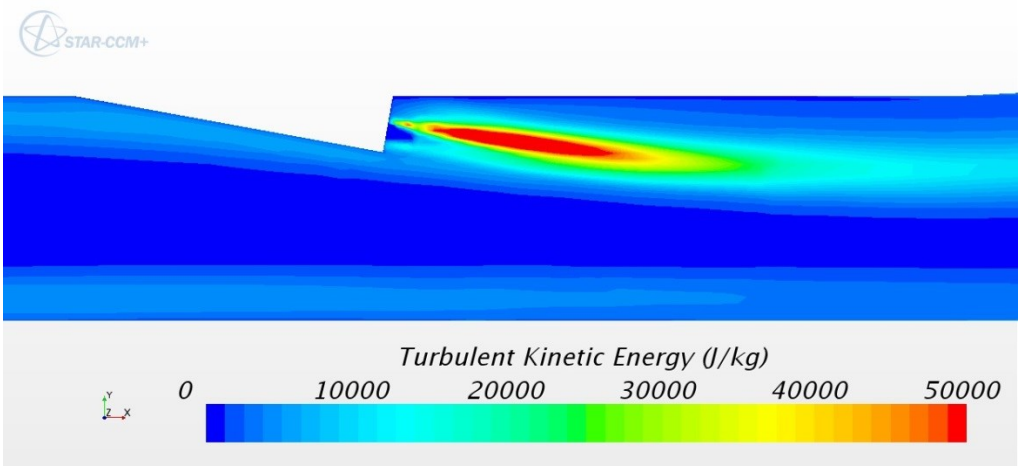

(b)

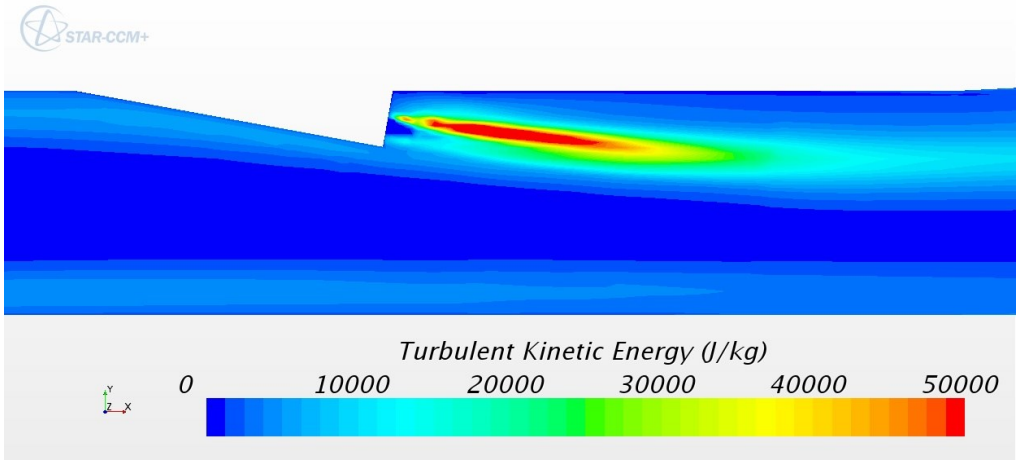

(c)

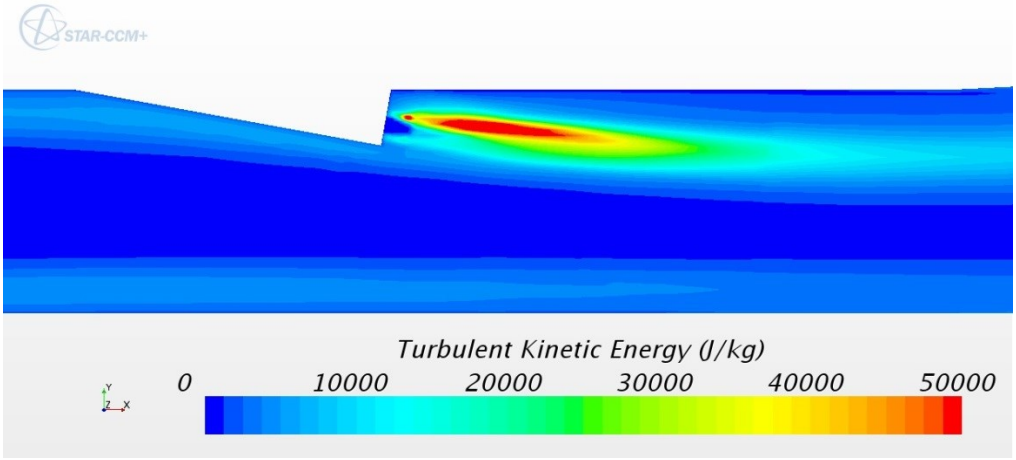

Figure 125 Turbulent kinetic energy plots on the fuel nozzle centerline plane (z = 2r) in the combustor for Configuration 4xr-TO
a) 4xr-V00, b) 4xr-V10-TO c) 4xr-V20-TO

(d)

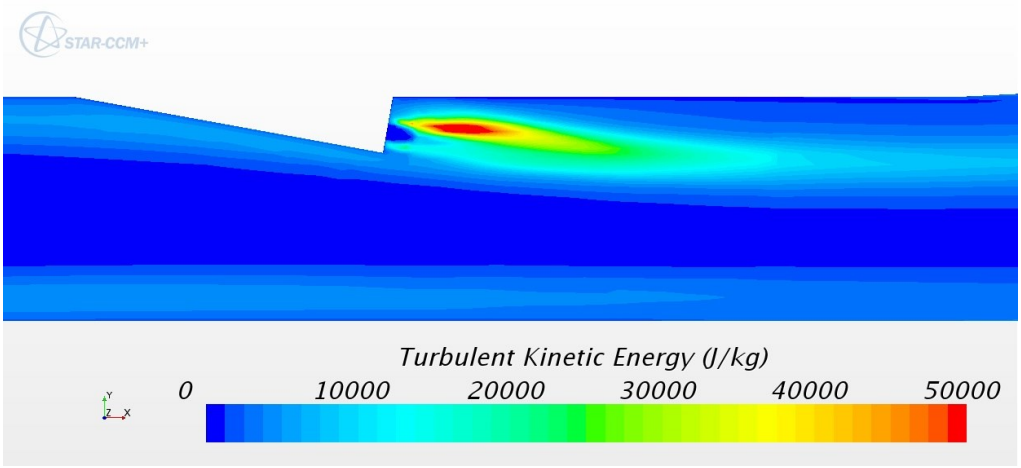

(e)

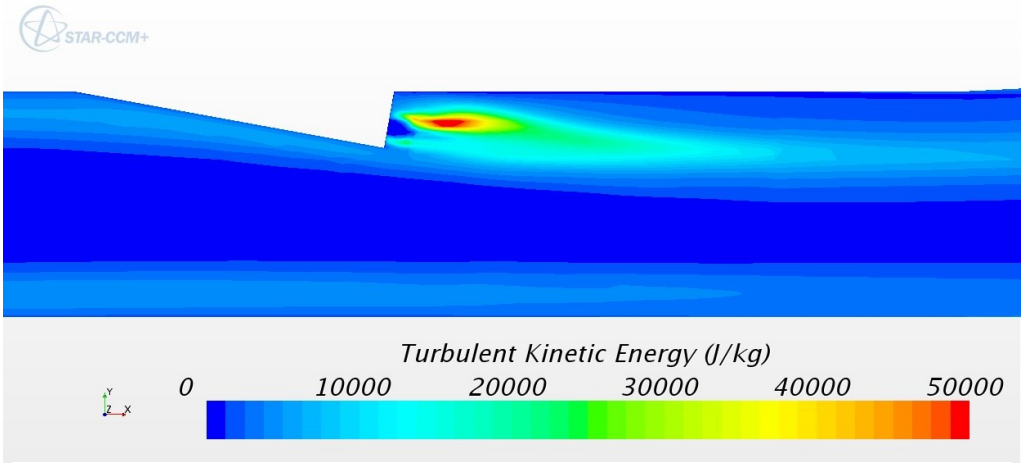

(f)

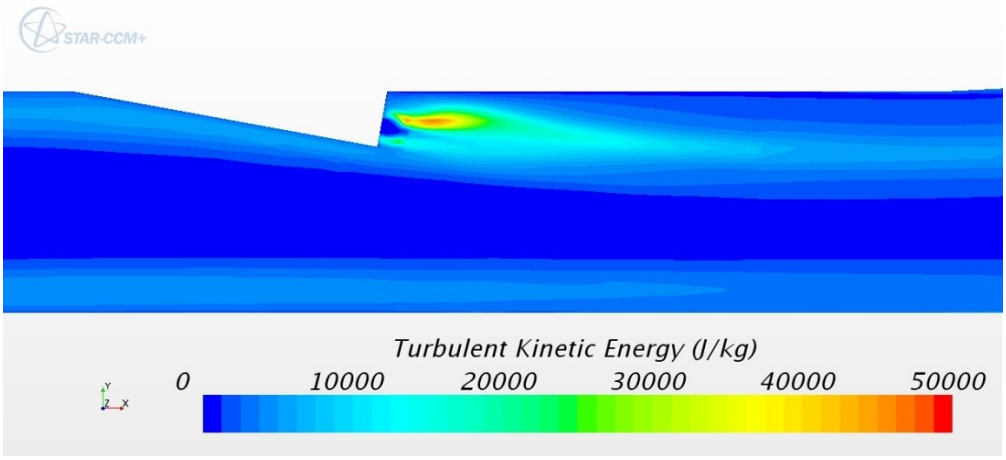

Figure 125 Turbulent kinetic energy plots on the fuel nozzle centerline plane (z = 2r) in the combustor for Configuration 4xr-TO
d) 4xr-V30-TO, e) 4xr-V40-TO, f) 4xr-V50-TO

a)

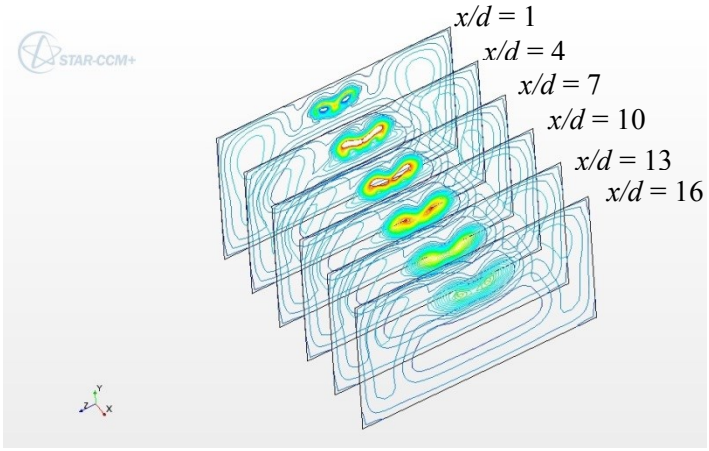

b)

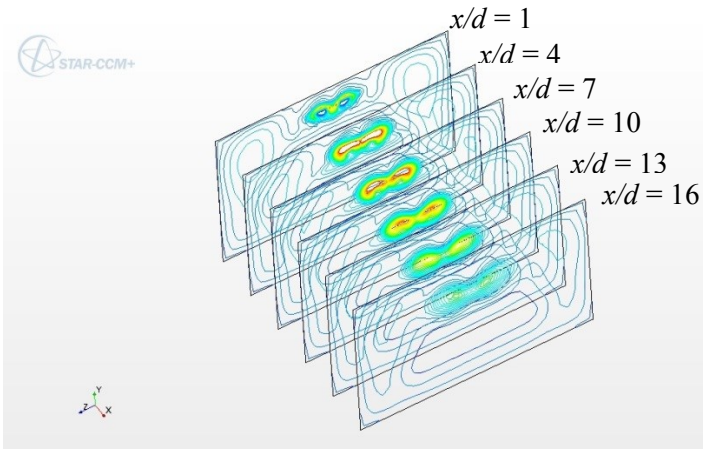

c)

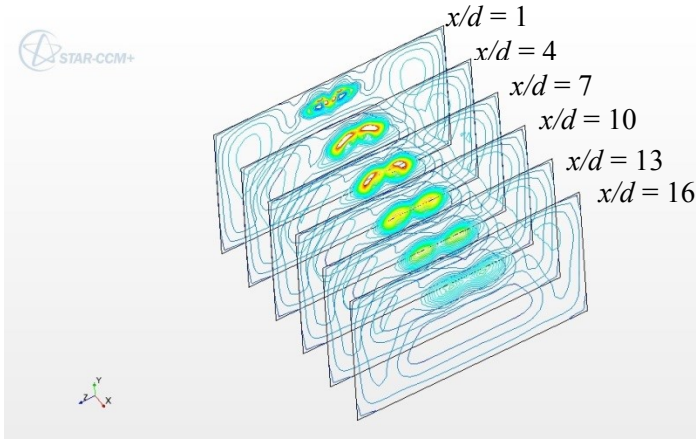

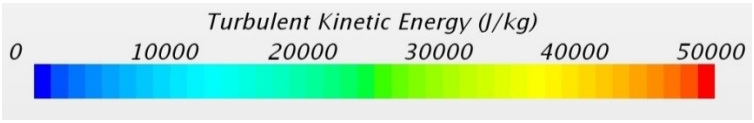

Figure 126 Turbulent kinetic energy contours in the combustor for Configuration 4xr-TO
a) 4xr-V00, b) 4xr-V10-TO, c) 4xr-V20-TO

d)

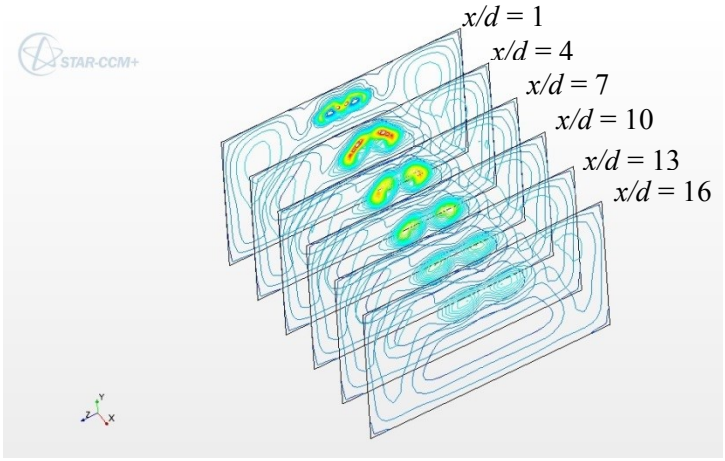

e)

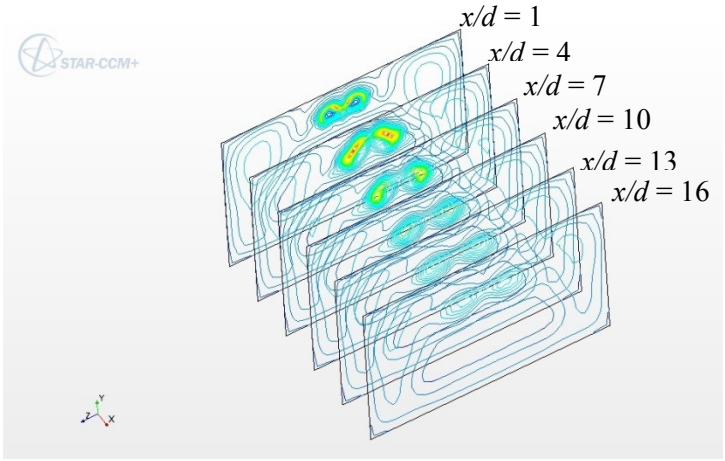

f)

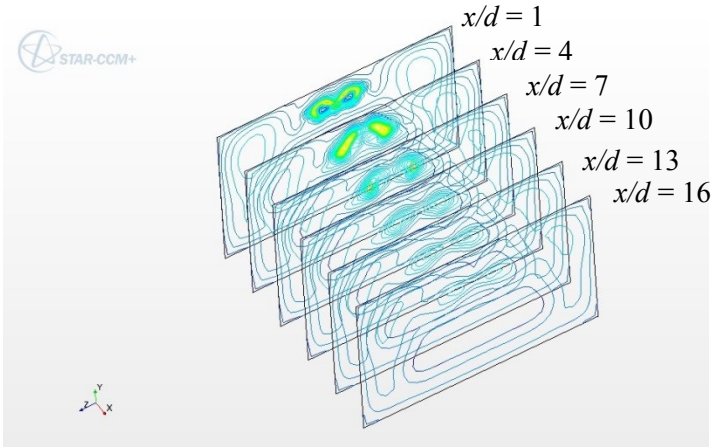

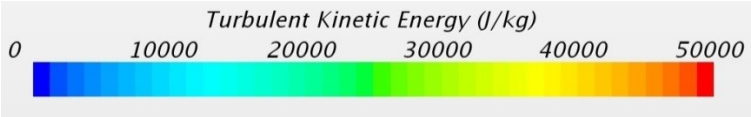

Figure 126 Turbulent kinetic energy contours in the combustor for Configuration 4xr-TO
d) 4xr-V30-TO, e) 4xr-V40-TO, f) 4xr-V50-TO

6.3.6 Distance Configuration 4xr, Swirl Pattern SD

Figure 127(a) shows the H_2O mole fraction contours on the fuel inlet and upper combustor walls for the non-swirling baseline case for the distance configuration 4xr. The high H_2O mole fraction zones on the fuel nozzle wall rotate as swirl increases and then moves unto the upper combustor wall. Figure 12(e) and (f) are very similar to one another suggesting the progression of the H_2O along the wall has decreased despite the increase in swirl.

Contour plots showing the progression of the H_2O mole fraction in the combustor are shown in Figure 128. Increasing the swirl lengthens the distance over which the fuel jets merge into one. This trend is not as obviously seen in the temperature contours shown in Figure 129.

Turbulent kinetic energy is shown on the left fuel injector centerline plane (z = -2r) in Figure 130, on the tunnel centerline (z = 0) in Figure 131 and on the right fuel injector centerline plane (z = 2r) in Figure 132. Figure 133 shows a progression of contour plots of TKE. At first there are two high TKE zones. The high TKE zone on the left side decreases as the swirl increases. Figure 114(e) shows only one high TKE zone at $x/d = 4$.

Table 13 shows the start location and length of the high TKE zone, the burning efficiency and the increase in burning efficiency due to swirl. The results show a similar trend as the 3xr-SD configuration. One major difference is that the start location of the high TKE zone plateaus at $0.24d$ downstream of the fuel injector exit and the start location of the high TKE zone increases with additional swirl. The high TKE zone length increases with swirl, reaches a maximum of $9.79d$ and then decreases as more swirl is added to the fuel jet.

As with the other simulation cases increasing swirl increased the burning efficiency. Configuration 4xr-V50-SD resulted in an impressive 20.5% increase in burning efficiency compared to the case with no swirl.

Table 13 Mixing Data for Configuration 4xr-SD

	High Turbulent Kinetic Energy Zone			
Configuration	*Zone start location (x/d)*	*Zone Length (d)*	*Burning Efficiency, η_{burn}*	*$\Delta \eta_{burn}$ (%)*
4xr-V00	2.07	8.19	0.73	n/a
4xr-V10-SD	0.68	9.79	0.73	1.1
4xr-V20-Sd	0.28	8.79	0.76	4.3
4xr-V30-SD	0.24	6.92	0.79	8.4
4xr-V40-SD	0.24	5.13	0.83	14.3
4xr-V50-SD	1.07	3.30	0.88	20.5

a)

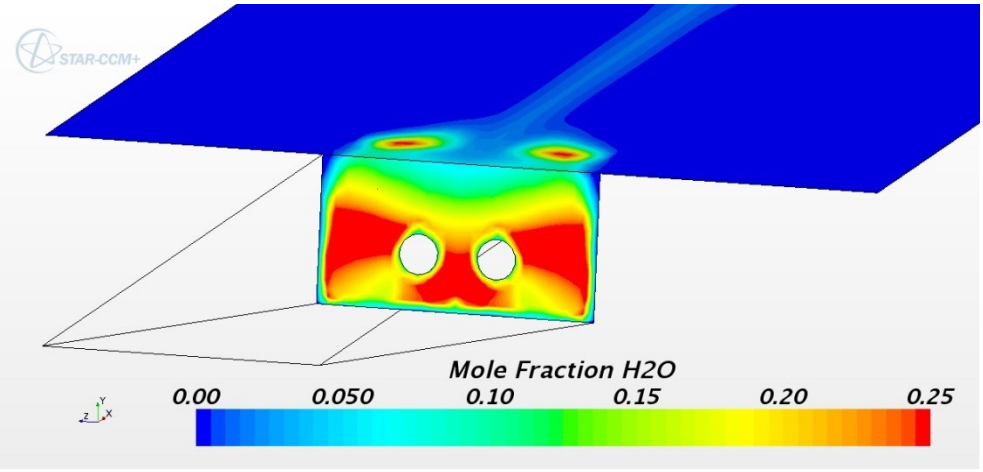

b)

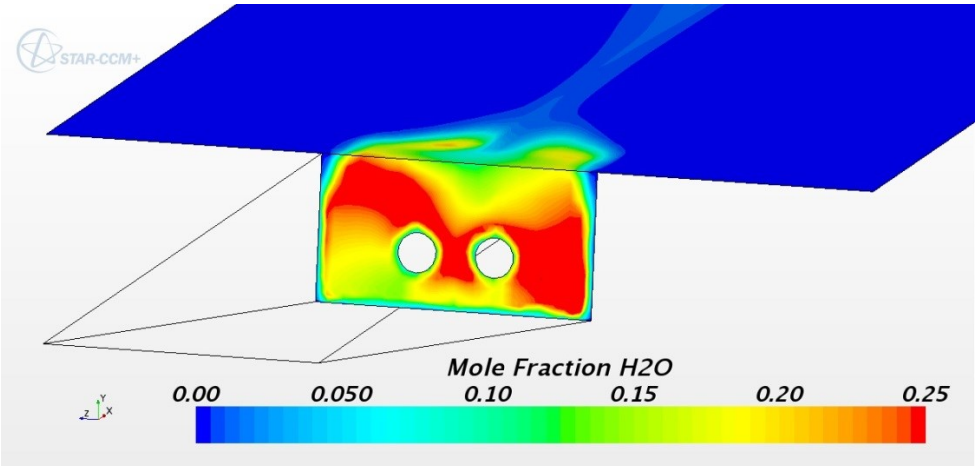

c)

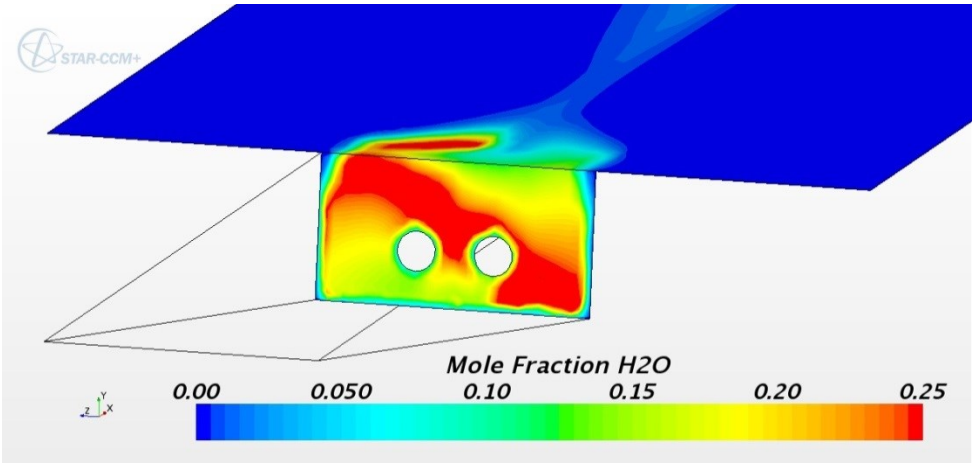

Figure 127 Mole fraction contours of H_2O on the fuel inlet wall and combustor upper wall for Configuration 4xr-SD
a) 4xr-V00, b) 4xr-V10-SD, c) 4xr-V20-SD

d)

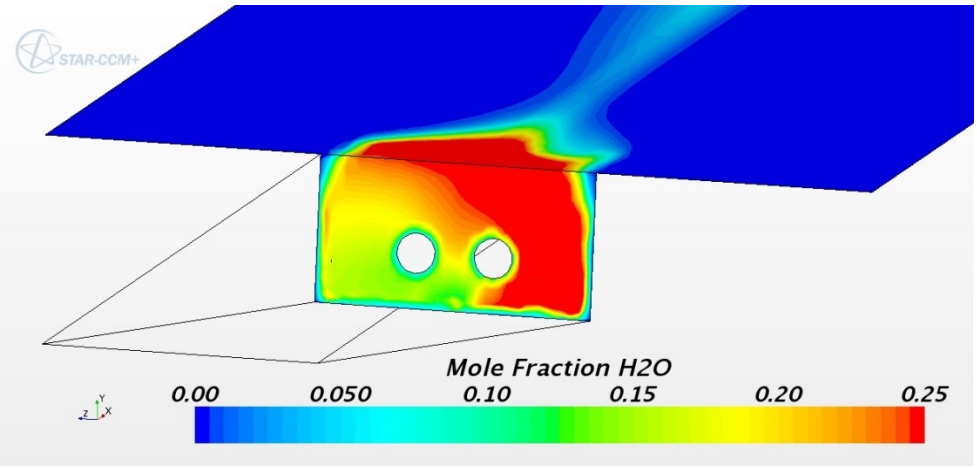

e)

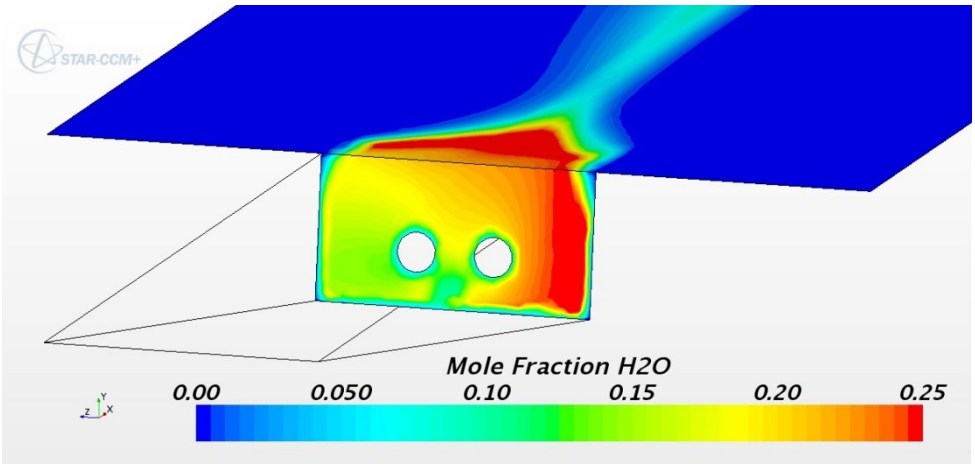

f)

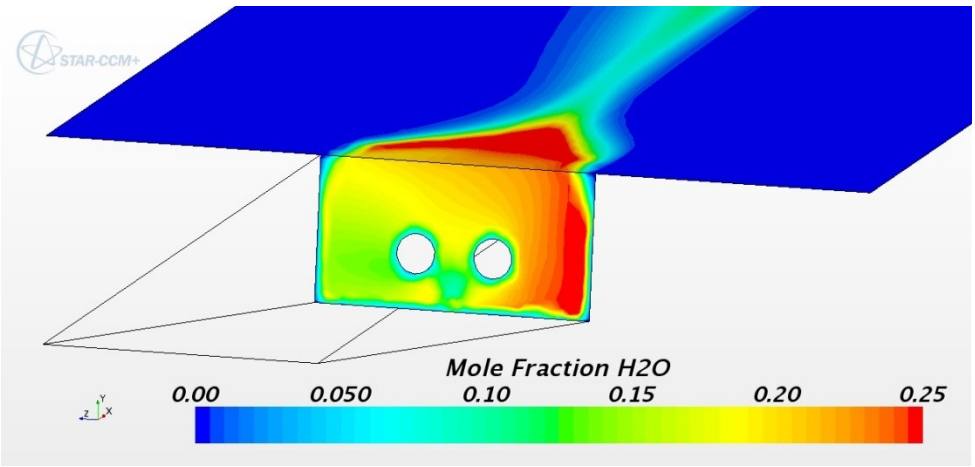

Figure 127 Mole fraction contours of H_2O on the fuel inlet wall and the combustor upper wall for Configuration 4xr-SD
d) 4xr-V30-SD, e) 4xr-V40-SD, f) 4xr-V50-SD

a)

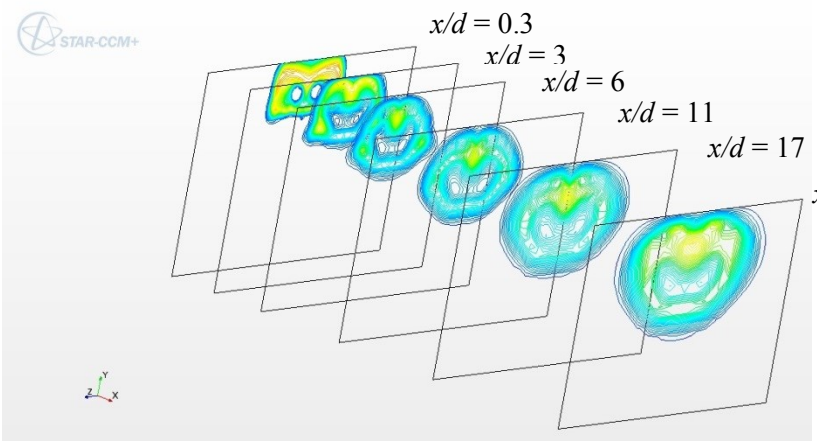

b)

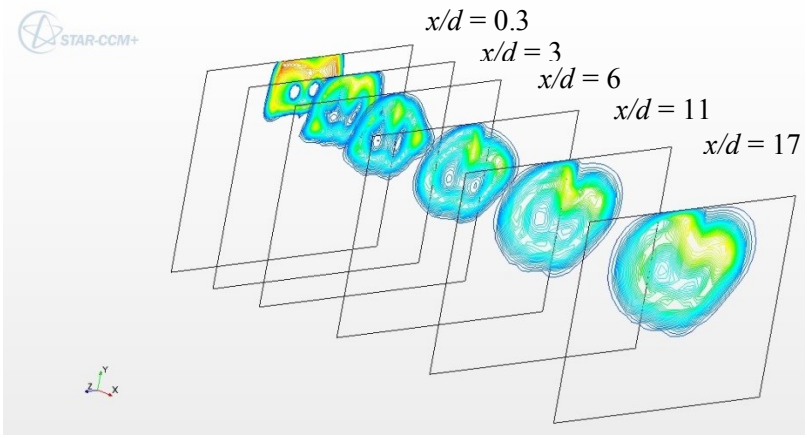

c)

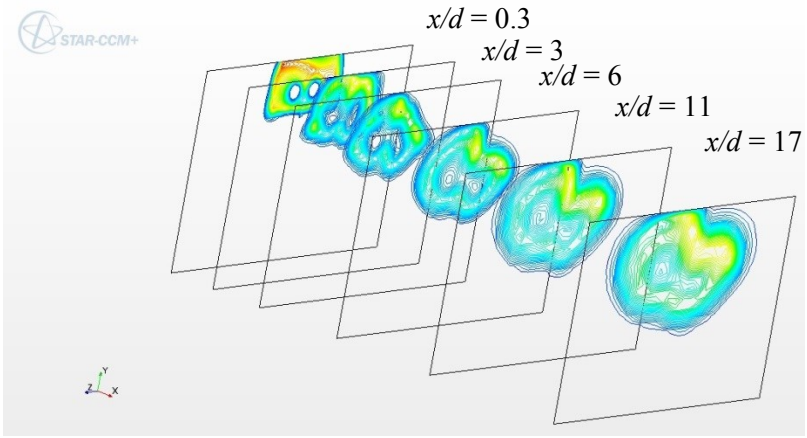

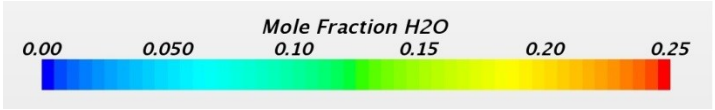

Figure 128 Mole fraction contours of H_2O in the combustor for Configuration 4xr-SD
a) 4xr-V00, b) 4xr-V10-SD, c) 4xr-V20-SD

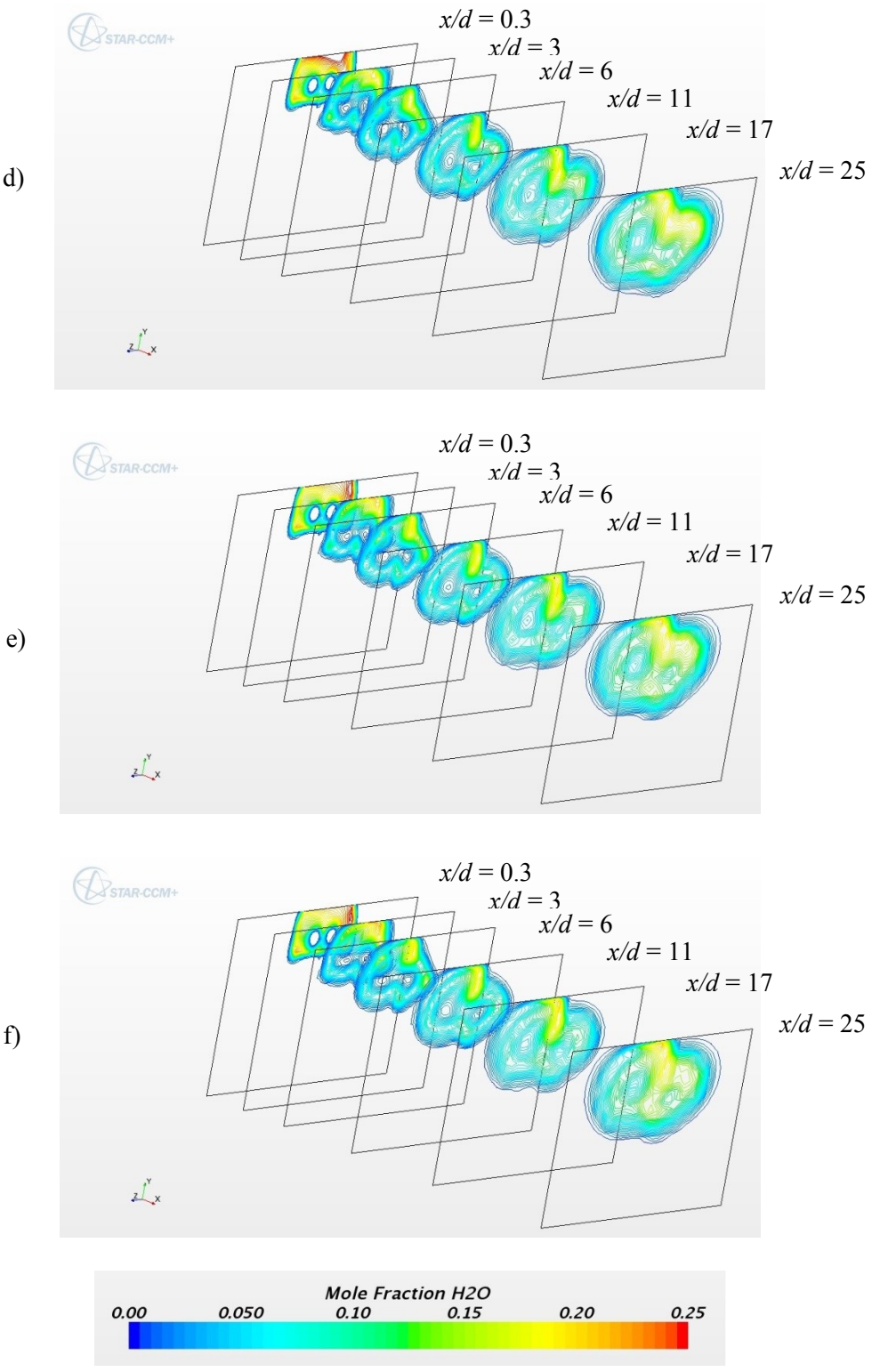

Figure 128 Mole fraction contours of H_2O in the combustor for Configuration 4xr-SD
d) 4xr-V30-SD, e) 4xr-V40-SD, f) 4xr-V50-SD

a)

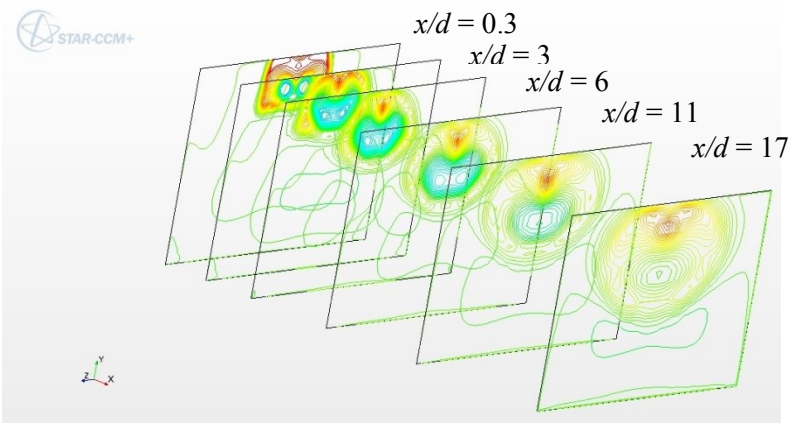

b)

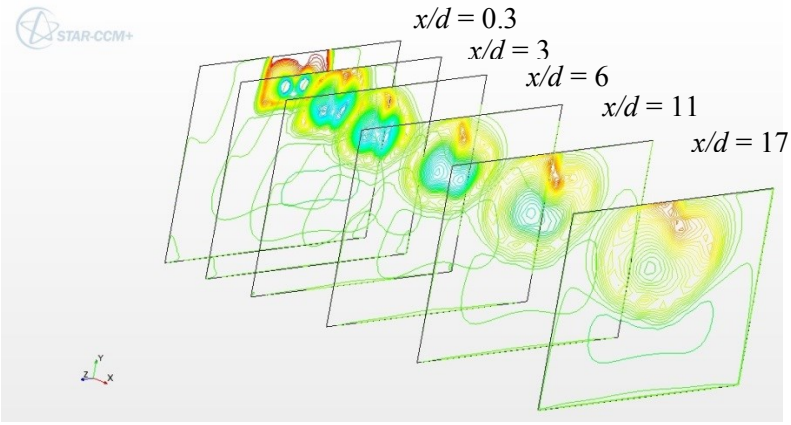

c)

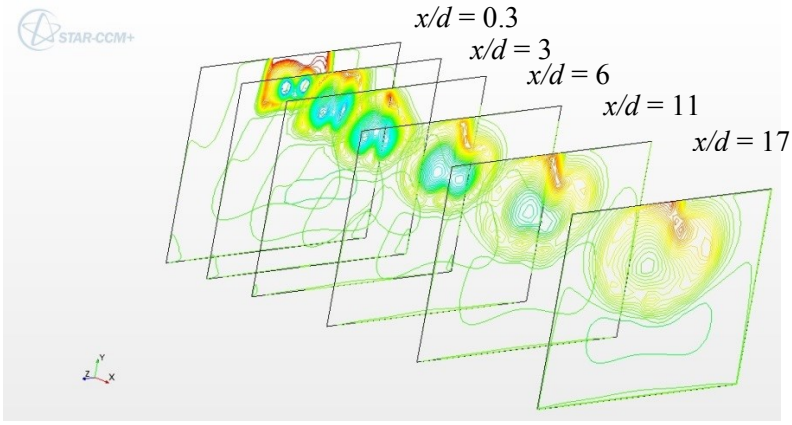

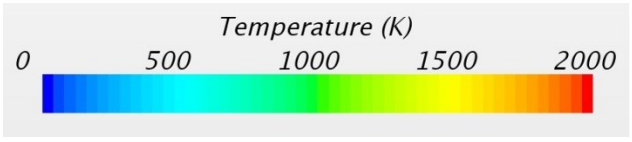

Figure 129 Temperature contours in the combustor for Configuration 4xr-SD
a) 4xr-V00, b) 4xr-V10-SD, c) 4xr-V20-SD

d)

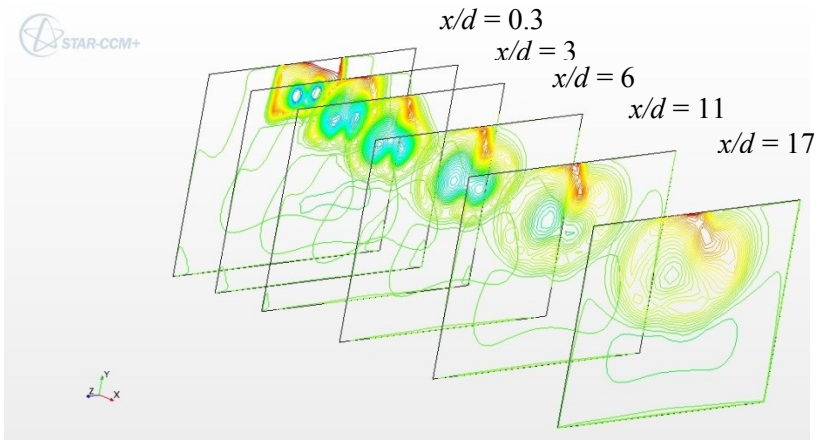

e)

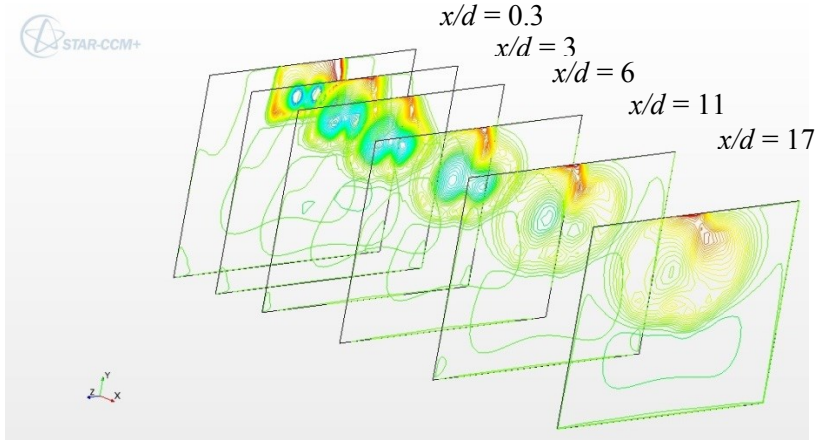

f)

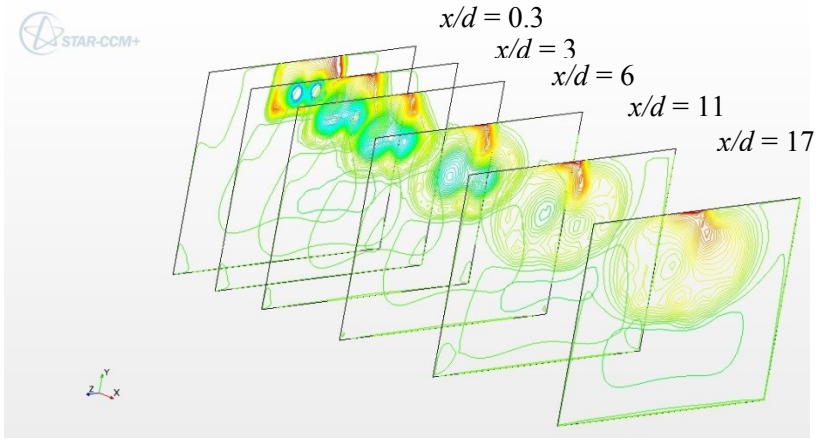

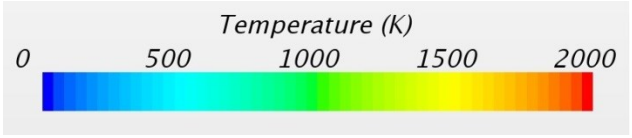

Figure 129 Temperature contours in the combustor for Configuration 4xr-SD
d) 4xr-V30-SD, e) 4xr-V40-SD, f) 4xr-V50-SD

(a)

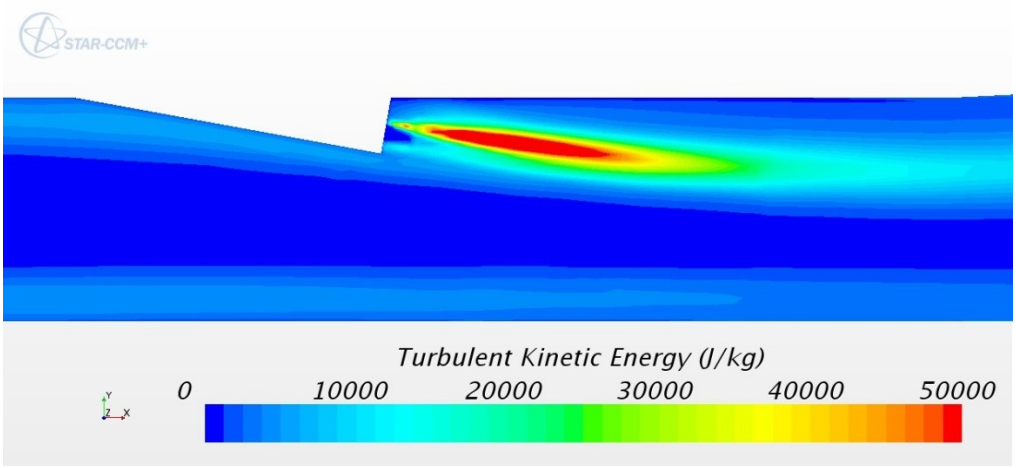

(b)

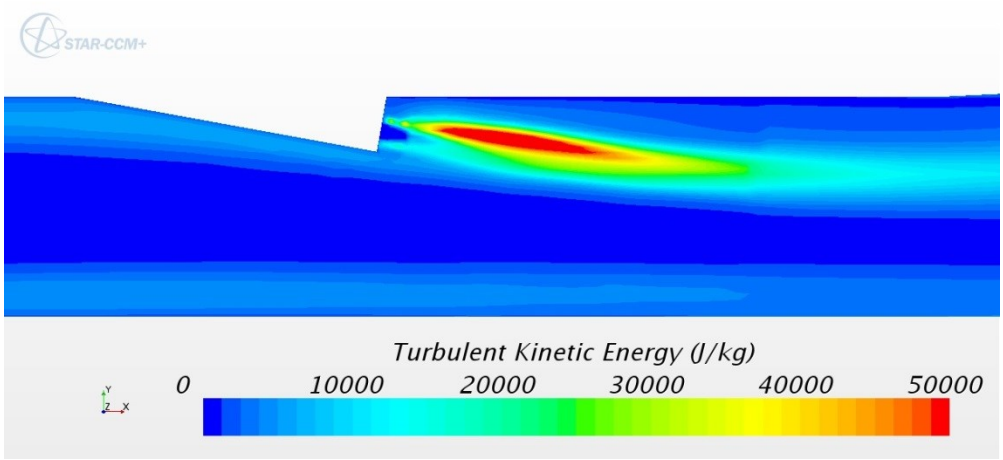

(c)

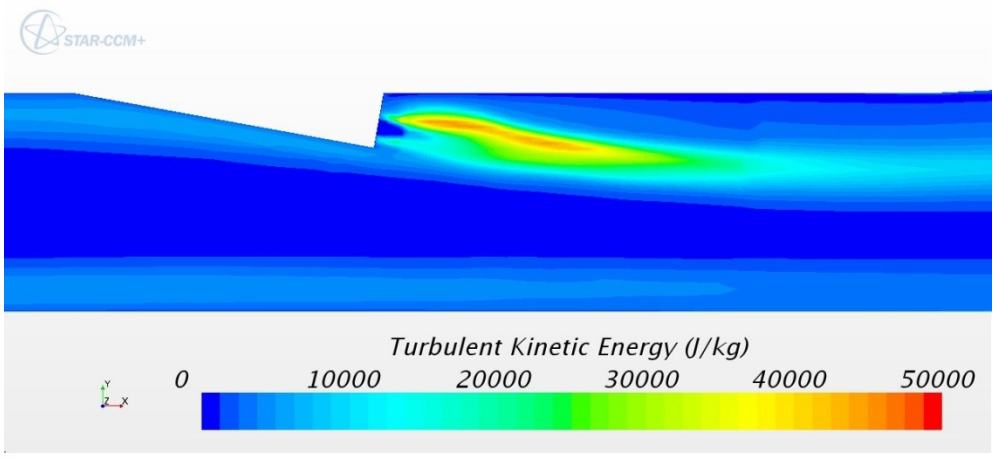

Figure 130 Turbulent kinetic energy plots on the left fuel nozzle centerline plane (z = -2r) in the combustor for Configuration 4xr-SD
a) 4xr-V00, b) 4xr-V10-SD, c) 4xr-V20-SD

(d)

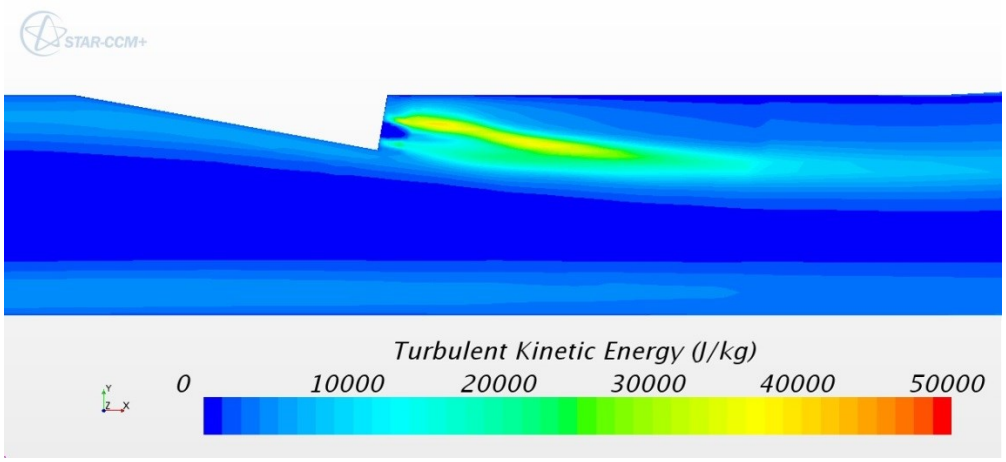

(e)

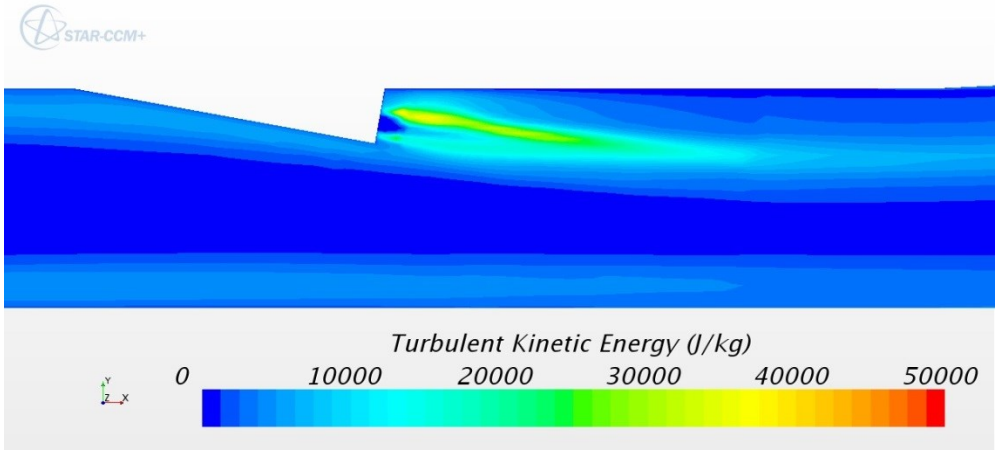

(f)

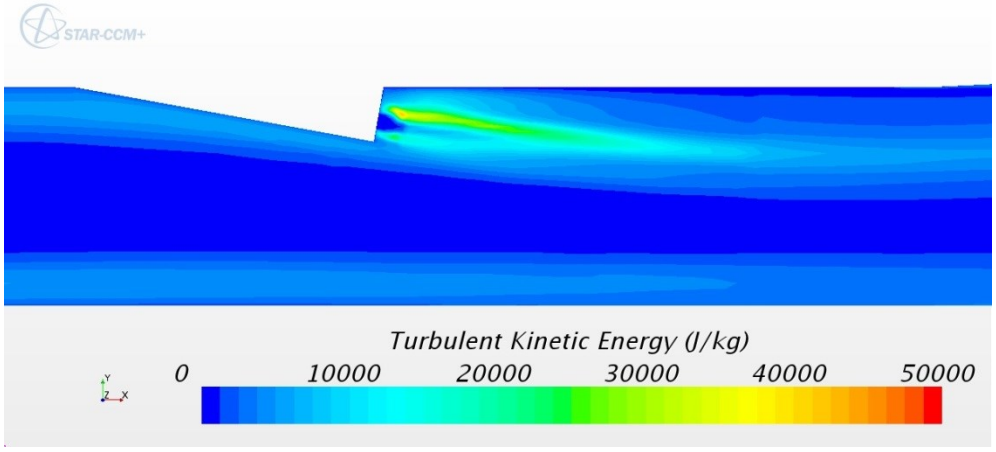

Figure 130 Turbulent kinetic energy plots on the left fuel nozzle centerline plane (z = -2r) in the combustor for Configuration 4xr-SD
d) 4xr-V30-SD, e) 4xr-V40-SD, f) 4xr-V50-SD

(a)

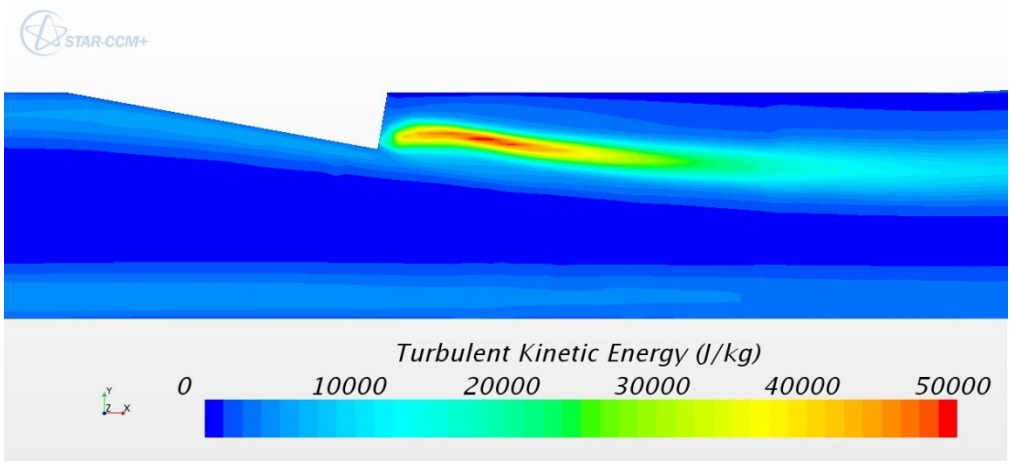

(b)

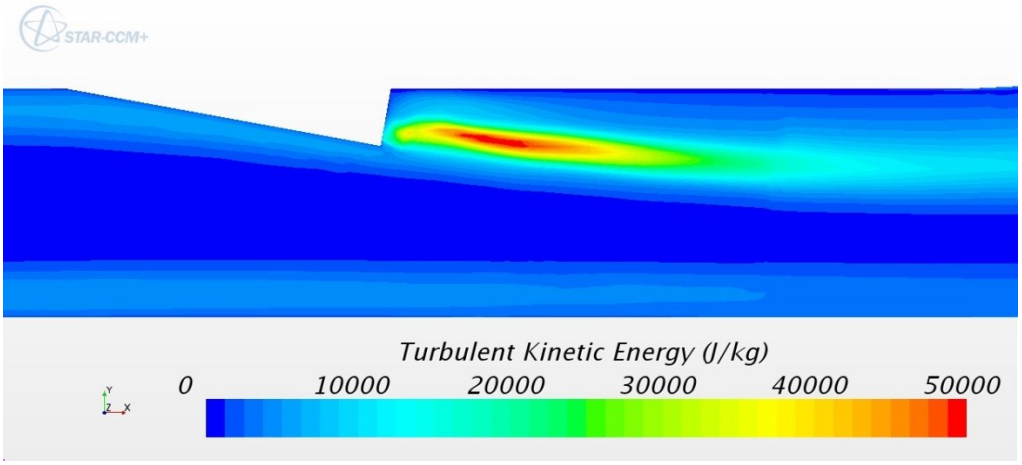

(c)

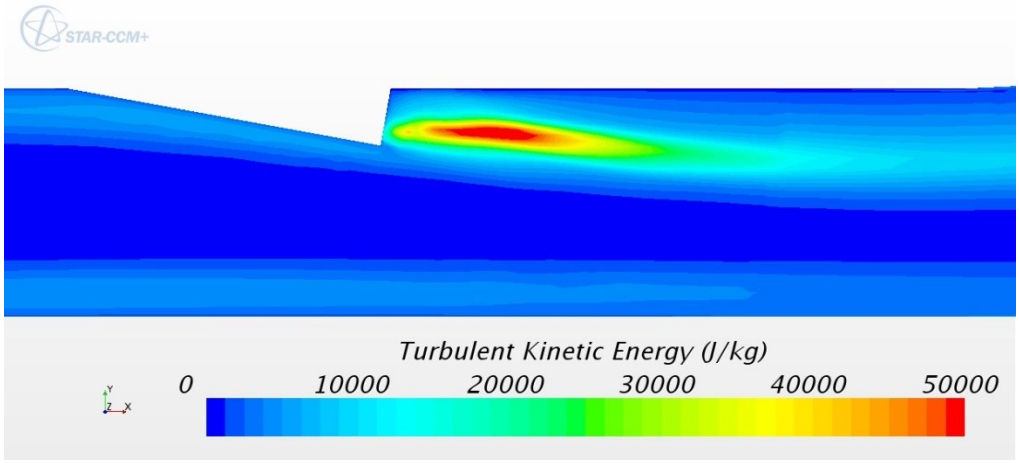

Figure 131 Turbulent kinetic energy plots on the centerline plane (z = 0) in the combustor for Configuration 4xr-SD
a) 4xr-V00, b) 4xr-V10-SD, c) 4xr-V20-SD

(d)

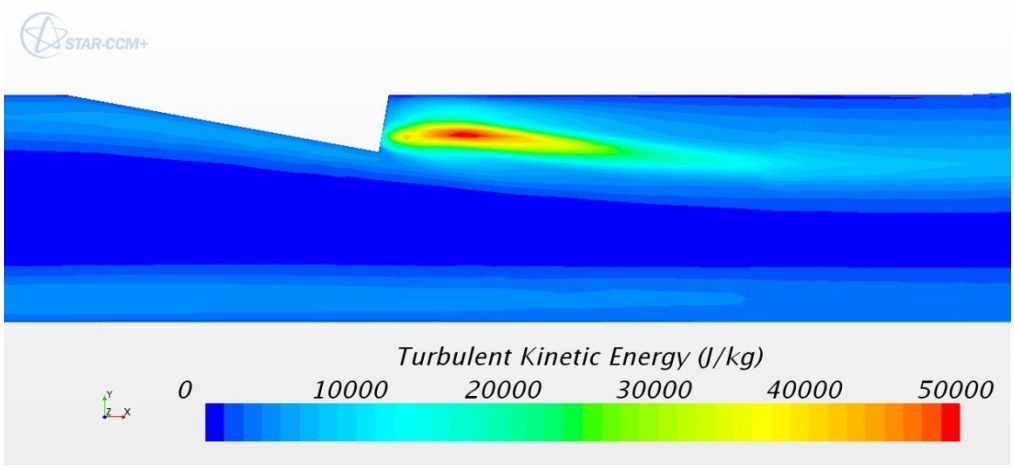

(e)

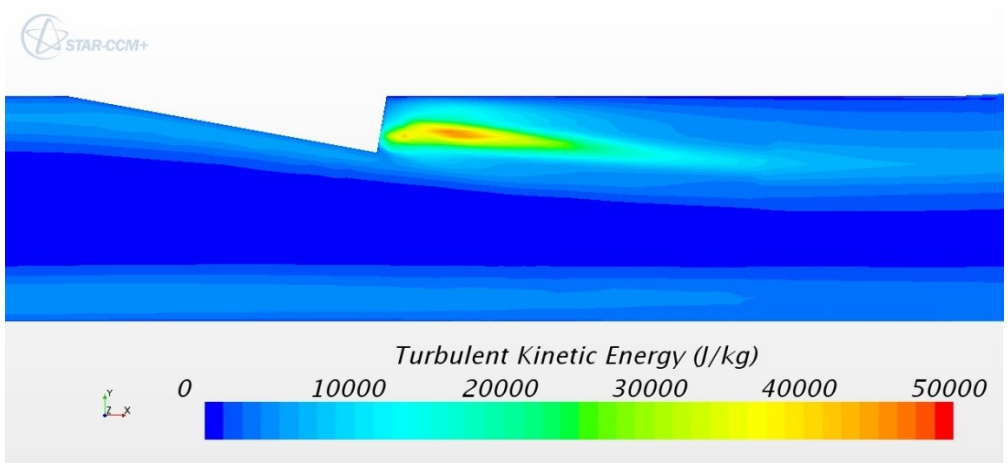

(f)

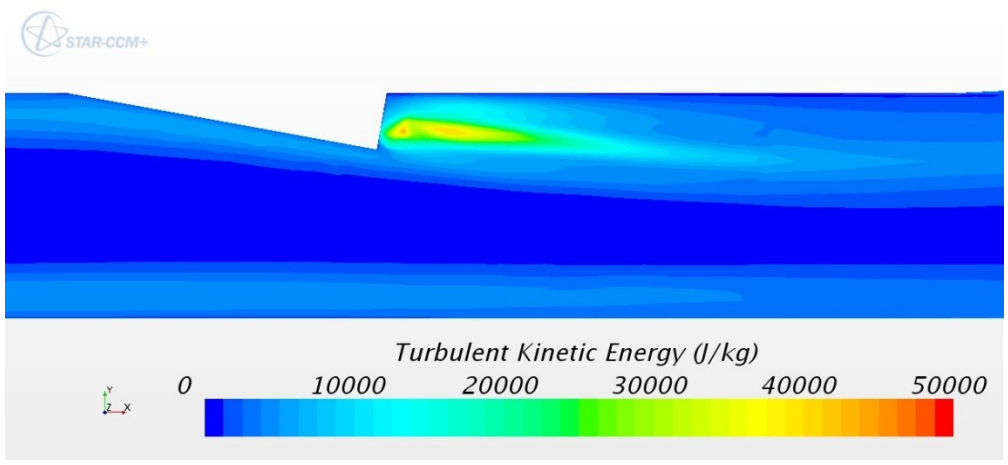

Figure 131 Turbulent kinetic energy plots on the centerline plane (z = 0) in the combustor for Configuration 4xr-SD
d) 4xr-V30-SD, e) 4xr-V40-SD, f) 4xr-V50-SD

(a)

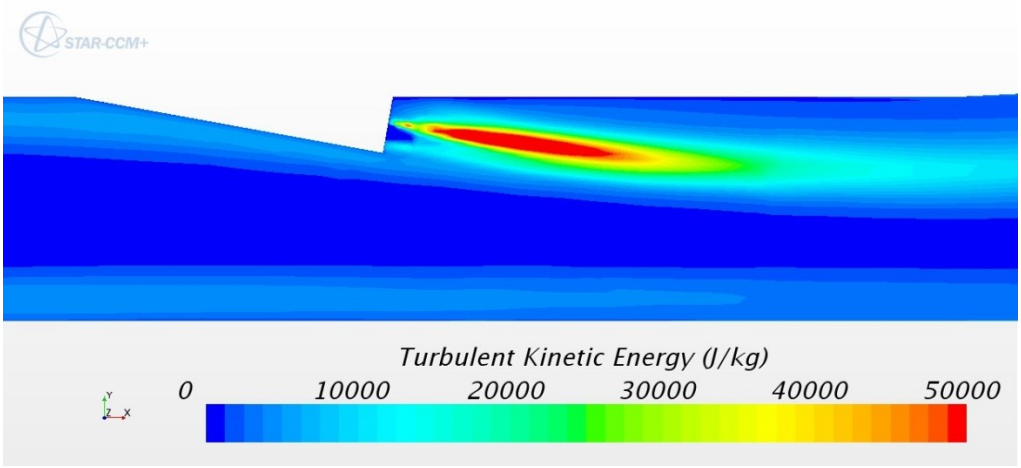

(b)

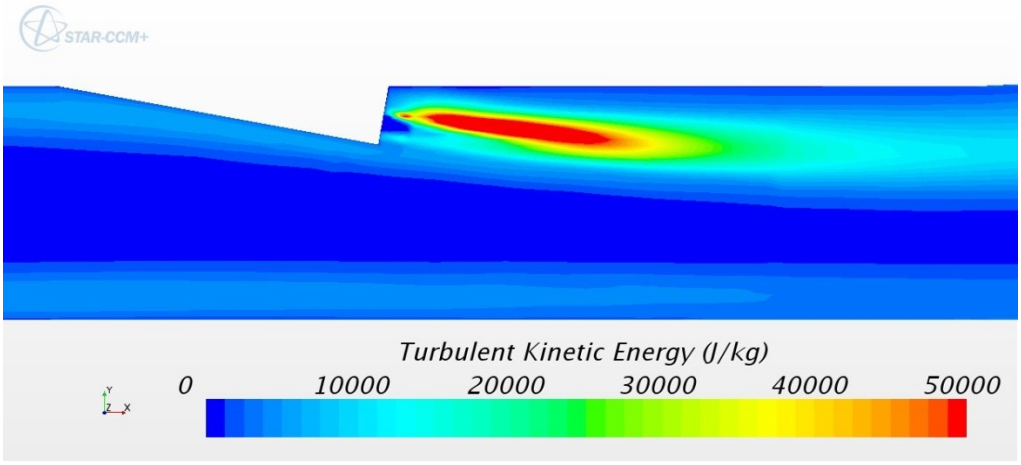

(c)

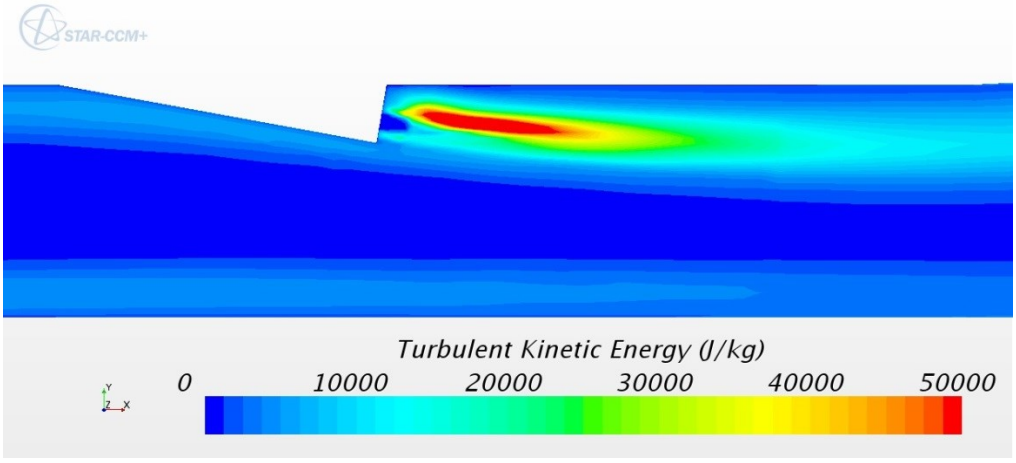

Figure 132 Turbulent kinetic energy plots on the right fuel nozzle centerline plane (z = 2r) in the combustor for Configuration 4xr-SD
a) 4xr-V00, b) 4xr-V10-SD, c) 4xr-V20-SD

(d)

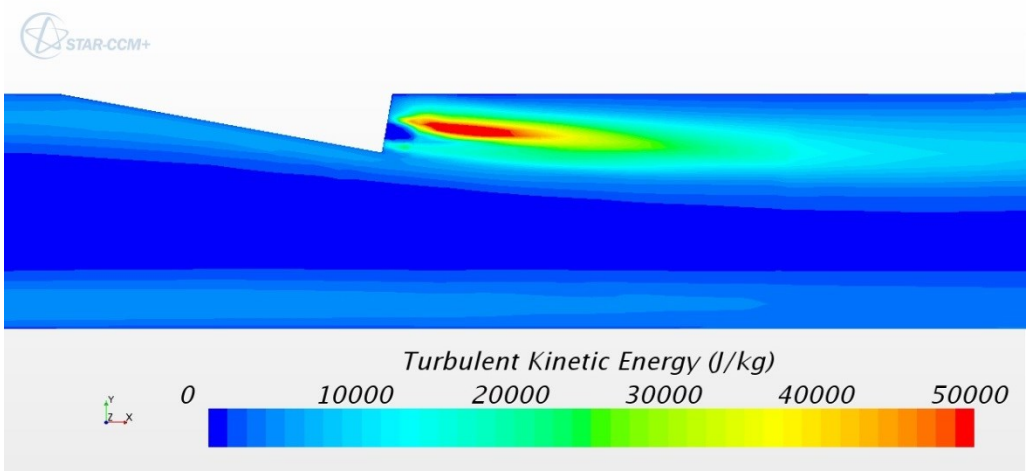

(e)

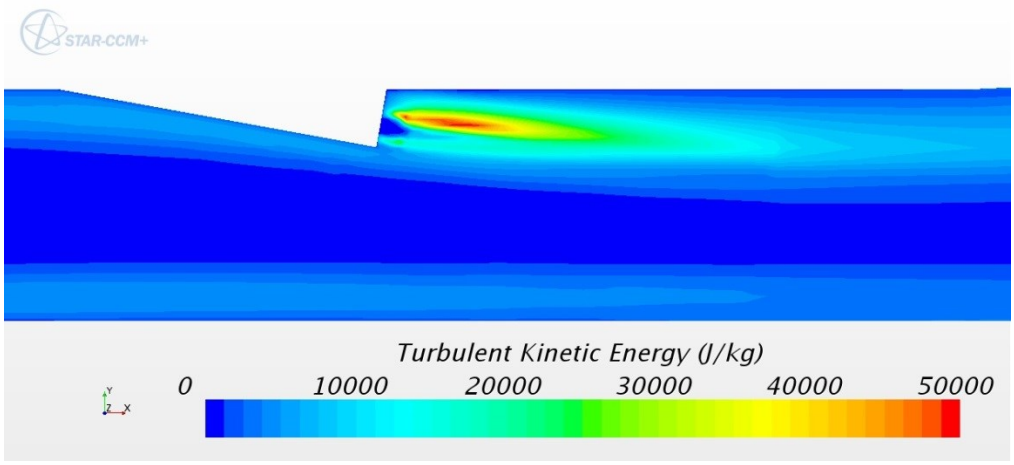

(f)

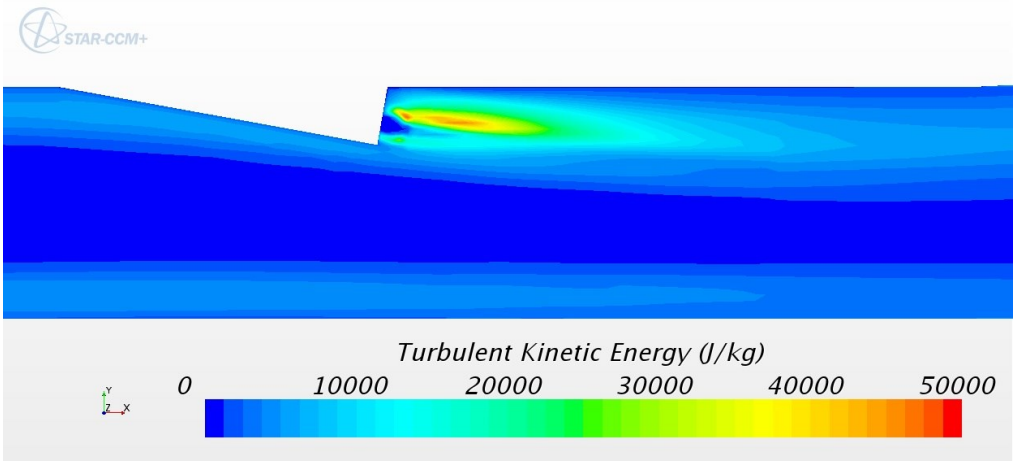

Figure 132 Turbulent kinetic energy plots on the right fuel nozzle centerline plane (z = 2r) in the combustor for Configuration 4xr-SD
d) 4xr-V30-SD, e) 4xr-V40-SD, f) 4xr-V50-SD

a)

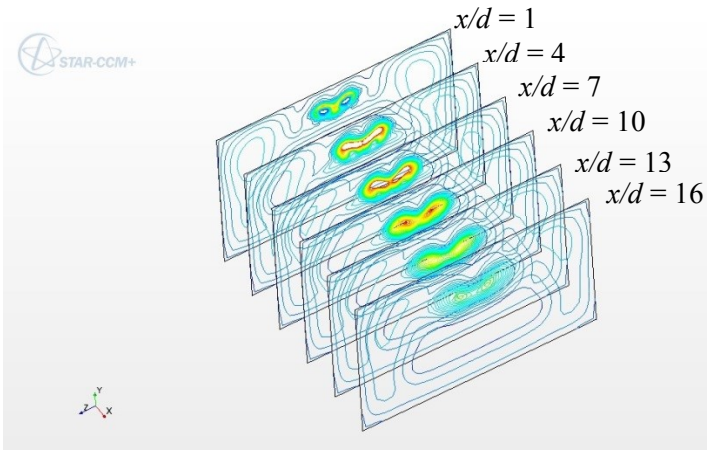

b)

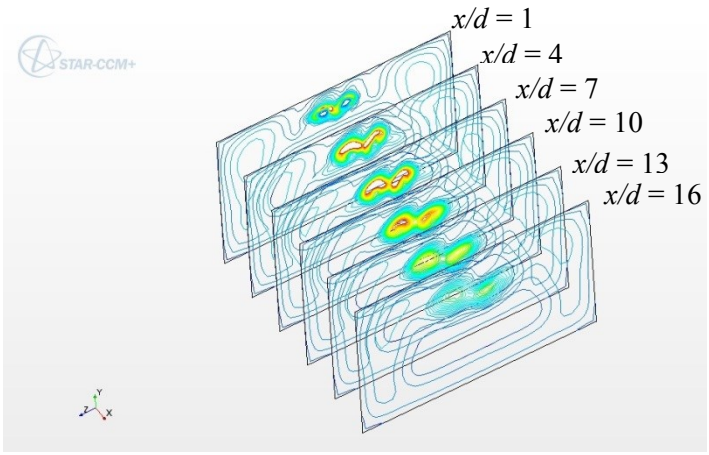

c)

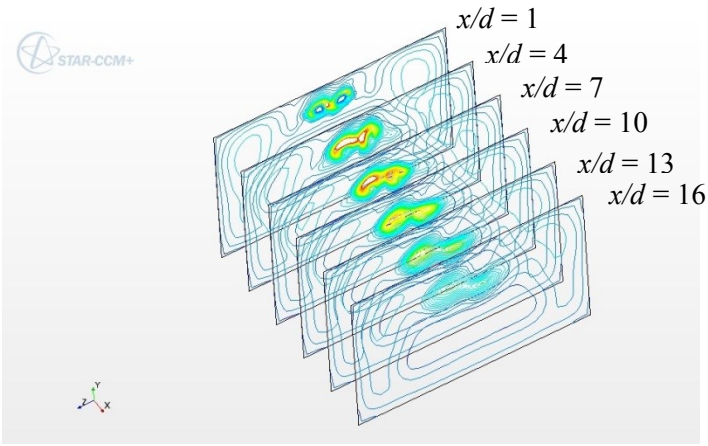

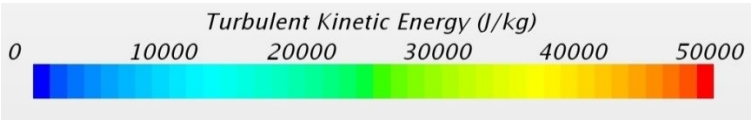

Figure 133 Turbulent kinetic energy contours in the combustor for Configuration 4xr-SD
a) 4xr-V00, b) 4xr-V10-SD, c) 4xr-V20-SD

d)

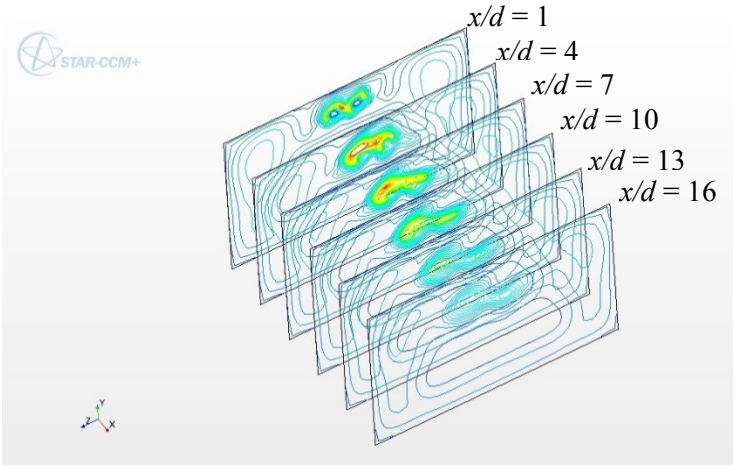

e)

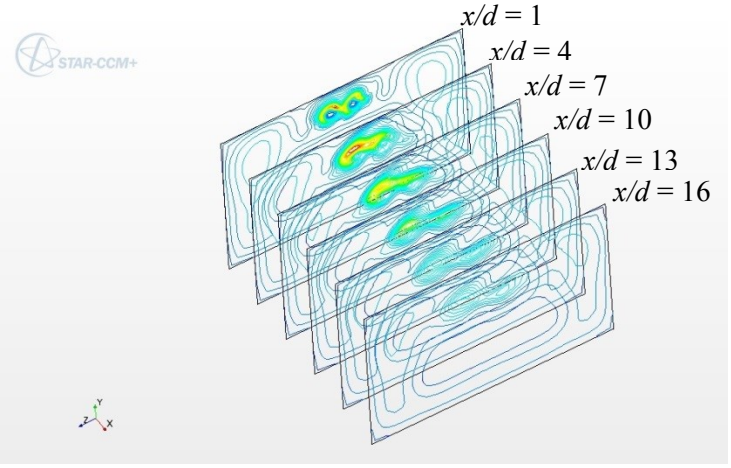

f)

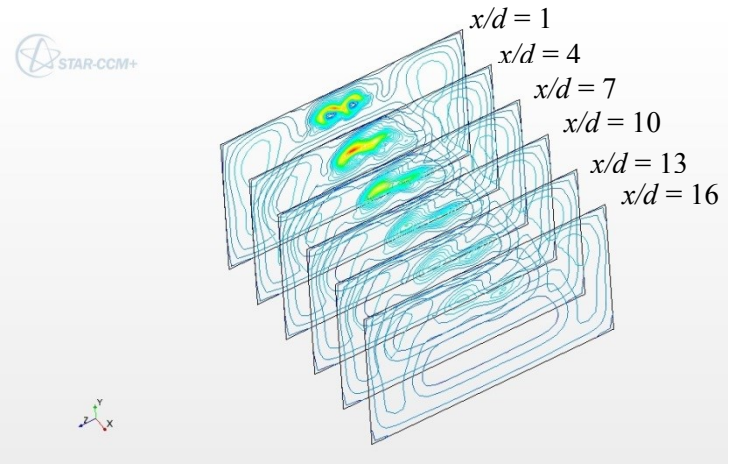

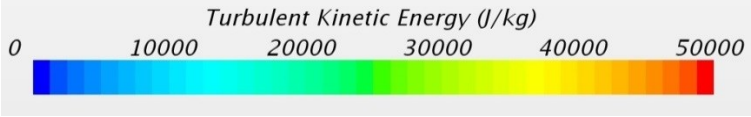

Figure 133 Turbulent kinetic energy contours in the combustor for Configuration 4xr-SD
d) 4xr-V30-SD, e) 4xr-V40-SD, f) 4xr-V50-SD

6.3.7 Distance Configuration 5xr, Swirl Pattern TI

Figure 134(a) shows the H_2O mole fraction contours on the fuel inlet and upper combustor walls for the non-swirling baseline case for the distance configuration 5xr. There are two small areas of high H_2O mole fraction zones on the upper combustor wall and one zones on the fuel nozzle wall. The high H_2O mole fraction zones on the upper combustor wall are not eliminated and the zones on the fuel nozzle wall do not rotate as swirl increases. The high H_2O mole fraction zones on the fuel nozzle wall increase in area moving towards the upper combustor wall and eventually combining with the zones on the upper combustor wall. Finally the high H_2O mole fraction zone starts to transfer to the upper combustor wall completely. The interaction of this swirl pattern produces similar results to high swirl in single fuel jet.

Figure 97 shows that the two fuel jets merge together with more distance as swirl in increased until they do not merge at all.

The temperature contours are shown in Figure 136 and indicate that temperature decreases with increasing fuel jet swirl.

Turbulent kinetic energy is shown on the tunnel centerline (z = 0) in Figure 137 and on the right fuel injector centerline plane (z = 2.5r) in Figure 138. The flow through the tunnel is symmetrical for this swirl pattern. Therefore Figure 138 is the same for the right and left fuel jets. There is no evidence of high TKE zones on the tunnel centerline. The high TKE zones on the fuel jet centerline decrease rapidly with increasing swirl. The rapid decrease of high TKE zones with increasing swirl is also seen in Figure 139.

Table 14 shows the start location and length of the high TKE zone, the burning efficiency and the increase in burning efficiency due to swirl. The results show a similar trend as the 5xr-

TI configuration. A major difference is that the high TKE zone is eliminated with the higher swirl configurations. The high TKE zone length decreases with swirl.

As with the other simulation cases increasing swirl increase the burning efficiency. Configuration 5xr-V50-TI resulted in an impressive 24.6% increase in burning efficiency compared to the case with no swirl.

Table 14 Mixing Data for Configuration 5xr-TI

	High Turbulent Kinetic Energy Zone			
Configuration	*Zone start location (x/d)*	*Zone Length (d)*	*Burning Efficiency,* η_{burn}	$\Delta\ \eta_{burn}$ *(%)*
5xr-V00	1.99	9.03	0.72	n/a
5xr-V10-TI	1.87	8.87	0.74	3.4
5xr-V20-TI	0.88	6.60	0.77	7.2
5xr-V30-TI	0.91	3.18	0.81	12.1
5xr-V40-TI	n/a	0	0.85	18.5
5xr-V50-TI	n/a	0	0.90	24.6

a)

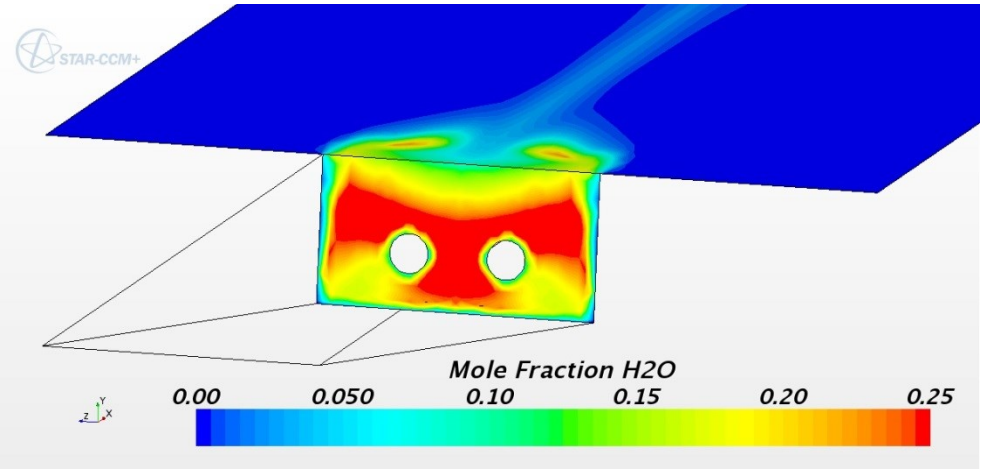

b)

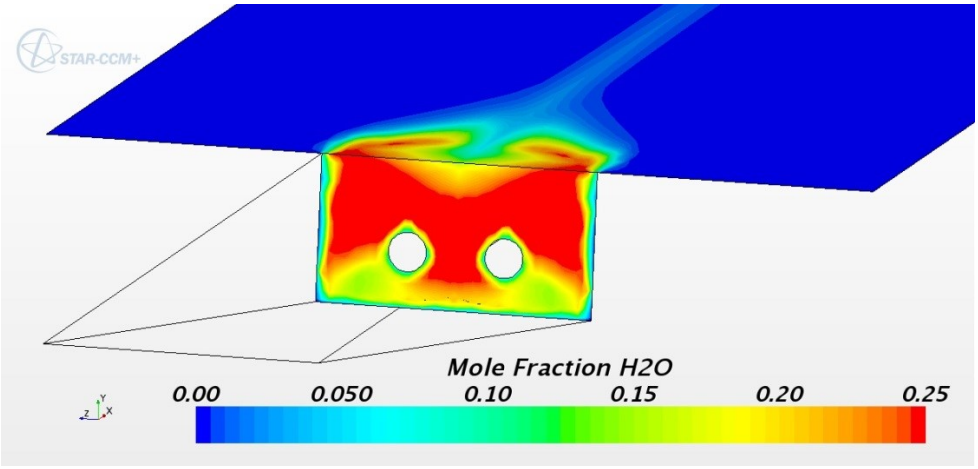

c)

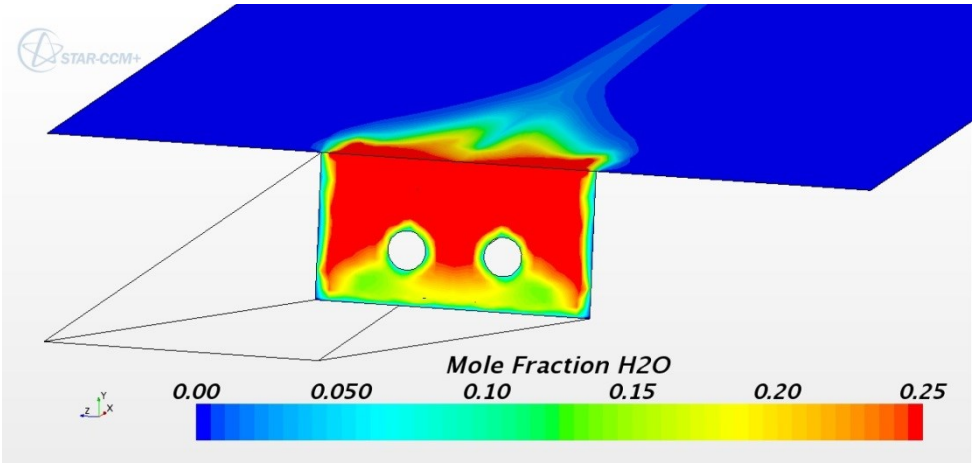

Figure 134 Mole fraction contours of H_2O on the fuel inlet wall and combustor upper wall for Configuration 5xr-TI
a) 5xr-V00, b) 5xr-V10-TI, c) 5xr-V20-TI

d)

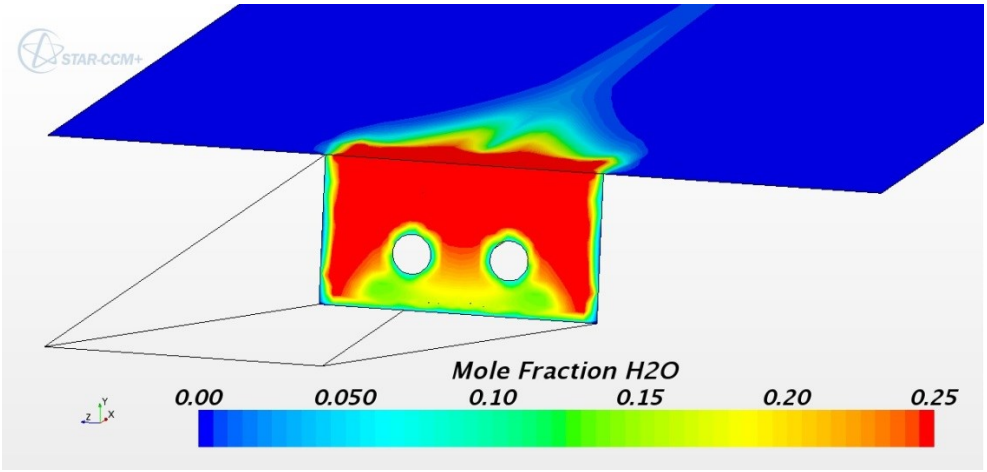

e)

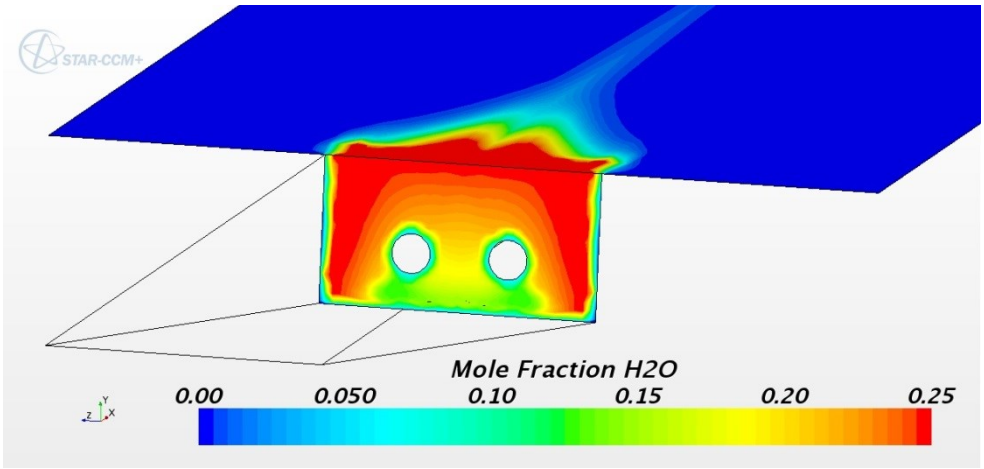

f)

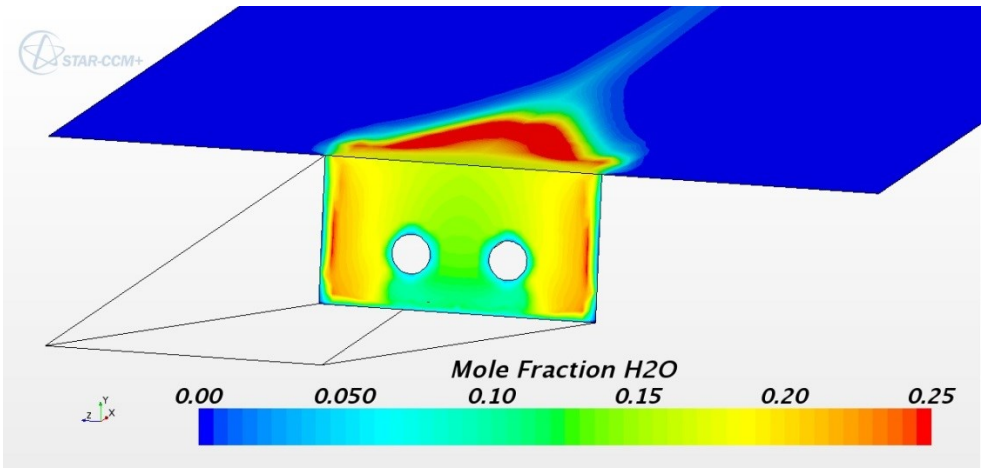

Figure 134 Mole fraction contours of H_2O on the fuel inlet wall and the combustor upper wall for Configuration 5xr-TI
d) 5xr-V30-TI, e) 5xr-V40-TI, f) 5xr-V50-TI

a)

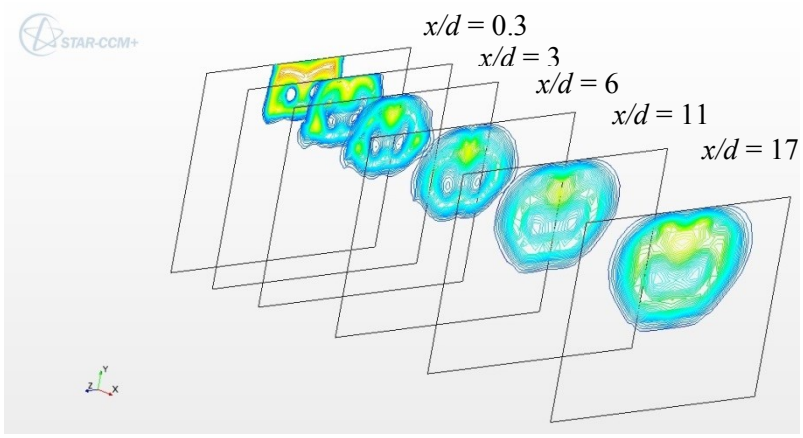

b)

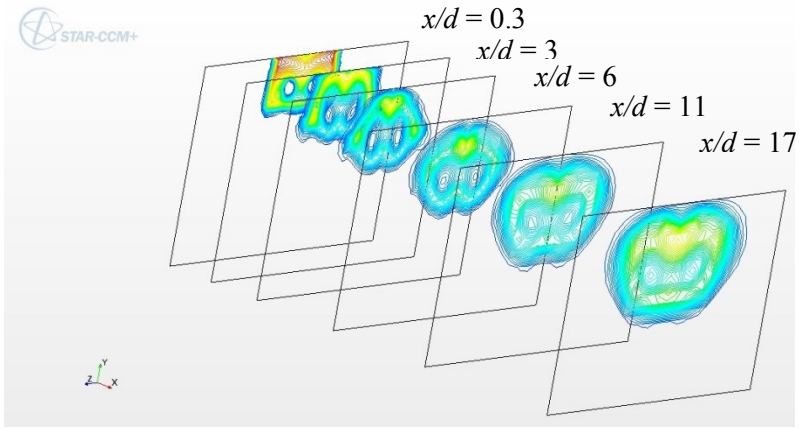

c)

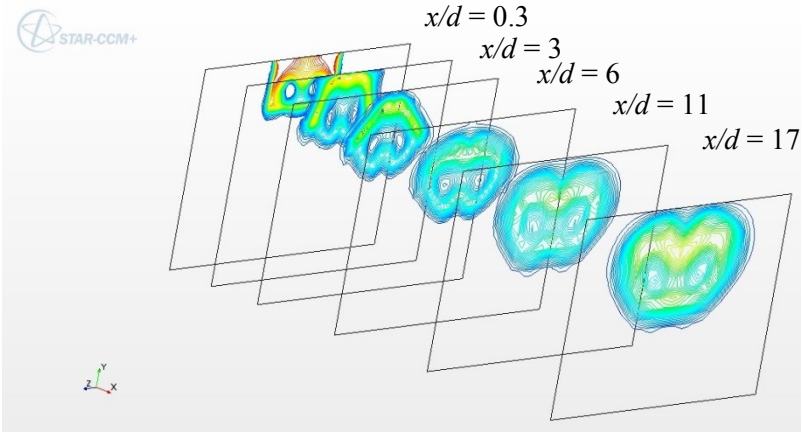

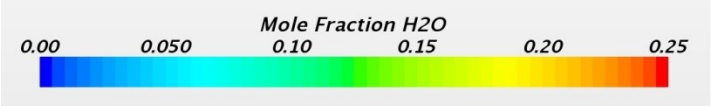

Figure 135 Mole fraction contours of H_2O in the combustor for Configuration 5xr-TI
a) 5xr-V00, b) 5xr-V10-TI, c) 5xr-V20-TI

d)

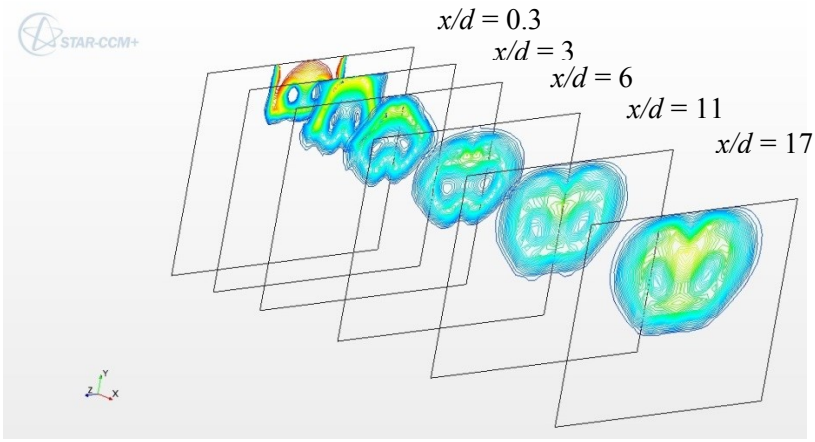

e)

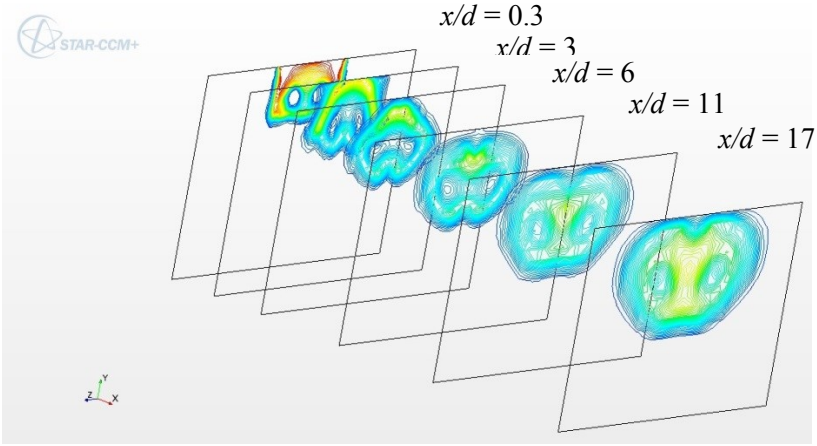

f)

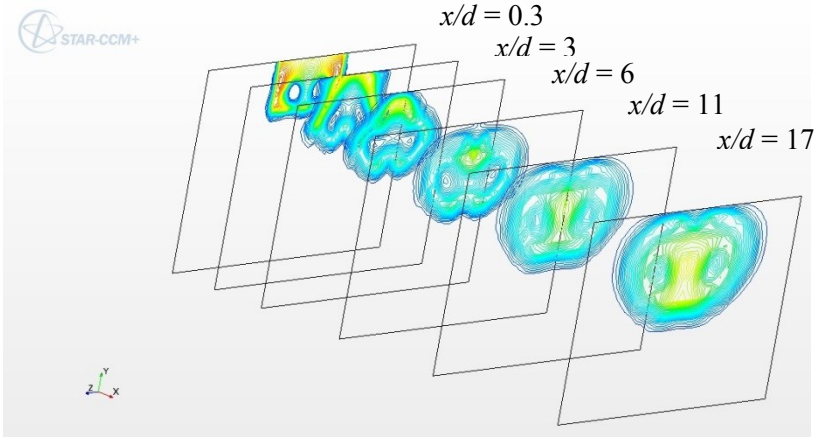

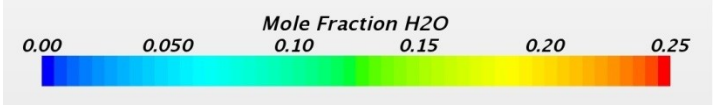

Figure 135 Mole fraction contours of H_2O in the combustor for Configuration 5xr-TI
d) 5xr-V30-TI, e) 5xr-V40-TI, f) 5xr-V50-TI

a)

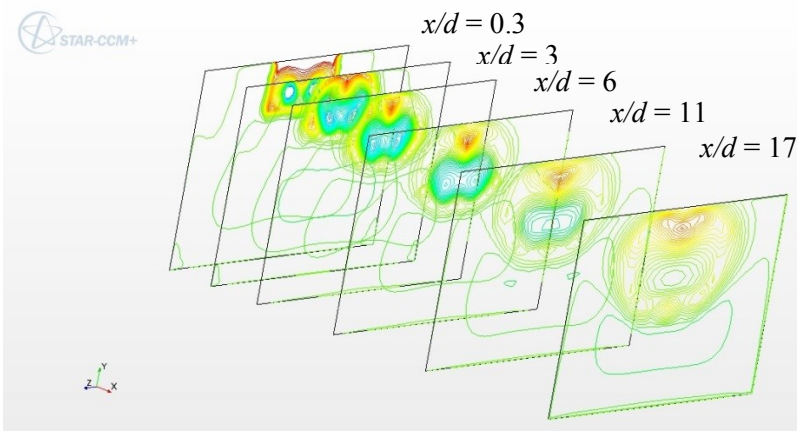

b)

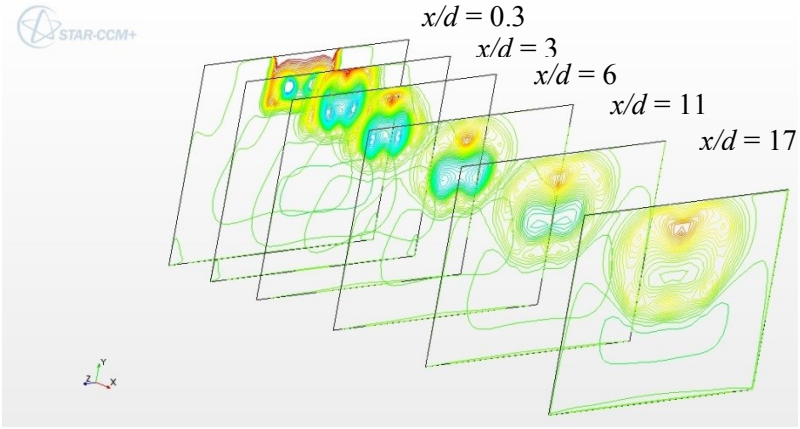

c)

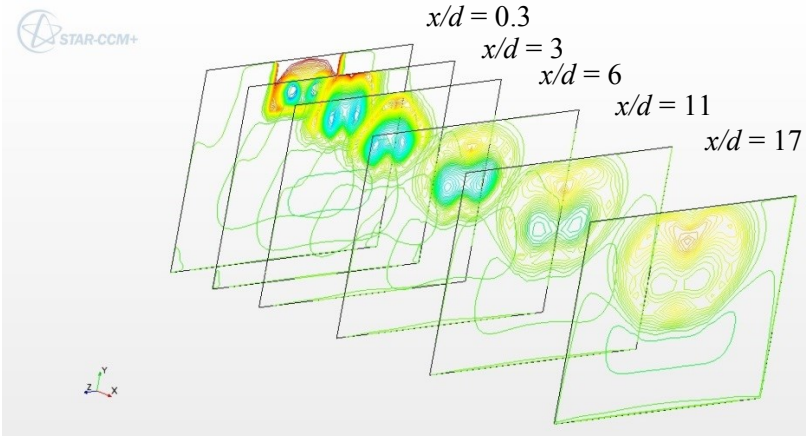

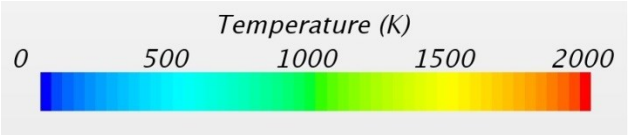

Figure 136 Temperature contours in the combustor for Configuration 5xr-TI
a) 5xr-V00, b) 5xr-V10-TI, c) 5xr-V20-TI

d)

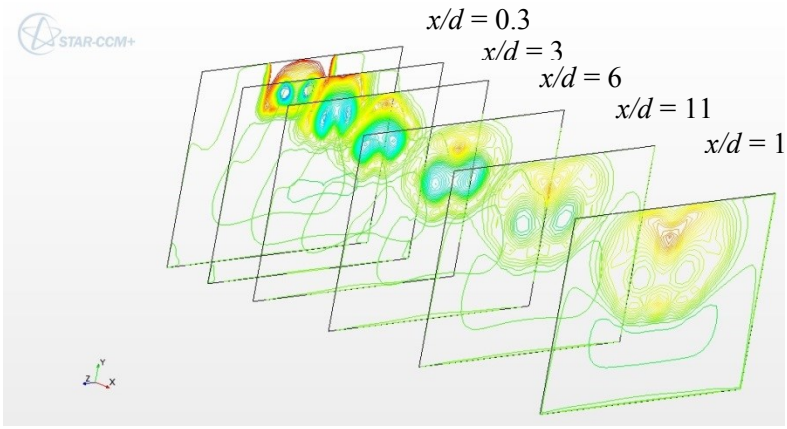

e)

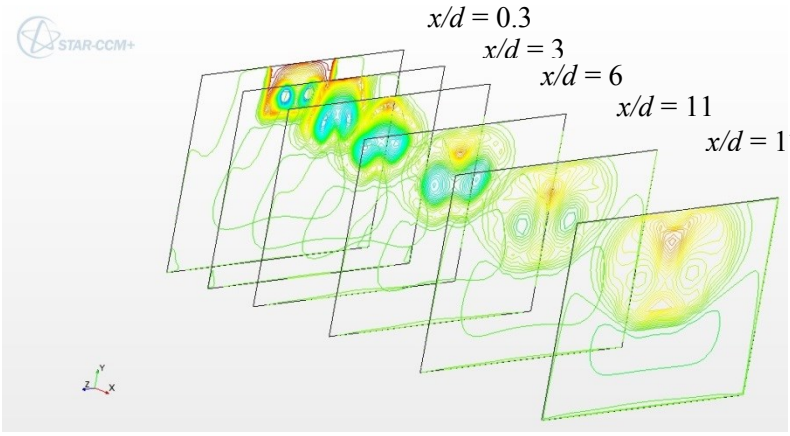

f)

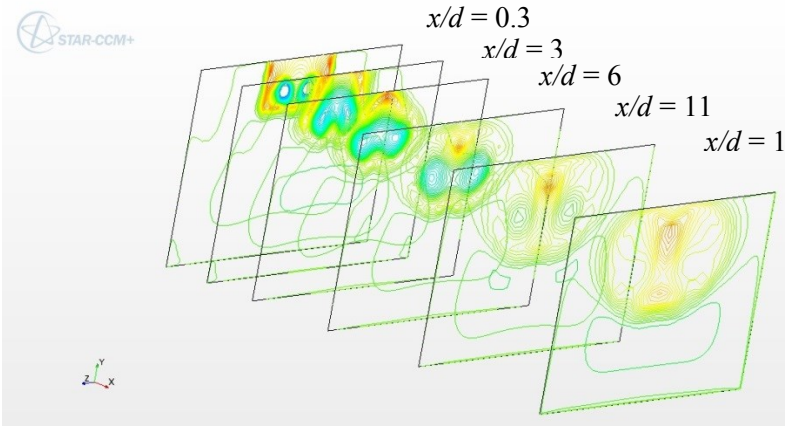

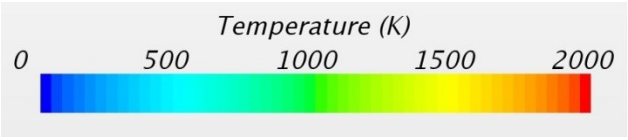

Figure 136 Temperature contours in the combustor for Configuration 5xr-TI
d) 5xr-V30-TI, e) 5xr-V40-TI, f) 5xr-V50-TI

(a)

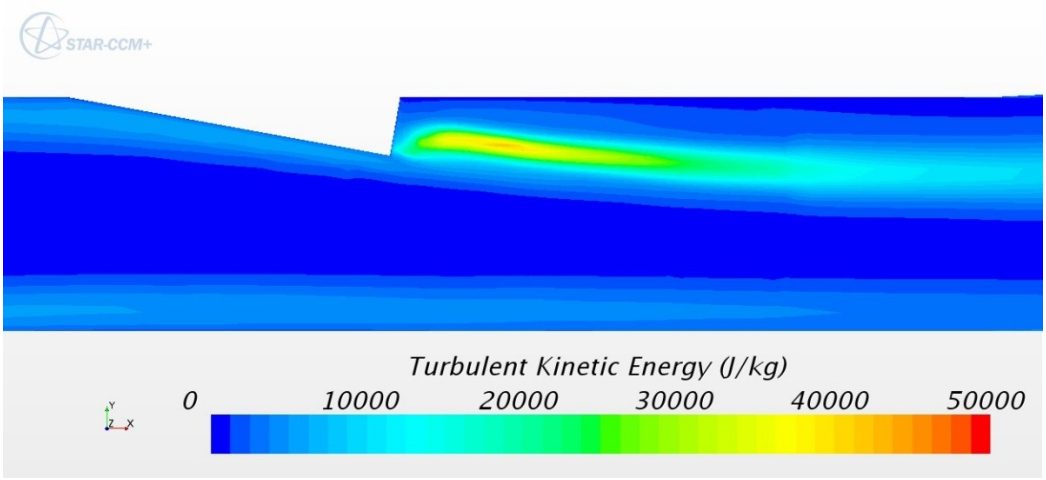

(b)

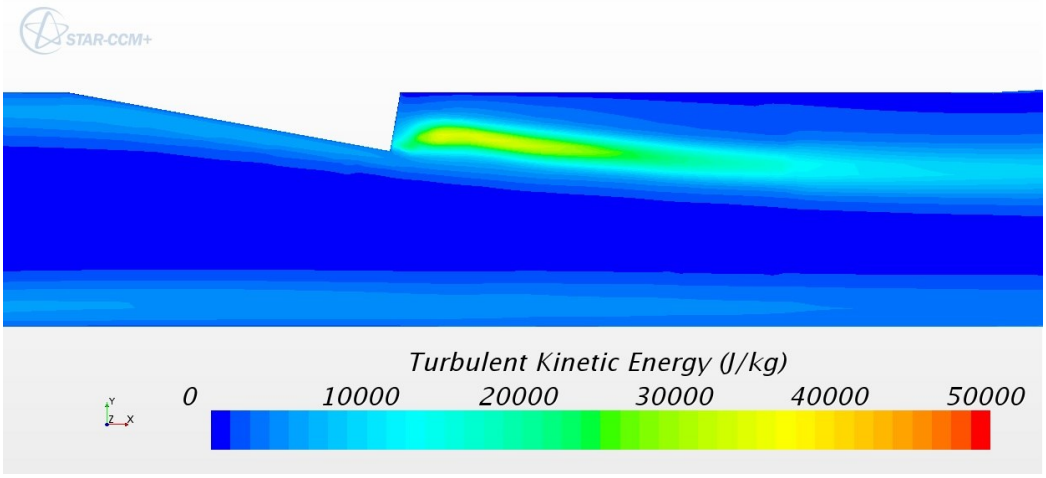

(c)

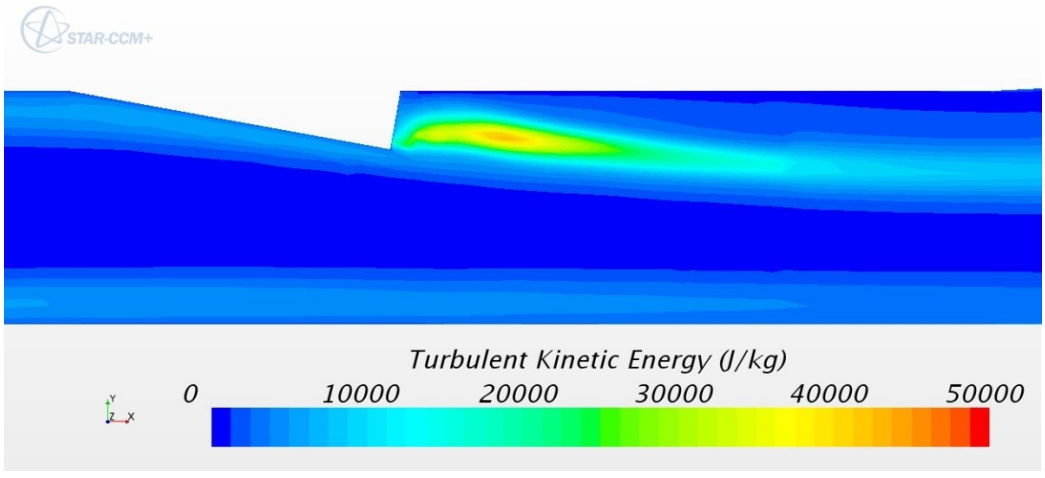

Figure 137 Turbulent kinetic energy plots on the centerline plane (z = 0) in the combustor for Configuration 5xr-TI
a) 5xr-V00, b) 5xr-V10-TI, c) 5xr-V20-TI

(d)

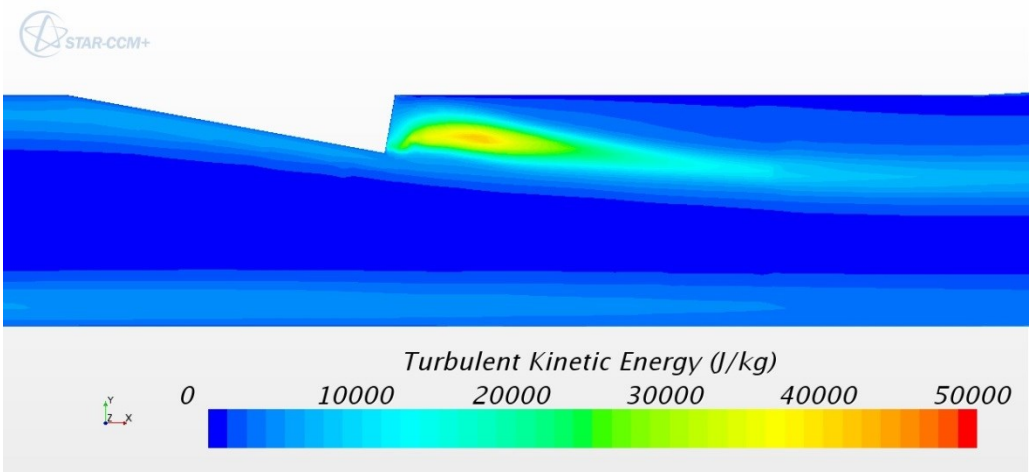

(e)

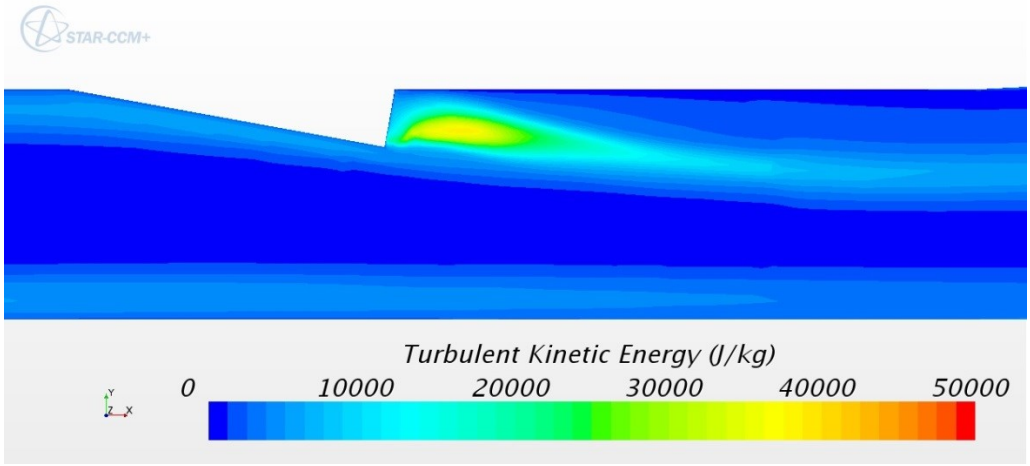

(f)

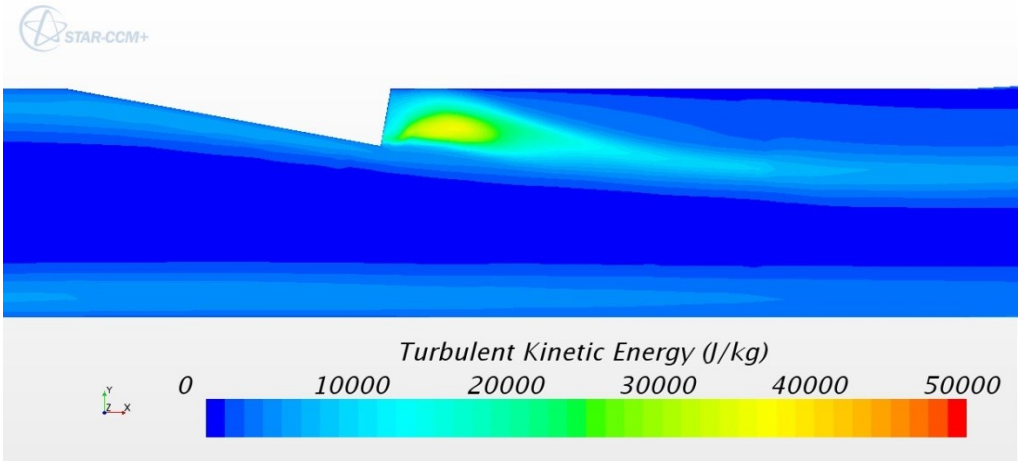

Figure 137 Turbulent kinetic energy plots on the centerline plane (z = 0) in the combustor for Configuration 5xr-TI
d) 5xr-V30-TI, e) 5xr-V40-TI, f) 5xr-V50-TI

(a)

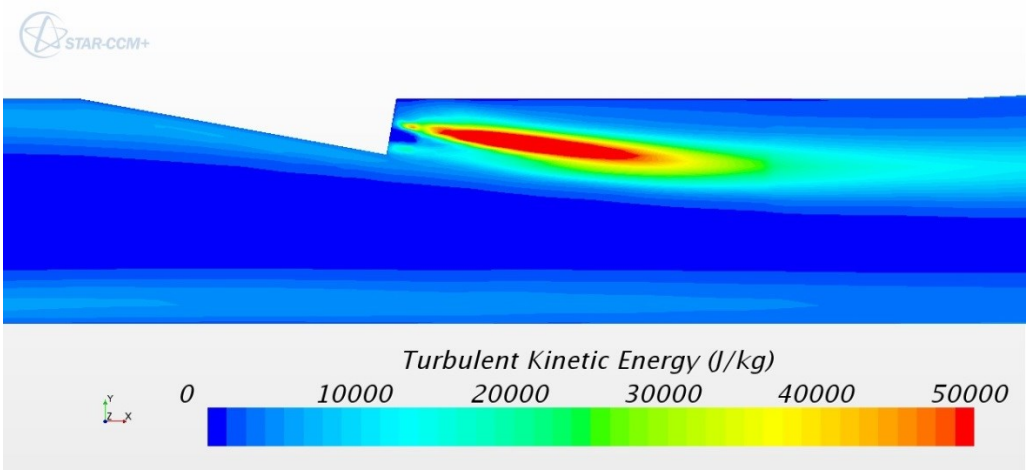

(b)

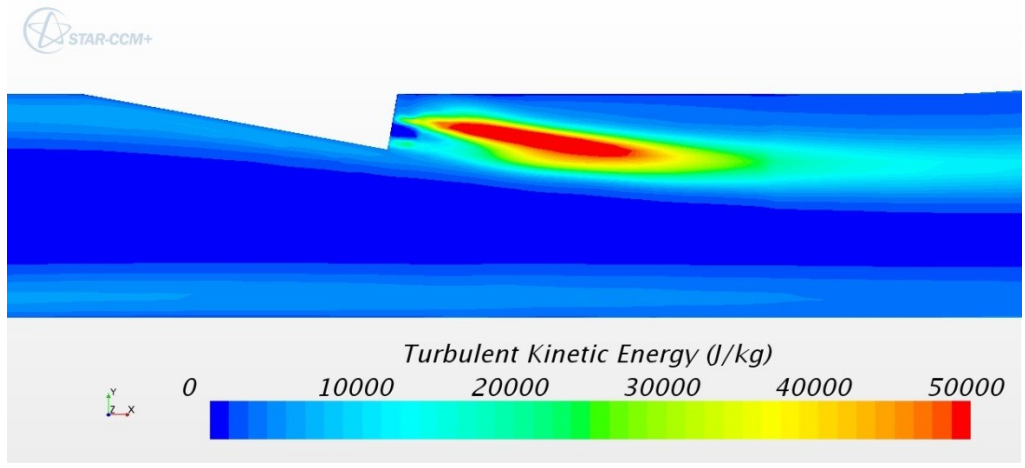

(c)

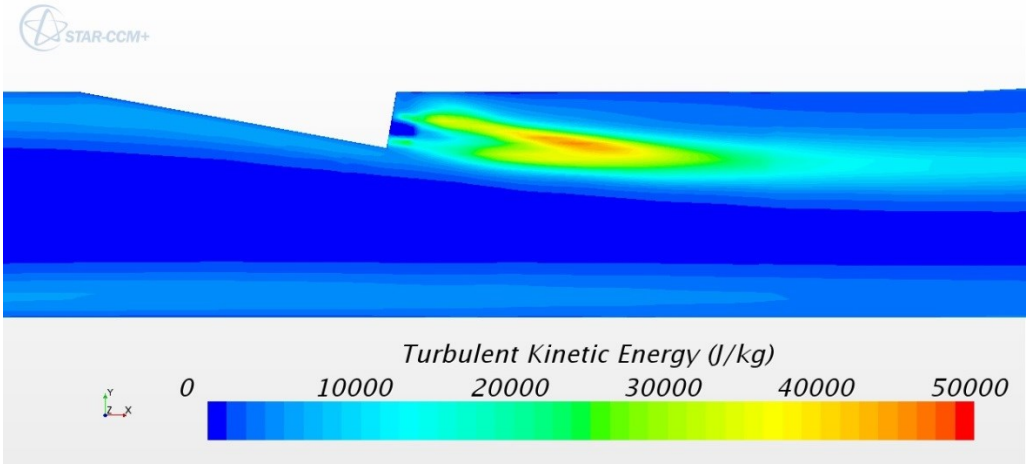

Figure 138 Turbulent kinetic energy plots on the fuel nozzle centerline plane (z = 2.5r) in the combustor for Configuration 5xr-TI
a) 5xr-V00, b) 5xr-V10-TI, c) 5xr-V20-TI

(d)

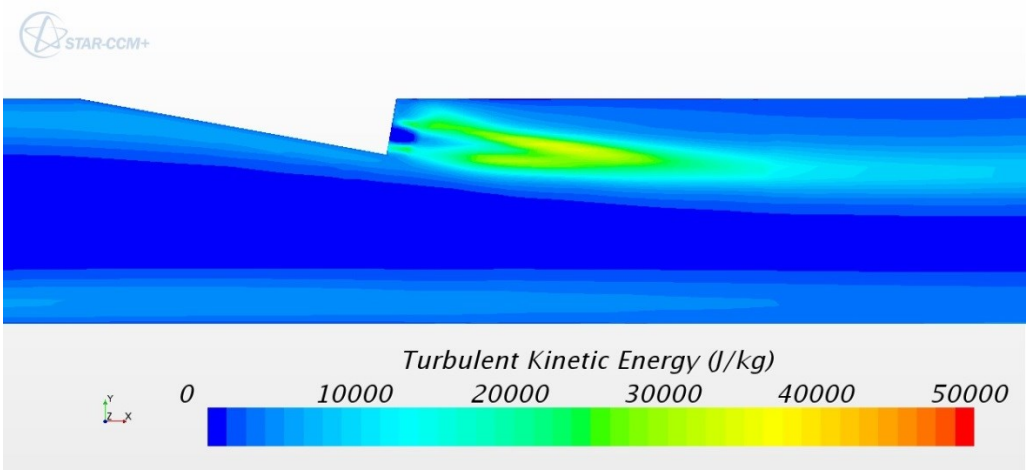

(e)

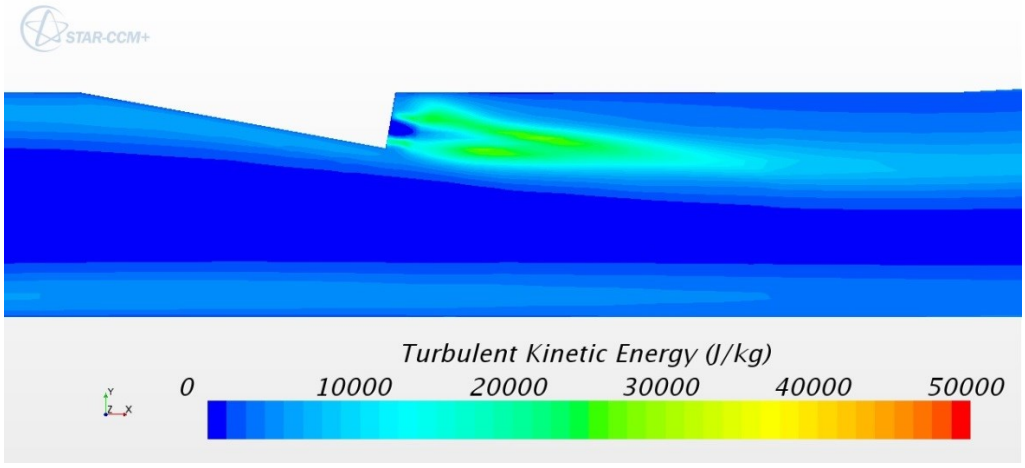

(f)

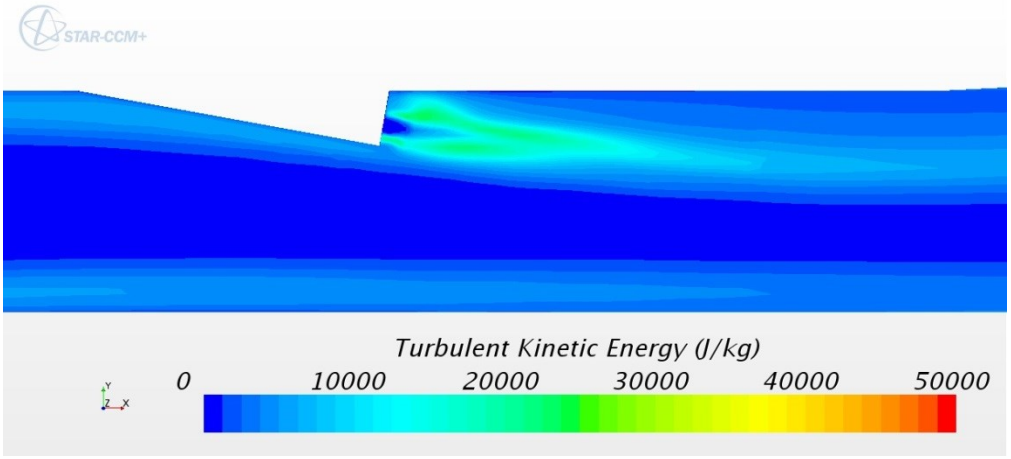

Figure 138 Turbulent kinetic energy plots on the fuel nozzle centerline plane (z = 2.5r) in the combustor for Configuration 5xr-TI
d) 5xr-V30-TI, e) 5xr-V40-TI, f) 5xr-V50-TI

a)

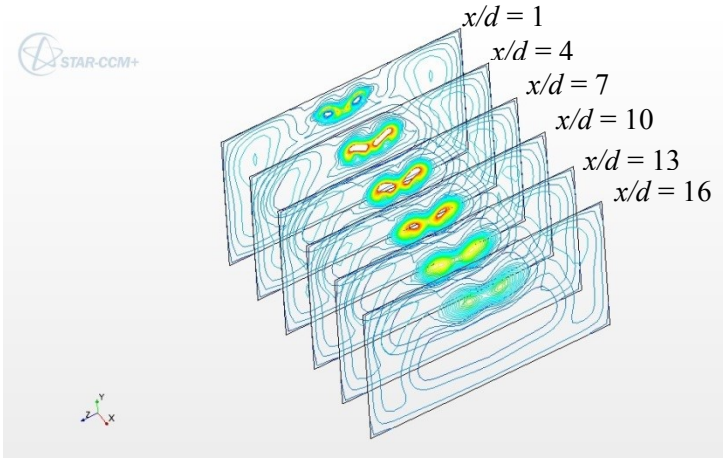

b)

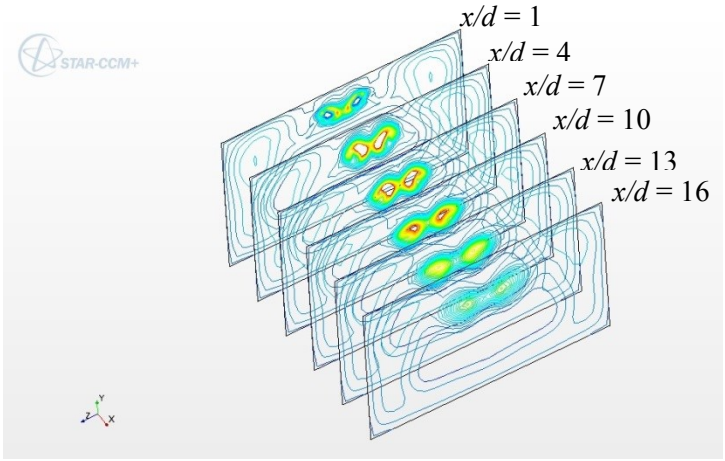

c)

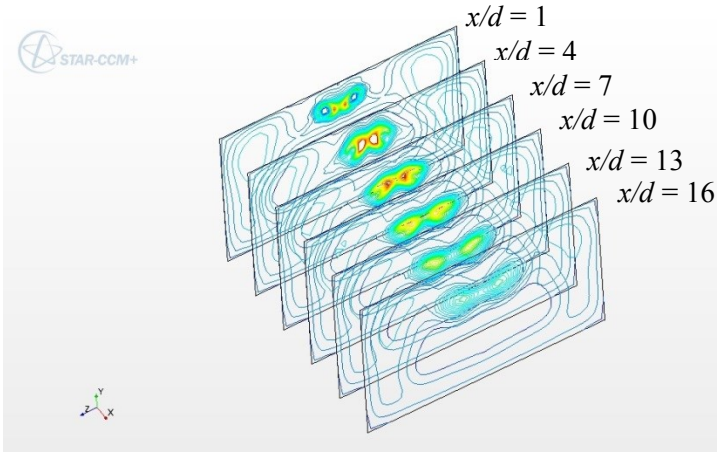

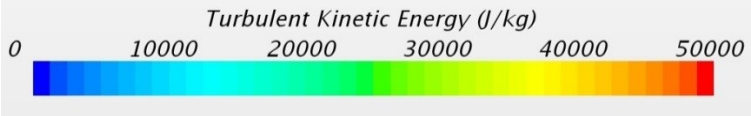

Figure 139 Turbulent kinetic energy contours in the combustor for Configuration 5xr-TI
a) 5xr-V00, b) 5xr-V10-TI, c) 5xr-V20-TI

d)

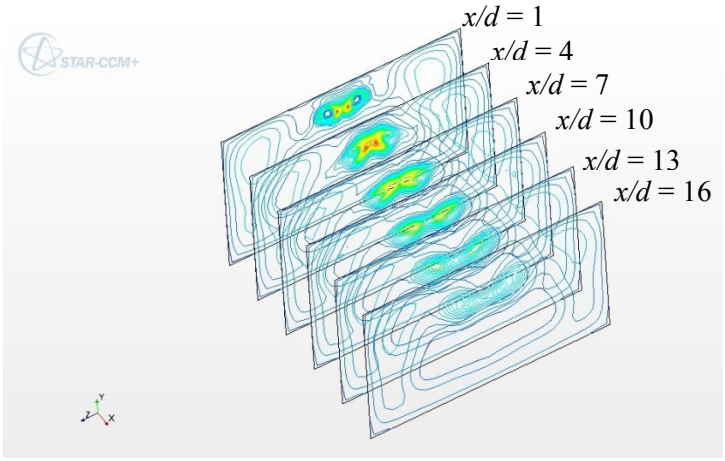

e)

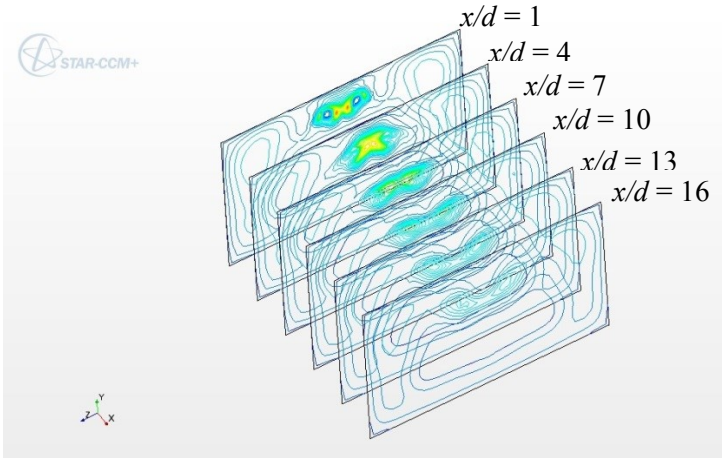

f)

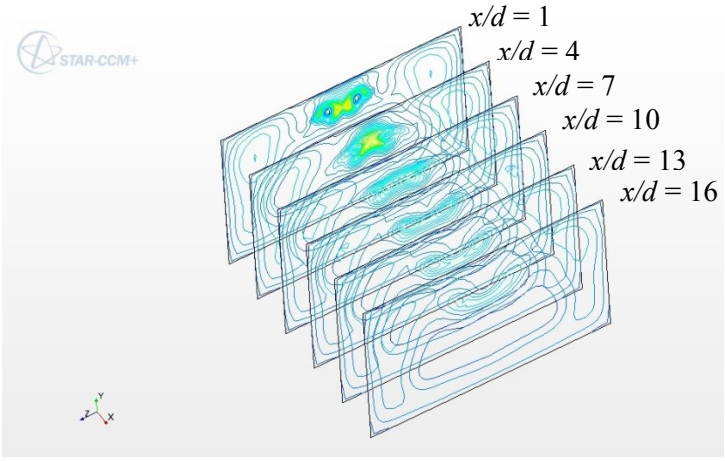

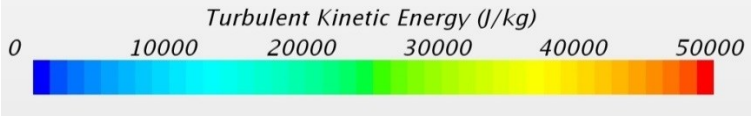

Figure 139 Turbulent kinetic energy contours in the combustor for Configuration 5xr-TI
d) 5xr-V30-TI, e) 5xr-V40-TI, f) 5xr-V50-TI

6.3.8 Distance Configuration 5xr, Swirl Pattern TO

Figure 140(a) shows the H_2O mole fraction contours on the fuel inlet and upper combustor walls for the non-swirling baseline case for the distance configuration 5xr. Once swirl is added to the non-swirling case three areas of high H_2O mole fraction zones develop on the fuel nozzle wall and none on the upper combustor wall. There are no indications that the high H_2O mole fraction zones formed on the fuel nozzle wall rotate as swirl increases. The high H_2O mole fraction zones on the fuel nozzle wall move outwards from the fuel injector exits and then moves unto the upper combustor wall. Finally the high H_2O mole fraction zone is eliminated from the fuel nozzle wall.

Figure 141 shows an interesting fluid dynamic phenomenon of the H_2 jets merging and then separating and then merging again.

Figure 142 shows temperature contours and the customary upside down heart shape of cooler temperature.

Turbulent kinetic energy is shown on the tunnel centerline (z = 0) in Figure 143 and on the right fuel injector centerline plane (z = 2.5r) in Figure 144. The flow through the tunnel is symmetrical for this swirl pattern. Therefore Figure 145 is the same for the right and left fuel jets. There are no high TKE zones on the tunnel centerline plane. The high TKE zones on the fuel jet centerline decrease with increasing swirl. re similar to those shown in Figure 79 for the single fuel jet configuration R2. Figure 145 shows a progression of contour plots of TKE.

Table 15 shows the start location and length of the high TKE zone, the burning efficiency and the increase in burning efficiency due to swirl. The results show a similar trend as the 3xr-TO configuration. One major difference is that the start location of the high TKE zone plateaus at 0.32*d* downstream of the fuel injector exit then the high TKE zone is eliminated. The high

TKE zone length increases with swirl, reaches a maximum of 8.83*d* and then decreases as more swirl is added to the fuel jet.

As with the other simulation cases increasing swirl increase the burning efficiency. Configuration 5xr-V50-TO resulted in an impressive 20.5% increase in burning efficiency compared to the case with no swirl.

Table 15 Mixing Data for Configuration 5xr-TO

	High Turbulent Kinetic Energy Zone			
Configuration	*Zone start location (x/d)*	*Zone Length (d)*	*Burning Efficiency, η_{burn}*	*$\Delta\ \eta_{burn}$ (%)*
5xr-V00	1.99	9.03	0.72	n/a
5xr-V10-TO	0.95	9.19	0.72	0.3
5xr-V20-TO	1.07	7.56	0.74	2.7
5xr-V30-TO	1.07	5.97	0.78	8.0
5xr-V40-TO	1.11	3.74	0.82	14.4
5xr-V50-TO	n/a	0.00	0.87	20.5

a)

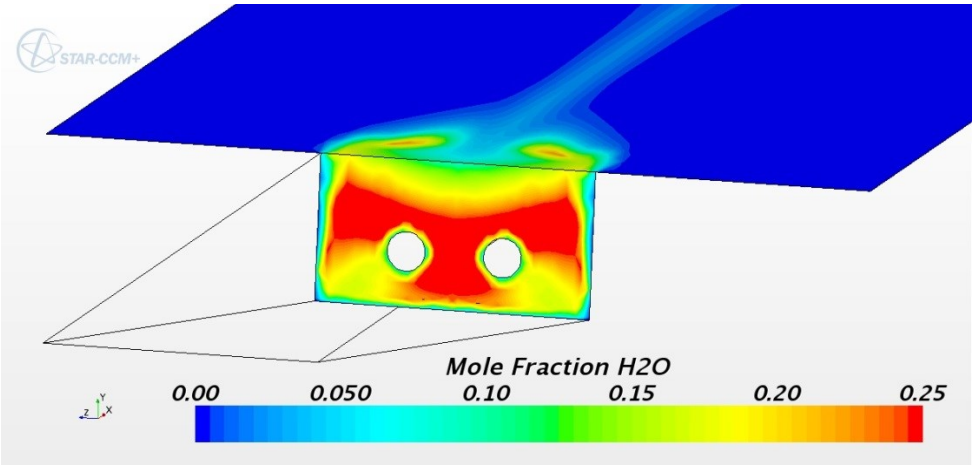

b)

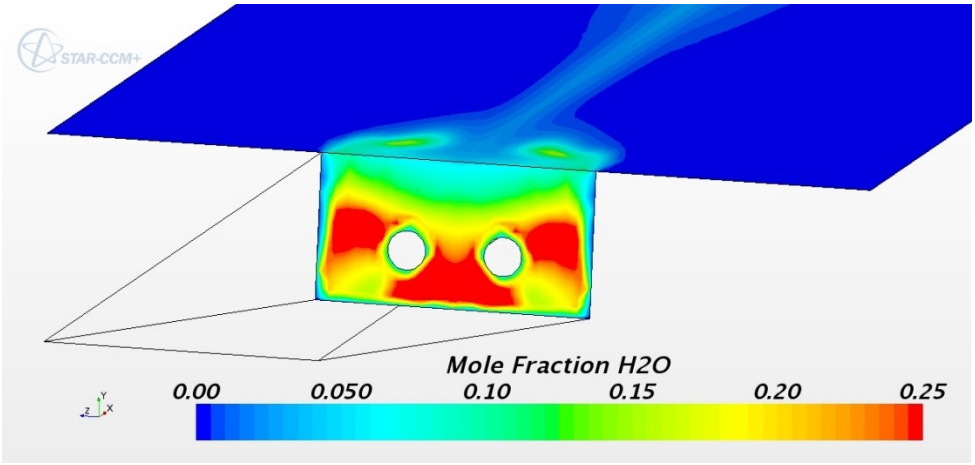

c)

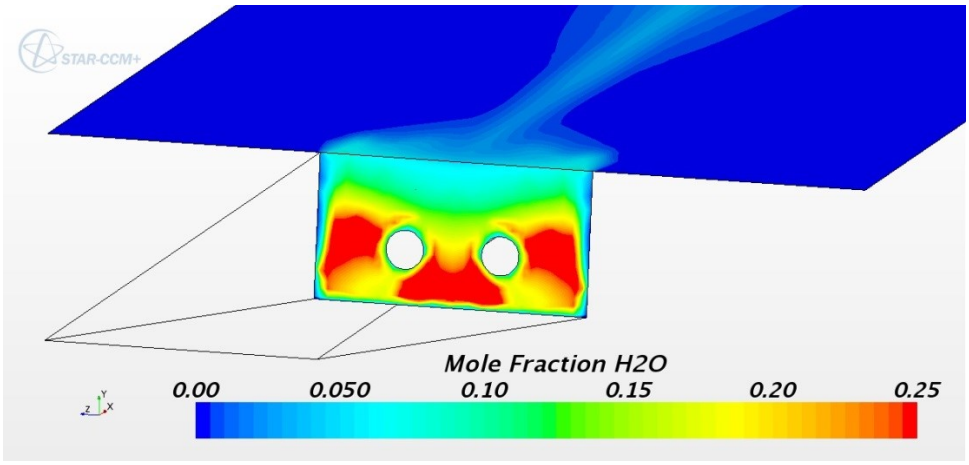

Figure 140 Mole fraction contours of H_2O on the fuel inlet wall and combustor upper wall for Configuration 5xr-TO
a) 5xr-V00, b) 5xr-V10-TO, c) 5xr-V20-TO

d)

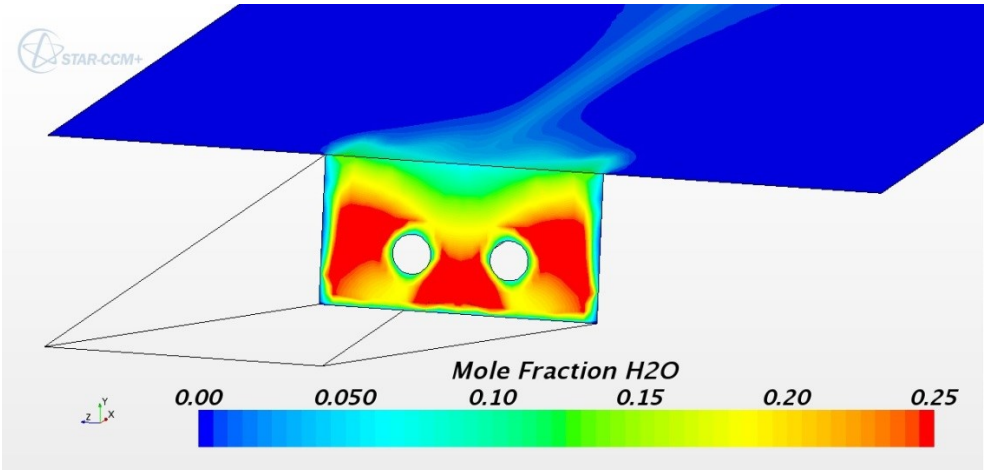

e)

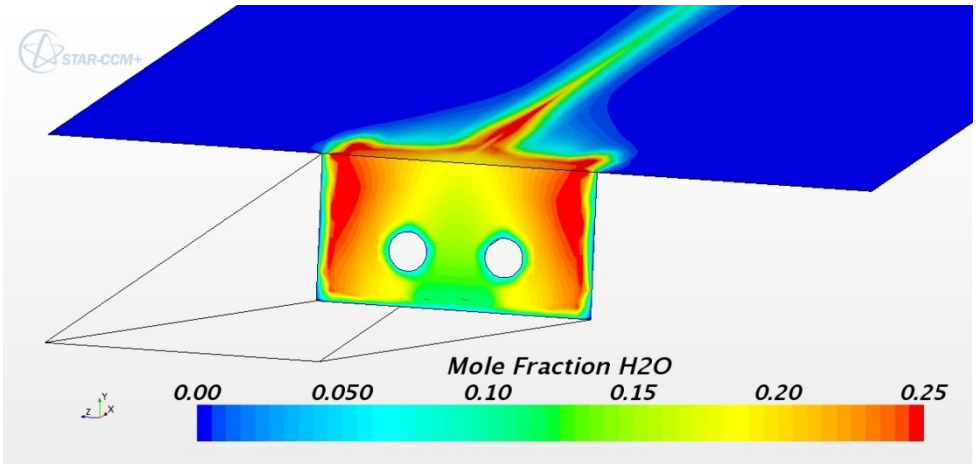

f)

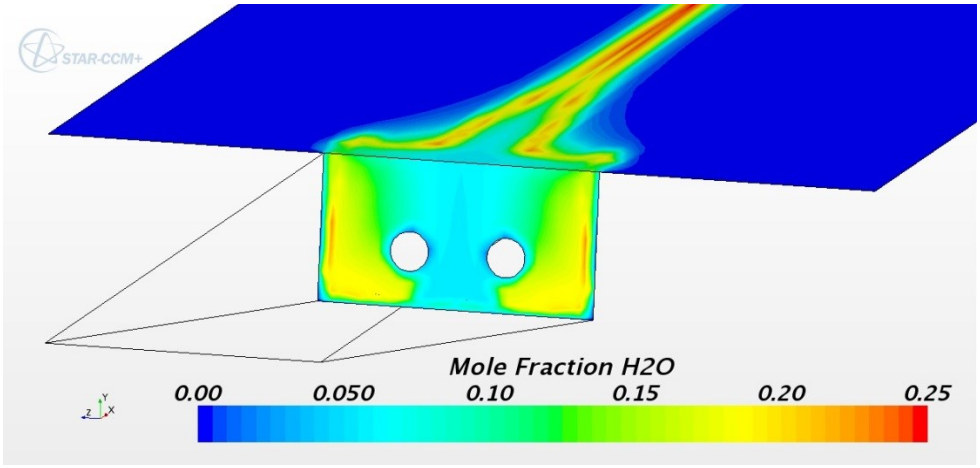

Figure 140 Mole fraction contours of H_2O on the fuel inlet wall and the combustor upper wall for Configuration 5xr-TO
d) 5xr-V30-TO, e) 5xr-V40-TO, f) 5xr-V50-TO

a)

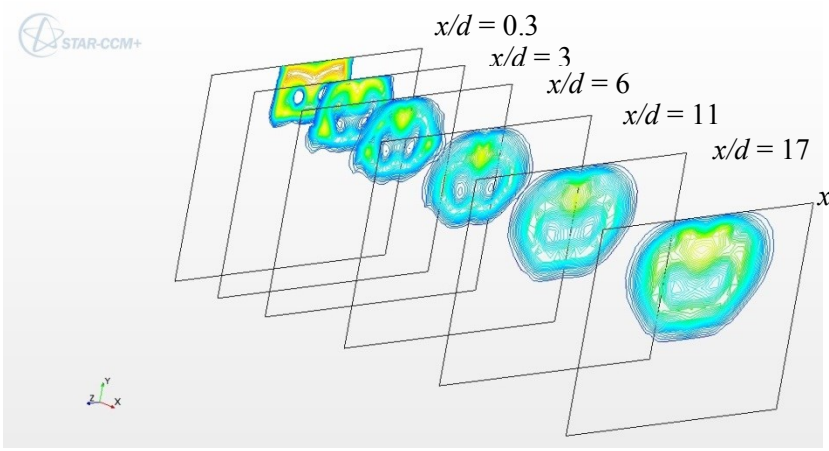

b)

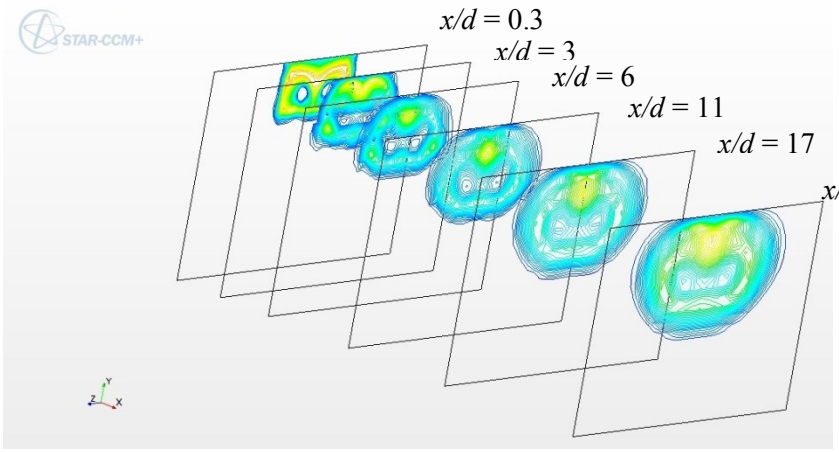

c)

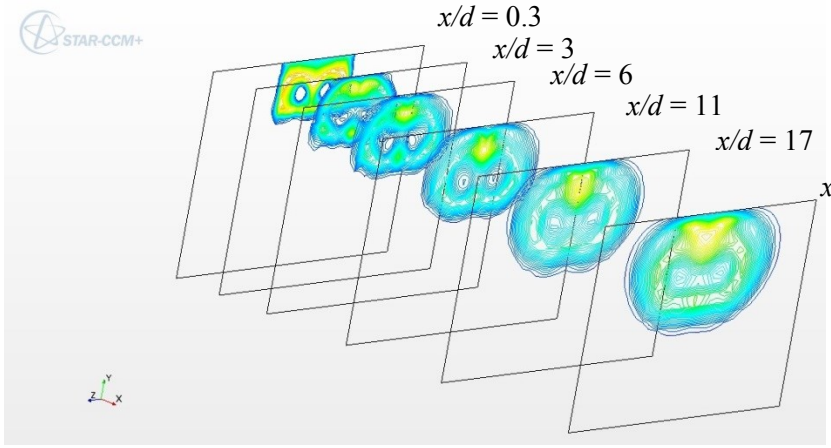

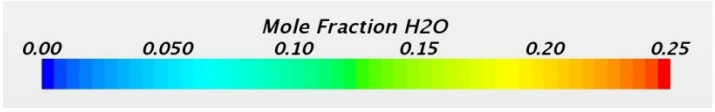

Figure 141 Mole fraction contours of H_2O in the combustor for Configuration 5xr-TO
a) 5xr-V00, b) 5xr-V10-TO, c) 5xr-V20-TO

d)

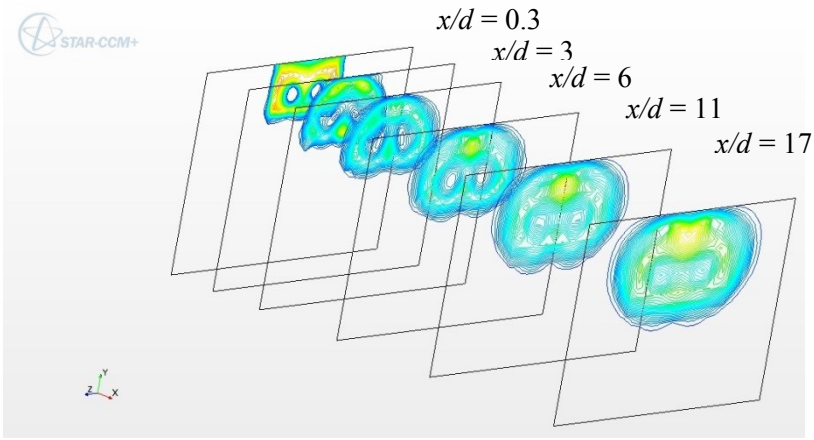

e)

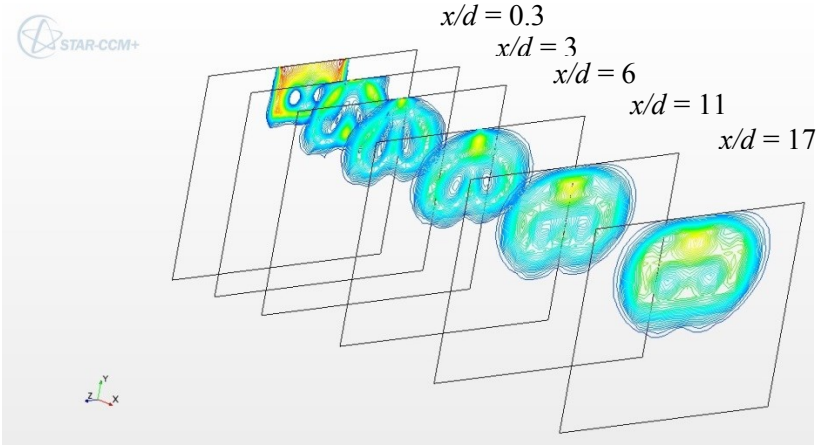

f)

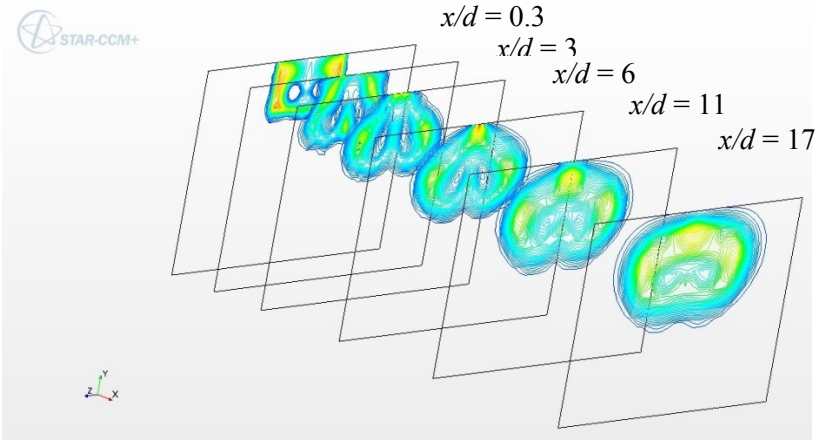

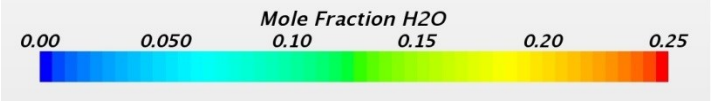

Figure 141 Mole fraction contours of H_2O in the combustor for Configuration 5xr-TO
d) 5xr-V30-TO, e) 5xr-V40-TO, f) 5xr-V50-TO

a)

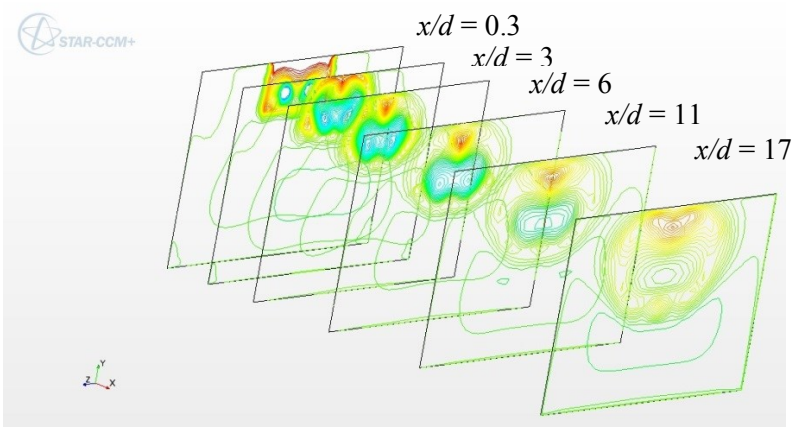

b)

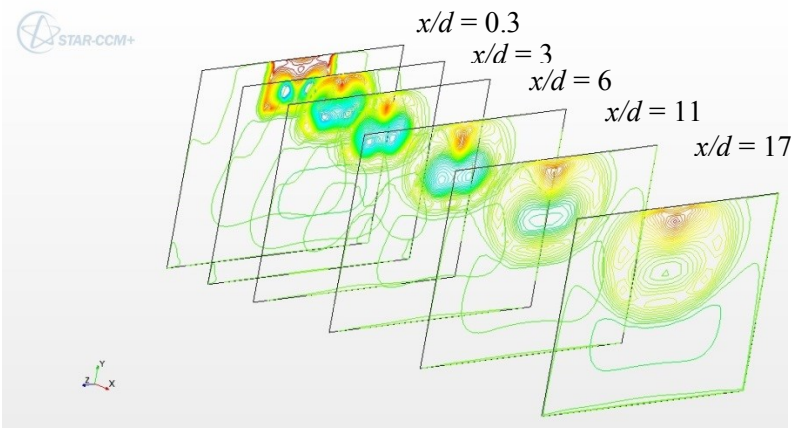

c)

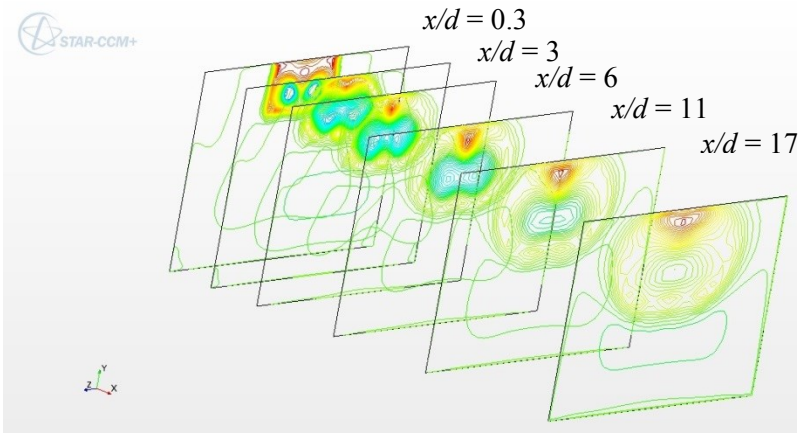

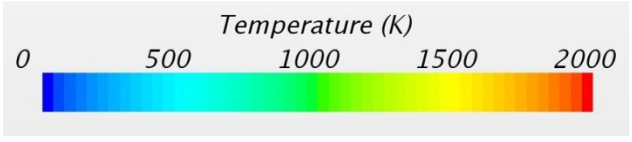

Figure 142 Temperature contours in the combustor for Configuration 5xr-TO
a) 5xr-V00, b) 5xr-V10-TO, c) 5xr-V20-TO

d)

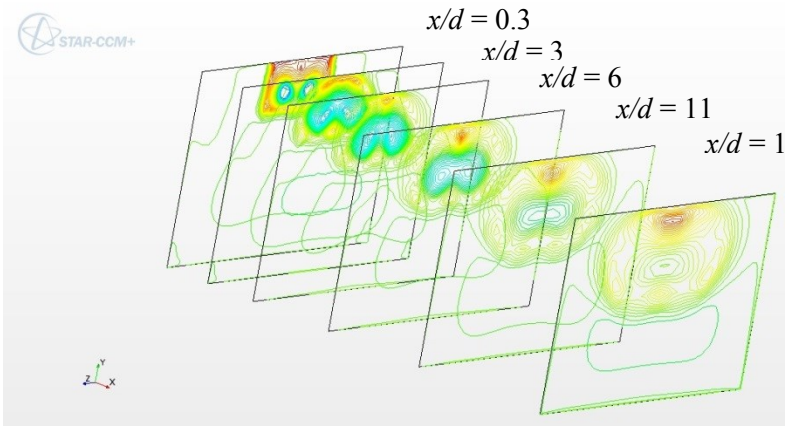

e)

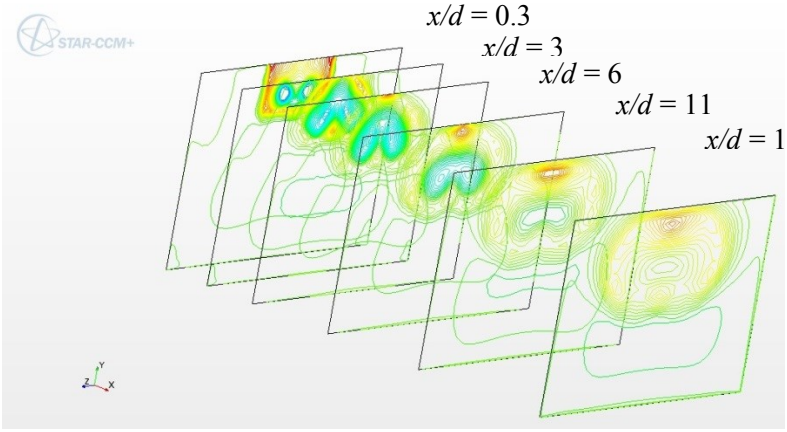

f)

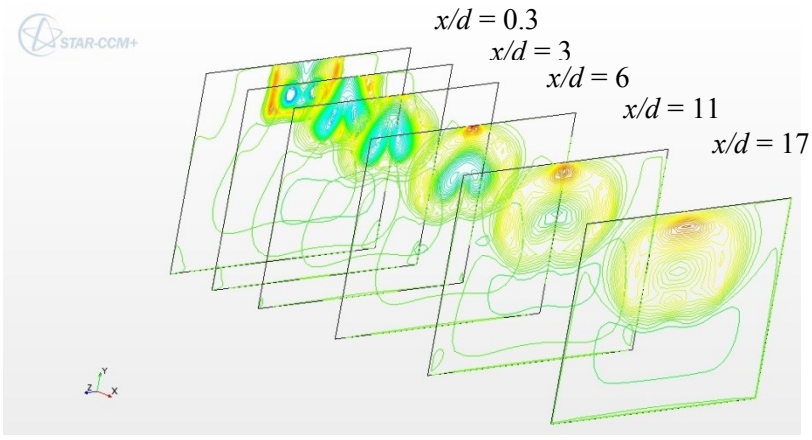

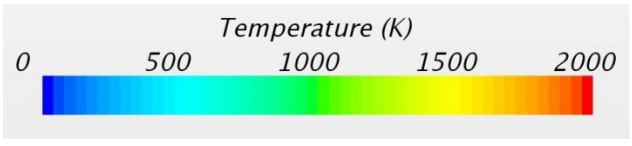

Figure 142 Temperature contours in the combustor for Configuration 5xr-TO
d) 5xr-V30-TO, e) 5xr-V40-TO, f) 5xr-V50-TO

(a)

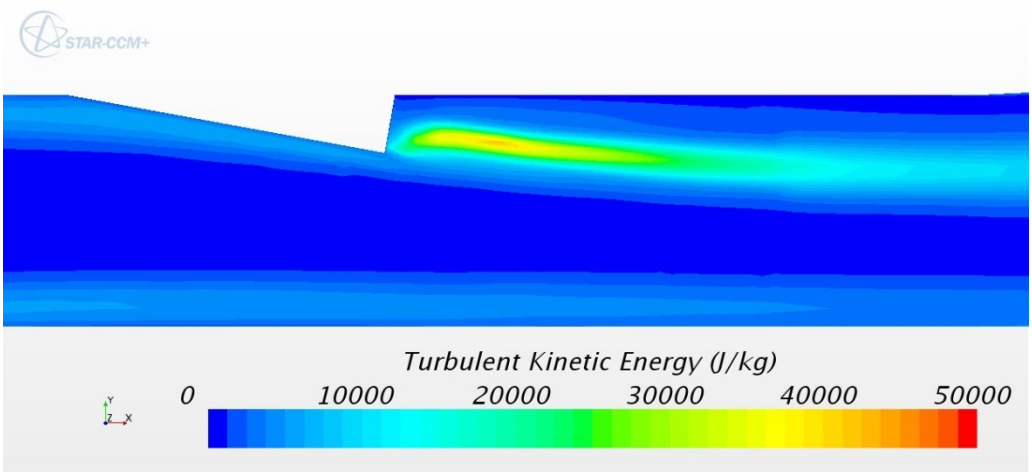

(b)

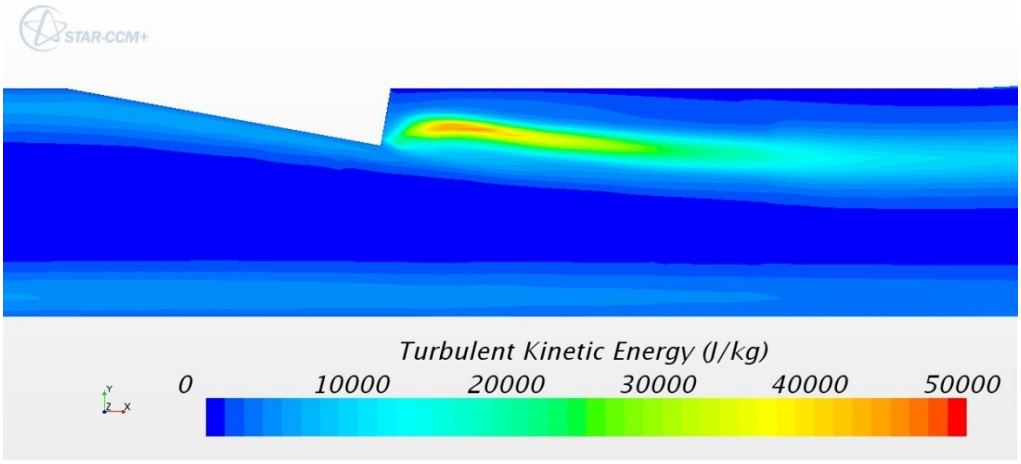

(c)

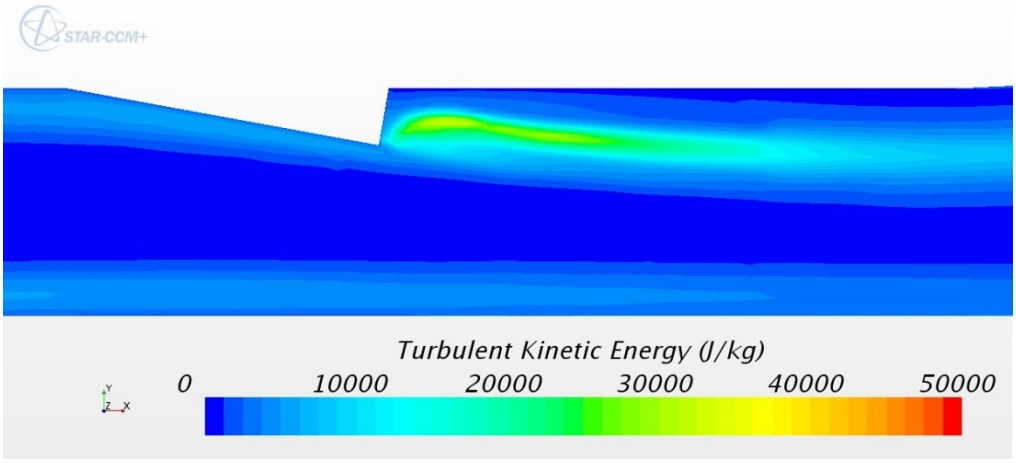

Figure 143 Turbulent kinetic energy plots on the centerline plane (z = 0) in the combustor for Configuration 5xr-TO
a) 5xr-V00, b) 5xr-V10-TO, c) 5xr-V20-TO

(d)

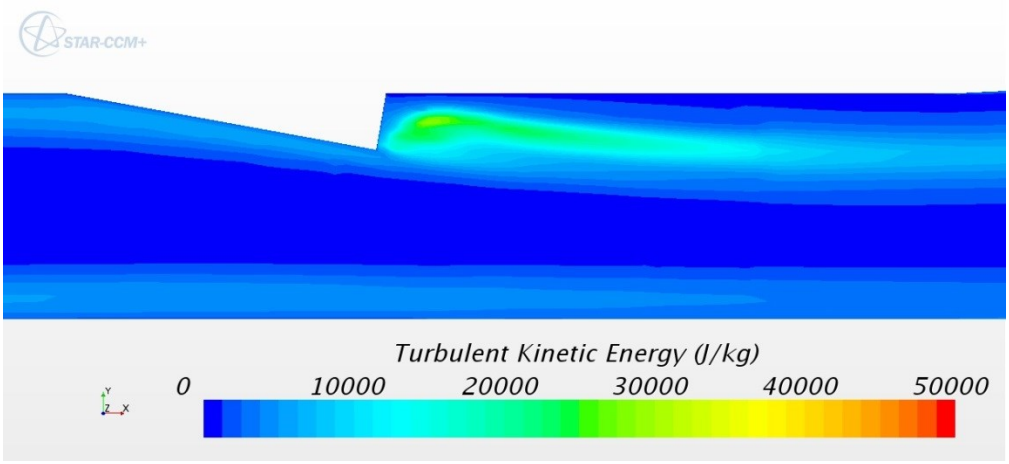

(e)

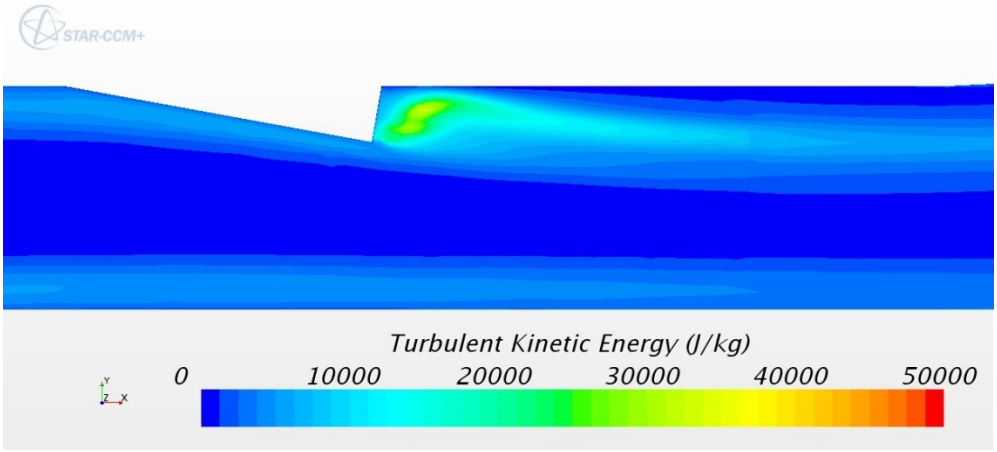

(f)

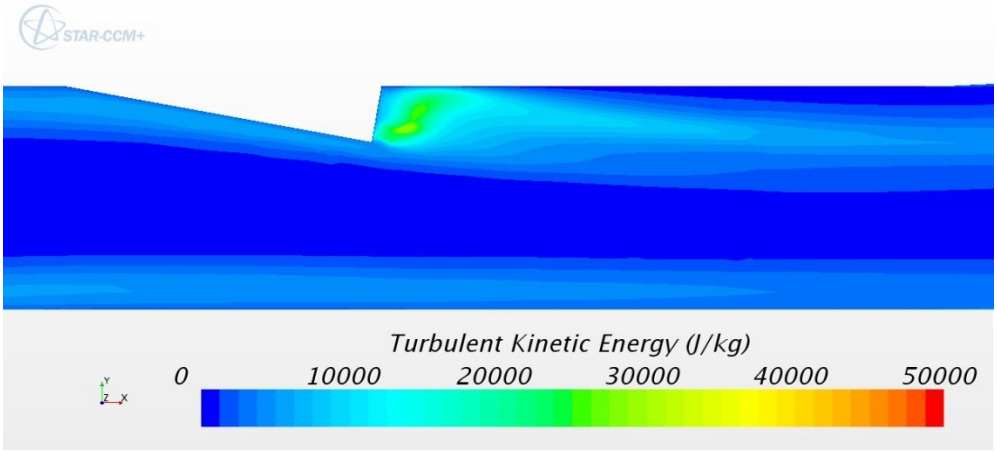

Figure 143 Turbulent kinetic energy plots on the centerline plane (z = 0) in the combustor for Configuration 5xr-TO
d) 5xr-V30-TO, e) 5xr-V40-TO, f) 5xr-V50-TO

(a)

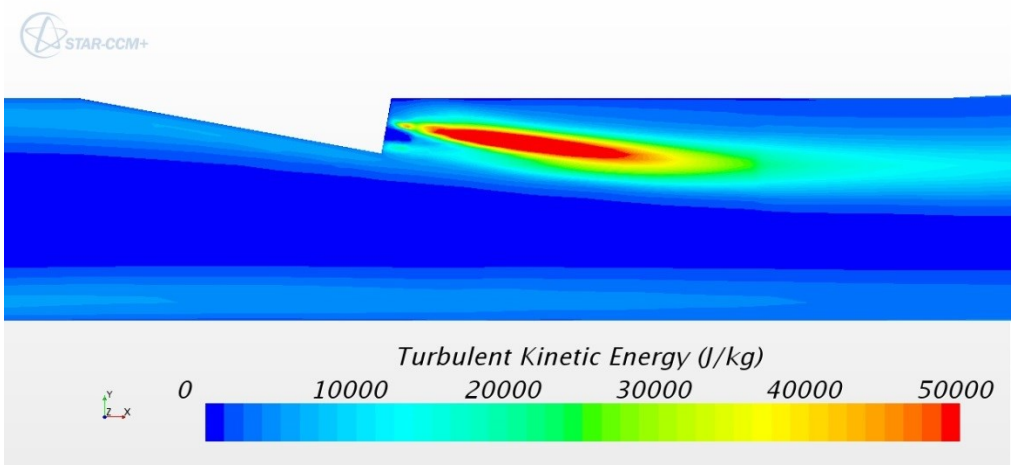

(b)

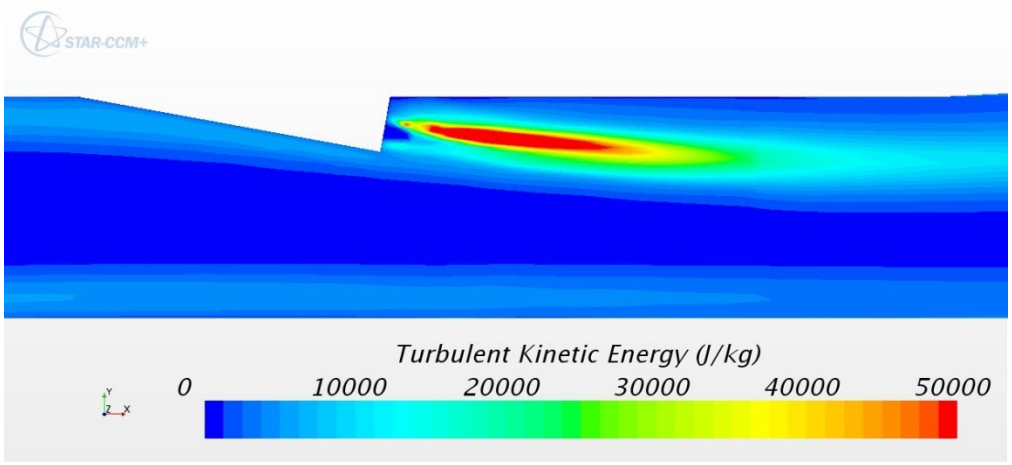

(c)

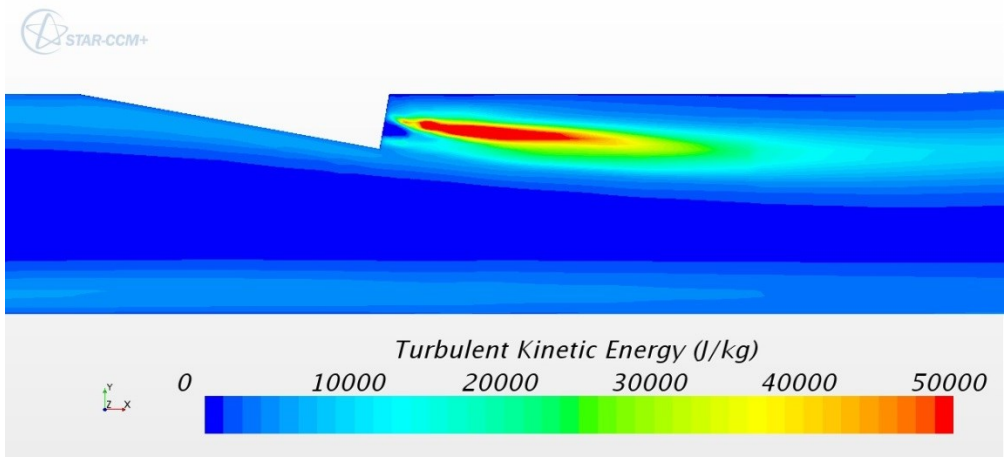

Figure 144 Turbulent kinetic energy plots on the fuel nozzle centerline plane (z = 2.5r) in the combustor for Configuration 5xr-TO
a) 5xr-V00, b) 5xr-V10-TO c) 5xr-V20-TO

(d)

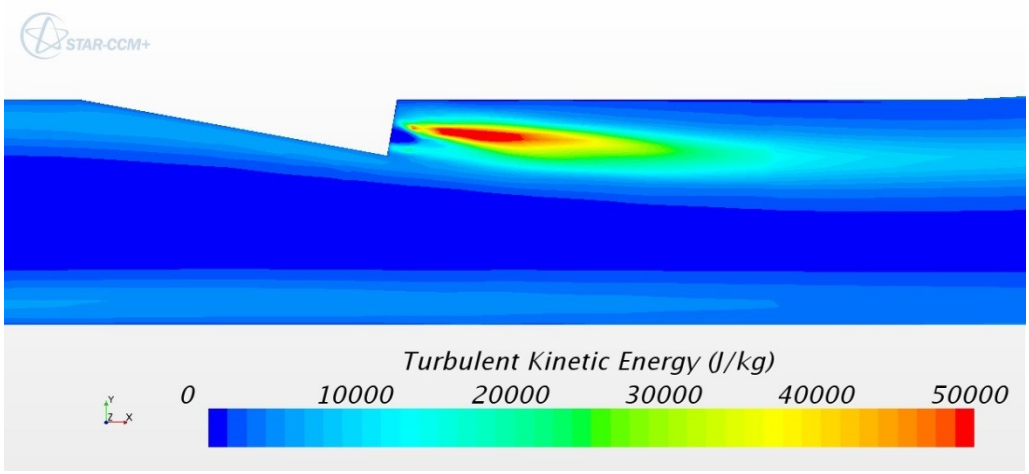

(e)

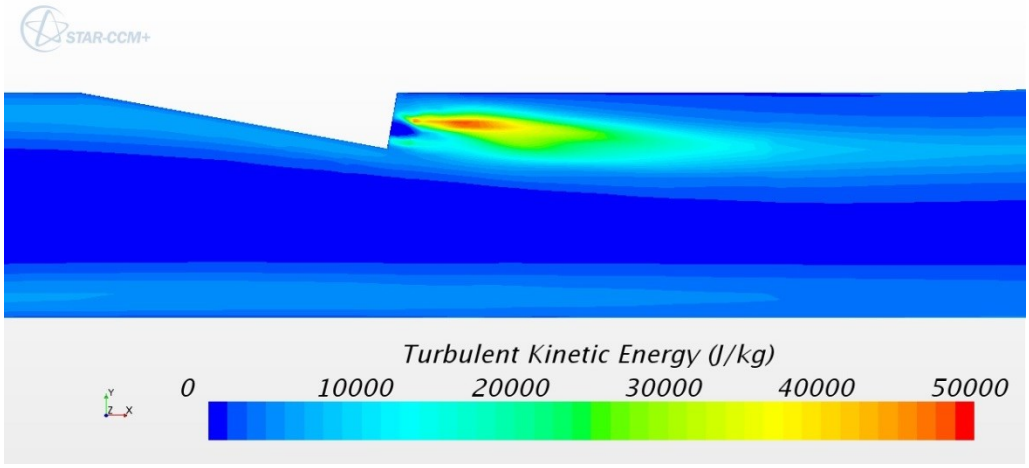

(f)

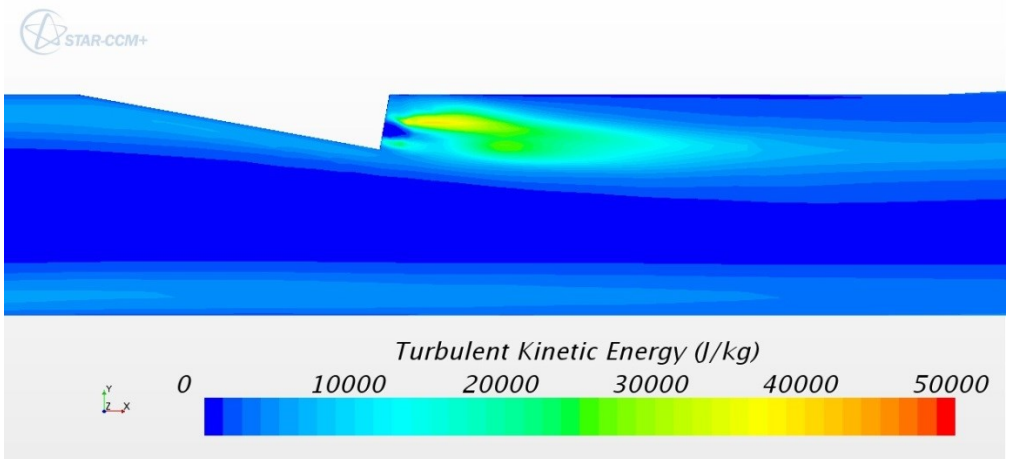

Figure 145 Turbulent kinetic energy plots on the fuel nozzle centerline plane (z = 2.5r) in the combustor for Configuration 5xr-TO
d) 5xr-V30-TO, e) 5xr-V40-TO, f) 5xr-V50-TO

a)

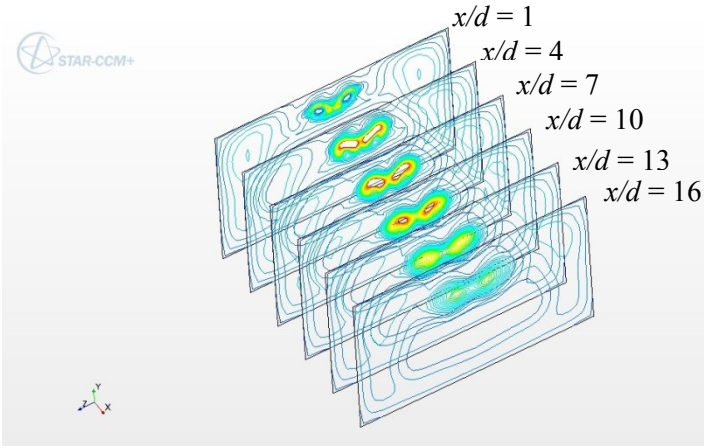

b)

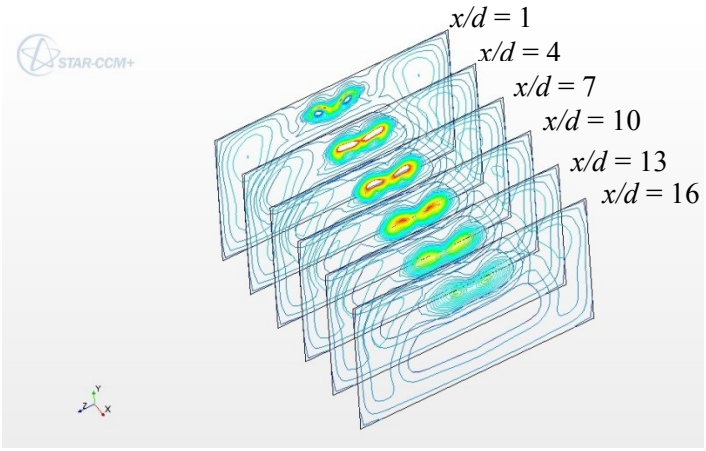

c)

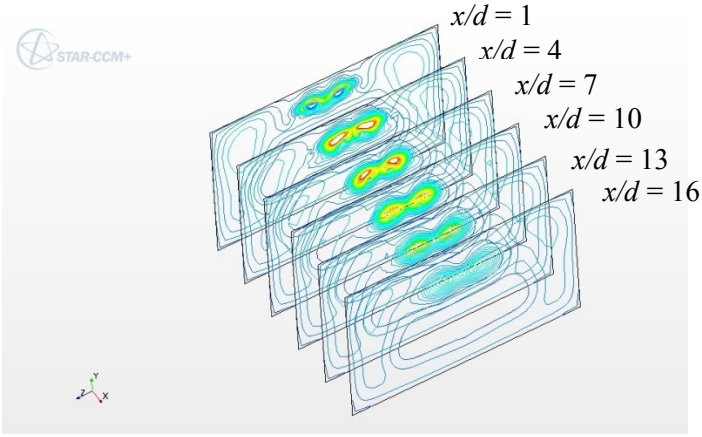

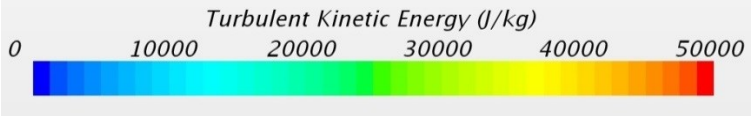

Figure 145 Turbulent kinetic energy contours in the combustor for Configuration 5xr-TO
a) 5xr-V00, b) 5xr-V10-TO, c) 5xr-V20-TO

d)

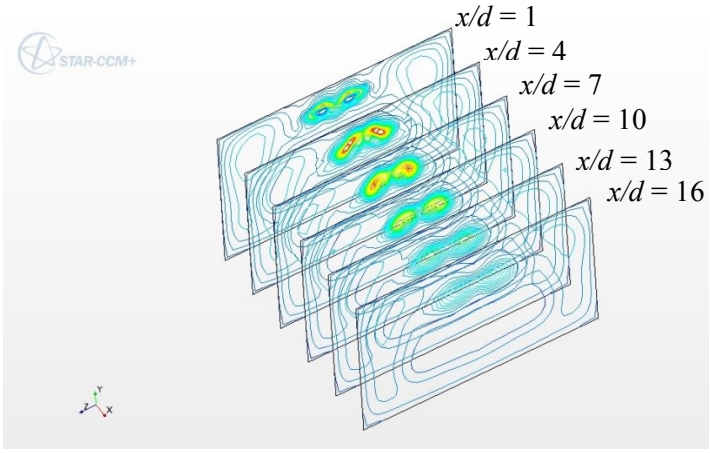

e)

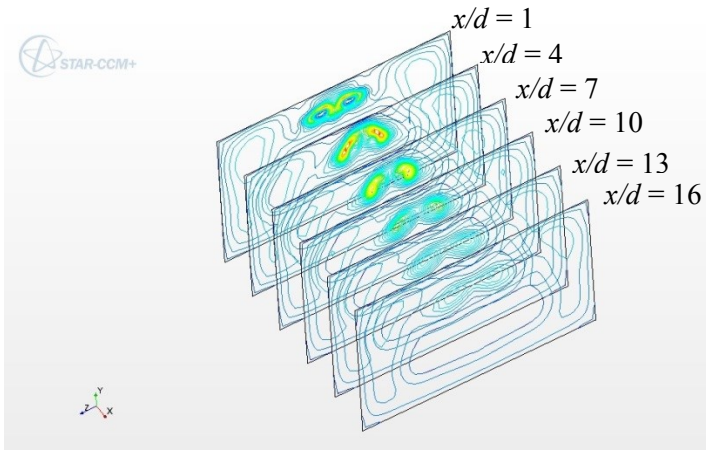

f)

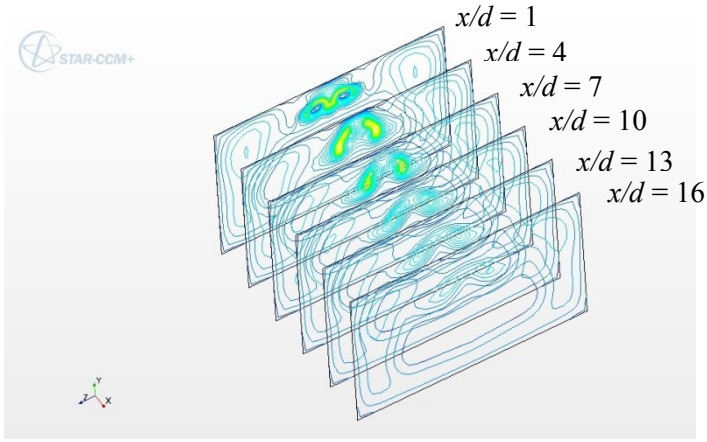

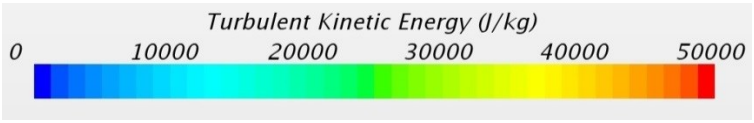

Figure 145 Turbulent kinetic energy contours in the combustor for Configuration 5xr-TO
d) 5xr-V30-TO, e) 5xr-V40-TO, f) 5xr-V50-TO

6.3.9 Distance Configuration 5xr, Swirl Pattern SD

Figure 146(a) shows the H_2O mole fraction contours on the fuel inlet and upper combustor walls for the non-swirling baseline case for the distance configuration 5xr. The high H_2O mole fraction zones on the fuel nozzle wall rotate as swirl increases and then moves unto the upper combustor wall.

Contour plots showing the progression of the H_2O mole fraction in the combustor are shown in Figure 147. Increasing the swirl lengthens the distance over which the fuel jets merge into one. Temperature contours are shown in Figure 148.

Turbulent kinetic energy is shown on the left fuel injector centerline plane (z = -2.5r) in Figure 149, on the tunnel centerline (z = 0) in Figure 150 and on the right fuel injector centerline plane (z = 2.5r) in Figure 151. Figure 152 shows a progression of contour plots of TKE. At first there are two high TKE zones. The high TKE zone on the left side decreases as the swirl increases. Figure 114(e) shows only one high TKE zone at $x/d = 4$.

Table 16 shows the start location and length of the high TKE zone, the burning efficiency and the increase in burning efficiency due to swirl. The results show a similar trend as the 3xr-SD configuration. One major difference is that the start location of the high TKE zone plateaus at 0.24*d* downstream of the fuel injector exit and the start location of the high TKE zone increases with additional swirl. The high TKE zone length increases with swirl, reaches a maximum of 9.79*d* and then decreases as more swirl is added to the fuel jet.

As with the other simulation cases increasing swirl increased the burning efficiency. Configuration 5xr-V50-SD resulted in an impressive 21.9% increase in burning efficiency compared to the case with no swirl.

Table 16 Mixing Data for Configuration 5xr-SD

	High Turbulent Kinetic Energy Zone			
Configuration	*Zone start location (x/d)*	*Zone Length (d)*	*Burning Efficiency,* η_{burn}	$\Delta\ \eta_{burn}$ *(%)*
5xr-V00	1.99	9.03	0.72	n/a
5xr-V10-SD	0.91	9.79	0.73	1.9
5xr-V20-SD	0.80	8.75	0.75	4.7
5xr-V30-SD	0.64	7.20	0.79	9.4
5xr-V40-SD	1.15	3.90	0.83	15.3
5xr-V50-SD	n/a	0.00	0.88	21.9

a)

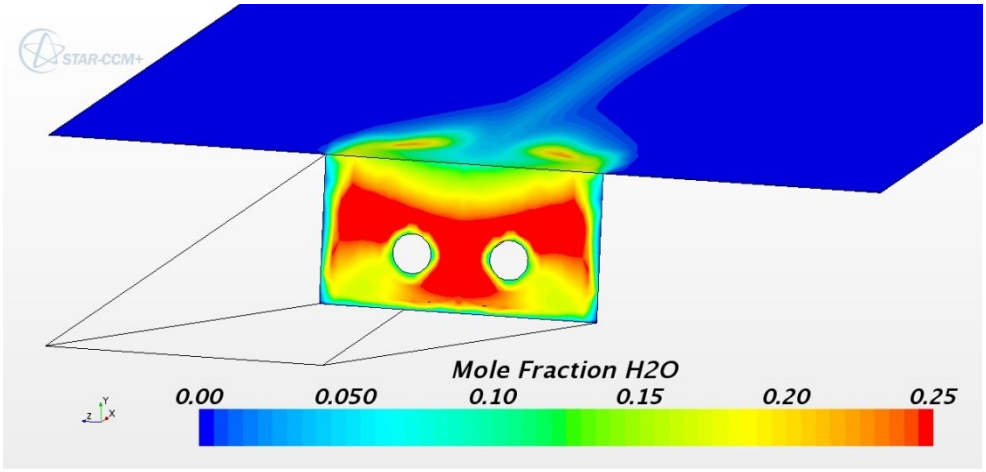

b)

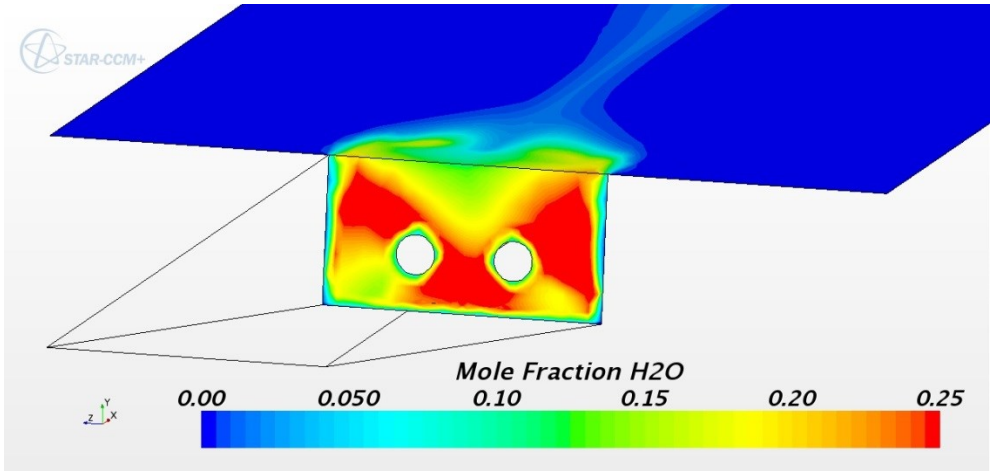

c)

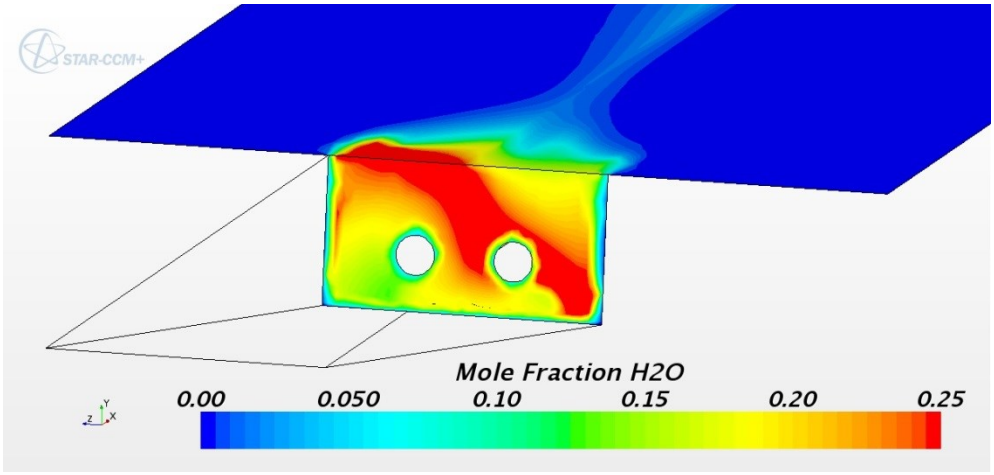

Figure 146 Mole fraction contours of H_2O on the fuel inlet wall and combustor upper wall for Configuration 5xr-SD
a) 5xr-V00, b) 5xr-V10-SD, c) 5xr-V20-SD

d)

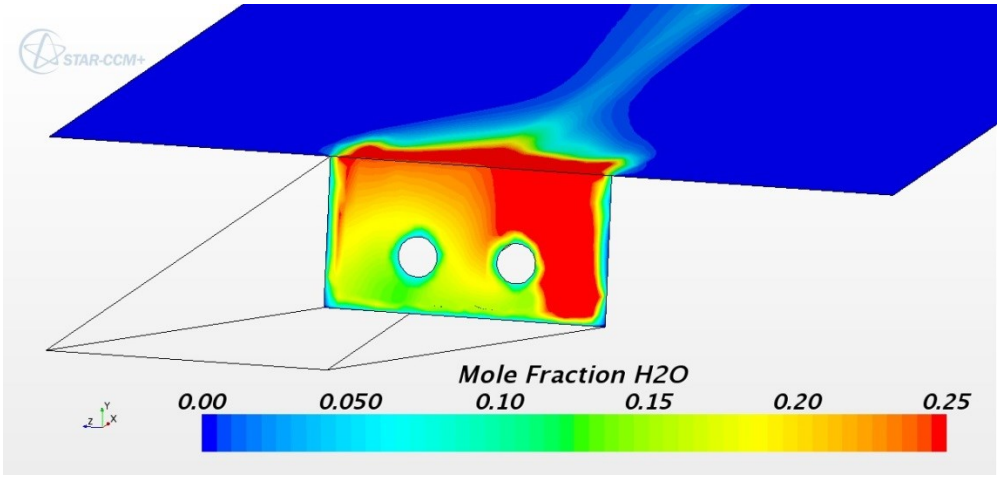

e)

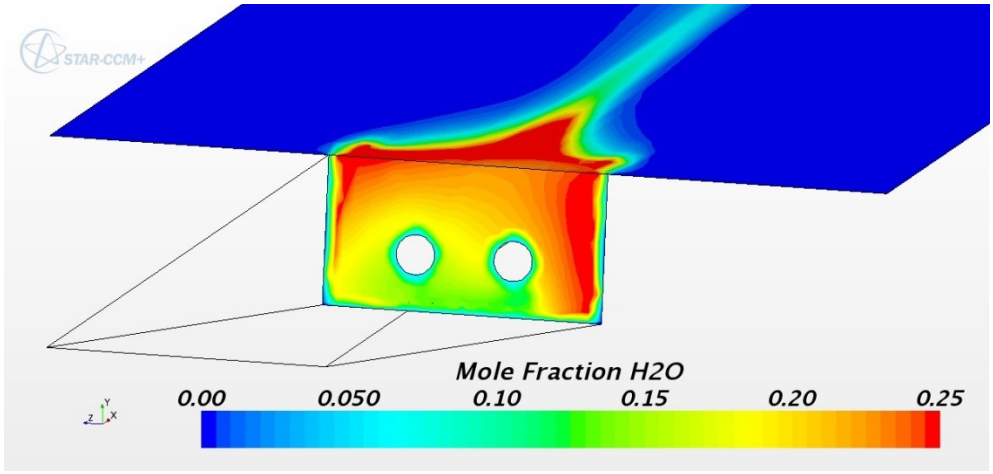

f)

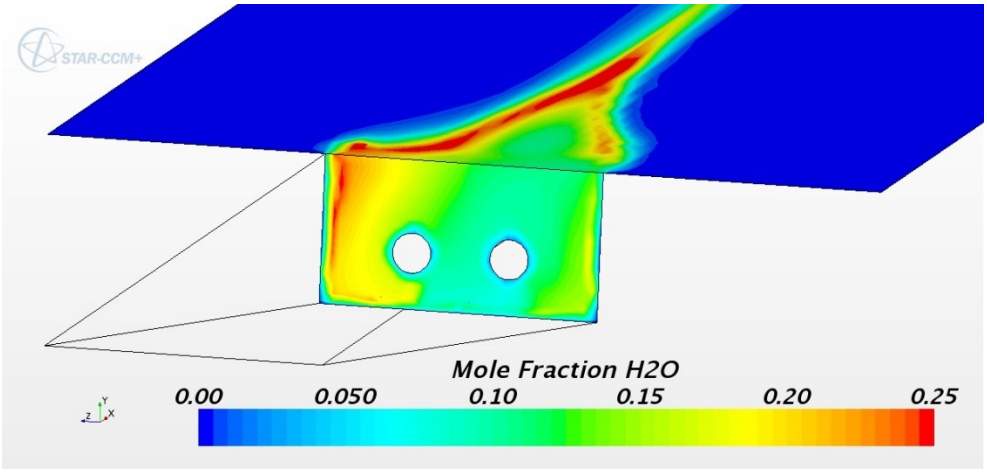

Figure 146 Mole fraction contours of H_2O on the fuel inlet wall and the combustor upper wall for Configuration 5xr-SD
d) 5xr-V30-SD, e) 5xr-V40-SD, f) 5xr-V50-SD

a)

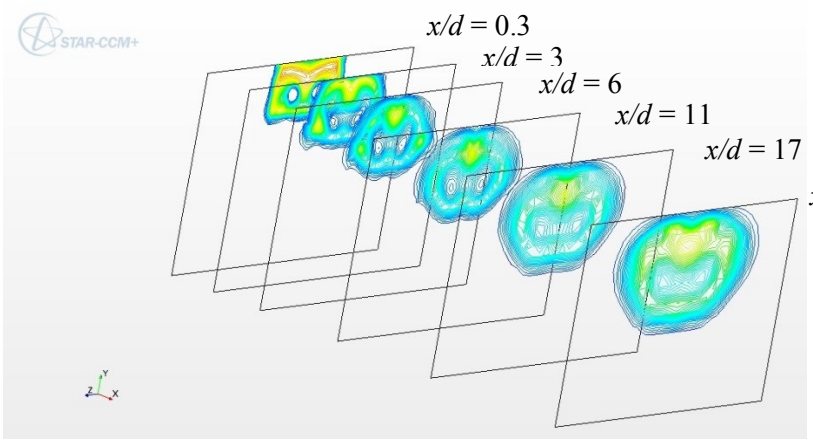

b)

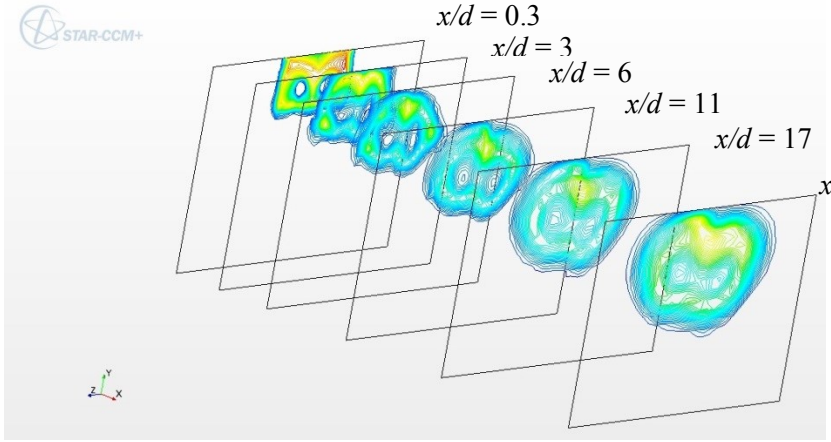

c)

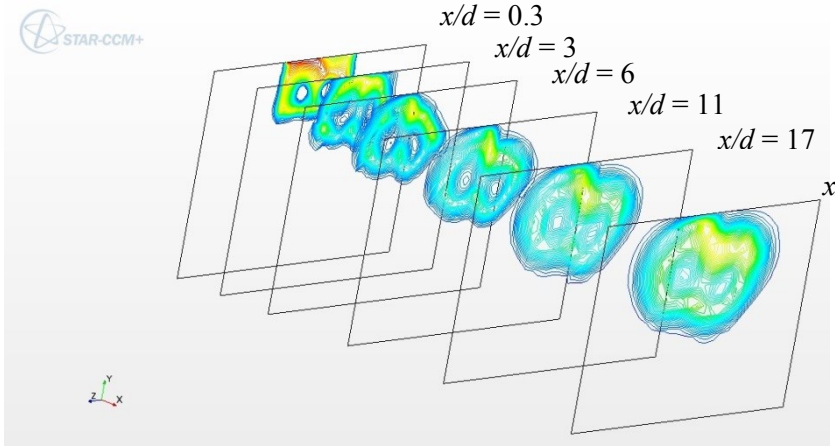

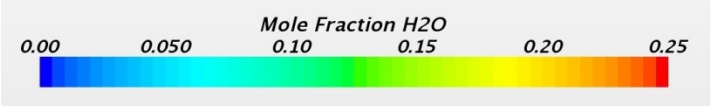

Figure 147 Mole fraction contours of H_2O in the combustor for Configuration 5xr-SD
a) 5xr-V00, b) 5xr-V10-SD, c) 5xr-V20-SD

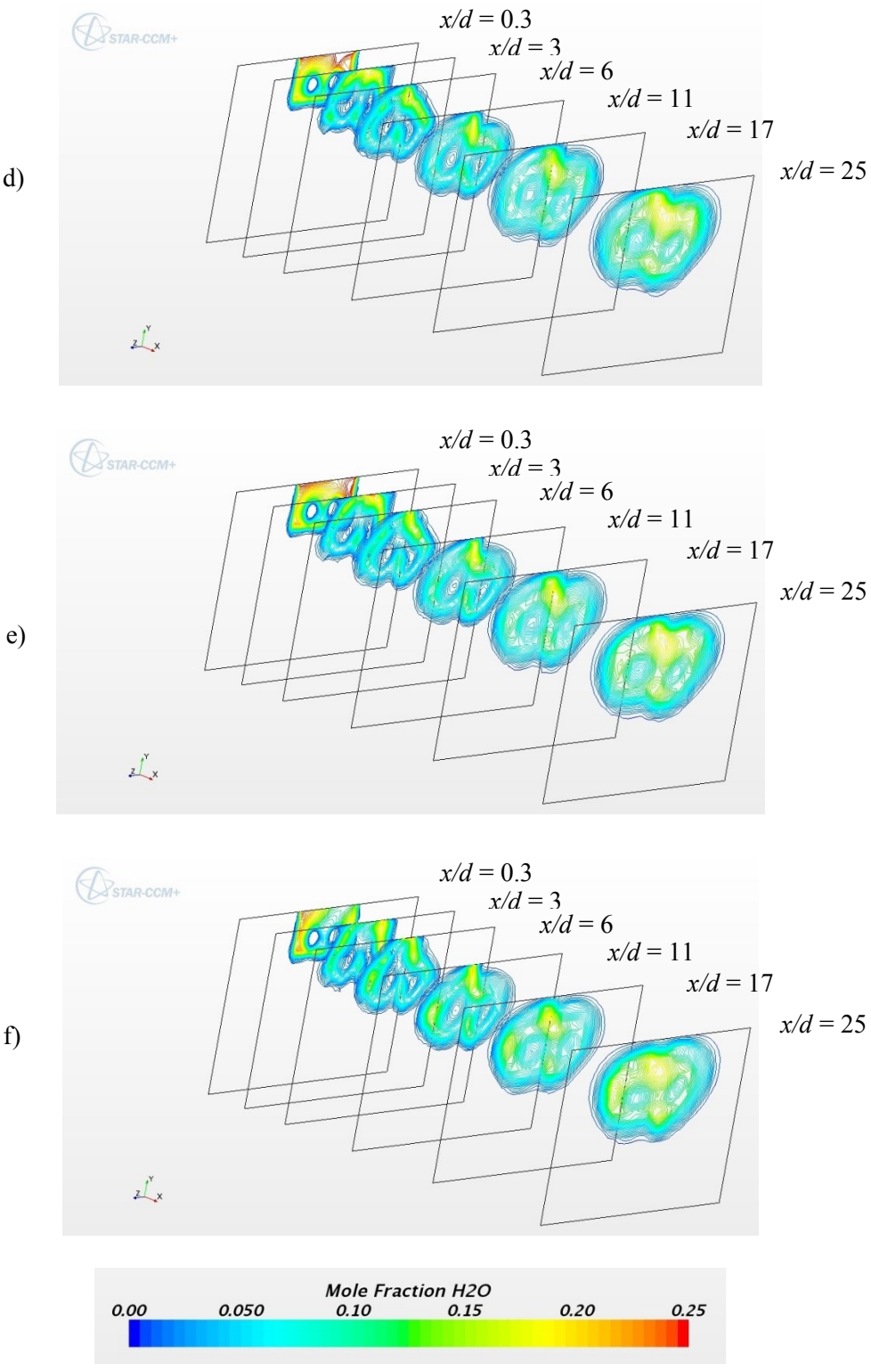

Figure 147 Mole fraction contours of H_2O in the combustor for Configuration 5xr-SD
d) 5xr-V30-SD, e) 5xr-V40-SD, f) 5xr-V50-SD

a)

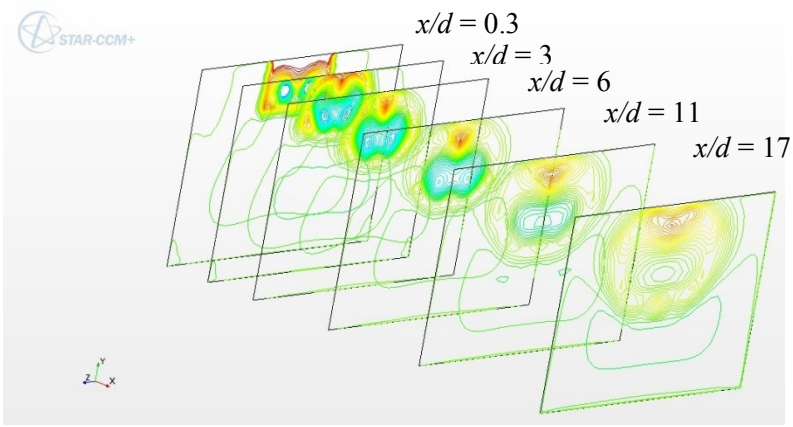

b)

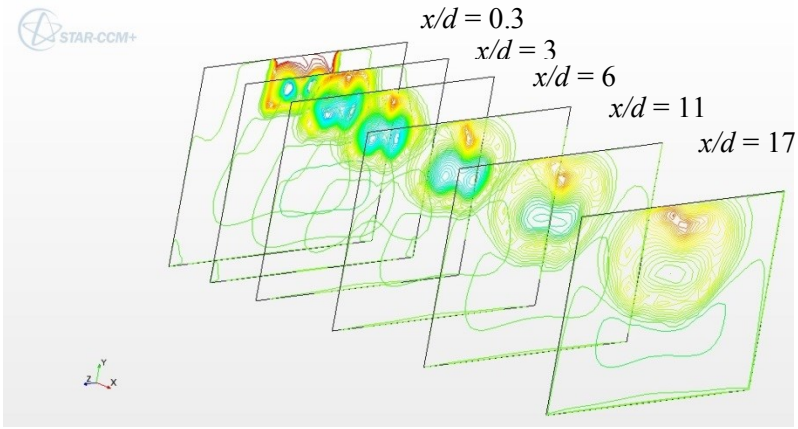

c)

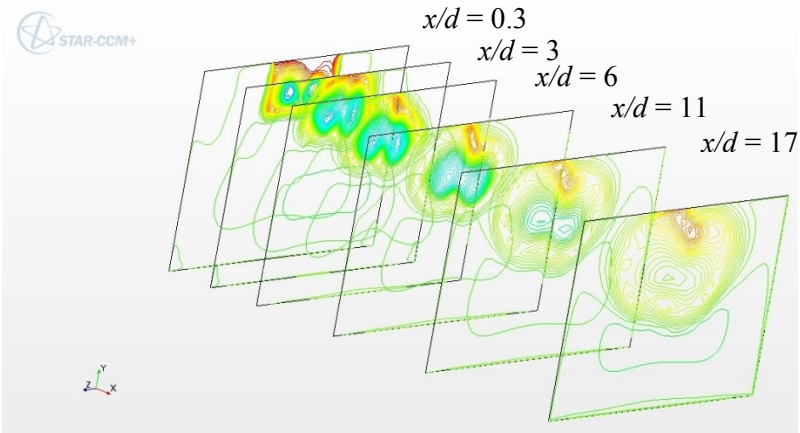

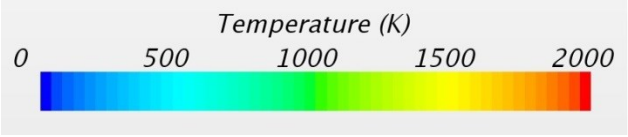

Figure 148 Temperature contours in the combustor for Configuration 5xr-SD
a) 5xr-V00, b) 5xr-V10-SD, c) 5xr-V20-SD

d)

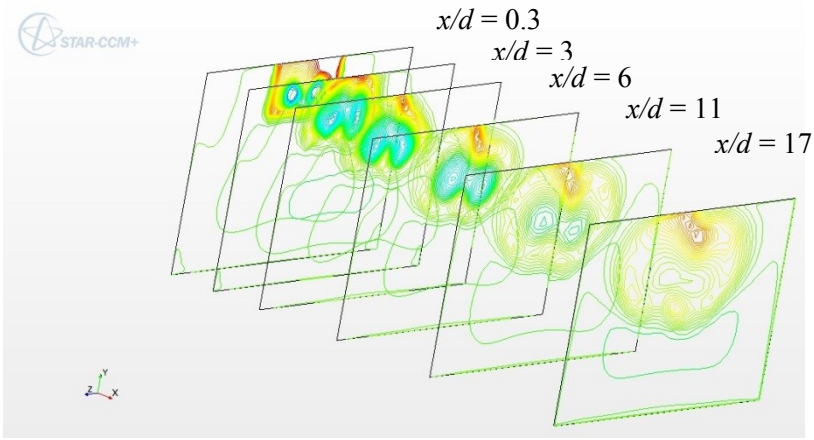

e)

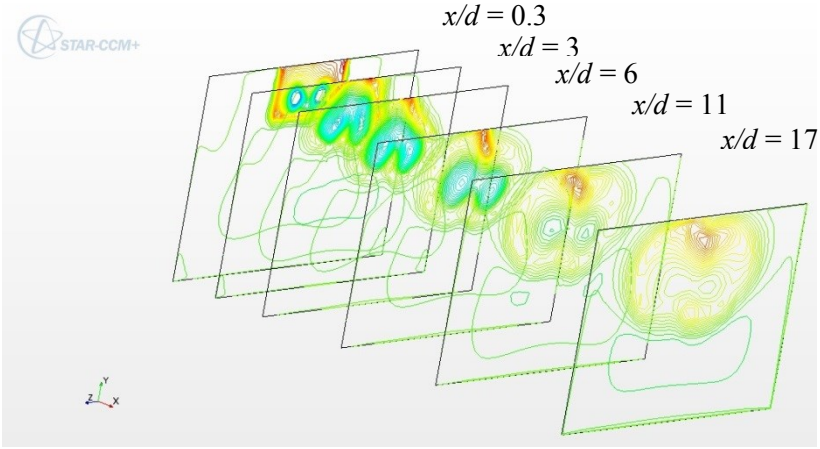

f)

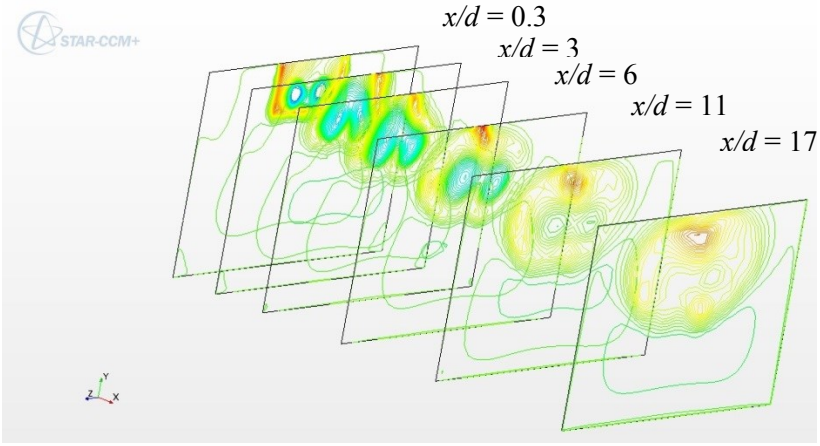

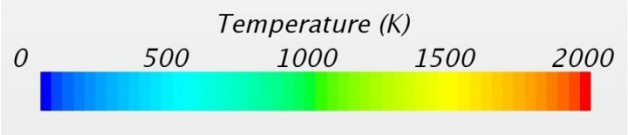

Figure 148 Temperature contours in the combustor for Configuration 5xr-SD
d) 5xr-V30-SD, e) 5xr-V40-SD, f) 5xr-V50-SD

(a)

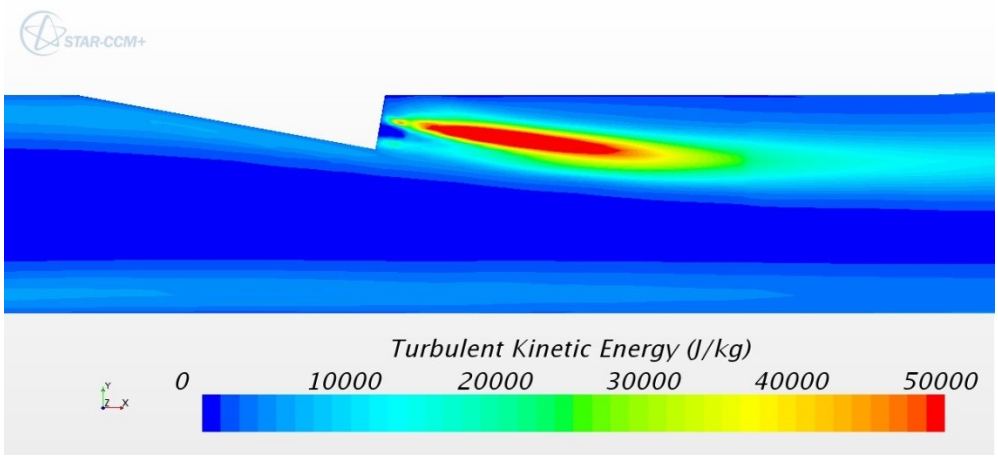

(b)

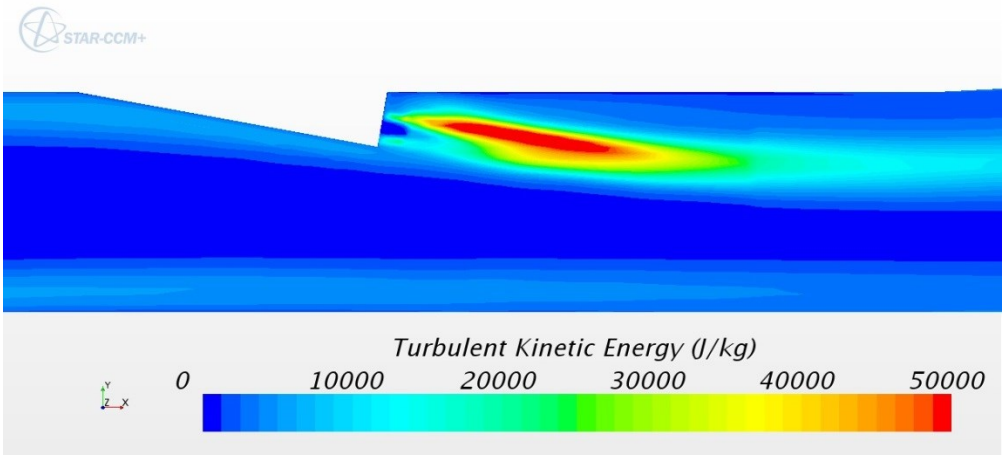

(c)

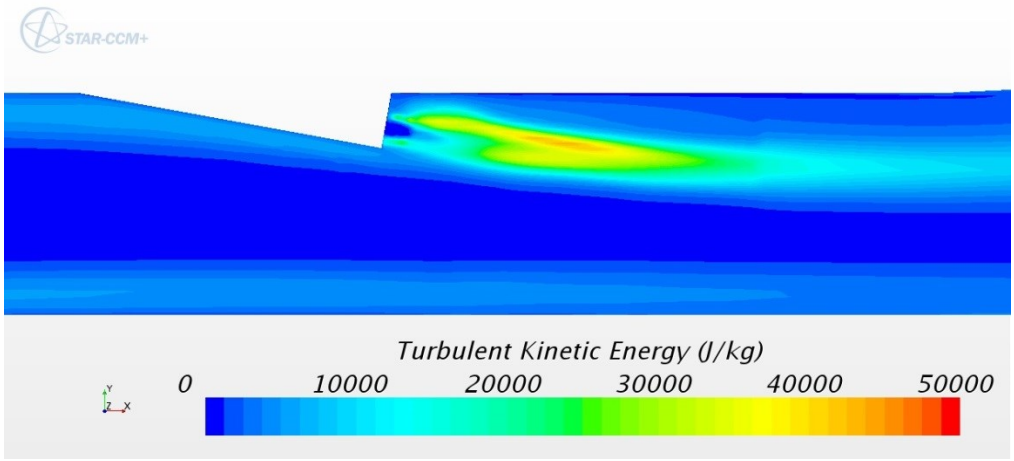

Figure 149 Turbulent kinetic energy plots on the left fuel nozzle centerline plane (z = -2.5r) in the combustor for Configuration 5xr-SD
a) 5xr-V00, b) 5xr-V10-SD, c) 5xr-V20-SD

(d)

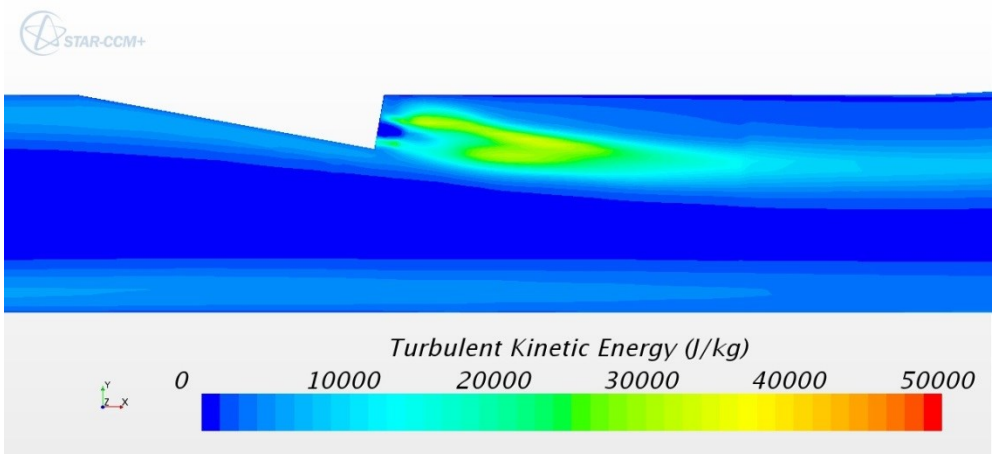

(e)

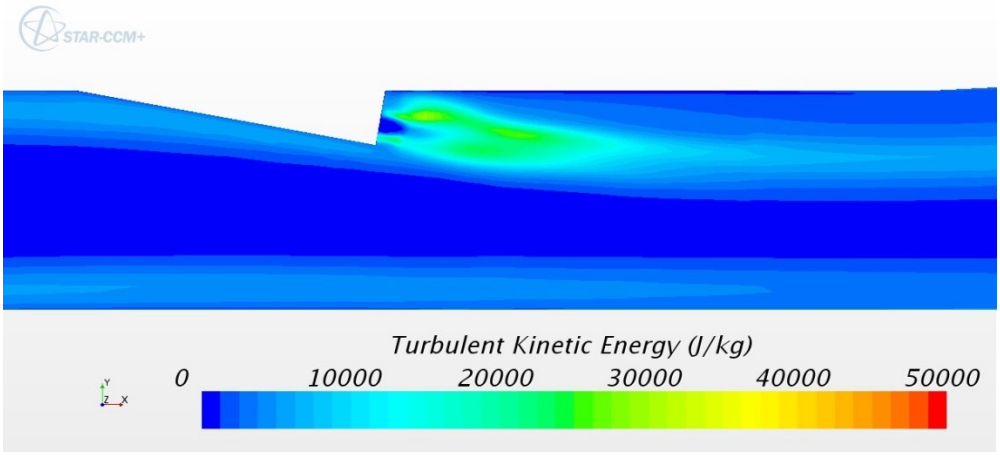

(f)

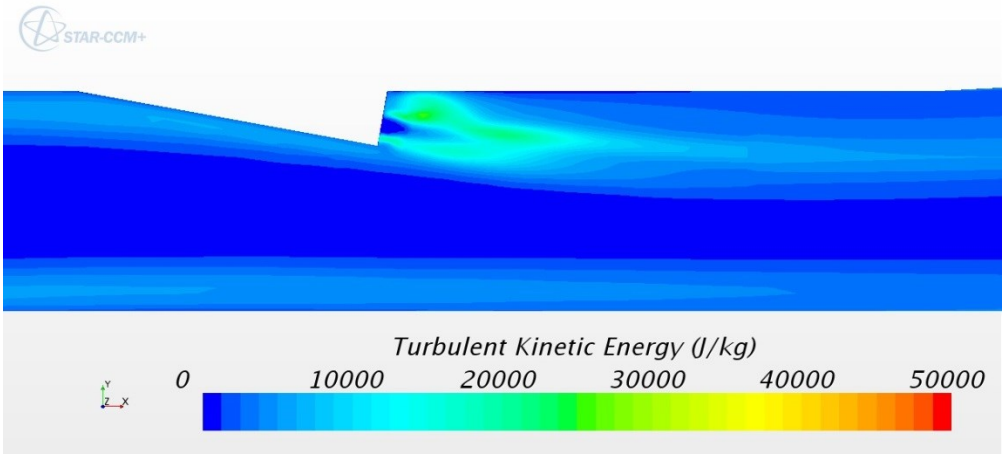

Figure 149 Turbulent kinetic energy plots on the left fuel nozzle centerline plane (z = -2.5r) in the combustor for Configuration 5xr-SD
d) 5xr-V30-SD, e) 5xr-V40-SD, f) 5xr-V50-SD

(a)

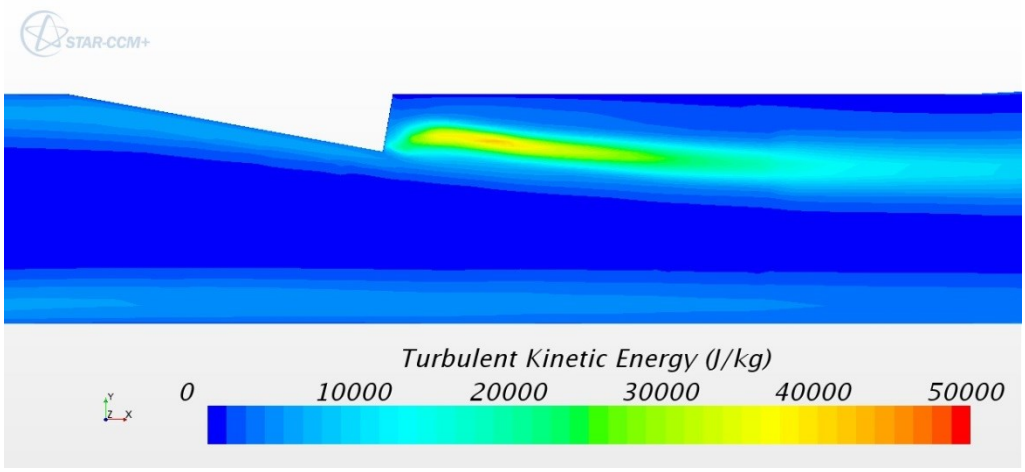

(b)

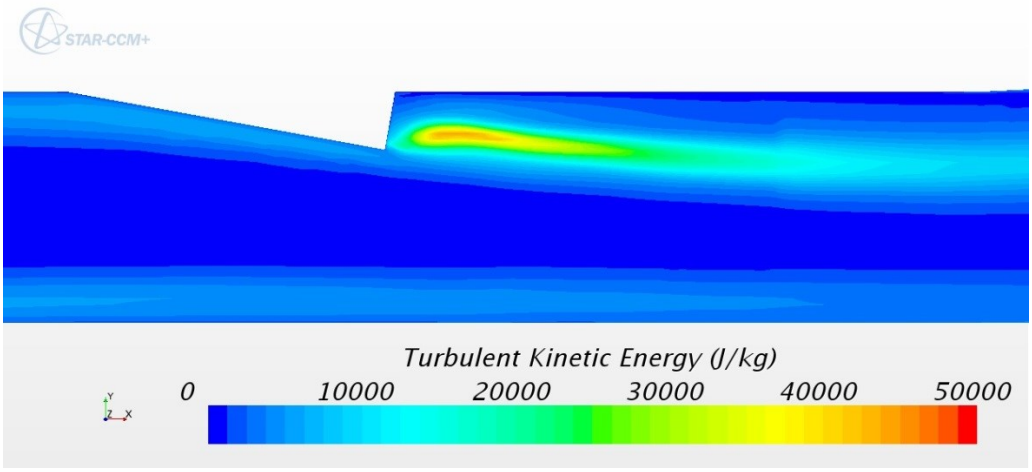

(c)

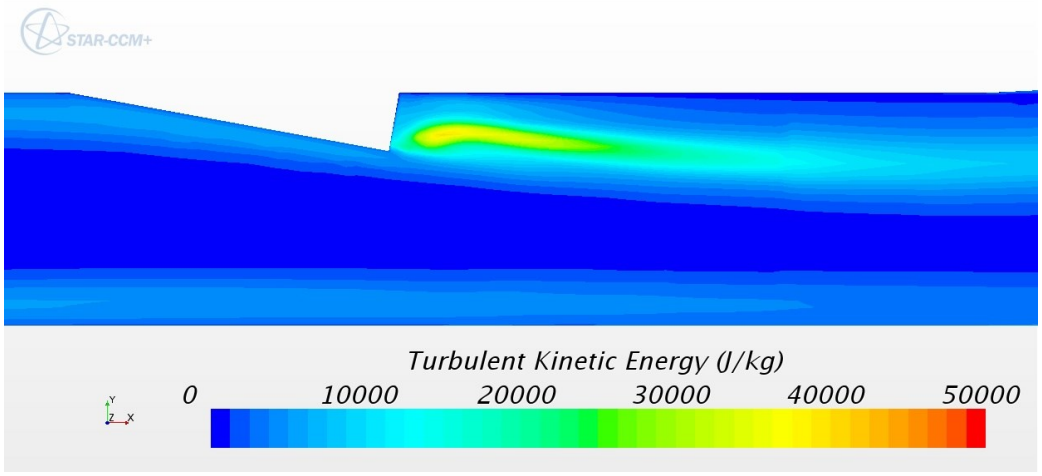

Figure 150 Turbulent kinetic energy plots on the centerline plane (z = 0) in the combustor for Configuration 5xr-SD
a) 5xr-V00, b) 5xr-V10-SD, c) 5xr-V20-SD

(d)

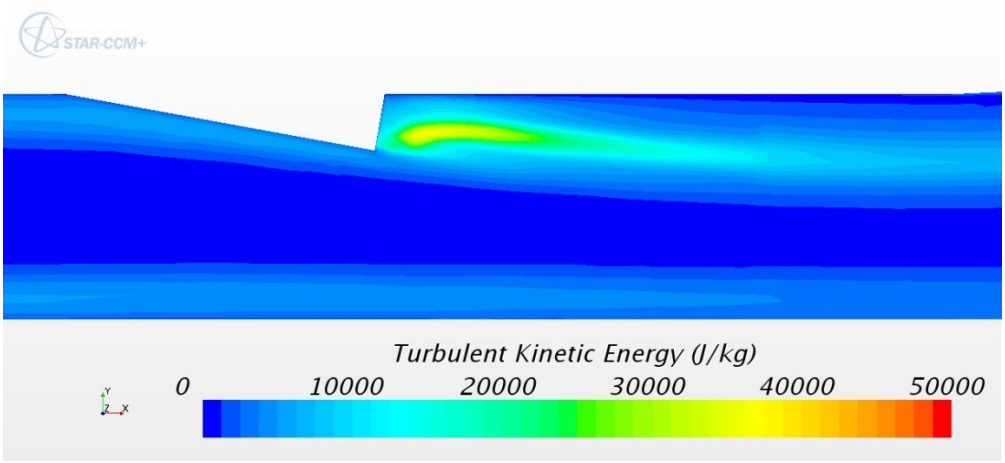

(e)

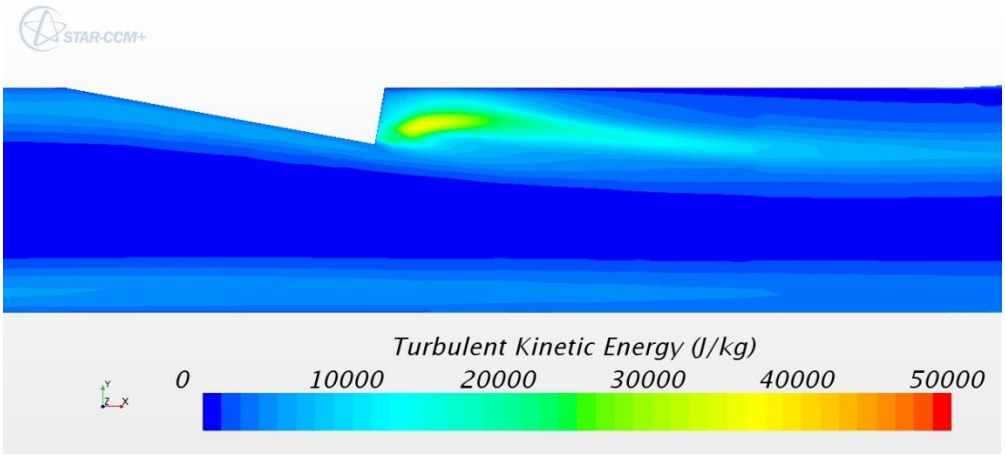

(f)

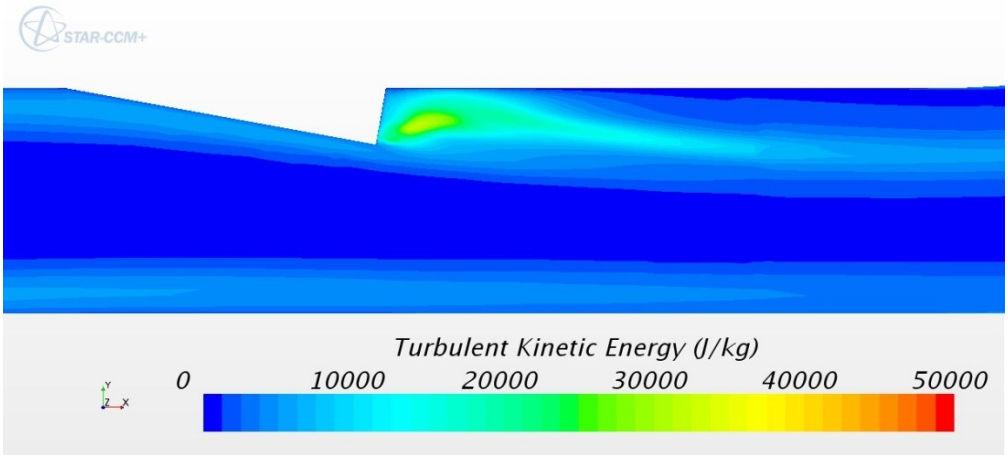

Figure 150 Turbulent kinetic energy plots on the centerline plane (z = 0) in the combustor for Configuration 5xr-TI
d) 5xr-V30-SD, e) 5xr-V40-SD, f) 5xr-V50-SD

(a)

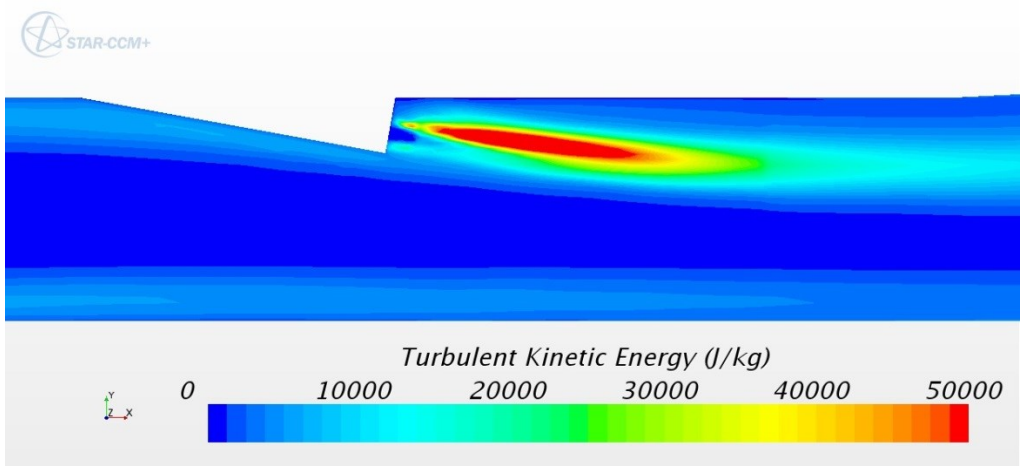

(b)

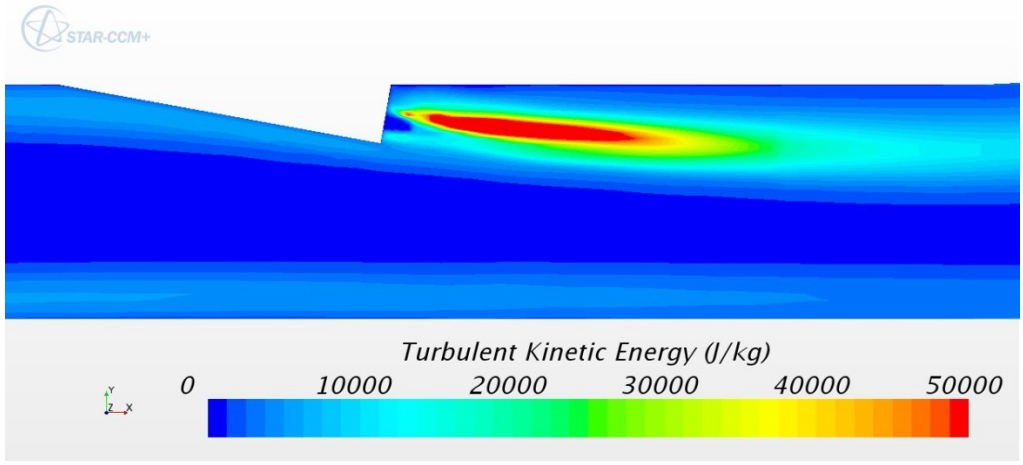

(c)

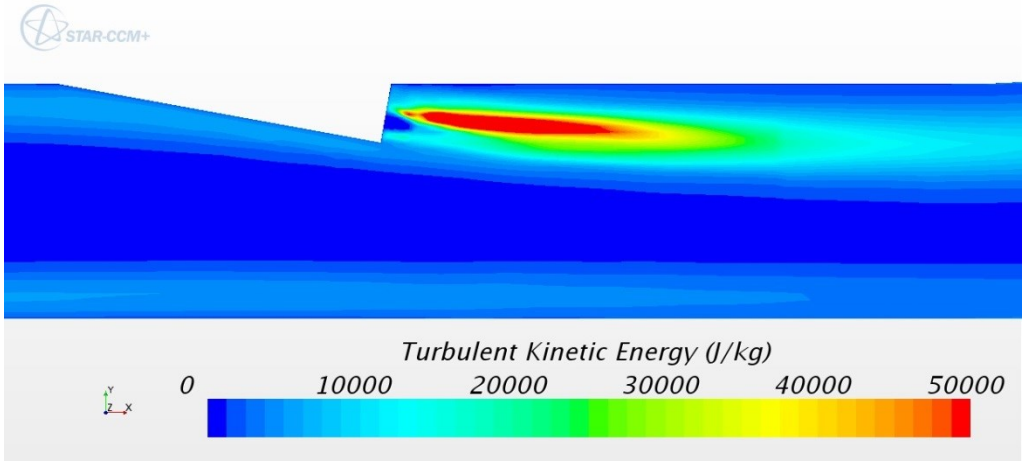

Figure 151 Turbulent kinetic energy plots on the right fuel nozzle centerline plane (z = 2.5r) in the combustor for Configuration 5xr-SD
a) 5xr-V00, b) 5xr-V10-SD, c) 5xr-V20-SD

(d)

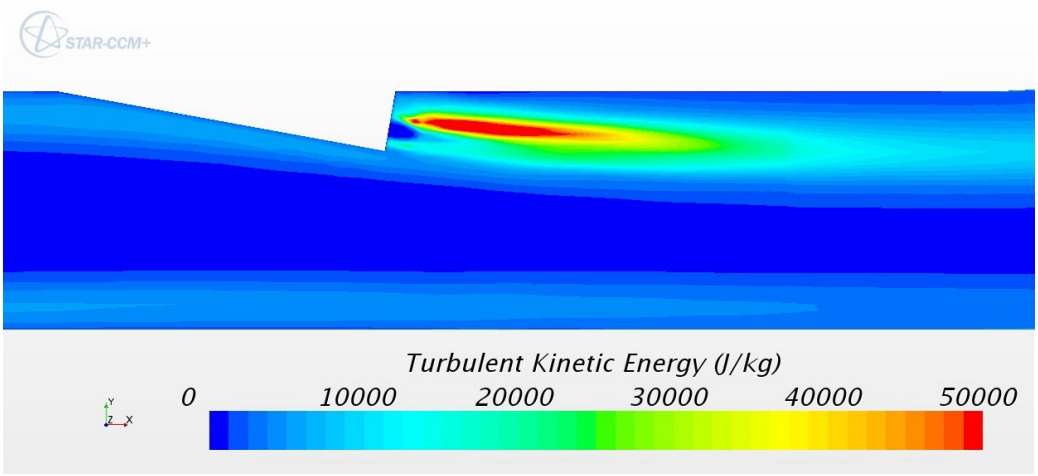

(e)

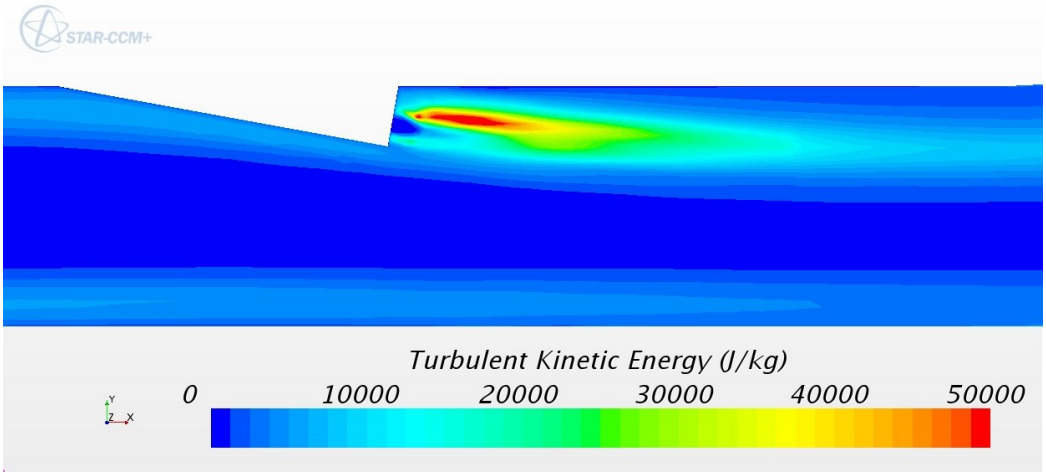

(f)

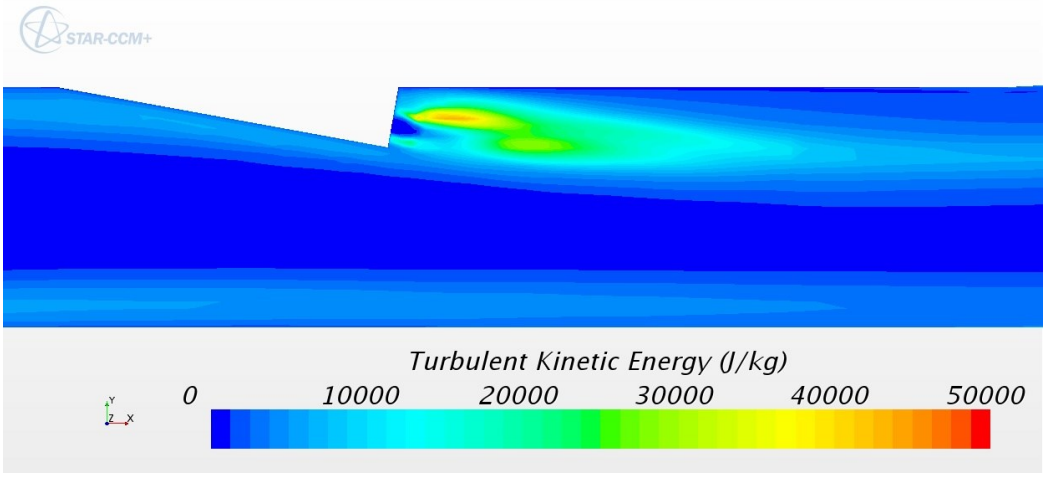

Figure 151 Turbulent kinetic energy plots on the right fuel nozzle centerline plane (z = 2.5r) in the combustor for Configuration 5xr-SD
d) 5xr-V30-SD, e) 5xr-V40-SD, f) 5xr-V50-SD

a)

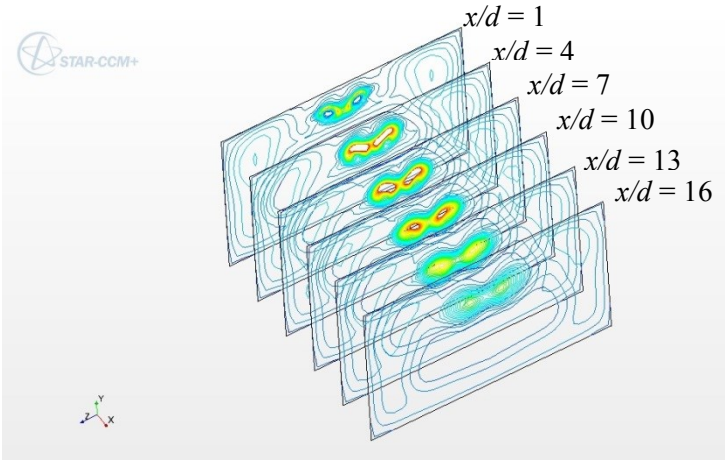

b)

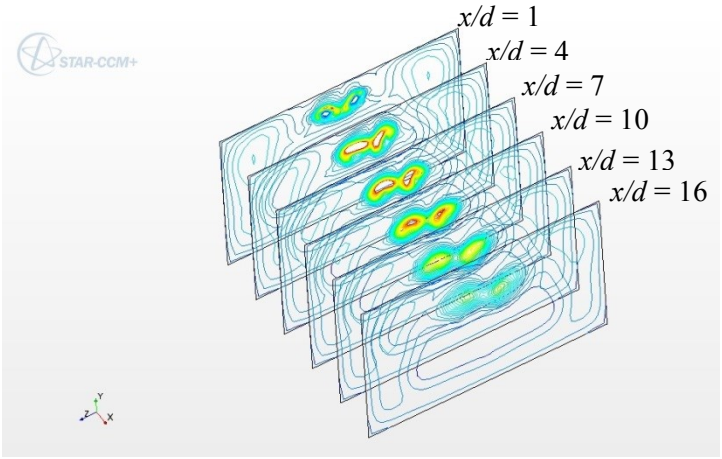

c)

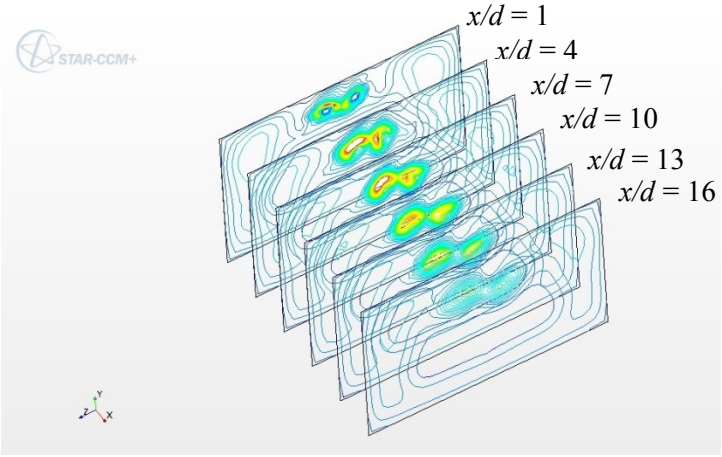

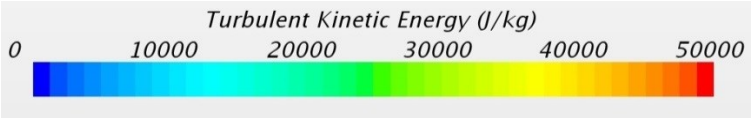

Figure 152 Turbulent kinetic energy contours in the combustor for Configuration 5xr-SD
a) 5xr-V00, b) 5xr-V10-SD, c) 5xr-V20-SD

d)

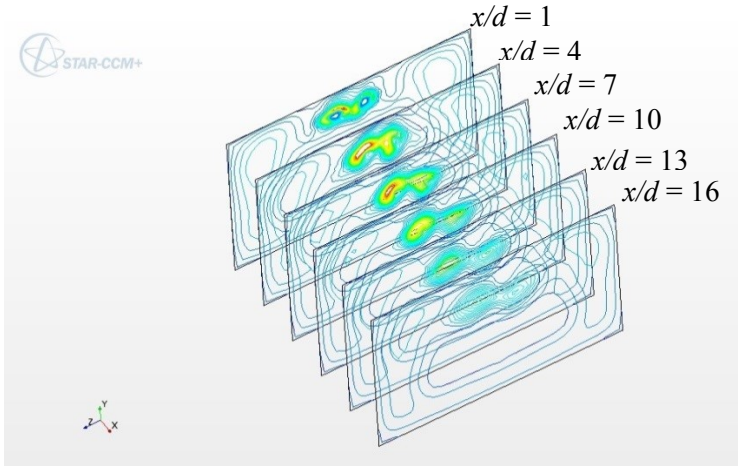

e)

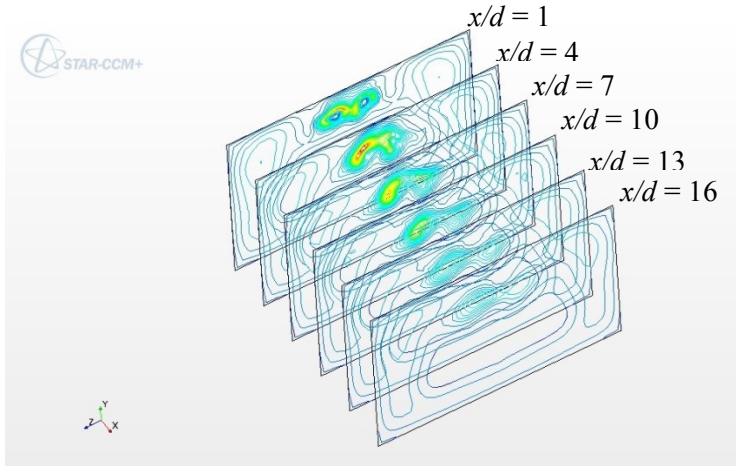

f)

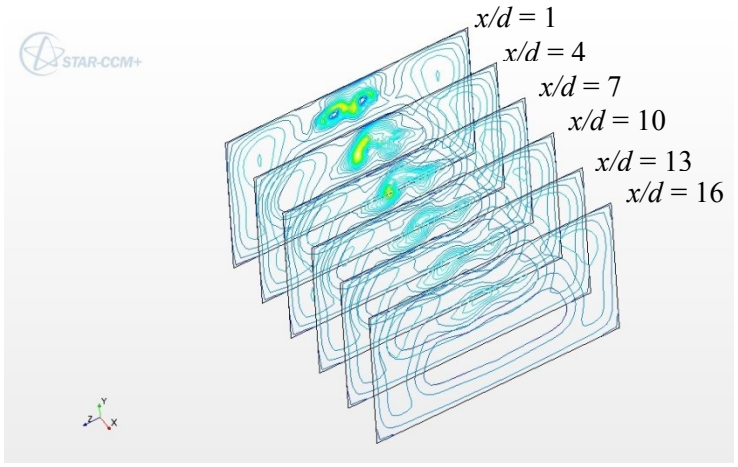

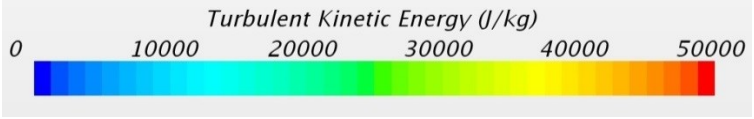

Figure 152 Turbulent kinetic energy contours in the combustor for Configuration 5xr-SD
d) 5xr-V30-SD, e) 5xr-V40-SD, f) 5xr-V50-SD

6.3.10 Summary of Distance Configuration and Swirl Patterns

Each swirl pattern had some general characteristics that were common regardless of distance configuration. In the case of the Top In, TI, swirl pattern the high H_2O mole fraction zones on the nozzle fuel wall tended to form on the top half of the wall. As swirl increased the high H_2O mole fraction zones moved to the left and right side of the fuel nozzle wall prior to transferring unto the upper combustor wall. High turbulent kinetic energy, TKE zones would form on either side of the tunnel symmetry plane but merge with increasing swirl.

The main characteristic of the Top Out, TO, swirl pattern was that high H_2O mole fraction zones on the nozzle fuel wall tended to form on the lower half of the wall. High TKE zones formed on either side of the tunnel symmetry plane for this swirl pattern as well.

The Same Direction, SD, swirl pattern was similar to the single nozzle swirl cases in that the high H_2O mole fraction zones on the nozzle fuel wall tended to rotate slightly with increasing swirl. A larger high TKE zone forms on the right fuel nozzle centerline plane than on the left fuel nozzle centerline plane. High TKE zones formed on either side of the tunnel symmetry plane but the zone on that is left of the tunnel symmetry plane the left fades before the one on the right side.

Increasing the distance between the two fuel injector exits affected the non-swirling baseline cases by decreasing the high TKE zone on the tunnel symmetry centerline plane. The high TKE zone on the fuel nozzle centerline plane increased with increasing distance between the fuel injector exits. The swirl pattern characteristics of the swirl patterns and the distance between the fuel injector exits combined to increase the burning efficiency of the model differently.

The Same Direction, SD, swirl pattern produced the greatest increase in burning efficiency for the 3xr distance configuration, while the Top Out, TO, swirl pattern produced the greatest increase in burning efficiency for the 4xr distance configuration and the Top In, TI, swirl pattern produced the greatest increase in burning efficiency for the 5xr distance configuration.

The maximum increase in burning efficiency compared to the corresponding non-swirling two nozzle baseline case was very impressive at 24.6% and was produced by the TI swirl pattern for the 5xr distance configuration.

The burning efficiency for the single nozzle non-swirling baseline case and the TI swirl pattern for the 5xr distance configuration was 0.70 and 0.90 respectively. The TI swirl pattern with a 5xr distance configuration had burning efficiency 29% greater than the single nozzle non-swirling baseline case. This too is considered to be a very impressive performance improvement in combustion efficiency due to swirl.

7 Conclusions and Recommendations

The main challenge associated with operating a scramjet engine is the short time that the fuel and oxidizer have to mix, ignite and combust in the combustion chamber due to the supersonic speed of both the fuel and oxidizer jets. The purpose of the research was to investigate mixing and combustion enhancement of fuel and oxidizer within the combustion chamber of a scramjet by introducing swirl to the fuel jet. The simulation model was based on the geometry of University of Virginia Supersonic Combustion Facility and boundary conditions and numerical parameters were based on an experimental case with combustion that was previously presented by Bhagwandin and Englom (2009) [69].

The scramjet simulation model consists of and isolator, a ramp fuel region for fuel injection, a combustor and a divergent nozzle. The simulation was modelled to provide 21% oxygen and 79% nitrogen at the isolator inlet at Mach 2. The fuel was hydrogen and was injected into the tunnel at Mach 1.7. The isolator and combustor were rectangular with constant area dimensions of 1.0" x 1.5". The width of the divergent nozzle was constant at 1.5" and the top wall diverged at 2.9°at the combustor exit.

The computational fluid dynamic software used for simulation of the scramjet model was STAR-CCM+. Since the main focus of the research was mixing in the combustor, a chemical non-equilibrium combustion model was used for the study. Also an SST k-ω turbulence model was chosen for the simulations.

7.1 Single Nozzle Fuel Jet Injection Swirl

Numerical results showed that the addition of swirl to a fuel jet increased mixing and entrainment of the fuel with the oxidizer. In addition results showed that mixing enhancement increased with swirl strength prior to the creation of a recirculation zone in the flow. The coaxial fuel jet was comprised of two regions; a non-swirling core jet flow and a swirling annular jet flow. The swirling annular jet flow represented the swirl produced with guide vanes. The swirl flow was defined to represent swirl guide vane angles of 10, 20, 30, 40 or 50 degrees. Three coaxial jet configurations with different core jet flow radius were investigated. The core jet flow radius/fuel inlet radius of 20%, 40% and 60% were simulated. Simulation results show that as the swirl strength of the fuel jet flow was increased the length of fuel jet potential core decreased and once the critical swirl number of 0.735 was reached the fuel jet would break down. This was seen with all three coaxial jet configurations. Swirl affected the fuel jet flow more as the radius of the non-swirling core of the jet decreases. In the case where the simulation model had a core jet flow radius/fuel inlet radius of 20% and the swirl represented 50 ° guide vanes the swirl was strong enough to break down the fuel jet creating two recirculation zones.

Contour plots of H_2O mole fraction indicated an increase in swirl assisted H_2O to form further upstream than a non-swirling fuel jet until the start of fuel jet breakdown. Fuel jet swirl promoted less H_2O to form on the upper combustor and more on the fuel nozzle wall. This indicated H_2O was forming further upstream with increased fuel jet swirl. As the critical swirl number was reached more H_2O would form on the upper combustor wall. After the critical swirl number was attained there was less H_2O on the fuel nozzle wall and the H_2O on the upper combustor wall was further downstream. Weak fuel jet swirl aided combustion to occur further upstream and within the short resident time of the fuel and air in the combustor.

The temperature within the non-swirling fuel jet case decreased when swirl was introduced to the fuel jet. The temperature decrease was seen throughout the combustor length especially on the upper combustor wall.

Turbulent kinetic energy is associated with eddies in turbulent flow that promotes mixing. As swirl was introduced to the fuel jet and increased high turbulent kinetic energy zones moved upstream closer to the fuel injector exit and the zone length increased providing a greater opportunity for the fuel and oxidizer to mix earlier and for a longer time. However, this behavior starts to reverse as the strong fuel jet swirl approaches the critical swirl number.

The burning efficiency measures how much injected fuel was consumed prior to reaching the nozzle exit. An increase in burning efficiency indicated an increase in the mixing of H_2 with O_2. In all the single nozzle cases the burning efficiency increased with increasing swirl. The maximum increase in burning efficiency compared to the non-swirling baseline case was 23.3%.

7.2 Dual Nozzle Fuel Jet Injection with Swirl

The research continued with two fuel jet injectors with swirl in order to investigate the possibility that interaction between two swirling jets, i.e., their coupling, would produce increased mixing. The two nozzle simulations had coaxial fuel jets with a non-swirling core flow radius/ fuel jet nozzle radius of 40%. The swirling annular fuel jet represented swirl induced by guide vanes of angles of 10° - 50° in ten degree intervals. Three swirl pattern and three distance configurations were simulated.

The first swirl pattern when viewed looking downstream had the right fuel annular jet swirling counter clockwise and the left fuel annular jet swirling clockwise and was named TI for fuel jets swirling towards each other at the top of the fuel nozzle wall. The swirl pattern, TO,

described the fuel jets swirling away from each other at the top of the fuel nozzle wall and had the right fuel jet swirling clockwise and the left fuel jet swirling counter clockwise. The third swirl pattern named SD had both the right and left fuel jet swirling in the same clockwise direction.

The first distance configuration was called 3xr to describe that the distance between the center points of the fuel jets were three times the fuel injector radius. Likewise the distance configuration 4xr described the distance between the center points of the fuel jets as four times the fuel injector radius. The third distance configuration was called 5xr to describe that the distance between the center points of the fuel jets were four times the fuel injector radius.

Each swirl pattern had some general characteristics that were common regardless of distance configuration. Simulations with swirl pattern TI showed high H_2O mole fraction zones tended to form on the top half of the fuel nozzle wall. As swirl increased the high H_2O mole fraction zones moved to the left and right side of the fuel nozzle wall prior to transferring unto the upper combustor wall. High turbulent kinetic energy zones would form on either side of the tunnel symmetry plane but merge with increasing swirl.

The main characteristic of the TO swirl pattern was that high H_2O mole fraction zones on the nozzle fuel wall tended to form on the lower half of the wall. High turbulent kinetic energy zones formed on either side of the tunnel symmetry plane for this swirl pattern as well.

The SD swirl pattern was similar to the single nozzle swirl cases in that the high H_2O mole fraction zones on the nozzle fuel wall tended to rotate slightly with increased swirl. A larger high turbulent kinetic energy zone formed on the right fuel nozzle centerline plane than on the left fuel nozzle centerline plane. High turbulent kinetic energy zones formed on either side

of the tunnel symmetry plane but the zone on that was left of the tunnel symmetry plane faded fades before the one on the right side.

Increasing the distance between the two fuel injector exits affected the non-swirling baseline cases by decreasing the high turbulent kinetic energy zone on the tunnel symmetry centerline plane. The high turbulent kinetic energy zone on the fuel nozzle centerline plane increased with increasing distance between the fuel injector exits. The swirl pattern characteristics of the swirl patterns and the distance between the fuel injector exits combined to increase the burning efficiency of the model differently.

The SD swirl pattern produced the greatest increase in burning efficiency for the 3xr distance configuration, while the TO swirl pattern produced the greatest burning efficiency increase for the 4xr distance configuration and the TI swirl pattern produced the largest burning efficiency increase for the 5xr distance configuration.

The maximum increase in burning efficiency compared to the corresponding non-swirling two nozzle baseline case was at the impressive level of 24.6% and was produced by the TI swirl pattern for the 5xr distance configuration.

The burning efficiency for the single nozzle non-swirling baseline case and the TI swirl pattern for the 5xr distance configuration was 0.70 and 0.90 respectively. The TI swirl pattern with a 5xr distance configuration had burning efficiency 29% greater than the single nozzle non-swirling baseline case. This is deemed significant performance improvement in combustion efficiency.

7.2 Recommendations for Future Studies

Based on the encouraging results achieved by this research fuel jet injection swirl, as a means to increase mixing within a scramjet combustor, merits further study. In the future, such studies could include:

- numerical simulation using a different combustor model such as the SCHOLAR benchmark case
- numerical study focusing on the effect of fuel jet injection swirl on a simulation model with nitrogen reacting and producing NO_X
- numerical simulation using fuel injection swirl that includes the physics of thermal radiation
- numerical study focusing on the dynamics and complex flow of coupling swirl jets
- experimental research using fuel jet injection swirl to obtain experimental data to compare with numerical data
- numerical and experimental studies focusing on the effect of fuel jet injection swirl on aeroacoustics properties

References

[1] J. D. Anderson Jr, Hypersonic and High Temperture Gas Dynamics, Reston: American Institute of Aeronautics and Astronautics, Inc., 2006.

[2] C. Segal, The Scramjet Engine - Processess and Characteristics, New York, New York: Cambridge University Press, 2009.

[3] A. K. Gupta, D. G. Lilley and N. Syred, Swirl Flows, Cambridge, USA: Abacus Press, 1984.

[4] S. Flesberg, "Aeroaccoustic Characteristics of Supersonic Rectangular Jets," M.Sc Thesis, The University of Kansas, Lawrence, 2000.

[5] Wikipedia, "Scramjet," 14 October 2014. [Online]. Available: en.wikipedia.org/wiki/Scramjet. [Accessed 29 October 2014].

[6] S. Farokhi, Aircraft Propulsion, 2nd ed., Chichester (UK): John Wiley & Sons Ltd., 2014.

[7] M. A. Vyas, W. A. Engblom, N. J. Georgiadis, C. J. Trefny and V. A. Bhagwandin, "Numerical Simulation of Vitiation Effects on a Hydrogen Fueled Dual-Mode Scramjet," in *AIAA 2010-1127*, Orlando, 2010.

[8] E. Curran, W. Heiser and D. Pratt, "Fluid Phenomena in Scarmjet Combustion Sysytems," *Annual Review Fluid Mechanics,* vol. 28, pp. 323-360, 1996.

[9] P. E. Dimotakis, "Turbulent Free Shear Layer Mixing and Combustion," *Progress in Astronautics and Aeronautics, AIAA,* vol. 137, pp. 265-340, 1991.

[10] G. Brown and A. Roshko, "On Density Effects and Large Structure in Turbulent Mixing Layers," *Journal of Fluid Mechanics,* vol. 64, no. 4, pp. 775-816, 1974.

[11] M. Wendt, R. Stalker and P. Jacobs, "Fuel Stagnation Temperature effects on Mixing with Supersonic Combustion Flows," *Journal of Propulsion and Power,* vol. 13, no. 2, pp. 274-280, 1997.

[12] D. Bogdanoff, "Compressibility Effects in Turbulent Shear Layers," *AIAA Journal,* vol. 21, no. 6, pp. 926-927, 1983.

[13] D. Papamoschou and A. Roshko, "Observations of Supersonic Free Shear Layers," in *AIAA 1986-162*, Manhattan Beach, CA, 1986.

[14] T. Rossmann, M. Mungal and R. Hanson, "An Experimental Investigation of High Compressibility Non-Reacting Mixing Layers," in *AIAA 2000-0063*, Reno, 2000.

[15] N. Chinzei, G. Masuya, T. Komuro, A. Murakami and K. Kudou, "Spreading of Two-Stream Supersonic Turbulent Mixing Layers," *Physics of fluids,* vol. 29, pp. 1345-1347, 1985.

[16] M. Day, W. Reynolds and N. Mansour, "Linear Stability Analysis and Structure of the Compressible Reacting Mixing Layer," in *AIAA 97-0761*, Reno, 1997.

[17] J. Drummond, M. Carpenter and D. Riggins, "Mixing and Mixing Enhancement in Supersonic Reacting Flowfields," *Progess in Astronautics and Aeronautics, AIAA,* vol. 137, no. High Speed Flight Propulsion Systems, pp. 383-455, 1991.

[18] L. Romagnosi, A. Ingenito, D. Cecere, E. Giacomazzi and C. Bruno, "Mixing and Turbulent Kinetic Energy Scaling in Compressible Reacting Flows," in *AIAA 2011-2364*, San Francisco, 2011.

[19] M. Samimy, M. Reeder and G. Elliot, "Compressibility Effects on Large Structures in Free Shear Flows," *Physics of Fluids,* vol. 4, no. 6, pp. 1251-1258, 1991.

[20] R. Portz and C. Segal, "Mixing in High Speed Flows with Thick Boundary Layers," in *AIAA 2004-3655*, Fort Lauderdale, 2004.

[21] A. Ferri, "Mixing-Controlled Supersonic Combustion," *Annual Review of Fluid Mechanics,* vol. 5, pp. 301-338, 1973.

[22] F. Povinelli and L. Povinelli, "Correlation of Secondary Sonic and Supersonic Gaseous Jet Penetration Into Supersonic Crossflows," NASA, Cleveland, OH, 1971.

[23] C. McClinton, "Effect of Ratio of Wall Boundary Layer Thickness to Jet Diameter on Mixing of a Normal Hydrogen Jet in a Supersonic Stream," NASA, Hampton, VA, 1974.

[24] D. Ballal and A. Lefebvre, "The Structure and Propagation of Turbulent Flames," *Proceedings of the Royal Society of London,* vol. 344, no. 1637, pp. 217-234, 1975.

[25] D. Ballal, "The Structure of a Premixed Turbulent Flame," *Proceedings of the Royal Society of London,* vol. 367, no. 1730, pp. 353-380, 1979.

[26] D. Ballal, "The Influence of Laminar Burning Velocity on the Structure and Propagation of Turbulent Flames," *Proceedings of the Royal Society of London,* vol. 367, no. 1731, pp. 485-502, 1979.

[27] J. P. Drummond, G. S. Diskin and A. D. Cutler, "NASA," 2006. [Online]. Available: http://www.ntrs.nasa.gov/archive/nasa/casi.ntrs.nasa.gov/20060020221_2006008471.pdf. [Accessed 24 09 2013].

[28] B. Armaly, F. Durst, J. Pereira and B. Schonung, "Experimental and Theoretical Investigation of Backward-Facing Step Flow," *Journal of Fluid Mechanics,* vol. 127, pp. 473-496, 1983.

[29] T. M. Abdel-Salam, S. N. Tiwari, S. K. Chaturvedi and T. O. Mohieldin, "Mixing and Combustion in Scramjet Combustor with Raised and Relieved Ramp," in *AIAA 2000-3709*, Huntsville, 2000.

[30] E. Jeong, S. O'Byrne, I. Jeung and A. F. P. Houwing, "Supersonic Combustion on Hydrogen Fuel Injection Locations in a Cavity Based Combustor," in *AIAA 2008-4576*, Hartford, 2008.

[31] Y. Haimovitch, E. Gartenberg and A. S. Roberts Jr., "Investigation of Ramp Injectors for Supersonic Mixing Enhancement," NASA, Hampton, USA, 1994.

[32] A. Trebs, M. Roa, S. Heister, W. Anderson and R. Lucht, "Ramp Injector Scale Effects on Supersonic Combsution," *Journal of Propulsion and Power,* vol. 30, no. 2, pp. 426-437, 2014.

[33] C. Kim, I. Jeung, B. Choi, T. Kouchi and G. Masuya, "Flowfield Characteristics of a Hypermixer Interacting with Transverse Injection in Supersonic Flow," *AIAA Journal,* vol. 50, no. 8, pp. 1742-1753, 2012.

[34] R. P. Fuller, P. Wu, A. S. Nejad and J. A. Schetz, "Comparison of Physical and Aerodynamic Ramps as Fuel Injectors in Supersonic Flow," *Journal of Propulsion and Power,* vol. 14, no. 2, pp. 135-145, 1998.

[35] A. Tomioka, A. Murakami, K. Kudo and T. Mitani, "Combustion Tests of a Staged Supersonic Combustor with a Strut," *Journal of Propulsion and Power,* vol. 17, no. 2, pp. 293-300, 2001.

[36] S. Lee, "Mixing Augmentation with Cooled Pylon Injection in a Scramjet Combustor," *Journal of Propulsion and Power,* vol. 28, no. 3, pp. 477-485, 2012.

[37] R. Kirchhartz, D. Mee, R. Stalker, P. Jacobs and M. Smart, "Supersonic Boundary-Layer Combustion:Effects of Upstream Entropy and Shear-Layer Thickness," *Journal of Propulsion and Power,* vol. 26, no. 1, pp. 57-66, 2010.

[38] A. Mack and J. Steelant, "Mixing and Combustion Enhancement in a Generic Scramjet Combustion Chamber," in *AIAA 2006-8134*, Atlanta, 2006.

[39] B. Parent and J. P. Sislian, "Hypersonic Mixing Enhancement by Compression at High Convective Mach Number," *AIAA Journal,* vol. 42, no. 4, pp. 787-795, 2004.

[40] J. Sislian and B. Parent, "Hypervelocity Fuel/Air Mixing in a Shcramjet Inlet," *Journal of Propulsion and Power,* vol. 20, no. 2, pp. 263-272, 2004.

[41] K. Kathiresan, A. Balamanio, M. Karthik, P. Gogulanathan, D. Thanikaivel Murugan and S. Ilakkiya, "CFD Analysis of Supersonic Coaxial Jets on Effect of SPearding Rates," *Journal of Engineering Research and Applications,* vol. 4, no. 4, pp. 29-35, 2014.

[42] A. Cutler and J. White, "An Experiemental and CFD Study of a Supersonic Coaxial Jet," in *AIAA 2001-0143*, Reno, 2001.

[43] A. Abdelhafez and A. Gupta, "Effect of Swirl on Mixing in Underexpanded Supersonic Airflow," *Journal of Propulsion and Power,* vol. 27, no. 1, pp. 117-131, 2011.

[44] T. Kouchi, N. Sakuranaka, M. Izumikawa and S. Tomioka, "Pulsed Transverse Injection Applied to a Supersonic Flow," in *AIAA 2007-5405*, Cincinnati, 2007.

[45] S. Kalidas and J. Kurian, "Enhancement of Supersonic Mixing with the Help of Pulsed Injection," in *AIAA 2007-5032*, Cincinnati, 2007.

[46] A. Cutler, G. Harding and G. Diskin, "High Frequency Pulsed Injection into a Supersonic Duct Flow," *AIAA Journal,* vol. 51, no. 4, pp. 809-818, 2013.

[47] L. Smith, "The Effects of Parallel Pusled Injection in Supersonic Flow," PhD Comprehensive Exam Proposal, Lawrence, 2014.

[48] T. Ombrello, C. Carter, J. McCall, F. Schauer, C. Tam, A. Naples, J. Hoke and K. Hsu, "Enhanced Mixing in Supersonic Flow Using a Pulse Detonation Combustor," in *AIAA 2012-0123*, Nashville, 2012.

[49] J. Frank, "Experimental Investigation of the Effect of Swirl on Mixing Enhancement of Supersonic Rectangular Jets," M.Sc Thesis, University of Kansas, Lawrence, 1994.

[50] S. Han and R. Taghavi, "Computational Study of Supersonic Jets from Swirl Inducing Nozzles," in *AIAA 2001-0673*, Reno, 2001.

[51] S. Farokhi and R. Taghavi, "Effect of Initial Swirl Distribution on the Evolution of a Turbulent Jet," *AIAA Journal,* vol. 27, no. 6, pp. 700-706, 1989.

[52] R. Gilchrist and J. Naughton, "An Experimental Study of Swirling jets with Different Initial Swirl Profiles," in *AIAA 2003-0639*, Reno, 2003.

[53] A. Benim, F. Gul and E. Pasqualotto, "Numerical Investigation of the Role of the Inlet Swirl Velocity Profile on Decay of the Swirl in Pipe Flow," in *IASME/WSEAS 238-243*, Athens, 2007.

[54] S. Murugappan and E. Gurmark, "A Novel Swirling Injector for Improving Mixing in High Speed Flows," in *AIAA 2003-4785*, Huntsville, USA, 2003.

[55] S. Murugappan, E. Gutmark, C. Carter, J. Donbar, M. Gruber and K. Y. HSU, "Transverse Supersonic Controlled Swirling Jet in a Supersonic Cross Stream," *AIAA Journal,* vol. 44, no. 2, pp. 290-300, 2006.

[56] M. Linck and A. Gupta, "Effect of Swirl and Combustion on Flow Dynamics in Luminous Kerosene Spray Flames," in *AIAA 2003-1345*, Reno, 2003.

[57] M. B. Linck and A. K. Gupta, "Effect of Combustion on Exhaust Jet Characteritics in a Pressurized, Swirl-Stabilized Spray Combustor," in *AIAA 2005-956*, Reno, 2005.

[58] A. D. Cutler and C. H. Johnson, "The Use of Swirling Jet Pairs to Provide Rapid Fuel Penetration in Scramjet Combustors," in *AIAA 95-0099*, Reno, 1995.

[59] S. Koike, T. Ito, K. Hirose, M. Hiroto, K. Takita and G. Masuya, "Measurement of Flow Field Produced by Ramp Vortices and Twin Swirl jets," in *AIAA 2005-3302*, Capua, Ce, Italy, 2005.

[60] A. D. Cutler, P. M. Danehy, S. O'Byrne, C. G. Rodriguez and J. P. Drummond, "Supersonic Combustion Experiments for CFD Model Development and Validation," in *AIAA 2004-266*, Reno, 2004.

[61] C. G. Rodriguez and A. D. Cutler, "Computational Simulation of a Supersonic Combustion Benchmark Experiment," in *AIAA 2005-4424*, Tucson, 2005.

[62] J. D. Anderson Jr, Fundamentals of Aerodynamics, New York: McGraw-Hill, 2007.

[63] L. N. Jones, "Modelling of Turbulent Swirling Flows," Ph.D Thesis, The University of Leeds, Leeds, 2004.

[64] Various, "CFD Online," GNU FDL, 1994. [Online]. Available: http://www.cfd-online.com/Wiki/RANS-based_turbulence_models. [Accessed 15 April 2014].

[65] V. A. Bui, "Simplified Turbulence Models for Confined Swirling Flows," *Engineering Applications of Computational Fluid Mechanics,* vol. 2, no. 4, pp. 404-410, 2008.

[66] C. Kannepalli, J. Chenoweth, S. Arunajatesan and A. Hosangadi, "A Hybrid RANS/LES Approach to Modelling of Swirling Jet Flows," in *AIAA 2008-3853*, Seattle, USA, 2008.

[67] C. Tourani, "Computaional Simulation of Scramjet Combustors - A Comparison Between Quasi-One Dimensional and 2-D Numerical Simulations," M.Sc Thesis, The University of Kansas, Lawrence, 2011.

[68] X. Jianwen and L. Jialing, "Application of Flamelet Model for the Numerical Simulation of Turbulent Combustion in Scramjet," ICMAR, Novosibirsk, 2008.

[69] V. A. Bhagwandin and W. A. Engblom, "Numerical Simulation of a Hydrogen-Fueled Dual Mode Scramjet Engine Using Wind-US," in *AIAA 2009-5382*, Denver, USA, 2009.

[70] M. Kindler, P. Gerlinger and M. Aigner, "Numerical Investigations of NOx-Formation in Scramjet Combustors using Wall and Strut Injectors," in *AIAA 2011-405*, Orlando, FL, 2011.

[71] "STAR-CCM+," CD-adapco, [Online]. Available: http://www.cd-adapco.com/products/star-ccm. [Accessed 2012].

[72] F. Zhouqin, S. Mingbo and L. Weidong, "Flamelet/Progress-Variable Model for Large Eddy Simulation of Supersonic Reacting Flow," in *AIAA 2010-6878*, Nashville, TN, 2010.

[73] D. Veynante and L. Vervisch, "Turbulent Combustion Modelling," *Progress in Energy and Combustion Science,* vol. 28, pp. 193-266, 2002.

[74] NASA, "The Langley Direct-Connect Supersonic Combustion Test Facility Brochure," 11 October 2005. [Online]. Available: http://hapb-www.larc.nasa.gov/Public/Facilities/Dcsctf/Wte_info/DCSCTF_brochure.html. [Accessed 29 October 2014].

[75] C. G. Rodriguez and A. D. Cutler, "Numerical Analysis of the SCHOLAR Supersonic Combustor," NASA, Hampton, VA, 2003.

[76] U. o. Virginia, "Mechanical and Aerospace Engineering," [Online]. Available: http://www.mae.virginia.edu/NewMAE/2011/02/supersonic-combustion-facility/. [Accessed 29 October 2014].

[77] K. Pandey and T. Sivasakthivel, "CFD Analysis of Mixing and Combustion of a Hydrogen Fueled Scramjet Combustor with a strut Injector by Using Fluent Software," *IACSIT International Journal of Engineering and Technology,* vol. 3, no. 5, pp. 446-453, 2011.

Appendix A: User Defined Functions

Tangential Velocity Component

($$Centroid(@CoordinateSystem("Laboratory.Cylindrical 1"))[0] >R_{CJF}) ? $tan\theta$

Where R_{CJF} (m) = 2.514E-4 for Configuration R2 (see Section 6.1.2)

= 5.028E-4 for Configuration R4 (see Section 6.1.2)

= 7.542E-4 for Configuration R6 (see Section 6.1.2)

and θ(°) = 10, 20, 30, 40, 50

Appendix B: Fuel Inlet Velocity Profiles

The fuel inlet axial and tangential velocities to produce the required swirl were normalized to V= 1754 m/s. The radial velocity, w = 0 m/s.

Configuration R2: R_{CJF}/R_I = 20%

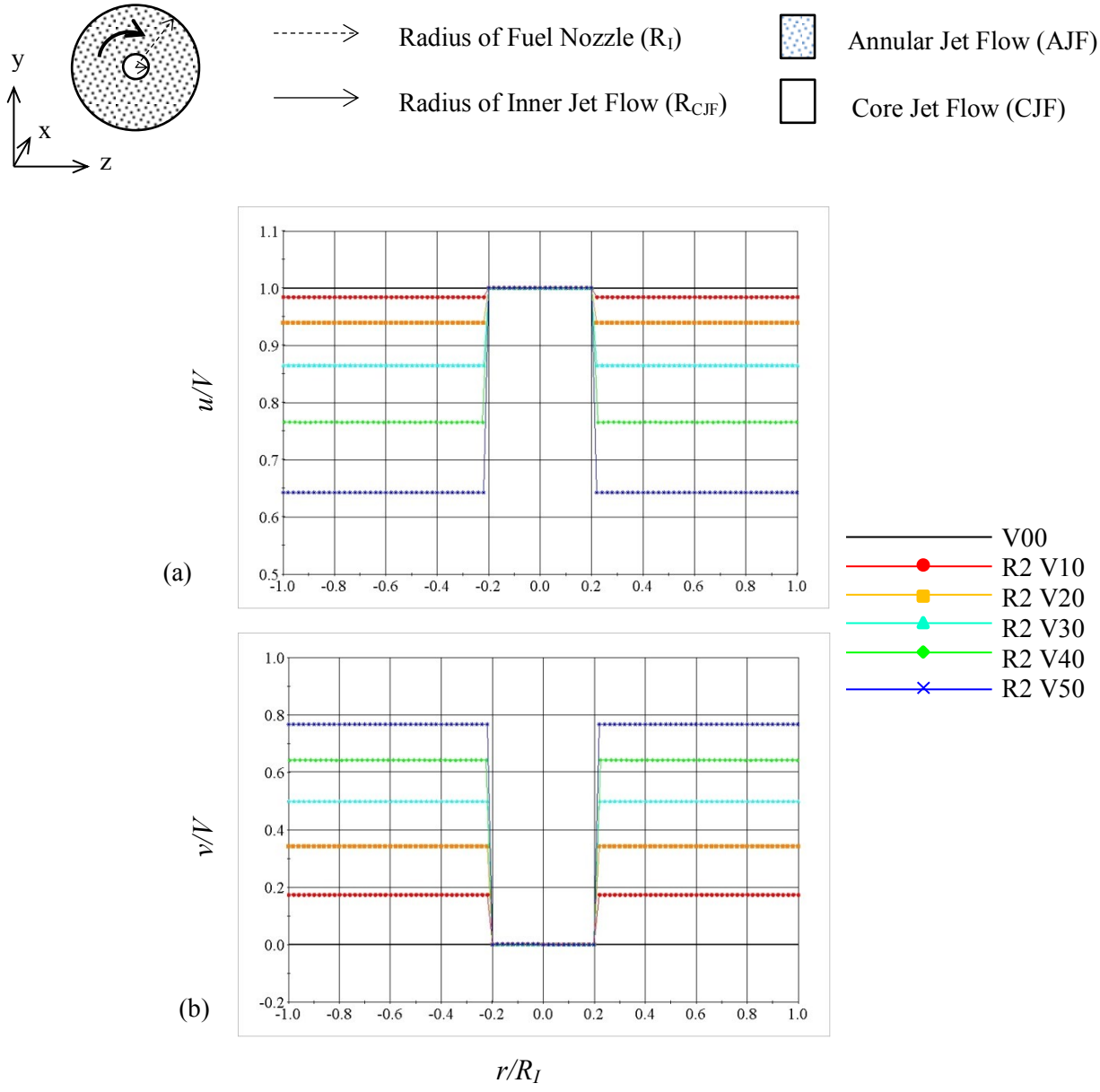

Figure B-1 Normalized fuel inlet velocity profile for Configuration R2
(a) axial, (b) tangential

Configuration R4: $R_{CJF}/R_I = 40\%$

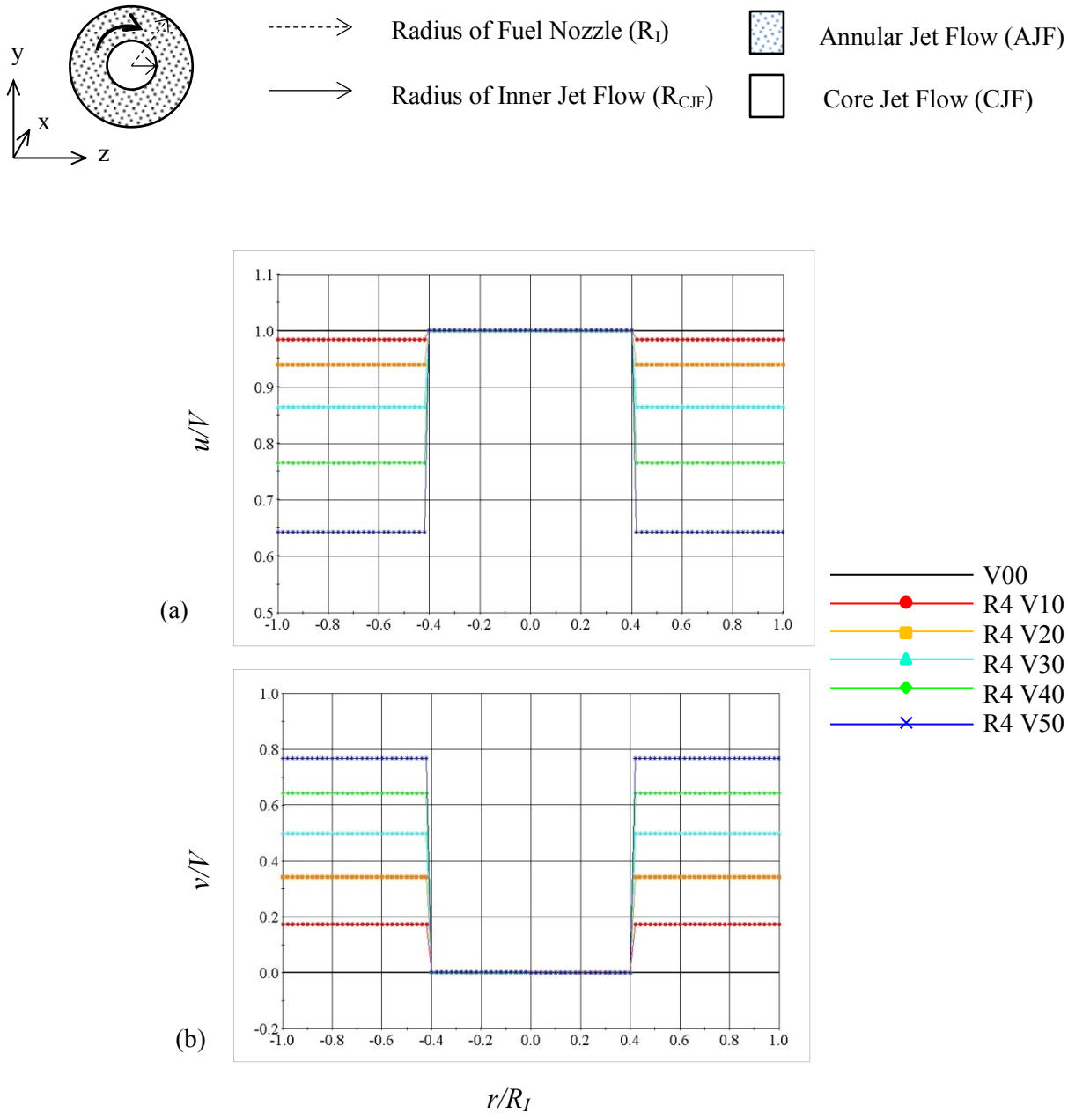

Figure B-2 Normalized fuel inlet velocity profile for Configuration R4
(a) axial, (b) tangential

Configuration R6: $R_{CJF}/R_I = 60\%$

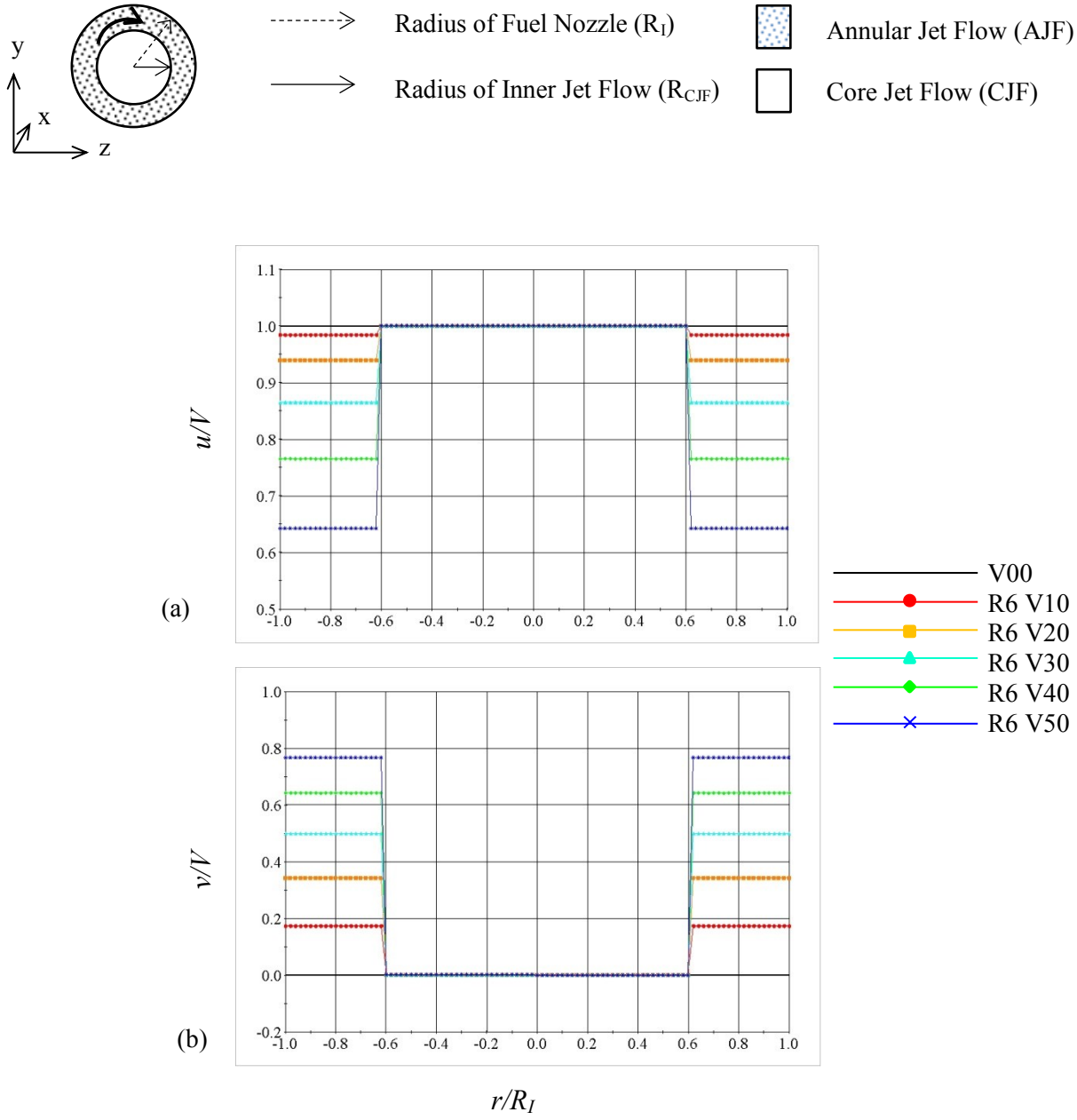

Figure B-3 Normalized fuel inlet velocity profile for Configuration R6
(a) axial, (b) tangential

Appendix C: Critical Swirl Number, S_{CRIT}

As previously discussed in Section 2.5 the critical swirl number is defined as the swirl number at which the jet flow breaks down and recirculation begins. By plotting the minimum velocity along the potential core of the fuel jet and swirl number for the configuration the critical swirl number is found when the minimum velocity along the potential core jet is zero. The critical swirl number, S_{CRIT} is approximately 0.735 as shown in Figure C-1.

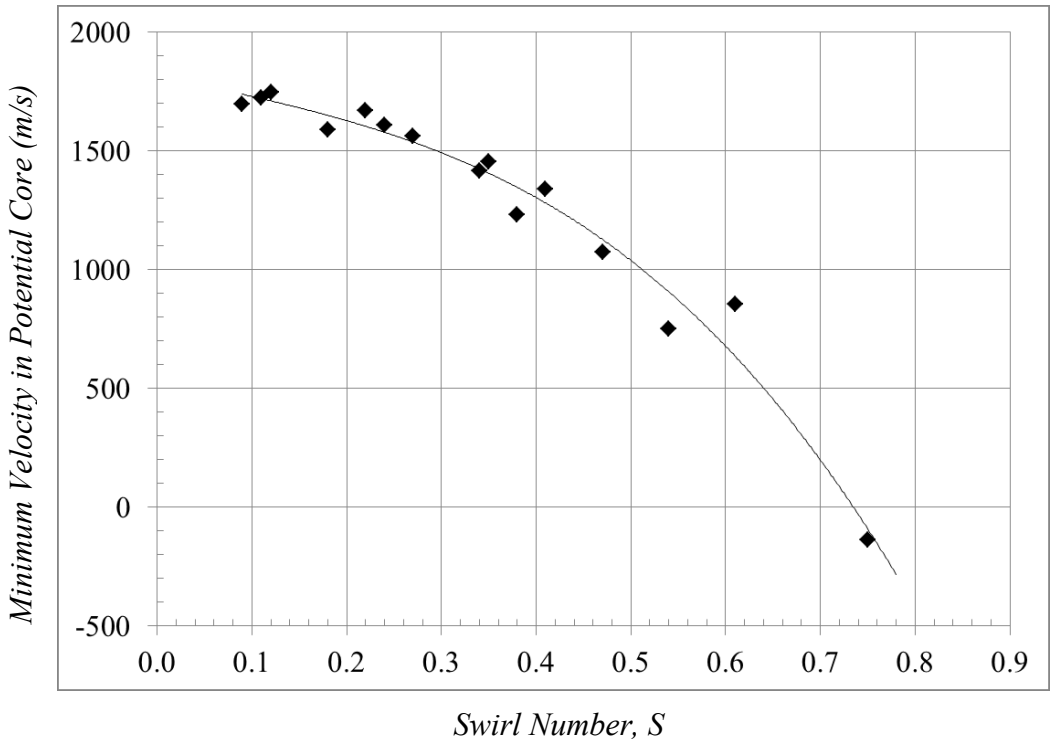

Figure C-1 Determination of critical swirl number, S_{CRIT}